# Nanophase and Nanocomposite Materials IV

**DISTRIBUTION STATEMENT A**
Approved for Public Release
Distribution Unlimited

MATERIALS RESEARCH SOCIETY
SYMPOSIUM PROCEEDINGS VOLUME 703

# Nanophase and Nanocomposite Materials IV

Symposium held November 26–29, 2001, Boston, Massachusetts, U.S.A.

**EDITORS:**

**Sridhar Komarneni**
The Pennsylvania State University
University Park, Pennsylvania, U.S.A.

**John C. Parker**
CirQon Technologies Corporation
Gurnee, Illinois, U.S.A.

**Richard A. Vaia**
Air Force Research Laboratory
Wright Patterson AFB, Ohio, U.S.A.

**G.Q. (Max) Lu**
University of Queensland
Brisbane, Queensland, Australia

**Jun-ichi Matsushita**
Tokai University
Hiratsuka, Japan

MRS
**Materials Research Society**
Warrendale, Pennsylvania

20020405 088

This work was supported in part by the Office of Naval Research under Grant Number N00014-02-1-0161. The United States Government has a royalty-free license throughout the world in all copyrightable material contained herein.

This work was sponsored in part by the Air Force Research Laboratory, Materials and Manufacturing Directorate.

Single article reprints from this publication are available through
University Microfilms Inc., 300 North Zeeb Road, Ann Arbor, Michigan 48106

CODEN: MRSPDH

Copyright 2002 by Materials Research Society.
All rights reserved.

This book has been registered with Copyright Clearance Center, Inc. For further information, please contact the Copyright Clearance Center, Salem, Massachusetts.

Published by:

Materials Research Society
506 Keystone Drive
Warrendale, PA 15086
Telephone (724) 779-3003
Fax (724) 779-8313
Web site: http://www.mrs.org/

Library of Congress Cataloging-in-Publication Data

Nanophase and nanocomposite materials IV : symposium held November 26–29, 2001, Boston, Massachusetts, U.S.A. / editors, Sridhar Komarneni, John C. Parker, Richard A. Vaia, G.Q. (Max) Lu, Jun-ichi Matsushita
p.cm.—(Materials Research Society symposium proceedings ; v. 703)
Includes bibliographical references and indexes.
ISBN 1-55899-639-7
I. Komarneni, Sridhar II. Parker, John C. III. Vaia, Richard A. IV. Lu, G.Q. (Max)
V. Matsushita, Jun-ichi VI. Materials Research Society symposium proceedings ; v. 703
2002

Manufactured in the United States of America

# CONTENTS

**Preface** ..... xv

**Materials Research Society Symposium Proceedings** ..... xvi

*NANOCOMPOSITE AND NANOFIBER MATERIALS*

**Processing, Dynamic Studies and Properties of Exfoliated Aerospace Epoxy-Organoclay Nanocomposites** ..... 3
Chenggang Chen and David Curliss

* **Molecular Engineered Porous Nanocomposites of Metal Oxide and Clay Using Surfactants** ..... 9
Huai Y. Zhu and Gao Q. Lu

**Study of $NiFe/SiO_2$ Nanocomposites** ..... 19
S. Hui, Y.D. Zhang, T.D. Xiao, Mingzhong Wu, Shihui Ge, W.A. Hines, J.I. Budnick, M.J. Yacaman, and H.E. Troiani

**Novel Synthesis of Aluminium Oxide Nanofibers** ..... 25
Huai Y. Zhu and Gao Q. Lu

*NANOSTRUCTURES I*

* **Self-Assembly of Metal Nanoclusters in Block Co-Polymers** ..... 33
Erica H. Tadd, John Bradley, Eugene P. Goldberg, and Rina Tannenbaum

**Salt-Induced Block Copolymer Micelles as Nanoreactors for the Formation of CdS Nanoparticles** ..... 43
Hanying Zhao and Elliot P. Douglas

* **Growth of Highly Oriented ZnO Nanorods by Chemical Vapor Deposition** ..... 49
Sai-Chang Liu and Jih-Jen Wu

**Nano-Cylinder Structure Studied by X-ray Diffraction** ..... 59
Gu Xu, Zhechuan Feng, Zoran Popovic, Jianyi Lin, and Jagadese J. Vittal

*Invited Paper

**Thermal Characterization of Nanowire Array in $a$-$Al_2O_3$ Matrix** ..... 65
Diana-Andra Borca-Tasciuc, Gang Chen, Yu-Ming Lin, Oded Rabin, Mildred S. Dresselhaus, Alexander Borshchevsky, Jean-Pierre Fleurial, and Margaret A. Ryan

* **Formation of Ordered Silica–Organic Hybrids by Self-Assembly of Hydrolyzed Organoalkoxysilanes with Long Organic Chains** ..... 71
Kazuyuki Kuroda and Atsushi Shimojima

**Polymerization in Inverse Microemulsion: An Effective Tool to Produce Biodegradable and Non-Biodegradable Nanoparticles** ..... 83
F. Lebon, C. Grandfils, R. Jérôme, I. Barakat, and L. Sartore

*NANOPHASE AND NANOCOMPOSITE MATERIALS I*

**Self-Energy Corrections to DFT-LDA Gaps of Realistic Carbon Nanotubes** ..... 93
Guido Satta, Giancarlo Cappellini, and Francesco Casula

**Casimir Forces Between ThermallyActivated Nanocomposites** ..... 99
Raúl Esquivel-Sirvent, Carlos Villarreal, and Cecilia Noguez

**Characterization of the Order-Annealing Response of Nanostructured Iron-Palladium Based Ferromagnetic Thin Films** ..... 105
Huiping Xu, Adam T. Wise, Timothy J. Klemmer, and Jörg M. K. Wiezorek

**Nanostructured $NiFe_2O_4$ Soft Magnetic Ferrite** ..... 111
Zongtao Zhang, Y. D. Zhang, T. D. Xiao, Shihui Ge, Mingzhong Wu, W. A. Hines, J. I. Budnick, J. M. Gromek, M. J. Yacaman, and H. E. Troiani

**Dynamic Fracture Mechanisms in Nanostructured and Amorphous Silica Glasses Million-Atom Molecular Dynamics Simulations** ..... 117
Laurent Van Brutzel, Cindy L. Rountree, Rajiv K. Kalia, Aiichiro Nakano, and Priya Vashishta

*Invited Paper

**A Non-Traditional Vapor-Liquid-Solid Method for Bulk Synthesis of Semiconductor Nanowires** ..... 123
Shashank Sharma, Mahendra K. Sunkara, Guoda Lian, and Elizabeth C. Dickey

**Catalyst-Free Growth of Large Scale $Ga_2O_3$ Nanowires** ..... 129
Ko-wei Chang, Sai-chang Liu, Liang-Yih Chen, Franklin Chau-Nan Hong, and Jih-Jen Wu

**Grain Size Dependent Magnetic Properties of Nanocrystalline $Sm_2Co_{17}$/Cu** ..... 135
L. Bessais, C. Djéga-Mariadassou, J. Zhang, V. Lalanne, and A. Percheron-Guégan

**Multi-functionalization of Silicon by Nanoparticles Through "Plug and Play" Approach** ..... 141
K. Prabhakaran, K.V.P.M. Shafi, A. Ulman, and T. Ogino

**Sol-Gel Processing of Low Dielectric Constant Nanoporous Silica Thin Films** ..... 147
Deok-Yang Kim, Henry Du, Suhas Bhandarkar, and David W. Johnson, Jr.

**Stress and Hardness of $CrN_x$ Films** ..... 153
G.C.A.M. Janssen, J.-D. Kamminga, and W.G.M. Sloof

**Formation of Gold Nanowires on MgO Surfaces** ..... 159
Akira Ueda, Richard R. Mu, Vanessa Saunders, Thurston Livingston, Marvin H. Wu, Vera L. Arantes, and Don O. Henderson

**Solvothermal Synthesis of Electrochemically Active Nanocrystalline Li-Ti-O Spinel** ..... 165
Dina Fattakhova, Petr Krtil, and Valery Petrykin

*SYNTHESIS AND CHARACTERIZATION I*

***In Situ* Analysis of the Chemical Vapor Synthesis of Nanocrystalline Silicon Carbide by Aerosol Mass Spectrometry** ..... 173
In-Kyum Lee, Markus Winterer, Horst Hahn, Christian Janzen, Dirk Lindackers, and Paul Roth

**Grain-Size-Dependent Thermal Transport Properties in Nanocrystalline Yttria-Stabilized Zirconia** ..... 179
Ho-Soon Yang, J.A. Eastman, L.J. Thompson, and G.-R. Bai

**Optical, Electrical and Microstructural Properties of Tin Doped Indium Oxide Films Made From Sintered Nanoparticles** ..... 185
Annette Hultåker, Anders Hoel, Claes-Göran Granqvist, Arie van Doorn, Michel J. Jongerius, and Detlef Burgard

*SYNTHESIS AND CHARACTERIZATION II*

**Sol-Gel Synthesis and Characterization of Neodymium-Ion Doped Nanostructured Titania Thin Films** ..... 193
Andrew Burns, W. Li, C. Baker, and S.I. Shah

* **Insight into the Formation of Ultrafine Nanostructures in Bulk Amorphous $Zr_{54.5}Ti_{7.5}Al_{10}Cu_{20}Ni_8$** ..... 199
André Heinemann, Helmut Hermann, Albrecht Wiedenmann, Norbert Mattern, Uta Kühn, Hans-Dietrich Bauer, and Jürgen Eckert

**Supersonic Nanocrystal Deposition for Nanostructured Materials** ..... 209
W.T. Nichols, D.T. O'Brien, G. Malyavanatham, M.F. Becker, and J.W. Keto

**Orientation of Aromatic Ion Exchange Diamines and the Effect on Melt Viscosity and Thermal Stability of PMR-15/Silicate Nanocomposites** ..... 215
Sandi Campbell and Daniel Scheiman

**Production and Magnetic Properties of Nanocomposites Made of Ferrites and Ceramic Matrices** ..... 223
H. A. Calderon, A. Huerta, M. Umemoto, and K. Cornett

*NANOPHASE AND NANOCOMPOSITE MATERIALS II*

**Crystalline-Amorphous Interface: Molecular Dynamics Simulation of Thermal Conductivity** ..... 231
Sebastian von Alfthan, Antti Kuronen, and Kimmo Kaski

*Invited Paper

**Fe/$SiO_2$ Nanocomposite Soft Magnetic Materials** ..... 237
S. Hui, Y.D. Zhang, T.D. Xiao, Mingzhong Wu, Shihui Ge, W.A. Hines, J.I. Budnick, M.J. Yacaman, and H.E. Troiani

**Preparation of Optically Transparent Films of Poly(methyl methacrylate) (PMMA) and Montmorillonite** ..... 243
Elena Vasiliu, Chyi-Shan Wang, and Richard A. Vaia

**Characterization of the Morphology of Faceted Particles by Transmission Electron Microscopy** ..... 249
Shirley Turner and David S. Bright

**Preparation of Copper Aluminium Oxide by Spray Pyrolysis** ..... 255
Ji Youn Rim, Shin Ae Song, and Seung Bin Park

**Temperature Dependence of Electroresistivity, Negative and Positive Magnetoresistivity of Graphite/Diamond Nanocomposites and Onion-Like Carbon** ..... 259
Anatoliy I. Romanenko, Olga B. Anikeeva, Alexander V. Okotrub, Vladimir L. Kuznetsov, Yuriy V. Butenko, Andrew L. Chuvilin, C. Dong, and Y. Ni

**Rapid-Solidification Effect on Magnetostriction in Iron-Based Ferromagnetic Shape Memory Alloy** ..... 265
Yasubumi Furuya, Takeshi Kubota, Teiko Okazaki, Mitsutaka Sato, and Manfred Wuttig

**Nanoscale Compositional Changes Along Fast Ion Tracks in Equilibrium Solid Solutions: A Computer Simulation of Ultra-Fast Solidification and Thermomigration** ..... 271
Edmundo M. Lopasso, Alfredo Caro, Eduardo Ogando Arregui, and Magdalena Caro

**Deposition of Polymer Thin Films on ZnO Nanoparticles by a Plasma Treatment** ..... 277
Peng He, Jie Lian, L. M. Wang, Wim J. van Ooij, and Donglu Shi

**Synthesis of Nanosized Lithium Manganate For Lithium-Ion Secondary Batteries** ..... 283
Hsien-Cheng Wang, Yueh Lin, Ming-Chang Wen, and Chung-Hsin Lu

*APPLICATIONS AND PROPERTIES I*

**Nanostructured Hydroxyapatite Coatings for Improved Adhesion and Corrosion Resistance for Medical Implants** ..... 291
Zongtao Zhang, Matthew F. Dunn, T. D. Xiao, Antoni P. Tomsia, and E. Saiz

**Characterization of Self-Assembled $SnO_2$ Nanoparticles for Fabrication of a High Sensitivity and High Selectivity Micro-Gas Sensor** ..... 297
R.C. Ghan, Y. Lvov, and R.S. Besser

**Fluorescence from Coated Oxide Nanoparticles** ..... 303
D. Vollath, I. Lamparth, and D.V. Szabó

**Nanocomposite Electrodes for Advanced Lithium Batteries: The $LiFePO_4$ Cathode** ..... 309
Shoufeng Yang, Yanning Song, Peter Y. Zavalij, and M. Stanley Whittingham

*APPLICATIONS AND PROPERTIES II*

* **Nanocomposite Coatings—Applications and Properties** ..... 317
Roger H. Cayton and R. W. Brotzman, Jr.

**Vanadium Oxide Nanotubes: Characterization and Electrochemical Behavior** ..... 323
Samuel T. Lutta, Arthur Dobley, Katana Ngala, Shoufeng Yang, Peter Y. Zavalij, and M. Stanley Whittingham

*NANOPHASE AND NANOCOMPOSITE MATERIALS III*

**Controlling the Microstructure and Magnetic Properties of Ferromagnetic Nanocrystals Produced by Ion Implantation** ..... 331
K.S. Beaty, A. Meldrum, J.P. Franck, K. Sorge, J. R. Thompson, C.W. White, R.A. Zuhr, L.A. Boatner, and S. Honda

**Innovative and Cost-Effective Microfabrication of Nanoceramic Components** ..... 337
Balakrishnan G. Nair

*Invited Paper

**Processing Effects on The Morphology of Hydrothermally Derived Nanocrystalline Lead Titanate** ..... 343
Zhiyuan Ye, Elliott B. Slamovich, and Alexander H. King

**Nanocomposite Based on Semiconductor Oxides $SnO_2/WO_3$** ..... 349
M.N. Rumyntseva, M.N. Boulova, D.A. Chareev, L.I. Ryabova, B.A. Akimov, and A.M. Gaskov

**Nickel Nanocomposite Thin Films** ..... 355
Honghui Zhou, A. Kvit, D. Kumar, and J. Narayan

**Thermal and Structural Characterization of Nanocomposite Iron Nitride-Alumina and Iron Nitride-Silica Particles** ..... 363
Ann M. Viano and Sanjay R. Mishra

**Structure and Nanocrystallites of Ni and NiO Three Dimensional Ordered Macromeshes** ..... 369
W.L. Zhou, L. Xu, A.A. Zakhidov, R.H. Baughman, and J.B. Wiley

**Substrate Dependence in the Growth of Three-Dimensional Gold Nanoparticle Superlattices** ..... 375
S. Sato, N. Yamamoto, H. Yao, and K. Kimura

**Topology and Electronic Structure of Onion-Like Carbon and Graphite/Diamond Nanocomposites** ..... 381
Lyubov G. Bulusheva, Alexander V. Okotrub, Vladimir L. Kuznetsov, Andrew L. Chuvilin, Yuriy V. Butenko, and Malcolm I. Heggie

**Mechanical Properties of Unsaturated Polyester/Montmorillonite Composites** ..... 387
A. Baran Inceoglu and Ulku Yilmazer

**Microwave Plasma CVD of Silicon Nanocrystalline and Amorphous Silicon as a Function of Deposition Conditions** ..... 393
J-H. Jeung, Hak-Gue Lee, Lihong Teng, and W.A. Anderson

**Dispersion of Functionalized Nanoclay Platelets in an Amine-Cured Epoxy Resin System** ..... 399
D. Raghavan, E. Feresenbet, D. Yebassa, A. Emekalam, and G. Holmes

**Single-Wall Carbon Nanotubes Synthesis by Means of UV Laser Vaporization: Effects of the Furnace Temperature and the Laser Intensity Processing Parameters** ..... 407
N. Braidy, M.A. El Khakani, and G.A. Botton

**Using Ion Beams to Modify Nanocrystalline Composites: Co Nanoparticles in Sapphire** ..... 413
A. Meldrum, K.S. Beaty, M. Lam, C.W. White, R.A. Zuhr, and L.A. Boatner

*SELF ASSEMBLY OF NANOPHASE AND NANOCOMPOSITE MATERIALS*

**Silver-Polyimide Nanocomposite Films Yielding Highly Reflective Surfaces** ..... 421
Robin E. Southward, C.J. Dean, J.L. Scott, S.T. Broadwater, and D.W. Thompson

**Investigating Catalytic Properties of Composite Nanoparticle Assemblies** ..... 427
M.M. Maye, J. Luo, Y. Lou, N.K. Ly, W.-B. Chan, E. Phillip, M. Hepel, and C.J. Zhong

**Surfactant Templated Assembly of Hexagonal Mesostructured Semiconductors Based on $[Ge_4Q_{10}]^{4-}$ (Q=S,Se)and $Pd^{2+}$ and $Pt^{2+}$ Ions** ..... 433
Pantelis N. Trikalitis, Krishnaswamy K. Rangan, and Mercouri G. Kanatzidis

**Studies of Intersubband Transitions in Arrays of Bi Nanowire Samples Using Optical Transmission** ..... 439
M.R. Black, K.R. Maskaly, O. Rabin, Y.M. Lin, S.B. Cronin, M. Padi, Y. Fink, and M.S. Dresselhaus

**The Role of the Interfaces in the Optical Effects of Large-Sized $SiC_xO_{1-x}N$ Nanocrystallites** ..... 445
K.J. Plucinski, H. Kaddouri, and I.V. Kityk

*SYNTHESIS, MODELING AND THEORY*

* **Intercalative Route to Heterostructured Nanohybrids** ..... 453
Jin-Ho Choy

*Invited Paper

**What Xe Nanocrystals in Al Can Teach Us in Materials Science** ..... 463
C. W. Allen, R. C. Birtcher, U. Dahmen, K. Furuya, M. Song, and S. E. Donnelly

**Exploring the Consequences of Negative Triple Junction Energy** ..... 469
Gaurav K. Gupta and Alexander H. King

**Magic Family of Discretly Sized Ultrabright Si Nanoparticles** ..... 475
G. Belomoin, J. Therrien, A. Smith, S. Rao, R. Twesten, S. Chaieb, M.H. Nayfeh, L. Wagner, and L. Mitas

**Optical Characterization and Modeling of Sulfur Incorporated Nanocrystalline Carbon Thin Films Deposited by Hot Filament CVD** ..... 481
S. Gupta, B. R. Weiner, and G. Morell

**Analysis of fhe Atomic-Scale Defect Chemistry at Interfaces in Fluorite Structured Oxides by Electron Energy Loss Spectroscopy** ..... 489
Y. Ito, Y. Lei, N.D. Browning, and T.J. Mazanec

*NANOSTRUCTURES II*

**$H_3PO_4$/Oxide Nanoparticles/Polymer Composites as Proton Conducting Membranes** ..... 497
D. Carrière, P. Barboux, M. Moreau, and J.-P. Boilot

*NANOPHASE AND NANOCOMPOSITE MATERIALS IV*

**Soft Reverse Current-Voltage Characteristics in $V_2O_5$ Nanofiber Junctions** ..... 505
Gyu-Tae Kim, Jörg Muster, Marko Burghard, and Siegmar Roth

**Growth of Solid and Hollow Nanowhiskers From Nanoscale Powders** ..... 511
R.T. Malkhasyan, R.K. Karakhanyan, and M.N. Nazaryan

**The Generation of a Carbon Nanotube-Cyclodextrin Complex** ..... 517
G.F. Farrell, G. Chambers, A.B Dalton, E. Cummins,
M. McNamara, R.H. Baughman, M. in het Panhuis, and H.J. Byrne

**Optical Nonlinearity of Sputtered $Co_3O_4$-$SiO_2$-$TiO_2$ Thin Films** ..... 523
Hiroki Yamamoto, Takashi Naito, and Kazuyuki Hirao

**Structure of Zirconia Nanoparticles Used for Pillaring of Clay** ..... 529
V.A. Sadykov, T.G. Kuznetsova, V.P. Doronin,
T.P. Sorokina, D.I. Kochubei, B.N. Novgorodov,
V.N. Kolomiichuk, E.M. Moroz, D.A. Zyuzin,
E.A. Paukshtis, V.B. Fenelonov, A.Ya. Derevyankin,
S.A. Beloshapkin, V.A. Matyshak, G.A. Konin, and
J.R.H. Ross

**Superconductivity of Embedded Lead Nanoparticles in Metallic and Amorphous Matrices** ..... 535
K. Chattopadhyay, V. Bhattacharya, and A.P. Tsai

**Fabrication of Metal Nanostructures in Mesoporous Silicas** ..... 541
Kuei Jung Chao and Chia Min Yang

**Synthesis of Epoxy and Block Oligomer Modified Clay Nanocomposite** ..... 547
Kang Hung Chen and Sze Ming Yang

**Doping and Electrochemical Capacitance of Carbon Nanotube-Polypyrrole Composite Films** ..... 553
Mark Hughes, George Z. Chen, Milo S. P. Shaffer,
Derek J. Fray, and Alan H. Windle

**Insertion of Inorganic-Biomolecular Nanohybrid into Eucaryotic Cell** ..... 559
Seo-Young Kwak, Sung-Ho Hwang, Yong-Joo Jeong,
Jong-Sang Park, and Jin-Ho Choy

**The Coercivity – Remanence Tradeoff in Nanocrystalline Permanent Magnets** ..... 565
Laura H. Lewis and David C. Crew

**Growth of Nanosize and Colloid Particles by Controlled Addition of Singlets** ..... 577
Vladimir Privman

**Author Index** ..... 587

**Subject Index** ..... 591

# PREFACE

This volume contains the proceedings of Symposium V, "Nanophase and Nanocomposite Materials IV," held November 26-29 at the 2001 MRS Fall Meeting in Boston, Massachusetts. This symposium is the fourth in this series, which began at the 1992 MRS Fall Meeting, long before nanotechnology had become a buzz word. As with the previous symposia in this series, the objective was to bring together scientists from many disciplines in order to share and discuss their results related to many aspects of nanophase and nanocomposite materials. Over two hundred papers from several countries on synthesis, characterization and property evaluation and applications of nanophase and nanocomposite materials were presented in both oral and poster sessions. All of the papers published in this proceedings have been refereed.

Sridhar Komarneni
John C. Parker
Richard A.Vaia
G.Q. (Max) Lu
Jun-ichi Matsushita

January 2002

## MATERIALS RESEARCH SOCIETY SYMPOSIUM PROCEEDINGS

Volume 664— Amorphous and Heterogeneous Silicon-Based Films—2001, M. Stutzmann, J.B. Boyce, J.D. Cohen, R.W. Collins, J. Hanna, 2001, ISBN: 1-55899-600-1
Volume 665— Electronic, Optical and Optoelectronic Polymers and Oligomers, G.E. Jabbour, B. Meijer, N.S. Sariciftci, T.M. Swager, 2002, ISBN: 1-55899-601-X
Volume 666— Transport and Microstructural Phenomena in Oxide Electronics, D.S. Ginley, M.E. Hawley, D.C. Paine, D.H. Blank, S.K. Streiffer, 2001, ISBN: 1-55899-602-8
Volume 667— Luminescence and Luminescent Materials, K.C. Mishra, J. McKittrick, B. DiBartolo, A. Srivastava, P.C. Schmidt, 2001, ISBN: 1-55899-603-6
Volume 668— II-VI Compound Semiconductor Photovoltaic Materials, R. Noufi, R.W. Birkmire, D. Lincot, H.W. Schock, 2001, ISBN: 1-55899-604-4
Volume 669— Si Front-End Processing—Physics and Technology of Dopant-Defect Interactions III, M.A. Foad, J. Matsuo, P. Stolk, M.D. Giles, K.S. Jones, 2001, ISBN: 1-55899-605-2
Volume 670— Gate Stack and Silicide Issues in Silicon Processing II, S.A. Campbell, C.C. Hobbs, L. Clevenger, P. Griffin, 2002, ISBN: 1-55899-606-0
Volume 671— Chemical-Mechanical Polishing 2001—Advances and Future Challenges, S.V. Babu, K.C. Cadien, J.G. Ryan, H. Yano, 2001, ISBN: 1-55899-607-9
Volume 672— Mechanisms of Surface and Microstrucure Evolution in Deposited Films and Film Structures, J. Sanchez, Jr., J.G. Amar, R. Murty, G. Gilmer, 2001, ISBN: 1-55899-608-7
Volume 673— Dislocations and Deformation Mechanisms in Thin Films and Small Structures, O. Kraft, K. Schwarz, S.P. Baker, B. Freund, R. Hull, 2001, ISBN: 1-55899-609-5
Volume 674— Applications of Ferromagnetic and Optical Materials, Storage and Magnetoelectronics, W.C. Black, H.J. Borg, K. Bussmann, L. Hesselink, S.A. Majetich, E.S. Murdock, B.J.H. Stadler, M. Vazquez, M. Wuttig, J.Q. Xiao, 2001, ISBN: 1-55899-610-9
Volume 675— Nanotubes, Fullerenes, Nanostructured and Disordered Carbon, J. Robertson, T.A. Friedmann, D.B. Geohegan, D.E. Luzzi, R.S. Ruoff, 2001, ISBN: 1-55899-611-7
Volume 676— Synthesis, Functional Properties and Applications of Nanostructures, H.W. Hahn, D.L. Feldheim, C.P. Kubiak, R. Tannenbaum, R.W. Siegel, 2002, ISBN: 1-55899-612-5
Volume 677— Advances in Materials Theory and Modeling—Bridging Over Multiple-Length and Time Scales, L. Colombo, V. Bulatov, F. Cleri, L. Lewis, N. Mousseau, 2001, ISBN: 1-55899-613-3
Volume 678— Applications of Synchrotron Radiation Techniques to Materials Science VI, P.G. Allen, S.M. Mini, D.L. Perry, S.R. Stock, 2001, ISBN: 1-55899-614-1
Volume 679E—Molecular and Biomolecular Electronics, A. Christou, E.A. Chandross, W.M. Tolles, S. Tolbert, 2001, ISBN: 1-55899-615-X
Volume 680E—Wide-Bandgap Electronics, T.E. Kazior, P. Parikh, C. Nguyen, E.T. Yu, 2001, ISBN: 1-55899-616-8
Volume 681E—Wafer Bonding and Thinning Techniques for Materials Integration, T.E. Haynes, U.M. Gösele, M. Nastasi, T. Yonehara, 2001, ISBN: 1-55899-617-6
Volume 682E—Microelectronics and Microsystems Packaging, J.C. Boudreaux, R.H. Dauskardt, H.R. Last, F.P. McCluskey, 2001, ISBN: 1-55899-618-4
Volume 683E—Material Instabilities and Patterning in Metals, H.M. Zbib, G.H. Campbell, M. Victoria, D.A. Hughes, L.E. Levine, 2001, ISBN: 1-55899-619-2
Volume 684E—Impacting Society Through Materials Science and Engineering Education, L. Broadbelt, K. Constant, S. Gleixner, 2001, ISBN: 1-55899-620-6
Volume 685E—Advanced Materials and Devices for Large-Area Electronics, J.S. Im, J.H. Werner, S. Uchikoga, T.E. Felter, T.T. Voutsas, H.J. Kim, 2001, ISBN: 1-55899-621-4
Volume 686— Materials Issues in Novel Si-Based Technology, W. En, E.C. Jones, J.C. Sturm, S. Tiwari, M. Hirose, M. Chan, 2002, ISBN: 1-55899-622-2
Volume 687— Materials Science of Microelectromechanical Systems (MEMS) Devices IV, A.A. Ayon, S.M. Spearing, T. Buchheit, H. Kahn, 2002, ISBN: 1-55899-623-0
Volume 688— Ferroelectric Thin Films X, S.R. Gilbert, Y. Miyasaka, D. Wouters, S. Trolier-McKinstry, S.K. Streiffer, 2002, ISBN: 1-55899-624-9

## MATERIALS RESEARCH SOCIETY SYMPOSIUM PROCEEDINGS

Volume 689— Materials for High-Temperature Superconductor Technologies, M.P. Paranthaman, M.W. Rupich, K. Salama, J. Mannhart, T. Hasegawa, 2002, ISBN: 1-55899-625-7
Volume 690— Spintronics, T.J. Klemmer, J.Z. Sun, A. Fert, J. Bass, 2002, ISBN: 1-55899-626-5
Volume 691— Thermoelectric Materials 2001—Research and Applications, G.S. Nolas, D.C. Johnson, D.G. Mandrus, 2002, ISBN: 1-55899-627-3
Volume 692— Progress in Semiconductor Materials for Optoelectronic Applications, E.D. Jones, M.O. Manasreh, K.D. Choquette, D. Friedman, 2002, ISBN: 1-55899-628-1
Volume 693— GaN and Related Alloys—2001, J.E. Northrup, J. Neugebauer, S.F. Chichibu, D.C. Look, H. Riechert, 2002, ISBN: 1-55899-629-X
Volume 695— Thin Films: Stresses and Mechanical Properties IX, C.S. Ozkan, R.C. Cammarata, L.B. Freund, H. Gao, 2002, ISBN: 1-55899-631-1
Volume 696— Current Issues in Heteroepitaxial Growth—Stress Relaxation and Self Assembly, E. Stach, E. Chason, R. Hull, S. Bader, 2002, ISBN: 1-55899-632-X
Volume 697— Surface Engineering 2001—Fundamentals and Applications, W.J. Meng, A. Kumar, Y-W. Chung, G.L. Doll, Y-T. Cheng, S. Veprek, 2002, ISBN: 1-55899-633-8
Volume 698— Electroactive Polymers and Rapid Prototyping, Y. Bar-Cohen, D.B. Chrisey, Q.M. Zhang, S. Bauer, E. Fukada, S.C. Danforth, 2002, ISBN: 1-55899-634-6
Volume 699— Electrically Based Microstructural Characterization III, R.A. Gerhardt, A. Washabaugh, M.A. Alim, G.M. Choi, 2002, ISBN: 1-55899-635-4
Volume 700— Combinatorial and Artificial Intelligence Methods in Materials Science, I. Takeuchi, C. Buelens, H. Koinuma, E.J. Amis, J.M. Newsam, L.T. Wille, 2002, ISBN: 1-55899-636-2
Volume 702— Advanced Fibers, Plastics, Laminates and Composites. F.T. Wallenberger, N. Weston, K. Chawla, R. Ford, R.P. Wool, 2002, ISBN: 1-55899-638-9
Volume 703— Nanophase and Nanocomposite Materials IV, S. Komarneni, R.A. Vaia, G.Q. Lu, J-I. Matsushita, J.C. Parker, 2002, ISBN: 1-55899-639-7
Volume 704— Nanoparticle Materials, R.K. Singh, R. Partch, M. Muhammed, M. Senna, H. Hofmann, 2002, ISBN: 1-55899-640-0
Volume 705— Nanopatterning—From Ultralarge-Scale Integration to Biotechnology, L. Merhari, K.E. Gonsalves, E.A. Dobisz, M. Angelopoulos, D. Herr, 2002, ISBN: 1-55899-641-9
Volume 706— Making Functional Materials with Nanotubes, P. Nikolaev, P. Bernier, P. Ajayan, Y. Iwasa, 2002, ISBN: 1-55899-642-7
Volume 707— Self-Assembly Processes in Materials, S. Moss, 2002, ISBN: 1-55899-643-5
Volume 708— Organic and Optoelectronic Materials, Processing and Devices, S. Moss, 2002, ISBN: 1-55899-644-3
Volume 709— Advances in Liquid Crystalline Materials and Technologies, P.T. Mather, D.J. Broer, T.J. Bunning, D.M. Walba, R. Zentel, 2002, ISBN: 1-55899-645-1
Volume 710— Polymer Interfaces and Thin Films, C.W. Frank, 2002, ISBN: 1-55899-646-X
Volume 711— Advanced Biomaterials—Characterization, Tissue Engineering and Complexity, 2002, ISBN: 1-55899-647-8
Volume 712— Materials Issues in Art and Archaeology VI, P.B. Vandiver, M. Goodway, J.R. Druzik, J.L. Mass, 2002, ISBN: 1-55899-648-6
Volume 713— Scientific Basis for Nuclear Waste Management XXV, B.P. McGrail, G.A. Cragnolino, 2002, ISBN: 1-55899-649-4
Volume 714E—Materials, Technology and Reliability for Advanced Interconnects and Low-k Dielectrics II, S. Lahiri, 2002, ISBN: 1-55899-650-8

**Prior Materials Research Society Symposium Proceedings available by contacting Materials Research Society**

# Nanocomposite and Nanofiber Materials

Mat. Res. Soc. Symp. Proc. Vol. 703 © 2002 Materials Research Society V1.2

# Processing, Dynamic Studies and Properties of Exfoliated Aerospace Epoxy-Organoclay Nanocomposites

Chenggang Chen[1] and David Curliss[2]
[1]University of Dayton Research Institute, 300 College Park, Dayton, OH 45469-0168, U.S.A.
[2]Air Force Research Laboratory, Materials and Manufacturing Directorate, WPAFB, OH 45433, U.S.A.

## ABSTRACT

Epoxy nanocomposites were prepared from the montmorillonite after organic treatment with a high $T_g$ epoxy resin (Shell Epon 862 and curing agent W). Investigation of the rheological characteristics showed that the addition of clay to the resin did not significantly alter the viscosity or cure kinetics and that the modified resin would still be suitable for liquid composite molding techniques such as resin transfer molding. DSC was performed to study the kinetics of the curing reactions in the modified resin. An *in situ* small-angle x-ray scattering (SAXS) experiment was used to try to understand the structural development during cure. Based on the *in situ* SAXS data, structural changes were monitored in real time during cure and analyzed. Results from wide-angle x-ray diffraction, SAXS, and transmission electron microscopy of the polymer-silicate nanocomposites were used to characterize the morphology of the layered silicate in the epoxy resin matrix. The glassy and rubbery moduli of the polymer-silicate nanocomposites were found to be greater than the unmodified resin due to the high aspect ratio and high stiffness of the layered silicate filler. The solvent absorption in methanol was also slower for the polymer-silicate nanocomposites.

## INTRODUCTION

Conventional composite materials are materials with a macroscopic combination of two or more distinct materials, having recognized interface between them [1]. They have been widely used in construction, transportation, electronics and consumer products. Composites with at least one solid phase with a dimension in the range of 1-100 nm can be defined as nanocomposites [2, 3]. Polymer-layered silicate nanocomposites are new hybrid materials of polymers with nanometer-thickness layered silicates. Due to the unique nanometer-size dispersion of the layered silicates with high aspect ratio and high strength in the polymer matrix, these materials generally exhibit improvements in properties even at low loading of layered silicate. These properties can include mechanical performance, ablation performance, thermal stability, barrier performance, and flame retardancy [4-7].

Layered silicates are abundant and important minerals in geological environments at or within roughly 20 km of the Earth surface [8]. There are many types of sheet silicates including clay mineral. The most widely used layered silicate for the nanocomposites is montmorillonite. Natural montmorillonite is constructed of repeating TOT layers composed of two silica tetrahedral sheets fused to an edge-shared octahedral sheet of alumina. The physical dimensions for these silicate sheets are around one hundred to several hundred nanometer in lateral and 1-nm in thickness. However, the individual sheets in the silicates are generally stacked together and hydrophilic, and thus are not compatible with the hydrophobic organic matrix polymer. Therefore, the challenge is to produce a layered silicate system compatible with the matrix

polymer. Fortunately, some silicon atoms in the silica tetrahedral layer and some alumina atoms in the octahedral layer are isomorphically substituted by alumina and magnesium, respectively. This generates negative charges that are counter-balanced by some cations such as $Na^+$, $K^+$ or $Ca^{2+}$ in the gallery. These cations can be easily exchanged with surfactant such as alkyl ammonium cations. The pendent organic group in the surface of the silicate sheets lowers the surface energy of silicate layers and make the layered silicate compatible with polymer matrix. Up to now, extensive research on the polymer layered silicate nanocomposites is being carried out and most of the research is focused on the preparation of the nanocomposite [4-7]. In this research work, the emphasis is placed on aerospace epoxy-silicate nanocomposites. In addition to the preparation and characterization of the nanocomposites, the processing and dynamic study are also performed to understand the exfoliation mechanism. The aerospace epoxy studied here is made from Shell Epon 862 (a low viscosity Bis-phenol F/epichlorohydrin-based liquid epoxy resin) and Epi-Cure curing agent W (diethyltoluenediamine). This epoxy system has high $T_g$ (155 °C) and low-viscosity, which is suitable for resin transfer modeling.

## EXPERIMENTAL DETAILS

The resin, cure agent, chemical modifiers and clays used in this research includes Shell Epon 862 (a bis-phenol F epoxy), Epi-Cure curing agent W, *n*-octadecylamine (Aldrich), hydrochloric acid (Aldrich), SNA (Southern Clay Products), and I.30E (Nanocor).

The preparation of organoclay, SC18, was as follows: 21.1 g of *n*-octadecylamine in the 750 mL of ethanol and water mixture solvent (v:v, 1:1) was added with aqueous hydrochloric acid (HCl, 1N, 67.5 mL). The mixture was stirred at ~70 °C. When the solution was clear, 67.5 g of SNA was added to the above mixture solution, and the suspension was continuously stirred for 4 hours at ~ 70 °C. The resultant mixture was filtered. The solid was washed with a mixture of warm ethanol and water, and dried.

Processing: Desired amount of Epon 862 and the corresponding amount of organoclay was mixed and stirred at ~ 70 °C. The mixture was degassed in the vacuum oven. Then the corresponding amount of curing agent W was added to the mixture and continued stirring. The resulting mixture was cast between glass plates spaced 0.25 inch apart and cured in a programmable Blue M oven using the following curing cycle: heat the cast in the oven to 121°C over 30 minutes, hold at 121°C for two hours, then heat to 177°C over 30 minutes and hold for another two hours at 177°C, and finally cool the cast in the oven to ambient.

Characterization: Wide-angle x-ray diffraction was performed in the Rigaku x-ray powder diffractometer. The generator power was 40 kV and 150 mA, and the scan mode was continuous with a scan rate of 0.6°/min. The scan 2θ range is from 2° to 10°. Some of small-angle x-ray scattering was performed at National Synchrotron Light Source at the Brookhaven National Laboratory (Beamline X27C with a one-dimensional detector). Some other small-angle x-ray scattering was taken using a flat film Statton camera on a Rigaku RU-200 with Cu $K_\alpha$ as its radiation with a wavelength of 1.5418 Å. The power was 50 kV and 150 mA and the exposure time was around 20 hours. The *in-situ* small-angle x-ray scattering experiment was also performed at National Synchrotron Light Source at the Brookhaven National Laboratory (Beamline X27C with a one-dimensional detector). The mixture of the organoclay with Epoxy and curing agent was mounted on the holder and sample was heated up at 2°C/min. The data was recorded every minute. DSC was performed on a TA Instruments differential scanning calorimeter 2920 modulated DSC at 2°C/min with air sweep gas. The sample for transmission

electron microscopy was microtomed in a Reichert-Jung Ultracut Microtome and mounted on 200 mesh copper grids. Transmission electron microscopy was performed using a Philips CM200 transmission electron microscope. The dynamic mechanical analysis was performed using a RHEOMETRICS ARES dynamic spectrometer using torsion bar geometry at a frequency of 100 rad/sec, a strain of 0.1 percent, and a heating rate of 2°C/min; while the viscosity test was carried out at a RHEOMETRICS ARES dynamic spectrometer using 25-mm diameter parallel plates geometry at a frequency of 10 rad/sec, a strain of 3 percent and a heating rate of 2°C/min.

## RESULTS AND DISCUSSION

SC18 is the organoclay prepared from Closite Na (CEC: ~ 92 meq/100 g) with *n*-octadecylammonium hydrogen chloride in the laboratory while I.30E is commercially available from Nanocor (CEC ~145 meq/100 g, also treated with *n*-octadecylammonium hydrogen chloride). The wide-angle x-ray diffraction shows that the interplanar spacing SC18 was increased to 18.0 Å from original 10.5 Å of Closite Na while the interplanar spacing of I.30E is 22.6 Å. This is consistent with the exchange capacities of their original sodium montmorillonite (92 meq vs 145 meq). These two organoclays are very well compatible with aerospace epoxy resins. A series of aerospace epoxy-organoclay nanocomposites were made with different loadings of SC18 and I.30E. The wide-angle x-ray diffraction of the nanocomposites shows that there is no peak at 2 θ scanning ranging from 2° to 10°, which generally indicates that the interplanar spacing is larger than 44 Å and nanocomposites are considered to be exfoliated structures. In order to confirm the morphology of the nanocomposite, small-angle x-ray diffractions were taken at National Synchrotron Light Source at Brookhaven National Laboratory and Rigaku RU-200, Table I. The interplanar spacing is larger than 100 Å when the organoclay loading is less than eight percent. Even the organoclay loading is as high as 10% for SC18, and 9.0% and 12.0% for I.30E, the interplanar spacing is as large as 90 Å, 88 Å and 68 Å, respectively. With the increment of the organoclay loading, the interplanar spacing began to decrease because of less epoxy resin between the nanosheets at the low loading of the organoclay. The weakness of the peak demonstrates the existence of the disordered structures. In addition, the interplanar spacing of the nanocomposites from the synthetic organoclay (SC18) is larger than those from commercial organoclay (I.30E) although the original interplanar spacing of the synthetic clay (~18 Å) is even smaller than that of commercial organoclay (I.30E, 22.6 Å). This is related to the cation-exchange capacity of the montmorillonite used for making nanocomposites. The higher cation-exchange capacity means that more organic group can be introduced into the gallery and interplanar spacing is also larger (22.6 Å). However, when the organoclay was mixed with epoxy resin, the organoclay with high cation-exchange capacity has more organic groups in the gallery, which perhaps slows the epoxy resin migrating into the gallery [9]. Thus it makes the gallery of the nanocomposite from montmorillonite (I.30E) with high cation-exchange capacity smaller than that with lower cation-exchange capacity (SC18).

Several images of transmission electron microscopy of these nanocomposites are taken. The original aggregates of the silicate sheets are disrupted and each individual sheet with nanometer-thickness was well dispersed in the epoxy resin. Some individual sheets are completely disordered while some still preserve the parallel alignment of layers. This is consistent with the results from small-angle x-ray scattering.

The viscosity study related to the I.30E/Epon862/W and Epon862/W was performed by dynamic mechanical analysis, Figure 1. At room temperature, the viscosity of the

**Table I.** Small-Angle X-ray Diffraction Data, Storage Moduli and Glass Transition Temperatures (Tg) of the Nanocomposites and Their Pristine Polymer

| | d-Spacing (Å) | | Tg (°C) | G' (dyne/cm$^2$) | |
|---|---|---|---|---|---|
| Clay | NSLS | Rigaku | Tan δ | Glassy (30°C) | Rubber (180°C) |
| NA | | | 154 | 1.14E10 | 1.03E8 |
| 1.0% SC18 | 249 | | | | |
| 3.0% SC18 | 135 | 135 | 145 | 1.23E10 | 1.39E8 |
| 6.0% SC18 | 129 | | 154 | 1.30E10 | 2.14E8 |
| 8.0% SC18 | 114 | | | | |
| 10.0% SC18 | 90 | 89/44 | 144 | 1.56E10 | 2.82E8 |
| 1.0% I.30E | 172 | | 153 | 1.20E10 | 1.24E8 |
| 3.0% I.30E | 126 | 125 | | | |
| 6.0% I.30E | 100/49 | 100/48 | | | |
| 9.0% I.30E | | 88/44 | 144 | 1.61E10 | 2.31E8 |
| 12.0% I.30E | | 68 | | | |

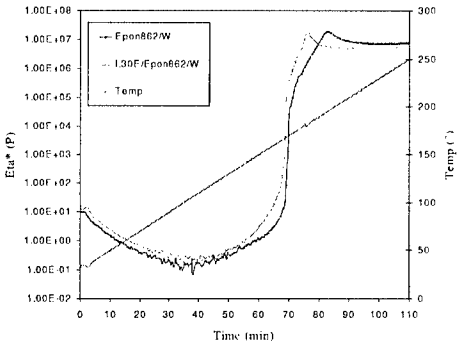


**Figure 1.** Viscosity of Epon862/W and 6% I.30E/Epon862/W at heating rate (2° C/min).

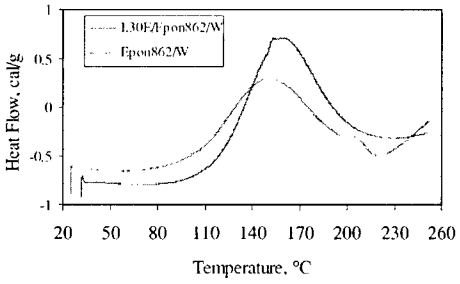


**Figure 2.** DSC of Epon862/W and 6% I.30E/Epon862/W at heating rate (2°C/min).

I.30E/Epon862/W is a little larger than that of Epon862/W as expected. However the increase is limited and the processable window is still wide for resin transfer modeling. As the temperature increases, the cross-linking polymerization takes place. After the polymer is formed, with the temperature continually increased the solid polymer will begin to soften into rubber state and the viscosity will be decreased to some extent. The shape of the viscosity vs. time and temperature are similar. The gelling takes place more quickly for the epoxy resin with organoclay. The time and temperature of the turning point of softening for I.30E/Epon862/W are also similar to that of Epon862/W, but are clearly shorter (7 minutes shorter) and lower (180 vs. 196 °C). This demonstrates that the organoclay has some catalytic effect on the polymerization of Epon862/W.

The DSC experiment of I.30E/Epon862/curing agent W and Epon862/curing agent W was performed. The DSC was shown in Figure 2. With the addition of the organoclay (I.30E) to the original Epon862/W resin, the nanocomposite system produces more exothermal heat

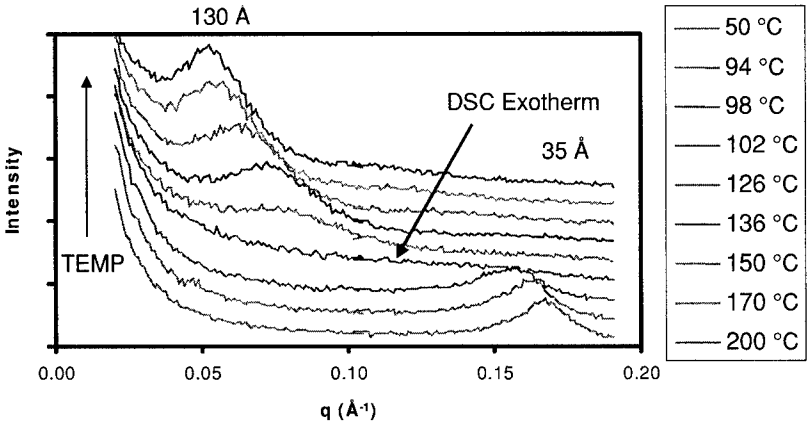


**Figure 3.** The *in-situ* small-angle x-ray scattering of 6% I.30E/Epon862/W at heating rate (2°C/min).

(49.2 vs 45.7 cal/g) at lower curing onset temperature (102.5 vs 122.5°C). This demonstrates that the organoclay has some catalytic effect on the cross-linking polymerization of Epon862 with curing agent W. This catalytic effect of the organoclay is consistent with the report for the rubber state epoxy system [10].

During processing, the morphology of the system changes. Since the organoclay has layered structure, the gallery interplanar spacing will change. The *in-situ* small-angle x-ray scattering at National Synchrotron Light Source at the Brookhaven National Laboratory provides powerful tools to monitor the structural evolution of the nanocomposite. The Epon 862 and organoclay was mixed in advance. When the corresponding curing agent W was added, the mixture was immediately mounted on the holder. The sample was heated at 2°C/minute. In order to be clear, some key data was chosen, Figure 3. When the Epon862 mixed with I.30E, the organoclay after organic treatment was compatible with the epoxy resin. Some epoxy resin will enter into the gallery of the clay. The interplanar was increased to 35 Å from original 22 Å. When the mixture was heated up at 2°C/min, for the I.30E/Epon862/W, the peak gradually shifts and becomes a little weaker, but not significantly. Amazingly, at ~102 °C, suddenly the ordered structure was collapsed and the exfoliation takes place. Later, a new clear peak appears and the intensity and interplanar spacing in increased gradually. The temperature for the collapse of the ordered structure is the same as the curing onset temperature from DSC. This is perhaps because the exothermal heat from curing at ~102 °C provides enough energy to make the nanoclay sheets expand quickly and exfoliation takes place. The results of the kinetics studies from *in-situ* small-angle x-ray scattering, DSC and rheological are well related.

The dynamic mechanical analysis, Table 1, shows that the storage modulus of the nanocomposites is higher than that of the pristine epoxy resin. Moduli increase with increased organoclay loading. Generally, the nanocomposites shows more significant improvement of storage modulus in the rubber state than that in the glassy states. The dynamic storage modulus can be increased up to more than 40% in the glassy state and 125% in the rubber state. This is

due to the high aspect ratio and high stiffness of the organoclay filler. The extra reinforcement from further nanosheet alignment in the rubber state perhaps is the reason for larger increase in the rubber state [11].

The effect of the addition of organoclay on the solvent uptake properties of Epon 862/W was examined. Three Epon 862/W panels were made with 0%, 3% and 6% I.30E. The degree of solvent uptake was evident due to the increased mass of the coupons over time. After 60 days, the percent mass gain is 14%, 10%, and 8% for 0%, 3%, and 6% I.30E/Epon862/W; respectively. The reduced transport rates observed for the polymer-silicate nanocomposites were attributed to the hindered diffusion pathways caused by the dispersion of the individual nanosheets of the layered silicate in the nanocomposites.

## CONCLUSIONS

Exfoliated aerospace epoxy organoclay nanocomposites are successfully made. The characterization from wide-angle x-ray diffraction, small-angle x-ray diffraction and transmission electron microscopy confirms the exfoliated nanostructure. Rheological, DSC and *in situ* small-angle x-ray scattering study shows that the organoclay has some catalytic effect for polymerization and that the exothermal heat at onset curing temperature is a key factor for nanosheets exfoliation. The morphology of the nanocomposites is also closely related to the CEC of the montmorillonite. The clay with lower CEC is more favorable for the polymer penetration. The dynamic storage of the nanocomposites was increased and the solvent absorption in methanol was slower for the nanocomposites.

## ACKNOWLEDGEMENTS

This material is based in part upon the work supported by Air Force Research Laboratory, Materials & Manufacturing Directorate (F33615-00-D-5006), and the Air Force Office of Scientific Research. Authors would also like to thank Dr. Richard Vaia and Dr. Dave Anderson for their help.

## REFERENCES

1. T.J. Reinhart, *Engineered Materials Handbook, Vol. 1, Composites Materials* (ASM International, 1987).
2. B.M. Novak, *Adv. Mater.* **5,** 422 (1993).
3. R.F. Ziolo, E.P. Giannelis, B.A. Weinstein, M.P. O'Horo, B.N. Granguly, V. Mehrot, M.W. Russell, D.R. Huffman, *Science* **257,** 219 (1992).
4. W.D. Nesse, *Introduction to Mineralogy,* (Oxford University Press, Oxford, 2000) p. 235.
5. E.P. Giannelis, *Adv. Mater.* **8** (1), 29 (1996).
6. P.C. LeBaron, Z. Wang, T. J. Pinnavaia, *Applied Clay Science* **15,** 11 (1999).
7. J.W. Gilman, *Applied Clay Science* **15,** 31 (1999).
8. M. Alexandre, P. Dubois, *Materials Science and Engineering* **28,** 1 (2000).
9. X. Kornmann, H. Lindberg, L.A. Berglund, *Polymer* **42,** 1303 (2001).
10. T. Lan, P.D. Kavirayna, T.J. Pinnavaia, *J. Phys. Chem. Solids* **57,** 1005 (1996).
11. P.B. Messermith, E.P. Giannelis, *Mater. Chem.* **6,** 1719 (2001).

Mat. Res. Soc. Symp. Proc. Vol. 703 © 2002 Materials Research Society V1.5

# Molecular Engineered Porous Nanocomposites of Metal Oxide and Clay Using Surfactants

Huai Y. Zhu and Gao. Q. Lu*
NanoMaterials Centre and Department of Chemical Engineering, The University of Queensland
St Lucia Qld 4072 Australia

## ABSTRACT

A novel synthesis route of metal oxide nanoparticles dispersed in a silicate framework is reported here. This composite nanostructure is highly thermally stable and porous, rendering large surface area and rich surface chemistry promising for catalytic applications. Aqueous solutions of metal salts were used as the precursors of the nanoparticles, and added in an aqueous dispersion of synthetic clay, laponite, in which the clay exists in exfoliated silicate sheets. Acid leaching of the clay sheets occurs in the reaction due to the strong acidity of the metal salt solution. Meanwhile, the metal hydrate ions polymerise because of the high pH of the clay dispersion and condense on the leached silicates. This mechanism is distinctly different from conventional pillaring process. The nanocomposites of various oxides and binary oxides were synthesised. By introducing polyethylene oxide surfactants, we obtained mesoporous nanocomposites with very large surface areas (400 –900 $m^2/g$) and porosity. These nanocomposites are superior catalysts or catalyst supports over of microporous pillared clays [1-3] due to their structure and surface properties.

## INTRODUCTION

The nanoparticles of transition metal oxides, in several nanometers range, are very attractive materials for uses in catalysis, because these nanoparticles often exhibit superior properties and performance due to their large specific surface area. However, agglomeration of ultra-fine particles adversely affects their performance, and recovering such catalysts is difficult. These problems seriously limit their applications. A feasible approach is to disperse nanoparticles of metal oxide within an inorganic media, such as layered clays, meanwhile maintaining most of the surface of metal oxides accessible to reactant molecules. This approach is similar, in some aspects, to the synthesis of pillared layered clays developed in late 1970s [1-2].

It is well known that hydrate cations of many metal elements exist stably in acidic environment. If the pH increases, the metal hydrate ions hydrolyze, forming polymerized hydroxyl ions (oligomers), and finally precipitates [4]. Actually, there are layered clays, which can form well-dispersed suspensions at high pH values. For instance, laponite, synthetic clay that is iso-structural with the smectite clays, has a pH between 9.5 and 10. This pH is effective for inducing hydrolysis of various metal ions. The clay platelets are small, about 20-30 nm in diameter. In a dilute aqueous dispersion the clay exists as discrete plates [5]. Therefore, laponite is an ideal inorganic medium to form nanometer-scale composite structures with various metal hydroxyl species. Aqueous solutions of metal hydroxyl species or positively charged sol particles (precursor solutions) can be readily obtained from inorganic salts. The development of pillared layered clays has provided very useful knowledge on the precursor solutions [1]. The structures

of various oligomers in precursor solutions have been comprehensively studied [6,7]. In many cases, the pillaring solutions for the synthesis of pillared layered clays can be used for the synthesis of nanocomposites.

## EXPERIMENTAL DETAILS

A general procedure for synthesis of metal oxide nanoparticles in clays is as follows: Laponite clay was dispersed into water in a designed ratio to form a clear dispersion. A certain amount of a polyethylene oxide (PEO) surfactants of small molecular weights, with a general chemical formula $C_{12\text{-}14}H_{25\text{-}29}O(CH_2CH_2O)_nH$ ($n$ = 5-12), was added into the laponite dispersion which then became opaque. The suspension was stirred for 2 hours to allow sufficient mixing. To this mixture, an aqueous solution of metal ions was added drop-wise with continuous stirring. Some solutions of metal ions were obtained following the method for preparing corresponding pillaring solutions. The pH was controlled at 3-5. For instance a solution containing zirconium hydroxyl oligomers can be readily prepared by reflux a $ZrOCl_2$ solution. After a stirring of 2 hour, the mixed suspension was maintained at 373K for two days. The precipitate was recovered from the mixture by centrifuging and washed with deionized water. The wet cake was dried in air and calcined at 773 K for 20 hours. The hydrolyzed metal hydroxyl species are converted to oxide particles of several nanometers, and porous nanocomposite structures of metal oxide and silicate are obtained.

## RESULTS AND DISCUSSION

We found that the porosity of the nanocomposite can be significantly increased by introducing polyethylene oxide (PEO) surfactants of small molecular weights. These surfactants have strong affinities to the surfaces of clay and metal hydrates. Therefore, they have a function of separating the hydrolyzed species of metal elements, preventing them from further agglomeration and sintering during the drying and heating processes. It is known that in the templated synthesis the pore size of the product is proportional to the molecular size of the surfactant [8-10]. But there is no such a trend observed in this study. The molecular size of the surfactant is not a sole determinant of the pore size of the product solids. During heating the surfactant volatilizes, leaving a rigid structure with high porosity. The BET specific surface area and porosity data of some nanocomposite samples are given in Table 1.

These oxide nanocomposites exhibit much larger surface areas and pore volumes, compared to pillared layered clays (pore volume of 0.15-0.40 $cm^3/g$ and the BET surface area 150-400 $m^2/g$). The pillared layered clays are microporous solids (pore size below 2 nm) with a moderate porosity, while the nanocomposites are mesoporous solids. The structures of these two classes of solids are also profoundly different. The TEM images of the pristine laponite and three nanocomposites (as representatives) are given in Fig 1.

**Table I.** BET specific surface area and pore volume of metal oxide nanocomposite samples.

| **Samples prepared w/surfactant** | | | **Samples prepared w/o surfactant** | | |
|---|---|---|---|---|---|
| Metal oxide | BET S.A. ($m^2/g$) | Vp ($cm^3/g$) | Metal oxide | BET S.A. ($m^2/g$) | Vp ($cm^3/g$) |
| $Al_2O_3$- | 542 | 0.709 | $Al_2O_3$- | 278 | 0.233 |
| $Al_2O_3/La_2O_3$- | 587 | 0.676 | $Al_2O_3/La_2O_3$- | 439 | 0.383 |
| $Al_2O_3/CeO_2$- | 599 | 0.775 | $Al_2O_3/CeO_2$- | 422 | 0.345 |
| $ZrO_2$ | 459 | 0.430 | $ZrO_2$ | 248 | 0.146 |
| $ZrO_2/CeO_2$ | 611 | 0.676 | $ZrO_2/CeO_2$ | 291 | 0.185 |
| $TiO_2$- | 635 | 0.776 | $TiO_2$- | 343 | 0. 405 |
| $Cr_2O_3$- | 670 | 0.461 | $Cr_2O_3$- | 894 | 1.124 |
| $Fe_2O_3$- | 434 | 0.547 | $Fe_2O_3$- | 419 | 0.307 |

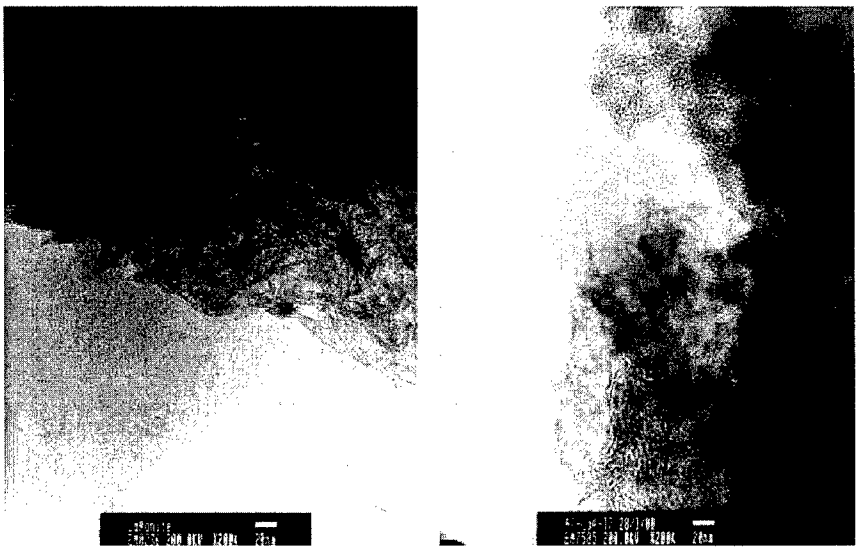

**(a)** **(b)**

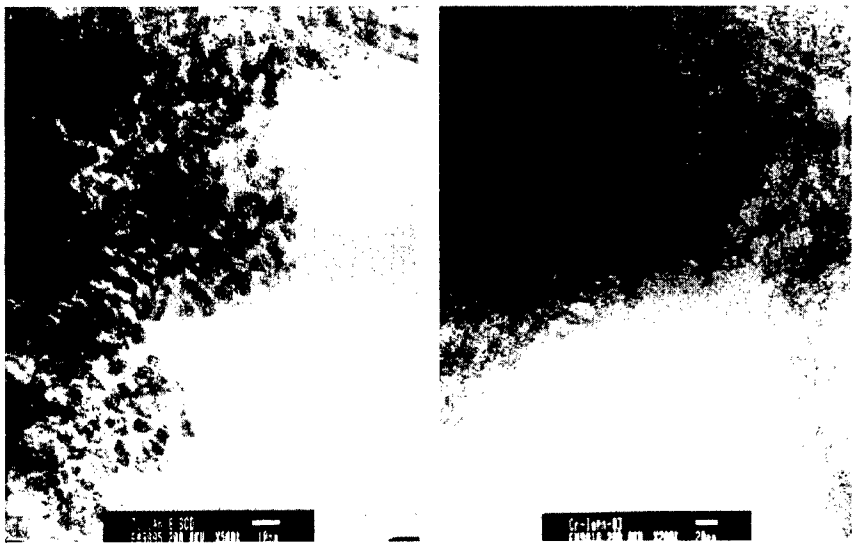

(c) (d)

**Figure 1.** TEM images of laponite clay and the calcined metal oxide nanocomposite samples. **(a)** laponite (**b**) $Al_2O_3$-nanocomposite (**c**). $TiO_2$-nanocomposite and (**d**) a $Cr_2O_3$-nanocomposite with low $Cr_2O_3$ content. The scale bars in the images indicate 20 nm.

Bundles of several clay platelets can be seen in the image of pristine laponite in Fig 1a, which aggregate in a poor long-range order. For pillared clays, the clay layers were regarded as inert with respect to reaction and almost intact in term of chemical composition during the pillaring process. However, layered clays can react with various acids even at moderate conditions [11-13]. Acid leaching is regarded as an effective means to activate clays. The acid leaching could result in remarkable changes in composition and structure of the clay layers. The extent of the reaction varies substantially from clay to clay.

Fig 1b is the image of the sample prepared from a solution containing Keggin ions [1,2,7] $[Al_{13}O_4(OH)_{24}]^{7-}$, and the laponite dispersion, $Al_2O_3$-composite. In this solid, thin stringy structure of about 1 and 2 nm thickness are observed, which are singular and paired silicate platelets, respectively. It is noted that these platelets are entangled but with a separation in the nanometer range. This indicates that the platelets are intercalated with nanoparticles of alumina. The Keggin ion solution has a weak acidity (pH of 3.0-3.5), and there is no obvious acid leaching from the laponite platelets, according to the results of chemical composition of the sample (in Table 2). Substantial loss of magnesium that is in the clay layer is an indicative of the acid leaching. Thus, the laponite platelets remain intact, in terms of composition and framework structure. When a more acidic solution containing sol particles of titanium (IV) hydrate, was used, laponite platelets are obviously involved in reaction. Most of magnesium in the clay platelets was leached out (Table 2). The solids obtained after calcination at 500°C contains mainly silica and titanium dioxide. X-ray powder diffraction pattern (not shown) indicates that

$TiO_2$ exists in anatase phase and we can see the aggregation of crystallites with random orientations in Fig 1c. The size of the anatase crystallites can be estimated from domains of regular texture in the image, being about 3-9 nm. Neither the x-ray pattern nor TEM image indicate any crystal form of silica or silicate although silica accounts for over 50% of the sample mass. The silica in the samples is more likely amorphous as reaction product of the laponite clay. Similar behaviors were observed for other transition metal oxide nanocomposites. Energy dispersing x-ray spectroscopy (EDS) was used to analyze the chemical compositions at different regions over a sample. At least 5 regions were taken for one sample and the average region size was about 15 nm in diameter. We found no obvious difference from region to region and the overall composition of the sample was uniform, for all samples. This means that in these samples metal oxide particles homogeneously disperse in exfoliated silicate media.

**Table II**. Major chemical composition of the samples shown in Fig 1.

| Sample | $SiO_2$ | $Al_2O_3$ | MgO | $TiO_2$ | $Na_2O$ | $Fe_2O_3$ | $Cr_2O_3$ |
|---|---|---|---|---|---|---|---|
| | (%) | (%) | (%) | (%) | (%) | (%) | (%) |
| Laponite | 51.10 | 0.07 | 23.20 | -* | 2.51 | - | - |
| $Al_2O_3$-composite | 41.49 | 27.91 | 17.38 | - | - | 0.04 | - |
| $TiO_2$-composite | 55.30 | 0.12 | 0.19 | 43.90 | - | 0.02 | - |
| $Cr_2O_3$-composite | 79.87 | - | 6.13 | - | - | 0.60 | 0.03 |

* Not detectable.

The image in Fig 1d provides more information on the structure of the reaction product derived from laponite. This solid was obtained after reaction of laponite suspension with a solution containing chromium hydroxyl ions. In this particular case, only a small amount of $Cr_2O_3$ is left in the product solid ($Cr_2O_3$ content below 1 %), which contains about 80 wt% of silica and 6 wt% of MgO, meanwhile most of the Mg content in the original laponite has been leached out during the synthesis. This solid provides a clear picture of the residue from the original laponite after reaction. The structure of this solid is strikingly different from that of the original laponite. Mesopores ranging from 3-20 nm can be seen in the image. These irregular pores reveal that the laponite platelets were seriously attacked, not only at edges but also on the basal surface of the platelets (gallery access mechanism [13], leaving a porous framework of silica.

$^{29}Si$ magic angle spinning nuclear magnetic resonance ($^{29}Si$ MAS-NMR) of the samples (Fig 2) also indicates the different structure change in silicate platelets caused by the reaction. $^{29}Si$ MASNMR spectrum of laponite displays two resonance peaks at –90 and 80 ppm. Such chemical shifts are correlated to the $SiO_4$ tetrahedra linked with 3 and 2 other $SiO_4$ tetrahedra ($Q^3$ and $Q^2$ sites), respectively. This is expected for the structure of laponite clay layer [14-15]. In the clay layer most $SiO_4$ tetrahedra are linked to 3 other $SiO_4$ tetrahedra, being in $Q^3$ sites but the tetrahedra at the edges of the clay layers are linked to 2 other $SiO_4$ tetrahedra and thus form the $Q^2$ sites. The smaller amount of $Q^2$ sites, compared with that of $Q^3$ sites, is responsible for the low intensity of the peak at -80 ppm.

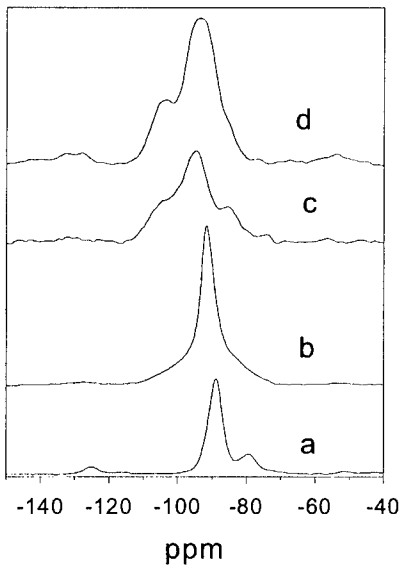


**Figure 2.** $^{29}$Si magic angle spinning nuclear magnetic resonance ($^{29}$Si MASNMR) of **a.** laponite clay; **b**, $Al_2O_3$-nanocomposite; **c**, $TiO_2$-nanocomposite; and **d**, $Cr_2O_3$-nanocomposite with low $Cr_2O_3$ content.

The chemical shifts for $Al_2O_3$-nanocomposite is similar to that of laponite, with a major resonance at –91.7 ppm. This means that the clay platelets remain almost intact during the reaction, being consistent with our observation in TEM image. The $TiO_2$-nanocomposite and $Cr_2O_3$- nanocomposite samples show substantially different MAS-NMR spectra. Broad resonance in the range from –110 to –80 ppm can be seen, reflecting poor short-range order. It also suggests a radical structure change of the silicate due to the reaction in the synthesis. The chemical shift at –104 ppm (a peak for $Cr_2O_3$-nanocomposite and a shoulder for $TiO_2$-nanocomposite) should be assigned to $Q^4$ sites where the $SiO_4$ tetrahedra linked with 4 other $SiO_4$ tetrahedra. In laponite clay structure there should be no $Q^4$ sites [16] and this is confirmed by the spectrum of the clay. Thus the $Q^4$ sites must have resulted from the profound structure changes of the silicate in the synthesis.

This evidence suggests that the clay layers could be seriously attacked if the acidity of the precursor solution is strong. On the other hand, the laponite dispersion with a high pH inevitably induces further hydrolysis of the metal hydroxyl oligomers in the precursor solution, forming larger species, the precursors of metal oxide nanoparticles. These large species most likely condense to the surrounding silicate platelets, because they carry opposite electric charges. This leads to a composite structure in which metal oxide particles of several nanometers in size are dispersed among the exfoliated silicate media.

According to this mechanism, it is possible to alter the particle size of the metal oxides by manipulating the acidity of the precursor solution. Indeed, as we increased the $H^+/Ti$ molar ratio of the precursor solution from 2.0 to 8.0, the mean size of anatase particle in the product $TiO_2$-composites increases from 3.7 to 9.0 nm. This finding is of importance, which allows us to effectively tailor the structure of these solids for various applications.

During last two decades, application of pillared clays as catalysts or catalyst supports for numerous chemical reactions has been attempted [3]. In general, better acidic characteristic, larger specific surface area, pore volume and pore size are required for catalysis purpose. As shown above, the properties of nanocomposites based on the above properties are remarkably superior to that of pillared clays and they are of great potential for these catalytic applications.

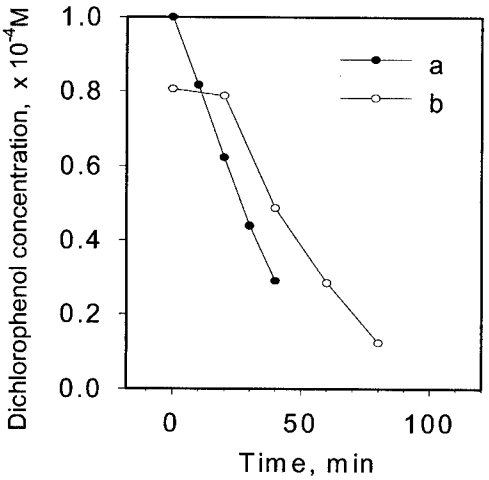


**Figure 3**. Catalytic performance of photocatalysts for photo-degradation of 2, 4-dichlorophenol. Curves **a** and **b** illustrate the performance of the ultra-fine $TiO_2$ powder P25 and a $TiO_2$-nanocomposite sample, respectively.

$TiO_2$-nanocomposite prepared in this study can be used as photocatalysts. It is well known that $TiO_2$ anatase nanoparticles are regarded as the best photo-catalysts for decomposing refractory organic pollutants in water and air [17-19]. The catalyst can be used for various processes such as odor elimination of drinking water, degradation of harmful organic contaminants, like herbicides, pesticides, refractive dyes, and oil spills in surface water systems. In Fig 3 catalytic performances for photo-degradation of 2, 4-dicholorophenol by a $TiO_2$-composite and P25, a commercial ultra-fine titanium dioxide powder supplied by Degussa, are compared. The overall photo-catalytic efficiency of the $TiO_2$-nanocomposite is comparable to that of P25, which is known to be the best commercial $TiO_2$ photo-catalyst and has a mean particles size of about 25 nm. The performance of the $TiO_2$-nanocomposite proves that most of the surface of $TiO_2$ crystals is accessible to the various molecules in solution. Furthermore, the $TiO_2$-nanocomposite contains about 45 % of $TiO_2$. Therefore, the activity per mass of $TiO_2$ for the $TiO_2$-nanocomposite is superior. Besides, it is very difficult to recover P25 powder from

water. This could leads to a potential difficulty in downstream separation. In contrast, the nanocomposite catalyst can be readily separated from aqueous solutions by settling and filtration. The silicate layers in the samples not only act as media allowing $TiO_2$ to disperse in nano-crystals but also link the distributed $TiO_2$ nano-crystals to large granules which can be recovered easily.

Besides, we also found that nickel catalysts supported on $ZrO_2$-nanocomposite result in high conversion rate for methane reforming with carbon dioxide. The catalyst maintains the high activity for over 180 hours (Fig 4), much longer than the catalyst supported activated $Al_2O_3$. The pore structure and surface nature of $ZrO_2$-nanocomposite can be tailored to obtain supports with higher surface area resulting in well-dispersed Ni catalysts. Carbon deposition on such catalysts was also suppressed due to the small nanoparticles of Ni metal well dispersed in the nanoporous support. The sintering deactivation is also reduced due to the excellent dispersion.

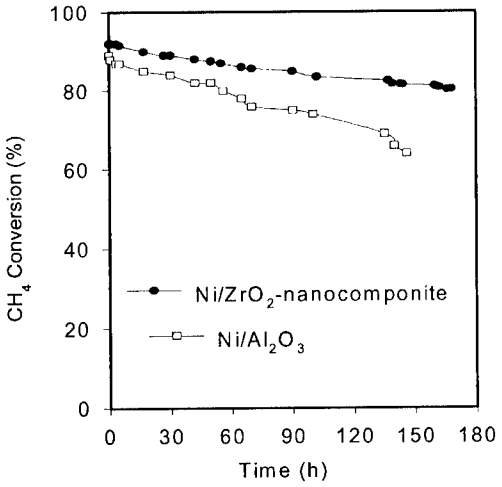


**Figure 4.** Performance of the nickel catalysts on a $ZrO_2$-nanocomposite and an activated alumina for methane reforming with carbon in a fixed bed reactor. The reaction conditions $CH_4/CO_2$ =1:1, $P$ = 1 atm and flow rate = 60 ml/min.

We also found very recently that $Fe_2O_3$-composite is an excellent catalyst for the photo-assisted Fenton degradation of azo-dye Orange II (Fig 5). This catalyst can significantly enhance the degradation of Orange II and has an excellent long-term stability. It is much cheaper than the Nafion-based catalysts used in Fenton reaction for water purification. It was also found that $H_2O_2$ molar concentration in solution, solution pH, UV light wavelength and power, and catalyst loading are the four main factors that can significantly influence the photo-assisted Fenton degradation of Orange II.

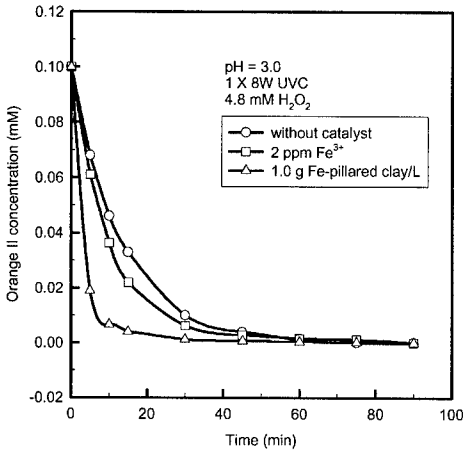


**Figure 5.** Orange II concentration as a function of irradiation time for systems without any catalyst, with 2 ppm $Fe^{3+}$ in solution, and with 1.0 g Fe-nanocomposite catalyst/L, respectively. The Orange II degradation is much faster in the presence of the Fe-nanocomposite catalyst than that without any catalyst.

## CONCLUSIONS

These findings in this work highlight the great potential of this novel synthesis of metal oxide nanocomposites as advanced catalytic materials. These solids can be readily granulated to designed shapes and the grains have good mechanical strength because of the presence of a silicate framework structure. Creating porous structures of transition metal oxides with large surface areas has attracted great research interest. Templated synthesis, invented in early 1990s for the synthesis of mesoporous silica or aluminosilicate [8,9] were also applied for this purpose. Successes have been achieved as various approaches, such as starting with metal alkoxides and conducting the synthesis in non-aqueous systems, were employed to overcome serious difficulties in the synthesis [20-22]. In comparison, the synthesis proposed in this study has a prominent advantage that it can be conducted in aqueous system at moderate conditions. Moreover, this synthesis utilises the reaction between the clay suspension and the oligomer solution to form composite nanostructure with assistance of PEO surfactant, being profoundly different from the synthesis of the well-known pillared clay materials. Actually, such a synthesis route is not limited to laponite, we have also prepared nanocomposites from natural layered clays such as saponite and hectorite. This new synthesis technique allows us to design and engineer composite nanostructures with desirable pore and surface properties.

## ACKNOWLEDGEMENTS

Financial Support from the Australian Research Council (ARC) and the University of Queensland are gratefully acknowledged. HYZ is indebted to Australian Research Council (ARC) for the QE II fellowship. The authors would like to thank Dr John Barry for his assistance in TEM imaging, and Dr Andrew Whittaker and Indriana Kartini for their assistance in NMR analysis. We also would like to thank Dr J-C. Zhao for providing data on photocatalytic degradation of dichlorophenol and Dr X. Hu for data on the Fenton reactions for Orange II removal.

## REFERENCES

1. R. Burch (Ed.), "*Pillared Clays*", *Catal Today*, Vol 2-3, (Elsevier, New York, 1988).
2. T.J. Pinnavaia, *Science*, **220**, 365-71 (1983).
3. A. Gil., L.M. Gandia, and M.A.Vicente, *Catal. Rev.* **42**(1/2) 145-212 (2000).
4. C.F. Baes and R.E. Mesmer, *The Hydrolysis of Cations*, (Wiley & Sons, New York, 1986).
5. D.W. Thompson and J.T. Butterworth, *J. Colloid Interface Sci.* **151**, 236-243 (1992).
6. K. Ohtsuka, Y. Hayashi and M. Suda, *Chem. Mater.* **5**, 1823-1829(1993).
7. R.A. Schoonheydt, H. Leeman, A. Scorpion, I. Lenotte and P. Grobet, *Clays Clay Miner.* **42**, 518-525(1994).
8. C.T. Kresge, M.E. Leonowicz, W.J. Roth, J.C. Vartuli and J.S. Beck, *Nature*, **359**, 710-712(1992)
9. S. Inagaki, Y. Fukushima, and K. Kuroda, *J. Chem. Soc. Chem. Commun.* 680-682. (1993).
10. Q. Huo, *et al*, *Nature*, **368**, 317-321(1994).
11. A. Corma, A. Mifsud, and E. Sanz, *Clay Miner.* **22**, 225-232(1987).
12. R. Mokaya and W. Jones, *J. Catal.* **153**, 76-85(1995).
13. H. Kaviratna and T.J. Pinnavaia, *Clays Clay Miner.* **42**, 717-723(1994).
14. M.A. Wilson, *NMR Techniques and Applications in Geochemistry and Soil Chemistry*. (Pergamon Press, Oxford, 1987)
15. S. Komarneni, C.A. Fyfe, G.J. Kennedy and H. Strobl, H. *J. Am. Ceram. Soc.* **69**, C45-C47 (1986).
16. A.C.D. Newman, *Chemistry of Clays and Clay Minerals*, (Mineralogical Society, Longman Sci & Tech., UK, 1987) p161.
17. G. Liu, X. Li, J. Zhao, H. Hidaka, and N. Serpone, *Environ. Sci. Technol.* **34**, 3982-3990(2000).
18. A. Fujishima, K. Hashimoto and T. Watanabe, *$TiO_2$ Photocatalysis Fundamentals and Applications*, (BKC, Inc., Tokyo. 1999) pp50-89.
19. A. L. Linsebigler, G.Q. Lu, and J.T. Yates, *Chem. Rev.* **95**, 735-758(1995).
20. D.M. Antonelli and J.Y. Ying, *Angew. Chem., Int. Ed. Engl.* **34**, 2014-2017(1995).
21. P. Yang, D.Y. Zhao, D.I. Margolese, B.F. Chmelka and G.D. Stucky, *Nature* **396**, 152-155(1998).
22. J.Y. Ying, C.P. Mehnert and M.S. Wong, Synthesis and applications of supramolecular-templated mesoporous materials. *Angew. Chem., Int. Ed,* **38**, 56-77 (1999).

Mat. Res. Soc. Symp. Proc. Vol. 703 © 2002 Materials Research Society V1.6

# Study of $NiFe/SiO_2$ Nanocomposites

S. Hui[1], Y.D. Zhang[1], T. D. Xiao[1], Mingzhong Wu[2], Shihui Ge[2], W. A. Hines[2], J. I. Budnick[2], M. J. Yacaman[3], and H. E. Troiani[4]
[1]Inframat Corporation, 74 Batterson Park Road, Farmington, CT 06032
[2]Physics Department and IMS, University of Connecticut, Storrs, CT 06269
[3]Department of Chemical Engineering, University of Texas, Austin, TX 78712
[4]CNM and Texas Materials Institute, University of Texas, Austin, TX 78712

## ABSTRACT

$(Ni_{75}Fe_{25})_v/(SiO_2)_{1-v}$ nanocomposites with v =0.5, 0.7, and 1.0, where 75 denotes the atomic percent of Ni in the Ni-Fe alloy phase and v denotes the volume fraction of the magnetic constituent in the composite, were synthesized using a wet chemical approach. The x-ray diffraction and TEM experiments show that the synthetic $NiFe/SiO_2$ is a two-phase composite system in that an amorphous insulating SiO2 layer coats each Ni-Fe particle. The Ni-Fe particle is in a fcc Ni-Fe alloy state. Its size can be controlled over a rather large range between 5 nm to 70 nm by adjusting the reaction parameters. Particular attention was paid to reduce the chemical reaction temperature so as to insure the smallness of the particle size. Meanwhile, measurements of the saturation magnetization indicated that the higher the heat treatment temperature, the more complete the chemical reaction to form the Ni-Fe alloys from precursor materials.

## INTRODUCTION

Magnetic nanocrystalline solids offer attractive properties for various applications such as the active component of ferrofluids [1], recording tapes [2], biomedical materials [3], separation techniques [4], as well as permanent magnets and soft magnetic materials [5-6]. Furthermore, nanocompositing opened new opportunities to develop novel magnetic materials [7]. Such materials provide great possibilities for the atomic engineering of materials with specific magnetic properties. Thin film nanocomposites with significantly improved high frequency properties have been developed based on the exchange coupling mechanism [8-9]. By coating magnetic nanoparticles with a second insulating phase, the following improvements could be achieved. Since the distribution of the two phases is homogenous on a nanometer scale, the aggregation of magnetic nanoparticles themselves is greatly limited. In this case, the magnetic materials can retain the nature of the nanocrystals. Therefore, the interaction of the magnetic particles could be adjusted and studied because the magnetic cores are kept at a well-defined distance. Coating the metallic magnetic nanoparticles prevents oxidation since the particles are extremely active and pyrophoric at ambient conditions. Coating with an insulating phase can improve the electrical resistivity of the magnetic materials. This maintains low eddy current losses for soft magnetic materials in high frequency applications. Coating also hinders the diffusion or the grain growth of metallic particles during the formation or sintering of the nanoparticles.

A wide variety of routes have been employed to synthesize magnetic nanocomposites, including sol-gel [10], sputtering [7], electrodeposition [11], high energy ball milling [12], microemulsion and reverse micelle techniques [13]. In order to dramatically increase the electric resistivity of metallic magnetic alloys while retaining their excellent soft magnetic properties (high saturation magnetization, high permeability, high Curie temperature, etc.),

$(Ni_{75}Fe_{25})_v/(SiO_2)_{1-v}$ nanocomposites were synthesized using a wet chemical approach. The magnetic properties of the nanoparticles were investigated for samples treated at different temperatures.

## EXPERIMENTAL

Nickel nitrate, iron nitrate, and tetraethoxysilane (TEOS) were used as received from Alfa Aesar. n-Ni-Fe/SiO2 nanocomposites were synthesized using a wet chemical solution technique, followed by oxidation and reduction under a controlled atmosphere at elevated temperatures. Starting materials were mixed in an organic solvent. The solvent is then removed by evaporation at elevated temperature. A further drying process is performed in an oven to obtain porous agglomerates. The agglomerates were then heated in an oxidizing atmosphere for a period of time. An this stage, impurity elements such as carbon, hydrogen, and nitrogen from the starting materials were burned out and the remaining materials precomposite of were nickel oxide, iron oxides, and silica. The precomposite powder was reduced at different temperatures in the range of 400-900 °C to form n-Ni-Fe/$SiO_2$ composites.

Thermogravimetric analysis (TGA) was conducted to determine the starting and finishing temperature for oxidation. Characterization of the crystal structure and particle size of the synthetic powder was carried out using x-ray diffraction (XRD) and high-resolution transmission electron microscopy (HRTEM). High-resolution transmission electron micrographs were obtained with a JEOL 4000 EX electron microscope. HRTEM specimens were prepared by dispersing the powders in methanol. Drops of this solution were then deposited on a carbon-grid and observed in the microscope. Bright field images, electron diffraction, and lattice images were carried out. The static magnetic properties of the synthetic powder were studied by using Quantum Design SQUID magnetometer at temperatures of 10 K and 300 K. Before the measurements, the samples were weighted accurately and then wrapped carefully in an adhesive tape.

## RESULTS AND DISCUSSION

In Figure 1 a typical TGA scan for the composite materials is presented. It can be seen in Figure1 that the unwanted organic start to burn-off at ~ 300 °C. However, a rather long time may be required to complete the oxidation and "clean" the precursor at this temperature. It appears that a higher temperature (*e.g.,* 500 °C) is necessary to complete the oxidation reactions.

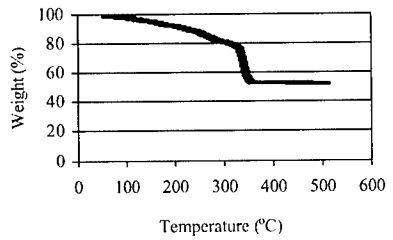


**Figure 1.** Weight change vs. temperature for precomposite powder of Ni-Fe/$SiO_2$ in oxygen.

Figure 2 shows the XRD patterns for the $(Ni_{75}Fe_{25})_{0.7}/(SiO_2)_{0.3}$ samples that were obtained by reducing the precursor in $H_2$ for 3 hours at various temperatures. For a comparison, the figure also includes the XRD pattern of a bulk-size Ni-Fe alloy sample. The results indicate that all of the synthetic $(Ni_{75}Fe_{25})_{0.7}/(SiO_2)_{0.3}$ samples have the face-centered cubic (fcc) structure. As shown in Figure 2, the linewidth of the diffraction peaks for the $(Ni_{75}Fe_{25})_{0.7}/(SiO_2)_{0.3}$ samples were significantly broader than that for the bulk Ni-Fe alloy sample, and highly dependent on the reduction temperature.

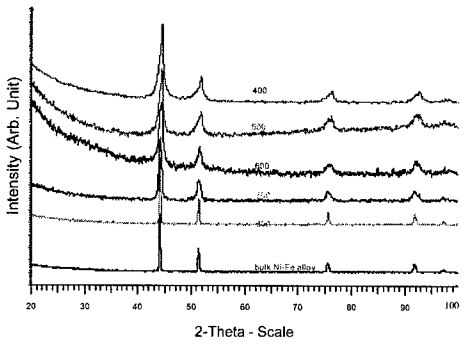


**Figure 2.** XRD pattern for bulk Ni-Fe alloy and n-$(Ni_{75}Fe_{25})_{0.7}/(SiO_2)_{0.3}$ samples prepared at different reduction temperatures (in degree C).

The particle size for nanostructured materials calculated from the Scherrer equation. Figure 3 shows the particle size of the synthetic $(Ni_{75}Fe_{25})_{0.7}/(SiO_2)_{0.3}$ as a function of the hydrogen reduction temperature. It reveals that when the reduction temperature is 700 °C or below, the particle size remains small (< 20 nm) with little change with reduction temperature. However, the size increases significantly with $H_2$ reduction temperatures beyond 700 °C.

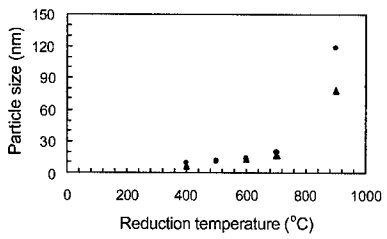


**Figure 3.** Variation of Ni-Fe particle size with reduction temperature in hydrogen: circles, $(Ni_{75}Fe_{25})_{0.7}/(SiO_2)_{0.3}$; triangles, $(Ni_{75}Fe_{25})_{0.5}/(SiO_2)_{0.5}$.

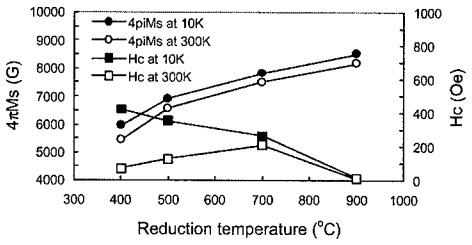


**Figure 4.** Magnetization and coercivity as a function of $H_2$ reduction temperature for n-$(Ni_{75}Fe_{25})_{0.7}/(SiO_2)_{0.3}$.

The static magnetic properties of n-$(Ni_{75}Fe_{25})_{0.7}/(SiO_2)_{0.3}$ are summarized in Figure 4 which shows the saturation magnetization and coercivity as a function of the $H_2$ reduction temperature for $(Ni_{75}Fe_{25})_{0.7}/(SiO_2)_{0.3}$ measured at 10 K and 300 K. The saturation magnetization of the bulk $Ni_{75}Fe_{25}$ alloy is 12000 G, which translates to the saturation magnetization of 8000 G for $(Ni_{75}Fe_{25})_{0.7}/(SiO_2)_{0.3}$ nanocomposite presuming the electronic as well as magnetic structure for the Ni-Fe nanoparticle is essentially the same as those for the bulk Ni-Fe alloy. It can be seen from Figure 4 that for the powder reduced at 900 °C, the saturation magnetization is actually 8600 G. This is due to the composition deviation in that the actual volume fraction of the Ni-Fe magnetic phase may be slightly greater than 0.7. By reducing at 700 °C, a saturation of 8000 G is obtained, which is 93% of the saturation magnetization. This indicates that the reduction temperature can be set to 700 °C at which the reduction process is essentially completed while the Ni-Fe particle size remains less than 20 nm. From Figure 4, it also can be seen that at low temperature the coercivity decreases with increasing reduction temperature, while at room temperature the coercivity increases as the reduction temperature increases from 400 °C to 700 °C. This is probably because some Ni-Fe particles in the nanocomposite reduced at 400 °C and 500 °C have small size due to lower reduction temperature and exhibit superparamagnetic behavior at room temperature.

Figure 5 shows the XRD diffraction patterns for the n-$(Ni_{75}Fe_{25})_{0.5}/(SiO_2)_{0.5}$ powders, which are the same as shown in Figure 2. The particle size dependence on the reduction temperature for n-$(Ni_{75}Fe_{25})_{0.5}/(SiO_2)_{0.5}$ is shown in Figure 3. It is clear that the thicker the $SiO_2$ coating, the smaller the Ni-Fe particle size obtained in the same reduction process.

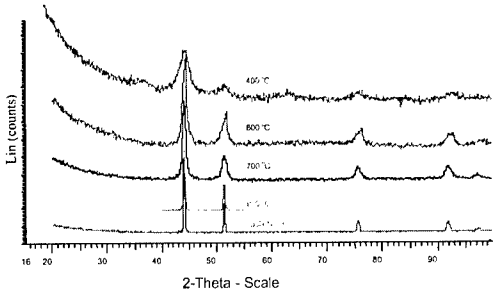


**Figure 5.** XRD pattern for n-$(Ni_{75}Fe_{25})_{0.5}/(SiO_2)_{0.5}$ and bulk Ni-Fe alloy.

In Figure 6 a typical TEM image is presented which shows the morphology for n-$(Ni_{75}Fe_{25})_{0.5}/(SiO_2)_{0.5}$ sample which was heat-treated in hydrogen at 700 °C. This image shows that all of the particles are embedded in an amorphous media different from the amorphous carbon of the support grid. The image in Figure 7 shows a typical particle size distribution for a portion of the sample. The width of the distribution is approximately 15 nm and it shows a peak centered around 15.5 nm, which is consistent with the size calculated from XRD. The particle range is between 5 and 30 nm, which is a relative large distribution in size. For this histogram, 31 particles were counted and analyzed. The typical length in the figure is an average between the maximum and minimum lateral dimensions measured from the TEM image.

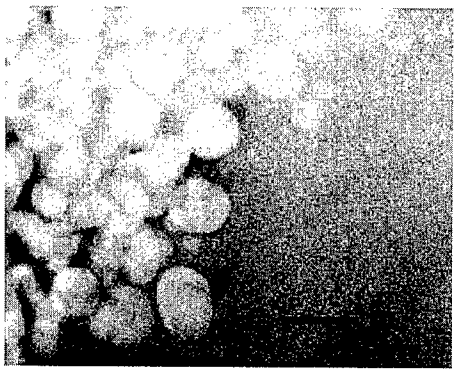

**Figure 6.** TEM image for the n-$(Ni_{75}Fe_{25})_{0.5}/(SiO_2)_{0.5}$ sample heat-treated in hydrogen at 700 °C. The bar in the figure corresponds to 100 nm.

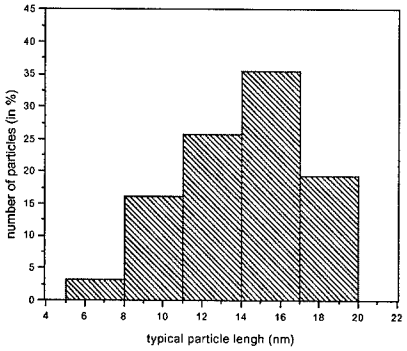


**Figure 7.** Particle size distribution from TEM study for n-$(Ni_{75}Fe_{25})_{0.5}/(SiO_2)_{0.5}$.

Figure 8 shows the variation of the saturation magnetization and coercivity as a function of reduction temperature in hydrogen. By reducing at 700 °C, a saturation magnetization of 5303 G was obtained. This corresponds to an 84% completion of the chemical reaction. It also can be seen from Figure 8 that, at both 10 K and 300 K, the coercivity decreases when the reduction temperature increases from 600 °C to 900 °C. However, for the nanocomposite reduced at 400 °C, the coercivities measured at 10 K and 300 K are quite different from each other. This may result from the superparamagnetic behavior of small size particles due to the low reduction temperature.

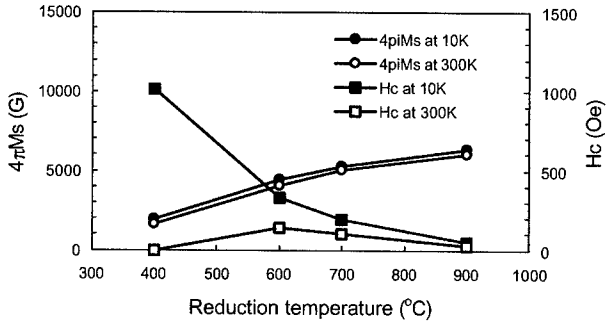


**Figure 8.** Magnetization and coercivity as a function of reduction temperature in hydrogen for n-$(Ni_{75}Fe_{25})_{0.5}/(SiO_2)_{0.5}$

An interesting result was observed on the $Ni_{75}Fe_{25}$ nanoparticle without a $SiO_2$ coating. The powder was synthesized using the same chemical route without adding tetraethoxysilane in the starting raw materials. While the powder reduced at 700 °C possesses essentially bulk size (micrometer size), that reduced at 400 °C possesses a mean particle size of only 18.5 nm. For $Ni_{75}Fe_{25}$ powder samples obtained by $H_2$ reduction at 400 °C and 700 °C respectively, the saturation magnetization for the two samples are the same, indicating that the chemical reaction can be completed at temperatures as low as 400 °C without the existence of $SiO_2$.

## CONCLUSIONS

$(Ni_{75}Fe_{25})_v/(SiO_2)_{1-v}$ (v = 0.5, 0.7) nanocomposites and nanostructured $Ni_{75}Fe_{25}$ alloys have been successfully synthesized using a wet chemical approach. The XRD and TEM studies show that the synthetic Ni-Fe/$SiO_2$ is a two-phase composite system in that the Ni-Fe particles are embedded in a common amorphous insulating $SiO_2$ matrix. The Ni-Fe particle is in a fcc Ni-Fe alloy state. Its size can be controlled in a rather large range between 5 nm to 70 nm by adjusting the reaction parameters. Measurements of saturation magnetization indicate that the higher the heat treatment temperature, the more complete the chemical reaction to form the Ni-Fe alloys from the precursor materials.

## ACKNOWLEDGMENTS

The work is supported by NASA Contract No. NAS3-01013.

## REFERENCES

1. A.P. Philipse, P.B. van Bruggen, and C. Pathmamanoharan, Langmuir **10**, 92-99 (1994).
2. K.O. Grady and H. Laidler, J. Magn. Magn. Mater. **200**, 616-633 (1999).
3. Q. Liu, Z. Xu, J.A. Finch, and R. Egerton, Chem. Mater. **10**, 3936-940 (1998).
4. L. Nixon, C.A. Koval, R.D. Noble, and G.S. Slaff, Chem. Mater. **4**, 117-121 (1992).
5. G.C. Hadjipanayis, WTEC Workshop Rep. R&D Status Trends Nanopart., Nanostruct. Mater., Nanodevices U. S., Proc., Meeting Date 1997 (International Technology Research Institute, Baltimore, Md, 1998), p. 107-112.
6. H. Fukunaga, Nippon Oyo Jiki Gakkaishi **19**(4), 791-6 (1995).
7. G.C. Hadjipanayis and G.A. Prinz, Science and Technology of Nanostructures Magnetic Materials (Plunum Press, New York, 1991).p.477.
8. Y. Hayakawa, A. Makino, H. Fujimori, and A. Inoue, J. Appl. Phys. **81**, 3747 (1997).
9. H. Fujimori, Sripta Met. Mat. **33**, 1625 (1995).
10. (a) G.M. Chow and K.E. Gonsalves, Novel Tech. Synth. Process. Adv. Mater., Proc. Symp. (1994), 155-63. Editor(s): J. Singh and S.M. Copley, Minerals, Metals & Materials Society, Warrendale, Pa.; (b) R. Monaci, A. Musinu, G. Piccaluga, G. Pinna, Mater. Sci. Forum (1995), 195 (Nanophase Materials), 1-6; (c) D. Niznansky, N. Viart, and J.L. Rehspringer, J. Sol-Gel Sci. Tech. **8**, 615-618 (1997).
11. R.D. Shull and L.H. Bennett, Nanostruct. Mater. **1**, 83-88 (1992).
12. (a) A.K. Giri, C. de Julian, J.M. Gonzalez, J. Appl. Phys. **76**(10, Pt. 2), 6573-5 (1994); (b) M. Pardavi-Horvath and L. Takacs, IEEE Trans. Magn. **28**, 3186-3188 (1992).
13. (a) S. Chang, L. Liu, and S.A. Asher, J. Am. Chem. Soc. **116**, 6739 (1994); (b) **116**, 6745 (1994).

Mat. Res. Soc. Symp. Proc. Vol. 703 © 2002 Materials Research Society V1.8

# Novel Synthesis of Aluminium Oxide Nanofibers

Huai. Y. Zhu and Gao. Q. Lu*

Nanomaterials Centre and Department of Chemical Engineering, The University of Queensland, Brisbane, 4072 Australia

## ABSTRACT

This report presents a novel synthesis method of alumina nanofibers at moderate conditions in aqueous systems through a surfactant-directed crystal growth process. In the presence of polyethylene oxide (PEO) surfactants, boehmite nanofibers of about 3 nm thick and 30-60 nm long formed from aluminium hydrate colloids. During the subsequent heating, the surfactant was evaporated and boehmite nanofibers were converted into γ-alumina nanofibers. The function of the PEO surfactant and the formation mechanism of the nanofibers are discussed. Alumina nanofibers are an ideal structural reinforcement for various nanocomposite materials. They are potential adsorbents with high adsorption capacity. Furthermore, their unique structure exhibits strong resistance to heating at high temperatures. The BET surface area of a typical sample after heating at 1200°C is as high as 68 $m^2/g$. This makes the material very promising as excellent substrates for catalysts of high thermal stability.

## INTRODUCTION

In recent years, nanomaterials have attracted great attention from academe and industry because of their superior properties and their potential for a wide range of applications. Surfactants have been widely used as templates in developing uniform mesoporous structure at a scale of several nano-meters [1-3]. The concept of surfactant templating was also applied to the synthesis of mesoporous alumina molecular sieves, because activated alumina is extensively used as industrial adsorbents, catalysts and catalyst supports [4]. Successes were achieved by using neutral surfactants [5,6)] or carboxylic acids [7], as templates and aluminium alkoxide as the alumina precursor. It would be of great interest to construct alumina nano-structures of other geometry (morphology). The alumina with other geometry in nano-meter level, for instance, nano-fibers, could be important advanced engineering materials. The unique aspect ratio of nano-fibers can lead to a wide range of applications in advanced ceramics, electronic, adsorption, and catalysis etc. Here we report the first synthesis of alumina nanofibers with very large porosity from inorganic salts with non-ionic polyethylene oxide (PEO) surfactants. In such a synthesis, the surfactant micelles induce important changes in morphology and growth of the nano-sized crystallite, rather than acting as templates for gel particles to condense around them. The formation mechanism of alumina nanofibers is distinctly different from the templating mechanism as observed in M41S synthesis. This new mechanism could constitute a new strategy of nano-structuring inorganic solids.

## EXPERIMENTAL

The PEO surfactant, with a general chemical formula $C_{12\text{-}14}H_{25\text{-}29}O(CH_2CH_2O)_nH$ (n = 5-30) was mixed with aluminium hydrate cake prepared from common inorganic salts like $NaAlO_2$, in a designed molar ratio of surfactant to aluminium (PEO/Al ratio). Details of synthesis can be

found in [8]. Boehmite (AlOOH) crystallite grows during a hydrothermal treatment at 100°C. The PEO surfactant introduced prior to the treatment can affect the crystalline growth. The hydrothermally treated samples were dried in air and calcined subsequently at 500°C. The calcination converted nano-crystallite boehmite to γ-alumina. A significant difference in crystal morphology can be observed by transmission electron microscopy (TEM). In Fig. 1, the TEM image of γ-alumina prepared with the PEO surfactant (Fig 1a) is compared with that of the γ-alumina prepared without the surfactant (Fig 1b).

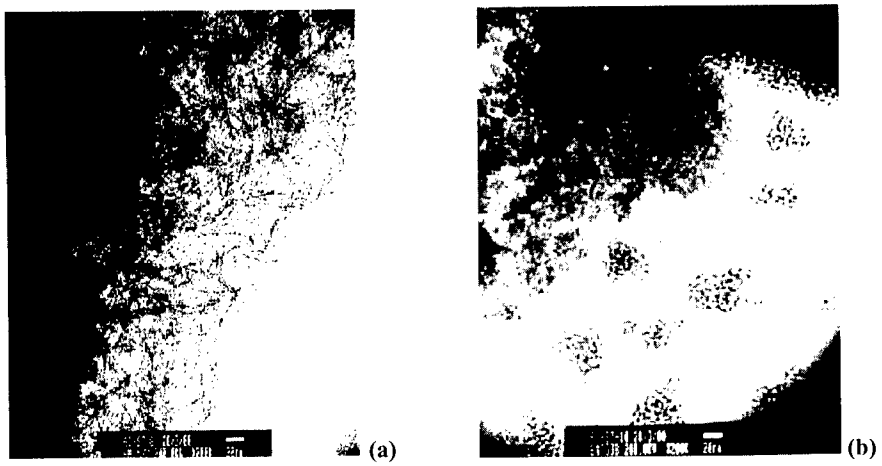


**Figure 1.** TEM images of (**a**) γ-alumina prepared with a PEO/Al ratio of 0.47, (**b**) γ-alumina prepared at the same conditions but without PEO surfactant. Nanofibers can be seen in (**a**) the sample prepared with PEO surfactant. The scale-bar is 20 nm.

## RESULTS AND DISCUSSION

The nanocrystallites in Fig 1a are nanofibers with a length over 60 nm, and a constant thickness of about 3 nm. In contrast, γ-alumina particles prepared without PEO addition as in Fig. 1b show irregular shapes. Evidently, introducing PEO surfactant results in the formation of alumina nano-crystallite with a fibrous morphology. It is postulated that boehmite nanofibers first formed from aluminium hydrate at a moderate hydrothermal condition. In the subsequent heating at 500°C, the surfactant was removed and boehmite is converted into γ-alumina, whilst the fibrous morphology was retained as shown in Fig 1a. However, the XRD patterns for the samples in Fig 1a and 1b are almost identical (Fig 2).

The random stacking of the alumina nanofibers (Fig 1a) results in a highly porous texture, as reflected by the nitrogen adsorption isotherms in Fig 3. It is known that nitrogen adsorption by a solid strongly depends on its porosity [9]. The alumina prepared without PEO adsorbed nitrogen at 77 K slightly over 300 $cm^3/g$ STP, whereas the sample prepared in the presence of PEO adsorbed as much as 1050 $cm^3/g$ STP. The extraordinarily large adsorption capacity indicates very large pore volumes in the samples prepared with PEO. The pore volume should be attributed to the inter-crystallite voids of the randomly stacked alumina nanofibers. An

important feature of the nanofiber structure is that it exhibits significant resistance to heating at high temperatures. The data of BET specific surface area and porosity of the samples calcined at three temperatures are given in Table 1.

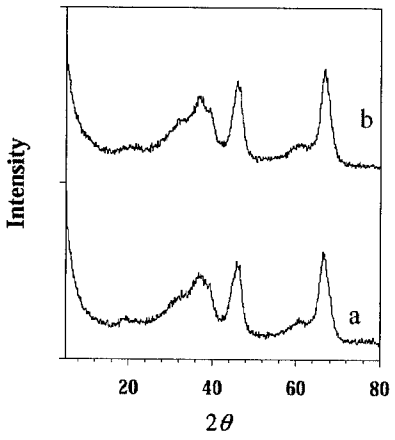


**Figure 2.** XRD patterns of γ-alumina. Patterns **a** and **b** are for samples **a** and b in Fig 1, respectively. The two patterns are almost identical

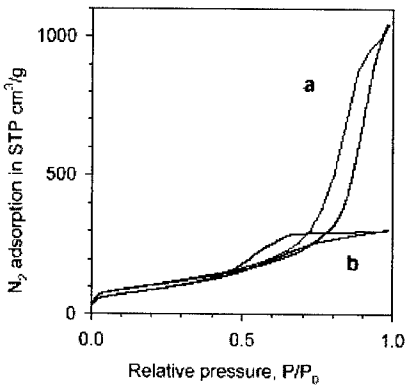


**Figure 3.** Nitrogen ads/desorption isotherms of the samples in Figure 1. For the sample prepared with PEO surfactant a steep increase in adsorption commences from a $P/P_0$ of about 0.7 (curve **a**), indicating a huge mesopore volume, whereas for sample b (w/o PEO) the adsorption capacity is low.

**Table I.** Surface area, mean pore radius and pore volume of alumina samples.

| PEO/Al ratio | BET S.A. ($m^2/g$) | Mean R (nm) | Pore volume ($cm^3/g$) |
|---|---|---|---|
| **After calcination at 500°C** | | | |
| 0 | 321.6 | 5.9 | 0.471 |
| 0.24 | 360.0 | 15.7 | 1.409 |
| 0.47 | 376.2 | 17.1 | 1.616 |
| 0.95 | 347.4 | 22.4 | 1.946 |
| 1.95 | 373.1 | 12.7 | 1.185 |
| **After calcination at 900°C** | | | |
| 0 | 154.2 | 7.2 | 0.433 |
| 0.24 | 179.4 | 15.5 | 1.131 |
| 0.47 | 198.7 | 15.5 | 1.406 |
| 0.95 | 189.3 | 21.8 | 1.545 |
| 1.95 | 183.9 | 15.5 | 1.129 |
| **After calcination at 1200°C** | | | |
| 0 | 4.6 | 10.5 | 0.032 |
| 0.24 | 13.4 | 11.4 | 0.077 |
| 0.47 | 48.6 | 16.0 | 0.391 |
| 0.95 | 50.2 | 16.1 | 0.404 |
| 1.95 | 43.4 | 15.3 | 0.333 |

To understand the function of the PEO surfactant, the weight loss of the dried sample as temperature increases from room temperature to 800°C was measured by thermogravimetric analysis (TGA). The main weight loss for the sample prepared without PEO is below 150°C, mainly due to dehydration, whereas for the samples prepared with PEO the greatest weight loss is observed between 200-300°C, due to volatilization. If heating was carried out in a nitrogen flow that passes a cooling trap, the surfactant could be readily recovered for reuse. This is an important merit in regard to environmentally friendliness and costs of the synthesis process. We also found that the pore volume (obtained from $N_2$ adsorption) is proportional to the weight loss. This suggests that the surfactant molecules were located in the inter-crystallite voids before the calcination step. The surfactant evaporates during heating, leaving a large number of mesopores in the sample. Because the pore size is far beyond the molecular size of the surfactant, the surfactant should have existed in the forms of micelles rather than in single molecule. A number of studies have also shown that PEO surfactants exist in rod-like or worm-like micelles in aqueous solutions [10-13]. It was reported that introducing polymer molecules of large molecular weight ($10^4$ to $10^6$) increased the porosity of activated alumina [14]. However, the additives, such as polyalcohols and cellulose, were simply regarded as space fillers in that work. The affinity of the additives to aluminium hydroxide surfaces was ignored. It is known that the conversion of boehmite to γ-alumina mostly takes place at above 300°C and the PEO surfactants evaporate at lower temperatures than this temperature. Because the nano-fiber morphology resulted from the presence of PEO surfactant, the surfactant-boehmite interaction should be the main force inducing the oriented growth to form nano-fiber crystallites. This morphology was retained even after the surfactant removal.

For the dried samples prepared with surfactant, a XRD peak of the greatest intensity at $2\theta$ = 20.8°, corresponding to d = 4.3Å, is observed (curve c in Fig 4), whilst the rest peaks are well matched with the pattern. This peak is believed to be due to the oxide groups of the surfactants because we found the intensity of this peak is proportional to the number of oxide groups in the surfactant. For the same surfactant used, the intensity of this peak is proportional to the surfactant amount in the dried samples, and if various PEO surfactants were introduced by the same amount, this increases with n, the number of oxide groups in a surfactant molecule. Indeed, a strong peak is also found in the XRD pattern of the pristine surfactant liquid at room temperature at a lower angle, $2\theta$ = 18.6 (Fig 4d), corresponding to d = 4.8Å. The comparison of XRD patterns for the same surfactant in different states, solid, partial melted, in mixture of boehmite and surfactant (in Fig 4), suggests that the surfactant in boehmite is in an intermediate state, with more close packing than that in pristine liquid. This can only be due to the interaction of the surfactant micelles with the boehmite crystallite surfaces. In liquid phase the alkyl chains of PEO surfactants prefer to stack close to each other, and so do their oxide groups, forming micelles. When the surfactant is dispersed in a polar media, such as in aqueous systems or polar surfaces, the oxide groups would form the outer surface of the micelles, being in contact with the polar media [10-12], in this case, the surface of boehmite crystallites. The shift in the diffraction peak to a lower angle is indicative of the interaction between oxide groups of the surfactants and the surface of boehmite crystallites. This hydrogen bonding seems not sufficiently strong to alter the intrinsic structure of boehmite crystallites, but could lead to changes in the stacking of oxide groups in the surfactants because the stacking of the surfactant molecules is more flexible. More importantly, this close bonding combined with the regular stacking of the PEO surfactant, regulates the growth of the boehmite crystallites to a certain direction during aging. This is the

fundamental mechanism underlying the oriented growth of alumina nano-fibers, which we term as surfactant-directed oriented growth (SDOG).

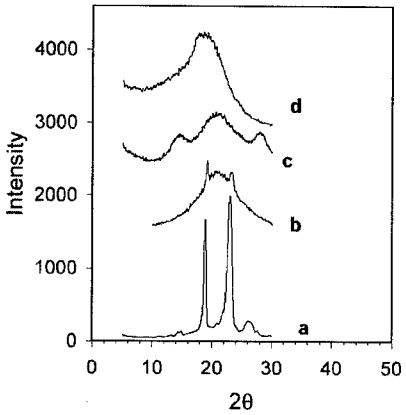


**Figure 4.** XRD patterns of a PEO surfactant in various states. **a** pure solid, b, partial melt, **c** in boehmite and **d** pure liquid.

The proposed SDOG process is schematically illustrated in Fig 5a. The structure of boehmite crystallite is given in Fig 5b. The corrugated layers of boehmite nano-crystallite are linked by hydrogen bonds. The surfactant micelles should take the configuration that the oxide chains linking to the surface of boehmite crystallite, while the alkyl chains point away from the surface (Fig 5b). The layered aggregates of boehmite crystallites are thus intercalated with surfactant micelles. The hydrogen bonding between the oxide groups and the boehmite crystallite surface reduces the chemical potential of the system. The stacking of the oxides groups of the surfactant micelles on the boehmite crystallite surface is more closely packed than in the pristine surfactant liquid. Therefore, the surfactant micelles attain a maximum number of hydrogen bonds with the -OH groups on boehmite surfaces.

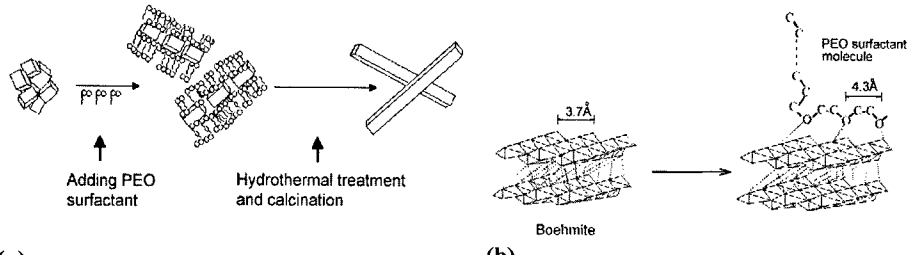


**Figure 5**. SDOG mechanism (**a**). boehmite in PEO surfactant, where PEO molecules form micelles of one dimension structure. The growth of boehmite crystals is regulated by the micelles through hydrogen bonding. During heating the boehmite nanofibers consolidate, and are converted to γ-alumina nano-s upon PEO removal. **b.** Boehmite corrugate structure and interaction with PEO molecules. The micelles are close packed on the surface of boehmite behaving as directing agents for the oriented growth of boehmite crystallite, thus inducing nano- morphology

High-temperature calcination may create acid sites with stronger acidity, which is more favorable for some catalytic reactions. We have found that Ni catalysts supported by our nano-alumina calcined at 900°C exhibit a superior performance for $NO_x$ reduction to catalysts supported on a commercial γ-alumina. Barium hexaaluminate (BHA) is reported to have high thermal stability above 1200°C, and it retained surface area of around 10 $m^2/g$ after heat treatments at 1200°C [16,17]. BHA has been used for catalytic combustion or steam reforming reaction. As a comparison, we simply impregnated the alumina nano- with $Ba(NO_3)_2$ solution and calcined the solid at 1200°C. The calcined catalyst still has a surface area of 35 $m^2/g$, which are a mixture of barium hexaaluminate and barium aluminate. This demonstrates that alumina nanofibers in this work are promising substrate for the synthesis of BHA catalysts.

## CONCLUSION

SDOG is a typical "synthesis with construction" mechanism [15], which is distinctly different from the conventional crystallization and the templated synthesis. The new strategy proposed in this work would be useful for low temperature, aqueous syntheses of oxides and other useful nano-structured ceramics and composites. It is expected that a comprehensive understanding of the SDOG mechanism will greatly assist us in developing new nanomaterials with desired morphology, tailorable size, porosity and surface chemistry.

## ACKNOWLEDGEMENTS

Financial Support from the Australian Research Council (ARC) and the University of Queensland's Strategic Funds are gratefully acknowledged. HYZ is also indebted to Australian Research Council (ARC) for the QE II fellowship. Thanks also to Dr. John Barry for TEM imaging and to Mr C. Lu and Ms X. Q. Yan for most of experimental data collection..

## REFERENCES

1. C. T. Kresge, M. E. Leonowicz, W. J. Roth, J. C. Vartuli, J. S.Beck, *Nature* **359,** 710 (1992).
2. S. Inagaki, Y. Fukushima, K. Kuroda, *J. Chem. Soc. Chem. Commun.* **680**, (1993).
3. Q. Huo, et al., *Nature* **368**, 317 (1994).
4. K. P. Goodboy, K. C. Dowing, in *Alumina Chemicals: Science and Technology Handbook*, Hart, L. D., Lense, E., Eds. (American Ceramic Society, Westervill, Ohio, 1990), p. 93.
5. P. Yang, D. Zhao, D. I. Margolese, B. F. Chmelka, G. D. Stucky, *Nature* **396**, 152 (1998).
6. S. A. Bagshaw, T. J. Pinnavaia, *Angew. Chem. Int. Ed. Engl.* **35**(10), 1102 (1996).
7. F. Vaudry, S. Khodabandeh, M. E. Davis, *Chem. Mater.* **8**, 1451 (1996).
8. H.Y. Zhu and G.Q. Lu, Patent WO 01/74713 A1, 11 Oct, 2001
9. S. J. Gregg, K. S. W. Sing, *Adsorption, Surface Area and Porosity* (Academic Press: New York, 1982).
10. P. G. Cummins, J. B. Hayter, J. Pemfold, E. Staples, Chem. *Phys. Lett.* **138**, 436 (1987).
11. P. G. Cummins, E. Staples, J. Pemfold, *Langmuir* **5**, 1195 (1989).
12. J. Pemfold, E. Staples, P. G. Cummins, *Adv. Colloid Interface Sci.* **34**, 451 (1991).
13. Z. Lin, L. E. Scriven, H. T. Davis, *Langmuir* **8**, 2200 (1992).
14. D. Basmadjian, N. Fulford, B. I. Parsons, D. S. Montgomery, *J Catal.* **1**, 547 (1962).
15. S. Mann, *Nature* **365**, 499 (1993).
16. G. Groppi, M. Bellotto, C. Cristiani, P. Forzatti, P. L. Villa, *Appl. Catal.* **104**, 101 (1993).
17. A. J. Zarur, J. Y. Ying, *Nature* **403**, 65 (2000).

# Nanostructures I

Mat. Res. Soc. Symp. Proc. Vol. 703 © 2002 Materials Research Society V2.1

## Self-Assembly of Metal Nanoclusters in Block Co-Polymers

Erica H. Tadd[1], John Bradley[1], Eugene P. Goldberg[2] and Rina Tannenbaum[1]*
[1]School of Materials Science and Engineering, Georgia Institute of Technology, Atlanta, GA 30332. [2]Department of Materials Science and Engineering, University of Florida, Gainesville, FL 32611.

## ABSTRACT

This paper describes the formation of cobalt and iron metal nanoclusters in various polymeric domains. The size of the particles, their size distribution and their geometry is controlled by the extent of the interfacial interactions between the polymeric phase and the growing metal fragments. Iron oxide particles are shown to exhibit various geometries as a function of the polymer medium and the temperature at which they are formed. The selective phase separation and particle confinement of cobalt clusters in the presence of $PS_{25300}$-b-$PMMA_{25900}$ block co-polymer was achieved due to the different reactivities of the functional groups in the blocks towards the metal fragments. Transmission electron micrographs showed that cobalt clusters aggregated primarily in the poly(methyl methacrylate) block, while no cobalt nanoclusters were observed in the polystyrene block, thus creating a patterned distribution that coincided with the morphology of the block copolymer.

## INTRODUCTION

Hierarchical materials are ordered on the molecular (10-100Å), nano (10nm-100nm) and meso (1μm-10μm) scales. This unique level of organization leads to specialized material properties that significantly differ from those of less ordered phases. However, optimal performance requires a degree of control over domain size and distribution, on all length-scales, which is not easily obtainable with current synthetic methods.

The development of a synthesis methodology to control the structure and properties of metallic nanocluster-polymeric composites requires detailed understanding of the interactions between the metal clusters and their polymeric environment, as well as the relationship between polymeric parameters and cluster formation. Although various studies have shown that polymers control cluster formation and properties [1-4], little is known regarding the details of this relationship. The large number of parameters (e.g. polymer molecular weight, chemistry and concentration) requires a systematic investigation. This paper describes the development of a *versatile and controllable* synthetic process for the formation of *three-dimensional, self-assembled nanoparticle arrays* in, and aided by, a *polymeric medium*. The development of appropriate synthetic and processing methods, which can produce finite, ordered domains with a given geometry, is a central theme in the design of hierarchical ordered structures [5-8].

## EXPERIMENTAL METHOD

The solution decomposition of $Co_2(CO)_8$ and $Fe(CO)_5$ to metal nanoclusters was performed in a sealed three-neck round-bottomed reaction vessel that was first evacuated and then flushed with $N_2$. A side neck was equipped with a thermometer, the middle neck with a reflux condenser, and the other neck with a gas inlet-outlet glass fitting. The thermometer outlet was also used for sampling. In order to drive the reactions away from

equilibrium and toward completion, the carbon monoxide gas formed during the reaction had to be continuously flushed away by the $N_2$ stream, while avoiding bubble formation. The jacketed reaction flask was equipped with tubing to circulate heated ethylene glycol around the reaction flask, thus keeping the contents of the flask at a constant temperature. The flask was connected to a vacuum line via the reflux condenser, which allowed strict control of the environment inside the flask at all times. The initial concentration of the metal carbonyl in the solution was $5 \times 10^{-3}$ M. The solution was allowed to react under a continuous nitrogen stream with constant stirring.

The decomposition of the metal carbonyl precursors in both polystyrene and poly(methyl methacrylate) homopolymers, and in the $PS_{25300}$-b-$PMMA_{25900}$ block co-polymer was monitored via Fourier transform infrared spectroscopy (FTIR) at low temperatures. The decomposition in poly(styrene), $\overline{M}_n$=250,000, was carried out in toluene at 90 °C and the decomposition in poly(methyl methacrylate), $\overline{M}_n$=300,000, was carried out in methylene chloride at 40 °C. The decomposition in the $PS_{25300}$-b-$PMMA_{25900}$ block co-polymer solution was carried out in toluene at 90 °C as well. The reaction at the low temperature spanned more than two weeks, but data was collected for only the first 192 hours. Aliquots from the reaction solution were placed into a demountable infrared liquid cell with NaCl windows and a 0.2 mm optical path. The flask was placed under nitrogen during sample removal to prevent oxidation of the metal clusters. The cell was not demounted during the experiment, and the sample removal and cell washing was performed by suction. FTIR spectra were collected on a Nicolet Nexus 870 spectrophotometer, with a resolution of 2 $cm^{-1}$ and 50 scans/spectrum.

After the decomposition reactions of $Co_2(CO)_8$ in 0.38 wt. % PS-b-PMMA co-polymer was complete, TEM samples were made by placing an aliquot of the solution onto a carbon coated TEM grid. These films constituted "bulk" block copolymer films. A high quality, free-standing film was also prepared to be microtomed by combining 1 mL of the block copolymer solution with 2 mL of a 30 wt. % solution of PS in toluene, $\overline{M}_n$ = 300,000. The final composition of these films was then 33% $PS_{25300}$-b-$PMMA_{25900}$ containing cobalt nanoparticles, and 67% PS homopolymer. The solution was added dropwise onto a glass slide until a film covered the entire surface. After allowing the solvent to evaporate, the film was removed from the slide by peeling off one corner of the film and applying water between the film and the slide. The hydrophobic interactions between the film and water caused the film to peel off easily. These films were microtomed and constituted "thinly sectioned" block copolymer films. The TEM imaging was conducted on both Hitachi HF-2000 field emission gun (FEG) and JEOL 2010, and a high resolution JEOL 4000EX. The operating voltage was 200 keV for all three microscopes.

## RESULTS AND DISCUSSION

The chemical reactivity of metal clusters is largely determined by the size of the particles, and therefore the ability to control particle size, particle size distribution and dispersion would imply an ability to determine the reactivity and interfacial behavior of the clusters in the polymer-metal cluster interfacial systems. The synthesis of metal clusters, which is designed to accommodate these size manipulations, consists of the decomposition of organometallic complexes under controlled conditions (the energy

source could be thermal, UV radiation or E-beam), to form uniform metal dispersions of very small particle size [9,10]. The process is best described in the following three stages (Figure 1): (a) The preparation of homogeneous solutions of metal complexes in a carefully selected solvent; (b) The mixing of the organometallic complex solution with a polymer solution in which the polymer of choice has been dissolved in the common solvent; and (c) The energy-induced decomposition of the organometallic complexes to form uniform metal dispersions of very small particle size in the polymer solution. The overall reaction may be described as follows:

$$nM_x(L)_y \xrightarrow{Energy,\ Controlled\ Atmosphere,\ Polymer,\ Solvent} M_k^{(0)}\ and/or\ M_j^{(i)}O_{ij/2} + nyL$$

(where M=metal; L=organic ligand; and k=nx).

This approach may afford unique opportunities for investigating fundamental aspects of nucleation and growth of metal clusters, as well as the properties of such nanoparticles as functions of cluster size, concentration and environment. Metallic fragments created by the energy-induced decomposition of metal complexes are highly reactive [11,12], which constitutes the driving force for the nucleation and growth mechanism to form nanocrystals. The size of the clusters formed is significantly influenced by the following parameters: (a) Reducing or oxidative atmospheres, (b) The diffusion of small cluster fragments through the medium and (c) The viscosity of the medium in which the diffusion takes place. Chemical reactivity, for instance, is found to be strongly related to the size of these metal clusters, since the size of the clusters largely determines their crystal structure.

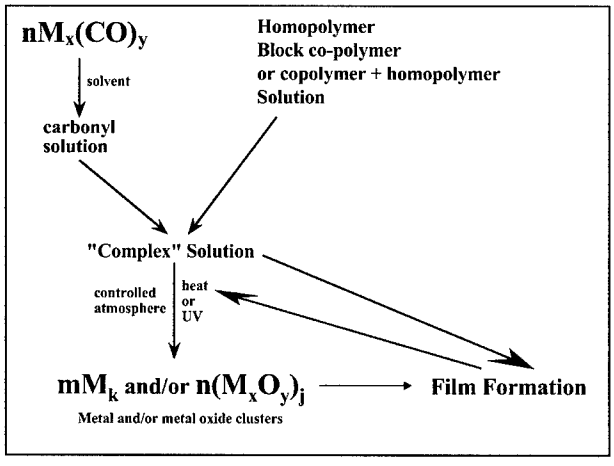


Figure 1: Schematic description of the synthesis methodology for the self-assembly of metal nanoparticles.

The thermal decomposition of cobalt carbonyls to metallic Co in polystyrene (PS) solutions has been used as a *model system* to test the chemical method under investigation. This process consists of a stepwise colloidal reaction mechanism [13-15], which is highly facilitated by the presence of macromolecules that provide the necessary solid state support and microenvironment which constitutes the driving force for cluster aggregation. As particle size grows, the mobility of the reactive metal fragments and their ability to diffuse through the solution and collide with each other decreases, and equilibrium is reached when the diffusion of the particles is too slow for observation in real time.

Experimental results of this model system (Figure 2), show that there is an inverse correlation between cobalt cluster size (measured by *Transmission Electron Microscopy*, TEM) and the PS concentration in the reaction solutions [16], accompanied by a considerable particle size distribution narrowing. When the excess polymer is washed off and the solvent is removed, the particles do not undergo additional growth, which indicates that they have been sufficiently coated by the "capping" polymer to prevent further aggregation.

When all the solvent has been removed from the polymer-containing solutions prior to decomposition (to form a polymer film), the smallest cobalt nanoparticles are formed. The ultimate result is a phase separated material in which the metal cluster and polymer phases are held together via the irreversible interfacial bonds created during the decomposition process. Moreover, the metallic nanoparticles are homogeneously dispersed throughout the polymer film, and given their small size, they exhibit high surface reactivity, and ensure good mechanical coupling of the particles to the polymer matrix.

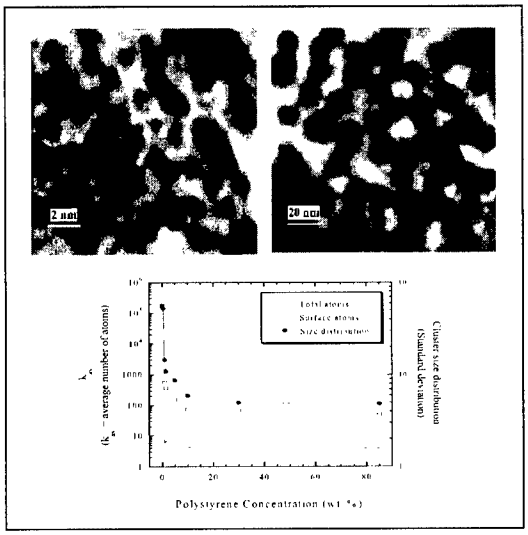


Figure 2: Co particles formed in polystyrene film (top left) and in a hydrocarbon solution (top right). The dependence of Co particle size, size distribution and abundance of surface atoms as a function of initial polymer concentration.

The synthetic method that we have developed for the controlled synthesis of metal nanoclusters can be extended to include also the manipulation of not only cluster size, size distribution and composition, but also geometrical shape. Biological systems have a unique ability to control crystal structure, phase, orientation and nanostructural regularity of inorganic materials [see, for example 17,18]. In biological hybrid systems it has been shown [17,18] that selected peptides can specifically bind to zinc-blende III-V semiconductor surfaces by discriminating between various crystallographic faces. These peptides are being used to grow nanoparticles and nanowires of specific crystallographic structure and orientation. Using these molecular interactions and specific nanoparticles, organic/inorganic hybrid materials may be organized into supramolecular architectures [for example, 19-21].

The preferred adsorption of the polymer chains to a particular crystalographic surface of the growing metal nano-clusters is clearly demonstrated in several Fe-polymer systems, as shown in Figure 3. The preferential adsorption of synthetic polymers to distinct crystallographic faces of the growing metallic fragment causes a distortion of the cluster shape, since the growth directions become differently hindered by the polymer. Hence, the result is a high degree of anisotropy in the cluster shape. In these systems, the protocol by which the decomposition reaction of $Fe(CO)_5$ in the presence of polymers is carried out is essential in determining the metal nanoparticle shape. Systems in which the same polymer has been used but the conditions of the thermal decomposition reaction were different, exhibited different particulate shape. For example, in the pesence of poly(vinylidene difluoride) (PVF2), the thermal treatment of the metal carbonyl-polymer complex solution that is concurrent with solvent removal and polymer film formation ("hot" method), gives rise to nanopyramids. On the other hand, the thermal treatment of the metal carbonyl-polymer complex solution that is performed after solvent evaporation at room temperature ("cold" method), gives rise to nanospheres [9]. In the former case, the solvent is present in the initial stages of the decomposition process, allowing a higher degree of mobility of the growing nanoclusters and the polymer chains, while in the latter case the metal carbonyl precursors are immobilized in the polymer film. Additional

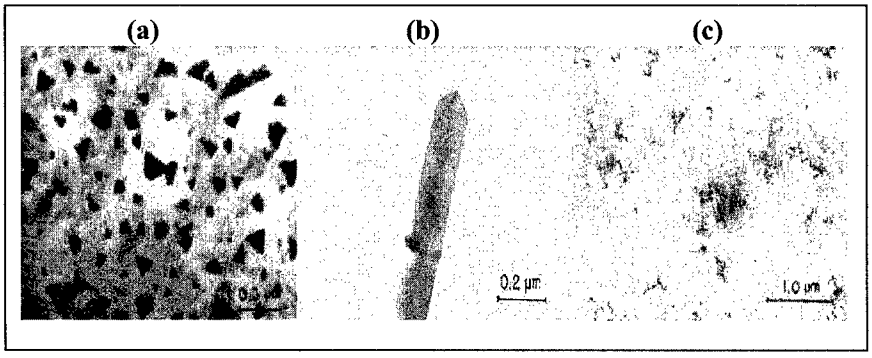


Figure 3: Shape control in the synthesis of iron nanoparticles via the decomposition of $Fe(CO)_5$ in the presence of (a) PVF2-nanopyramids; (b) PMMA-nanorods; and (c) Poly(carbonate)-nanostrings [9].

examples include the formation of Fe nanorods via the decomposition of $Fe(CO)_5$ in the presence of poly(methyl methacrylate) (PMMA), and the formation of nanostrings in the presence of poly(carbonate) (PC). This latter nanostructure is accompanied by extensive scission of the polymer chains, which may be partly responsible for the formation of the small Fe particles organized as nanostrings [9]. These examples are comprised of preliminary results, and a comprehensive study of these phenomena are currently underway. It is our intention to concentrate on the Fe and Co systems in the presence of PVF2, PMMA and PC, in order to establish the protocols for specific nanocluster polymer-induced geometry control as a function of polymer concentration and polymer molecular weight.

A direct extension of the methodology developed here is the creation of *polymer-induced, self-assembled, multi-functional nanoparticulate materials*, i.e. materials in which the metal clusters are phase separated within the polymer according to a predetermined spatial architecture. This spatial architecture can be achieved by the utilization of the phase separation and microdomain formation in multi-component polymers with self-organizing properties, i.e. *block copolymers*, for the anisotropic synthesis of nanoparticulate composites [22-24]. Hence, these block copolymers will be used as a structural and chemical template to produce a controllable, predetermined, self-developing spatial arrangement of clusters [24]. This implies that if the metal clusters are to aggregate in a particular polymeric domain, there should exist a driving force that would direct the phase separation such that certain areas in the polymer will be more reactive than others toward the metal clusters. This can be achieved by using *di-block copolymers* as a model system, in which one block will have reactive groups and the other block will be "inert" toward the metal clusters. One of the main features of block copolymers is the incompatibility between different parts of the same polymeric chain and the formation of microdomains [25]. The microdomain structure may consist of spheres, cylinders or lamellae, depending on the molecular weight of the blocks, their relative concentrations, the solvents used and the interfacial properties of the blocks. By carrying out the decomposition of the metal carbonyls in a di-block copolymer which was designed to phase separate in one of the main microdomain structures, we expect to obtain a high concentration of metal clusters in the domains occupied by the reactive block, and hence the spatial distribution of the clusters will conform to the spatial pattern created by the block copolymers. In this manner, it will be possible to concentrate the metal clusters in an ordered array of complex and highly ordered structures, as shown in Figure 4a. The homogeneous dispersion of the metal nanoclusters within the reactive block will provide certain physical and chemical properties inherent to metallic systems (e.g. mechanical strength, electrical conductivity, etc.), and thus create distinct functional regions within the polymeric material.

The selective incorporation of metal clusters into block copolymers may be achieved by three main pathways: (a) The exposure of block copolymer films to metal vapors, resulting in the selective adsorption of the metal atoms onto the more reactive block; (b) The impregnation of block copolymer films with a metal salt, with a subsequent reduction of the salt to form metallic clusters in the reactive block domains; and (c) The homogeneous mixing of the block copolymers with the organometallic precursors followed by the in-situ phase separation and self-assembly of both metal clusters and copolymer microdomains [22-24,26,27]. In the first two approaches, the

block copolymers are first allowed to self assemble into their distinct microdomains, and are subsequently exposed to the metallic moiety. Under these conditions, there are significant differences in the size and dispersion of the metallic clusters between the bulk copolymer films and the thin (microtomed) films, due to the rates of diffusion and penetration depth of the metallic precursors. Moreover, if the polymers are below their $T_g$, the interfacial adhesion between polymer chains and the growing clusters is severely hindered, and therefore, the limitation on metal cluster size is due to nucleation and growth kinetics and not to a polymer "capping" effect. The third method, and the one that we have developed, is designed to circumvent these issues by performing the nucleation and growth of the metal clusters and the phase separation of the block copolymers *in-situ*, in a homogeneous solution of both components. Under these conditions, nucleation and growth of the clusters will be limited not only by reaction kinetics, but also by the direct interaction with the available reactive sites on the polymer. Hence, the difference in the reactivity of the two blocks toward the metal will be fully exhibited.

Preliminary results for the cobalt-poly(styrene-*b*-methyl methacrylate) block copolymer system (Figure 4c), show a distinct segregation of the cobalt clusters in defined regions, similar to the "worm-like" distribution achieved by Cohen et al. in their microtomed Ag-block copolymer samples [24]. The actual microstructure exhibited by the metal-containing block copolymers is strongly influenced and complicated by the phase behavior of block copolymer in solution prior to metal incorporation, irrespective to the method used. In dilute solutions, the blocks form micelles [27] where one of the blocks forms the core of the micelle (the block less favored by the solvent used), and the other forms the shell. After the incorporation of the metal nanoparticles, the solvent is evaporated, and it is expected that a phase transition will take place resulting in a microstructure that corresponds to the block copolymer composition. However, our own preliminary results and the results in the literature [22-24,26,27] suggest that this phase transformation is incomplete, either due to some degree of crosslinking caused by the metal nanoparticles or by the change in phase behavior of the block copolymers as a result of the presence of the nanoclusters (Figure 4b,c).

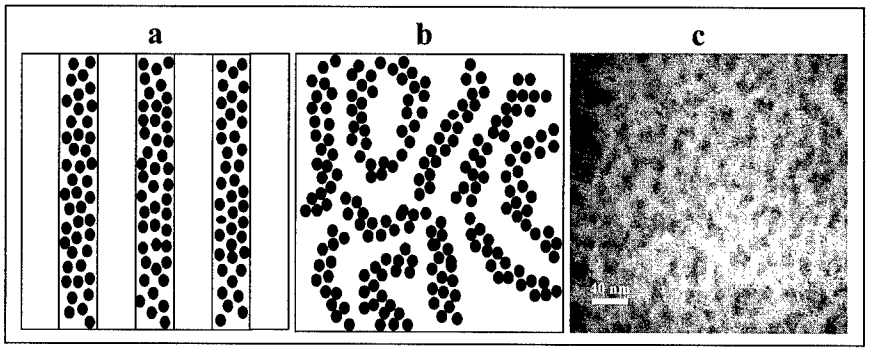


Figure 4: Cobalt nanoparticle size distribution in the PS-PMMA block co-polymer domains. (a) Idealized lamellar phases; (b) Arrested phase transformation; (c) TEM micrograph of particle distribution.

The average particle size is ~ 50 Å, and it does not change upon film formation. Moreover, particle size and microdomain distribution is independent of film thickness, and is a function of the initial polymer solution concentration in the decomposition reaction.

Additional insight into the strength of the interaction between the cobalt nanoparticles and the PMMA block was obtained by probing the diffusion of the cobalt particles from the PMMA domain into a large PS domain. For this purpose, the $PS_{25300}$-*b*-$PMMA_{25900}$ block copolymer solutions used in this work were doped with high molecular weight polystyrene homopolymer. The addition of a homopolymer to a diblock copolymer has the effect of increasing the domain size of the common block for a particular morphology [27-30], if the total concentration of the homopolymer component is within the concentration regime commensurate with that morphology. In this particular case, since the molecular weight of the polystyrene homopolymer far exceeded (six fold) the combined molecular weights of both blocks, the block copolymer and the homopolymer behaved as a macrophase and microphase separated blend [31-33]. Figure 5 shows a HRTEM image of a "thinly sectioned" microtomed film of a high molecular weight polystyrene ($\overline{M}_n = 300{,}000$) blended with the $PS_{25300}$-*b*-$PMMA_{25900}$ block copolymer, that contained cobalt precursors which were then decomposed ***in situ*** according to the cluster synthesis used in these experiments. The decomposition of the cobalt precursors in the polymer medium occurred either before or after the addition of the PS homopolymer. The distribution of the cobalt particles within the polymeric matrix was similar in both cases. The particles were concentrated in the block copolymer, specifically in the PMMA microdomain, without any traces of cobalt clusters in the polystyrene homopolymer phase. No cobalt particle diffusion from the poly(methyl methacrylate) domain to the polystyrene domain was observed, as evidenced by the irreversible confinement of the cobalt particles in the more reactive block.

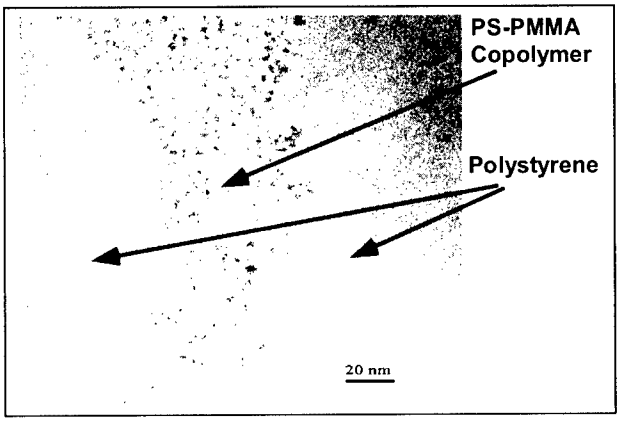


Figure 5: HRTEM image of a microtomed film of the homopolymer/block co-polymer blend showing cobalt particle confinement in the block phase.

## SUMMARY

The results presented in this paper demonstrate that the incorporation of metal nanoclusters, synthesized via an ***in situ*** decomposition of metal carbonyl precursors into a block copolymer, generates an uneven dispersion of the particles, with a preferential aggregation in the poly(methyl methacrylate) block. This can be explained by the reactive adsorption of the PMMA block onto the metal cluster surface, through the interaction of the carbonyl group of the polymer with the metal. This is supported by experimental results obtained with Fourier Transform Infrared (FTIR) spectroscopy that are described elsewhere [34]. The morphology of the system did not conform to the expected lamellar structure, due to the fact that the $PS_{25300}$-b-$PMMA_{25900}$ block copolymer that was used forms micelles in the solvent of choice (in this case toluene), with the poly(styrene) block constituting the shell and the poly(methyl methacrylate) block constituting the core of the micelles. The preferential incorporation of the cobalt nanoclusters into the poly(methyl methacrylate) block has the effect of immobilizing the micellar structure, thus preventing the expected phase transformation to the expected lamellar morphology upon removal of the solvent. Moreover, when this block copolymer was mixed with a high molecular weight poly(styrene) homopolymer, the common poly(styrene) moieties did not enhance the mutual solubility of the homopolymer and the block copolymer, and the material behaved as a macrophase and microphase separated blend.

## ACKNOWLEDGEMENTS

The authors thank NSF-ERC (through the Packaging Research Center), the Georgia Tech Foundation, and the College of Engineering at Georgia Tech for financial support.

## REFERENCES

1. Addadi, L.; Weiner, S. *Angew. Chem. Int. Ed. Engl.* **1992**, *31*, 169.
2. Belcher, A. M.; Hansma, P. K.; Stucky, G. D.; Morse, D. E. *Acta Mater.* **1998**, *46*, 733-736.
3. McGrath, K. M. *Adv. Mater.* **2001**, *13*, 989.
4. Pileni, M.-P.; Ninham, B. W.; Gulik-Krzywicki, T.; Tanori, J.; Lisiecki, I.; Filankembo, A. *Adv. Mater.* **1999**, *11*, 1358.
5. Alivisatos, A. P.; Barbara, P. F.; Castleman, A. W.; Chang, J.; Dixon, D. A.; Klein, M. L.; McLendon, G. L.; Miller, J. S.; Ratner, M. A.; Rossky, P. J.; Stupp, S. I.; Thompson, M. E. *Adv. Mater.* **1998**, *10 (16),* 1297-1336.
6. Stupp, S. I.; Keser, M.; Tew, G. N. *Polymer* **1998**, *39(19)*, 4505-4508.
7. Stupp, S. I.; Pralle, M. U.; Tew, G. N.; Li, L.; Sayar, M.; Zubarev, E. R. *MRS Bull.* **2000**, *25(4)*, 42-48.
8. Grier, D. G. *MRS Bull.* **1998**, *23(10)*, 21-23.
9. Tannenbaum, R.; Goldberg, E. P.; Flenniken, C. L. "Metal-containing polymeric systems", Eds. Carraher C., Pittman C. U. and Sheats J., Plenum Press, New York **1985**, p. 303-340.
10. Tannenbaum, R.; Flenniken, C. L.; Goldberg, E. P *J. Polym. Sci. Phys. Ed.* **1990**, *28*, 2421.
11. Klaubunde, K. J.; Tanaka, Y. *J. Molec. Catal,* **1983**, *21*, 57.

12. Kanai, H.; Tan, B. J.; Klaubunde, K. J. *Langmuir* **1986**, *2(6)*, 760.
13. Kernizan, C. F.; Klabunde, K. J.; Sorensen, C. M.; Hadjipanayis, G. C. *J. Appl. Phys.* **1990**, *67(9)*, 5897.
14. Tannenbaum, R. *Langmuir* **1997**, *13(19)*, 5056, and pertinent references therein.
15. Rotstein, H. G.; Novick-Cohen, A.; Tannenbaum, R. *J. Stat. Phys.* **1998**, *90(1/2)*, 119.
16. Rotstein, H. G.; Novick-Cohen, A.; Tannenbaum R. *J. Phys. Chem. B* **2001**, to appear.
17. Smith, B. l.; Schäffer, T. E; Viani, M.; Thompson, J. B.; Frederick, N. A.; Kindt, J.; Belcher, A.; Stucky, G. D.; Morse, D. E.; Hansma, P. K. *Nature* **1999**, *399*, 761-763.
18. Whaley, S. R.; English, D. S.; Hu, E. L.; Barbara, P. F.; Belcher, A. M., *Nature* **2000**, *405*, 665-668.
19. Ahmadi, T. S.; Wang, Z. L.; Green, T. C.; Henglein, A.; El-Sayed, M. A. *Science* **1996**, *272*, 1924-1925.
20. Petroski, J. M.; Wang, Z. L.; Green, T. C.; El-Sayed, M. A. *J. Phys. Chem. B* **1998**, *102*, 3316-3320.
21. Bradley, J. S.; Tesche, B.; Busser, W.; Maase, M.; Reetz, M. T. *J. Am. Chem. Soc.* **2000**, *122*, 4631-4636.
22. Morkved, T. L.; Wiltzius, P.; Jaeger, H. M.; Grier, D. G.; Witten, T. A. *Appl. Phys. Lett.* **1994**, *64(4)*, 422-424.
23. Caruso, F.; Möhwald, H. *Langmuir* **1999**, *15(23)*, 8276-8281.
24. Clay, R. T.; Cohen, R. E. *Supramolecular Science* **1995**, *2*, 183-191.
25. Bates, F. S.; Fredrickson, G. H. *Ann. Rev. Phys. Chem.* **1990**, *41*, 525-557.
26. Hashimoto, T. ; Harada, M. ; Sakamoto, N. *Macromolecules* **1999**, *32*, 6867-6870.
27. Spatz, J. P.; Mössmer, S.; Hartmann, C.; Möller, M.; Herzog, T.; Krieger, M.; Boyen, H. –G.; Ziemann, P.; Kabius, B. *Langmuir* **2000**, *16*, 407-415.
25. Li, R.R., Dapkus, P.D., Thompson, M.E., Jwong, W.G., Harrison, C., Chaikin, P.M., Register, R.A., Adamson, D.H. *Applied Physics Letters* **2000**, *76 (13)*, 1689-1691.
26. Bronstein, L.M., Valetsky, P.M., Solodovnikov, S.P., Seregina, M.V., Register, R.A. *Macromol. Symp.* **1996**, *106*, 73-86.
27. Winey, K. I.; Thomas, E. L.; Fetters, L. J. *Macromolecules* **1992**, *25(1)*, 422-428.
28. Winey, K. I.; Thomas, E. L.; Fetters, L. J. *Macromolecules* **1991**, *24(23)*, 6182-6188.
29. Winey, K. I.; Thomas, E. L.; Fetters, L. J. *Macromolecules* **1992**, *25(10)*, 2645-2650.
30. Whitmore, M. D.; Noolandi, J. *Polym. Eng. Sci.* **1985**, *25 (17)*, 1120-1121.
31. Pepin, M. P.; Whitmore, M. D. *Macromolecules* **2000**, *33(23)*, 8644-8653.
32. Jeon, K. –J.; Roe, R. –J. *Macromolecules* **1994**, *27(9)*, 2439-2447.
33. Roe, R. –J. *Polym. Eng. Sci.* **1985**, *25(17)*, 1103-1109.
34. Tadd, E. H.; Bradley, J.; Tannenbaum, R. *J. Phys. Chem. B* **2001**, *105*, 0000-0000 (to appear).

Mat. Res. Soc. Symp. Proc. Vol. 703 © 2002 Materials Research Society V2.3

# SALT-INDUCED BLOCK COPOLYMER MICELLES AS NANOREACTORS FOR THE FORMATION OF CdS NANOPARTICLES

Hanying Zhao, Elliot P. Douglas

Department of Materials Science and Engineering, University of Florida, Gainesville, FL 32611, USA

## ABSTRACT

A novel preparation method of CdS nanoparticles in the core or corona of micelles is presented. Poly(styrene-*block*-2-vinylpyridine) (PS-*b*-P2VP) and cadmium ions form aggregates of single micelles, called compound micelles, upon addition of the cadmium acetate salt into a solution of the block copolymer in tetrahydrofuran. The growth of CdS nanoparticles is confined to the core of single micelles after introduction of hydrogen sulfide gas into the solution. UV-visible spectroscopy, fluorescence spectroscopy, and transmission electron microscopy were employed to characterize the prepared core-embedded CdS nanoparticles. Corona-embedded CdS nanoparticles were prepared by dropping the core-embedded CdS nanoparticles into water with a low pH value. The location change of the CdS nanoparticles was accompanied by a structural change of the micelles, a change from compound micelles to single micelles. In a single micelle, CdS nanoparticles distribute randomly in the corona. The size of the nanoparticles increases slightly after the transition.

## INTRODUCTION

The synthesis of semiconductor nanoparticles or clusters is emerging in the fields of materials science and colloid science because of their wide range of optical and electronic properties [1-5]. Many people have prepared nanoparticles in micelles formed by block copolymers [6-7]. A micelle core can be regarded as a nanosized reaction vessel, and the growth of colloidal particles can be limited to the micelle core. Recently in our group we prepared CdS nanoparticles in the core (core-embedded) and corona part (corona-embedded) of salt-induced micelles [8-9]. The size of CdS nanoparticles can be controlled by changing 2VP:$Cd^{2+}$ molar ratio and block copolymer concentration in THF etc.

## EXPERIMENTAL DETAILS

The synthesis of the PS-*b*-P2VP block copolymer was performed using sequential anionic polymerization. The molecular weight of the block copolymer is $25.5 \times 10^3$ g/mol ($M_n$) with a polydispersity of 1.30, measured by GPC relative to PS standards. The content of 2-vinylpyridine units in the block copolymer is about 35 mol% as measured by $^1$H-NMR.

Preparation of core-embedded CdS nanoparticles: PS-*b*-P2VP block copolymer was dissolved in THF at different concentrations under vigorous stirring for 1 hour. $Cd(Ac)_2.2H_2O$ dissolved in a mixture of methanol and THF (1:2 V/V), was added to the polymer solution. The light yellow solution of core-embedded CdS nanoparticles was prepared by introducing $H_2S$ gas into the complex solution.

Preparation of corona-embedded CdS nanoparticles: Corona-embedded CdS nanoparticles were prepared by dropping varying amounts of core-embedded CdS nanoparticles solution into water with a low pH value and then removing THF in the solution under vacuum.

UV-Visible absorption spectra were recorded on a Shimadzu UV-Vis spectrophotometer (UV-2401PC), by scanning the CdS-containing solution in a 1-cm quartz cell. Steady-state fluorescence spectra were obtained on an SPEX Fluorolog spectrophotometer equipped with a 450W Xe arc-lamp and a PMT detector. The excitation wavelength was 350 nm and the bandwidths were 10 nm for excitation and emission. Fluorescence measurements were obtained on the colloidal suspensions contained in quartz cuvettes. Electron microscopy was performed on a Zeiss EM 10A transmission electron microscope operated at 100 kV. TEM samples were prepared by depositing a droplet of micelle solution or CdS-containing colloidal solution (<0.1 mg/ml) onto a copper grid which had been coated with Formvar/Silicon monoxide film.

## RESULTS AND DISCUSSION

In a previous paper we have demonstrated that upon addition of cadmium ions into a solution of PS-*b*-P2VP block copolymer in THF, a solvent for both of the blocks, compound micelles form due to complexation of $Cd^{2+}$ with the 2-vinylpyridine (2VP) units [8]. A compound micelle is an assembly of single micelles. A core of a single micelle is composed of $Cd^{2+}$/2VP complexes and a corona is composed of PS blocks. The growth of a CdS nanoparticle is confined to the core of a single micelle.

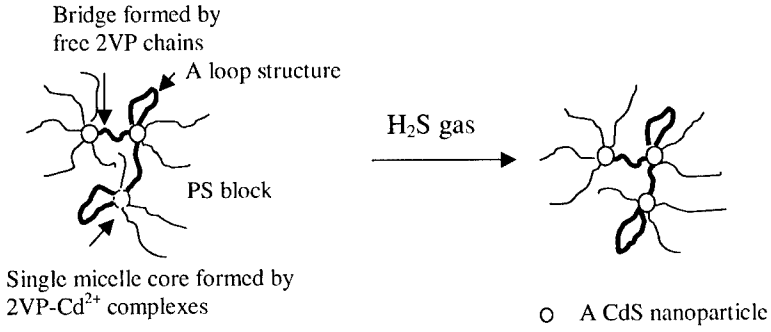


**A Compound micelle**

**Figure 1** Schematic representation of the formation of a compound micelle, and preparation of CdS nanoparticles in a compound micelle.

Figure 2 are three UV-visible absorption spectra of nanoparticles prepared at different 2VP:$Cd^{2+}$ molar ratios. The absorption edge of the curves shifts with the change of the molar ratio. When the molar ratio is 1:0.5, the absorption edge is at about 458 nm (particle diameter of 3.8 nm). However, when the ratio is 1:0.77 and 1:2.31, it red-shifts to 470 and 485 nm.

corresponding to particle diameters of 4.2 and 4.5 nm, respectively. This result indicates that larger nanoparticles can be prepared at lower 2VP:$Cd^{2+}$ molar ratios.

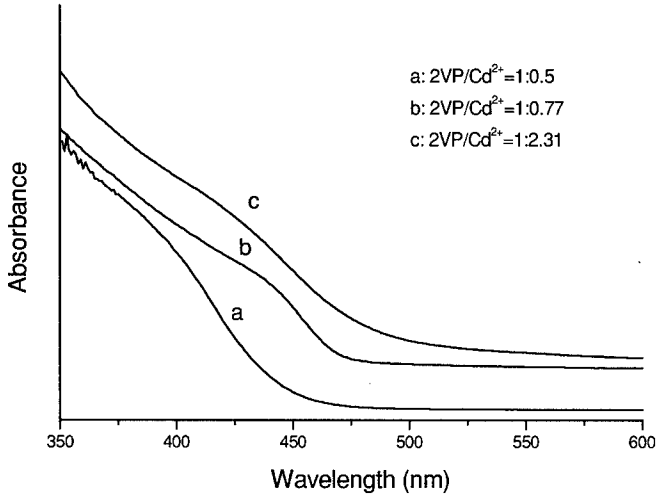


**Figure 2** UV-visible absorption spectra of CdS nanoparticles in salt induced micelles at different 2VP : $Cd^{2+}$ molar ratios. The concentration of the block copolymer in THF is 26.6 g/L.

Holding the 2VP:$Cd^{2+}$ molar ratio constant (1:0.5), the effect of block copolymer concentration in THF on the size of CdS nanoparticles was investigated. Figure 3 shows three typical UV-Visible absorption curves of CdS nanoparticles prepared from the PS-*b*-P2VP-$Cd^{2+}$ solutions with concentrations of 10, 2.5 and 1.0 g/L. It can be seen that the absorption edge blue-shifts with decreasing concentration. It is noted that a weak maximum develops at about 370 nm at low concentration. This maximum is characteristic of CdS nanoparticles with a comparatively small size and narrow size distribution.

The stability of CdS nanoparticles in solution was also investigated. The CdS nanoparticles prepared in the block copolymer micelle solutions are very stable if the 2VP: $Cd^{2+}$ molar ratio is above 1:2. Precipitation was not observed even after storage of the solutions at room temperature for more than two months. UV-Visible absorption spectra shows that CdS-containing solutions measured after 12 days storage red-shifts 19 nm compared to freshly prepared CdS nanoparticles in solution. No further red-shift is observed after an additional 33 days of storage.

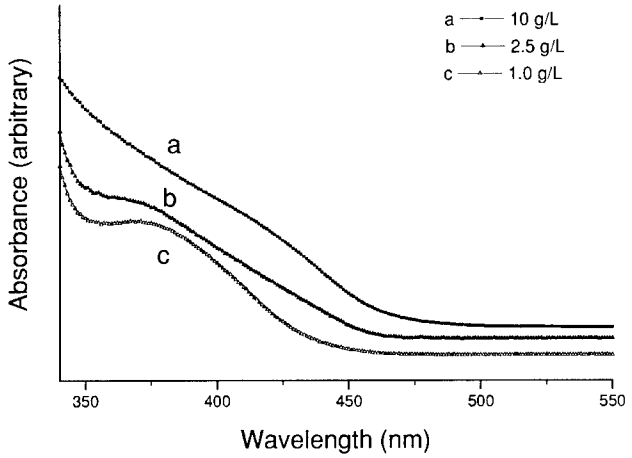


**Figure 3** UV-visible absorption spectra of CdS nanoparticles in salt induced micelles prepared from PS-*b*-P2VP/$Cd^{2+}$ in THF at different block copolymer concentrations. The 2VP : $Cd^{2+}$ molar ratio is 1:0.5. The plots are shifted vertically for clarity.

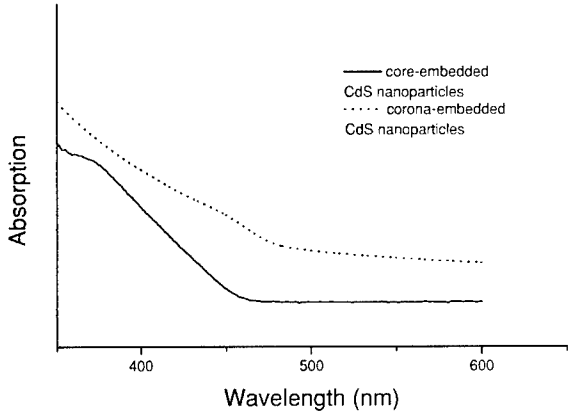


**Figure 4** UV-Vis absorption spectra of core-embedded CdS nanoparticles and corona-embedded CdS nanoparticles. The concentration of the block copolymer in THF is 2.5 g/L and the molar ratio of 2VP units to $Cd^{2+}$ is 1:0.5.

Figure 4 shows UV-vis spectra of core-embedded and corona-embedded CdS nanoparticles in THF. For the core-embedded CdS nanoparticles solution with a polymer concentration of 2.5 mg/ml, the absorption edge is at about 457 nm, however, the absorption edge red-shifted to 474 nm when the core-embedded CdS nanoparticles solution was dropped into water with a pH value of 3.3 (corona-embedded nanoparticles). The average diameter of the core-embedded CdS particles is about 3.7 nm, and after the transition it increases to about 4.4 nm, which indicates that some nanoparticles aggregated into bigger nanoparticles during the transition from core-embedded nanoparticles to corona-embedded nanoparticles.

Figure 5 is a TEM image of corona-embedded CdS nanoparticles prepared by dropping 1 ml of the core-embedded CdS nanoparticle solution into 20 ml of water with a pH value of 3.3. Examining the TEM image carefully, it can be found that there are more nanoparticles in the corona region. This morphology is just like a colloidal core-shell structure. This TEM image strongly proves that nanoparticles are located around the corona of the micelles and form a "red currant" morphology [10]. The diameters of the nanoparticles range from 2 to 5 nm.

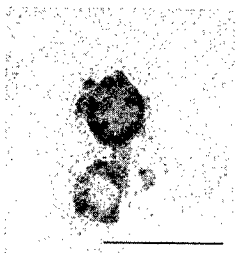

**Figure 5** A TEM image of corona-embedded CdS nanoparticles prepared by dropping 1 ml of the core-embedded CdS nanoparticle solution into 20 ml water with a pH value of 3.3. The Scale bar on the TEM image represents 100nm.


## ACKNOWLEDGMENTS

We would like to thank Dr. Jill Verlander Reed, and Ms. Melissa Ann Lewis, College of Medicine, electron microscopy core facility, University of Florida, for performing the TEM. and Prof. Kirk S. Schanze, Mr. Benjamin S. Harrison, Department of Chemistry, University of Florida, in fluorescence measurements and analysis. Financial support of the Center for Materials in Sensors and Actuators (MINSA, Grant No. DAAD19-00-1-0002) is gratefully acknowledged.


## References:


1. A. Henglein, *Chem. Rev.* **89**, 1861(1989).
2. L. Spanhel, M. Hoasse, H. J. Weller and A. Henglein, *J. Am. Chem. Soc.*, **109**, 5649 (1987).
3. A. Henglein and M. Gutierrez, M. *Ber. Bunsenges. Phys. Chem.*, **87**, 852 (1983).
4. Y. Wang and N. Herron, *J. Phys. Chem.*, **95**, 525 (1991).

5. W. P. McConnell, J. P. Novak, L. C. Brousseau, R. R. Fuierer, R. C. Tenent and D. L. Feldheim, *J. Phys. Chem. B*, **104**, 8925 (2000).
6. M. Antonietti, E. Wenz, L. Bronstein, M. Seregina, M. *Adv. Mater.*, **7**, 1000 (1995).
7. M. Antonietti, S. Forster, J. Hartmann and S. Oestreich, S, *Macromolecules* **29**, 3800 (1996).
8. H. Zhao, E. P. Douglas, B. S. Harrison and K. S. Schanze, *Langmur*, in press
9. H. Zhao and E. P. Douglas, submitted to *Chemistry of Materials*
10. A. B. R. Mayer, *Polym. Adv. Technol.*, **12**, 96 (2001).

Mat. Res. Soc. Symp. Proc. Vol. 703 © 2002 Materials Research Society V2.4

# Growth of Highly Oriented ZnO Nanorods by Chemical Vapor Deposition

Sai-Chang Liu and Jih-Jen Wu
Department of Chemical Engineering, National Cheng Kung University, Tainan, Taiwan

## ABSTRACT

Highly-oriented ZnO nanorods were grown on the fused silica substrates by a thermal CVD technique using Zinc acetylacetonate ($Zn(C_5H_7O_2)_2$). The substrate was heated to 500°C and the vaporization temperature of $Zn(C_5H_7O_2)_2$ was keep at around 135°C. X-ray diffraction and TEM analyses reveal that the nanorods are preferentially oriented toward the c-axis direction. Photoluminescence (PL) and absorption measurements show a strong emission at around 380nm which corresponds to the near band-edge emission of the bulk ZnO. Moreover, the negligible green emission band in PL spectrum and the absence of $E_1(LO)$ mode of the ZnO crystal in Raman spectrum indicate a low concentration of oxygen vacancy in the highly-oriented ZnO nanorods.

## INTRODUCTION

One-dimensional nanometer-sized semiconductor materials, i.e. nanowires and nanorods, have attracted considerable attention due to their unique properties and suitability for fundamental studies of the roles of dimensionality and size in their physical properties as well as for the application to optoelectronic nanodevices [1]. ZnO exhibits a direct band gap of 3.37 eV at room temperature with a large exciton binding energy of 60 meV. The strong exciton binding energy which is much larger than that of GaN(25 meV) as well as the thermal energy at room temperature(25 meV) can ensure an efficient exciton emission at room temperature under low excitation energy [2,3]. In consequence, ZnO is recognized as a promising photonic material in the blue-UV region. Room temperature UV lasing properties have been indeed demonstrated with ZnO epitaxial films, microcrystalline thin films and nanoclusters recently [4,5]. Moreover, room temperature UV lasing in ZnO nanowires has been demonstrated very recently [6]. The synthesis of one-dimensional single crystal ZnO nanostructures has been of growing interest owing to their promising application in nanoscale optoelectronic devices. Single crystalline ZnO nanowires have been synthesized successfully using VLS growth methods [6,7,8] at rather high temperatures for the VLS mechanism proceeding. Besides, single crystalline ZnO nanobelts have also been reported by simply evaporating the ZnO powders at a high temperature of 1400°C [9]. However, high density and well-ordered nanostructures will be needed from practical application

point of view. Here, we present a simple catalyst-free CVD approach for the growth of the highly-oriented ZnO nanorods at a low temperature of around 500°C.

## EXPERIMENTAL DETAILS

ZnO nanorods were grown in a two-temperature-zone furnace (see figure 1). Silicon wafers and fused silica plates were employed as substrates. They were cleaned in an ultrasonic bath of acetone for 20 min. Zinc acetylacetonate hydrate ($Zn(C_5H_7O_2)_2 \cdot xH2O$, Lancaster, 98%) placed in a glass cell was loaded into the low temperature zone of the furnace which was controlled to be at 130-140°C to vaporize the solid reactant. The vapor was carried by a 500-sccm $N_2/O_2$ flow into the higher temperature zone of the furnace in which substrates were located at 200 Torr. ZnO nanorods were grown directly on bare fused silica or silicon substrates at 500°C. It should be noted that there were no metal films, which are employed as catalyst in VLS method, pre-coated on the substrates.

The morphology and size distribution as well as elemental analyses of the nanorods were examined using SEM equipped with an EDS. The crystal structure of the nanorods was analyzed using XRD and HRTEM. Optical properties were characterized by absorption spectrometry as well as by photoluminescence spectrometry using a Xe lamp with an excitation wavelength of 325nm at room temperature.

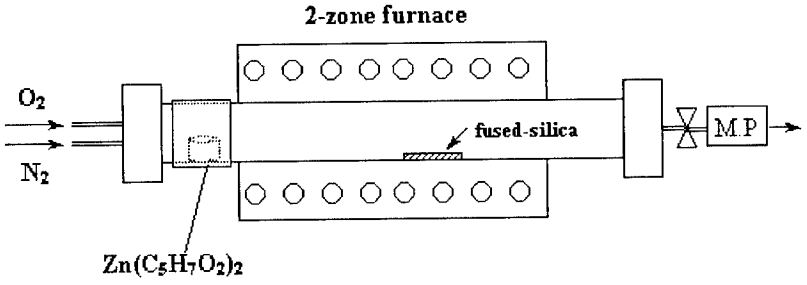


**Figure 1.** Schematic diagram of the experimental setup.

## RESULTS AND DISCUSSION

As shown in figure 2, ZnO nanorods were grown directly on bare fused silica or silicon substrates at 500°C. A high density of highly-oriented nanorods with a diameter in the range of 60-80 nm uniformly formed over the entire substrate at a vaporizing temperature of 135°C and $N_2/O_2$ flow rates of 250/250 sccm. The energy dispersive spectrometry (EDS) taken from the nanorods shows that the atomic composition ratio of Zn:O is about 1:1. Size control of the highly-oriented ZnO nanorods diameters was achieved by adjusting the growth condition. Figure 3 shows that the ZnO nanorods with smaller diameters (~ 45nm) are obtained by increasing $N_2$ flow rate to 500 sccm.

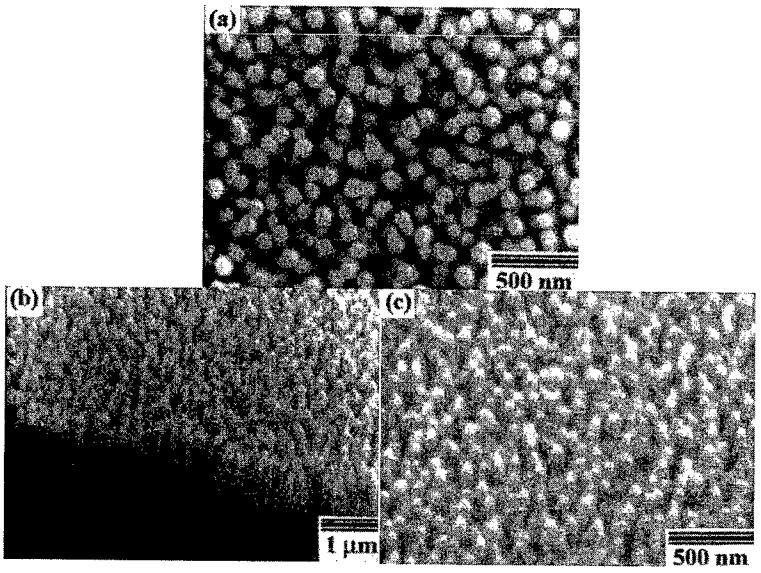


**Figure 2.** SEM images of ZnO nanorods grown on the fused silica substrates at $N_2/O_2$ flow rates of 250/250 sccm. (a) Top view, (b) and (c) 45° tilted view.

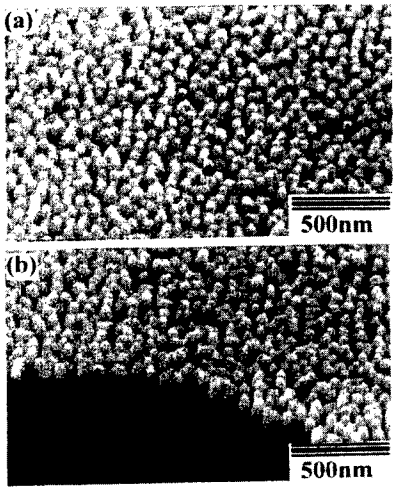


**Figure 3.** SEM images of ZnO nanorods grown on the fused silica substrates at $N_2/O_2$ flow rates of 500/250 sccm. (a) and (b) 45° tilted view.

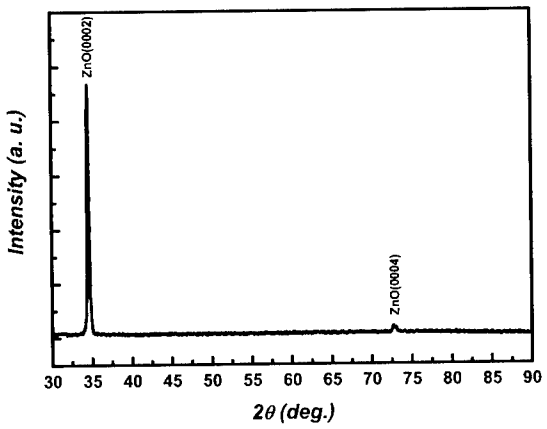


**Figure 4.** XRD pattern of ZnO nanorods on a fused silica substrate.

The crystal structure of the nanorods was examined by X-ray diffraction (XRD). Figure 4 shows a typical XRD pattern of the highly-oriented ZnO nanorods grown on a fused silica substrate. The two peaks are indexed as (0002) and (0004) of the wurtzite structure of ZnO, indicating that the nanorods are preferentially oriented toward the c-axis direction.

Further structural characterization of the ZnO nanorods was performed using transmission electron microscopy (TEM). Figure 5(a) shows a cross-sectional image of the ZnO nanorods, on a fused silica substrate, with a diameter in the range of 80-100 nm. It reveals that all nanorods were grown with a direction perpendicular to the substrate. Moreover, there is no additional metal particle appeared on the top or the bottom of the rods, implying a catalyst-free approach for the growth of the highly-oriented ZnO nanorods at a low temperature is achieved. Typical bright-field and dark-field images of the ZnO nanorods are illustrated in figure 5(b) and figure 5(c), respectively. The dark-field image indicates that the nanorod possesses the single crystalline structure. Figure 5(d) shows a high-resolution TEM image of a nanorod. The lattice spacing of 0.257 nm is corresponding to the d-spacing of (0002) crystal planes, confirming the XRD analysis that the ZnO nanorods are preferentially oriented toward the c-axis direction, as shown in figure 4.

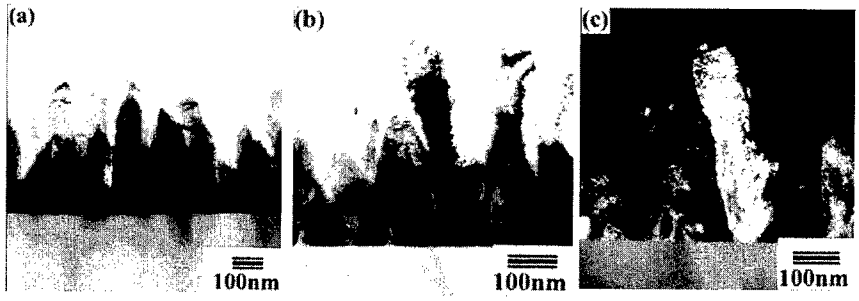


**Figure 5(a)(b)(c).** TEM cross-sectional images of ZnO nanorods grown on fused silica substrates at a vaporizing temperature of 138°C. (a) Low magnification image shows nanorods grown with a direction perpendicular to the substrate. (b) and (c) Typical bright-field and dark-field images of the ZnO nanorods, respectively.

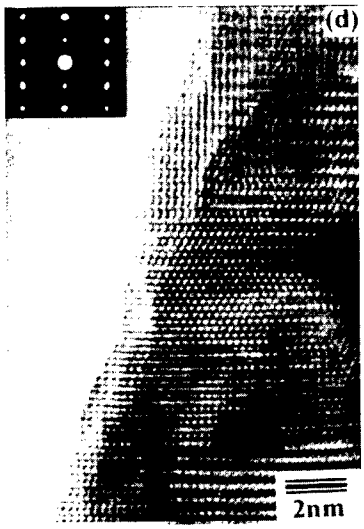


**Figure 5(d).** High-resolution TEM image of a single crystalline ZnO nanorods and the corresponding electron diffraction pattern (inset).

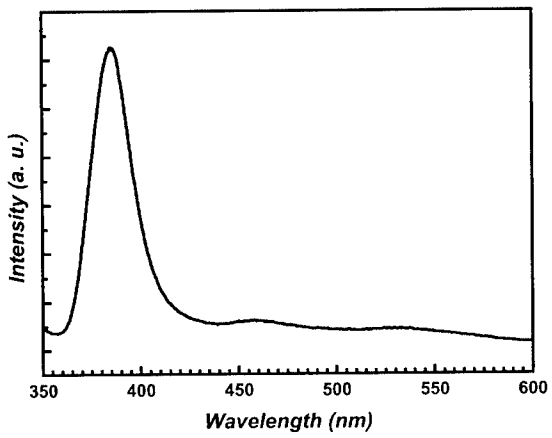


**Figure 6.** Typical photoluminescence spectrum of ZnO nanorods.

Figure 6 shows the PL spectrum of the ZnO nanorods with a diameter in the range of 60-80 nm. Three emitting bands, including a strong ultraviolet emission at around 380 nm, a very week blue band (440-480 nm) as well as an almost negligible green band (510-580 nm), were observed. Among them the UV emission must be contributed to the near band edge emission of the wide band gap ZnO. It has been suggested that the green band emission is corresponding to the singly ionized oxygen vacancy in ZnO and results from the recombination of a photogenerated hole with the single ionized charge state of this defect [10]. Thus the almost negligible green band in figure 6 shows that there is very low concentration of oxygen vacancy in the highly-oriented ZnO nanorods. The observation of blue band emission (440-480 nm) of ZnO film has been also reported using cathodoluminescence [11]. However, the mechanism of this emission is not clear yet.

In addition to photoluminescence measurement, we also used absorption spectrometry to further examine the optical property of the highly-oriented ZnO nanorods. As illustrated in figure 7, the absorption spectrum at room temperature shows that there is an absorption peak at around 380nm, which is consistent with the result of PL measurement. The Raman spectrum of the highly-oriented ZnO nanorods grown on fused silica substrate is shown in figure 8. Only the ZnO $E_2$ mode at 437cm$^{-1}$ is appeared in this spectrum. The absence of the $E_1$(LO) mode at 583cm$^{-1}$ of the ZnO associated with oxygen deficiency [12] indicates the high quality of the ZnO nanorods as the negligible green band in the PL spectrum.

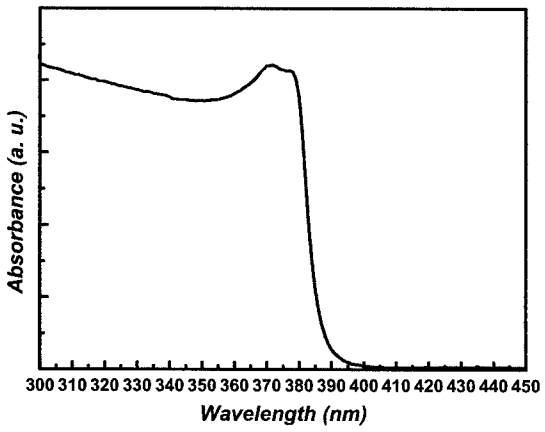


**Figure 7.** Absorption spectrum of the ZnO nanorods at room temperature.

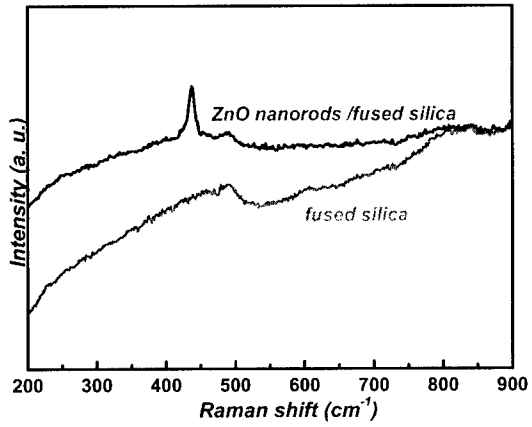


**Figure 8.** Raman spectra of the bare fused silica substrate and the ZnO nanorods grown on it.

## CONCLUSIONS

A simple catalyst-free CVD method for the growth of the highly-oriented ZnO nanorods at low temperature has been demonstrated in this report. The nanorods grown on fused silica are preferentially oriented toward the c-axis direction. Photoluminescence (PL) and absorption characteristics of the ZnO nanorods shows a strong UV light emission peaked around 380 nm at room temperature. PL and Raman measurements also show a concentration of oxygen vacancy in the highly-oriented ZnO nanorods. We believe the presented approach is a simple one for practical application to nanoscale optoelectronic devices.

## ACKNOWLEDGEMENTS

The authors would like to thank prof. Y. Chen and Dr. K. H. Chen for technical support. The financial support of this work, by the National Council in Taiwan under contracts no. NSC89-2214-E-006-052 and NSC90-2214-E-006-023, is gratefully acknowledged.

## REFERENCES


1. C. M. Lieber, Solid State Commun. **107,** 607 (1998).
2. Y. Cheng, D. M. Bagnall, H. Koh, K. Park, K. Hiraga, Z. Zhu, T. Yao, J. Appl. Phys. **84,** 3912 (1998).
3. A. Ohtomo, M. Kawasaki, Y. Sakurai, I. Ohkubo, R. Shiroki, Y. Yoshida, T. Yasuda, Y. Segawa, H. Koinuma, Mater. Sci. Eng. **B 56,** 263 (1998).
4. D. M. Bagnall, Y. F. Chen, Z. Zhu, T. Yao, S. Koyama, M. Y. Shen, T. Goto, Appl. Phys. Lett. **70,** 2230 (1997).
5. P. Zu, Z. K. Tang, G. K. L. Wong, M. Kawasaki, A. Ohtomo, H. Koinuma, Y. Segawa, Solid State Commun. **103**, 459 (1997).
6. M. H. Huang, S. Mao, H. Feick, H. Yan, Y. Wu, H. Kind, E. Weber, R. Russo, P. Yang, Science. **292,** 1879 (2001).
7. M. H. Huang, Y. Wu, H. Feick, N. Tran, E. Weber, P. Yang, Adv. Mater. **13**, 113 (2001).
8. Y. C. Kong, D. P. Yu, B. Zhang, W. Fang, S. Q. Feng, Appl. Phys. Lett. **78,** 407 (2001).
9. Z. W. Pan, Z. R. Dai, Z. L. Wang, Science. **291,** 1947 (2001).
10. K. Vanheusden, W. L. Warren, C. H. Seager, D. R. Tallant, J. A. Voigt, B. E. Gnade, J. Appl. Phys. **79,** 7983 (1996).
11. Z. Fu, B. Lin, G. Liao, Z. Wu, J. Cryst. Growth. **193,** 316(1998).
12. X. L. Xu, S. P. Lau, J. S. Chen, G. Y. Chen, B. K. Tay, J. Cryst. Growth. **223,** 201(2001).

Mat. Res. Soc. Symp. Proc. Vol. 703 © 2002 Materials Research Society V2.6

# Nano-Cylinder Structure Studied by X-ray Diffraction

Gu Xu, Zhechuan Feng,[1] Zoran Popovic,[2] Jianyi Lin[3] and Jagadese.J. Vittal[4]
Department of Materials Sci. & Eng., McMaster University, Hamilton, L8S 4L7, Canada
[1]Axcel Photonics Inc., 45 Bartlett Street, Marlborough, Massachusetts, 01752
[2]Xerox Research Center of Canada, Mississauga, Ontario, L5K 2L1, Canada
[3]Department of Physics, National University of Singapore, 119260, Singapore
[4]Department of Chemistry, National University of Singapore, 119260, Singapore

## ABSTRACT

The study of nano-cylinder structure has attracted much attention due to the application of multi-wall carbon nanotubes (MWCNTs). While some TEM observations indicate that they are formed by seamless concentric cylinders, other TEM and high pressure X-ray diffraction studies suggest that they look like scrolls of graphite sheets. Although many people now accept the concentric cylinder model, there has been no confirmation reported. On the other hand, this structural difference of MWCNTs plays a crucial role in determining the properties and suitability for future applications. For example, the periodical boundary condition can only be imposed for cylinders, but not for scrolls. To resolve this issue, we employed high-resolution X-ray diffraction to measure detailed profiles of the Bragg peaks for high-purity MWCNTs. We then identified some unusual observations unique to the nano-cylinder structure, followed by the analysis of the structural difference in the Fourier transform between nanotubes formed by scrolls and concentric cylinders. The simulation results are then compared with the experimental data to reveal the structural details.

## INTRODUCTION

The determination of nano-sized structures has been a great challenge to materials scientists and engineers. As a recent example, the cylindrical nature of multi-wall carbon nanotubes (MWCNT) has been much debatable [1-11]. While most of the transmission electron microscopy (TEM) observations indicate that they are formed by seamless concentric cylinders [1,2], some TEM and high-pressure X-ray diffraction studies suggest that they look like scrolls of graphite sheets [10,11]. This structural difference of MWCNT plays a crucial role in determining the properties and suitability for future applications, because, e.g., the periodical boundary condition can only be imposed for cylinders, but not for scrolls [12,13]. Although many people accept the concentric cylinder model, there has been no confirmation reported. To resolve this issue, we present high resolution x-ray diffraction results of high purity MWCNT made by catalytic decomposition, where non-equal Bragg peak breaths and shifting of the peak positions were observed. We then identify some unusual observations unique to the nano-cylinder structure, followed by the analysis of the structural difference in the Fourier transform between nanotubes formed by scrolls and concentric cylinders. The simulation results are then compared with the experimental data to reveal the structural details.

## EXPERIMENTAL

The x-ray diffraction intensities of carbon nanotube samples were recorded on a Philips X'Pert-MRD Diffractometer with an instrumental broadening of <0.003°/2θ (about 12 arc second) using Cu $K\alpha_1$ radiation ($\lambda$=0.15406nm). High purity carbon nanotube samples were prepared by catalytic decomposition of CO using Ni-MgO as the catalyst [14]. This method allows for a good control of the product and over 95% purity [15]. TEM studies show that they have a fairly uniform outer diameter of 20-30nm, each containing about 15 layers of carbon sheets, and extending up to 10 μm in length [14,15]. The resulting θ–2θ scan from 10-100°/2θ is shown in Fig.1a, which was indexed according to graphite structure, with (hk0) representing the reciprocal space of a graphitic layer, and (00l) for the stacking of the layers [11]. Local enlargements of (002) and (004) Bragg peaks are plotted in Fig.1b (taken by 5 min/step).

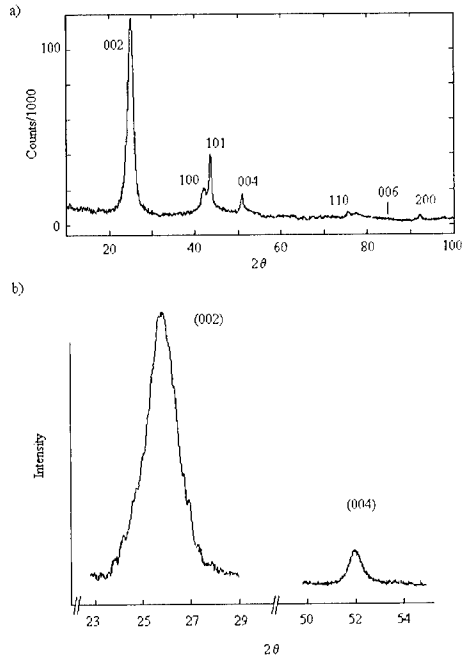


**Figure 1.** High resolution x-ray diffraction data (θ–2θ scans) of multi-wall carbon nanotubes; a) the entire data set (with Si peaks removed); b) enlargements of (002) and (004) Bragg peaks ($k=4\pi\sin\theta/\lambda$).

## RESULTS AND DISCUSSION

From the data, two unusual observations can be made. First of all, the full width at half maximum (FWHM) for the 1st Bragg peak is about 1.45°/2θ, and for the 2nd peak 0.65°/2θ. This produces a ratio of 2.23 of the peak breaths in 2θ, and a ratio of 2.42 in wave vector k ($=4\pi\sin\theta/\lambda$). It is quite unusual because the usually the peak width (measured by k) is related to q/N [16], where q is the peak value of k and N is the number of repeats. The other unusual feature is that the two Bragg peak positions are not obeying the integer multiples of wave vector q, 2q. For example, if we take the 2nd Bragg peak position (2θ = 51.96°) to be the 2q, the 1st peak then should be located at 2θ = 25.30°, rather than shown by the data of 2θ = 25.87°. This also rules out the possibility of having two sets of diffraction peaks, one of which is broader and has a very high effective static Debye-Waller factor, such that the 2nd order Bragg peak becomes much weaker than the 1st.

On the other hand, non-equal peak breaths were also observed in the low resolution x-ray diffraction (XRD) data from the existing literature [11, 17-20], and from a recent neutron diffraction experiment [21], where the (004) peaks were found to be wider than (002). Although this could also be attributed to the lattice distortion, it produces a much higher layer number [19]. From the enlargements of neutron diffraction data [21], the same "mismatch" for the peak positions can also be found, where (004) does not sit on 2q but right-shifted. Apart from the fact that the XRD data were collected using both Cu $K\alpha_1$ +$K\alpha_2$ lines, they are mostly based on the samples made by arc evaporation of graphite, rather than catalytic decomposition of CO. In some cases the sample purity was about 60% [19]. Although most of them found no strong (101) peak, due presumably to the expected misalignment between the graphite layers, the works of Pasqualini [20] and Burian et al [21] suggested that it is possible to have lateral correlation. Therefore, it is likely that they exist in the samples of high purity.

## NUMERICAL SIMULATION AND CONCLUSIONS

To resolve the exact structure, a numerical analysis is developed next, to compute the diffraction intensity by the nano-cylinders. For the micro-meter long carbon nanotubes intertwined in space, they can be considered as a collection of randomly distributed tubule segments, which are located at $\mathbf{r'}$ (=x',y',z'), and described by cylindrical co-ordinates $\mathbf{r}$=(r,φ,z):

$$I(\mathbf{k}) \propto |\Sigma_R \rho(\mathbf{R})\exp(i\mathbf{kR})|^2 = |\Sigma_{r'}\exp(i\mathbf{kr'})\int_{cy}d\mathbf{r}\rho(\mathbf{r})\exp(i\mathbf{kr})|^2 \qquad (1)$$

where $\mathbf{R} = \mathbf{r} + \mathbf{r'}$, $\mathbf{k} = (k_x,k_y,k_z)$, and the integral is performed within each segment. Because all segments have different orientations, the local co-ordinate axes (e.g., the tube axis z) vary the orientation from segment to segment. Therefore, we can label the integral of segments by F(k,r'), and equation (1) becomes (with * denotes the complex-conjugate):

$$\Sigma_{r'}\Sigma_{r''}F(\mathbf{k},\mathbf{r'})F^*(\mathbf{k},\mathbf{r''})\exp(i\mathbf{k}(\mathbf{r'}-\mathbf{r''})) = \Sigma_{r'}|F(\mathbf{k},\mathbf{r'})|^2 + \Sigma_{r'\neq r''}F(\mathbf{k},\mathbf{r'})F^*(\mathbf{k},\mathbf{r''})\exp(i\mathbf{k}(\mathbf{r'}-\mathbf{r''})) \qquad (2)$$

where r'' is also used for the location of the tube segment. Before the quantitative calculation of F(k,r'), from the work of Saito et al [17], we learn that for the tube segment, the reciprocal space

consists of annular rings and disks centered around the tube axis. Thus F(k,r') is real and the 2nd exp(ik(r'-r")) in equation (2) can be converted into a cosine function. Due to the random orientation and location of the tube segments, the second part of equation (2) will mostly vanish except at the overlap points of two mis-aligned ring sets, which are further modulated by the cosine factor. Thus the resulting intensity will follow the average of $|F(k)|^2$ over all orientations. The annular rings are then extended into spheres in the reciprocal space, to make the diffraction pattern powder-like. This powder-like nature of the sample can easily be verified by the diffraction measurement at various sample orientations, which was also performed in this study where no sample an-isotropy was detected. Therefore, the Bragg peaks can be calculated from the Fourier transform of any cylindrical segment. According to the convention of graphite structure, (00L) are used to denote reciprocal space along the radial direction of the cylinder, thus only the (r, φ) plane is needed in the calculation (Fig.2a,b). Moreover, the original 3D integral can be further reduced to 2D [22].

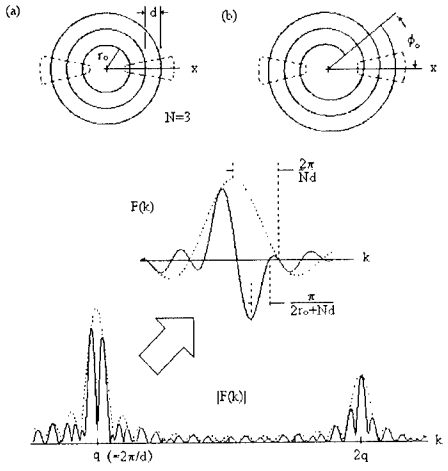


**Figure 2.** a) Cross-section of multi-wall nanotubes formed by concentric cylinders; b) Cross-section formed by scrolls of graphite sheets; both a) and b) employ polar coordinates r and φ; c) Numerical result of Fourier transform from a), with N=15, $r_o$=3.3d and $F_2$=-$F_1$/2 following equation 1; d) Enlargement of the 1st Bragg peak of c).

As an example, the numerical result of Eq.2 for Fig.2a is shown in Fig.2c. Only two inputs are needed. One is the number of layers, N=15, which can also be estimated from the width of the (002) Bragg peak of the data using Debye Formula [16]. The other is the ratio of $F_1/F_2$, where $F_n$ being the structure factors for one carbon layer, which forms one repeat unit cell along r-direction. Two Bragg peaks appeared, as indicated by the dashline. The location of the Bragg peak, q, is determined by the periodicity of the repeated structure, d, whereas the overall

peak breadth decided by the number of repeats, N, and the relative peak heights dependent on the choice of $F_n$. However, since $r_o$+Nd/2> Nd/2, the period of cos(k($r_o$+Nd/2)) is always *smaller* than that of sinc(kNd/2) (Fig.2d). Thus the resulting transform will follow the solid line of Fig.2c, 2d, where the dashlined peak is split into two or more narrower peaks. The above interference will be varied not only by $r_o$, but also by $\varphi_o$ for scrolls (Fig.2b). To see this, four representative cases within a cycle have been illustrated by Figs.3a-d. If the nanotube has a scroll form, because $\varphi_o$ can be arbitrary for each nanotube, the observed diffraction will become the intensity average of the entire cycle. The result is shown in Fig.3e, where the Bragg peak breadths become equal for both q and 2q. This means, the interference has been *averaged out* for scrolls. Due to the discrete nature of $r_o$ ($\propto (n^2+m^2+nm)^{1/2}$, where n,m specify the chiral vector of the inner most cylinder) [23], the intensity average over $r_o$ will *not*, in general, remove the interference effect. For example, when there exists a preferential $r_o$, and it is chosen to be the value in between Fig.3d and 3a, after the average the result shows that the 2nd peak has only 2/5 the width of the 1st (Fig.3f).

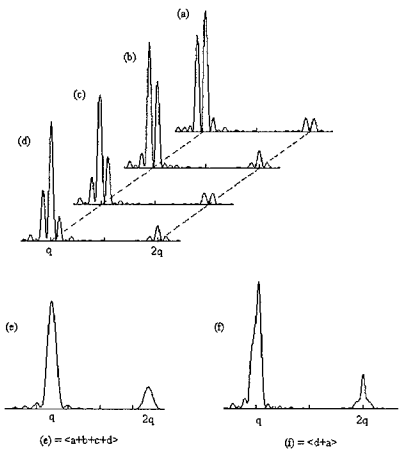


**Figure 3.** Amplitude square of the Fourier transform of a scroll oriented by $\varphi_o$, with N=15, $F_2$=-$F_1$/2 and $r_o$=3.05d; a) $\varphi_o=\pi/4$, b) $\varphi_o=\pi/2$, c) $\varphi_o=3\pi/4$, d) $\varphi_o=\pi$. The same set also serves to illustrate the results for concentric cylinders, which are very similar and without involving $\varphi_o$; they represent the changing $r_o$ with: a) $r_o$= 3.425d, b) $r_o$=3.30d, c) $r_o$=3.175d, d) $r_o$=3.05d; e) Overall $|F(k)|^2$ for scrolls, which has been averaged over the entire cycle of $\varphi_o$ from 0 to $\pi$; f) Example of $|F(k)|^2$ for concentric cylinders, with a small $r_o$ variation between a) and d).

Therefore, the Bragg peak widths (FWHM) must be equal for scrolls, whereas they are, in general, not the same for concentric cylinders (unless the inner radius follows a uniform distribution over a certain range, e.g., several d-spacing). The conclusion can be easily drawn from the comparison of the numerical results and the experimental data, which are in good agreement with Fig.3f for cylinders. In the meantime, it clearly rejects the scroll form (Fig.3e). In

addition to the confirmation of cylinder model, it is interesting to see that the inner tube diameter $r_0$ does follow a non-uniform distribution for our nanotubes.

To conclude, some unusual diffraction physics was obtained from high resolution x-ray diffraction of high purity MWCNT, in addition to the previous low resolution XRD measurements of low purity samples found in literature. The Fourier analysis not only shows that our multi-wall carbon nanotubes are made of concentric cylinders, but also reveals there is a non-uniform distribution of inner tube diameter. Also, the interference effect discussed in this paper is unique for concentric cylinders because the central canal is separating two identical multiwalls (not only in contrast to scrolls but also in contrast to irregular grains).

## REFERENCES


1. S. Iijima, *Nature* **354,** 56 (1991).
2. T.W. Ebbesen and P.M. Ajayan, *Nature* **358,** 220 (1992).
3. A. Thess, R. Lee, P. Nikolaev, H. Dai, P. Petit, J. Robert, C. Xu, Y.H. Lee, S.G. Kim, A.G. Rinzler, D.T. Colbert, G.E. Scuseria, D. Tomanek, J.E. Fischer and R.E. Smalley, *Science* **273,** 483 (1996).
4. M. Ge and K. Sattler, *Science* **260,** 515 (1993).
5. R. Saito, M. Fujita, G. Dresselhaus and M.S. Dresselhaus, *Appl. Phys. Lett.* **60,** 2204 (1992).
6. Z. Zhang and C.M. Lieber, *Appl. Phys. Lett.* **62,** 2792 (1993).
7. J.W.G. Wildoer, L.C. Venema, A.G. Rinzler, R. E. Smalley and C. Dekker, *Nature* **391,** 59 (1998).
8. T. W. Odom, J.L. Huang, P. Kim and C.M. Lieber, *Nature* **391,** 62 (1998).
9. A. Hassanien, M. Tokumoto, Y. Kumazawa, H. Kataura, Y. Maniwa, S. Suzuki and Y. Achiba, *Appl. Phys. Lett.* **73,** 3839 (1998).
10. V.P. Dravid, X. Lin, Y. Wang, X.K. Wang, A. Yee, J.B. Ketterson and R.P.H. Chang, *Science* **259,** 1601 (1993).
11. O. Zhou, R.M. Fleming, D.W. Murphy, C.H. Chen, R.C. Haddon, A.P. Ramirez and S.H. Glarum, *Science* **263,** 1744 (1994).
12. N. Hamada, S. Sawada and A. Oshiyama, *Phys. Rev. Lett.* **68,** 1579 (1992).
13. M.S. Dresselhaus, G. Dresselhaus and R. Saito, *Phys. Rev. B.* **45,** 6234 (1992).
14. P. Chen, H.B. Zhang, G.D. Lin, Q. Hong and K.R. Tsai, *Carbon* **35,** 1495 (1997).
15. P. Chen, X. Wu, J.Y. Lin, H. Li and K.L. Tan, *Carbon* **38,** 139 (2000).
16. B.E. Warren, *X-ray diffraction,* (Addison-Wesley, New York, 1969).
17. Y. Saito, T. Yoshikawa, S. Bandow, M. Tomita and T. Hayashi, *Phys. Rev. B.* **48,** 1907 (1993).
18. S. Bandow, *J. Appl. Phys.* **80,** 1020 (1996).
19. D. Reznik, C.H. Olk, D.A. Neumann and J.R.D. Copley, *Phys. Rev. B.* **52,** 116 (1995).
20. E. Pasqualini, *Phys. Rev. B.* **56,** 7751 (1997).
21. A. Burian, J.C. Dore, H.E. Fischer and J. Sloan, *Phys. Rev. B.* **59,** 1665 (1999).
22. G. Xu, Z.C. Feng, Z. Popovic, J. Lin and J. J. Vittal, *Advanced Materials* **13,** 264 (2001).
23. R. Saito, G. Dresselhaus, and M.S. Dresselhaus, *Physical properties of carbon nanotubes,* (Imperial College Press, London, 1998).

Mat. Res. Soc. Symp. Proc. Vol. 703 © 2002 Materials Research Society V2.7

# Thermal Characterization of Nanowire Array in $a$-$Al_2O_3$ Matrix

Diana-Andra Borca-Tasciuc[1†], Gang Chen[1], Yu-Ming Lin[2], Oded Rabin[2], Mildred S. Dresselhaus[2,3], Alexander Borshchevsky[4], Jean-Pierre Fleurial[4], and Margaret A. Ryan[4],
[1]Mechanical Engineering Department,
Massachusetts Institute of Technology, Cambridge, MA 02139, USA
[2]Physics Department,
Massachusetts Institute of Technology, Cambridge, MA 02139, USA
[3]Electrical Engineering Department,
Massachusetts Institute of Technology, Cambridge, MA 02139, USA
[4]Jet Propulsion Laboratory/California Institute of Technology,
4800 Oak Grove Drive, MS 277-207, Pasadena, CA 91109, USA

## ABSTRACT

Thermal properties characterization of Bi nanowires is critical in order to validate the predicted enhancement of their thermoelectric figure-of-merit. In this paper we report the effective thermal diffusivity of Bi nanowires array embedded in $a$-$Al_2O_3$ (alumina) template. The composite material consists of 85% alumina and approximately 15% Bi nanowires with a diameter of 40 nm and an average length of 40 μm. Measurements are performed along the nanowire axis. A thermal wave is produced at the front side of the sample and it is monitored at the backside through a fast thermoelectric effect. A one-dimensional heat conduction model is used to extract the thermal diffusivity.

## INTRODUCTION

The efficiency of a thermoelectric device is limited by the thermoelectric figure-of-merit of the material $Z = \sigma S^2/k$, where S is the Seebeck coefficient, $\sigma$ is electrical conductivity, and k is the thermal conductivity. Currently, the best commercially available thermoelectric material $(BiSb)_2Te_3$ has a ZT of ~1, however thermoelectric devices based on this material cannot compete in performance with other well-established technologies.

Several approaches have been explored to increase the thermoelectric figure-of-merit [1,2]. Among those, low-dimensional thermoelectric materials structures such as quantum wells, superlattices and nanowires have been extensively investigated [3-7]. As predicted by Hicks and Dresselhaus [2,8], quantum effects in low-dimensional systems may result in increased density of states near Fermi level and consequently increased electrical conductivity and Seebeck coefficient. Furthermore, increased scattering of heat carriers from interfaces leads to a decreased thermal conductivity in such systems. In light of these, theoretical studies done on bismuth nanowires estimate a significantly enhanced thermoelectric figure-of-merit [5]. However, experimental measurements must be carried out in order to validate the theoretical estimations. While electrical properties and Seebeck coefficient of bismuth nanowires have been characterized [9], another key property of a material candidate to thermoelectric applications, thermal conductivity, has yet to be determined experimentally. However, manipulation and preparation of test specimens of nanometer size is not an easy task. Therefore, a first approach in

† Visiting student from UCLA.

exploring thermal properties of nanowires is to characterize them embedded in another media with known thermal properties

In this paper we report thermal diffusivity measurements of Bi nanowires in amorphous $Al_2O_3$ matrix. The composite material has 85% alumina and approximately 15% Bi nanowires. The nanowires are highly ordered, with a diameter of 40 nm and an average length of 40 μm. Thermal diffusivity measurement is carried out in the direction along the nanowire axis. Modulated heating is applied to the front side of the sample and the amplitude and phase of the temperature signal is monitored at the backside by a fast responding thermocouple. The thermal diffusivity is extracted by fitting the experimental data to a one-dimensional heat transport model. Preliminary results suggest that thermal diffusivity of the composite material is $1.3x10^{-6}m^2s^{-1}$. In order to extract the thermal diffusivity of Bi nanowires further investigation of thermal properties of the host alumina template must be carried out.

## SAMPLE PREPARATION

The template used for the preparation of Bi nanowires is an anodic porous alumina, with highly ordered nanochannels formed by the anodization of aluminum. Thermal characterization was initially performed on commercially available templates (Whatman, Anodisc). However, SEM micrographs (Fig. 1(a)) of Whatman templates have shown that templates are not uniform and they have variable diameter across the thickness. Uniform pore size is critical in order to obtain consistent quantum effects once the pores are filled with material of interest. To overcome these inconveniences, templates of uniform pore diameter were fabricated through a two-step anodization process [10]. Figure 1 (b) is a SEM micrograph of a fabricated alumina template. The structure of porous alumina can be described as self-ordered array of cells with cylindrical pores of diameter as low as 10 nm and depth exceeding 1000 μm [11,12]. The pore geometry can be controlled by the oxidization conditions. The templates were filled by pressure injection with molten Bi [13]. Figure 1(c) represents a SEM micrograph of an alumina template filled with Bi nanowires with a uniform pore diameter of 40 nm. A layer of excess Bi resulted from pressure injection process is present on one side of the sample. The thickness of these samples is typically tens of microns (50-70 μm) and consequently samples are very fragile and difficult to handle.

## MEASUREMENT TECHNIQUE

The thermal diffusivity of alumina templates (empty or filled with Bi) was measured

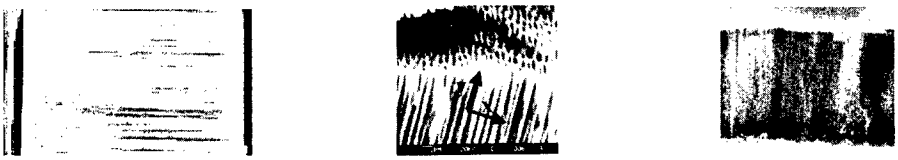

(a) (b) (c)

**Figure 1.** SEM micrographs: (a) Cross-section of a commercially available alumina template (0.02 μm Whatman, Anodisc). (b) Fabricated alumina template. y represent the direction along the pore axis and x represent the direction perpendicular to the pore axis.(c) Bi filled alumina template. The non-uniform top layer is excess Bi.

along the pore/nanowire axis (y-direction in Fig. 1(b)). Figure 2 shows a schematic of the experimental set up. In this technique, ac optical heating is applied at the front side of the sample and a fast thermoelectric effect is used to detect the temperature rise at the backside.

The ac heating is produced by the absorbed light coming from a tungsten lamp and modulated by a chopper. The area of the light spot is of few $mm^2$ in order to insure one-dimensional heat conduction across the sample thickness, which is in the order of tens of microns. In case of transparent samples (such as empty alumina templates) a thick copper layer (about 1μm thick) was deposited on the front side of the sample in order to absorb the incident light.

The amplitude and phase of the temperature signal are monitored at the backside by a fast responding thermocouple. The junction of the thermocouple consists of a point contact between a sharp metallic wire and the sample surface, which has to be electrically conductive [14,15]. Since the junction has zero thermal mass the thermocouple is expected to be very fast responding. Previous experiments carried out in our laboratory demonstrated that the thermocouple junction could respond to frequencies higher than 100 KHz [14,15]. A second wire is connected to the sample surface far from the heated spot in order to close the electrical circuit. The thermocouple voltage consists of the Seebeck voltage drop across the sharp wire ($V_w$ in Fig. 2) and the in-plane Seebeck voltage drop on sample surface ($V_s$ in Fig. 2). The second wire attached to the sample experiences no temperature difference between its ends and therefore has no contribution to the thermocouple voltage. The thermocouple voltage is measured by a lock-in amplifier at the modulation frequency. The data collection is automatically and controlled by a LabView program.

## MODELING AND CALIBRATION

The modulated heating at the front side of the sample produces an AC temperature rise at the backside. Under the assumption of one-dimensional heat conduction and adiabatic boundary condition the complex temperature rise at the backside of the sample is given by:

$$T(L) = \frac{2Pe^{mL}}{Akm(1 - e^{2mL})} \qquad (1)$$

where

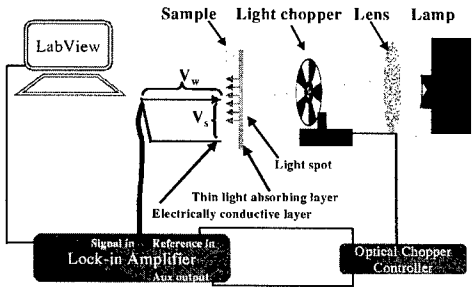


**Figure 2.** Experimental set-up.

$$m = \sqrt{i\frac{2\pi f}{\alpha}} \qquad (2)$$

and P is power, A is area, k is sample thermal conductivity, f is frequency, L is sample thickness and $\alpha$ is thermal diffusivity. The expression contains both the amplitude and phase of the temperature rise.

The thermal diffusivity can be determined by comparing the calculated phase and the normalized amplitude of the AC temperature rise with the experimental signal.

The technique was tested on glass slides (VWR International, Micro Cover Glasses) of two different thicknesses. The glass slides were covered by e-beam deposition with 1 μm of copper on one side to absorb the light and with a thin (500 nm) layer of gold on the other side for electrical conduction. Figure 3 (a and b) is an example of the normalized amplitude and phase for glass slides of two different thicknesses of 147 (±12) μm and 240 (±12) μm. The dots are experimental data and the continuous line is the fitting curve. The measured thermal diffusivity is $6.2\times10^{-7}$ $m^2s^{-1}$ for the 147 μm thickness sample and $5.6\times10^{-7}m^2s^{-1}$ for the 240 μm sample. The difference in the measured thermal diffusivity could be explained by the relatively high uncertainty in the thickness measurement. The value of measured thermal diffusivity is relatively close to the one reported by a manufacturer (Corning) of similar type of glass: $6.9\times10^{-7}$ $m^2s^{-1}$[16].

## RESULTS

The thermal diffusivity characterization of commercially available (Whatman, Anodisc) empty alumina templates was performed first. Figure 4 (a and b) shows the experimental signals and the fitted phase and normalized amplitude for Whatman templates of two different pore diameter and porosities. The thermal diffusivity of the 0.02 μm pore diameter Whatman template (36% porosity) is found to be $5\times10^{-7}$ $m^2s^{-1}$. The value is close to the thermal diffusivity of the 0.1 μm pore diameter template (50% porosity) $4.7\times10^{-7}$ $m^2s^{-1}$. However, template roughness (estimated to be thousands of Å) may affect these results since the sharp wire may not be in good contact with the solid part of the template underneath. Currently, different methods are investigated in order to cross-check these results.

It should be mentioned that thermal conductivity of the 0.02 μm Whatman templates was measured through a different technique before [17]. In this technique a microfabricated heater/temperature sensor was used to measure the anisotropic thermal conductivity of the

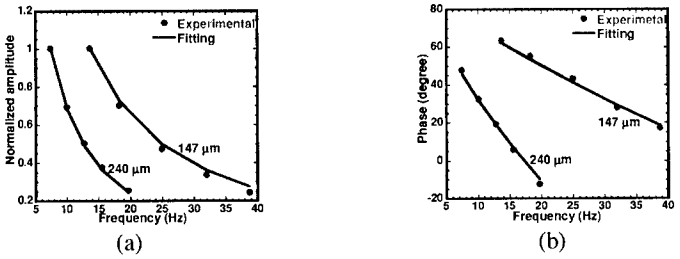


**Figure 3.** Normalized amplitude (a) and phase (b) of glass slides of two different thicknesses. The dots represent experimental data points and the continuous line is the fitting.

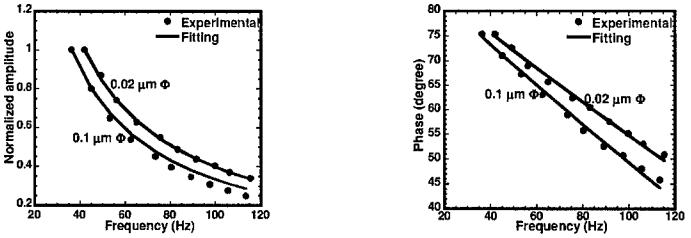


(a) (b)

**Figure 4.** Normalized amplitude (a) and phase (b) of Whatman anodic alumina templates of 0.02 μm pore diameter (36 %) and 0.1 μm pore diameter (50% porosity).

template. The effective thermal conductivity measured along the pore axis was 1.47 W/mK. However this measurement required density/porosity and specific heat of amorphous porous alumina for data interpretation. Since these parameters were difficult to estimate a relatively high uncertainty remains associated with the above result. However, the low value of the measured thermal conductivity suggested that the alumina template is a good candidate for thermoelectric applications.

Finally the effective thermal diffusivity of Bi filled alumina template was measured. The excess Bi layer was used for electrical connection in thermocouple measurement. The incident light was directly absorbed at the other side of the sample. Figure 5 (a and b) shows the experimental signals and the fitted normalized amplitude and phase. Preliminary results suggest that thermal diffusivity of the filled sample is $1.3 \times 10^{-6}$ $m^2 s^{-1}$. The calculated phase and normalized amplitude at low frequencies agrees well with the experimental data. However, at higher frequencies there is a difference between predictions and experiment. Although the reason for this is still under investigation a possible explanation could be the thermal mass of the Bi layer from the backside of the sample. It should be emphasized that this result is preliminary. The thermal diffusivity measurement was carried out on a single sample of relatively small size. More measurements on samples with different thicknesses and of larger area must be carried out in order to confirm the result. Furthermore, in order to extract the thermal diffusivity of Bi nanowires and compare it with thermal diffusivity of bulk Bi ($8 \times 10^{-6}$ $m^2 s^{-1}$), thermal diffusivity measurement of the fabricated template must be carried out.

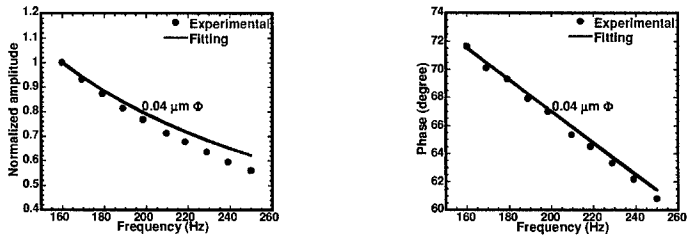


(a) (b)

**Figure 5.** Normalized amplitude (a) and phase (b) of Bi filled alumina template.

## CONCLUSION AND FUTURE WORK

A simple and fast technique was applied to characterize thermal properties of thin membranes. Thermal diffusivity measurements of Bi filled alumina template were carried out at room temperature. The results suggest that thermal diffusivity of the filled template is larger then thermal diffusivity of the empty alumina template. Currently, efforts are on way to characterize the 40 nm diameter template in order to extract the thermal diffusivity of Bi nanowires.

## ACKNOWLEDGMENTS

This work is supported by DoD/ONR MURI on low-dimensional thermoelectrics (N00014-97-1-0516). D. B.-T. thanks to Jianping Fu, Ronggui Yang, and Arvind Narayanaswamy for the manuscript review.

## REFERENCES

1. *Recent trends in thermoelectric materials research*,T.Tritt (volume editor) *Semicond. Semimet.* **69-71** (2001)
2. L.D. Hicks and M. S. Dresselhaus, *Phys. Rev. B*, **47**, 12727 (1993).
3. T. Koga, X. Sun, S. B. Cronin, M. S. Dresselhaus, K. L. Wang, and G. Chen, *J. Com.-Aided Mat. Design*, **82**, 830 (1997).
4. T. Koga, X. Sun, S. B. Cronin, and M. S. Dresselhaus, *Appl. Phys. Lett.*, **75**, 2438 (1999).
5. X. Sun, Z. Zhang, and M. S. Dresselhaus, *Appl. Phys. Lett*, **74**, 4005 (1999).
6. T. C. Harman, P. J. Taylor, D. L. Spears, and M. P. Walsh, *J. Electron. Mat.*, **29**, L1 (2000).
7. M. S. Dresselhaus, G. D. Dresselhaus, X. Sun, Z. Zhang, S. B. Cronin, T. Koga, J. Y. Ying, and G. Chen, *Micros. Thermophys. Eng.*, **3**, 89 (1999).
8. L.D. Hicks and M. S. Dresselhaus, *Phys. Rev. B*, **47**, 16631 (1993).
9. S. B. Cronin, Y. M. Lin, T. Koga, X. Sun, J. Y. Ying, and M. S. Dresselhaus, *Proceedings ICT'99*, 554 (1999).
10. Y.-M. Lin, *Fabrication, Characterization and Theoretical Modeling of Te-doped Bi Nanowire Systems for Thermoelectric Applications*, M.S. Thesis, Massachusetts Institute of Technology, (2000).
11. D. Crouse, Y. Lo, A. E. Miller, and M. Crouse, *Appl. Phys. Lett.*, **76**, 49 (2000).
12. H. Masuda, H. Yamada, M. Satoh, H. Asoh, M. Nakao, and T. Tamamura, *Appl. Phys. Lett.*, **71**, 2770 (1997).
13. Z. Zhang, J. Y. Ying, and M. S. Dresselhaus, *J. Mater. Res.*, **13**, 1745 (1998).
14. T. Borca-Tasciuc, and G. Chen, *Intl. J. Thermophys*, **19**, 557 (1998).
15. T. Borca-Tasciuc, and G. Chen, *Proc. 1999 Natl. Heat Transf. Conf.*, (CD ROM) (1999)
16. www.abrisa.com -distributor of Corning glass. At the date this paper was written, the URL referenced herein were deemed to be useful supplementary material to this paper. Neither the author nor the Materials Research Society warrants or assumes liability for the content availability of URLs referenced in this paper.
17. D.-A. Borca-Tasciuc, *Thermal Characterization of Nanochanneled Alumina*, M.S. Thesis, University of California Los Angeles, (2001).

Mat. Res. Soc. Symp. Proc. Vol. 703 © 2002 Materials Research Society V2.8

# Formation of Ordered Silica–Organic Hybrids by Self-Assembly of Hydrolyzed Organoalkoxysilanes with Long Organic Chains

Kazuyuki Kuroda[1,2] and Atsushi Shimojima[1]

[1]Department of Applied Chemistry, Waseda University,
Ohkubo-3, Shinjuku-ku, Tokyo 169-8555, Japan

[2]Kagami Memorial Laboratory for Materials Science and Technology, Waseda University,
Nishiwaseda-2, Shinjuku-ku, Tokyo 169-0051, Japan

## ABSTRACT

Various layered hybrid films prepared from organoalkoxysilanes with long organic chains, based on the self-assembly of the hydrolyzed species, are reviewed. Morphological control of transparent and oriented films was achieved by cohydrolysis and polycondensation with tetraalkoxysilanes, followed by dip- or spin-coating. In addition to alkyltrialkoxysilanes, alkyldimethylmonoalkoxy- and alkylmethyldialkoxy-silanes were also used as the structural units, implying that the inorganic–organic interface can be designed at a molecular level. In these cases, co-condensation in the precursor solution plays an essential role in the formation of homogeneous and ordered films. Alkenyltriethoxysilanes with terminal C=C bonds were also employed to prepare layered hybrid films. Interlayer chains were polymerized upon UV irradiation, and the resulting films exhibited a significant increase in the hardness if compared with the films before polymerization. Hybrid films thus obtained are a new class of materials and of great interest for a wide range of materials chemistry.

## INTRODUCTION

Organoalkoxysilanes are widely used as structural units to construct a variety of silica-based hybrid materials [1–3]. Because simple sol–gel reactions of alkoxysilanes usually result in the formation of amorphous materials [4], much efforts have been made in the structural control on a nanometer-length scale [5–8]. Such an attempt is of great interest from the possibility to produce novel hybrid materials with unique structures and properties.

Self-organization of organosilane molecules is a promising technique for the construction of ordered hybrid materials. The process relies on the amphiphilic nature of hydrolyzed organosilane molecules containing both hydrophilic silanol groups and hydrophobic alkyl chains. While many studies have focused on the interfacial deposition of alkylsiloxane monolayers [9], researchers have recently shown that the process can be extended to the formation of multilayered hybrids by the reaction in solution states [10–12]. We reported the formation of multi-bilayer aggregates by hydrolysis and polycondensation of alkyltrialkoxysilanes in homogeneous solutions [12]. These are a new class of layered materials consisting of organic two-dimensional arrays and siloxane networks linked by covalent Si–C bonds.

Although the layered hybrids derived from alkyltrialkoxysilanes are obtained as powders, transparent and oriented thin films can be obtained by cohydrolysis and polycondensation with tetraalkoxysilane under well-controlled conditions [13]. This synthetic approach can be extended to the development of a variety of hybrid materials by the molecular design of starting organoalkoxysilane with varied alkyl chain lengths, controlled numbers of the organic groups, and various functionalities in the organic groups.

In this paper, we present a review of the recent developments conducted in our laboratory on the formation of ordered hybrid films derived from the organoalkoxysilane–tetraalkoxysilane systems [14–16]. In addition to the alkyltrialkoxysilane with various chain lengths, alkyldimethylalkoxysilane and alkylmethyldialkoxysilanes as well as alkenyltrialkoxysilane were used as the starting molecules (figure 1). This approach will lead to the formation of highly organized architectures by a simple sol–gel route using various organoalkoxysilanes.

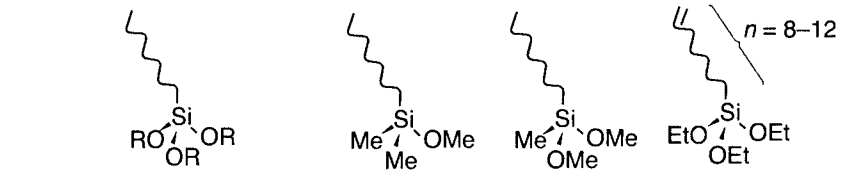


**Figure 1.** Organoalkoxysilanes used in this study.

## LAYERED HYBRID FILMS DERIVED FROM C*n*TES–TEOS SYSTEMS

Precursor solutions were prepared by cohydrolysis and polycondensation in the C*n*TES–TEOS–EtOH–$H_2O$–HCl system [14]. The $^1H$ NMR spectra of the reaction mixtures revealed that the signals due to ethoxy groups ($SiOC\underline{H}_2CH_3$, at around 3.8 ppm) almost disappeared within the first period of 15 min. The $^{29}Si$ NMR spectra of the solution in the C18TES–TEOS system revealed that the signals assigned to the monomeric species of both alkoxysilanes disappeared after the reaction at 40 °C for 90 min. Although the signals due to oligomeric species were not clearly resolved, the co-condensation between C*n*TES and TEOS should occur because sufficient evidences have already been reported in similar systems [17,18].

Thin films were deposited on glass substrates by dip-coating. However, the structural ordering and the macroscopic homogeneity of the films depended largely on the alkyl chain length as well as the solution temperature during the deposition. In the C10TES–TEOS system, transparent films exhibiting a sharp diffraction peak ($d$ = 3.48 nm) were formed at around room temperature (20–25 °C). The layered structure of the film was confirmed by TEM (not shown). Although the films prepared at lower temperatures (10 and 15 °C) also exhibited sharp diffraction peaks, they were not homogeneous and the $d$ values were rather variable. In contrast, the deposition at higher temperatures up to 30 °C resulted in the formation of homogeneous films with a disordered nanostructure. Similar trends were also observed for the systems with $n$ = 8 and 12 .

In the case of $n \geq 14$, neither transparent nor well-ordered films were deposited from the solution at around room temperature. Figure 2 shows the variation in the XRD pattern of the hybrid films in the C14TES–TEOS system. The films obtained at around room temperature exhibited very broad peaks. However, the intensity of the peaks progressively increased as the solution temperature increases, and transparent and highly ordered films were obtained at 30–35 °C. The effect of the solution temperature was more clearly observed for the systems with $n$ = 16 and 18. In these cases, well-ordered films with sharp and intense peaks were formed at 40–45 °C and 55–60 °C, respectively.

The incorporation of the Q units in the C*n*TES-derived hybrids contributed to the thermal stability. The layered hybrid derived from C18TES alone melted into an amorphous state upon heating above ~110 °C [12]. In contrast, the layered product

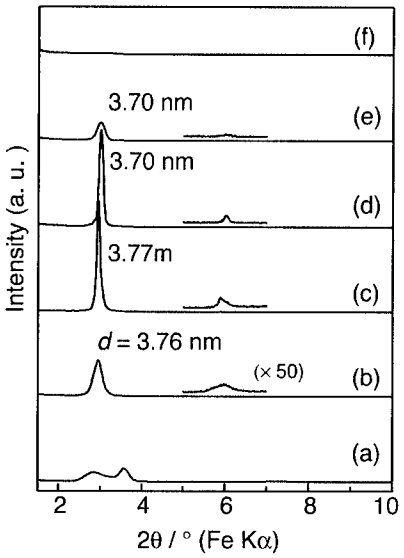


**Figure 2.** XRD patters of the hybrid films in the C14TES–TEOS system prepared at various temperatures: (a) 20 °C, (b) 25 °C, (c) 30 °C, (d) 35 °C, (e) 40 °C, and (f) 45 °C.

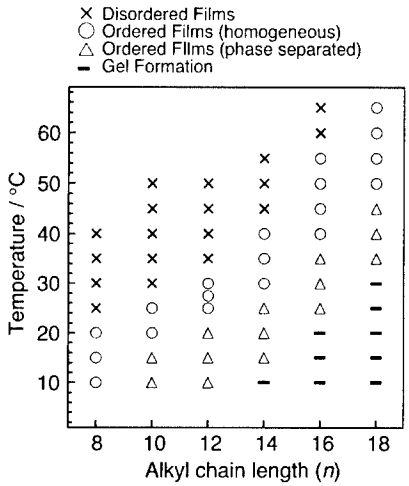


**Figure 3.** Variation of the products derived from the C*n*TES–TEOS systems ($n$ = 8–18) depending on the solution temperatures.

derived from the C18TES–TEOS system retained the structure even at 170 °C, suggesting that the product was comprised of more stable siloxane networks.

Figure 3 summarizes the variation of the nanostructure and the macroscopic morphology of the resulting hybrids depending on the solution temperature during the film formation. Transparent and ordered films are formed at higher temperatures with increasing chain length, suggesting that the self-assembly of alkylsiloxane oligomers depend essentially on the solution temperature. When a substrate is withdrawn from the reaction mixtures, silicate species in the solutions are concentrated by the evaporation of the solvent, and finally polycondensed to form siloxane networks. The formation of oriented multilayered films requires uniform and continuous organization, presumably from solid–liquid and liquid–vapor interfaces, during this coating process. In the cases of C*n*TES with longer chains ($n \geq 14$), the films deposited at lower temperatures exhibited a less-ordered structure. This behavior is probably attributed to the random nucleation of the layered aggregates caused by a slight decrease in the temperature as well as the evaporation

of the solvent during the film formation. The suppression of the segregation of the layered aggregate appears to play an important role in the formation of oriented films. In all the systems, further increase in the deposition temperature caused the structural disordering and eventually led to amorphous films. This is explained by the general behavior of amphiphilic assemblies that become isotropic states at higher temperature. The films may be solidified by the siloxane formation prior to the self-organization.

Figure 4 represents the basal spacings of the well-ordered films as a function of the alkyl chain length. For comparison, the *d* values for the layered hybrids derived from C*n*TES (*n* = 12–18) alone are also shown. As we reported previously, the products derived from C*n*TES alone are comprised of a bilayer structure with *all-trans* chains almost perpendicular to the siloxane layers [12]. In contrast to the linear relationship in these products, the *d* spacing of the films increases continuously in the range of *n* = 8 to 14, but decreases between *n* = 14 to 16. It is reasonable to assume that the thickness of the siloxane layer is almost constant independent of the chain lengths, because the TEOS/C*n*TES ratio is identical in all the systems. Therefore, the above behavior should be attributed to the variation in the conformation and/or the packing arrangement of the interlayer alkyl chains depending on the alkyl chain length.

The difference in the conformations of the alkyl chains in the films was confirmed by $^{13}C$ CP/MAS NMR. The $^{13}C$ signals ascribed to the interior methylene carbons appear at 30 ppm for *n* = 8–14, suggesting the presence of *gauche* conformers. However, the

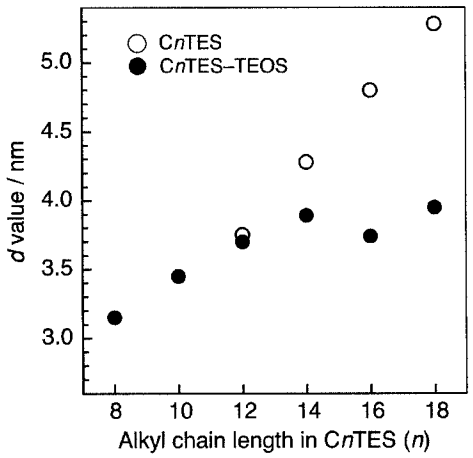


**Figure 4.** Variation in the *d* values as a function of the number of carbon atoms in the alkyl chain: The layered hybrid films derived from the C*n*TES–TEOS systems (filled circles) and the layered hybrids derived from C*n*TES alone (open circles).

relative intensity of the signal at 33 ppm, indicative of the chains in *all-trans* conformations, increases as the chain length increases to $n = 16$ and 18.

The packing arrangements of the interlayer chains can be divided into two types, i.e. interdigitated monolayer and bilayer structures, according to the representative models for amphiphilic lamellar phases [19]. In the cases of $n$ = 8–12, the alkyl chains are supposed to adopt a bilayer structure with disordered state, based on our study on the layered hybrid films derived from C*n*TMS ($n$ = 8–12)–TMOS systems [13]. However, in the cases of $n$ = 16 and 18, the observed $d$ spacings appear to be too small for the similar bilayer structures, considering that the chains are longer and take more extended states. Indeed, the $d$ value of the film in the C18TES–TEOS system is considerably smaller than that of a bilayer structure derived from C18TES alone (figure 4), although there is no significant conformational difference in both of the products. It is considered that the alkyl chains are arranged in an interdigitated monolayer with a rather ordered state. Such interlayer structures are also reported for the alkylsilylated derivatives of crystalline layered polysilicates [20,21], and may arise from the increases in the distance between alkylsilyl groups due to the presence of co-condensed Q units.

## LAYERED HYBRID FILMS DERIVED FROM C*n*TMS–, C*n*MeDMS–, AND C*n*Me$_2$MMS–TMOS SYSTEMS

In these systems, hybrid films were prepared by cohydrolysis and polycondensation of C*n*TMS ($n$ = 8, 10, 12)–TMOS–THF–$H_2O$–HCl mixtures, followed by spin-coating on glass substrates [15]. As shown in figure 5, the XRD patterns of the hybrid films derived from the C10TMS–, C10MeDMS–, and C10Me$_2$MMS–TMOS systems showed sharp diffraction peaks with the $d$ spacings of 3.56, 3.67, and 4.06 nm, respectively. The structural ordering and the macroscopic morphology of the films are strongly affected by the reaction time in the precursor solutions. The solutions at the earlier stages of the reactions afford inhomogeneous films with phase separated morphologies. On the other hand, further reactions in the precursor solutions caused the disordering of the nanostructures, and finally led to the formation of amorphous films. Controlled reaction in the precursor solutions was needed for the formation of well-ordered and transparent hybrid films.

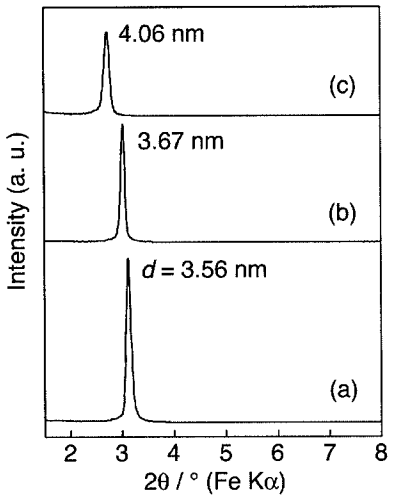


**Figure 5.** XRD patterns of the hybrid films derived from (a) C10TMS–, (b) C10MeDMS–, and (c) $C10Me_2MMS$–TMOS systems.

The TEM images of the ordered films showed well-defined stripes due to the lamellar structures, and the periodicities agree closely with the *d* spacings measured by XRD. The layered structures of these films were also confirmed by the structural collapse upon calcination at 450 °C for 6 h to remove organic constituents.

The formation of siloxane networks in the films was confirmed by $^{29}Si$ MAS NMR. The spectra for all the systems showed the signals assigned to the $Q^2$ (–90 ppm), $Q^3$ (–100 ppm), and $Q^4$ (–110 ppm) units derived from TMOS. In addition, the signals due to the organosiloxane units derived from C10TMS, C10MeDMS, and $C10Me_2MMS$ are observed at the $T^2$ (–55 ppm) and $T^3$ (–65 ppm), $D^1$ (shouldered peak at –10 ppm) and $D^2$ (–16 ppm), and $M^1$ (13, 7 ppm) regions, respectively.

Similar hybrid films were prepared when the alkyl chain lengths in alkylmethoxysilanes were 8 and 12. The formation of ordered films required longer reaction time in the precursor solution with increasing chain length. This is in part ascribed to the difference in the condensation rate depending on the chain length. In this manner, the reaction time in the precursor solution was optimized depending on the number of methoxy groups and alkyl chain lengths. Figure 6 shows the relationship between the *d* values of the resulting hybrid films and the alkyl chain lengths of the alkylmethoxysilanes used. The *d* value increases continuously with increasing chain lengths and exhibit larger value as the number of methoxy groups decreases.

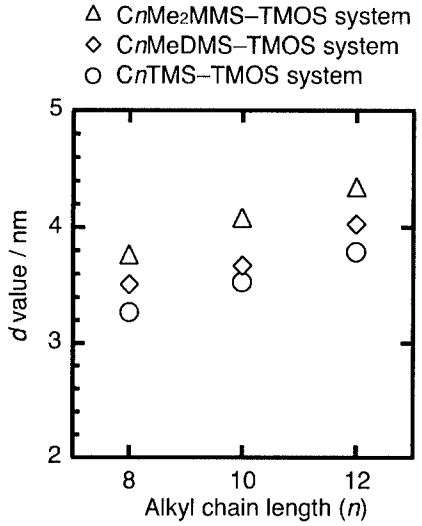


**Figure 6.** Variation in the *d* values of the hybrid films as a function of the alkyl chain length in the alkylmethoxysilanes.

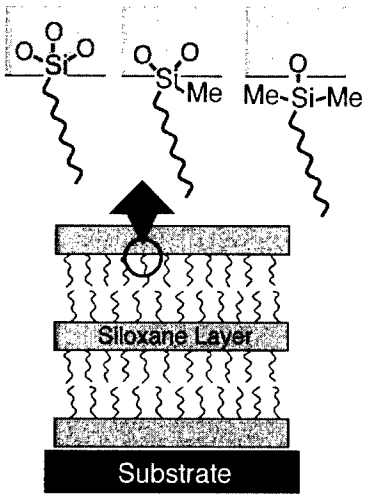


**Figure 7.** Proposed structural models for the hybrid films derived from C*n*TMS–, C*n*MeDMS–, and C*n*Me$_2$MMS–TMOS systems.

The structural models for the hybrid films are schematically illustrated in figure 7. The films have multilayered structures consisting of a bilayer arrangement of alkyl chains that are covalently attached to siloxane layers. The observed difference in the *d* value with varying the number of methoxy groups in the starting alkylmethoxysilanes (figure 6) is probably attributed to the variation in the interfacial structures. It is supposed that the trialkoxysilyl groups are in part integrated into the siloxane networks due to their cross-linking abilities, while the substitution of methyl groups for methoxy groups results in the grafting on the external surface of silica layers.

In the present system, co-condensation between alkylmethoxysilanes and TMOS in the precursor solution plays a crucial role in the formation of ordered hybrid films. This is supported by the fact that neither transparent nor ordered films were obtained by the hydrolysis and polycondensation of alkylmethoxysilane alone. In the $^{29}$Si NMR spectra of the precursor solutions, the signals due to monomeric species almost disappeared and those of the oligomeric species including substantial amounts of co-condensed units were observed. These results provide a strong evidence that the origin of the self-assembly in

this system is quite different from that of the conventional single-component systems using alkyltrialkoxysilanes alone [12]. The alkylsiloxane oligomers formed by the co-condensation can be regarded as amphiphilic molecules containing both hydrophobic alkyl chains and hydrophilic silanol groups. We suppose that the construction of ordered films relies on the self-assembly of these oligomeric species by the rapid evaporation of the miscible solvent during the spin-coating procedure.

## LAYERED SILICA/ORGANIC POLYMER HYBRID FILMS DERIVED FROM v-C*n*TES–TEOS SYSTEMS

Multilayered hybrid films were also prepared from v-C*n*TES–TEOS–EtOH–$H_2O$–HCl mixtures [16]. The films before UV irradiation showed sharp diffraction peaks with the *d* spacing of ca. 3.0–3.6 nm, depending on the chain lengths. The films are considered to have a bilayer arrangement of alkenyl chains, because the *d* spacings of the films are similar to those of the films derived from C*n*TES–TEOS systems (see figure 4). The IR spectrum of the v-C8TES-derived film before the UV irradiation (figure 8a) shows the absorption bands due to the siloxane framework (1000–1200 $cm^{-1}$, 450 $cm^{-1}$) and the terminal double bonds in the organic groups at 3079 $cm^{-1}$ (=CH stretching), 1642 $cm^{-1}$ (C=C stretching), and 910 $cm^{-1}$ (=$CH_2$ out-of-plane deformation). These results suggest that the films are composed of lamellar structures containing vinyl functionalities within the interlayers.

The film exposed to the UV light still retained the structural order with a slight decrease in the *d* value in the XRD pattern. As shown in figure 9, the TEM image of the film derived from the v-C8TES–TEOS system shows well-defined stripe patterns whose periodicity corresponds to the *d* spacing determined by XRD . The polymerization of organic chains was evidenced by the substantial decrease in the IR absorption bands ascribed to the terminal double bonds (figure 8b). Because the interlayer organic chains in this system appear to adopt a bilayer structure, polymerization should have proceeded either within layers or between adjacent layers. The resulting hybrid film exhibited a remarkable increase in the hardness and the scratch resistance if compared with the film before the organic polymerization.

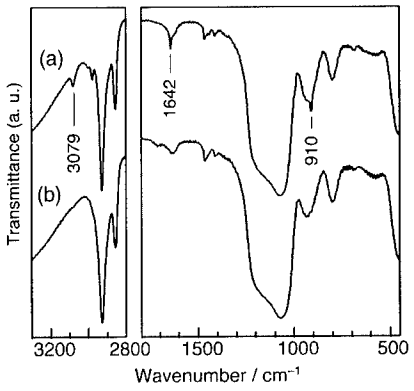


**Figure 8.** FT-IR spectra of the films derived from the v-C8TES–TEOS system (a) before and (b) after the UV irradiation.

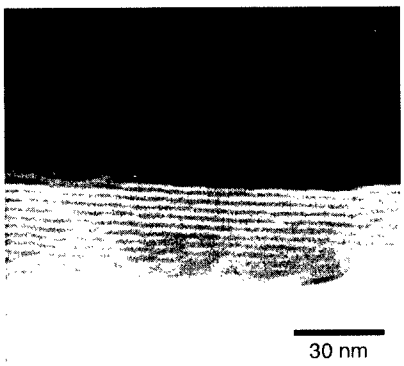


**Figure 9.** TEM image of the hybrid film derived from the v-C8TES–TEOS system after the UV irradiation. (The film was powdered for the observation.)

All these results indicate the formation of inorganic–organic hybrid films with a lamellar structure in which the siloxane layers and the organic polymer are linked by Si–C bonds. With regard to the silica-organic polymer hybrids, intercalation of organic polymers into the interlayer spaces of crystalline layered silicates has attracted much attention for the possibility to provide new properties [22]. Covalent linking between organic moieties and silica interlayers can also be attained by using a silane coupling agent such as γ-methacryloxypropyltrimethoxysilane [23]. However, the present approach is quite different in utilizing the molecular self-assembly of organoalkoxysilane–tetraalkoxysilane system, which enabled the morphological control into the transparent and oriented thin films.

## CONCLUSIONS

We have presented the formation of multilayered hybrid films consisting of alternating organic and siloxane layers by the sol–gel reaction of a series of organoalkoxysilanes and tetraalkoxysilane. This approach is quite simple and effective for the construction of ordered hybrids with precisely controlled nanostructures, macroscopic homogeneities, and compositions. The introduction of tetraalkoxysilane contributes to the

morphological variation and increases the thermal stability that could not be attained by hydrolysis and condensation of alkyltrialkoxysilane alone. It is of great interest that the ordered hybrid films were also obtained from alkyldimethylmethoxysilane and alkylmethyldimethoxysilane in the presence of TMOS. In these systems, co-condensation between alkylmethoxysilane and TMOS in the precursor solutions is essential for the self-organization. The overall results provide an access to the generalized synthesis of ordered hybrid films utilizing various organoalkoxysilanes with hydrophobic organic groups.

## ACKNOWLEDGMENTS

This work was financially supported by the Grant-in-Aid for COE research and for JSPS Fellows from the Ministry of Education, Culture, Sports, Science and Technology.

## REFERENCES

1. U. Schubert, N. Hüsing and A. Lorenz, *Chem. Mater.* **7**, 2010 (1995).
2. C. Sanchez, F. Ribot and B. Lebeau, *J. Mater. Chem.* **9**, 35 (1999).
3. D. A. Loy, B. M. Baugher, C. R. Baugher, D. A. Schneider and K. Rahimian, *Chem. Mater.* **12**, 3624 (2000).
4. C. J. Brinker and G. W. Scherer, "Sol–Gel Science", Academic Press, San Diego (1990).
5. C. J. Brinker, Y. Lu, A. Sellinger and H. Fan, *Adv. Mater.* **11**, 579 (1999).
6. A. Stein, B. J. Melde and R. C. Schroden, *Adv. Mater.* **12**, 1403 (2000).
7. B. Boury, R. J. P. Corriu, V. L. Strat, P. Delord and M. Nobili, *Angew. Chem. Int. Ed.* **38**, 3172 (1999).
8. Y. Lu, H. Fan, N. Doke, D. A. Loy, R. A. Assink, D. A. LaVan and C. J. Brinker, *J. Am. Chem. Soc.* **122**, 5258 (2000).
9. A. Ulman, *Chem. Rev.* **96**, 1533 (1996).
10. Y. Fukushima and M. Tani, *J. Chem. Soc., Chem. Commun.* 241 (1995).
11. Q. Huo, D. I. Margolese and G. D. Stucky, *Chem. Mater.* **8**, 1147 (1996).
12. A. Shimojima, Y. Sugahara and K. Kuroda, *Bull. Chem. Soc. Jpn.* **70**, 2847 (1997).
13. A. Shimojima, Y. Sugahara and K. Kuroda, *J. Am. Chem. Soc.* **120**, 4528 (1998).

14. A. Shimojima and K. Kuroda, *Langmuir*, in press.
15. A. Shimojima, N. Umeda and K. Kuroda, *Chem. Mater.* **13**, 3610 (2001).
16. A. Shimojima and K. Kuroda, *Chem. Lett.* 1310 (2000).
17. L. Delattre and F. Babonneau, *Mater. Res. Soc. Symp. Proc.* **346**, 365 (1994).
18. S. A. Rodríguez and L. A. Colón, *Chem. Mater.* **11**, 754 (1999).
19. G. J. T. Tiddy, *Phys. Rep.* **57**, 1 (1980).
20. M. Ogawa, S. Okutomo and K. Kuroda, *J. Am. Chem. Soc.* **120**, 7361 (1998).
21. A. Shimojima, D. Mochizuki and K. Kuroda, *Chem. Mater.* **13**, 3603 (2001).
22 E. P. Giannelis, *Adv. Mater.* **8**, 29 (1996).
23. K. Isoda, K. Kuroda and M. Ogawa, *Chem. Mater.* **12**, 1702 (2000).

Mat. Res. Soc. Symp. Proc. Vol. 703 © 2002 Materials Research Society V2.9

# Polymerization in Inverse Microemulsion: An Effective Tool to Produce Biodegradable and non Biodegradable Nanoparticles

Lebon F[1,2]., Grandfils C.[3], Jérôme R.[3,4], Barakat I.[3], Sartore L.[5]

[1]Dip. Scienze Biomediche e Biotecnologie, Univ. di Brescia, Brescia, Italy

[2]Ist. Nazionale di Fisica della Materia (INFM), Brescia, Italy

[3] Interfacultary Biomaterial Centre, University of Liège, Belgium

[4] CERM (Center for Education & Research on Macromolecules), University of Liège, Belgium

[5] Dip. di Chimica e Fisica per l'Ingegneria e i Materiali, Università di Brescia, Brescia, Italy

## ABSTRACT

Potential of polymerization in inverse microemulsions has been illustrated by the preparation of crosslinked nanoparticles with functional groups on the surface. Nonbiodegradable polyacrylamide nanoparticles have been prepared, with the purpose to use these stable monodisperse lattices as enzymatic reactors and in diagnostic applications. Their size is in the 50 to 90 nm range and they contain a model enzyme (alkaline phosphatase) immobilized. In another example, monodisperse biodegradable nanoparticles of polyamidoamines with a size from 90 to 130 nm have been prepared. They are envisioned for intravenous administration because of a low content of non-metabolized material and absence of toxicity.

## INTRODUCTION

The term "microemulsion" has been defined by Danielsson and Lindmann [1] as "a system of water, oil and amphiphile, which is a single phase, optically isotropic and thermodynamically-stable liquid solution". For other workers, a microemulsion refers to dispersion of very small droplets in a medium. In contrast to emulsions, which are opaque, unstable, and contain 1-10 μm droplets, the colloidal particles spontaneously formed in microemulsions are typically up to nanometric-scale globular droplets of the minor solvent, each one surrounded by a surfactant monolayer and thus dispersed in the bulk solvent. The nanoscale compartmentalization in inverse microemulsions (water-in-oil microemulsion, w/o) can be used as a structured reaction medium for the controlled formation of colloids.

Previous papers [2] have reported on an original way to immobilize enzyme within latex particles of reticulated polyacrylamide starting from an inverse microemulsion with a mixture of surfactants AOT (Sodium bis(-ethylhexyl)sulfosuccinate) and Brij30 (polyethylene glycol lauryl ether) in hexane. It is now well-established that the constituents of the reverse micellar system

can modify the interfacial rigidity of the droplets, the interdroplet interaction and ultimately the size and size distribution of the final nanoparticles[3]. The purpose of this work is to show that polymerization in inverse microemulsion can be successfully used for synthesis of calibrated biodegradable and non biodegradable latex particles. We have prepared non-biodegradable nanoparticles of crosslinked polyacrylamide/acrylic acid copolymers, and studied their size and stability after purification and redispersion increasing the functional groups content. The preparation of functionalized biodegradable nanoparticles of biocompatible vinyl-terminated macromonomers based on polyamidoamines was also accomplished and the effect of polymer nature on the particle size was studied.

## EXPERIMENTAL DETAILS

Non biodegradable nanoparticles were prepared from a mixture of 18.4 wt % surfactants, 73.8 wt % hexane and 7.8 wt % aqueous phase, i.e. a composition in the microemulsion domain of the pseudo-ternary phase diagram. The organic phase consisted of hexane and a pair of anionic-nonionic surfactants, i.e., AOT and Brij30 in a 34/66 weight ratio. The aqueous phase contained acrylamide (2M), acrylic acid (from 0 to 0.6 M), bis-acrylamide (0.05M) and ammonium persulfate (0.05M) and the enzyme (alkaline phosphatase; 10 µg/ml) in a Tris buffer (pH 10, 0.1M). In a typical polymerization, the aqueous phase was dispersed in the oil phase under stirring and an inert atmosphere was maintained during the whole reaction. The polymerization was initiated by addition of tetraethylmethylenediamine (TEMED) and carried out at 25°C for 30 min. The TEMED/$(NH_4)_2S_2O_8$ molar ratio was 1/1. Cold acetone (poor solvent) was added to the polymerization medium in order to precipitate the polymer. After centrifugation at 15,000 rpm for 5 min, the upper phase was removed and replaced by fresh acetone. This purification was repeated four times, and the nanolatex was redispersed in water. The aqueous dispersion was immediately dialyzed against water (10,000 cut off dialysis membrane) and then lyophilized. The dry powder was stored at low temperature (4°C).

Biodegradable nanoparticles based on polyamidoamines were prepared by radical polymerization of polyamidoamines oligomers (BAC-2MP and MBA-2MP). These dimacromonomers resulted from polycondensation [4] of an excess of 2,2-bis(acrylamido acetic acid) (BAC) and N,N'-methylene-bis-acrylamide (MBA), respectively, with 2-methylpiperazine (2MP) (figure 1).

Polymerization proceeded under the same conditions as before, except for the aqueous phase composition. Indeed, the dimacromonomer (2% w/w) and the initiator (ammonium persulfate; 0.5 M) in Tris buffer (0.1 M, pH 8) were dispersed in the organic one under stirring followed by the addition of TEMED (0.3 M in the reaction medium). After reaction under nitrogen at 30°C for 24 h, the nanoparticles were purified by repeated precipitation/redispersion cycles. Then the sample was passed through a membrane of regenerated cellulose with a cut off 100,000 and the dispersion was finally lyophilized.

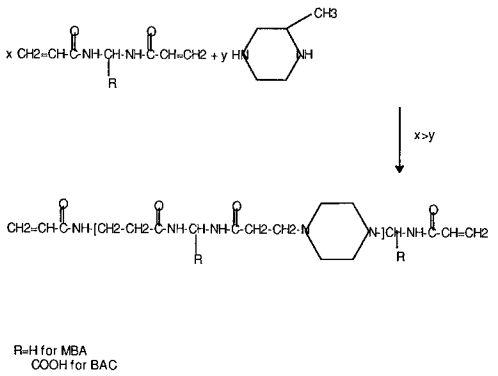


**Figure 1:** General synthesis of PAA oligomers: x/y=1.41 for sample I (BAC-2MP) and III (MBA-2MP); x/y=1.16 for sample II (BAC-2MP) and IV (MBA-2MP)

Gel permeation chromatograms (GPC) were recorded with TSK-GEL3000 PW and G4000 PW columns eluted with Tris buffer (pH8.1, 0.1M) in NaCl (0.2M) and calibrated with home-made PAA standards [5].

Size distribution of the latex was measured by quasi elastic light scattering (linear correlator, BI-2030, Brookhaven Instruments Corp., NY). The autocorrelation function was determined with argon ion laser (2W) operating at 488 nm and 20 mW. Time-dependent light scattering fluctuations were usually measured at 90 degree. The concentration of the suspension is around 5 mg/ml.

The determination of the zeta potential was performed using a Malvern Zetasizer. The colloidal suspensions (around 1 mg/ml) were placed in the electrophoretic cell where a potential of ±150 mV was established.

## RESULTS AND DISCUSSION

Polyacrylamide nanoparticles of increasing content of acrylic acid have been prepared, and the size and size distribution have been measured by PCS measurements for dispersions of the purified latex in a Tris buffer at pH 8. Table 1 shows that the particle size is in the range of 60 to 77 nm when the acrylic acid content of the copolymer is smaller than 15 mol%. There is a sharp increase in size when this acrylic acid content is exceeded, which indicates an aggregation of small particles into larger ones. These aggregates cannot be desegregated by ultrasound irradiation.

**Table 1:** Characterization of polyacrylamide nanoparticles

| AA (M) | η*=[AA]/[Am+AA] | Particle size (nm) | Zeta potential (mV) |
|---|---|---|---|
| 0.0 | 0.00 | 55 | 0.03 ± 0.5 |
| 0.1 | 0.05 | 77 | -11.80 ± 1.9 |
| 0.2 | 0.09 | 70 | -18.15 ± 1.6 |
| 0.3 | 015 | 70 | -34.10 ± 2.0 |
| 0.4 | 0.17 | 158 | -29.60 ± 0.6 |
| 0.6 | 0.25 | 132 | -30.40 ± 5.2 |

*molar ratio of acrylic acid in the comonomers feed

The zeta potential has been measured for the same samples as for PCS. Data in table 2 show that the amount of acrylic acid available on the surface of the particles can be modulated by the composition of the comonomers feed. When the acrylic acid content is increased up to 15 mol%, the zeta potential is more negative and the colloidal stability is improved. Beyond this content, the zeta potential levels off, and the nanoparticle dispersions become less stable.

As demonstrated by Candau et al. [6], the acrylic acid has an interfacial behavior and is presumably located at the w/o interface before polymerization. In agreement with Antonietti et al. [7], during the polymerization, a transfert of monomer and comonomer between the interface and the aqueous core could affect the surfactant head group interactions and then the curvature of the interface. At higher concentration in acrylic acid, the transfert is expected to increase involving an increase of the attractive force between particles.

Polymerization in inverse microemulsion has also been carried out in order to prepare biodegradable nanoparticles based on polyamidoamines (PAA). This synthetic polymer consists of regularly alternating amido and tertiary amino groups, and it is water soluble. Radical polymerization of PAA oligomers in inverse microemulsion leads to nanoparticles that can be functional depending on the staring macromonomers. In this work, two series of nanoparticles have been prepared with carboxylic acid group attached to PAA (BAC series) and with non functionalized PAA (MBA series), respectively. $M_n$ and $M_w/M_n$ of the dimacromonomers are listed in table 2.

**Table 2:** Characterization of dimacromonomers polymerized in inverse microemulsion

| | x/y | GPC | |
|---|---|---|---|
| | | $M_n$ | $M_w/M_n$ |
| BAC-2MP | 1.41 (I) | 725 | 1,45 |
| | 1.16 (II) | 1250 | 1,48 |
| MBA-2MP | 1.41 (III) | 635 | 1,51 |
| | 1.16 (IV) | 1020 | 1,43 |

PCS analysis of the BAC-2MP nanoparticles shows a main population with a particle size centered at 107 and 113 nm in case of 30 and 15 mol% of BAC, respectively. A second population of larger particles (> 500 nm) is also observed. Figure 2 shows a population MBA-2MP nanoparticles centered at 91 nm for 30 mol% MBA and very large (340 nm) and polydisperse particles when the MBA content is 15 mol%.

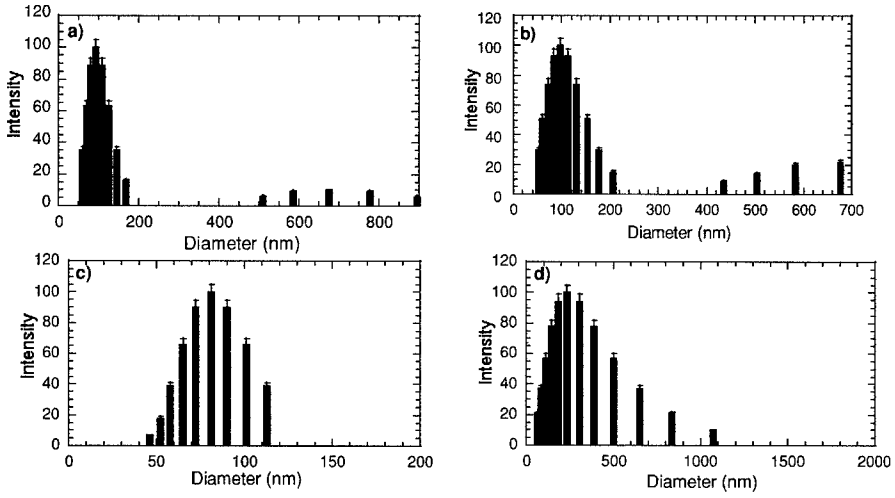


**Figure 2.** Quasi-elastic laser light spectrum of polyaamidoamines nanoparticle purified and dispersed in Tris buffer pH=8, 0.1M **a)** I **b)** II **c)** III **d)** IV

These measurements show that the latex size of the BAC-2MP and MBA-2MP nanoparticles depends on the average molecular weight of the dimacromonomer. As a rule, the

size increases with the molecular weight, and ultimately aggregates can be formed as observed in case of MBA-2MP. Indeed the reaction medium becomes turbid when the sample IV is prepared.

This behavior might be explained by a decrease in the crosslinking density when $M_n$ of the dimacromonomer is increased. This effect was previously reported for crosslinked polyacrylamide nanoparticles [2]. Nevertheless, additional experiments are required to support this explanation. The higher stability of the BAC-2MP nanoparticles suggests that the carboxylic acid groups improve the colloidal stability by electrostatic repulsions.

## CONCLUSIONS

Polymerization in inverse microemulsion is an efficient technique to prepare monodisperse nanoparticles of crosslinked polyacrylamide bearing carboxylic acids on the surface. An increase in the acrylic acid content of the comonomers feed up to 15 mol% improves the colloidal stability. Higher content has an adversary effect on the stability, which may lead to latex aggregation. Modulation of either the particle size or the content of carboxylic acid is an important parameter for diagnostic applications. Indeed, occurrence of non selective adsorption of proteins could be prevented and sites for the grafting of sensors can be made available.

Inverse microemulsion polymerization has also proved efficiency for the preparation of biodegradable nanoparticles based on a biocompatible and non toxic polymer: polyamidoamine. Latex prepared from functionalized macromonomer (BAC-2MP) have been prepared with a size of ca. 100 nm.

## ACKOWLEDGMENTS

F. Lebon is indebted to FRIA (Brussels, Belgium) for a PhD grant.

## REFERENCES

1. I. Danielson, B. Lindmann, *Colloids Surfaces*, **3**, 391 (1981)

2. a) C. Daubresse, C. Grandfils, R. Jérôme, P. Teyssié, *J. Colloid and Interface Sci.* **168**, 222 (1994)- b) C. Daubresse, C. Grandfils, R. Jérôme, P. Teyssié, *Colloid Polym. Sci.* **274**, 482 (1996)

3. a) P.D.I. Fletcher, A.M. Howe, B.H. Robinson, *J. Chem. Soc. Faraday Trans. I* **83**, 985 (1987)- b) A.S. Bommarius, J.F. Holzworth, D.I.C. Wang, T.A. Hatton, *J. Phys. Chem.* **94**, 7232 (1990)- c) S. Sarcar, N. Munshi, T.K. Jain, A.N. Maitra, *Colloids Surf. A* **88**, 169 (1994)

4. P. Ferruti, M. A. Marchisio, R. Barbucci, *Polymer* **26**, 1336 (1985)

5. F. Bignotti, P. Sozzani, E. Ranucci, P. Ferruti, *Macromolecules* 27, 7171 (1994)

6. a) F. Candau, *Macromol. Symp.* **92**, 169 (1995)- b) Y. S. Leong, S. Candau, F. Candau, *In Surfactants in Solution;* K.L. Mittal, M. Lindman, Eds; Plenum: New-York, 1984; Vol.3, p.1897

7. M. Antonietti, R. Basten, S. Lohman, *Macromol. Chem. Phys.***196**,2,441 (1995)

# Nanophase and Nanocomposite Materials I

Mat. Res. Soc. Symp. Proc. Vol. 703 © 2002 Materials Research Society V3.1

# Self-Energy corrections to DFT-LDA Gaps of Realistic Carbon Nanotubes

Guido Satta, Giancarlo Cappellini, and Francesco Casula
INFM and Dipartimento di Fisica, Università di Cagliari, I-09042 Cagliari, Italy

## ABSTRACT

Since their discovery carbon nanotubes have attracted much interest for their peculiar electronic properties which go from metallic to semiconducting behaviour, depending both on diameter and chirality. The exact value of their band gap is obviously a crucial point to be addressed because it enters in the nanotube application as microelectronic devices. By making use of an efficient GW scheme, previously tested on bulk systems, as well as of a model screening function, we obtaind for the first time excitation energies and band-gap values for carbon nanotubes. Results for $(6,0)$ and $(7,0)$ will be presented and discussed.

## Introduction

Since their discovery [1] in 1991 carbon nanotubes have attracted much attention for their peculiar mechanical and electronic properties. As it is well known, their structure can be thought as obtained by rolling up a graphite sheet in such a way that the carbon atoms along a given direction are arranged in parallel rings orthogonal to the tube axis. If after the wrapping procedure a lattice site of a graphite sheet turns out to coincide with the site originally displaced by a vector

$$\mathbf{c} = n\mathbf{a_1} + m\mathbf{a_2}, \tag{1}$$

$\mathbf{a_1} = (a\sqrt{3}, 0)$ and $\mathbf{a_2} = (a\sqrt{3}/2, 3a/2)$ being the graphite lattice vectors, the nanotube is uniquely identified by the indices (n,m). Actually both the tube diameter d and the chiral angle, i.e. the angle between $\mathbf{c}$ and $\mathbf{a}_1$, can be easily expressed in terms of n and m:

$$d = \frac{\sqrt{3}\sqrt{n^2 + m^2 + nm}}{\pi} a, \tag{2}$$

$$d = \ tg\theta = \frac{\sqrt{3}m}{2n + m}, \tag{3}$$

$a = 1.42\mathring{A}$ being the nearest neighbor distance of carbon atoms in graphite. For obvious geometrical reasons chiral angles range between $\theta = 0$ and $\theta = \pi/6$, where the two limiting cases are strictly speaking not chiral ones. The $\theta = 0$ and $\theta = \pi/6$ wrappings correspond to (n,0) and (n,n) indices and are popularly known as zig-zag nanotubes and armchair nanotubes respectively.

Carbon nanotubes diameters range in the nanometer size, whilst their lenght is in the millimiter size, and small changes in helicity and diameter can shift their electronic character from insulating to semiconducting and to metallic. Moreover spontaneous or induced mechanical distortions can dramatically affect their properties. If one now takes into account the possibility of growing multiwalled nanotubes, i.e. co-axial carbon tubes, or of arranging them in bundles, one can easily understand how many different physical properties can be obtained by modifying the same basic object. Obviously these systems have

been submitted to theoretical investigation, in order to reproduce the experimental results and to predict specific material properties. [2, 5]

We have reported in a previous paper [6] the results of our calculations on several armchair and zig-zag single-wall finite nanotubes, performed by the discrete variational method (DVM) within DFT-LDA approximation. We refer to the original paper, as well as to other DVM-based papers for discussing the reliability of such computational approach [7, 8, 9]. In principle our results should be of comparable quality with any LDA results for similar systems. Actually we can use them also for estimating the electronic properties of infinite nanotubes, provided that the border effects in the local densities of states go rapidly to zero, as soon as states localized on the inner carbon rings are considered. In this way we have been able to obtain predictions for the gaps of quite large carbon nanotubes in reasonable agreement with previous LDA results, if any, and with a very reasonable computational effort.

Still remains the problem of a direct determination of the LDA gaps in infinite carbon nanotubes as well as the problem of correctly estimating their excitation properties. In fact, DFT-LDA approximation has been successfully used for determining the ground-state electronic properties of a large class of materials ranging from bulk systems, surfaces and etherostructures to atoms and clusters. [10] On the other hand if DFT-LDA is used to determine the quasiparticle (QP) spectra of many-electron systems in most cases results are in disagreement with experiments.[10] For example, in the case of bulk semiconductors, assumption of the Kohn-Sham (K-S) eigenvalues as electronic QP energies leads to a systematic underestimate of the electronic transition energies with respect to the experiment (*band-gap problem*). [11, 12, 13]

QP properties of many-electron systems are correctly evaluated starting from the QP equations, in which the full electronic self-energy operator appears. [14] The self-energy operator is treated usually in the GW approximation (GWA) by starting from DFT-LDA eigenvalues and eigenfunctions used to evaluate the one-electron Green function and the screened Coulomb interaction.[11, 12] Until now the numerical effort required to calculate the dynamical screened interaction (W) for the GW self-energy has restricted the systematic solution of the QP problem mainly to simple structures. [15] In this work for the first time GW self-energy corrections for the (6,0) and (7,0) nanotubes have been calculated. The present results demonstrate the possibility to apply our method to larger graphene systems.

## Computational Method

*Ab initio* calculations of the electronic properties of infinite isolated carbon nanotubes have been performed by using a plane wave basis set and ionic pseudopotentials for Carbon after Troullier and Martins [16]. Angular components of ionic pseudopotentials up to $l = 2$ have been included . In particular we have considered the case of zig-zag nanotubes with indeces (6,0) and (7,0). A repeated-cell approach has been used, and in order to correctly simulate the isolated structures of nanotubes, distances in the directions orthogonal to the nanotube axis have been accurately chosen. Moreover we have performed two different kinds of convergence tests, i.e. with respect to energy cutoff and to dimensions of the simulation cell. In the case of the (6,0) structure a $3a$x$12a$x$12a$ cell with 24-atom basis has been used. (see figure 1)

While $3a = 8$ *a.u.* is the length of the unitary structure to be repeated along the graphene

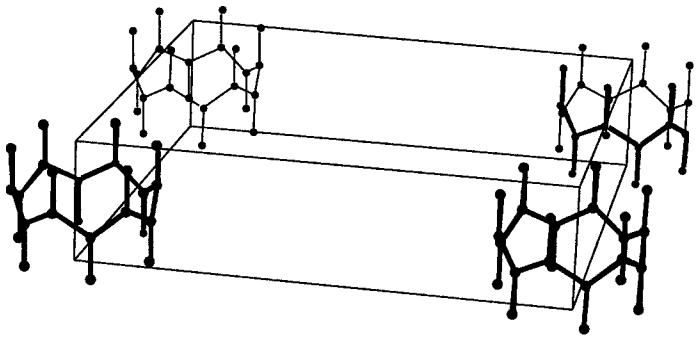

Figure 1: simulation cell for (6,0) structure

nanotube, the $32a.u.$ sides garantee a sufficiently large distance between atoms belonging to different nanotubes (as a term of comparison the interplanar distance in graphite is $d = 6.34$ $a.u.$. ).

Within our simulation cell the minimal distance between carbon atoms belonging to different nanotubes turns out to be greater than 23 a.u. For what attains to the energy cutoff, values up to 30 $Ry$ have been considered. In sampling the first BZ for calculating the nanotube charge density only the $\Gamma$ point has been used. This choice has been obviously dictated by the need of drastically reducing the computational effort in such a large unit cell. On the other hand the BZ of the system is correspondingly small, which should justify our choice, as we shall see later on in the discussion of the results. The same technicalities have been used in calculating LDA energies of $(7,0)$ nanotube.

An efficient DFT-GW method has been used to determine the quasiparticle correction of the band-gap of (6,0) and (7,0) nanotubes. It has been originally developed for the calculation of quasiparticle energies of cubic semiconductors [17] and then succesfully extended to systems of lower symmetry such as SiC polytypes [18] and oxides [19]. Local fields effects in the screening of the material are described within an LDA-like approximation, and dynamical effects are treated by expanding the self-energy operator to linear order in energy. The anisotropy of the inverse dielectric matrix is taken into account simply averaging over three directions:

$$\frac{1}{\epsilon_\infty} = \frac{a}{\epsilon_{||}} + \frac{b}{\epsilon_\perp} \tag{4}$$

$a$ and $b$ being two weighting factors which take into account the different screening properties along the tube and in the orthogonal directions. If we imagine to start from the structure of the graphitic plane we have that $\epsilon_{||}$ is the in plane component and $\epsilon_\perp$ is the component perpendicular to the plane. This simple approximation permits us the use of a cubic cell to perform self-energy calculations with a strong reduction of computational effort. In

Table I: Band gap energies for $(6,0)$ and $(7,0)$ zig-zag nanotubes calculated with DVM approch (first column) DFT-LDA approach (second column). In the third column previous DFT-LDA results after Ref.[20]

| (n,m ) | DVM | LDA(pw) | LDA(Ref.[20]) |
|---|---|---|---|
| $(6,0)$ | 0.0 | $Metal(-0.74)$ | $Metal(-0.83)$ |
| $(7,0)$ | 1.04 | 0.18 | 0.09 |

Table II: GW quasi-particle corrections to band gap energies for $(6,0)$ and $(7,0)$ zig-zag nanotubes calculated with different $\epsilon_\infty$ values (see text).The energies are in eV

| $\epsilon_\infty$ | $(6,0)$ | $(7,0)$ |
|---|---|---|
| 240 | 0.04 | |
| 7.06 | 0.41 | 0.651 |

order to keep a sufficiently large distance between atoms of different isolated nanotubes the cube side must be at least twice as large as the minimal $3a$ one, so that 8 carbon rings are included along the cell vertical axis. In this way the minimal distance between atoms belonging to different (6,0) nanotubes turns out to be at least 1.14 times the minimal distance between atoms belonging to different planes in graphite. In (7,0) nanotubes the corresponding distance is 0.91 times that of graphite. The results for the gap values will confirm this assumption. The self-energy correction of the eigenvalue $E^0_{n\mathbf{k}}$ relative to the Bloch state $|n\mathbf{k}>$ is calculated according to equation [17]

$$\Delta_{n\mathbf{k}} = E_{n\mathbf{k}} - E^0_{n\mathbf{k}} = \frac{[\Sigma^{COH}_{n\mathbf{k}} + \Sigma^{SEX}_{n\mathbf{k}} + \Sigma^{DYN}_{n\mathbf{k}}(E^0) - V^{XC}_{n\mathbf{k}}]}{1+\beta_{n\mathbf{k}}}, \tag{5}$$

where the terms appearing in the third member of the equation are the static Coulomb Hole (COH) and Screened Exchange terms (SEX), the expectation value of the DFT-LDA exchange-correlation potential,and of the two dynamical terms $\Sigma^{DYN}$ and $\beta$ (see Refs. [17] and [18]). The singularity of the Coulomb potential in the screened-exchange part of the electronic self-energy is treated by using auxiliary functions of the appropriate symmetry [18].

## Results and Discussion

In Tab. I we have shown the results of our LDA calculation for the $(6,0)$ and $(7,0)$ nanotubes compared with previous results. We note the our result for the gap of the $(7,0)$ structure is slightly different from the result of Ref. [20]. This difference can be reasonably explained by taking into account the different cutoff, and the different relaxation of the structure.

In any case our calculations reproduce the same trend previously reported in ref. [20], with semiconduting properties for the $(7,0)$ structure and metallic properties for the $(6,0)$ one. The band structure and the energy-level ordering results in good agreement too.

In Tab. II we have reported the GW corrections to the band gap values obtained with our method for the (6,0) and (7,0) zig-zag nanotubes. The corrections are calculated with $\epsilon_\infty$ obtained from equation (4) . The two components are estimated from graphite parameter, in particular we follow ref. [21] and we put the value $\epsilon_\perp = 2.4$ and for $\epsilon_{||}$ we use a value 100 times greater [21]. With $a = 1$ and $b = 0$, i.e. complete metallic screening, for the $(6,0)$ a very small GW correction results. On the other hand even with a more semiconducting behaviour $\epsilon_\infty = 7.06$, obtained with $a = 2/3$ and $b = 1/3$ in equation 4 the structure maintains a metallic character. For the $(7,0)$ nanotube we confirm including GW corrections the DFT-LDA prediction of a semiconducting behaviour, with a enhancement of the gap due to self-energy corrections.

To summarize, we have presented in this paper DFT- LDA calculations with GW corrections for the band-gap of $(6,0)$ and $(7,0)$ carbon nanotubes. Our DFT-LDA results have been compared with previous theoretical ones in order to prove the accuracy of the present computational method. For $(6,0)$ nanotube our LDA results are in good agreement with previous similar calculations and our GW corrections confirm the metallic character of this tube. On the other hand $(7,0)$ nanotubes appears to be semiconductors with a relevant GW gap correction. Since C nanotubes as small as $3,3)$ ones have been detected [22, 23], one can expect that specific measurements even for small nanotubes can be available in the next future, thus eventually confirming our predictions. Moreover the combination of different approaches, say cluster calculations, repeated cell ones and GW corrections, depending on the properties one is looking for, turn to be very useful in addressing such kind of systems.

## REFERENCES


1. S. Iijma, Nature **354**, 56 (1991)

2. R. Saito, G. Dresselhaus, and M.S. Dresselhaus, *Physical Properties of Carbon Nanotubes* (Imp. Coll. Press, London 1996); M.S. Dresselhaus, G 2E Dresselhaus, and P.C. Ecklund, , *Science of Fullerenes and Carbon n Nanotubes* (Academic Press, San Diego 1996)

3. N. Hamada, S. Sawada, and A. Oshiyama, Phys.Rev. Lett. **68**, 1579 (1 992))); please note that in this reference, because of another choice of graphite lattice vectors, nanotubes are differently labelled: eg (2n,n) stays for armchair nanotubes.

4. R. Saito, M. Fujita, G. Dresselhaus, and M.S. Dresselhaus, Appl. Phys. Lett. **60**, 2204 (1992); R. Saito, M. Fujita, G. Dresselhaus, and M.S. Dresselhaus, Phys.Rev. B**46**, 1804 (1992)

5. J.W. Mintmire, B.I. Dunlap, and C.T. White, Phys.Rev.Lett. **68**, 631 (1992)

6. F.Casula, G. Cappellini, and G.Satta, Ann SNS, in press **(2001)**

7. J. Yang, W. Kelin, F.Casula, G. Mula, Phys. Rev. B **47**, 4025 (1993)

8. J. Yang, F. Toigo, and W. Kelin, Phys. Rev. B **50**, 79155 (1994), and references therein

9. M. Porcu, G. Satta, F.Casula, G. Mula, Mat. Res. Symp. Proc. **491**, 149 (1998)

10. R.O. Jones and O.Gunnarson, Rev. Mod. Phys. **61**, 689 (1989)

11. M.S. Hybertsen and S.G. Louie, Phys. Rev.Lett. **55**, 1418 (1985); Phys.Rev.B **34**, 5390 (1986)

12. R.W. Godby, M. Schlüter, L.J. Sham, Phys. Rev. **37**, 10159 (1988)

13. L.J. Sham,M. Schlüter,Phys. Rev. B **32**,3883(1985)

14. L. Hedin, Phys. Rev. **139**, A796 (1963)

15. G.Onida, L. Reining, R.W. Godby, R. Del Sole, W. Andreoni, Phys. Rev. Lett. **75**, 818 (1995)

16. Troullier and J.L. Martins, Phys. Rev. B **43**, 1993 (1991)

17. F. Bechstedt, R. Del Sole, G. Cappellini and L. Reining, *Solid State Comm.* **84**, 765 (1992)

18. B. Wenzien, G. Cappellini, F. Bechstedt , Phys. Rev. B **51**, 4397 (1995)

19. G. Cappellini, S. Bouette-Russo,B. Amadon, C. Noguera, F. Finocchi, Journal of Phys.: Cond. Matter **12**, 3671 (2000)

20. X. Blase, L. X. Benedict, E. L. Shirley, S.G. Louie, Phys. Rev.Lett. **72**, 1878 (1994)

21. M. F. Lin, Kenneh W.-K. Shung, Phys. Rev. B **50**, 17744 (1994)

22. L.C. Qin, X. Zhao, K. Hirahara, Y. Miyamoto, Y. Ando, and S.Iijma, Nature **408**, 50 (2000)

23. N. Wang, Z.K. Tang, G.D. Li, and J.S. Chen, Nature **408**, 50 (2000)

Mat. Res. Soc. Symp. Proc. Vol. 703 © 2002 Materials Research Society V3.3

# Casimir Forces between ThermallyActivated Nanocomposites

Raúl Esquivel-Sirvent, Carlos Villarreal, and Cecilia Noguez
Instituto de Física, Universidad Nacional Autónoma de México,
Circuito de la Investigación Científica, Ciudad Universitaria,
México, DF, 04510, México.

## ABSTRACT

We present a theoretical study of the modification of Casimir forces between nanocomposite slabs that exhibit a metal-dielectric transition. In particular, we consider slabs made of $VO_2$ precipitates in sapphire, whose effective dielectric function is calculated within a mean field approximation. The results for the Casimir force as a function of the separation of the slabs, show that at a fixed separation the magnitude of the force changes as temperature increases from 300 K to 355 K. The possible applications of these results to Casimir devices is discussed.

## INTRODUCTION

In 1948 Casimir [1] showed that two parallel plates separated by a distance $a$ and made of a perfect conductor will attract each other with a force per unit area given by

$$F = -\frac{\pi^2 hc}{240a^4}. \qquad (1)$$

This force is attributed to the quantum vacuum fluctuations of the electromagnetic field. Indeed, Casimir forces appear whenever the mode distribution of a fluctuating field is modified by the presence of boundaries [2]. Although Casimir forces are small (0.13 dynes for 1 $mm^2$ plates separated by one micron) they have been measured through a series of ingenious experiments. Lamoreaux [3] reported an agreement with theory at the level of 5% using an electromechanical system based on a torsion balance. More recent experiments performed by Mohideen with atomic force microscopes achieved precisions close to 1% [4]. In another experiment, a micromachined torsional device was employed to measure the Casimir attraction between a plate and a spherical metallic surface [5].
The original formulation of Casimir was for perfect conductors motivating Lifshitz to propose in 1956 a theory for vacuum forces between semi-infinite dielectric media [6]. The corresponding theory for finite dielectric systems has been developed in last few years [7].

With the advent of novel experimental techniques associated to the development of micro electromechanical systems (MEMS), and instruments such as the atomic force microcope (AFM) different proposals related with the technological uses of the Casimir forces have been investigated. For example, the deflection of a thin microfabricated rectangular strip due to Casimir forces was calculated by Serry *et al.* [8]. According to their results, the strength of these forces is high enough as to buckle the strip and limit the operation of MEMS. Maclay [9] has also suggested to build MEMS devices in order to study the properties and energy balance of MEMS when static or vibrating membranes are

placed on the top of open rectangular cavities. The proposed experimental configuration consists of an array of open rectangular metallic cavities. A top plate suspended by micromecanical springs may be used to measure the sign and magnitude of the Casimir interaction between the plate and the cavity array.

In a recent paper [10], we discussed the possibility of controlling the strength of Casimir forces using heterostructures made of materials with different dielectric properties such as metals and semiconductors. This kind of structures would be also useful in the building of Casimir engines in which part of the energy cycle could be driven by the Casimir interactions. Such a cycle has been proposed by Pinto [11] in order to design a vacuum energy transducer, using optically active elements. He estimated that the power per unit area of this Casimir engine could be as high as 1 kW/m$^2$. Based on these ideas, in this work we study a system made of nanocomposite slabs that exhibit a metal-dielectric transition. In particular, we consider slabs made of $VO_2$ precipitates in sapphire [12], whose effective dielectric function is calculated within a mean field approximation. These nanocomposites undergo a first order phase transition which changes their dielectric response from semiconducting to metallic.
This behavior would allow to build devices in which the Casimir forces could be modified not only by changing the separation between the slabs, but also by temperature variations as we show in this paper.

## THEORY

Consider two parallel slabs made of a dielectric of thickness $d$ and separated by a distance $a$. The Casimir force between dielectric media considering only wave vectors perpendicular to the slabs is given by [7]

$$F = \frac{2\hbar}{\pi c}\mathrm{Re}\int_0^\infty d\omega\omega\left[1-\frac{1-|r(\omega)|^2}{\left|1-r^2(\omega)e^{2i\omega a/c}\right|^2}\right] \qquad (2)$$

where the $r(\omega)$ is the frequency-dependent reflection coefficient. To calculate $r(\omega)$ the dielectric function of the slabs is needed. For a nanocomposite slab made of a host material with a dielectric function $\varepsilon_h(\omega)$ and inclusions with dielectric function $\varepsilon_i(\omega)$, the effective dielectric response $\varepsilon_M(\omega)$ can be calculated within a mean field approximation as [13]

$$\frac{\varepsilon_M}{\varepsilon_h} = 1+3f\alpha+f^2\alpha^2\left[3+2\log\frac{8+\alpha}{8-2\alpha}\right] \qquad (3)$$

where $f$ is the volume fraction of the inclusions and $\alpha$ is the effective polarizability given by the Maxwell Garnett theory. This expression for the effective dielectric function includes higher order corrections in the volume fraction and is a first approximation beyond

single particle mean field theories. To model the dielectric function of the $VO_2$ precipitates embbeded in sapphire we considered a Lorentz model for both $\varepsilon_h(\omega)$ (sapphire) and $\varepsilon_i(\omega)$ ($VO_2$). The parameters appearing in Lorenz formula for these materials have been taken from Ref.[14]. In the case of $VO_2$, these parameters change as a function of temperature due to the phase transition.

## RESULTS

The system we study consists of two parallel planar nanocomposite slabs separated a distance $a$ and with a thickness of $d$=0.1 microns. The volume fraction of the $VO_2$ precipitates was arbitrarily set at 20 %. In figures (1a) and (1b), we present the real and imaginary parts of the dielectric function as calculated from Eq.(3). The dielectric function is shown for two different temperatures, $T_{sc}$ = 300 K, and , $T_m$ = 355 K. The first temperature corresponds to the semiconducting state, and the second to the metallic one.

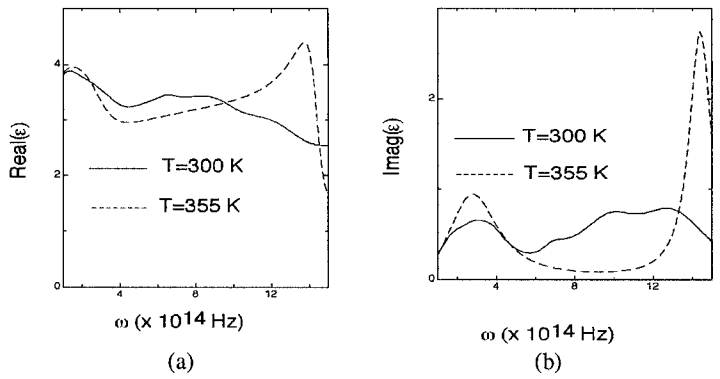


**Figure 1.** (a) Frequency dependence of the real part of the effective dielectric function for the semiconducting ($T_{sc}$ = 300 K) and metallic phases ($T_m$ = 355 K). (b) Frequency dependence of the imaginary part of the effective dielectric function for the semiconducting ($T_{sc}$ = 300 K) and metallic phases ($T_m$ = 355 K).

In figure (2) we present the calculated reflectance of a nanocomposite slab for the semiconducting and metallic phases based on our results for $\varepsilon_M(\omega)$ . The metallic case shows a significant deviation with respect to the semiconducting one at an angular frequency of 1.5 x $10^{15}$ Hz. The changes in $r(\omega)$ as a function of temperature should be reflected in the calculation of the Casimir force. This is indeed the case, as shown in figure (3) where we plot the force as a function of the separation $a$. The force is normalized to the ideal case. The ideal case is when the slabs are made of a perfect conductor. As shown in the figure, after a separation of roughly 0.3 μm the magnitude of the force is different. This is understood from Eq. (2) since at a given separation of the slabs the modes that will

contribute more to the force are those with a wavelength that fit within the slabs. This is, modes with a frequency of $\omega = \pi c/a$. The region of small separations ($a$<0.2 μm) the force is the same at the two temperatures since these separations correspond to frequencies at which the reflectivity of the material is very small and the mode density within the slabs is similar to that of vacuum resulting in a negligible Casimir force.

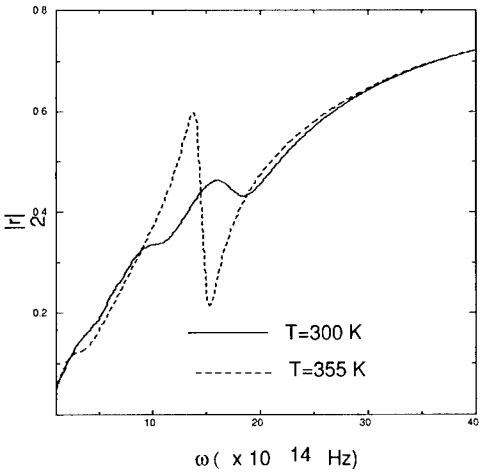


**Figure 2.** Frequency dependence of the reflectance of the nanocomposite slab at $T_{sc}$, and $T_m$. In the frequency region around $1.5 \times 10^{15}$ Hz the reflectance differs at the two temperatures.

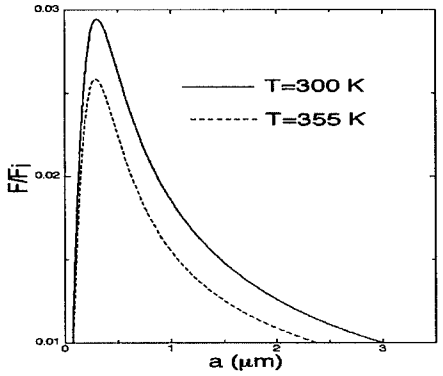


**Figure 3.** Casimir force as a function of the nanocomposite slab separation $a$ . The dashed curve corresponds to the metallic phase, while the continuous one corresponds to the semiconducting phase. The force is normalized with respect to the perfectly conducting case given by equation (1).

## CONCLUSIONS

We have explored the possibility of using the dielectric properties of nanocomposite slabs that exhibit a metal-dielectric transition to modulate the Casimir forces. In this work, we considered slabs made of $VO_2$ precipitates in sapphire. The results for the Casimir force as a function of the separation of the slabs show that at a fixed separation the magnitude of the force changes as temperature increases from 300 K to 355 K. This effect could be used in principle, as part of a thermodynamic cycle of a micromachined motor similar to the one proposed by Pinto [11] but working at ambient temperature.

## ACKNOWLEDGMENTS.

This work has been partially supported by NASA Breakthrough Propulsion Physics Program.

## REFERENCES

1. H. B. G. Casimir, Proc. Kon. Ned. Akad. Wet. **51**, 793 (1948); G. Plunien, B. Muller and W. Greiner, Phys. Rep. **134**, 87 (1986) ; L. S. Brown and G. J. Maclay, Phys. Rev. **184,**1272 (1969); S. Hacyan, R. Jáuregui, F. Soto, and C. Villarreal, J. Phys. A **23**, 2401 (1990).

2. A. Larraza, C. D. Holmes, R. T. Susbilla and B. Denardo, J. Acoust. Soc. Am. **103**, 2267 (1998).
3. S. K. Lamoreaux, Phys. Rev. Lett. **78**, 5 (1997).
4. U. Mohideen and Anushree Roy, Phys. Rev. Lett. **81**, 4549 (1998); B. W. Harris, F. Chen, and U. Mohideen, Phys. Rev. A **62**, 052109 (2000).
5. H. B. Chan, V. A. Aksyuk, R. N. Kliman, D. J. Bishop and F. Capasso, Science **291**, 1942 (2001).
6. E. M. Lifshitz, Sov. Phys. JETP **2**, 73 (1956).
7. D. Kupiszewska and J. Mostowski, Phys. Rev. A, **41**, 4636 (1990); D. Kupiszewska, Phys. Rev. A, **46**, 2286 (1992) ; R. Matloob, A. Keshavaraz, and D. Sedighi, Phys. Rev. A, **60**, 3410 (1999).
8. F. M. Serry, D. Walliser and J. Maclay, J. Appl. Phys. **84**, 2501 (1998).
9. J. Maclay, in *Proceedings of STAIF-99 (Space Technology and Applications International Forum-1999, Albuquerque, NM, January, 1999)*, edited by M.S. El-Genk, AIP Conference Proceedings 458, American Institute of Physics, New York, 1999.
10. R. Esquivel-Sirvent , C. Villarreal, and G.H. Cocoletzi, Phys. Rev. A (2001).
11. F. Pinto, Phys. Rev. B **60**, 14740 (1999).
12. L. A. Gea, and L. A. Boatner, Appl. Phys. Lett., **68**, 3081 (1996); L.A. Gea, J.D. Budai, and L.A. Boatner, J. Mater. Res. **14**, 2602 (1999).
13. R. G. Barrera, C. Noguez, and E.V. Anda, J. Chem. Phys. **96**, 1574 (1992).
14. H. W. Verleur, A.S. Barker, and C. N. Berglund, Phys. Rev. **172**, 788 (1968).

Mat. Res. Soc. Symp. Proc. Vol. 703 © 2002 Materials Research Society V3.4

# Characterization of the order-annealing response of nanostructured iron-palladium based ferromagnetic thin-films

Huiping Xu[1)], Adam T. Wise[1)], Timothy J. Klemmer[2)] and Jörg M. K. Wiezorek [1)]

1) Department of Materials Science & Engineering, University of Pittsburgh, 848 Benedum Hall, Pittsburgh, PA 15261, USA;
2) Seagate Technology, 2403 Sidney Street, Pittsburgh, PA 15203, USA;

## Abstract

A combination of XRD and TEM techniques have been used to characterize the response of room temperature magnetron sputtered Fe-Pd thin films on Si-susbtrates to post-deposition order-annealing at temperatures between 400-500°C. Deposition produced the disordered Fe-Pd phase with (111)-twinned grains approximately 18nm in size. Ordering occurred for annealing at 450°C and 500°C after 1.8ks, accompanied by grain growth (40-70nm). The ordered FePd grains contained (111)-twins rather than {101}-twins typical of bulk ordered FePd. The metallic overlayers and underlayers selected here produced detrimental dissolution (Pt into Fe-Pd phases) and precipitation reactions between Pd and the Si substrate.

## Introduction

Tetragonal intermetallic phases, such as FePt, CoPt, MnAl and FePd, are of interest as active ferromagnetic materials in thermally stable high-information density thin film data storage media [1]. Due to their high magnetocrystalline anisotropy (~$10^7$-$10^8$ erg/cm$^3$) theoretical estimates predict thermally stable grain sizes resistant to spontaneous magnetization reversal in the range of approximately 3-5nm for these intermetallics [2]. Utilization of these intermetallic phases, which derive their attractive magnetic properties from their tetragonal ordered $L1_0$-type crystal structures with an easy magnetization axis parallel to the c-direction, promises up to about one order of magnitude increase in data storage densities with respect to current Co-based media.

Recent research on ferromagnetic intermetallic thin films for potential storage media applications focused mostly on FePt, CoPt and on property measurements, whereas relatively little published work on the structural evolution of FePd thin films during post-deposition treatments exists. FePd thin films have been grown successfully by molecular beam epitaxy (MBE) [3] and by magnetron sputtering on Pt-underlayers on MgO substrates [4]. The latter method allows more rapid deposition and is currently popularly employed in most industrial operations. Unlike MBE, magnetron sputtering without substrate heating usually produces intermetallic films that consist of the disordered solid solution rather than the ordered phases. In principle, substrate heating can be used to induce ordering during deposition but is usually accompanied by undesirable grain growth, producing less than optimal magnetization behavior [4]. Post-deposition annealing procedures that induce the ordering transformation offer potential control of the ordered phase grain size in room temperature sputtered Fe-Pd thin films. The development of optimized processing strategies for these nanostructured intermetallic materials systems, including potential alloying schemes, requires a basic understanding of the microstructural response of as-deposited Fe-Pd based thin films to annealing. Therefore, here exploratory studies have been performed of the microstructural response of magnetron sputtered Fe-Pd based thin films to post-deposition order-annealing. Combinations of X-ray diffraction (XRD) and imaging and analytical techniques of transmission electron microscopy (TEM) have been used in the characterization of the as-deposited and annealed films. Based on the experimental observations possible pathways for the evolution of the nanoscale microstructure are identified and discussed for the films studied here.

## Experimental Procedure

FePd based thin films with nominal thickness of 100nm have been prepared by RF-magnetron sputtering at room temperature directly on Si substrates and on Si substrates with various metallic underlayers. Targets of an equiatomic Fe-Pd alloy together with high-purity elemental metal targets have been employed and all films were capped with a 5nm thick overlayer of Pt. Some pertinent parameters and compositions of deposited films are collated in table 1. Cleaved sections of the deposited films have been encapsulated in silica quartz tubes. The tubes have been evacuated down to ~$10^{-3}$torr and were then refilled with a reduced atmosphere of argon gas. Sequences of evacuation and argon refilling have been repeated three times before establishing a final partial pressure of ~$25x10^{-3}$ torr of argon in the tubes. The encapsulated films have been annealed isothermally at three different temperatures (400°C, 450°C and 500°C) for times between 1.8ks to 7.2ks. Plan-view and cross-sectional samples of the as-deposited and annealed films for transmission electron microscopy (TEM) have been prepared by standard methods. The structure of the films was characterized by a combination of X-ray diffraction (XRD) and TEM and scanning TEM (STEM) using Phillips X-pert diffractometers and a Jeol2000fx and a Tecnai F20, respectively. Compositional analyses of cross-sections have been performed by energy-dispersive X-ray spectroscopy (EDS) in the TEM and EDS-maps have been obtained by STEM.

**Table I:** Composition and dimensions of the magnetron sputtered FePd based thin films.

| Sample ID | Overlayer | Active layer | Underlayer | Substrate |
|---|---|---|---|---|
| #810 | Pt , 5nm | Fe-Pd, 100nm | Ti, 20nm | Si <100> |
| #811 | Pt , 5nm | Fe-Pd, 100nm | NiCr, 15nm, Ta, 5nm | Si <100> |
| #813 | Pt , 5nm | Fe-Pd, 100nm | none | Si <100> |

### Results

*As-deposited thin films*

Symmetric (θ/2θ)-XRD and glancing incidence scans for the three samples (for brevity not reproduced here) indicated that a significant <111>-fiber texture with the fiber-axis normal to the substrate developed in the active layers and that they consisted of the disordered fcc-phase γ-(Fe,Pd). The TEM analyses of the cross-sections of the as-deposited thin films confirmed the nominal compositions (spot-EDS) and desired dimensions for the various layers as summarized in table 1 (Fig. 1). Moreover, the γ-(Fe,Pd) layer exhibited a columnar morphology with about five individual grains of average grain size (18±4)nm constituting the columnar grains (Fig. 1). The individual γ-(Fe,Pd) grains exhibited profuse internal faulting (Fig. 1). Selected area and micro-diffraction (SAD and μD) together with bright field (BF) and dark field (DF) imaging tilting experiments have been used to determine that these faults are twins on {111}-planes parallel to the substrate/film interface (SAD in Fig. 1b). The SAD pattern (SADP) of Fig. 1b has been obtained from groups of columnar grains of similar orientations with <110>-zone axes approximately parallel to the electron beam. The twin-conjugation plane normal, $\mathbf{g}_{hkl}$=111, is marked by a solid white line and the open circles highlight some twin-reflections in Fig. 1b.

*Annealed thin films*

No structural changes were detected in XRD scans of the isothermally annealed samples (for brevity not reproduced here) for isothermal treatments at 400°C for up to 7.2ks. Structural changes associated with the annealing response of the Fe-Pd based thin films were observed for annealing at 450°C and at 500°C after 1.8ks. Apparent ordering of γ-(Fe,Pd) to $\gamma_1$-FePd, a loss of

Pt and the formation of additional phases could be inferred qualitatively from the XRD data. TEM imaging and diffraction analyses of cross-sections of the annealed films have been performed and a number of microstructural changes have been identified. The TEM observations confirmed that the active layer ordered to $\gamma_1$-FePd with the tetragonal $L1_0$-structure (Fig. 2 & 3). The ordered FePd grains exhibited twinning on {111} (Fig. 2b). Furthermore, the local loss of the Pt-overlayer has been observed (Fig. 2). In regions that retained the Pt-overlayer the active layer exhibited a columnar grain structure with the increased average grain size of approximately 40-70nm (Fig. 2,3). PdSi precipitates of up to about 250nm in size formed periodically at the film/substrate interface and consistently in regions of the film where the Pt-overlayer had disintegrated (Fig. 2, 3). The PdSi precipitates have been characterized by EDS, SAD and μD. These buried precipitates exhibited an approximately equiatomic composition, $Pd_{48}Si_{52}$ (all in mol%), and their structure was determined to be consistent with an ordered orthorhombic MnP-type structure (Pnma) with $a_0$=5.617Å, $b_0$=3.391Å and $c_0$=6.153Å [5]. The additional peaks observed in the XRD scans for some of the annealed samples that were not associated with FePd, Pt, Ti and Si could be indexed consistent with respect to the orthorhombic PdSi phase. The ordered $\gamma_1$-FePd grains that formed in the vicinity of the buried PdSi precipitates also exhibited internal twining on {111} but the columnar grain morphology of the active layer was largely lost (Fig. 3). The composition of these latter $\gamma_1$-phase grains (Fig. 3) was determined by EDS to be $Fe_{53}Pd_{36}Pt_{11}$ (in mol%). Hence, significant amounts of Pt, dissolved into the $\gamma_1$-phase matrix, which may be described as approximately equiatomic in composition with respect to the ratio of Fe to (Pd + Pt). EDS mapping by STEM has been utilized to analyze the area depicted in Fig. 3, allowing a correlation of element distributions in the annealed film. Comparison of the STEM BF image and elemental O- and Fe-maps (Fig. 4) reveals a strong correlation between the spatial distribution of oxygen and Fe. The regions that exhibited significant correlation between strong enrichment in O and Fe have been labeled $Fe_xO_y$ in Fig. 2 and 3. Hence, it appears reasonable to conclude that interspersed with the $\gamma_1$-phase grains Fe-based oxides formed in regions where the Pt-overlayer disintegrated in response to the isothermal annealing (Fig. 2-4). Such oxide formation was not detected in the regions with columnar $\gamma_1$-FePd and intact Pt-overlayer. However, the EDS analyses of these latter regions indicated significant enrichment of the Ti-underlayer with Pd (e.g. Fig. 2, label Ti-Pd).

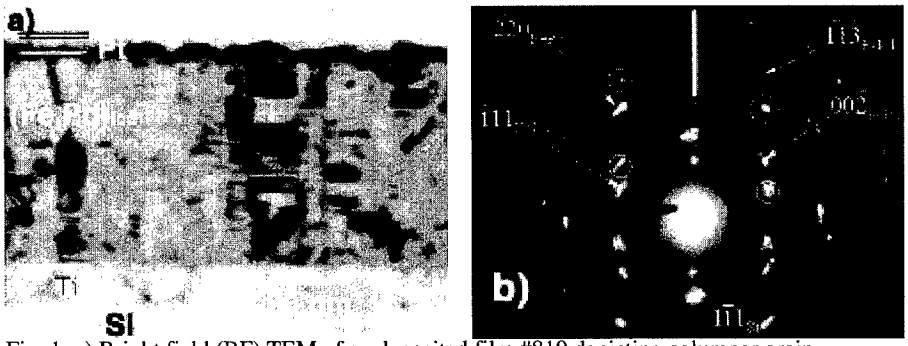


Fig. 1: a) Bright field (BF) TEM of as-deposited film #810 depicting columnar grain morphology. b) selected area diffraction pattern (SADP) from strongly diffraction region, approximately in center of a), for BD ~ <110> of g-(Fe,Pd); open circles mark (111)-twin spots and white line marks direction of conjugation plane normal.

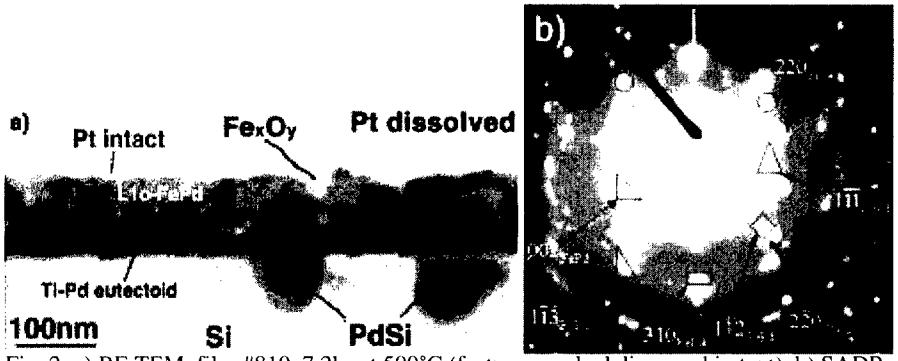


Fig. 2: a) BF-TEM, film #810, 7.2ks at 500°C (features marked discussed in text). b) SADP from region $L1_0$-FePd in a) for approximate beam direction (BD) of [110]; open circles mark (111)-twin spots, triangles and rectangles mark superstructure spots from $\gamma_1$-FePd.

## DISCUSSION

Room temperature magnetron sputtering of Fe-Pd films on Si-substrates and under the conditions employed here produces an active layer with columnar morphology comprised entirely of disordered $\gamma$-(Fe,Pd) grains, which are profusely twinned on (111) parallel to the film/substrate interface plane and on average approximately 18nm in diameter. In response to isothermal annealing at 400°C for up to 7.2ks no microstructural changes were detected by XRD. Annealing at the higher temperatures of 450°C and 500°C for times as short as 1.8ks induced the transformation of the disordered $\gamma$-(Fe,Pd) phase to $L1_0$-ordered $\gamma_1$-FePd in the active layer. The ordering of the Fe-Pd phase was accompanied by significant grain growth, producing elongated grains with their largest dimension normal to the film and with maximum diameters in the range of 40-70nm. The typically about five disordered grains that comprised the columnar grains in the as-deposited films are usually separated by low-angle grain boundaries (LAGB). It appears reasonable to propose that some of these LAGB have been eliminated and adjacent prior $\gamma$-(Fe,Pd) grains in a column of grains coalesced to form the larger elongated grains of the ordered phase during annealing. The transformation from the disordered phase to the ordered phase is associated with a volume change of approximately 1.7% and a reduction in symmetry of the crystal structure. Hence, in order to minimize the attendant transformation strains the characteristic polytwin structures with dodecahedral {101}-twin conjugation develop during the ordering process in bulk samples of $\gamma_1$-FePd [6]. Interestingly, the ordered $\gamma_1$-FePd grains in the annealed thin films studied here retained a large density of the octahedral (111)-conjugated twins. Presumably, these (111)-twins have been inherited from the disordered phase. Dodecahedral {101}-twins, characteristic of $\gamma_1$-FePd bulk samples [6], have not been observed. Hence, it is tempting to speculate that a critical grain size exists for the $\gamma_1$-FePd phase below which the transformation strain

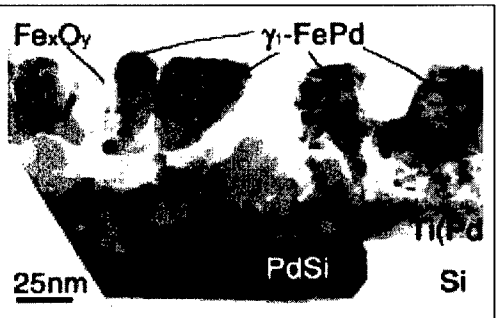


Fig. 3: Film #810, annelaed for 7.2ks at 500°C. BF TEM of region in vicinity of PdSi precipitate at film/substrate interface. See text for details

induced {101}-conjugated twins do not form during isothermal annealing. The additional degree of freedom afforded by the thin film geometry as compared with bulk samples may influence such a scaling effect in the microstructural response to isothermal ordering. The observation regarding the twin fault plane is interesting, because the nature of the defect structures in the ordered phase is predicted to significantly affects magnetic hysteresis behavior and requires further investigation.

In addition to the desirable ordering transformation a number of undesirable microstructural changes were detected. Intermetallic precipitates of an orthorhombic PdSi phase formed periodically at the film/substrate interface. Pd from the active layer grains diffused into the Ti-underlayer. The Pt-overlayer locally dissolved and Pt was incorporated as a solute into the $\gamma_1$-phase grains. The consistent correlation between local loss of the Pt-overlayer and formation of the buried PdSi precipitates may be indicative of some synergism between the inward (toward the substrate) diffusion of Pt and Pd. The $\gamma_1$-FePd grains in the active layer above the PdSi precipitates have an approximately equiatomic composition with respect to the ratio of Fe to the sum of Pd plus Pt. This is consistent with Pt atoms from the dissolving Pt-overlayer migrating into the active layer forming solute species in the Fe-Pd grains. The polycrystalline Pt-overlayer was only one grain thick and GB's exhibited considerable local curvature and signs of surface grooving prior to annealing (Fig. 1a). With thermal activation during annealing a driving force exists to initiate the inward diffusion of Pt into the active layer from these curved and grooved GB's. Hence, it appears reasonable to propose that the local decomposition of the Pt-overlayer involved diffusion of Pt, preferentially from grooved GB's in the overlayer, along the boundaries between the columns of grains in the active layer, followed by irrigation of the LAGB between individual Fe-Pd grains in adjacent columns. Once the Pt reached the LAGB's between individual active layer grains, incorporation into the lattices of the ordering $\gamma$-phase and/or the already ordered $\gamma_1$-phase would require bulk diffusion. The buried PdSi precipitates grew into the Si-substrate (Fig. 2,3). Thus, diffusion of Pd from the active layer through the underlayer into the substrate occurred. At a temperature of 760°C a eutectic of Pd and $Pd_3Si$ exists in the Si-Pd binary system. Neither of these phases has been observed in the films studied here, which is not surprising, since annealing was performed well below the eutectic temperature. However, considering a solid-state reaction between Pd and Si that starts with a Si-rich composition and if Pd is the faster diffusing species, the binary phase diagram indicates that at temperatures at or below 500°C the line compound PdSi would be predicted. Hence, the observed growth morphology, crystal structure and composition of the intermetallic PdSi precipitates at the film/substrate interface is consistent with the Si-Pd phase diagram. Based on the phase diagram of the Ti-Pd binary system, at or below 500°C solid state diffusion of Pd into the Ti-underlayer could potentially produce eutectoid mixtures of Ti, $Ti_4Pd$ and $Ti_2Pd$, depending on the local Pd

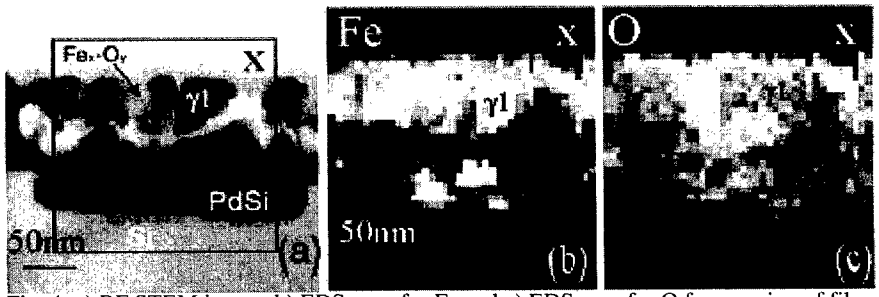

Fig. 4: a) BF STEM image, b) EDS-map for Fe and c) EDS map for O from region of film #810 shown in Fig. 3. The X marks identical positions in each figure, b) and c) have the same scale, $\gamma_1$ marks an ordered FePd grain and $Fe_xO_y$ marks Fe-based oxide.

composition. Interestingly, Pd enrichment of the Ti underlayer was detected by EDS analyses in the regions between the buried PdSi precipitates (label in Fig. 2). Thus, Pd diffused into the underlayer and eutectoid Ti-Pd mixtures would form prior to PdSi precipitates. The Pd diffusion into and through the Ti layer is a required intermediate step in the formation of the PdSi phase, which locally lead to disintegration of the Ti-underlayer. Gaseous species, such as O, present in the residual Ar-based atmosphere of the silica-quartz tubes during annealing also diffused into the film. This process was rapid after the protective Pt-overlayer locally disintegrated resulting in Fe-oxides near the PdSi precipitates. PdSi precipitation depleted adjacent active layer grains of Pd, rendering them less precious and less oxidation resistant. Observation of the Fe-oxides in the regions with disintegrated Pt-overlayer and buried PdSi precipitates is consistent with the oxidation of the Pd-depleted active layer grains (Fig. 3,4). Similar observation to those presented here for film #810 have been made for the other films. The undesirable microstructural changes reported here are attributed to the interplay of the solid-state reactions between Pt-metal atoms and the Fe-Pd based phases and between Pd and the chosen metal-underlayers and Si-substrate respectively, together with the residual oxygen partial pressure present in the annealing environment. Ti and NiCr are unsuitable diffusion barriers to prevent detrimental reactions between Pd and Si. Pt is unsuitable as an overlayer for Fe-Pd based active layers.

## CONCLUSIONS

A combination of XRD and TEM techniques have been used to characterize the response of room temperature magnetron sputtered Fe-Pd thin films on Si susbtrates to post-deposition order-annealing. The main conclusions of this preliminary study can be summarized as follows:

- As-deposited active layers consist of the disordered phase with (111)-twinned grains approximately 18nm in size.
- The Fe-Pd orders upon annealing in excess of 1.8ks at 450°C and 500°C.
- Ordered FePd grains in annealed films grew to maximum dimensions of 40-70nm and exhibit (111)-twins. Dodecahedral {101}-twins typical of the ordered FePd in the bulk were not observed.
- Pt dissolves into Fe-Pd phases and is unsuitable as an overlayer.
- The metallic underlayers were unsuitable to prevent detrimental precipitation reactions between Pd and the Si substrate.
- Post-deposition treatments of room temperature sputtered films are susceptible to local oxidation and thus should be performed in ultra-high vacuum or otherwise controlled inert atmospheres.

## ACKNOWLEDGMENTS

The authors thank the Office of Research of the University of Pittsburgh, Small Grants Program, Central Research Development Fund, and Seagate Technology for financial support of this study, and Tom Nuhfer, Department of Materials Science and Engineering, Carnegie-Mellon University, for assistance with the EDS mapping by STEM.

## REFERENCES

[1] T.J. Klemmer, D. Hoydick, H. Okumura, B. Zhang, W.A. Soffa, Scripta Metall. **33**, 1793 (1995).
[2] D. Weller, A. Moser, IEEE Trans. Magn., **35**, 4423 (1999).
[3] P.R. Aitchison, J.N. Chapman, V. Gehanno, I.S. Weir, M.R. Scheinfein, S. McVitie, A. Marty, J. Magn. Magn. Mat., **223**, 138 (2001).
[4] A. Cebollada, P. Caro, J.L. Menendez, F. Briones, D. Garcia, A. Hernando, J.A. Garcia-Diaz, J. Magn. Mat., **203**, 162 (1999).
[5] J.H. Westbrook, *Intermetallic Compounds*, (Robert E. Krieger Publishing Co., Huntington, NY, 1977).
[6] B. Zhang, M. Lelovic, W.A. Soffa, Scripta Metall. **25**, 1577 (1991).

Mat. Res. Soc. Symp. Proc. Vol. 703 © 2002 Materials Research Society V3.5

# Nanostructured $NiFe_2O_4$ Soft Magnetic Ferrite

Zongtao Zhang[1], Y. D. Zhang[1], T. D. Xiao[1], Shihui Ge[2], Mingzhong Wu[2], W. A. Hines[2], J. I. Budnick[2], J. M. Gromek[2], M. J. Yacaman[3], and H. E. Troiani[4]
[1]Inframat Corporation, 74 Batterson Park Road, Farmington, CT 06032
[2]Physics Department and Institute of Materials Science, University of Connecticut, Storrs, CT 06269
[3]Department of Chemical Engineering, University of Texas, Austin, TX 78712
[4]CNM and Texas Materials Institute, University of Texas, Austin, TX 78712

**ABSTRACT:** $NiFe_2O_4$ is an important high frequency soft magnetic material due to its ultra high resistivity; however, its initial permeability is rather low. Conventional magnetic ferrites are manufactured through ceramic processing. In an effort to explore innovative approaches for fabricating ferrite materials with improved performance, a study of fabricating nanostructured $NiFe_2O_4$ using wet chemical approaches has been carried out. The synthetic $NiFe_2O_4$ precursor was synthesized by a citrate reaction method followed by calcinating at various temperatures. Systematic studies concerning the crystallographic structure, the nanostructure and morphology of the particle, the phase homogeneity, the conditions for chemical reaction completion, and the magnetic properties have been carried out using x-ray diffraction, transmission electron microscopy, and magnetic measurements. The results show that by using a citrate reaction approach, pure phase and stoichiometric $NiFe_2O_4$ can be fabricated easily, and the particle size can be controlled on a nanometer scale, even at high calcination temperatures. In addition, a comparative study of the $NiFe_2O_4$ fabricated by conventional ceramic processing and this new citrate processing will be presented.

## INTRODUCTION

The development of personal computers and electronic equipment and devices is proceeding in the direction of miniaturization and high frequency operation. With high resistivity, ferrites play a leading role in many high frequency applications such as power electronics, communications, consumer electronics, and microwave equipment. Among the various types of ferrite magnetic materials [1-3], $NiFe_2O_4$ represents one of the best ferrites for ultra high frequency applications.

Since their discovery in the 1940's, ferrites were fabricated via ceramic processing which involved a solid state reaction between the constituent metal oxides at high temperatures. Although there have been a substantial improvement in the properties of conventional ferrites, the progresses are limited and the magnetic properties of the ferrites cannot satisfy the increasing demand for high quality ferrite products. In the request for improved magnetic properties, perhaps the most important task is to develop a novel synthesis approach. Based on this consideration, an aqueous solution reaction technique was developed to synthesis nanophase $NiFe_2O_4$ particles. This report deals with the synthesis of $NiFe_2O_4$, and its structural and magnetic properties.

## EXPERIMENTS

Low temperature synthesis approaches based on the aqueous synthesis method have been developed in recent years to synthesis very fine $NiFe_2O_4$ (n-$NiFe_2O_4$) particles [4-5]. The

synthesis method used in this work is as follows. The parent materials are iron (III) citrate, nickel nitrate, and citric acid. First, the iron citrate tri-hydrate and the nickel citrate tri-hydrate were dissolved separately in DI water. The two clear solutions were mixed together and slowly dried until the solution was concentrated and became sticky. The concentrated mixture was further dried in an oven at 40 °C for 8 hours. The dried powder was crushed and passed through a 60 mesh screen. The crushed powder was calcined in the temperatures between 100 to 900 °C for 2 hours in a controlled oxygen atmosphere. Characterization of the crystal structure and particle size of the synthetic powders was carried out using x-ray diffraction (XRD) with Cu $K\alpha_1$ radiation. The nanostructure of the $NiFe_2O_4$ particle was also examined using high-resolution transmission electron microscopy (HRTEM) and Mossbauer effect (ME) experiments. Static magnetic properties of the synthetic $NiFe_2O_4$ nanoparticles were measured using a Quantum Design SQUID magnetometer at temperatures between 10 K and 300K.

## RESULTS AND DISCUSSION

**Structure** Figure 1 shows the XRD pattern for the n-$NiFe_2O_4$ powder samples calcined at 100, 500, 700, and 900 °C. For comparison, the figure also includes the XRD pattern of a bulk-size conventional $NiFe_2O_4$ powder sample. The x-ray diffraction results identify that all of the synthetic $NiFe_2O_4$ powders have the same spinel $NiFe_2O_4$ structure. As shown in Figure 1, the linewidths of XRD diffraction peaks for the n-$NiFe_2O_4$ are significantly broader than that for the bulk $NiFe_2O_4$ sample. From the linewidth of the main peak (at 35.7°), the mean particle size of the $NiFe_2O_4$ nanoparticle samples calcined at different temperatures was calculated according to the Scherrer equation [6]. Figure 2 shows the particle size of the synthetic $NiFe_2O_4$ nanoparticles as a function of the calcination temperature. It can be seen that when the calcination temperature

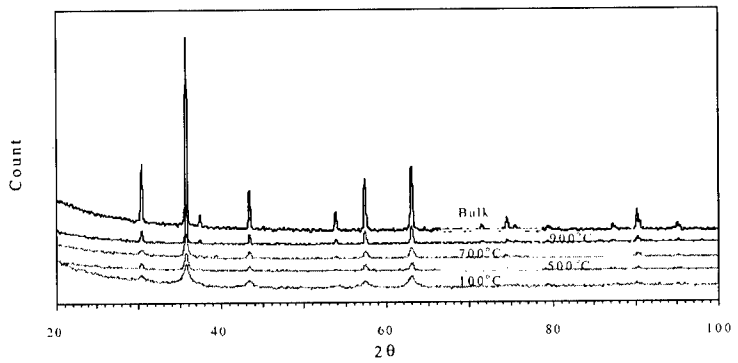


**Figure 1.** XRD pattern for nanostructured $NiFe_2O_4$ and microsized (bulk) $NiFe_2O_4$

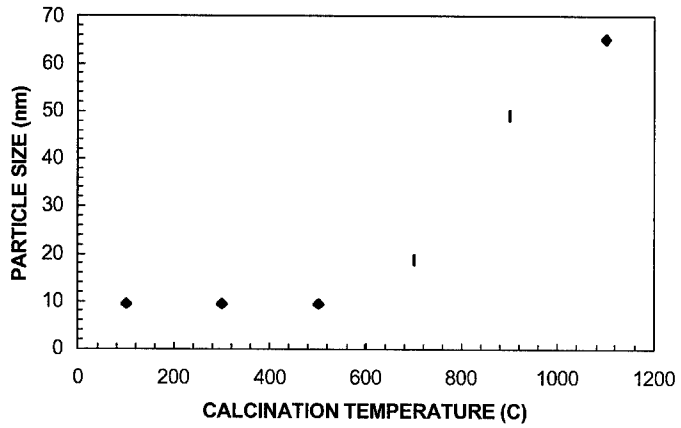


**Figure 2.** The particle size of n-$NiFe_2O_4$ as a function of the calcination temperature

is 500 °C or below, the $NiFe_2O_4$ particle size remains small (10 nm) with little change with temperature; while beyond 700 °C, the particle size significantly increases with increasing calcination temperature.

High-resolution transmission electron microscopy experiments were carried out to study the nanostructure of the synthetic $NiFe_2O_4$ samples. Bright field images, electron diffraction, and lattice images were obtained. A typical HRTEM image showing the morphologies of the $NiFe_2O_4$ nanoparticle materials is presented in Figure 3. This image shows many nanoparticles. It is very interesting that several nanoparticles appear for this particular set of lattice fringes, implying that it is possible that the particles do not have a random orientation. Many Moire fringes are distinguished, the array of nanoparticles is 3-D.

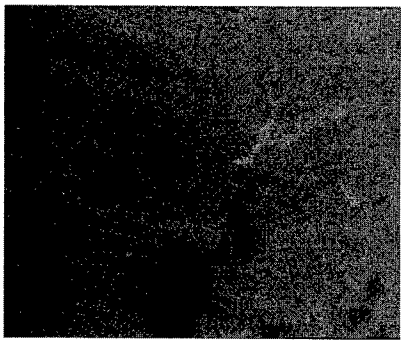

**Figure 3.** A typical atomic resolution TEM image showing the morphology of the$NiFe_2O_4$ nanoparticles. The bar corresponds to 20 nm.

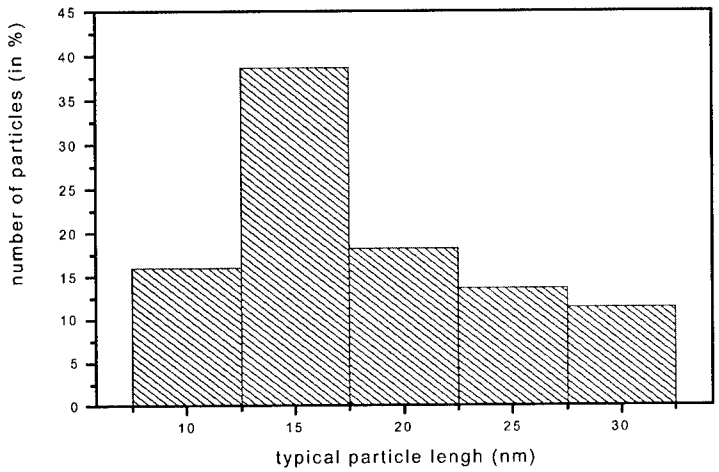


Fig. 4. Particle size distribution of $NiFe_2O_4$ obtained by TEM

The image shows a rather dispersive particle size distribution between 10nm and 30 nm. Figure 4 shows the particle size distribution obtained by TEM. The width of the distribution is approximately 25 nm and there is a peak centered around 15 nm. For this histogram, 54 particles were counted and analyzed. The typical length in the figure is an average between the maximum and minimum lateral dimensions measured from the TEM image.

It was found in this study of nanostructured ferrites that the nanostructured ferrite particle may consist of an outer amorphous shell and an inner crystalline core such that the relative shell thickness increases with the reduction in the particle size. To gain some insight into the nanostructure of the synthetic $NiFe_2O_4$ nanoparticles, a ME experiment has been carried out on these samples. The results indicate that the $NiFe_2O_4$ calcined at low temperatures possess a dominantly amorphous structure. With increasing calcination temperature, the crystalline constituent increases until 700 $^0$C, beyond which, crystalline phase becomes dominant. The details of the ME study will be published elsewhere [7].

**Static magnetic properties of $NiFe_2O_4$ nanoparticles**

Figure 5 shows typical magnetization curves measured at 10 K and 300 K for the n-$NiFe_2O_4$ powder sample calcined at 700°C. It can be seen from the figure that the magnetization of n-$NiFe_2O_4$ is close to saturation for a field of 10 kOe. The saturation magnetization of the powder at 10K is obtained to be 3410G. Figure 6 shows the saturation magnetization as a function of calcination temperature. Starting from 400 °C, calcination at an elevated temperature makes the $NiFe_2O_4$ phase more completely formed, thus the saturation magnetization increases with increasing the calcination temperature. For conventional bulk $NiFe_2O_4$, the saturation magnetization at 10 K is 3800 G. As shown in Figure 6, the same value can be reached for the as-synthesized nanosized $NiFe_2O_4$ when calcination occurs at 700 °C or higher.

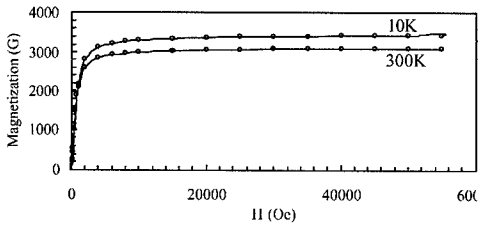


**Figure 5.** Magnetization curves for the 700°C calcined n-$NiFe_2O_4$ powder sample measured at 10 K and 300 K.

Figure 7 shows the temperature dependence of low field magnetization for the n-$NiFe_2O_4$ calcined at 100 °C. In this measurement, the sample was cooled from room temperature to 4.2 K in a zero magnetic field (ZFC), and then a 100 Oe field was applied. The magnetization on the 700 °C calcined sample; the result is shown in Figure 8. As can be seen from the figure, the monotonic increase of the magnetization with increasing temperature and the complete irreversible change of magnetization when reducing the temperature clearly prove that the particle size is larger for the 700 °C calcined sample.

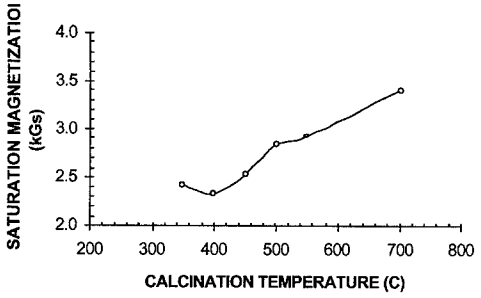


**Figure 6.** The variation of saturation magnetization measured at 10 K with calcination temperature for nanostructured $NiFe_2O_4$.

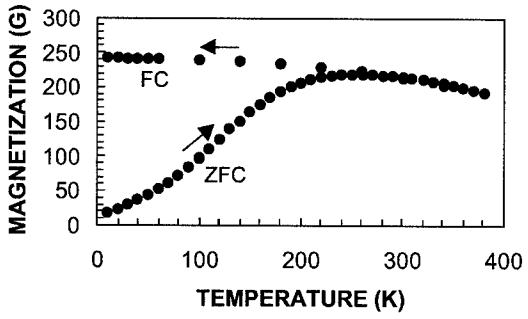


**Figure 7.** Magnetization in a field of 100Oe as a function of temperature for the 100 °C calcined n-$NiFe_2O_4$ powder sample. The arrows indicate the direction of the temperature variation.

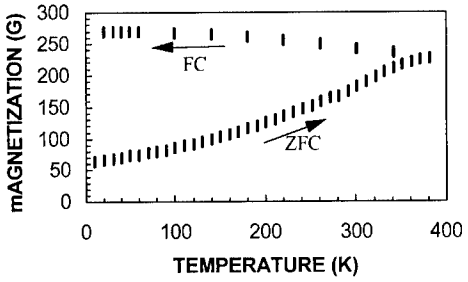


**Figure 8.** Magnetization as a function of temperature for the 700 °C calcined n-$NiFe_2O_4$ powder sample. The arrows indicate the direction of the temperature variation.

## CONCLUSIONS

Based on the structural and magnetic properties, it is determined that the synthetic nanostructured $NiFe_2O_4$ possesses high phase purity and controllable particle size. By calcining at 700°C, the synthetic $NiFe_2O_4$ nanoparticle possesses a saturation magnetization of 3841Gs and a particle size of about 20 nm. These characteristics are favorable for fabricating a nanophase $NiFe_2O_4$ ferrite.

## ACKNOWLEDGMENTS

The work at Inframat Corporation is supported by US Air Force Contract No. F29601 01-C-0141.

## REFERENCES

1. B. Viswanathan and V.R.K. Murthy, *Ferrite materials: science and technology* (Narosa Publishing House, New York, 1990).
2. A. Goldman, *Handbook of modern ferromagnetic materials* (Kluwer Academic Publishers, Boston, 1999).
3. J. Smit and H. P. J. Wijn, *Ferrites* (Philips', Holland, 1959).
4. A. Verma, T. C. Goel, and R. G. Mendiratta, Mat. Sci. Tech. **16**, 712 (2000).
5. A. Srivastava, P. Singh, and M. P. Gupta, J. Mat. Sci. **22**, 1489 (1987).
6. H. Lipson and H. Steeple, *Interpretation of X-Ray Powder Diffraction Patterns* (St Martin's Press, New York, 1970) p. 256.
7. D. P. Yang, Y. D. Zhang, and Zongtao Zhang, (to be published).
8. D.L. Leslie-Pelecky and R. D. Rieke, Chem. Mater. **8**, 1770 (1996).

Mat. Res. Soc. Symp. Proc. Vol. 703 © 2002 Materials Research Society V3.9

# Dynamic Fracture Mechanisms in Nanostructured and Amorphous Silica Glasses Million-Atom Molecular Dynamics Simulations.

**Laurent Van Brutzel, Cindy L. Rountree, Rajiv K. Kalia, Aiichiro Nakano, and Priya Vashishta**
Concurrent Computing Laboratory for Materials Simulations,
Biological Computation and Visualization Center,
Department of Physics and Astronomy, Department of Computer Science, Louisiana State University, Baton Rouge, Louisiana 70803

## ABSTRACT

Parallel molecular dynamics simulations are performed to investigate dynamic fracture in bulk and nanostructured silica glasses at room temperature and 1000 K. In bulk silica the crack front develops multiple branches and nanoscale pores open up ahead of the crack tip. Pores coalesce and then they merge with the advancing crack-front to cause cleavage fracture. The calculated fracture toughness is in good agreement with experiments. In nanostrucutred silica the crack-front meanders along intercluster boundaries, merging with nanoscale pores in these regions to cause intergranular fracture. The failure strain in nanostructured silica is significantly larger than in the bulk systems.

## INTRODUCTION

Amorphous silica (a-$SiO_2$) is widely used in various technological applications because of its unique chemical and physical properties. However, the brittle nature and poor shock resistance of silica have precluded its use as a structural material. With the synthesis of "ductile" nanophase ceramics, there is renewed hope that novel amorphous nanostructured silica systems that fracture more gracefully than conventional bulk a-$SiO_2$ will find use in structural applications. However, any hope to enhance mechanical properties rests on understanding crack initiation and propagation at the atomic scale. Ten years ago Simmons and al. carried out the first Molecular Dynamics simulations to investigate brittle fracture in a-$SiO_2$ [1-3]. They showed that the crack in a-$SiO_2$ is not only initiated by the surface defects but also has an origin in the intrinsic structure. Nevertheless, these simulations were not large enough to study the propagation on a largest scale.

We present here results of Molecular Dynamics (MD) simulations on crack propagation and fracture in both bulk a-$SiO_2$ and nanostructured a-$SiO_2$ at low and high temperatures. These simulations, involving a million-atom each, are performed with reliable inter-atomic potentials on parallel computers using highly efficient algorithms. In the bulk system at room temperature (300 K), we find that the crack-front propagates by merging with the cavities that open up just ahead of it. In contrast, the bulk system at 1000 K many more cavities both close and far from the crack-tip appear. Those far from the crack-tip coalesce before merging with the main crack forming a secondary crack. In the nanostructured a-$SiO_2$ at room and high temperature, we observe intergranular fracture with the crack meandering along the nanoparticle boundaries. The observed crack propagation and fracture behavior in both bulk and nanostructured silica are related to the inherent intermediate range order in these systems.

## COMPUTATIONAL PROCEDURE

MD simulations of silica are performed with a reliable inter-atomic potential, consisting of two-body and three-body terms [4]. The two-body terms contain the effects of charge transfer, electronic polarization, and steric repulsion. The three-body terms is a Stillinger-Weber like potential involving bond bending and bond stretching effects. The potential is validated through a detailed comparison with various experimental results on bulk silica glass such as elastic moduli, static structure factor, and phonon density of states [5, 6].

Fracture simulations in bulk and nanostructured silica glasses are performed on systems containing a million atoms each. The two bulk a-$SiO_2$ systems were prepared by melting β-cristobalite at 3500 K, thermalizing it for 30,000 time steps, before cooling it gradually to 3000 K where it was again thermalized for 30,000 time steps. Following this procedure of gradual cooling and thermalization, the system was cooling down to 5 K and then subjected to conjugate-gradient quench which brought down the temperature to 0 K. This system was then heated to 300 K where it was further thermalized for 50,000 time steps, subsequently, the temperature was raised to 1000 K and this system was also relaxed for 50,000 time steps.

The nanostructured system was prepared by cutting out spheres of radius 40 Å from the well thermalized bulk amorphous system [7]. These spherical nanoparticles were relaxed with the conjugate gradient technique. Subsequently, 100 of these nanoparticules were randomly placed in a box and consolidated at 1000 K with the application of a hydrostatic pressure that was gradually increased to 16 GPa. Keeping the pressure fixed, the system was cooled from 1000 K to 300 K and the system was relaxed for 30,000 time steps. Subsequently the pressure was slowly decreased to zero. This consolidated system at 0 GPa and 300 K has a density of 2.04 g/cc which is close to the bulk density (2.2 g/cc). The nanostructured glass at 1000 K was obtained by heating the room temperature system and subsequently thermalizing it for 30,000 time steps.

To simulate dynamic fracture the periodic boundary conditions are removed. A triangular notch of length 50 Å and width 40 Å is created on one edge of the simulation box by removing atoms. The pre-notched systems is then subjected to an external strain by displacing the atoms included in the top and the bottom layers of the simulation box. The width of these layers is approximately equal to a cut-off. The strained systems is subsequently relaxed under isothermal conditions before increasing the strain further. In all the systems studied we applied a strain rate of 0.01/ps.

## RESULTS AND DISCUSSION

Figure 1 shows snapshots of notch and pores in bulk a-$SiO_2$ at 300 K for different values of strains. Pores were analyzed by dividing each system into voxels of size 4.5 Å and then identifying empty voxels with a common edge or corner. Figure 1(a) shows the initial notch. Figure 1(b) displays that in bulk a-$SiO_2$ at 300 K small pores open up directly ahead of the crack tip when the strain exceeds 3.4%. In a region approximately of 50 Å ahead of the crack tip, pores coalesce to form cavities of dimensions between 20 Å and 60 Å. With further increase in

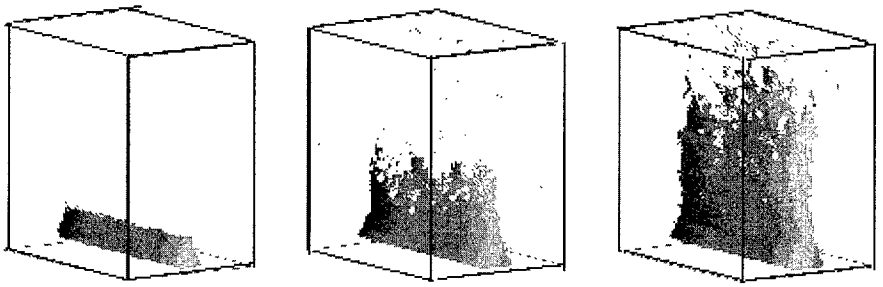


**Figure 1.** Snapshots of pores and cracks in bulk a-$SiO_2$ at 300 K. Fig. 1(a) shows the initial notch and fig. 1(b) and 1(c) show its evolution into several branches and the appearance of nanoscale pores at a strain of 3.4% and 6% respectively.

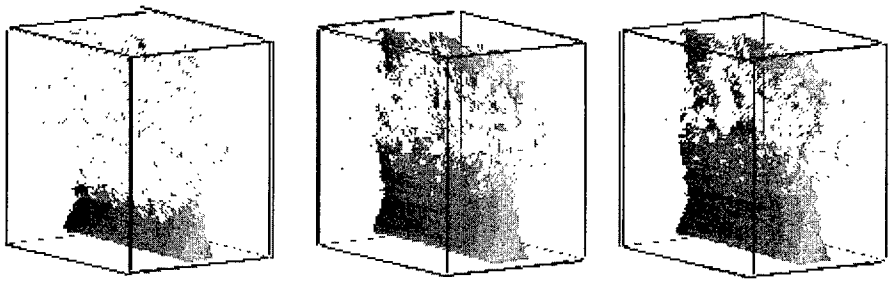


**Figure 2.** Snapshots of pores and cracks in bulk a-$SiO_2$ at 1000 K. The system at 1000 K shows little progression of the pre-notch even at a strain of 5.3% (fig. 2(a)). However in fig. 2(b), further increase in strain causes the crack-front to move significantly and in fig. 2(c) several cavities appear as a result of coalescence of nanoscale pores forming a distinct secondary crack.

the strain (Fig. 1(c)) the number of cavities increases and they form multiple branches on the crack-front. Finally, the system ruptures completely at a strain of 6.5 %.

Figure 2 shows many features of crack and pore evolution in a-$SiO_2$ at 1000 K similar to those observed at room temperature, the crack-front propagates by growth and coalescence of cavities. Nevertheless, the onset of crack in a-$SiO_2$ at 1000 K occurs at a strain of 5.3% whereas at room temperature it appears around 2%. Further analysis reveals that the glass at 1000 K has pores 100 Å ahead of the crack tip leading to the formation of a secondary crack, whereas in the room temperature system, pores are mostly combined closer to the crack tip.

Figures 3 show crack and pore evolution in nanostructured a-$SiO_2$ at 300 K. Small pores are formed in interfacial regions along nanoparticule boundaries even in the absence of the applied strain. As the strain increases pores grow, and some of them merge with the main crack while

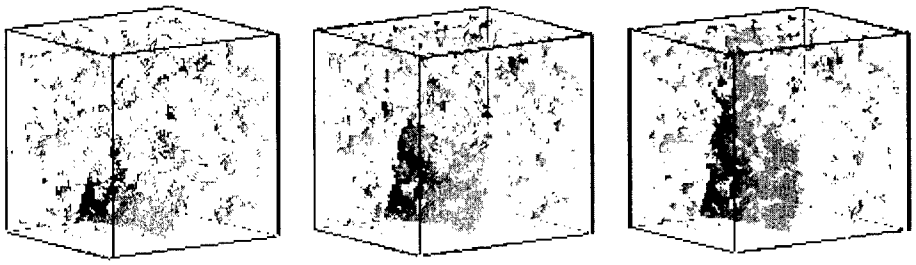


**Figure 3.** Snapshots of pores and cracks in nanostructured a-$SiO_2$ at 300 K. Fig. 3(a) displays the initial distribution of pores; in fig. 3(b) the pores show the interfacial regions between the clusters; and fig. 3(c) shows the evolution of the crack through the interfacial regions.

others coalesce to form a secondary cracks approximately 100 Å ahead the crack tip. At a strain of 9 %, the primary and secondary cracks merge to cause intergranular fracture.

Quantitatively, the similarities and differences between the three systems can be seen in Fig. 4(a) where the porosities are plotted as a function of the applied strain. The two bulk a-$SiO_2$ systems have nearly the same porosities up to a strain of 3.5%. With further increase in the strain, the porosity rises more sharply in the room temperature glass than in the system at 1000 K. In order to characterize more precisely the correlation between the number of pores and crack propagation the strain dependence of crack tip positions is also analyzed. In figure 4(b) the

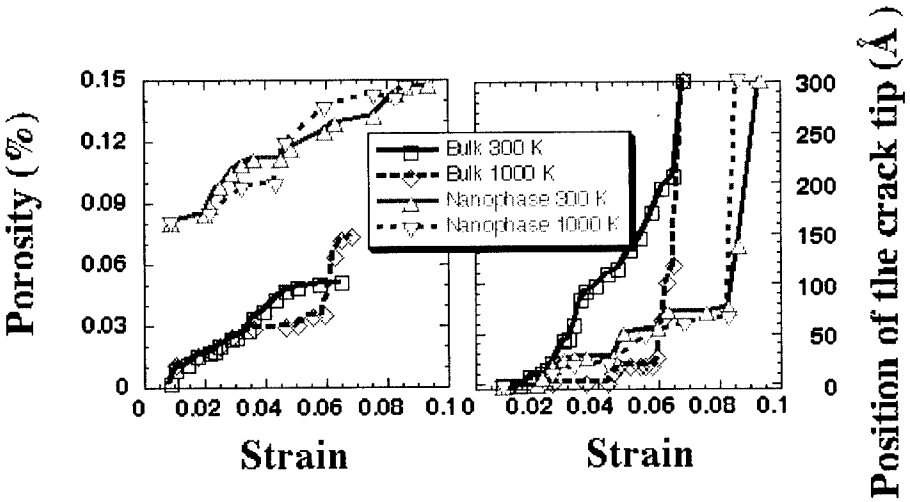


**Figure 4.** (a) Percentage of porosity as a function of strain. (b) Position of the crack tip as a function of the applied strain.

position of the crack tip in a-$SiO_2$ at 300 K advances linearly while in others systems it grows intermittently with increasing. The intermittent growth is much more accentuated in the nanostructured systems. The plateaus in Fig. 4(b) reflect the growth of bigger cavities and/or the formation of secondary cracks ahead of the crack tip. This behavior makes difficult to determine precisely the crack tip velocities, although average crack tip speeds can be estimated. In the case of a-$SiO_2$ at 300 K the crack propagation starts at a strain of 2 % and it advances at a speed of ~800 m/s up to a strain of 6.4 %. This corresponds to half of the Rayleigh wave speed in the material. In the case of a-$SiO_2$ at 1000 K the crack tip advances at a strain of 4.2 % reaching a plateau within a small increment of strain. The crack tip hardly advances until the strain reaches 6%. Subsequently, the primary crack tip coalesces with the secondary crack. These results strongly indicate that the strain energy in a-$SiO_2$ at 300 K is dissipated along the crack tip, whereas in a-$SiO_2$ at 1000 K the strain energy is also dissipated in the formation and growth of pores into secondary crack.

Strained nanostructured silica systems also exhibit alternating plateaus and crack growth. In the nanostructured system at 300 K the onset of crack growth occurs at a strain of 1.5 % followed by a plateau at strains between 3 % and 4.5 %. Further increase in strain results in an other plateau. Finally, at a strain of 8.2 % the system undergoes intergranular fracture. These results provide clear evidence that the strain energy supplied to this system is dissipated via the creation of pores. As a result, this system fracture at a higher strain than its bulk counterparts.

Hence, the augmentation of the temperature in the case of the a-$SiO_2$ enhances the creation of pores. In the case of the nanostructured the presence of many pores intrinsic of the material plays the same role than the augmentation of the temperature. Therefore, the influence of the temperature in the nanostructured material is smaller than in the bulk.

We have also examined the relationship between structural correlations and crack growth in the bulk and nanostructured a-$SiO_2$. Experiments and atomic simulations have shown that amorphous silica consists of corner-sharing $SiO_4$ tetrahedra which form mostly 5-, 6- and 7-membered rings [8]. In so far as the short-range order is concerned, pair-distribution functions and bond-angle distributions do not reveal any notable differences and the corner-sharing tetrahedral structure is mostly unaffected during crack propagation. The influence of

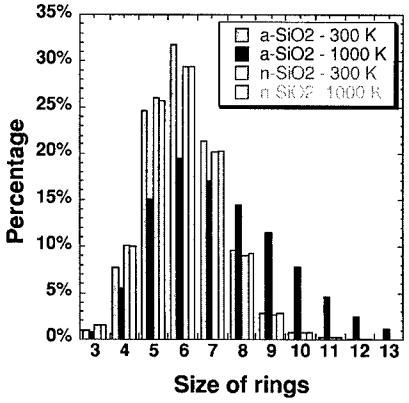


**Figure 5.** Distribution of the membered rings for the bulk a-$SiO_2$ and nanophase a-$SiO_2$ (n-$SiO_2$) at 1 % of strain corresponding to the strain just before the crack propagation.

intermediate-range order on crack initiation is analyzed through the ring distribution. Figure 5 shows these distributions for the four systems just before the onset of crack propagation. (Rings are identified by a procedure described in [8]). The two bulk systems have significantly different ring distributions: At 300 K, nearly 80% of the rings have 3 to 7 members and only 12% are 8-13 membered rings; at 1000 K, the population of 3- to 7-membered rings drops to 52% while the percentage of 8-13 membered rings increases to 42%. (Note that a 13-membered ring has the same size as a 10 Å pore.) Thus, pores in bulk a-$SiO_2$ at 1000 K initiate from the breakup of large rings that are distributed uniformly throughout the volume of the systems. In contrast, the nanostructured systems have nearly the same ring distributions indicating that, in both cases, pores in the interfacial regions grow by breaking up all size rings.

## CONCLUSIONS

In conclusion, these million-atom MD simulations show that advancing crack-fronts in bulk silica develop multiple branches and pores which coalesce among themselves and also with the crack-front. The strain energy dissipated in creating nanoscale pores causes the system at higher temperature to fracture at a much higher value of strain. In nanostructured silica glasses pores develop mainly in intergranular regions, crack-fronts meander along intercluster boundaries and they coalesce with pores to cause intergranular fracture. In this case temperature has small influence on the onset of crack.

## ACKNOWLEDGMENTS

We would like to thank Dr. E. Bouchaud for stimulating discussions and Dr. K. Hideaki for his technical help. This work was supported by U.S. DOE, AFOSR, NSF and Biological Computation and Visualization Center (BCVC). Simulations were performed on the 32-processor PC cluster in the Concurrent Computing Laboratory for Materials Simulations at Louisisana State University.

## REFERENCES

1. R. Ochoa, Th. P. Swiler and J. H. Simmons, J. Non-Cryst. Solids **128**, 57 (1991)
2. Th. P. Swiler, T. Varghese and J. H. Simmons, J. Non-Cryst. Solids **181**, 238 (1995)
3. Th. P. Swiler, J. H. Simmons, A. C. Wright, J. Non-Cryst. Solids **182**, 68 (1995)
4. P.Vashishta, R. K. Kalia, and J. P. Rino, Phys.Rev. B **41**,12197 (1990)
5. S. Susman, K. J. Volin, D. L. Gridsditch, J. P. Rino, R. K. Kalia, and P. Vashishta, Phys. Rev. B **43**, 1194 (1991)
6. W. Jin, P. Vashishta, and R. K. Kalia, Phys. Rev. Lett. **69**, 1387 (1992)
7. T. Campbell, R. K. Kalia, A. Nakano, F. Shimojo, K. Tsuruta and P. Vashishta, Phys. Rev. Lett. **82**, 4018 (1999)
8. J. P. Rino, I. Ebbsjo, R. K. Kalia, A. Nakano, P. Vashishta, Phys. Rev. B **47**, 3053 (1993)

Mat. Res. Soc. Symp. Proc. Vol. 703 © 2002 Materials Research Society V3.10

# A Non-Traditional Vapor-Liquid-Solid Method for Bulk Synthesis of Semiconductor Nanowires

Shashank Sharma, and Mahendra K. Sunkara*
Department of Chemical Engineering, University of Louisville,
Louisville, KY 40292, USA
Guoda Lian and Elizabeth C. Dickey
Department of Chemical and Materials Engineering, University of Kentucky,
Lexington, KY 40506, USA
* Corresponding author: mahendra@louisville.edu

## ABSTRACT

Multiple silicon nanowires were synthesized using large gallium pools and microwave plasma. Results showed that nanowires growing out of different sized large gallium drops show little variation in diameters, suggesting that our non-traditional technique can be used to synthesize bulk amounts of monodispersed nanowires out of thin films of molten gallium.

## INTRODUCTION

Size constraints and surface effects induce novel characteristics in materials at nanoscale.[1-6] In order to utilize nanometer scale structures in applications such as electronic, optoelectronic, and catalytic, bulk amounts of nanostructures will be required with tunable composition and structure. In this regard, bulk synthesis of semiconductor nanowires has been traditionally achieved using several variations of transition metal catalyzed techniques such as vapor-liquid-solid (VLS). [7-20] In such techniques, the nanowire diameter is limited by the catalyst droplet size. However, creation of nanometer size catalyst droplets is a non-trivial task. Furthermore, given the fact that transition metals form high solubility eutectics with various semiconductor elements, it would be very difficult to obtain abrupt compositionally modulated structures. Nanowires have also been synthesized by restrictive growth methods such as nanotube-confined reactions [21-23] and with atomic scale step edges as templates. [24] In all of these techniques, it will be difficult to control the nanowire diameter and diameter distribution.

Recently our group demonstrated bulk synthesis of silicon nanowires using gallium as the molten metal solvent and microwave plasma to carry out the gas phase chemistry. [25] It was reported that multiple nuclei form and grow as nanowires out of a large gallium pool. Thus, this gallium and microwave plasma based technique eliminates the need for nanometer sized metal droplets and has a potential to work at much lower temperatures than the conventional techniques using transition metals. However, there are certain important aspects of this technique that remained unaddressed. In this paper, we discuss issues related to control over nanowire diameter and diameter distribution in our non-transition metal-based technique. We also present evidence for in-situ generation of silyl radicals thus confirming silicon source to be through gas phase.

## EXPERIMENTAL DETAILS

The experimental setup for bulk synthesis of silicon nanowires has been previously described. [25] Chemical vapor transport experiments were also performed, in which gallium-covered p-BN and quartz substrates surrounded by silicon pieces were exposed to a diluted hydrogen plasma. An Ocean Optics® optical emission spectrometer (OES) was used to identify the various species in the plasma. Individual nanowires were analyzed for crystallinity and composition using high-resolution transmission electron microscopy (HRTEM) (200kV JEOL model 2010F) and energy-dispersive X-ray spectroscopy (EDX).

## RESULTS AND DISCUSSIONS

Figure 1(a) shows a SEM micrograph of several fibers growing out of a large gallium pool after a typical growth experiment. Figure 1 (b) shows very straight silicon nanowires grown out of a gallium pool.

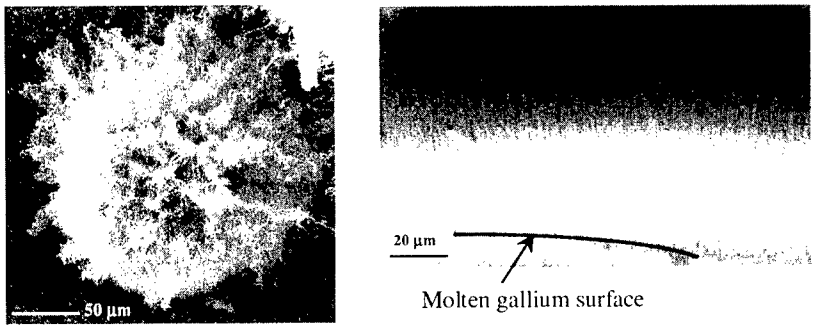


(a) (b)

**Figure1.** (a) Multiple silicon fibers ~20 nm thick, grown out of a 200 µm gallium drop. (b) Straight silicon filaments ~25 nm thick, obtained after another experiments under different conditions.

In traditional VLS methods, nanowire diameter is determined by the transition metal droplet size. Thus, in order to obtain a uniform nanowire diameter distribution, monodispersed catalyst particles need to be created on a solid substrate. However, it has been reported that there is an inherent limitation in controlling the nanowire diameter. [27] Formation of the transition metal-Si alloy before nucleation causes the nanowires in general to be thicker than the metal droplet. Thus, it is difficult to absolutely control the nanowire diameter.

In our non-traditional technique discussed in this paper, the critical nuclei diameter can be defined based on the classical nucleation theory as

$$d_c = \frac{4\Omega\alpha}{RT \ln(\frac{C}{C_\infty})} \qquad (1)$$

where, $d_c$, $\Omega$, $\alpha$, C and $C_\infty$ represent critical nucleus diameter, molar volume, surface free energy, concentration of silicon within liquid alloy and equilibrium concentration at temperature T, respectively. Thus unlike in traditional VLS methods, the nanowire diameter in our technique is determined by the solute supersaturation in molten gallium and substrate temperature. Figure 2 shows variation of critical nucleus diameter as a function of temperature for a particular dissolved solute concentration and as a function of dissolved solute concentration at a particular temperature. It can be seen that at a specific dissolved silicon concentration in molten gallium, critical nucleus size increases with increasing temperature due to greater influence of temperature on the equilibrium solubility.

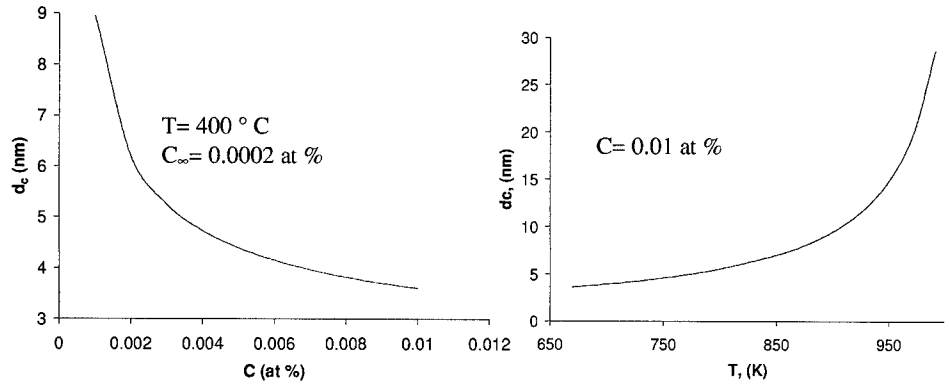


(a) (b)

**Figure 2.** Variation of the critical nucleus diameter defined by eqn (1) as a function of (a) dissolved solute concentration in molten gallium at a particular temperature, and (b) temperature for an arbitrary dissolved silicon concentration of 0.01 at %.

The liquid phase solute supersaturation is dependent on silicon supply at the V-L interface and the substrate temperature. The vapor phase silicon supersaturation is determined by substrate temperature, gas temperature, pressure, diluent gas and dilution fraction. Independent control over these parameters will enable a tighter control over nanowire diameter and diameter distribution. However in our current experimental setup, these parameters are related in a convoluted manner. Figures 2 (a)-(c) demonstrate that nanowires grown under different sets of experimental conditions have different diameters. Figure 2 (d) shows a representative diameter distribution of nanowires grown out of a 1.3 mm diameter gallium droplet at a substrate temperature of 700 ºC. For a particular set of experimental conditions, mean diameters of the nanowires grown out of different sized gallium droplets were very close to each other. Please see Table I. Thus it could be possible to synthesize silicon nanowires with a narrow diameter distribution using a thin film of gallium.

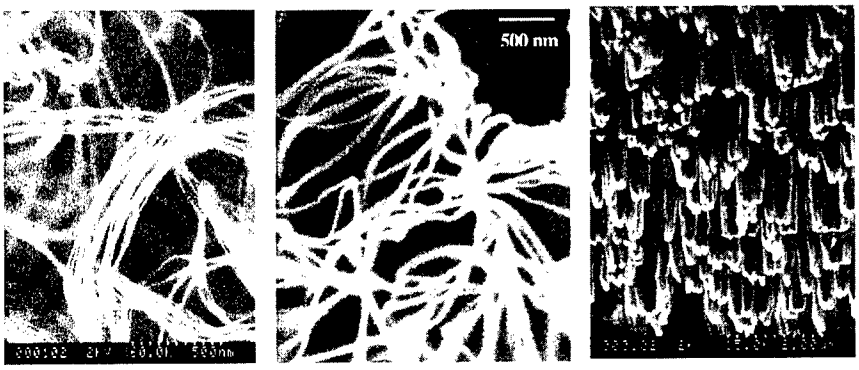


(a) (b) (c)

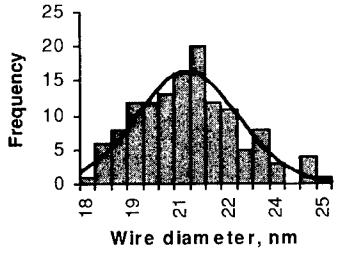


(d)

**Figure 2.** Bulk amounts of silicon nanowires obtained in three different experiments. Process parameters are (a) ~10 nm dia, 1000 W MW power, 30 torr total pressure, 0.25 sccm $H_2$/100 sccm $N_2$, 6 hrs (b) ~21 nm dia, 1000 W, 50 torr, 2.0 sccm $H_2$/100 sccm $N_2$, 4 hrs (c) ~150 nm dia, 900 W, 50 torr, 0.75 sccm $H_2$/100 sccm $N_2$, 5 hrs. (d) Diameter distribution of the nanowires grown under process conditions of (b); mean wire dia: 21.4 nm.

**Table I.** Mean nanowire diameters grown under different set of experimental conditions.

| MW Power (W) | Pressure (Torr) | H2 flow rate in 100 sccm N2 (sccm) | Temperature (deg C) | Duration (hrs) | Droplet size (μm) | Mean wire dia (nm) | SD (nm) |
|---|---|---|---|---|---|---|---|
| 850 | 40 | 0.8 | 580 | 12 | 800 | 24.2 | 0.8 |
| 850 | 40 | 0.8 | 580 | 12 | 1300 | 25.0 | 1.0 |
| 1000 | 50 | 2 | 695 | 4 | 71.75 | 35.3 | 2.8 |
| 1000 | 50 | 2 | 695 | 4 | 305 | 34.4 | 2.6 |
| 1000 | 50 | 2 | 695 | 4 | 1219 | 34.3 | 3.1 |
| 850 | 50 | 10 | 701 | 9 | 217.3 | 21.4 | 1.6 |
| 850 | 50 | 10 | 701 | 9 | 364.7 | 20.4 | 2.1 |

Gallium is not known to act as a catalyst for gas decomposition or dehydrogenation reactions. In our experiments, Silyl species are produced by atomic hydrogen etching of the exposed silicon substrate. In order to confirm this hypothesis, silicon nanowire growth experiments were performed using gallium covered non-silicon substrates surrounded by small silicon pieces. Figure 4 (a) shows silicon nanowires grown on a pyrolytic boron nitride substrate covered with Gallium droplets. Figure 4 (b) shows an optical emission spectrum taken during these chemical vapor transport experiments. A SiH peak was identified, [28-30] providing evidence of in-situ production of silyl radicals.

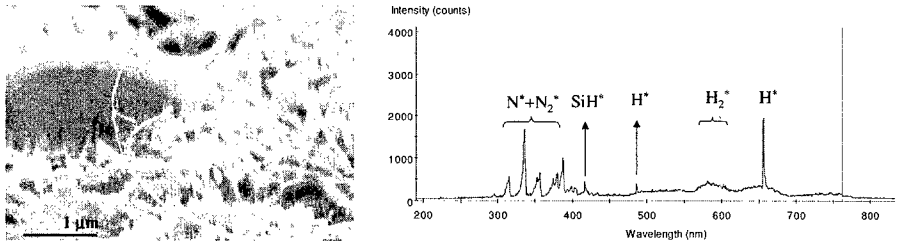


(a) (b)

Figure 3. (a) Silicon nanofibers obtained using PBN substrate covered with gallium droplets and surrounded by silicon pieces, exposed to the nitrogen plasma containing atomic hydrogen. (b) An optical emission spectrum of the plasma taken in the experimental conditions of (a).

## CONCLUSIONS

It is possible to grow monodispersed silicon nanowires out of a gallium film using our non-traditional technique, as demonstrated by a very narrow diameter variation exhibited by the nanowires grown out of different sized gallium drops.

## ACKNOWLEDGMENTS

We acknowledge partial support from NSF through a CAREER grant (CTS #9876251) and an infrastructure grant (EPS 0083103).

## REFERENCES

1. C.M. Lieber, Solid State Comm 107 (11), 607-616 (1998).
2. C.Wu, Prism 10(3), 21-26 (2000).
3. S-W Chung, J-Y Yu, and J.R. Heath, Appl. Phys. Lett. 76 (15), 2068-2070 (2000).
4. F.C.K. Au et al., Appl. Phys. Lett. 75 (12), 1700-1702 (1999).
5. A. Zunger and L-W Wang, Appl. Surf. Sc. 102, 350-359 (1996).
6. A.M. Saitta, F. Buda, G. Fiumara, and P.V. Giaquinta, Phys. Rev. B 53 (3), 1446-1451 (1996).
7. R.S. Wagner and W.C. Ellis, Appl. Phys. Lett. 4 (5), 89 (March 1964).
8. A.M. Morales and C.M. Lieber, Science 279, 208 (1998).

9. J. Westwater, D.P. Gosain, S. Tomiya, S. Usui, H. Ruda, J. Vac. Sc. Technol. B 15 (3), 554 (1997).
10. Y.F. Zhang, Y.H. Tang, N. Wang, D.P. Yu, C.S. Lee, I. Bello, S.T. Lee, Appl. Phys. Lett. 72 (15), 1835 (1998).
11. Y. Wu and P. Yang, Chem. Mater. 12, 605 (2000).
12. Y.F. Zhang, Y.H. Tang, N. Wang, C.S. Lee, I. Bello, and S.T. Lee, Phys. Rev. B. 61 (7), 4518 (15 February 2000).
13. E.F. Kukovitsky, S.G. L'vov, and N.A. Sainov, Chem. Phys. Lett. 317, 65 (2000).
14. X.H. Chen, F.M. Deng, X.N. Lu, G.T. Wu, M. Wang, H.S. Yang, and X.B. Zhang, J. Crystal Growth 222, 163 (2001).
15. L T-Nga, K. Hernadi, and L. Forró, Adv. Mat. 13 (2), 148 (2001).
16. S. Motojima, I. Hasegawa, S. Kagiya, M. Momiyama, M. Kawaguchi, and H. Iwanaga, Appl. Phys. Lett. 62 (19), 2322 (10 May 1993).
17. Y.H. Tang, N. Wang, Y.F. Zhang, C.S. Lee, I. Bello, and S.T. Lee, Appl. Phys. Lett. 75 (19), 2921 (1999).
18. X. Duan, Y. Huang, Y. Cui, J. Wang, and C.M. Lieber, Nature 409, 66 (4 January 2001).
19. M.H. Huang, Y. Wu, H. Feick, N. Tran, E. Weber, and P. Yang, Adv. Mat. 13 (2), 113 (16 January 2001).
20. M. He, I. Minus, P. Zhou, S.N. Mohammed, J.B. Halpern, R. Jacobs, W.L. Sarney, L. Salamancha-Riba, and R.D. Vispute, Appl. Phys. Lett. 77 (23), 3731 (4 December 2000).
21. W. Han, S. Fan, Q. Li, and Y. Hu, Science 277 (5330), 1287 (1997).
22. C. –H. Kiang, J. –S. Choi, T. T. Tran, and A. D. Bacher, J. Phys. Chem. B 103, 7449 (1999).
23. N.R.B. Coleman, M.A. Morris, T.R. Spalding, and J.D. Holmes, J. Am. Chem. Soc. 123, 187-188 (2001).
24. P. Scheier, B. Marsen, M. Lonfat, W. –D. Schneider, and K. Sattler, Surf. Sci. 458, 113 (2000).
25. M.K. Sunkara, S. Sharma, R. Miranda, G. Lian, and E.C. Dickey, Appl. Phys. Lett. 79 (10), 1546 (3 September 2001).
26. S. Sharma, M.K. Sunkara, H. Li, and G.D. Lian, Manuscript in preparation to be submitted to the Journal of Applied Physics, (November 2001).
27. Y. Cui, L.J. Lauhon, M.S. Gudiksen, J. Wang, and C.M. Lieber, Appl. Phys. Lett. 78 (15), 2214 (9 April 2001).
28. M. Imaizumi, K. Yamaguchi, K. Okitsu, M. Yamaguchi, T. Hara, T. Ito, I. Konomi, K.M. Jones, and M.M. Al-Jassim, J. Appl. Phys. 88 (11), 6848 (2000).
29. S.V. Hattangady, G.G. Fountain, R.A. Rudder, and R.J. Markunas, J. Vac. Sci. Tech. A. 7, 570 (1989).
30. U. Fantz, Plasma Phys. Control. Fusion 40, 1035 (1998).

Mat. Res. Soc. Symp. Proc. Vol. 703 © 2002 Materials Research Society V3.15

# Catalyst-free Growth of Large Scale $Ga_2O_3$ Nanowires

Ko-wei Chang, Sai-chang Liu, Liang-Yih Chen, Franklin Chau-Nan Hong, and Jih-Jen Wu
Department of Chemical Engineering, National Cheng Kung University
Tainan, Taiwan

## ABSTRACT

Large scale of straight $Ga_2O_3$ nanowires is grown on a fused silica substrate by a simple catalyst-free CVD method using Ga metal and $N_2$ / $H_2O$ reactants. The $Ga_2O_3$ nanowires with diameters ranging from 60 to 150 nm can be as long as several micrometers. XRD and TEM analyses indicate that the $Ga_2O_3$ nanowires exhibit a monoclinic structure. PL characteristic of the $Ga_2O_3$ nanowires shows a UV emission of 375 nm at room temperature.

## INTRODUCTION

The synthesis of nanometer scale one-dimensional materials, for example $\beta$-SiC [1-3], GaN [4,5], $In_2O_3$ [6], and Si [7,8], has received intensive research because of their great potential for fundamental studies of the roles of dimensionality and size in their physical properties as well as for the application to optoelectronic nanodevices [9].

Gallium oxide, $\beta$-$Ga_2O_3$, is a wide band gap compound ( Eg = 4.9 eV), and has potential applications in optoelectronic devices including flat panel displays, solar energy conversion devices, and high temperature stable gas sensors [10,11]. Even more, upon optical excitation through the band gap, $\beta$-$Ga_2O_3$ exhibit up to three different emissions, UV, blue, and green [12-14]. Recently, $\beta$-$Ga_2O_3$ nanowires have been synthesized by an arc discharge method [15], and physical deposition [16]. Here, we present a simple catalyst-free CVD approach for the growth of the straight $\beta$-$Ga_2O_3$ nanowires at a temperature of 800°C.

## EXPERIMENTAL DETAILS

The schematic representation of the $\beta$-$Ga_2O_3$ nanowires growth apparatus is shown in Fig. 1. Typically, an excess amount of molten gallium (Alfa Aesar, 99.99%) was placed on the fused silica substrate A (1x1$cm^2$) that was put in the end of the $Al_2O_3$ boat. The fused silica substrate B (1x1$cm^2$) was put away from substrate A about 3mm. An $Al_2O_3$ plate (4x4$cm^2$) put on the

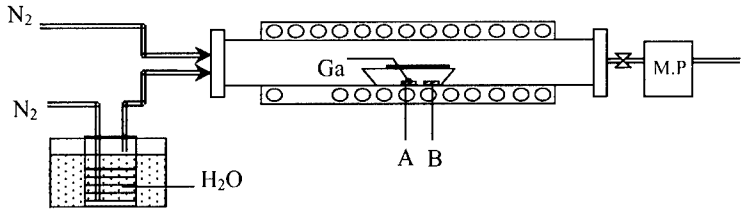


**Fig. 1** Schematic diagram of the high temperature furnace used for the synthesis of the straight $\beta$-$Ga_2O_3$ nanowires.

top of the $Al_2O_3$ boat was used to increase the reactants space time in the $Al_2O_3$ boat. Then the $Al_2O_3$ boat was inserted into the center of a 3 in. diameter furnace. Before the synthesis process, the furnace was evacuated to a base pressure of $1x10^{-2}$ Torr. The temperature of the furnace was increased to 800°C within 1 hr at a constant $N_2$ flow of 200 sccm and a pressure of 500 Torr. As the temperature reached 800°C, the $H_2O$ vapor was carried from an isothermal bath by another $N_2$ flow into the furnace. The synthesis processes were conducted under the following condition: furnace temperature, $H_2O$ vapor rate, $N_2$ flow rate, furnace pressure of 800°C, 3 sccm, 200 sccm and 500 Torr, respectively. After the 6-hr reaction, the furnace was cooled to room temperature and white products were deposited on the fused silica substrate B.

The morphology and size distribution of the products were examined using SEM (Hitachi, S-4200). The crystal structure of the products was analyzed using XRD (Rigaku) and HRTEM (JEOL 2010), which equipped with an EDS. Micro-Raman with 514.5 nm photons was also employed to characterize the products. Photoluminescence studies were conducted with a Hitachi F-4500 fluorescence spectrophotometer with a Xe lamp at room temperature. The excitation wavelengths were 320 nm.

## RESULTS AND DISCUSSION

Figure 2(a) shows a typical SEM image of the products on the fused silica substrate. Large scale of needle-like nanowires was formed with random direction on the fused silica substrate with diameters in the range of 60-150 nm. Fig. 2(b) shows a cross-sectional image of the nanowires, it reveals that the length of the nanowires is about several ten micrometers.

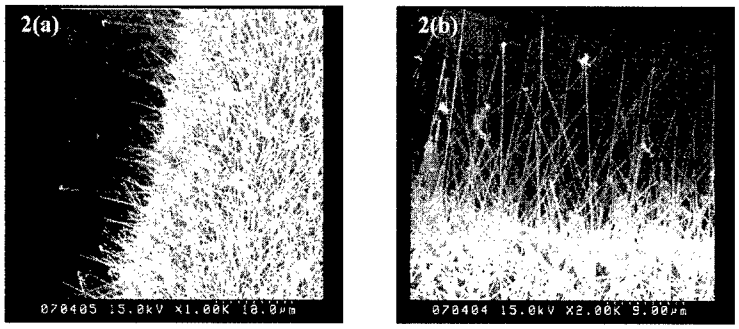


**Fig.2** SEM images of large quantity of $\beta$-$Ga_2O_3$ nanowires grown on fused silica substrates. (a) 45° tilted view, (b) cross-section.

The typical XRD pattern of the nanowires is shown in Fig.3. The diffraction peaks can be indexed to a monoclinic structure of $\beta$-$Ga_2O_3$ with lattice constant a=5.8 Å, =3b. Å,4=1c2 . 2 3 Å, $\beta$= 1 0°3Further structural characterization of the $\beta$-$Ga_2O_3$ nanowires was performed using TEM. As shown in Fig.4 (a), the image reveals that the surfaces of the nanowire are smooth without any step edge and sheathed amorphous phase. Moreover, there is no additional metal particle appeared at the ends of the wires, implying a non-VLS approach for the growth of the straight $\beta$-$Ga_2O_3$ nanowires is achieved. Fig. 4(b) shows a high-resolution TEM image of the individual nanowire. The insert shows a corresponding selected area electron diffraction pattern.

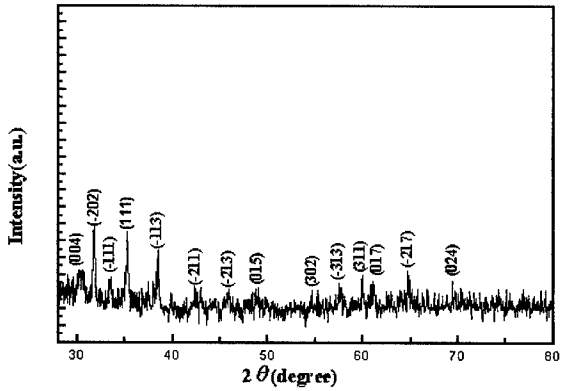


**Fig.3** XRD spectrum of the synthesized product.

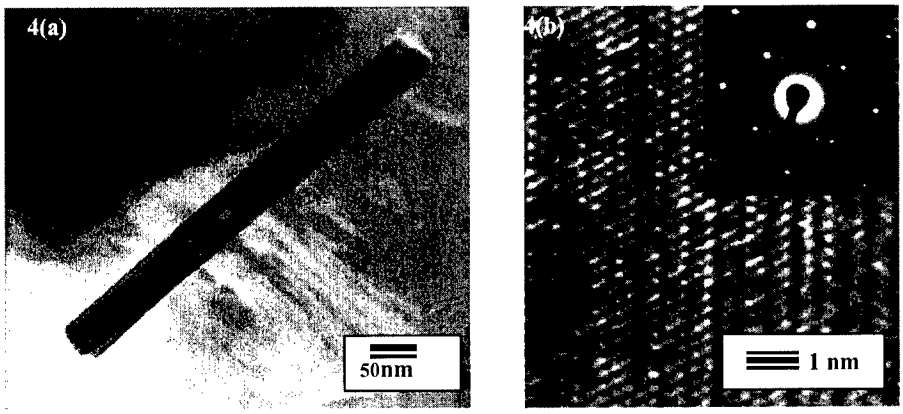


**Fig.4** (a) High resolution TEM image of individual nanowire. (b) Lattice image of the individual nanowire, and a corresponding selected area electron diffraction pattern (inset).

The composition of the Gallium oxide nanowires is confirmed by EDX. As shown in Fig. 5, the EDX spectrum reveals that the nanowires are composed of gallium and oxygen without any additional metal. Quantitative analysis shows that the atomic ratio of Ga :O is about 2:3. The Raman spectrum of the $\beta$-$Ga_2O_3$ nanowires is shown in Fig. 6. The peaks appeared in this spectrum are consistent very well with the FT-Raman spectrum of the $\beta$-$Ga_2O_3$ nanowires produced by arc discharge [15].

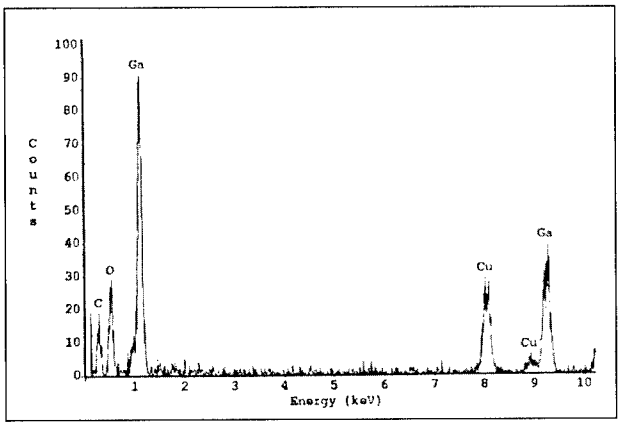


**Fig.5** EDX spectrum of the $\beta$-$Ga_2O_3$ nanowires on a fused silica substrate.

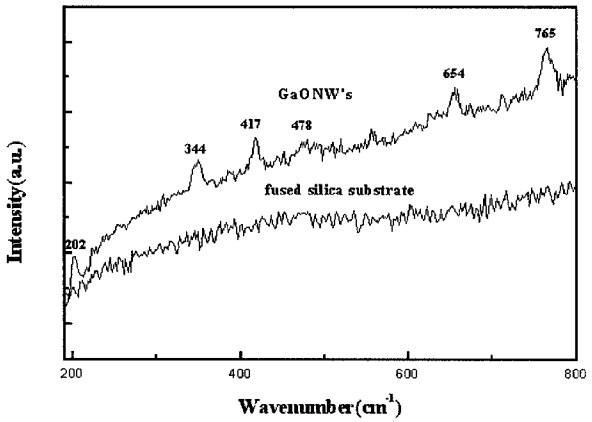


**Fig.6** Raman spectrum of the $\beta$-$Ga_2O_3$ nanowires.

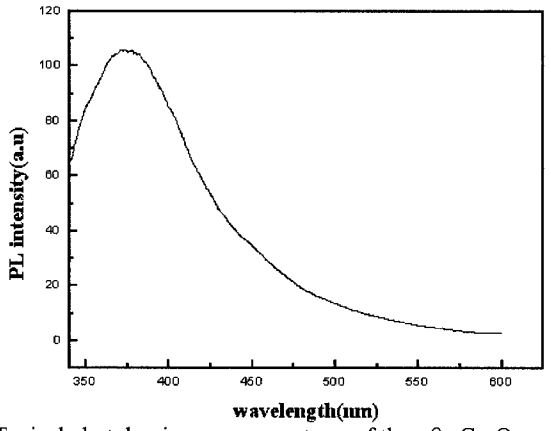


**Fig.7** Typical photoluminescence spectrum of the $\beta$ - $Ga_2O_3$ nanowires.

To examine the optical properties of the $\beta$-$Ga_2O_3$ nanowires, the photoluminescence(PL) measurement was conducted at room temperature. As shown in Fig. 7, the broad PL emission band is mainly located in the UV region with its maximum intensity centered at 375 nm.

## CONCLUSION

Large scale of straight $Ga_2O_3$ nanowires was synthesized on a fused silica substrate by a simple catalyst-free CVD method using Ga metal and $N_2$ / $H_2O$ reactants. The $Ga_2O_3$ nanowires, which have diameters ranging from 60 to 150 nm and lengths of several micrometers, are

identified to be monoclinic $Ga_2O_3$ using XRD. PL emission band centered at 375 nm are observed at room temperature.

## ACKNOWLEDGMENTS

The authors would like to thank Dr. K.H. Chen and Prof. Y. Chen for technical support. The financial support of this work, by the National Council in Taiwan under contracts No. NSC 89-2214-E-006-052, is gratefully acknowledged.

## REFERENCES

1. X.T. Lai, H.Y. Peng, Frederick C.K. Au, N. Wang, I. Bello, C.S. Lee, and S.T. Lee, *Appl. Phys. Lett.* **76**,294 (2000).
2. H. J. Dai, E.W. Wong, Y.Z. Lu, S.S. Fan, C.M. Lieber, *Nature* **375**,769 (1995).
3. W.Q. Han, S.S. Fan, Q.Q. Li, W.J. Liang, B.L. Gu, D.P.Yu, *Chem. Phys. Lett.* **265**,374 (1997).
4. G.S. Cheng, S.H. Chen, X.G.Zhu, Y.Q. Mao, L.D. Zhang, *Materials Science and Engineering* **A286**, 165 (2000).
5. M. He, I. Minus, P. Zhou, S. N. Mohammed, J. B. Halpern, R. Jacobs, W. L. Sarney, L. Salamanca-Riba, R. D. Vispute, *Appl. Phys. Lett.* **77**, 3731 (2000).
6. C.H. Liang, G.W.Meng, Y. Lei, L.D. Zhang, *Adv. Mater.* **13**,No.17, 1330 (2001).
7. A.M.Morales, C.M. Lieber, *Science* **279**,208(1998).
8. Y.F. Zhang, Y.H.Tang, N. Wang, D.P. Yu, C.S.Lee, I. Bello, S.T. Lee, *Appl. Phys. Lett.* **72**,1835 (1998).
9. C. M. Lieber, *Solid State Communication.* **107**, 607 (1998).
10. M. Ogita, N. Saika, Y. Nakanishi, and Y. Hatanaka, *Appl. Surf. Sci.* **142**,188 (1999).
11. D.D. Edwards, T.O. Mason, F. Goutenoir, and K.R. Poeppelmeier, *Appl. Phys. Lett.* **70**,1706 (1997).
12. Laurent Binet, and Didier Gouruer, *J. Phys. Chem Solids,* **59**, 8, 1241 (1998)
13. Blasse, G. and Bril, A., *J. Phys. Chem. Solids*, **31**,707 (1970).
14. Harwig, T., Kellendonk, F., and Slappendel, *S., J.Phys. Chem. Solids*, **39**,675 (1978).
15. Y.H. Lee, Y.C. Choi, W.S. Kim, Y.S. Park. S.M. Lee, D.J. Bae, *Adv. Mater.* **12**,No 10, 746 (2000).
16. H.Z. Zhang, Y.C. Kong, Y.Z. Wang, X. Due, Z.G. Bai, J.J. Wang, D.P. Yu, Y. Ding, Q.L. Hang, S.Q. Feng, *Solid State Communication*, **109**,677(1999).

Mat. Res. Soc. Symp. Proc. Vol. 703 © 2002 Materials Research Society V3.16

# Grain Size Dependent Magnetic Properties of Nanocrystalline $Sm_2Co_{17}$/Cu

L. Bessais[1,2], C. Djéga-Mariadassou[1], J. Zhang[1], V. Lalanne[1], and A. Percheron-Guégan[1]
[1] LCMTR, UPR209, CNRS, 2/8 rue Henri Dunant, B.P. 28 F-94320 Thiais, France.
[2] IUFM de Créteil, F-94861 Bonneuil sur Marne, France.

## ABSTRACT

The evolution of both micro structural and magnetic properties of the $Sm_2Co_{17}$−Cu powder, is studied as a function of soft co-milling time. The average grain size in the range 20 - 50 nm was determined by transmission electron microscopy coupled with x-ray diffraction using the Rietveld method. The particle shape and chemical distribution were investigated by elemental mapping, using wavelength dispersive x-ray analysis with electron microprobe analysis. The coercivity evolution shows that an optimum value of 6 kOe is obtained after 5 h co-milling. The microstructure analysis indicates that both materials are well mixed in nanometer scale. This technique appears as a potential route to synthesize nanocrystalline $Sm_2Co_{17}$ isolated by non-magnetic metal Cu.

## INTRODUCTION

Tremendous interest in the binary rare-earth transition metal (RE-TM) alloys exists because of their superb magnetic properties [1]. Most commercial high strength magnets are made from either the binary compound $SmCo_5$ or the compound $Sm_2Co_{17}$. New core-shell structure as $Sm_2Co_{17}$/Cu presents a great interest in the magnetic recording field. High-density storage material requires small magnetically independent particles above their superparamagnetic critical diameter (lower than 20 nm). Thus the powder coating process seems to be an appropriate way to obtain isolated ferromagnetic particles. Magnetic nanostructures often exhibit distinctly different behavior than their bulk counterparts [2]. The ideal medium for high-density magnetic recording with low noise consists of magnetically isolated nanoscale grains [3,4]. For such small grain high magnetocrystalline anisotropy is needed to avoid the magnetization fluctuation caused by thermal effect and demagnetizing field. In the last few years, Sm-Co system has received considerable attention due to the high anisotropy [5,6]. In order to magnetically isolate the grains different solutions have been proposed such as physical separation of the grains [7] and segregation of a nonmagnetic phase at the grain boundaries [8]. Current studies have investigated Sm-Co particles prepared by annealing Sm-Co thin film on different substrates and under layers.
This study deals with the grain size dependence of magnetic properties of nanocrystalline $Sm_2Co_{17}$ particle soft co-milled with Cu nanoparticules in order to get potential candidates for magnetic recording. The requirements for such goal are monodomain magnetically isolated grains of 20 to about 50 nm with magnetization $\mu_0 M_s \sim 0.5$ T and coercivity $H_C \sim 5$kOe. The special choice of $Sm_2Co_{17}$ results from its semi-hard magnetic character.

## EXPERIMENTAL DETAILS

The intermetallic $Sm_2Co_{17}$ was prepared by mechanical alloying technique. High-purity powders Sm (99.99%) and Co (99.8%), were used. All chemicals were handled inside a glove box under high-purity argon gas. They were carefully weighed, in the stoichiometric ratio 2:17, inside the box to give SmCo mixtures, and placed immediately into stainless steel jars. Next the powders

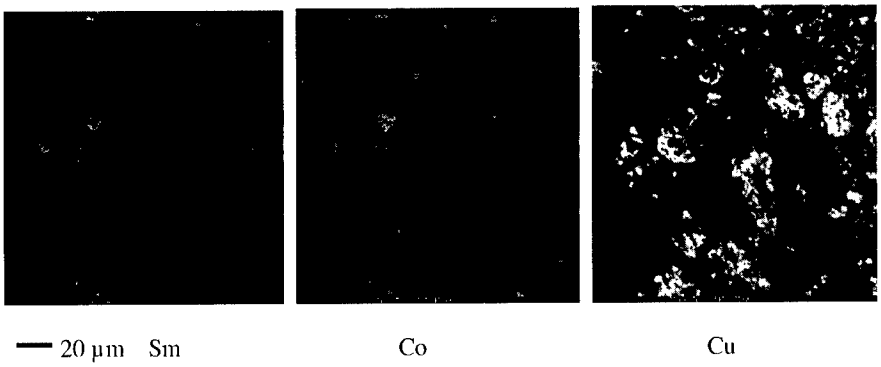


Figure 1: The image of element mapping of $Sm_2Co_{17}$−Cu co-milled 30 min.

were ball-milled in a high energy (power 10) Fritsch P7 planetary ball mill to form an ultra-fine layered microstructure. The mixtures were sealed in hardened steel vial together with five 15 mm diameter steel balls. A ball to powder mass ratio of 15:1 was used with milling time of 5 hours. The as-milled powder were wrapped in Tantalum foil and sealed into silica tubes under a vacuum of $5x10^{-7}$ Torr, then annealed at 800 °C for 30 min. Particle size was reduced by means of hydrogenation-deshydrogenation technique (HD)

$Sm_2Co_{17}$ powder and Cu nanoparticles, produced by cryogenic melting technique [9], were soft co-milled using the same planetary miller but with power 5 and 25 steel balls with diameter 7.3 mm. The milling time was varied from 30 min to 5 hours. The particle shape and the chemical distribution of samples milled 30 min, 2h and 3h were investigated by elemental mapping using wavelength dispersive x-ray analysis by electron microprobe analysis (EPMA).

Bright-field transmission electron micrographs (TEM) were taken using a JEOL 2010 high-resolution microscope operating at 200 kV. TEM sample preparation consisted of encapsulating milled powder in a room-temperature-cured epoxy and microtoming with a diamond knife to a thickness of approximately 100 nm.

The crystal structure was deduced from x-ray-diffraction (XRD) patterns, registered on a Brucker diffractometer with automatic divergence slit (CuKα radiation $\lambda$ = 1.541 78 Å). The grain size of the sample was determined from XRD patterns using Rietveld method.

The magnetic properties of all samples were measured using a vibrating sample magnetometer equipped with a 7 T superconducting magnet in Max-Planck-Institute for Metal Research, Stuttgart, Germany.

## DISCUSSION

After annealing the as-milled (Sm,Co) powders, the Rietveld analysis confirms the existence of hexagonal $Sm_2Co_{17}$ with $P6/mmm$ space group. The diffraction crystallite size (DCS) is around 50 nm. From scanning electron microscopy (SEM) the particle size is evaluated in the range of 20 $\mu$m. One particle should contain a large number of crystallites. Afterwards, the particle size is reduced down to 5 - 10 $\mu$m by HD technique. The final magnetic characteristics are obtained by further soft co-milling with Cu: (i) reduction of crystallite size at most down to 20 nm (ii)

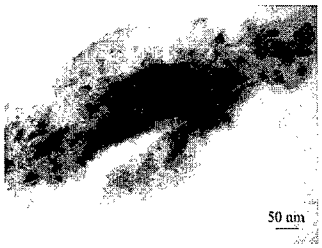


Figure 2: Transmission electron micrograph of $Sm_2Co_{17}-Cu$ co-milled 2 h.

separation and coating of $Sm_2Co_{17}$ crystallite.
The EPMA images for samples with Cu co-milled half an hour are shown, as an example, in figure 1. It can be deduced that the particle size of $Sm_2Co_{17}$ reduces monotonously from about 10 $\mu$m for sample milled 30 min to 1 $\mu$m for samples milled 2 h. For the sample milled 2 h, the $Sm_2Co_{17}$ particles are homogeneously separated by Cu particles. Figure 2 shows the TEM micrograph for the sample milled 2 hours. The TEM investigation shows that the grain size is in the range of 10-20 nm. The EDX analysis carried out by TEM didnot show neither a region of pure $Sm_2Co_{17}$ nor pure Cu. This indicates that the materials are well mixed in nanometer scale. The XRD patterns of all samples can be indexed by hexagonal $Sm_2Co_{17}$ with additional cubic Cu phase. After soft co-milling with Cu nanoparticles, $Sm_2Co_{17}$ powder keeps hexagonal $P6/mmm$ structure but with much broader reflections. The DCS and the microstrain rate have been determined from x-ray diffraction patterns using Rietveld method. The obtained $Sm_2Co_{17}$ DCS is plotted as a function of milling time and shown in figure 3. The grain size of $Sm_2Co_{17}$ decreases monotonously with milling time whereas the grain size of Cu remains constant. One can notice from figure 3 a slow decrease of $Sm_2Co_{17}$ grain size from 2 h to 5 h of co-milling time. This behavior means that it is possible to reduce the DCS to within 20 nm a value required for the high-density magnetic recording.

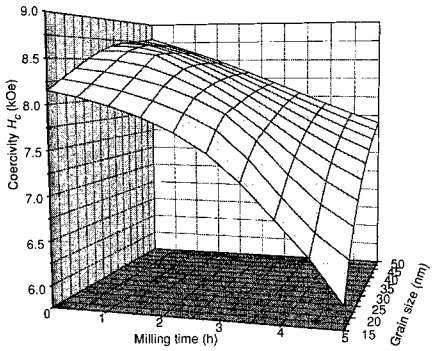


Figure 3: The dependence of room temperature coercivity ($H_C$) on $Sm_2Co_{17}$ grain size and co-milling time.

The room temperature hysteresis loop for sample before co-milling and after 5 hours co-milling are comparatively shown in figure 4. The room temperature coercivity ($H_C$) and remanence ratio ($M_r/M_s$) as a function of co-milling time is illustrated in figure 5. It can be seen that $M_r/M_s$ decreases rapidly from the 0.58 for the unmilled powder down to 0.52 after only half an hour milling. Then, with milling time, it decreases slightly to 0.5 for 5 h milled powder. On the contrary, the coercivity keeps almost constant at the beginning of milling. After 1 h milling $H_C$ decreases monotonously from 8.6 kOe to 6.0 kOe for sample milled 5 hours. This value is an optimum value for magnetic recording application. The powder after 5 hours co-milling possesses suitable magnetic and microstructure properties (magnetically separated grains) for high-density recording application.

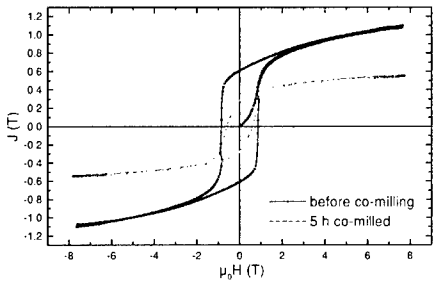


Figure 4: Hysteresis loops of co-milled $Sm_2Co_{17}-Cu$ powder.

From figure 3 it can be seen that the coercivity remains constant as the grain size decreases from 50 nm before co-milling to 30 nm after 1 h co-milling. $H_C$ decreases rapidly with further decreasing grain size. Two competing effects can explain this: the co-milling refines the grain size and reduces the coercivity. However, meanwhile the co-milling breaks the exchange coupling between the grains (which is proved by the reduction of $M_r/M_s$), it tends to enhance the coercivity.

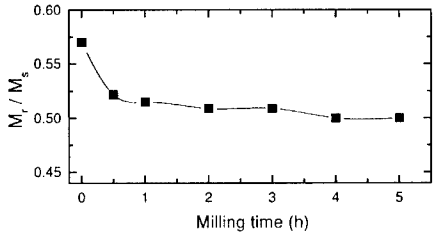


Figure 5: The dependence of the remanence ratio $M_r/M_s$ on co-milling time.

After 1 h milling the exchange coupling between grains is completely broken, further reducing grain size, from 30 nm to 10 nm, leads to decreasing the coercivity. For a fine particle system, the decrease in $H_C$ with decreasing grain size is due to thermal effect. Hence, the temperature dependence of the coercivity should obey the $H_C \propto T^{1/2}$ law. The coercivity of sample milled 5 hours at different temperature are obtained and plotted as a function of $T^{1/2}$ in figure 6. It shows a linear relation between $H_C$ and $T^{1/2}$, and indicates that the reduction of coercivity for small grain size (see figure 4) is a consequence of thermal effect, and 15 nm is near the superparamagnetic limit for $Sm_2Co_{17}$ powder.

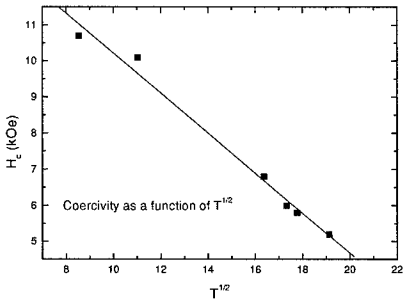


Figure 6: The coercivity for 5 h milled sample as a function of $T^{1/2}$

## CONCLUSION

* After soft co-milling with Cu nanoparticles, nanocrystalline Sm-Co powder remains hexagonal with $P6/mmm$ structure.
* The diffraction crystallite size of $Sm_2Co_{17}$ decreases from 50 nm before co-milling down to 15 nm after 5 h co-milling.
* TEM shows that the grain size is in the range of 10 - 20 nm after 5 h co-milling. The material is well mixed in nanometric scale, consistent with the DCS study.
* The coercivity decreases to 6.0 kOe after 5 h co-milling.
* By co-milling with Cu nanoparticles, the microstructure as well as the magnetic properties of $Sm_2Co_{17}-Cu$ powder can be controlled by milling conditions. Thus, this technique is a potential way to synthesize nanocomposite $Sm_2Co_{17}-Cu$ particles isolated by non-magnetic metal Cu with suitable magnetic properties and microstructure for high-density recording.

## ACKNOWLEDGMENTS

This work is supported by the CNRS under the Programme Matériaux n° 236. J. X. Zhang wishes to thank Max-Planck-Institute für Metallforschung for use of its facilities.

## REFERENCES


1. K.H.J. Buschow, *Rep. Prog. Phys.* **54,** 1123 (1991).
2. D. L. Leslie-Pelecky and R. D. Rieke, *Chem. Matter.* **8,** 1770 (1996).
3. M. H. Kryder, M. Messner, and L. R. Carley, *J. Appl. Phys.* **79,** 4485 (1996).
4. D. N. Lambeth, E. M. T. Velu, G. H. Bellesis, L. L. Lee, and D. E. Laughlin, *J. Appl. Phys.* **79,** 4496 (1996).
5. S. A. Romero, D. R. Cornejo, F. M. Rhen, A. C. Neiva, M. H. Tabacniks, and F. P. Missell, *J. Appl. Phys.* **87,** 6965 (2000).
6. S. Takei, Y. Otagri, A. Morisaka, and M. Matsumoto, *J. Appl. Phys.* **85,** 6145 (1999).
7. T. Yamashita, L. T. Chan, T. Fujiwara, and T. Chen, *IEEE Trans. Magn.* **27,** 4727 (1991).
8. G Xiao, and L. C. Chien, *J. Appl. Phys.* **63,** 4252 (1988).
9. Y. Champion, and J. Bigot, *Scripta Materialia* **35,** 517 (1996).

Mat. Res. Soc. Symp. Proc. Vol. 703 © 2002 Materials Research Society V3.17

# Multi-functionalization Of Silicon By Nanoparticles Through "Plug and Play" Approach

K. Prabhakaran * , K.V.P.M. Shafi[+], A. Ulman[+] and T. Ogino
Nippon Telegraph and Telephone Corporation (NTT)
Basic Research Laboratories, 3-1 Morinosato Wakamiya, Atsugi, Japan 243-0198
[+] Polytechnic University, NY, USA
* prab@will.brl.ntt.co.jp, Tel: 81 462 40 3474, Fax: 81 462 40 4718

## ABSTRACT

In this paper, we demonstrate a "Plug and Play" approach, whereby externally synthesized nanoparticles of desired functions and size are incorporated into the semiconductor, followed by the manipulation of surface chemical bonds in order to achieve multiple functionality. Sonochemically synthesised $Fe_2O_3$ nanoparticles were introduced onto device quality Si wafers. On annealing the particle-treated Si wafer in ultra high vacuum, oxygen changes the bonding partner from Fe to Si and desorb as SiO at ~ 760°C, leading to the formation of uniform sized Fe nanoparticles ( size ~6-8 nm) on the surface and the sample shows ferromagnetic behaviour. More importantly, the particle treated Si exhibits light emission at wavelengths 1.57, 1.61 and 1.65 microns (full width at half maximum ~ 20 meV). Emission in this wavelength range is crucial for optical communications and is highly desired from a Si based material. Further, oxidation of this material leads to the formation of a selective capping layer of $SiO_2$. Thus, by manipulating the surface chemical bonds, we are able to introduce optical, magnetic, metallic and insulating functions to Si. Additionally, the particles exhibit self-assembly on a patterned Si surface. We believe that this approach is universal and the material developed here is compatible with the planar Si technology, bringing us closer to realization of Si based monolithic electronics.

## INTRODUCTION

Realization of nanoscale devices depends crucially on the successful fabrication of nanostructures and their functionalization. Techniques such as, lithography, self-organization, atom manipulation using scanning tunneling microscope tip, chemical bond manipulation, control and design of surface atomic steps, or a combination of some of these, are employed to achieve these goals [1-4]. However, there are major problems encountered in these approaches which limit the advancement in this field. They are mainly associated with the poor controllability of the size, positioning as well as the functionality of the nanostructures. In order to ovecome these problems, we propose a "Plug and Play" approach, where externally synthesized nanoparticles of desired functions and size are incorporated into the semiconductor, followed by the manipulation of surface chemical bonds. This would enable fabrication of tailor-made structures on the whole wafer surface. In this paper, we demonstrate this idea, by taking the example of the interaction of $Fe_2O_3$ nanoparticles with device quality Si, Ge wafers and graphite.

## EXPERIMENTAL

Sonochemically synthesised $Fe_2O_3$ nanoparticles (spherical shape, size ~6-8 nm) [5] were introduced onto device quality Si wafers, from an ethanol suspension, kept in ultrasonic bath for a period of 30 min. They are rinsed in running water and dried with nitrogen gas. Si wafers are prior cleaned chemically. These samples are introduced into ultrahigh vacuum chamber (UHV) and degassed at around 100°C for a couple of hours. The samples are heated to a particular temperature and kept for 15-20 min. and the photoemission measurements are performed at room temperature. For achieving complete reduction, final anneal was performed at around 850°C for 3 min. In some cases, an ultrathin layer of Si was deposited onto this sample at around 500°C followed by anneal at 550°C for about 10-15 hrs. The samples are examined by a variety of other techniques, such as atomic force microscopy, photoluminescence, magnetic measurements, mapping of Auger signals, after taking it out of the chamber. The nature of the surface species was characterised *in-situ* by photoelectron spectroscopy. Samples were transferred to the molecular beam epitaxy (MBE) chamber where evaporation of Si was carried out by using an electron beam. The samples were examined, outside the chamber, by a variety of technique. Additionally, we have examined the surface transformation by employing highly surface sensitive synchrotron radiation photoelectron spectroscopy and the results will be published elsewhere 6

## RESULTS AND DISCUSSION

Figure 1 shows an AFM image of a planar Si(111) which was treated with the nanoparticles and subsequently annealed in UHV at 850°C. As can be seen, the particles are of uniform size and nucleate at step edges and annealing results in the etching of Si as SiO species and leads to the reduction of the iron oxide to elemental Fe. The XPS results shown in figure 2 clearly indicate the occurrence of the reaction,

$$Fe_2O_3 + 3\,Si \Rightarrow 2\,Fe + 3\,SiO$$

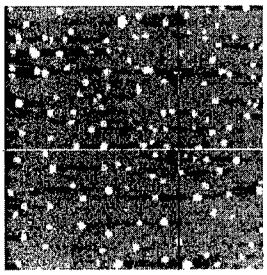

**Figure 1**

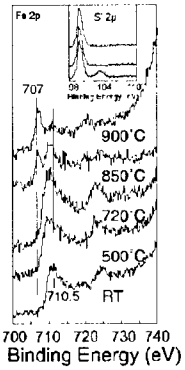


**Figure 2**

Figure 1 AFM image from the nanoparticle treated Si sample. The dot like structures are nanomagnets of Fe.

Figure 2 shows the thermal transformation of iron oxide particles by reaction with substrate silicon atoms

At these temperature and pressure the SiO is volatile and desorbs immediately, driving the reaction to completion, as is evident from x-ray photoelectron spectroscopy (Figure 2). The chemical shift in Fe $2p_{3/2}$ core level (3.5 eV) in the annealed sample, and the disappearance of the signal due to oxygen in Si 2p as well as O 1s regions, unequivocally establish the occurrence of this reaction. In essence, this reaction is similar to the reduction of iron oxide by carbon in the preparation of steel at ~1500°C. However, in the case of a surface reaction, the temperature is reduced due to desorption of SiO species. Interestingly, we have observed complete reduction of $Fe_2O_3$ nanoparticles to Fe at 450°C when deposited on Ge surfaces. Thus, the temperatures in which SiO and GeO species desorb dictate the reduction temperature in the Si and Ge cases, respectively.

Figure 3 depicts the photoluminescence (PL) spectrum recorded from this sample, showing sharp emission at three wavelengths—excited by He-Ne laser—1.57, 1.61 and 1.65 μm. This is the first report on multiple and narrow width light emission from a well-defined and device compatible Si based material that is of great significance for fiber optics communications [7]. Although weak, there is emission even at room temperature (RT). The emission at 1.57 □m originates from traces of the semiconducting silicide, β-$FeSi_2$, which is formed by the reaction of $Fe^o$ and $Si^o$. The β-$FeSi_2$, a covalent and environmentally friendly semiconductor possessing a direct bandgap (Eg ~ 0.8 eV), has been a topic of intense study recently as a candidate for a Si-based light emitter. [8-11]. They employed the method of implanting Fe ions into Si wafers and formed precipitates of iron silicide of various sizes. [11]

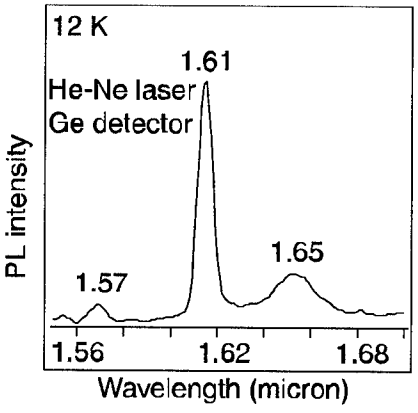


Figure 3

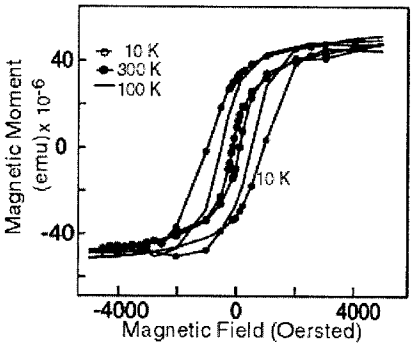


Figure 4

Figure 3. PL spectrum recorded from the nanoparticle treated Si sample at 12 K. Figure 4. Magnetization data measured on the nanoparticle treated Si sample at various temperatures, clearly showing the ferromagnetic behaviour. Hysteresis loop opens at low temperature

The emission intensity could be further increased by depositing a thin overlayer of Si, using molecular beam epitaxy (MBE) mode, followed by annealing at 530°C for several hours. The reflection high-energy electron diffraction monitored *in situ* during the Si MBE and subsequent annealing provides support for this reaction. The emission intensity decreased on raising the sample temperature, suggesting that the process is thermally activated, and indicating that the origin is exciton related. The observation of features at similar energies in the absorption spectrum from these samples supports this view. However, further measurements are required to fully understand the emission mechanism from this novel material. We have fabricated a series of samples by a variety of methods (such as Fe deposited or Fe implanted into Si, and nanoparticle treated Ge), examined the PL spectra, and found that none other than the nanoparticle-treated Si exhibits this behaviour. Secondary ion mass spectroscopy (SIMS) failed to detect any Fe diffused into the bulk.

The Si wafer with the as-incorporated amorphous $Fe_2O_3$ particles exhibits superparamagnetic behaviour, which is characteristic of amorphous nanoparticles. However, after annealing, the samples show soft ferromagnetic property as shown in Figure 4. This behaviour is attributed to the fact that the oxide particles are transformed to crystalline nanoparticles of Fe. The magnetic measurements were performed using a superconducting quantum interference device (SQUID). It was observed that the coercivity increases when the sample temperature is lowered to 10 K. This type of material might have tremendous impact in the area of magnetic semiconductors or spintronics and memory devices [12,13] . We have further introduced insulating features to this material by oxidation, which results in the preferential formation of an $SiO_2$ capping layer, thus preserving the light emitting and magnetic properties. The nanoparticles exhibit self-assembly on patterned Si wafers. Figure 5 shows that the periphery of the dot and trench patterns is decorated by uniform sized nanoparticles. This is due to their preferential nucleation on reactive centres in the step-bunched regions. Element mapping of the SEM image performed micro-Auger mapping indicates that these structures consist predominantly of elemental Fe.

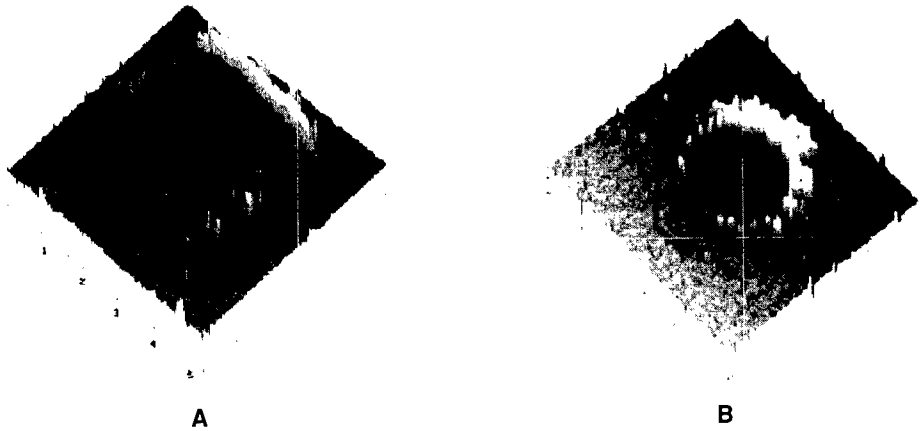


Figure 5 Self-organization of Fe nanoparticles formed by the reduction of iron oxide particles on patterned silicon substrates. A and B are dot and trench patterns

In conclusion, we have demonstrated, for the first time, that manipulating the properties of amorphous $Fe_2O_3$ nanoparticles on Si results in multiple light emission (narrow fwhm) and multiple functionality (magnetic, metallic, semiconducting, insulating, and optical) and clearly show an "all in one" or "all from one" approach. The amorphous $Fe_2O_3$ nanoparticle changed their properties from superparamagnetic to soft ferromagnetic by their reduction to metallic Fe. The subsequent reaction of $Fe^0$ with $Si^0$ results in the formation of $\beta$-$FeSi_2$, a semiconductor that emits light in wavelengths that are critical for fiber optics communication. The spatial distribution of the nanoparticles could be controlled by proper patterning of the Si wafer. While ion beam synthesis, which introduces a large number of defects in the Si substrate, this "plug and play" approach is compatible with the existing planar Si technology, and therefore is a promising candidate for realising monolithic integration of optical and magnetic features along with integrated circuits.

● Corresponding author Tel: 81 46 240 3474; Fax: 81 46 240 4718

**ACKNOWLEDGEMENTS**

We thank all the members of the surface science group in NTT Basic Research Laboratories for the help and support for carrying out this work. We also thank Drs. Tsubaki and Yamauchi for help with magnetic and PL measurements respectively.

## REFERENCES

1.Issues in Nanotechnology, Cover page article, *Science* **290**, 1524 (2000).

2.T. Ogino, H. Hibino, Y. Homma, Y. Kobayashi, K. Prabhakaran, K. Sumitomo, H. Omi, *Acc. Chem. Res.* **32**, 447 (1999).

3.D. E. Gittins, D. Bethell, D. J. Schiffrin, R. J. Nichols, *Nature* **408**, 67 (2000)

4. K. Prabhakaran,

5. K.V.P.M. Shafi, Y. Koltypin, A. Gedanken, R. Prosorov, J. Balogh, J. Lendvai, I. Felner, *J. Phys. Chem.* **B 101**, 6409 (1997).

6. K. Prabhakaran, Y. Watanabe, K.G. Nath, Y. Homma, K.V.P.M. Shafi, Y. Homma and T. Ogino, Proc. Of Meeting of Silicide Semiconductors, Osaka, Jpn. Soc. For Appl. Phys. 2001.

7. L. T. Canham, in *Frontiers of Nano-Optoelectronic Systems*, L. Pavesi and E. Buzaneva, Eds., Kluwer Academic: Dordrecht, 2000, pp. 85-98.

8. D. Leong, M. Harry, K. J. Reeson, K. P. Homewood, *Nature* **387**, 686 (1997).

9 .T. Suemasu, Y Iikura, T. Fujii, K. Takakura, N. Hiroi, and F. Hasagawa, *Jpn. J. Appl. Phys.* **L620**, 38 (1999)

10. T. Suemasu, Y. Negishi, K. Takakura, and F. Hasegawa, *Jpn. J. Appl. Phys.* **39**, L1013 (2000).

11. K, Lefki, P. Muret, N, Cherief ard R. C. Cinti, *J. Appl, Phys.* **69**, 352, (1991).

12. K. S. Suslick *Science* **247**, 1439 (1990); E. B. Flint, K. S. Suslick, *Science* **253**, 1397 (1991).

13. J. Shi, S. Gider, K. Babcock, D. D.. Awschalom, *Science* **271**, 937 (1996).

Mat. Res. Soc. Symp. Proc. Vol. 703 © 2002 Materials Research Society V3.21

# Sol-Gel Processing of Low Dielectric Constant Nanoporous Silica Thin Films

Deok-Yang Kim[1], Henry Du[1], Suhas Bhandarkar[2], and David W. Johnson, Jr.[3]
[1]Department of Chemical, Biochemical, and Materials Engineering, Stevens Institute of Technology, Hoboken, NJ 07030, U.S.A.
[2]Bell Laboratories, Lucent Technologies, Murray Hill, NJ 07974, U.S.A.
[3]Agere Systems, Murray Hill, NJ 07974, U.S.A.

## ABSTRACT

Tetramethyl ammonium silicate (TMAS) is known as a structuring agent in zeolite synthesis. We report its first use to prepare porous silica films for low k dielectric applications in microelectronics. A solution of TMAS 18.7 wt. % was spin coated on silicon substrates with a 3000 Å thick thermal oxide. The spin coated films were subsequently heat-treated at 450°C to obtain porous silica. The use of TMAS solution without gelation led to films of only moderate porosity value of 10%. The addition of methyl lactate, a gelling agent, significantly increased film porosity and improved the pore size distribution. For example, 50% porosity and uniform pore size distribution (average pore size ~ 40 Å) has been achieved. Dielectric constants (k) of our porous films are as low as 2.5.

## INTRODUCTION

There has been intensive research on low dielectric constant materials for metal-insulator interconnects in integrated circuits. A variety of materials have been explored so far, including polymers [1], inorganic-organic hybrid [2] and porous silica [3-6]. Among those candidates, porous silica is the most promising because it has high tunability of porosity and thermal stability. Tetramethylammonium (TMA) cation salts have been used as common structure-directing agents in the synthesis of zeolite [7]. This quartenary ammonium ion is known to form hydrates in aqueous solution. Water associated with the TMA ion is partially displaced by silicate in the synthesis of zeolite to form precursors for nucleation centers, allowing for the structure-direction to occur. TMA ions have strong affinity to silicate ions, which allows effective screening and dispersing of silicate ions in the solution. Nuclear magnetic resonance study of tetramethyl ammonium silicate (TMAS) has shown that it forms oligomers at high pH [8]. The sol-gel chemistry of TMAS system is much simpler than that of typical TEOS- based recipe because it does not need to use co-solvent (i.e. methanol). The unique feature of TMAS sol-gel process is kinetically controllable gelation with hydrolyzable ester [9]. The addition of ester reduces the pH value down to a level below 10 where gelation takes place in this system. Introduction of positive charge dissipates the space charge on silicate and allows the silica monomers to coalesce under the influence of attractive van der Waals forces. Spin coating has been used to deposit the porous thin silica films on desired substrates. This technique can be easily adapted to a manufacturable process.

## EXPERIMENTS

An aqueous solution consisting of 18.7 wt.% TMAS in water (Aldrich, 99.99+% purity, LOT 06301HU) was used. The ratio between TMA cation to Si atom is 1:2. Silicon

wafers with a 3,000 A thermal oxide were used as substrates for spin coating using a Model PC101 spinner by Headway Research, Inc. All the wafers were used as-received without any pretreatment process. Approximately 2 mL of TMAS liquid was dispensed onto the stationary substrate, which was then accelerated to the process speed of interest. The deposition was carried out at spin speeds ranging from 2,000 to 7,000 rpm for 30s during which time most of the water evaporated. Partially gelled silica films were obtained using a similar method. In addition, 0.8 equivalent mol ester (i.e. methyl lactate, 98 wt.%, Aldrich) was introduced to the solution before spin coating. Spin coating did not start until the solution reached the about-to-gel point, approximately 6/7 of its gelation time. After spin deposition, the wafers were heat-treated in a tube furnace at 450 °C for an hour in air to remove any residual solvent and carbon contents.

The thickness and refractive index of the heat-treated porous silica films were measured by a SENTECH SE801 spectroscopic ellipsometer. The ellipsometric data from a 350nm to 800nm was fit to a Cauchy dispersion model. The thickness values of the films were further measured using profilometry. Selected samples were also examined using a LEO 1530 field emission scanning electron microscope (FESEM) in a cross-section geometry. Powder samples of gelled TMAS were prepared for BET measurement. The powder was gelled with methyl lactate and dried quickly using air sprayer on hot plate so as to yield nearly the same evaporation condition as in spin coating. A nitrogen isotherm at 77 K on the powder was conducted with Micromeritics ASAP 2010. A Pt-silica-Pt parallel-plate capacitor structure was fabricated for dielectric measurements. The top and bottom Pt electrodes were electron-beam evaporated and sputter deposited, respectively. Top electrode area was 1.13 $mm^2$. The dielectric constant of the porous films was calculated based on their capacitance values at 1 MHz.

## RESULTS AND DISCUSSION

Fig.1 shows the dependence of thickness on spin speed for TMAS films as well as partially gelled TMAS films. As expected, the thickness of both types of silica films decreases as the spin speed increases due to increased shear forces exerted on the liquid before drying. The partially gelled films are three to four times thicker as compared to the films without the gelling agent. These results can be understood as follows. At the about-to-gel point, the solution containing gelling agent experiences an abrupt increase in viscosity, which better withstands the centrifugal force of spin coating. According to Bornside's model [10], the thickness of spin coated film is roughly proportional to one-third power of viscosity of the fluid used. For example, a tripled film thickness means that the viscosity is increased by $3^3 = 81$ times. This dramatic increase in the viscosity of solution can only be attributed to the process of gelation rather than the shear thickening of the fluid. Shear thickening can at most double the viscosity of the original solution.

Illustrated in Fig. 2 is refractive index versus the spin speed for TMAS only films and partially gelled TMAS films. The refractive index is not a strong function of the spin speed, indicating the insensitivity of the film porosity to the spin speed. The refractive index of the partially gelled films is significantly lower than that of the TMAS films without the gelling agent.

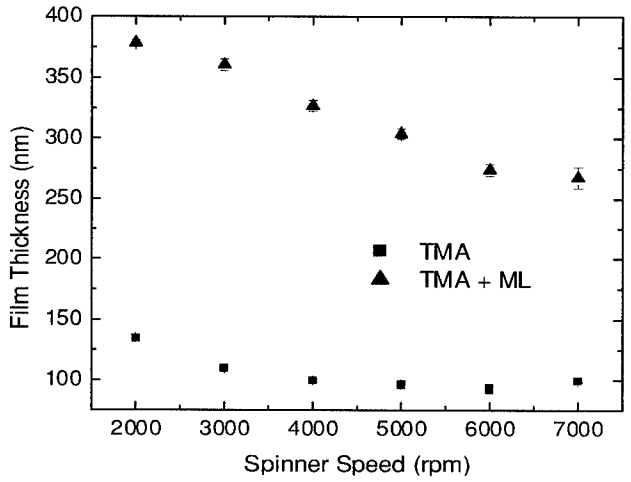


**Figure 1.** Thickness data of TMAS films vs spinner speed

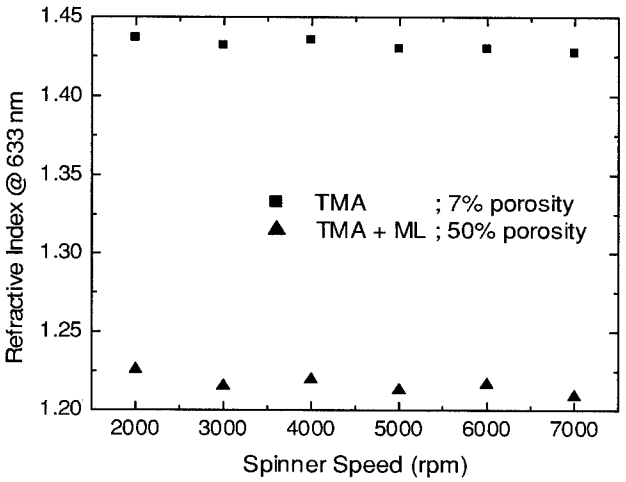


**Figure 2.** Refractive index data of TMAS films vs spinner speed

Bruggemann effective medium layer model [11] based on refractive index data was used to estimate the porosity of these films. Fig. 3 (a) describes the assumption this model makes. It is assumed that the film has small spherical inclusions (in this case, pores filled with air) in silica with a different index of refraction, $n_i$. The fraction of inclusion can thus be calculated using the equation in Fig. 3 (a). Fig. 3 (b) shows that the theoretically calculated curve based on this model fits well with the experimental data of one of the samples. This technique allows us to evaluate the porosity of films indirectly with ease even though we can not get pore size or pore distribution information. TMAS films without gelling agent contain less than 10% porosity whereas partially gelled films have 50% porosity on average. As gelation takes place, the silica network starts cross-linking and pore structure begins to evolve.

Enough time was allowed for partial gelation till about-to-gel point before significant evaporation occurred during spin coating. Therefore, when evaporation takes place in spin coating of these films, the already formed silica network would resist collapsing and pores created during gelation would remain intact. This mechanism is responsible for the higher porosity of partially gelled films. Shown in Fig. 4 is a cross sectional SEM micrograph, which gives the general morphological appearance of partially gelled porous silica thin film. In contrast, TMAS without gelling agent would experience quick evaporation of solvent and precipitate relatively dense silicates on the substrate. Further cross section SEM analysis revealed the existence of cluster-like precipitates in TMA only silicate films.

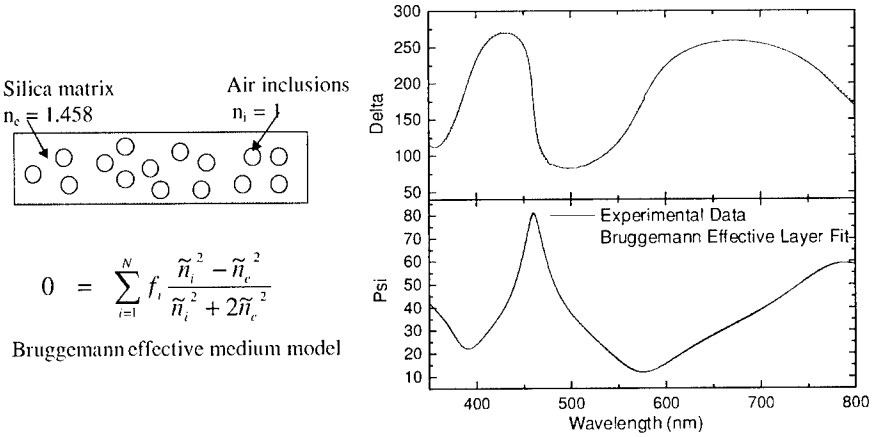


**Figure 3.** (a) Schematic diagram of Bruggemann effective layer model (b) two curves fitting of Psi and Delta values over wavelength range of 350 - 800 nm

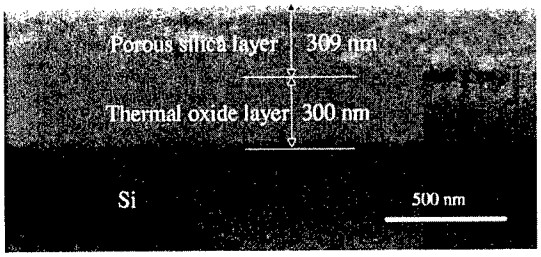


**Figure 4.** Cross sectional SEM of a partially gelled silica film at 4,000 rpm spin

TMAS gel with gelling agent shows a typical adsorption and desorption curve of mesoporous materials (type IV), based on the BET analysis of the corresponding powder samples shown in Fig. 5. The specific surface area of the porous silica is about 790 $m^2/g$. A BJH desorption curve study shows a very narrow pore size distribution of average diameter of ~ 40 Å for this material. Low angle x-ray diffraction experiments did not reveal any evidence of ordered pore structures. Silica films from TMAS with gelling agent are therefore considered to contain randomly distributed ~ 40 Å size pores.

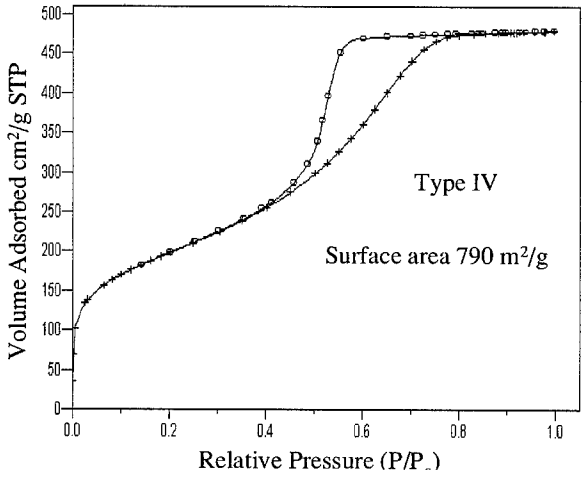


**Figure 5.** $N_2$ isotherm curve by BET measurement

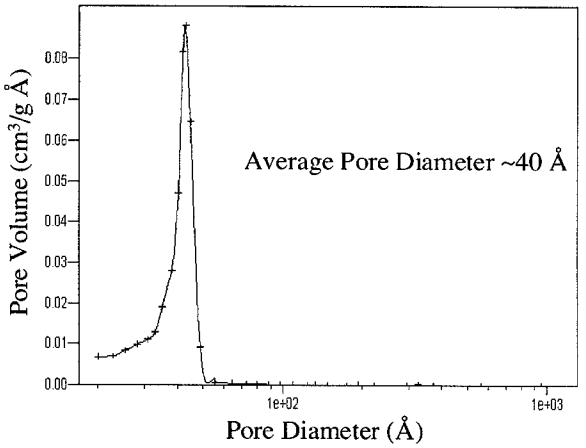


**Figure 6.** BJH desorption curve (pore size distribution) by BET measurement

Accurate dielectric measurements of silica films can be challenging because they are terminated with hydroxyl (-OH) groups and thus highly hydrophilic. Any moisture uptake in the porous thin films would significantly affect the measured values of the dielectric constants. Extra care was therefore taken by immediately storing the porous silica films in a dry nitrogen ambient after the heat treatment, Pt metallization and capacitance measurement. The lowest dielectric constant on 50 % porous TMAS films was 2.5 at 1 MHz.

## CONCLUSION

Two different types of TMAS thin films were fabricated via sol-gel processing. Partially gelled TMAS films have high porosity (~ 50%) and narrow pore size distribution of small pores (~40 Å). These films would be good candidates for low k application with further hydrophobic treatment as well as for host materials of larger pore arrays from surfactants.

## ACKNOWLEDGEMENT

This research is funded by the Stevens-Lucent Cooperative Research Program. The authors thank Dr. Glen Kowach of Agere systems for insightful discussions.

## REFERENCES

[1] T.M. Lu and J.A. Mopre, *MRS Bull.*, **22**, 28 (1997).
[2] A. Fidalgo and L. Ilhargo, *J. Sol-Gel Sci. & Tech.*, **13**, 433 (1998).
[3] S. Baskaran, J. Liu, K. Domansky, N. Kohler, X. Li, C. Coyle, G.E. Fryxell, S. Thevuthasan, and R.E. Williford, *Adv. Mater.*, **12**, 291 (2000).
[4] C.J. Hawker, J.L. Hedrick, R.D. Miller, and Willli Volksen, *MRS Bull.*, **25**, 54 (2000).
[5] S. Seraji, Y. Wu, M. Forbess, S.J. Limmer, T. Chou, and G. Cao, *Adv. Mater.*, **12** 1695 (2000).
[6] M. Jo, H. Park, D. Kim, S. Hyun, S. Choi, and J. Paik, *J. Appl. Phys.*, **82**, 1299 (1997).
[7]M.E. Davis and R.F. Lobo, *Chem. Mater.*, **4**, 756 (1992).
[8] R.K. Harris and C.T.G. Knight, *J. Mol. Struc.*, **78**, 273 (1982).
[9] J.B. MacChesney, D.W. Johnson Jr., S. Bhandarkar, M.P. Bohrer, J.W. Fleming, E.M. Monberg, and D.J. Trevor, *J. Non-Cryst. Sol.*, **226** , 232 (1998).
[10] D.E. Bornside, C.W. Macosko, and L.E. Scriven, *J. Electrochem. Soc.*, **138**, 317 (1991).
[11] D.A.G. Bruggemann, *Ann. Phys.*, **24**, 636 (1935)

Mat. Res. Soc. Symp. Proc. Vol. 703 © 2002 Materials Research Society V3.24

# Stress and Hardness of $CrN_x$ films

G.C.A.M.Janssen, J.-D.Kamminga[1], W.G.M.Sloof
Department of Material Science and Technology, Delft University of Technology, the Netherlands,
e-mail: g.c.a.m.janssen@tnw.tudelft.nl;
[1]Netherlands Institute for Metals Research, Delft, the Netherlands

## ABSTRACT

Chromium nitride films $CrN_x$ with x ranging form 0 to 1 were deposited by reactive PVD. Both stress and hardness in the films are a function of the composition. The growth stress and hardness for the majority of the films can be related through the Hall Petch relation. It is shown that the hardest films fall outside this relation. It is also shown that the hardest films are nanocrystalline. It is argued that the hardness of these films is a consequence of the nanocrystallinity of these films.

## INTRODUCTION

Chromium nitride coatings are succesfully applied in tribological systems where corrosion, oxidation and intense wear are expected [1]. Hardness of the coating is one of the key parameters to the succesful performance of the coating. Wear and corrosion resistant coatings are preferably in a state of compressive stress. The stress in the films at room temperature is the sum of the tensile growth stress generated at the column boundaries, the compressive growth stress generated by the ion bombardment on the growing film, and the thermal stress.

Typically deposition conditions are chosen such that the compressive stress from the ion bombardment is larger than the tensile stress from the columnar growth, leading to corrosion and wear resistant films. In the work reported in this paper however conditions were chosen such that the tensile stress is still visible. It turns out that growth stress and hardness can be related through the Hall-Petch relation for most $CrN_x$ films. The hardest films obtained in this work fall outside that relation, indicating that the deformation mechanism for these films is different.

## EXPERIMENTAL

Chromium nitride films were deposited on ball bearing steel and silicon in a Hauzer HC 139 PVD machine by reactive sputter deposition. The base pressure in the system was always below $1\times10^{-6}$ mbar. In all experiments an argon flow of 115 sccm was led into the reaction chamber. The chamber was pumped by a 2200 l/s turbomolecular pump resulting in an argon partial pressure of $3\times10^{-3}$ mbar. By sputter deposition in an argon/nitrogen mixture $CrN_x$ films are deposited, with x depending monotonically on the nitrogen flow. The nitrogen flow was varied from 0 to 150 sccm, resulting in films ranging from pure chromium to CrN. All depositions were done at 180°C.

The samples performed a planetary motion in the chamber; i.e. the substrate table rotated around its axis and the samples were mounted on rods on the substrate table, which also rotated about their axes (Fig.1). All depositions were carried out for 75 minutes. The thickness of the resulting film decreases monotonically with increasing nitrogen flow during deposition. Pure chromium films were 1.7 micron thick, CrN films were 1.1 micron thick.

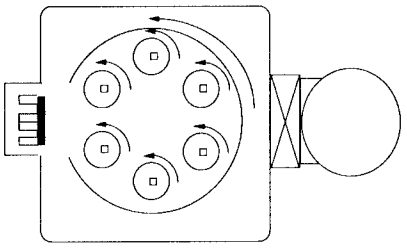

**Fig.1.** Schematic lay out of the PVD installation. On the left is shown the target with magnet assembly and plasma in front of the target. In the middle the planetary system, on the right the turbomolecular pump.

The microstructure of the film was studied by X-ray diffraction both for films deposited on ball bearing steel and on Si wafers. The composition of the films was measured by EPMA. The film for which the EPMA yielded $CrN_{0.48}$ was also the film with the sharpest X-ray peak for $Cr_2N$. In accordance with the accuracy of the EPMA of 2 at%. The hardness and the reduced modulus; $E_Y/(1-\nu^2)$ were measured by nano-indentation on a Hysitron/Digital Instruments nano-indenter on samples deposited on polished ball bearing steel. The stress in the films was studied by wafer curvature measurements from films deposited on 100 mm Si-wafers <100>.

## RESULTS

All films showed a columnar structure in cross sectional SEM, with columns of increasing diameter over the film thickness. The final width of the columns at the surface was on the order of 100 nm. A TEM micrograph of the $CrN_{0.43}$, i.e. chromium rich $Cr_2N$ film, on ball bearing steel is shown in Fig. 2. The hardness, reduced modulus and stress in the films are reported in Figs. 3, 4, and 5. For the $CrN_{0.43}$ film a maximum in hardness of 18 GPa was obtained. A second but lower maximum in the hardness of 9 GPa was obtained at a composition of $CrN_{0.73}$ i.e. chromium rich CrN. In contrast, the hardness of stoichiometric Cr, $Cr_2N$, and CrN films is only 5, 7 and 4 GPa respectively. The reduced modulus exhibits a broad maximum at stoichiometric $Cr_2N$.

**Fig.2.** Cross sectional TEM micrograph of a 1.3 micron thick $CrN_{0.43}$ film on ball bearing steel. Apart from a columnar structure faults inside the columns can be seen.

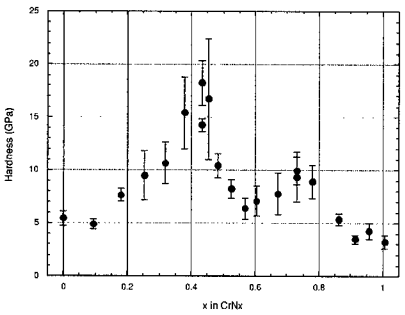


**Fig.3.** Hardness of $CrN_x$ films versus composition. The hardest films are chromium rich $Cr_2N$ films.

In Fig.6 the X-ray diffraction spectra for the $CrN_{0.43}$ and $CrN_{0.48}$ films are presented, these films resulted from deposition in an $Ar/N_2$ mixture with respectively 30 and 35 sccm nitrogen. A small difference in nitrogen flow leads to a large difference in microstructure of the film as is witnessed by the X-ray spectrum.
A crystallite size of 8 nm was estimated from the broadness of the diffraction peaks for the $CrN_{0.43}$ films, using the Scherrer equation [2]. This is not in correspondence with the width of the columns, as observed in SEM. Close inspection of the TEM micrograph (Fig.2) showed two length scales: the width of the colums that develop in the film and the size of unfaulted regions within the columns. Apparently the intra-columnar length scale causes the diffraction line broadening.

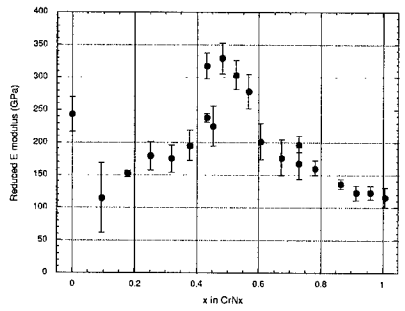


**Fig.4.** Reduced modulus of the $CrN_x$ films versus composition. The modulus shows a broad peak for stoichiometric $Cr_2N$.

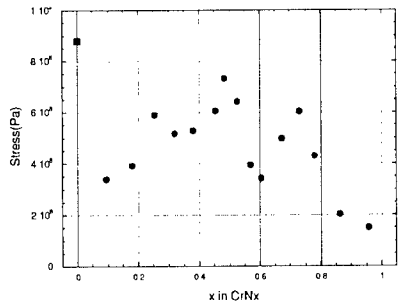


**Fig.5.** Stress in Cr (square) and $CrN_x$ films (dots) versus composition.

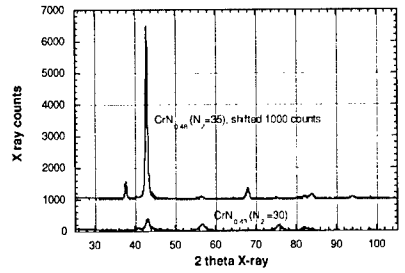


**Fig.6.** X-ray diffraction spectra taken on films deposited at 30 sccm $N_2$ flow and 35 sccm $N_2$ flow. Although the composition differs only slightly, the microstucture is considerably different.

## DISCUSSION

In none of the films a mixture of phases was observed. This is particularly intruiging for $CrN_{0.43}$, the composition of the hardest films. Only $Cr_2N$ peaks with pronounced broadening were identified in the X-ray spectrum taken on the $CrN_{0.43}$ film. No bcc Cr was observed in the $CrN_{0.43}$ films indicating the absence of Cr crystals. Assuming that the excess Cr in these films is located at the grain boundaries of 8 nm crystallites, we calculate the thickness of the chromium at the grain boundaries to be less than one atomic layer. Apparently, during deposition the mobility of the excess chromium is so small that this growth mode prevails over the growth of a two phase mixture, thereby forcing the growth of a nanocrystalline material.

In remainder of the text we will use the stress measurements for a discussion on the microstructure . First we discuss the tensile stress in the films. During deposition a bias voltage of 75V was applied to the substrate. A compressive stress was expected due to ion peening. The resulting tensile stress is explained in hindsight from the observation that, due to the planetary motion, the substrate is not in contact with the plasma for the major part of the time. During all

of this time film growth takes place, unaided by ion bombardment, leading to tensile stress. We checked this hypothesis by depositing a 1.1 micron chromium film with the substrate stationary for the target. This film exhibited a compressive stress of 900 MPa. Work is in progress to deposit films in compressive stress on planetary mounted substrates.

The observed stress at room temperature is the sum of the growth stress (1), the effect of ion bombardment (2) and the thermal stress (3). The linear thermal expansion coefficients of Cr and Si are $7\times10^{-6}K^{-1}$ and $3.2\times10^{-6}K^{-1}$ respectively. Thus the thermal stress in the pure Cr film at room temperature is 140 MPa. From the measured linear thermal expansion coefficient for $CrN_{0.43}$: $\alpha= 9.3\times10^{-6}$, a thermal stress of 220 MPa is calculated [3]. This thermal stress is assumed to be present in all $CrN_x$ samples. The compressive stress due to ion peening is assumed to be 40 MPa for all films, based on the lowest measured stress of 180 MPa for $CrN_{0.95}$ films.

Let us assume that the tensile growth stress is generated at the column boundaries of the growing film. Assuming that the average column boundary relaxes by a fixed distance, this means that the colums in the film will have to stretch by the same amount [4]. Therefore the strain in the film ($\varepsilon$) will be inversely proportional to the column size ($d$). Of course this straining of the film will have to be weighted over the film thickness, due to the evolution of the columns over the thickness. For the time being it is assumed that the column evolution is comparable for all films. Then:

$$\varepsilon=\frac{\sigma_{growth}(1-\nu)}{E_Y}\propto\frac{1}{d} \qquad (1)$$

with the Youngs modulus $E_Y$ and Poisson ratio $\nu$.

In many systems the Hall-Petch relation is observed. Hardness is inversely proportional to the square root of the grain size. Here we identify columns with grains for all but the nano-crystalline films.

$$Hardness\propto\frac{1}{\sqrt{d}} \qquad (2)$$

Originally this relation was proposed on the basis of dislocation pile up. However the grain boundary acting as a barrier for transfering the resolved shear stress from one grain to the next was also proposed as a mechanism [5]. In Fig.7 we plot the hardness versus $\sqrt{\varepsilon}$. The majority of the points obey the Hall Petch relation. Four points fall outside the curve. The two points with the low hardness are pure chromium and $CrN_{0.1}$. The two points with the high hardness are the points for $CrN_{0.38}$ and $CrN_{0.46}$, both nano-crystalline $Cr_2N$. First of all it is surprising to note that $CrN_x$ films with x ranging from 0.17 to 1.0 obey the same Hall Petch relation. Bcc Cr for $0.18<x<0.35$, hcp $Cr_2N$, for $0.40< x<0.65$ and fcc CrN for $x>0.70$ all obey the same Hall Petch relation.

Now, if the plasticity of our films is indeed dislocation based we can explain the marked different behaviour of the nano-crystalline films. The width of the columns determines the stress in all films and the hardness in the "micro-crystalline" films. In the case of the nano-crystalline films the stress is still determined by the width of the columns, but the hardness is determined by the size of the unfaulted regions (8 nm).

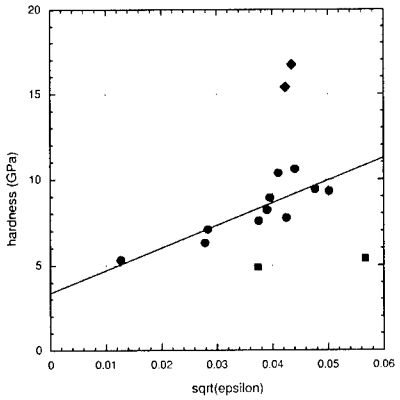


**Fig.7.** Hardness versus $\sqrt{\varepsilon}$. Most films obey the Hall-Petch relation (dots). Chromium films (squares) obey the Hall Petch relation with different coefficients. Nano-crystalline films (diamonds) fall outside the hall-Petch relation.

## CONCLUSION

For chromium nitride films deposited by reactive sputter deposition under tensile stress the hardness depends strongly on the composition. The hardest films are chromium rich $Cr_2N$ films. It is shown that the hardness is a consequence of the nano-crystallinity of the material. The maximum obtained hardness in our experiments was 18 GPa.

## ACKNOWLEDGEMENTS

We acknowledge the TEM preparation and microscopy of dr V. Svetchnikov of our department. This research was carried out under project number MC6.00087 in the framework of the Strategic Research programme of the Netherlands Institute for Metals Research in the Netherlands (www.nimr.nl). This work is part of the research programme of the Stichting voor Fundamenteel Onderzoek der Materie (FOM, financially supported by the Nederlandse Organisatie voor Wetenschappelijk Onderzoek (NWO)).

## REFERENCES

1. P.E.Hovsepian et al., Surface and Coatings Technology **116-119**, 727 (1999]
2. B.E.Warren, X-ray diffraction, (Assison-Wesley, Reading, Masschusetts, 1969) p.251
3. R.Hoy, to be published
4. F.A.Doljack and R.W.Hoffman, Thin Solid Films, **12**, 71 (1972)
5. John Price Hirth and Jens Lothe, Theory of dislocations, 2nd ed. (John Wiley, New York, 1982) p.778

Mat. Res. Soc. Symp. Proc. Vol. 703 © 2002 Materials Research Society V3.25

# Formation of Gold Nanowires on MgO Surfaces

Akira Ueda[1], Richard R. Mu[1], Vanessa Saunders[1], Thurston Livingston[1], Marvin H. Wu[1], Vera L. Arantes[2], and Don O. Henderson[1]
[1]Chemical Physics Laboratory, Department of Physics, Fisk University, Nashville, TN 37208, U.S.A.
[2]FEAU-Universidade do Vale do Paraiba, Sao Jose Campos, SP, Brazil

## ABSTRACT

Gold nanowires were fabricated on the stepped MgO (100) surfaces. The stepped MgO (100) surfaces were produced by polishing (100) surfaces at an inclined angle ~1° toward a [110] direction. An atomic force microscope image indicates that gold nanowires have grown at the steps on MgO (100) surface with a height of ~ 2 nm and a width of ~60 nm.

## INTRODUCTION

Recently nano-size materials have been paid attentions due to their diverse potentials in the fields of laser, optics, computer, electronics, biomedical science, and so on. Moreover, the nano-size materials provide the fields to study fundamental physics such as the quantized conductivity and the quantum Hall effect [1].

Regardless of any actual applications at this stage, the gold nanowire formation on MgO (100) surfaces was attempted. As shown later in the experimental results section, we have observed that the annealing single crystalline MgO (100) surface at high temperature in an oxidizing atmosphere can cause the step formation along two possible [110] directions on the (100) surface. By tilt-polishing the surface toward one of [110] directions by an angle of ~1°, we may depress the step formation of the other of two possible [110] directions, as shown in Fig.1.

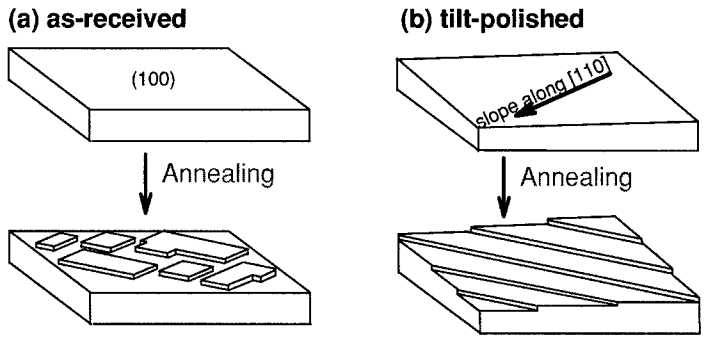


**Figure 1** Schematic model of the regulated steps for the tilt-polished MgO surface. (a) Two possible [110] directional step edges can be formed on an as-received MgO (100) surface. (b) One-directional step edges can be formed on the tilt-polished MgO surface.

Once we obtain such regulated steps, we may fabricate gold nanowires by depositing gold and by a suitable annealing recipe. We expect that gold atoms have the tendency to accommodate at the step sites, and the accumulation of the gold atoms leads to the formation of gold nanowires.

During this research, we have come across a series of recent publications by Himpsel's group [2] in which the step arrays of Si were formed on a Si (111) 7x7 reconstructed surface by miscutting a Si substrate and special annealing procedures. They also deposited $CaF_2$ to make some patterns for the formation of nanowires or quantum dots, which is similar to the way of the lithographic procedures. Their method on Si has been established and the applications are also in a process. For our case, the substrate is a single crystalline MgO that is transparent in visible-near IR range, and it may have an advantage for the optical applications.

## EXPERIMENTAL

The substrates were purchased from Princeton Scientific Corp. (Princeton, NJ) and were cut into smaller pieces suitable for the optical transmission measurements and the atomic force microscopy. The transmission measurements were made with a UV-Vis-NIR spectrophotometer (Hitachi U3501), and the morphologic images were made with an atomic force microscope (AFM, Digital Instrument Nanoscope III). The tilt-polishing was carried out with a home-made polishing device with three kinds of alumina polishing powders with water and with ortho-phosphoric acid. After polishing, the MgO substrates were annealed at 1200°C with a tube furnace in an oxidization atmosphere (an oxygen flowing tube furnace). The annealed substrates were observed with the AFM to see how the steps were formed. Gold was deposited to the substrates by using an e-beam evaporation device (Thermionics model 100-0030) in a high vacuum chamber with a background pressure of $10^{-7}$ torr. The gold deposited samples were observed with the AFM and the transmission measurements were carried out before and after every thermal annealing.

## RESULTS AND DISCUSSION

### The preparation of substrates

Fig.2 shows the AFM images of a flat MgO (a) as-received [4 μm x 4 μm] and (b) annealed substrates [8 μm x 8 μm], which was annealed at 1200°C in an oxidizing atmosphere for 5 h. In every pair of images in this paper, the left image is for the height mode and the right image is for the amplitude mode of Tapping AFM. The sides of the image frames are along the directions of crystal axes [100]. According to our cross-section analysis, the as-received substrate has a roughness of less than 1 nm as rms (the root mean square for the entire image of 512 x 512 pixels). Although it has a fairly flat surface, the morphology does not show an atomically flat surface, as shown in Fig.2 (a). On the other hand, although the annealed substrate has many steps with different edge lengths, there are atomically flat terraces between steps and the average step height is in the order of 1 nm (the cross-section analysis is not shown). The step edges are running along two possible crystal directions of [110].

This step formation along two possible crystal directions [110] of MgO led to the idea that the step arrays along only one direction of crystal axes [110] may be formed by tilt-polishing the substrate toward other [110] direction, as mentioned in the introduction and shown in Fig.1. Although our procedure for tilt-polishing and annealing is not well established yet, we have obtained nearly regulated step arrays. In Fig.3, the AFM images [2 μm x 2 μm] and the cross-section analysis are given for the MgO substrate tilt-polished and annealed at 1200°C in the oxygen atmosphere for 20 h. In Fig.3 (a), the step edges are running nearly along only one of [110] directions, which is diagonally from top-left to bottom-right. There is a crystal-like particle in the middle in this image, which is probably a MgO crystal island that was not completely annealed with the main MgO substrate. In Fig.3 (b), the cross-section analysis shows that the average step height is about 2-3 nm and the separation between steps is in the order of 100 nm.

**(a) As-received flat MgO substrate**

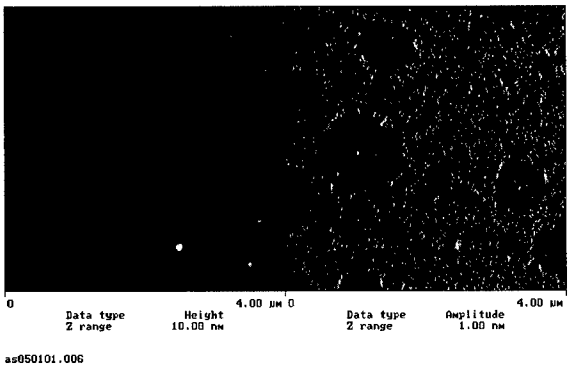


**(b) Annealed flat MgO substrate**

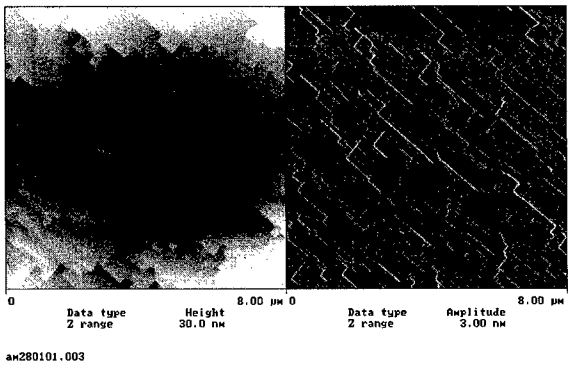


**Figure 2** AFM images of MgO substrates (a) as-received and (b) annealed at 1200°C in an oxidizing atmosphere for 5 h.

**(a) Substrate with the tilt-polishing and annealing**

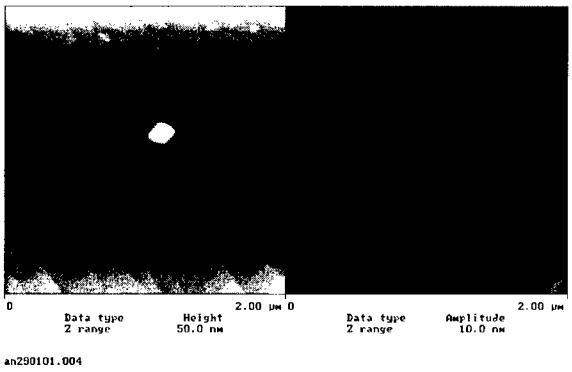


**(b) Cross-section analysis**

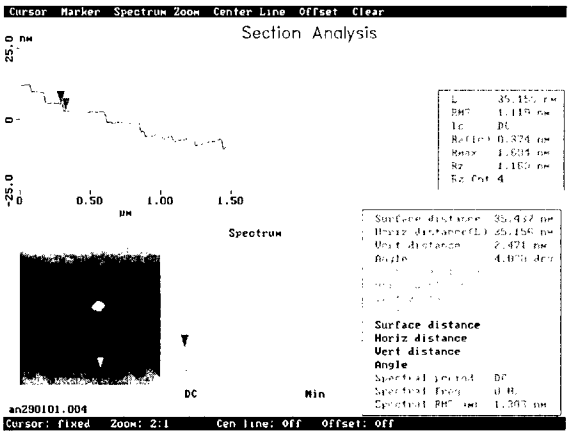


**Figure 3** AFM image of MgO substrate with the tilt-polishing and annealing in $O_2$ at 1200°C for 20 h, with the cross-section analysis.

**The gold deposited MgO**

The prepared MgO substrate with the step arrays was deposited with gold of 25 Å by using an electron-beam evaporator and was gradually annealed up to 800°C. Fig.4 shows the AFM images and the cross-section analysis, which indicates that there are higher rims on the step edges. In this image [8 µm x 8 µm], there are several crystal islands, which may interact with steps to disturb the step formation.

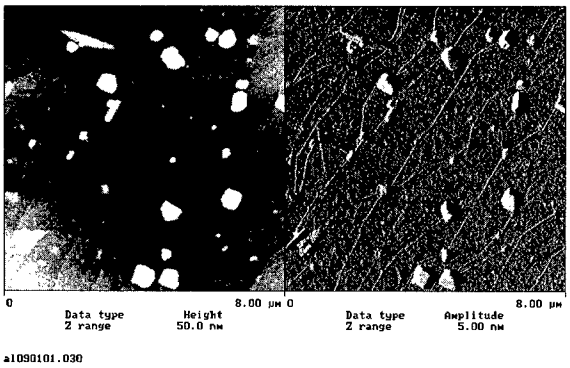


**Figure 4** The AFM images of a MgO surface deposited with gold and annealed. The MgO substrate was prepared by tilt-polishing and annealing, as mentioned in the text, and was deposited with gold of 25 Å by using an electron-beam evaporator and gradually annealed up to 800°C.

Fig.5 shows the cross-section analysis of a portion of Fig.4. The cross-section that we chose is marked with a line in the small image located at the left-bottom corner of each figure, and the numerical data are shown on the right. Fig.5 (a) shows the heights of two rims, and the rims are higher than the terrace level by ~2 nm. Fig.5 (b) shows the widths of two rims, and their widths are in the rage of 50-70 nm, which includes some uncertainty due to the AFM tip dimension, as known in AFM imaging. As shown in Fig.4, all the rims formed at the steps in the AFM image have similar dimensions, according to our observation.

We claim that these rims are gold nanowires by utilizing the regulated step arrays. There are MgO islands on the substrate, and gold particles are on the terraces as well. For the application purposes, we need to improve the substrate preparation: (1) The elimination of crystal islands, (2) the regulation of the step arrays, (3) the suitable conditions for the deposition of gold to the substrates, and (4) the suitable condition for the annealing of samples to form gold nanowires.

## CONCLUSION

We claim that gold nanowires have been formed by utilizing the regulated step arrays, which were created by tilt-polishing and annealing at a high temperature. At this stage, the preparation of MgO substrates is not well established yet, and there are problems to fabricate gold nanowires: (a) The elimination of crystal islands and the regulation of the step arrays, and (b) the suitable conditions for the deposition of gold and the annealing of the samples. We would like to continue to seek for the solutions to these problems.

**(a) The cross-section analysis for the heights of gold nanowires**

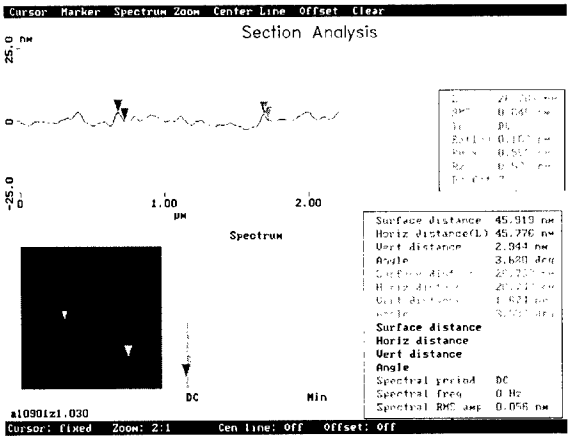


**(b) The cross-section analysis for the widths of gold nanowires**

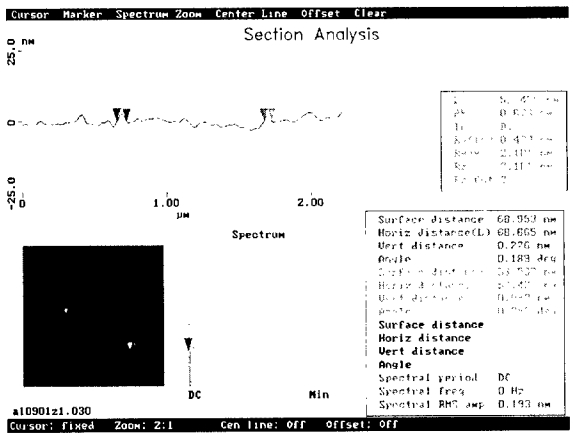


**Figure 5** The cross-section analysis of gold nanowires. The measurement of (a) the heights and (b) the widths for two nanowires.

## REFERENCES

[1] John H. Davies, "The Physics of Low-Dimensional Semiconductors", (Cambridge University Press, New York, 1998)
[2] F.J. Himpsel et al. Visit the web site: http://uw.physics.wisc.edu/~himpsel/wires.html and papers therein, *e.g.* J. Viernow et al., Appl. Phys. Lett. **72**, 948 (1998); J.-L. Lin et al., J. Appl. Phys. **84**, 255 (1998); A. Kirakosian et al., Appl. Phys. Lett. **79**, 1608 (2001).

Mat. Res. Soc. Symp. Proc. Vol. 703 © 2002 Materials Research Society V3.26

# Solvothermal Synthesis Of Electrochemically Active Nanocrystalline Li-Ti-O Spinel

Dina Fattakhova, Petr Krtil ,
J. Heyrovsky Institute of Physical Chemistry, Dolejskova 3, 18223 Prague, Czech Republic
Valery Petrykin,
Materials and Structures Laboratory, Tokyo Institute of Technology, Nagatsuta, Midori, 4259 Yokohama, Japan

## ABSTRACT

Nanocrystalline Li-Ti-O spinel samples were prepared by solvothermal reaction of $TiO_2$ with lithium hydroxide in water and ethanol. The hydrothermal reaction proceeds at temperature higher than 130 °C. The reaction proceeds via dissolution-precipitation mechanism and its course is not sensitive to titanium dioxide polymorph used in the reaction. Product of the reaction in water has cubic rock salt type structure. It converts, however, to spinel if annealed to temperatures exceeding 250 °C. The re-crystallization is accompanied with water removal from the structure. Solvothermal reaction in ethanol leads directly to a product with spinel structure without need for annealing. Both products are active for Li insertion; theelectrochemical activity. The specific capacity ranges between 100 and 160 mAh/g depending on the annealing temperature.

## INTRODUCTION

Nano-crystalline materials play an important role in design of new electrochemical energy related applications namely in development of new rechargeable batteries or photo-electrochemical cells. The use of nano-crystalline materials allows one to improve both the size and quality[1,2] of the electrode-electrolyte interface as well as to shorten significantly the characteristic diffusion lengths. Nanocrystalline Ti(IV) based oxides, particularly $TiO_2$ anatase and $Li_4Ti_5O_{12}$ spinel make prospective materials for 2V lithium ion batteries.

Solvothermal synthsis in Ti oxides chemistry is usually used to prepare large crystals of perovskites [3,4]. The potential of the hydrothermal synthesis in preparation of nanocrystals was, on the other hand, also demonstrated on controlled growth of anatase nanocrystals in tetramethylammonium containing solutions at 190-270 °C [5]. Li-Ti-O ternary phases are usually prepared by solid-state reaction at elevated temperatures. Hydrothermal synthesis of electrochemically active nanocrystalline Li-Ti-O ternary phases like e.g. $Li_4Ti_5O_{12}$ spinel has not been reported.

## EXPERIMENTAL

Nanocrystalline titanium dioxide (Bayer) was used as starting materials in syntheses. Parallel experiments were performed on anatase (PKP 5538) and mixture of anatase and rutile (1:3, P25 Bayer). All other chemicals in all experiments, i.e. LiOH and NaOH were obtained from Fluka. The water used in experiments was of Millipore MilliQ quality, used ethanol was of p.a. grade.

Reactions were carried out in poly(tetrafluoroethylene) (PTFE) - lined stainless steel autoclaves. The molar ratio of $TiO_2$ and LiOH in reaction mixture ranged between 2:1 and 1:5; the pH of the reaction mixture was adjusted to 14 by addition of concentrated NaOH solution. Syntheses were performed at temperatures between 130-200°C for 2 - 24 hours. Products of the reactions were filtered and carefully washed with water.

X-ray power diffraction of the prepared materials was measured using Siemens X500 powder X-ray diffractometer and CuK$\alpha$ radiation. Crystal morphology and size distribution was examined by field-emission SEM S-4500 (Hitachi). Additional estimate of crystal size distribution was done by Fourier transform analysis of peak shapes in X-ray diffractograms using Winfit program [6].Thermal analysis of hydrothermal powders was performed on NETZSCH STA 409 TG/DTA apparatus complemented with mass spectrometer QMS 403/4 (Balzers) allowing for qualitative analysis of gases evolved during heating.

The electrochemical activity of prepared phases was examined by cyclic voltammetry in three-electrode arrangement with Li counter and reference electrodes on PAR263A potentiostat in 1M solution of $Li(CF_3SO_2)_2N$ in 1:1 (w/w) mixture of ethylene carbonate (EC) and dimethoxyethane (DME). Li-Ti-O electrodes were prepared by mixing of powder samples with teflonized carbon black (ca 15% of carbon black).

## DISCUSSION

X-ray powder diffraction patterns of the starting titania and materials prepared in water and ethanol at 200 °C are shown in Fig. 1. The solvothermal synthesis at this temperature leads to complete removal of starting material. The products of both reactions contain small amounts of lithium carbonate, which was not removed by washing. The diffraction pattern of the product prepared in water shows three resolved diffraction peaks at approximately 4.81 Å, 2.81 Å and 1.54 Å. The broad peak at about 18 ° could be attributed to an amorphous phase. Such a phase, however, was not found in SEM. The diffraction peaks of the material prepared in water show good agreement with those of cubic rock salt $LiTiO_2$ ($a \approx 4.14$ Å, *Fm3m*). Annealing of the material prepared in water leads to its re-crystallization to spinel structure (*Fd3m*). This process is accompanied by removal of the structural water, which starts at temperatures above 250 °C.

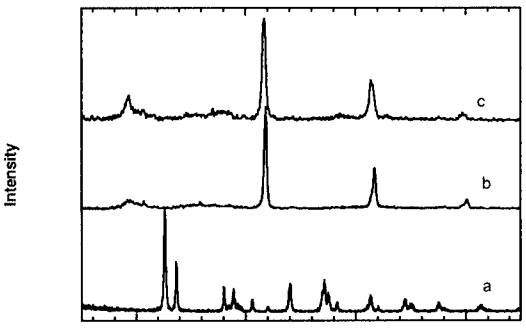


**Figure 1** X-ray diffraction patterns of: a) the starting $TiO_2$ (mixture of rutile and anatase 1:3), b) product of the reaction in water, c) product of the reaction in ethanol. In both cases the reaction proceeded at 200 ° for 24 hours.

The diffraction pattern of the material prepared in ethanol, on the other hand, shows good agreement with that of $Li_4Ti_5O_{12}$ spinel (a=8.357 Å). Small amounts of a material identical with product of the reaction in water can be traced in diffraction pattern. We attribute the presence of this impurity phase to the fact that the used ethanol contained ca 5 % of water (v/v). Low intensity of the signal and rather broad diffraction peaks indicate small crystal size of the prepared materials.

Analysis of the XRD patterns indicates average coherent domain size in the range 10-25 nm. SEM measurements, however, revealed the actual particle size to be about twice bigger. Slightly bigger particles were found in the case of water prepared materials. The reaction time has no pronounced effect on the particle growth. Also the annealing of the materials to temperatures below 500 °C does not lead to pronounced particle size increase.

## ELECTROCHEMICAL BEHAVIOR

Insertion behavior of the Li-Ti-O oxides prepared by solvothermal reaction is shown in Fig. 2. For both hydrothermal as well as solvothermal materials the lithium insertion and extraction proceeds in single step. The standard potential characterizing the thermodynamics of the

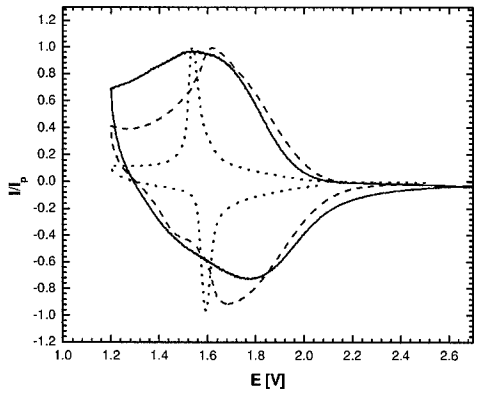


**Figure 2** Cyclic voltammograms of Li insertion into solvothermally prepared Li-Ti-O spinel annealed at 0, 200 and 300 °C. The material was prepared by reaction at 200 °C in water.

**Table 1** Standard potential of the Li insertion into Li-T-O oxides prepared in water and ethanol

| Annealing temperature | $E^0$[V] | |
|---|---|---|
| | $H_2O$ | Ethanol |
| 0 | 1.616 | 1.664 |
| 200 | 1.740 | 1.649 |
| 300 | 1.577 | 1.561 |

insertion process obtained are summarized in Table 1. The annealing causes a shift of the standard potential towards more negative potentials what indicates an increase in activation barriers for the insertion process. The specific capacity of the materials is between 100-160 mAh/g and improves with increasing temperature of the post-synthesis treatment. The upper specific capacity values are comparable with those reported for microcrystalline Li-Ti-O spinels. The kinetics of the insertion process into solvothermally prepared nanocrystaline spinels is, however, superior to that of materials prepared at high temperature (see Figure 3).

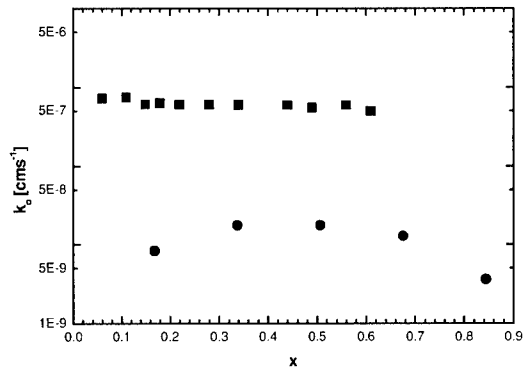


**Figure 3** Heterogeneous rate constant of the lithium insertion into high temperature prepared (circles) and solvothermally prepared $Li_4Ti_5O_{12}$ spinel


## ACKNOWLEDGEMENT

This work was supported by the Grant agency of the Czech Republic under contract 203/99/0879. The authors also appreciate kind help of Dr. Grygar with thermal analyses.

## REFERENCES


([1]) C. Martin, D. Mitchell in *Electroanalytical Chemistry* (I. Rubinstein and A.J. Bard Eds.), **21** M. Dekker, New York, 1999, p. 1.
([2]) P. Krtil, D. Fattakhova, L. Kavan, S. Burnside, M. Grätzel, *Solid State Ionics*, **135**, 101, 2000..
([3]) Lucka, M.M., Anderko, A.; Riman, R.E. *J. Amer. Ceram. Soc.* **1995,** *78*, 2609.
([4]) Oledzka, O.; Brese, N.E.; Riman, R.E. *Chem. Mater.* **1999**, *11*,1931.
([5]) Burnside, S.D.; Shklover, V.; Barbé, C; Comte, P.; Arendse, F., Brooks, K., Grätzel, M. *Chem. Mater* **1998**, *10*, 2419
([6]) Krumm, S.; *Acta Universitatis Carolinae Geologica*, **1994**, *38*, 253.

# Synthesis and Characterization I

Mat. Res. Soc. Symp. Proc. Vol. 703 © 2002 Materials Research Society V4.6

# In-situ Analysis of the Chemical Vapor Synthesis of Nanocrystalline Silicon Carbide by Aerosol Mass Spectrometry

In-Kyum Lee, Markus Winterer, Horst Hahn, Christian Janzen[1], Dirk Lindackers[1], Paul Roth[1]
Darmstadt University of Technology, Institute of Materials Science,
Petersenstr. 23, 64287 Darmstadt, Germany
[1]Institut of Combustion and Gasdynamics, Gerhard-Mercator University,
47048 Duisburg, Germany

## Abstract

An Aerosol Mass Spectrometer (AMS) is a combination of a Quadrupol- (QMS) and a Particle Mass Spectrometer (PMS) and enables the in-situ analysis of gas phase processes for the generation of nanoparticles. Size distributions of ultrafine silicon carbide particles in the range of $10^4$ atomic mass units (amu) to $10^7$ amu are measured in the PMS. Simultaneously, molecular species up to 300 amu can be detected in the QMS. Aerosols containing nanocrystalline silicon carbide are produced from tetramethylsilane (TMS) by thermal decomposition. In situ process analysis with the AMS as a function of process parameters was performed to elucidate the formation and growth mechanism of SiC nanoparticles.

## 1. Introduction

Powders of small grain size, narrow size distribution, low agglomeration and high purity are required for the production of solid nanocrystalline materials and the exploitation of size effects in applications (Winterer 2001 and multiple references therein). The synthesis of particles from the gas phase is one important technique to produce ultrafine particles with a narrow size distribution and high purity. Chemical Vapor Synthesis (CVS) is a method to generate particles in the size range below 10 nm, narrow size distribution, geometric standard deviation smaller than 1.2 and low degree of agglomeration. Silicon Carbide is an advanced ceramic material for high performance applications. Sintering of SiC to high density is very difficult because of low diffusion coefficient even at high temperatures due to strong covalent bonds. Ultrafine particles of SiC are promising for the production of dense bulk solids due to the small grain size of such powders. Up to now, CVS powders have been analysed only by ex situ methods (Klein 1998). In situ analysis methods of CVS processes have to be compatible with high temperatures, low pressures, high particle number concentration and very small particle size of the order of a few nanometers. One instrument which meets those requirements is called AMS, which has been used for particle size measurements in premixed low pressure flames (Roth 1993, Homann 1987).

## 2. Methodology

### Chemical Vapor Synthesis

In the Chemical Vapor Synthesis (CVS) process a precursor vapor with carrier gas is delivered into a hot wall reactor. The precursor is thermally decomposed and particles form by coagulation and sintering. Process parameters like temperature, pressure, mass flow, precursor concentration, precursor material and reactor geometry influence the time-temperature history of the particles and determine the particle size and chemical purity of the powder. For the synthesis of SiC the precursor, TMS, is evaporated at room temperature and is directly delivered through a thermal mass flow controller into the reactor. To adjust residence time and precursor concentration an additional helium flow is used. The mass flow of helium is controlled by a second thermal mass flow controller. The total, absolute pressure is measured with a Baratron capacitance gauge. The continuous gas flow is produced by a combination of a roots blower and a sliding vane pump and stabilised at different pressures by means of a butterfly valve (figure1).

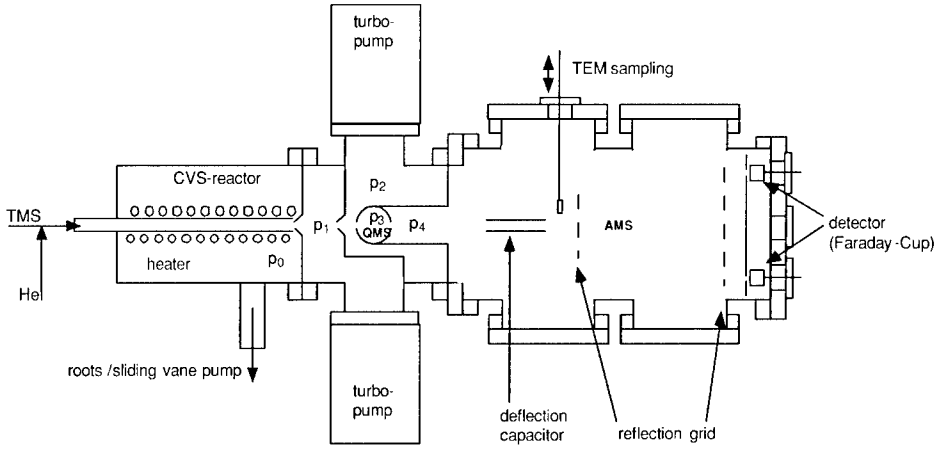


**Figure 1.** CVS reactor attached to the Aerosol Mass Spectrometer for in situ process analysis.

## Aerosol Mass Spectrometer

A new Aerosol Mass Spectrometer (AMS) was constructed by combining a Quadrupol Mass Spectrometer (QMS) (Balzers, QMA 430 with QMG 422) and a Particle Mass Spectrometer (PMS) (Roth 1993) (figure 1). Molecular species in the mass range 0-300 atomar mass units (amu) can be measured in the QMA. Particulate Species in the mass range $10^4$ to $10^7$ amu, corresponding to a diameter of 1 to 35 nm for SiC, can be measured in the PMS. The aerosol from the reaction chamber, which is in the continuous pressure regime ($p_0$) is supersonically expanded through a nozzle (0.8 mm diameter) into the first vacuum chamber ($p_1$, figure 1). Due to the high pressure ratio larger than $10^4$ a molecular free jet is generated, where all reactions, coagulation and sintering processes are quenched. The pressure in the first vacuum chamber is smaller than $10^{-3}$ mbar and pumped by a 1000 l/s turbomolecular pump (Pfeiffer Vakuum TMP 1001 SG). The center of the molecular free jet is extracted by a sharp edged skimmer (Molecular Beam Dynamics Standard Model 1, with 0.5mm orifice diameter) to generate a molecular beam ($p_2$, figure 1). The molecular beam (aerosol) is ionised in a cross beam ion source, which is part of the QMA, by electron impact ($p_3$, figure 1). Molecular species up to a mass of 300 amu can be analysed in the QMA. The separation of the particles is realised by their electrical charge and their inertia. A detailed description of the fundamentals of the PMS is given in (Roth 1993). The molecular beam enters a homogeneous electrical field, which is perpendicular to the molecular beam direction. The electrical field is realised by a capacitor with 100 mm in length and a distance of 20 mm. Charged particles are accelerated in the electrical field in direction of the field lines. Outside the electrical field the particles move in a straight line. For fixed geometric conditions of the detector the voltage $U_k$ selects particles of a certain kinetic energy carrying z elementary charges. By varying the voltage and therefore the electrical field of the capacitor a signal $I(U_k)$ is detected.

$$U_k = \text{const.} \frac{m_p}{ze} \frac{v_p^2}{2} \qquad (1)$$

where $U_k$ is the deflection voltage, $m_p$ the particle mass, $v_p$ the particle velocity, e the elementary charge, z the number of charges and I is the current measured by the ion detectors of the Faraday cup. With the information of the kinetic energy of the particles mass distributions can be determined if the particle velocity is known. The particle velocity is measured in an electrical

chopping system with a synchronously pulsed repelling potential. By sweeping the chopping frequency of the repelling potential a periodic signal is measured. The determination of the particle velocity is then given by the following equation:

$$v_p = \Delta f_{min}\,(I_{min})\; l_{rg} \qquad (2)$$

where $v_p$ is the particle velocity, $\Delta f_{min}\,(I_{min})$ the frequency of the signal at minimum signal intensity, and $l_{rp}$ the distance of the reflection grids. Figure 3 and 4 show a typical measurement.

## 3. Results and Discussion

**Detection of the Molecular Species (QMA):**

The thermal decomposition of TMS in the CVS reactor was measured using the QMS at different temperatures of the hot wall reactor at otherwise constant process parameters (2000 Pa, 800 sccm He and 30 sccm TMS; sccm stands for standard cubic centimeter). The decomposition of the TMS precursor (m/e = 73) starts at about 1173K and the signal vanishes at about 1673 K where the precursor is completely decomposed (figure 2). With increasing temperature an increase of lower hydrocarbon groups and also an increase of carbon and hydrogen is observed. Also observed is the occurrence of species of masses higher than 88 amu at the beginning of the precursor decomposition. This indicates that formation of nano SiC takes place by a polymerisation reaction as discussed by Fritz (Fritz 1986). With increasing temperature the signal of the higher masses decreases. It is not clear if species of higher masses decompose with increasing temperature or whether the polymerisation reaction goes on to form nano SiC. A signal in the PMS is observed as soon as a decrease of the TMS signal is measured in the QMS. Therefore, at 1173 K TMS is decomposed and converted to SiC particles. The intensity of this signal increases from 1173 K to 1473 K.

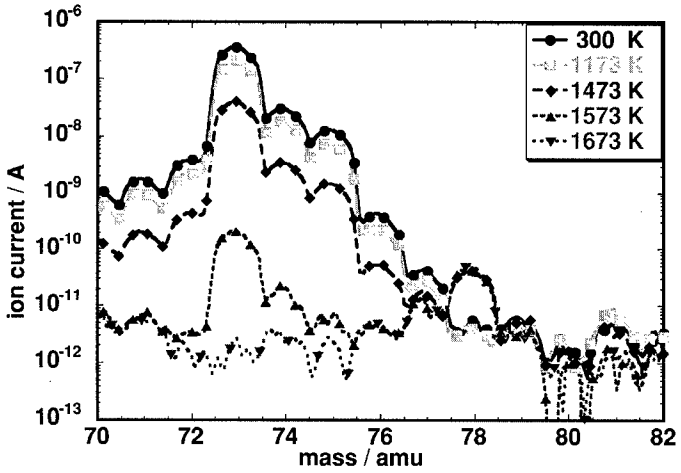


**Figure 2.** Quadrupol mass spectrum of the tetramethylsilane base peak (m/e 73 at 70 eV) at different temperatures.

**Detection of the Particular Species (PMS):**

In the following plots the classification by the deflection voltage and the velocity determined at the maximum intensity of the deflection voltage are shown. The synthesis conditions were as follows: T = 1323 K, p = 2000 Pa, 800 sccm He flow and 30 sccm TMS flow. It was found that particle charging by an external ion source is not necessary. The SiC particles are charged bipolarly in the CVS process as detected by switching the polarity of the deflection voltage. The maximum intensity at the kinetic energy filter is measured at 130 V. A velocity of 530 m/s was detected. The particle size distribution calculated from these data is shown in figure 5.
The distribution is fitted by a lognormal function and a particle mean diameter of approximately 13.5 nm with a geometric standard deviation of about 1.1 is deducted.
This PMS size distribution is compared with a TEM sample, which was taken directly from the molecular beam (figure 5). Altough only approximately 120 particles were measured by TEM the size distribution (histogram) shows a good agreement with the PMS data. In contrast the measured ion current in the PMS (figure 3) is about 4 pA at the maximum, which corresponds to about $10^7$ single charged particles. The size distribution from the TEM data was also fitted by a lognormal function and gives a mean particle diameter of 15.7 nm with a geometric standard deviation of 1.3. Measurements with increasing He flow (800/1200/1500 sccm) but otherwise constant process conditions, i.e.shorter residence time result in a decrease of particle diameter (14.9, 10.8, 8.9 nm (± 0.5 nm)). These trends are also predicted by a monodisperse reaction coagulation sintering model (Winterer, 2001).

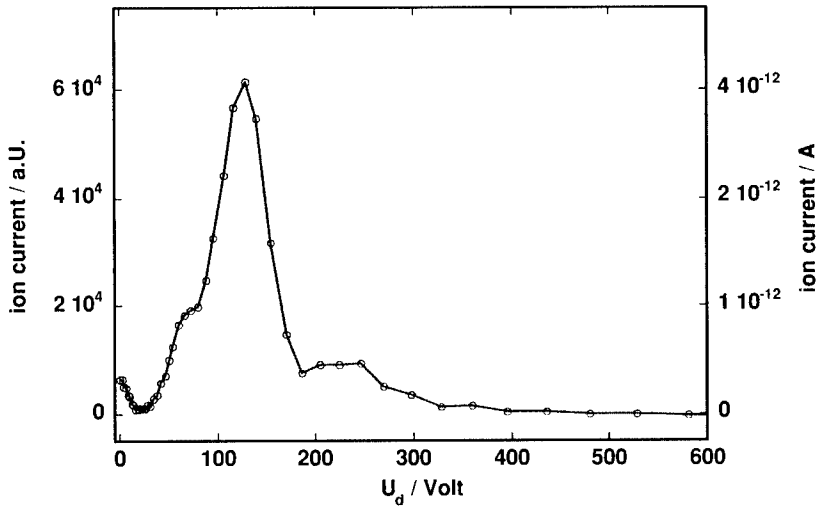


**Figure 3.** Measured kinetic energy distribution

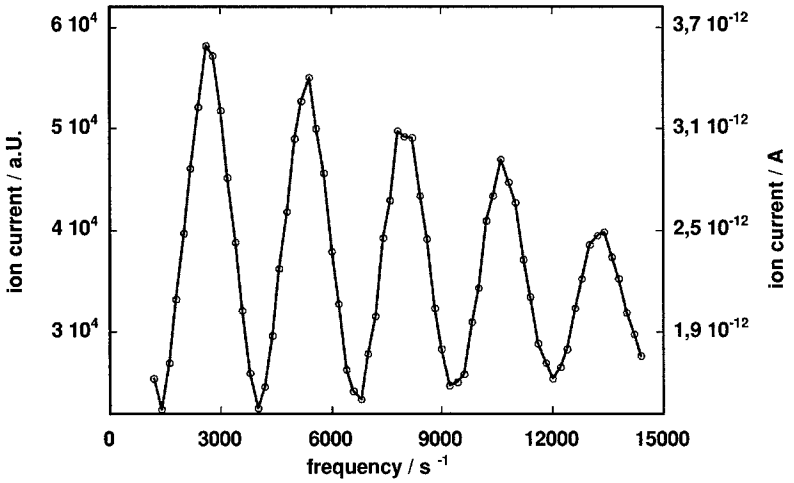


**Figure 4.** Measured particle velocity.

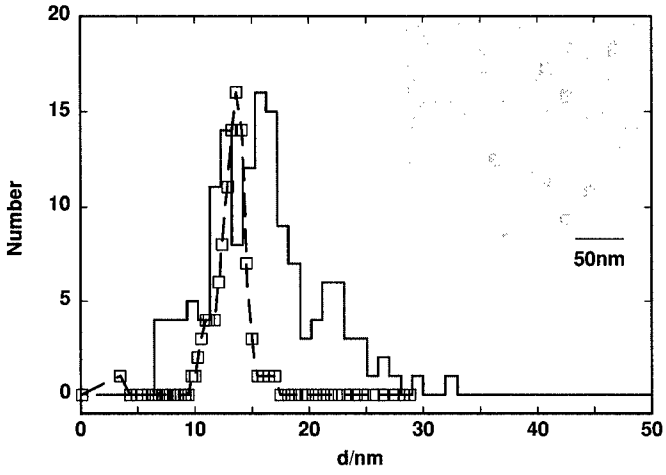


**Figure 5.** Particle size distribution from PMS measurements (squares) compared with TEM sampling (full line).

## 4. Conclusions

The AMS allows the in situ analysis of high temperature, low pressure gas phase processes. Particular and molecular type species can be detected simultaneously allowing the optimisation of the particle size distribution and the determination of precursor decomposition kinetics. The synthesis of nano SiC by thermal decomposition of TMS has been analysed. At about 1173 K the beginning of TMS decomposition is observed. At this point particles are detected in the PMS. Particle sizes between 1-35 nm of SiC can be measured in the PMS with an accuracy of about 8 % in size or 25 % in mass in the measured range. To simulate CVS processes with particle size distributions models without restriction to monodispersity have to be used , e.g. a sectional model (Landgrebe 1990).

## References


Fritz, G., *Carbosilanes Syntheses and Reactions*, Springer, **1986**.
Homann, K.H., Traube J., *Ber. Bunsenges. Phys. Chem.*, **91**, 828-833 (1987).
Klein, S., Winterer, M., Hahn, H., *Chem. Vap. Dep.*, **4**, 143-149 (1998).
Landgrebe, J.D., Pratsinis, ., S.E., *J. Colloid Interface Sci.*, **139**, 63-86 (1990).
Roth, P. and Hospital, A., *J. Aerosol Sci.*, **25**, 61-73 (1994).
Winterer, M., *Synthesis and Characterisation of Nanocrystalline Ceramics*, (2001) to be published by Springer Heidelberg.

Mat. Res. Soc. Symp. Proc. Vol. 703 © 2002 Materials Research Society V4.7

# GRAIN-SIZE-DEPENDENT THERMAL TRANSPORT PROPERTIES IN NANOCRYSTALLINE YTTRIA-STABILIZED ZIRCONIA

Ho-Soon Yang, J.A. Eastman, L.J. Thompson, and G.-R. Bai
Argonne National Laboratory, Materials Science Division
Argonne, IL 60439

## ABSTRACT

Understanding the role of grain boundaries in controlling heat flow is critical to the success of many envisioned applications of nanocrystalline materials. This study focuses on the effect of grain boundaries on thermal transport behavior in nanocrystalline yttria-stabilized zirconia (YSZ) coatings prepared by metal-organic chemical vapor deposition. A strong grain-size-dependent reduction in thermal conductivity is observed at all temperatures from 6–480 K. The behavior is due primarily to the effect of interfacial (Kapitza) resistance on thermal transport. In response to the application of heat to a material, interfacial resistance results in a small temperature discontinuity at every grain boundary, an effect that is magnified in nanocrystalline materials because of the large number of grain boundaries. The observed behavior in YSZ is compared with predictions derived from a diffuse-mismatch model. Implications for the possible development of improved thermal barriers based on nano-layered structures with large interfacial thermal resistance are discussed.

## INTRODUCTION

The efficiency of gas turbine engines is dictated by the maximum sustained operating temperature of their typically Ni- or Co-based alloy turbine rotors. Recent studies have concluded that significant near-term progress in increasing turbine engine operating temperatures is more likely to come from the development of improved thermal barrier coatings (TBCs), typically yttria-stabilized zirconia, than from the design of new alloys. New processing techniques that result in TBC microstructures with lower thermal conductivity could lead either to higher operating temperatures of turbine engines, resulting in greater efficiency, or thinner coatings for the same operating temperature, which would reduce overall weight. Using nanocrystalline YSZ coatings offers the possibility of lowering thermal conductivity, and may also provide additional benefits for TBC applications because of the possibility of improved toughness and ductility compared to that of coarser-grained ceramics.

Recent studies of thermal conductivity in nanocrystalline YSZ coatings have shown a very strong grain size dependence for average grain sizes below approximately 40 nm [1]. Studies of the grain size and temperature dependence of the thermal conductivity in YSZ have been interpreted in terms of the interfacial (Kapitza) resistance to thermal transport [2]. This report summarizes the results of those studies and extends them to include a comparison of the experimental observations with predictions of a diffuse mismatch model.

## EXPERIMENTAL PROCEDURES

Nanocrystalline YSZ coatings with thicknesses of 500-to-1200 nm were grown on polished polycrystalline $\alpha$-$Al_2O_3$ substrates by metal-organic chemical vapor deposition [1]. Samples with controlled average grain sizes from 10-100 nm were produced by varying the processing conditions, primarily the substrate temperature. Yttria contents for all samples used in this study varied from 8-15 mol.%, resulting in formation of the expected cubic fluorite-type structure [3]. Samples were found to contain approximately 10% porosity based on nanoindentation [1] and small-angle neutron scattering studies [4], independent of grain size. No dependence of thermal conductivity on $Y_2O_3$-content was observed, providing additional confidence that the observed behavior was due to intrinsic grain-size effects.

Thermal conductivity was measured using the 3$\omega$ method [5,6]. A typically 25 $\mu$m-wide and 300 nm-thick Au/Cr line was patterned onto the sample surface by electron beam evaporation and photolithography for use as both sample heater and thermometer in these measurements. Samples were placed in a liquid-helium cryostat in a low pressure gaseous helium environment for thermal conductivity measurements at temperatures from 6-280 K. Measurements from 280-480 K were performed in vacuum using a high-temperature probe station [7]. The data were corrected to account for the approximately 10% porosity in the samples.

## RESULTS AND DISCUSSION

Recent studies of thermal conductivity in nanocrystalline YSZ coatings have shown a very strong grain size dependence for average grain sizes below approximately 40 nm [1]. As seen in Fig. 1, at room temperature the thermal conductivity of YSZ with 10 nm grain size is reduced more than a factor-of-two compared to that of coarse-grained coatings. In the case of YSZ, this reduction is primarily due to the increasing contribution with decreasing grain size of the interfacial (Kapitza) resistance to thermal transport, which, as shown in Fig. 2, results in a temperature discontinuity at every interface in response to an applied heat flux. The temperature difference across a single grain can be described, therefore, as the sum of the temperature difference across a single grain interior region and the average temperature discontinuity at a grain boundary. The measurable thermal conductivity of a polycrystalline material, $k$, can be defined [2, 8] as:

$$k = \frac{k_o}{1 + \frac{k_o R_k}{d}}, \qquad (1)$$

where $k_o$ is the grain interior thermal conductivity, $d$ is the grain size, and $R_k$ is the Kapitza resistance [2, 8]. The parameters $k_o$ and $R_k$ can be determined by fitting plots of $k$ vs. $d$ to Eq. 1. A typical fit is shown in Fig. 1. The obtained values of the Kapitza conductance, $G = 1/R_k$, are shown as closed circles in Fig. 3. The conductance increases as temperature increases and plateaus in the vicinity of 300 K.

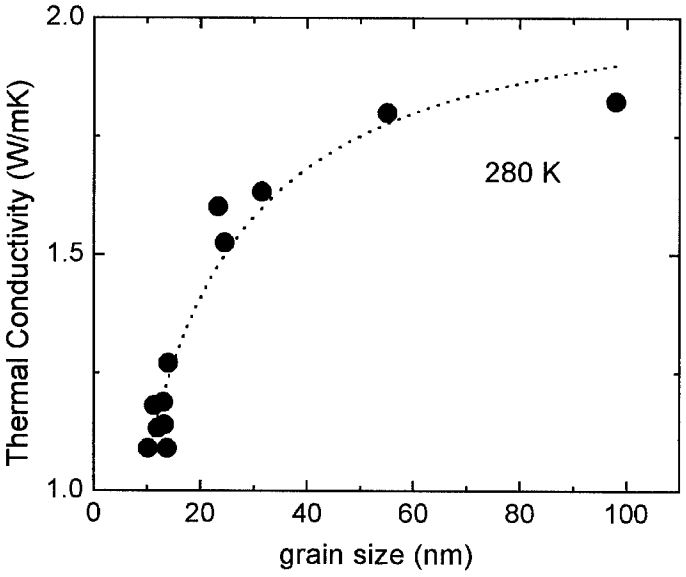


**Figure 1.** Thermal conductivity versus grain size at 280 K. Line represents a fit to Eq. 1.

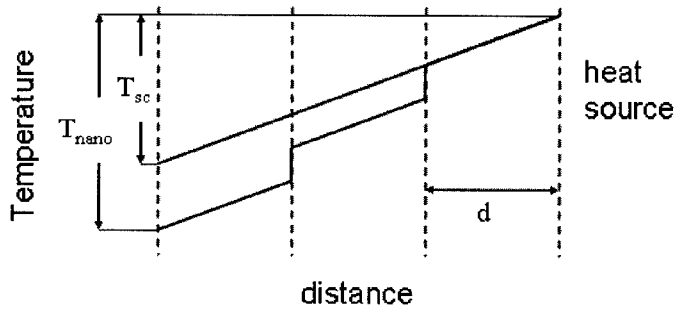


**Figure 2.** Schematic representation of the one-dimensional temperature profile across single crystal and polycrystalline material in response to an applied heat flux. The temperature drop across a nanocrystalline material, $T_{nano}$, is larger than that across a single crystal, $T_{sc}$ due to the many temperature discontinuities at grain boundaries. This results in a reduction of the net thermal conductivity, which becomes increasingly significant as grain size is reduced.

The Kapitza conductance is the derivative of the net heat flux transmitted across an interface with respect to the temperature difference across the interface. In the diffuse mismatch model, it is assumed that all phonons are scattered diffusely at an interface and the correlation between the incoming and outgoing phonons is completely destroyed by the scattering [9]. The transmission probability is determined by a mismatch between phonon densities of states. The Kapitza conductance can be expressed as

$$G = \frac{1}{4}\sum_j v_{1,j} \int_0^\infty \alpha_1 \hbar\omega \frac{d}{dT}\{D_j(\omega) n(\omega,T)\} d\omega \ , \qquad (2)$$

where $v_{1,j}$ and $D_j(\omega)$ are the velocity and the density of states for phonons with mode $j$ on the incident side of the interface, respectively, $\alpha_1$ is the transmission probability across the interface, and $n(\omega)$ is the occupation number of a phonon with energy $\hbar\omega$ [5]. Assuming that both sides of an interface have an identical structure ($\alpha_1$ assumed to equal 0.5 in this case), Eq. 2 is calculated for polycrystalline YSZ using the Debye model. The results of the calculation are denoted as open circles in Fig. 3. At all temperatures, the

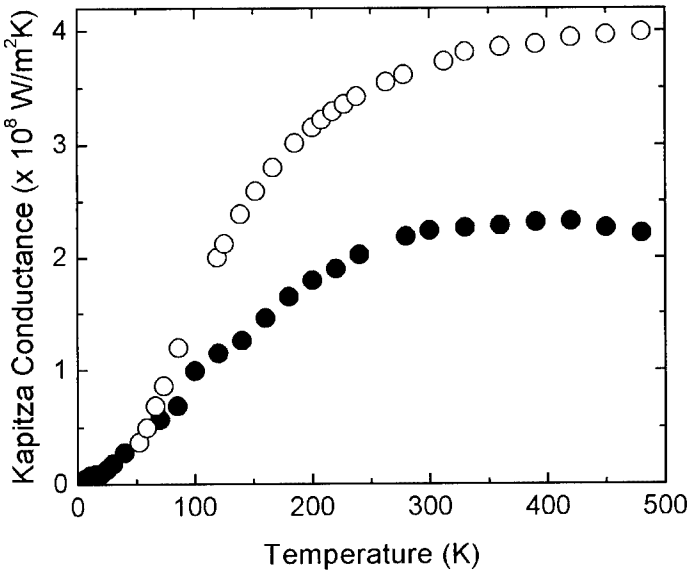


**Figure 3.** Kapitza conductance, $G$, for YSZ derived from the measured grain-size dependent thermal conductivity (●) and predicted with the diffuse mismatch model (○).

calculation of $G$ with the diffuse mismatch model predicts higher Kapitza conductance values than those obtained from fits of the measured $k$ vs. grain size to Eq. 1. The structures on both sides of a grain boundary would be different due to the random orientation of grains in polycrystalline materials. This needs to be considered in determining the transmission coefficient. However, simply using a value for $\alpha_1$ other than 0.5 does not improve the agreement with the $G$ values calculated using Eq. 1. The deviation of the calculated $G$ becomes larger with increasing temperature because the Debye model breaks down at high temperatures. For this reason, we believe that the $G$ values calculated from Eq. 1 are more accurate than those determined from a diffuse mismatch approach.

While YSZ is the material of choice in most current TBC applications, our studies suggest that an effective new strategy in designing TBC's with lower thermal conductivity could be to search for materials with large Kapitza resistance. Little is currently known about the magnitude of the average Kapitza resistance in different materials. At nanocrystalline grain sizes, materials with bulk thermal conductivity larger than that of YSZ could actually have a smaller net thermal conductivity. Nanocomposites of two or more dissimilar materials could be prime candidates for future TBC applications, both because the interfaces in such systems could exhibit large Kapitza resistance, and because formation of composite microstructures is a strategy that has been demonstrated to be effective in stabilizing nanocrystalline grain sizes to the high temperatures that would be encountered.

## CONCLUSIONS

The observed grain size dependent reduction in thermal conductivity of nanocrystalline YSZ is believed to arise primarily due to the Kapitza resistance to thermal transport at grain boundaries. The temperature-dependent Kapitza resistance in polycrystalline materials can be determined from measurements of grain-size dependent thermal conductivity and compared with the predicted values obtained from a diffuse mismatch model. Even in a highly defective material like YSZ, a substantial reduction in thermal conductivity is obtained by increasing the number-density of grain boundaries through grain refinement to the nanometer scale. Comparisons of the magnitude of the average Kapitza resistance in YSZ with that in other material are desirable. It is possible that future studies of other materials could lead to the development of improved thermal barriers by identifying materials possessing both low bulk thermal conductivity and large Kapitza resistance.

This work is supported by the U. S. Department of Energy, Office of Science, under Contract W-31-109-Eng-38.

## REFERENCES


1. G. Soyez, J.A. Eastman, L.J. Thompson, R.J. DiMelfi, G.-R. Bai, P.M. Baldo, A.W. McCormick, A.A. Elmustafa, M.F. Tambwe, and D.S. Stone, *Appl. Phys. Lett.*, **77**, no. 8, pp. 1155 (2000).
2. Ho-Soon Yang, G.-R. Bai, L.J. Thompson, and J.A. Eastman, submitted to *Acta Mater.* (2001).
3. JCPDS File 30-1468, International Committee for Diffraction Data, *Power Diffraction File* (Joint Committee on Power Diffraction Standards, Philadelphia, 1977).
4. W. Wagner, J. A. Eastman, G.-B. Bai, and L.J. Thompson, in preparation.
5. D. G. Cahill, A. Bullen, S.-M. Lee, *High Temp.-High Press.* **32**, 135 (2000).
6. D. G. Cahill, M. Katiyar, J. R. Ableson, *Phys. Rev. B* **50**, no. 9, 6077 (1994).
7. Micro Probe Station, MMR Technologies, Inc.
8. Ce-Wen Nan, R. Birringer, D. R. Clarke, H. Gleiter, *J. Appl. Phys.* **81**, no. 10, 6692 (1997).
9. E. T. Swartz, and R. O. Pohl, Rev. Mod. Phys. **61**, 605 (1989).

Mat. Res. Soc. Symp. Proc. Vol. 703 © 2002 Materials Research Society V4.10

# OPTICAL, ELECTRICAL AND MICROSTRUCTURAL PROPERTIES OF TIN DOPED INDIUM OXIDE FILMS MADE FROM SINTERED NANOPARTICLES

**Annette Hultåker[A], Anders Hoel and Claes-Göran Granqvist**
Department of Materials Science, The Ångström Laboratory, Uppsala University,
P O Box 534, SE-751 21 Uppsala, Sweden.
[A] Corresponding author: Phone: +46 18 471 31 32, Fax: +46 18 500 131,
E-mail: Annette.Hultaker@Angstrom.uu.se

**Arie van Doorn and Michel J. Jongerius**
Philips CFT, PO Box 218, 5600 MD Eindhoven, The Netherlands

**Detlef Burgard**
Nanogate GmbH, Gewerbepark Eschberger Weg, 66121 Saarbrücken, Germany

## ABSTRACT

Thin transparent and electrically conductive films of tin doped indium oxide (ITO) were made by sintering of nanoparticle dispersions. The resistivity decreased to $1 \cdot 10^{-2}$ Ωcm upon treatment at 800°C, while the luminous transmittance remained high. The property evolution was connected with sintering and densification as studied by Scanning Electron Microscopy, X-ray Diffraction, X-ray Fluorescence and Elastic Recoil Detection Analysis.

## INTRODUCTION

Films of tin doped indium oxide (ITO) are able to combine high visible transparency with good electrical conductivity. They are widely used in modern technology such as for flat panel displays, solar cells, switchable and low-emissivity windows, as well as for electromagnetic shielding [1]. The most prevalent production methods for ITO films are sputtering and evaporation.

Many applications, including flat panel displays, require patterned ITO layers. The pattering is commonly achieved by etching which, however, is a time consuming and environmentally less favourable method. An attractive alternative would be to print the ITO structure directly onto a substrate.

The purpose of this work is to investigate the microstructural, optical, and electrical properties of thin films made from an ITO nanoparticle dispersion. The ultimate goal is to develop a technique allowing thin lines of ITO to be applied by printing.

## FILM PREPARATION AND STRUCTURE

ITO particles were produced by a wet-chemical method. The average primary particle diameter and crystallite sizes were both approximately 16 nm. The tin to indium atomic ratio was 5%. 1.1 μm thick films were prepared by spin-coating a dispersion of the particles onto Corning 1737 glass and $Al_2O_3$ substrates. The thickness was measured by a mechanical stylus Dektak 3030 profilometer. Post deposition sintering was carried out in the $300°C \leq T_s \leq 800°C$ range for 2 hours. The temperature was ramped by 10°C per minute.

The crystalline structure was investigated by X-ray Diffraction using a Siemens D5000 unit operating with $CuK_\alpha$ radiation. The diffractograms were consistent with an $In_2O_3$ structure (Powder Diffraction File 06-0416). Crystallite sizes were evaluated from the (222) peak of ITO by Scherrer's method [2]. For all samples only a minor shift in the peak location, as compared to $In_2O_3$ was noticed. Hence, the enlargement of the lattice parameter due to tin atom incorporation is small.

Microstructures were studied with Scanning Electron Microscopy (SEM), using a Leo 1550 instrument. Figure 1 gives a high-resolution image of agglomerated ITO nanoparticles treated at 500°C. It is obvious that the particles are loosely packed, i.e. that the relative density $\gamma$ is much less than unity. Quantitative measurements using Elastic Recoil Detection Analysis (see e.g. [3]) and X-ray Fluorescence [4] indicated that the relative density was approximately 30% for samples sintered at 300 to 500°C.

Figure 2 presents SEM micrographs for samples treated at 400, 650, and 800°C. The corresponding average particle sizes determined from these pictures are 16, 19, and 34 nm. However, at 650°C when the particles have started growing the crystallite size still remains at 16 nm. At 800°C the grain and crystallite sizes are again equal.

It is obvious that a fully dense, sintered structure has not yet been reached at 800°C. According to conventional sintering theory [5], the grain growth severely slows down the sintering rate.

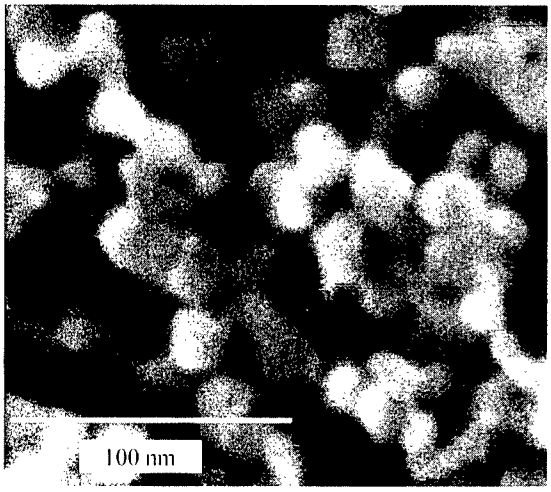


**Figure 1**: High-resolution SEM image of nanoparticle-based ITO film, heat treated at 500°C.

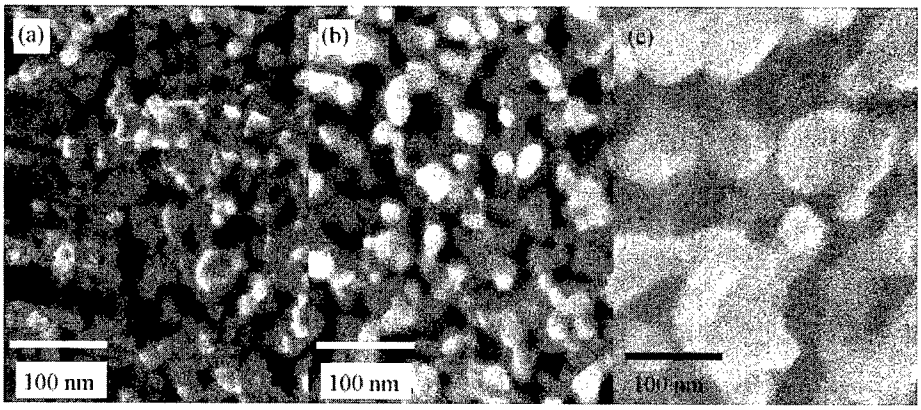


**Figure 2**: SEM images of nanoparticle-based ITO films sintered at 400°C (a), 650°C (b) and 800°C (c).

## OPTICAL AND ELECTRICAL PROPERTIES

Spectral normal transmittance ($T$) and near-normal reflectance ($R$) were measured in the $300 \leq \lambda \leq 2500$ nm wavelength range on a Perkin Elmer Lambda 9 spectrophotometer equipped by an integrating sphere. The resistivity ($\rho$) was calculated from resistance values measured by a square-probe. The data were taken on samples that had aged in room temperature and ambient atmosphere for several months. This generally means that the value of the resistivity has increased by a factor three, as compared to newly sintered samples. No effect of the specific substrate material was noticed.

Figure 3 illustrates $T(\lambda)$ and $R(\lambda)$ for five different sintering temperatures. It is found that $T(\lambda)$ is high across the $400 < \lambda < 700$ nm interval, pertinent to luminous radiation, and significant changes occur only at 800°C. Values of the luminous transmittance $T_{lum}$, determined by integrating over the sensitivity of the eye, are reported in Figure 4. Clearly, $T_{lum}$ exceeds 90% except when the sintering temperature is 800°C.

The magnitude of the resistivity drops monotonically, as the sintering temperature is increased, as apparent from Figure 4, and reaches $10^{-2}\Omega$cm at 800°C.

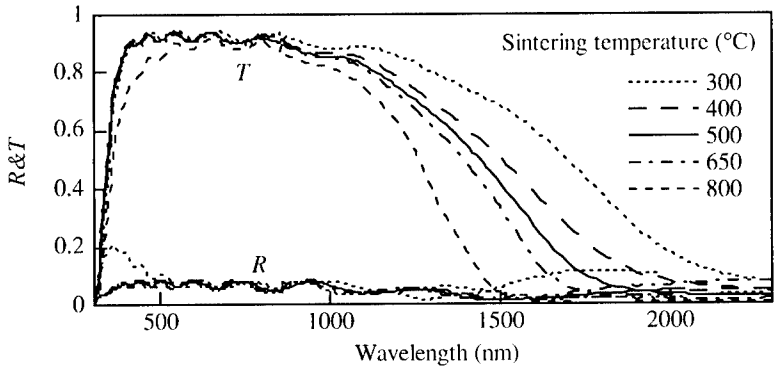


**Figure 3**: Spectral reflectance ($R$) and transmittance ($T$) for nanoparticles-based ITO films sintered at the shown temperatures.

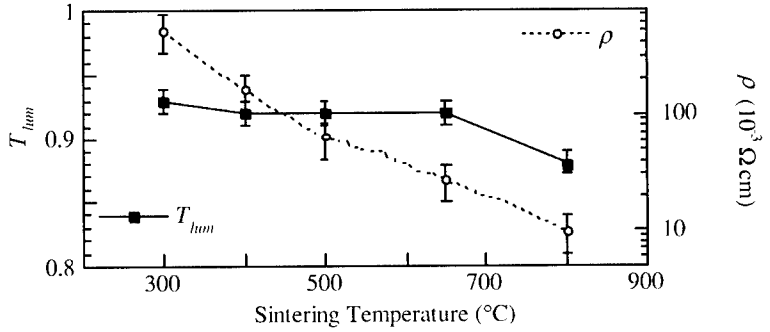


**Figure 4:** Luminous transmittance ($T_{lum}$) and resistivity ($\rho$) as a function of sintering temperature for nanoparticle-based ITO films.

## DISCUSSION AND CONCLUSIONS

We made transparent and electrically conducting ITO films by spin-coating a nanoparticle dispersion and ensuing heat treatment. A high luminous transmittance could be combined with a moderately low resistivity, whose value dropped as sintering progressed to higher temperatures. This relationship is connected with grain growth and densification, but no detailed modelling is possible yet. We note that earlier work [6, 7] on sol-gel produced ITO films have stated resistivities as low as 2 to $4 \cdot 10^{-4}$ Ωcm, which are only a factor three off from the lowest resistivity reported for highly transparent ITO layers [8, 9]. A comparison between our data and the former ones is hampered by the fact that the effects of sample ageing were not reported in the cited literature.

## ACKNOWLEDGEMENTS

This work has been financially supported by the European Union through the Brite-Euram contract BRPR-CT96-0346 ("Printracon"). Further support was obtained from Anna-Maria Lundins Scholarship Foundation, Smålands nation, Uppsala, Sweden.

Yanwen Zhang at the division of Ion Physics, The Ångström Laboratory, Uppsala University is acknowledged for the ERDA measurements.

## REFERENCES

1. R. G. Gordon, MRS Bull. **25**, 52-57 (2000).
2. M. F. Toney, in *Encyclopedia of Materials Characterization*, edited by C. R. Brundle, C. A. Evans, Jr., S. Wilson and L. E. Fitzpatrick, (Butterworth-Heinemann and Manning Publ. Co., Stoneham and Greenwich, 1992) pp. 207-208.
3. Y. Zhang, H. J. Whitlow, T. Winzell, I. F. Bubb, T. Sajavaara, K. Arstila and J. Keinonen, Nucl. Instr. Meth. B **149**, 477-489 (1999).
4. T. C. Huang, in *Encyclopedia of Materials Characterization*, edited by C. R. Brundle, C. A. Evans, Jr., S. Wilson and L. E. Fitzpatrick, (Butterworth-Heinemann and Manning Publ. Co., Stoneham and Greewich, 1992) pp. 338-348.
5. M. J. Mayo, Int. Mat. Rev. **41**, 85-115 (1996).
6. J. Liu, E. Rädlein and G. H. Frischat, Phys. Chem. Glasses **40**, 277-281 (1999).
7. Q. Wei, H. Zheng and Y. Huang, Sol. Energy Mater. Sol. Cells **68**, 383-390 (2001).
8. T. Minami, T. Yamamoto, Y. Toda and T. Miyata, Thin Solid Films **373**, 189-194 (2000).
9. A. Suzuki, T. Matsushita, T. Aoki, Y. Yoneyama and M. Okuda, Jpn. J. Appl. Phys. **40**, L401-L403 (2001).

# Synthesis and Characterization II

Mat. Res. Soc. Symp. Proc. Vol. 703 © 2002 Materials Research Society V5.2

# SOL-GEL SYNTHESIS AND CHARACTERIZATION OF NEODYMIUM-ION DOPED NANOSTRUCTURED TITANIA THIN FILMS

**Andrew Burns[(1)], W. Li[(1)], C. Baker[(1)] and S.I. Shah[(1,2)]**
[(1)]Department of Material Science and Engineering
[(2)]Department of Physics and Astronomy
University of Delaware, Newark, DE 19716

## ABSTRACT

Nd doped $TiO_2$ nanostructured thin films were prepared by sol-gel technique on quartz and Si substrates using $TiCl_4$ precursor. As-deposited amorphous films were annealed to form anatase phase in the thin films. The film grain size increased with annealing temperature. Above 800°C, rutile began to segregate and the grain size decreased slightly.

The photodegradation of 2-chlorophenol (2-CP) was studied. Doping $TiO_2$ with $Nd^{+3}$ reduced the photodegradation time. The difference in the ionic radii of $Nd^{+3}$ and $Ti^{+4}$ and the oxygen affinities of Nd and Ti were responsible for this effect. These differences help promote electron trapping, thereby increasing the lifetime of the holes which are responsible for the oxidation of 2-CP.

## 1. INTRODUCTION

Contaminants from industrial waste pose a major environmental threat to air and water. As of 1990, the EPA estimated that 10,000 U.S. public water sources contained pesticides or other contaminants linked to cancer and to kidney and nervous system damage. A method is needed to effectively neutralize these and other pollutants. Semiconductor photocatalysis offers a promising solution. Nanostructured semiconductors effectively catalyze aqueous reactions, which break down harmful organic pollutants to relatively harmless constituent chemicals.

Semiconductor photocatalysis takes advantage of the valence/conduction bandgap specific to semiconductor molecules. Incoming photons with energies at or above the bandgap will cause valence electrons to become excited and move to the conduction shell, leaving holes in the valence band. These excited charge carriers can react with molecules adsorbed on the semiconductor surface, thus acting as catalysts [1]. There are several competing effects, which limit the effectiveness of the catalysts. Most of the activated charge carriers will undergo recombination before reaching the surface to interact with adsorbed molecules. Up to 90% of the generated carriers are lost within a nanosecond of generation. As the grain size decreases, the probability of volumetric recombination also decreases, along with creating greater surface area for adsorption, thus making nanostructured systems particularly viable. However, there is an optimum in the particle size. As the particle size decreases, the probability of surface recombination increases, thereby limiting the minimum particle size.

Among the most viable nanoparticles for photocatalysis applications is titanium dioxide. $TiO_2$ is stable in aqueous media and is tolerant of both acidic and alkaline solutions. It is inexpensive, recyclable, reusable and relatively simple to produce. It also forms nanostructures more readily than other catalysts. Furthermore, its bandgap

includes the redox potential for the $H_2O/•OH$ reaction (-2.8V), thus allowing degradation of many organic compounds [2]. Unfortunately, the large (3.2 eV) bandgap of $TiO_2$, lies in the UV range, so that only 5-8% of sunlight photons have the requisite energy to activate the catalyst. A visible light ($\lambda$ = 400-800nm) catalyst would be much more effective and efficient.

There are several ways to increase the efficiency of $TiO_2$ as a catalyst. Decorating the particle surface with noble metals increases the surface charge transfer by stabilizing the electron-hole pairs once they reach the catalyst surface. Another option is sensitization in which catalyst is coated with a lower-bandgap material (organic dyes, CdS, etc.) which, upon activation, creates electron-hole pairs which can be transferred to the host $TiO_2$ and made available for photocatalysis. A related field of interest is photovoltaics, which uses the principle of dye sensitized $TiO_2$ [3]. Unfortunately, all of the known sensitizers are toxic or unstable in aqueous medium, thus making them inappropriate for application in photocatalysis. Doping the catalyst with certain metal ions can increase its effectiveness by introducing trapping sites. Trapping of electrons or holes at these sites effectively increases their lifetime and, therefore, the probability that they will reach the surface without suffering recombination and participate in the desired photocatalysis reaction. Some possible dopant ions include $Nd^{+3}$, $Cr^{+3}$, $Pd^{+4}$ and $Fe^{+3}$. Selection of the dopants depends on the reaction of interest. Not all dopants work efficiently for all reactions. For example, $Fe^{+3}$ works well for the catalysis of $CHCl_3$ [4] but not for 2-chlorophenol [5].

This study describes the preparative methodology used in making $TiO_2$ nanostructured thin films on quartz substrates via sol-gel method. The purpose of this study was to determine the effects of preparation conditions and Neodymium dopant concentration on nanostructured thin film titania. Effects on the physical and photochemical properties are investigated.

## 2. EXPERIMENTAL PROCEDURES

The Neodymium-doped $TiO_2$ nanostructured thin films were synthesized from titanium tetrachloride (Fluka 98%) and Neodymium (III) acetylacetonate hydrate (Aldrich) precursors in ethanol (Pharmco 200 Proof) by the sol-gel method previously described [6]. The Nd-precursor was massed to yield the desired molar ratios with $TiO_2$ and sonicated in 20ml ethanol to yield a homogenous opaque purple solution. 2 ml of $TiCl_4$ was added drop-wise to this solution. The reaction was carried out at room temperature under a fume hood due to the large amount of HCl gas evolved in this reaction. The product was allowed to rest until all HCl gas had dissipated, leaving a transparent, slightly viscous, yellow solution. This solution was allowed to evaporate for several hours to remove excess ethanol.

For physical and compositional measurements, quartz substrates and Boron (P-Type) doped silicon wafers (VSI) were dip coated in the solution and removed at approximately 2cm/min. For photodegradation experiments, 1" x 10" quartz tubes were coated by a similar method. These films were allowed to air dry in a desiccator (to avoid hydrolysis) overnight, followed by calcination in a stainless steel tubular furnace operating between 500° and 875°C under flowing $O_2$. Crystal growth was analyzed via X-ray diffraction and SEM.

Structural characterization of the doped and undoped $TiO_2$ samples was carried out by X-ray diffraction (XRD). $\theta$-$2\theta$ scans were recorded using Cu $K_\alpha$ radiation in a Rigaku D-Max B diffractometer equipped with a graphite crystal monochromator. Precise $2\theta$ positions and the full width at half maxima of the diffraction peaks were obtained by using XFIT software [7]. Compositions of the samples were determined by X-ray photoelectron spectroscopy (XPS) and energy dispersive X-ray spectroscopy (EDS). A SSI-M Probe XPS was used employing Al $K_\alpha$ exciting radiation. In addition to the survey scans, high resolution scans in the Ti 2p, Nd 4d, O 1s, and C 1s regions were also recorded. The Ti 2p and dopant 4d regions were used to measure the composition of the nanoparticles and to ascertain the valence states of Ti and the dopant. The doping concentration in $TiO_2$ was also confirmed by a JEOL energy dispersive x-ray spectrometer using a 20.0keV electron beam for X-ray excitation. The measurement of average particle size and surface morphology were performed by means of Scanning Electron Microscopy (SEM) in a JEOL SEM operating at 15.0 kV.

Photodegradation experiments were performed in the photocatalytic reactor system. This bench-scale system consisted of a cylindrical Pyrex-glass cell, 12 cm inside diameter and 30 cm high, with an inside reflective surface. A 100 Watts Hg lamp was used which was immersed in the solution with the cold air-cooling jacket. The maximum energy emission of UV at the wavelength of 365 nm was achieved in 4 minutes after the lamp was turned on. At the cooling jacket, an energy density of 5.3 $mW/cm^2$ was measured and the photon flux was calculated to be $4.42 \times 10^{-4}$ Einstein/min. An aqueous solution (1000 mL) of 2-CP and the quartz tube coated with 10 mg $TiO_2$ nanoparticles were placed in the photoreactor cell. A magnetic stirrer was used in the suspension and $O_2$ was supplied through compressed air for the oxidation reaction. During illumination, the pH value of whole suspension was controlled at 9.5. After illumination, samples were collected at regular intervals in a test-tube and each sample suspension was filtered by 0.2-$\mu$m filter and then analyzed by high performance liquid chromatograph (HPLC).

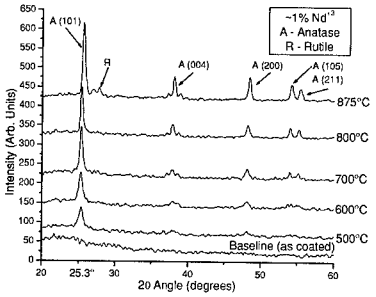


Fig.1. XRD patterns of as-deposited and annealed Nd-doped $TiO_2$ nanostructured thin films.

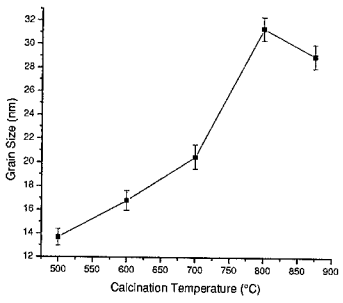


Fig.2. Grain size of Nd-doped $TiO_2$ films as a function of the calcination temperature.

The total organic carbon (TOC) of a sample solution was measured at constant irradiation time intervals using a DC-190 high temperature TOC analyzer. The $Cl^-$ ion was analyzed by ion chromatograph (Dionex Bio LC Chromatography) equipped with an electrochemical detector and a Dionex PAX-100 metal-free anion column (25 cm long, 4.6 mm I.D.). The eluent solution was a mixture of 80 % $H_2O$, 10% acetonitrile and 10% 191-mM NaOH. The flow rate was 1 mL/min and the injection loop volume was 50 µL. The activity of the photocatalytic decomposition of 2-CP was again estimated from the yield of carbon dioxide, determined gravimetrically as $BaCO_3$, from the yield of carbon dioxide as decreasing results of electric conductivity for $Ba(OH)_2$ solution. $HCO_3^-$ in a sample solution was measured by ion and liquid chromatography.

## 3. RESULTS

Figure 1 shows the X-ray diffraction pattern obtained from films grown on quartz substrates and annealed at temperatures ranging from 500 °C to 875 °C. The as-grown thin film was amorphous and did not show and x-ray structure. From 500°C to 700°C only peaks related to anatase structure were evident. Above 800°C, films contained a mixture of both the anatase and rutile phases of TiO2. The anatase (101) peak was used to determine the grain size by Scherrer's formula [8]. The results of the grain size analysis are presented in Fig. 2. The grain sizes increases at first, as the calcination temperature is raised from 500°C to 800°C and then decreases slightly as the calcination temperature is further raised above 800°C. The grain size ranges between 14 to 30 nm. The initial increase in grain size with temperature is as expected. Slight decrease in the grain size above 800°C correlates with the formation of rutile phase. Such grain size decrease has been reported previously and explained in terms of the intragranular rutile segregation in the anatase matrix [9].

No Nd related phases were observed by the x-ray diffraction analysis. This suggests that there is no Nd segregation in amounts large enough to be detected by XRD. Most of the Nd resides as substitutional or interstitial impurity.

The surface structure of the films was analyzed by SEM, as shown in Fig. 3. The particle sizes found by SEM generally concur with those determined by XRD, though some agglomeration is apparent. The surfaces of the samples are flat with no noticeable protrusions commonly associated with dip coating methods.

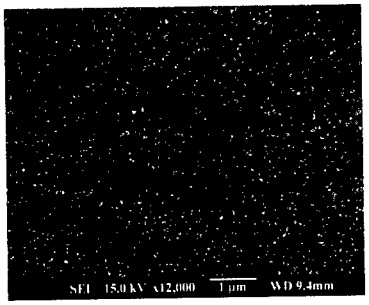


Fig. 3. SEM micrograph of the Nd-doped $TiO_2$ film surface.

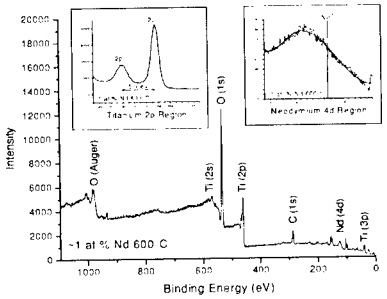


Fig. 4. XPS survey and high resolution Ti 2p and Nd 4d regions.

The valence state and the cation composition in the films were determined by X-ray photoelectron spectroscopy and energy dispersive spectroscopy. Fig. 4 shows the XPS survey for a Nd doped sample. Only peaks associated with Ti, O and Nd were observed. Nd concentration was measured to be about 1 at%. The inserts in Fig. 5 are the magnified Ti 2p and Nd 4d regions. The Ti 2p region shows two peaks located at 458.5 eV and 464.2 eV, respectively. The peaks for metallic $Ti^0$ are expected at 455 ($2p_{3/2}$) and 459 ($2p_{1/2}$) eV [10]. The shifts in Ti ($2p_{3/2}$) and Ti ($2p_{1/2}$) peak positions are due to the presence of tetravalent $Ti^{4+}$, as expected in $TiO_2$. The change in the separation between the Ti ($2p_{3/2}$) and Ti ($2p_{1/2}$) peaks is also consistent with the formation of $TiO_2$ [10,11].

The analysis of the Nd 4d region is relatively problematic due to the low concentration; however, the peak is shifted from the metallic position indicating Nd-O bonding. The detailed analysis of this peak is currently being carried out. The composition of the cations was confirmed by EDX analysis.

The photodegradation experiments were carried out on samples doped with about 1% Nd. The activities for the photodegradation for 2-CP are presented in Fig. 5. The figure also shows the photoactivity of the undoped Degussa P25 standard. The results show that the activities for the photodegradation of 2-CP have been enhanced with the addition of Nd. The time of 90% destruction of 2-CP has been reduced to 25 minutes from 60 minutes in the case of Degussa P25. Assuming that the fraction of absorbed photons by $TiO_2$ is 1, the apparent quantum yields can be calculated. The apparent quantum yields are shown in Table I. The quantum yield of 2-CP suspension with Nd doped $TiO_2$ catalyst is almost 2.5 times that of Degussa P25.

For the oxidation of 2-chlorophenol, the trapping of electrons is critical. In nanostructured $TiO_2$ thin films, electron trapping reduces surface recombination and allows holes to diffuse to the particle surface and participate in the oxidation reaction. Any dopant that effectively increases the localized positive charge will improve the oxidation of chlorophenol. The effective ionic radii of $Nd^{3+}$ and $Ti^{4+}$, are 0.983 Å and 0.605 Å, respectively [12,13]. The large difference in the ionic radii causes dilation of the lattice and localized charging. The high oxygen affinities of Nd cause a strong

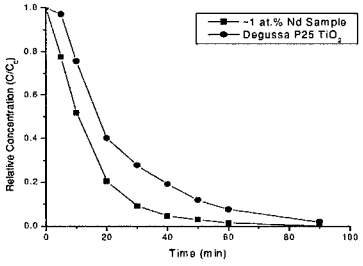


Fig. 5. 2-CP photodegradation with Nd-doped $TiO_2$ and Degussa P25 standard $TiO_2$.

**Table I: Photodegradation Analysis**

| Catalyst | Initial Rate $10^6 \cdot R_{in}$ (mol/min) | Photon Flux $10^4 R_{o_{(365)}}$ (Einstein/min) | Quantum Yield $-10^2 \Phi_{2CP} = R_{in}/R_{o_{(365)}}$ |
|---|---|---|---|
| ~1 at.% Nd Dopant | 15.5 | 4.42 | 3.5 |
| Degussa P25 | 11.7 | 4.42 | 2.7 |

dopant-oxygen bond. This effectively creates a localized positive charge around Ti and/or forms an oxygen vacancy. Both of these possibilities help form electron traps and increase the lifetime of holes.

## 4. CONCLUSION

We have prepared Nd doped $TiO_2$ nanostructured thin films on quartz and Si substrates by standard sol-gel technique using $TiCl_4$ as precursor. As-deposited films were amorphous and required a post-deposition calcination. Calcination caused anatase formation. The anatase grain size grew with calcination temperature. Above 800°C, rutile started to segregate from the anatase phase and the anatase grain size decreased slightly.

Photocatalysis measurement on the degradation of 2-CP indicated a reduction in the degradation time by the addition of Nd to $TiO_2$. This reduction is related to the difference in the ionic radii of $Nd^{+3}$ and $Ti^{+4}$ and the oxygen affinities of Nd and Ti. The larger $Nd^{+3}$ ionic radius causes localized charge perturbations and the higher oxygen affinity of Nd induced the formation of oxygen vacancy. Both these effects help promote electron trapping, increasing the lifetime of the holes which are responsible for the oxidation of 2-CP.

## 5. REFRERENCES


1. D. Beydoun, R. Amal, G. Low, S. McEvoy, Journal of Nanoparticle Research 1: 439-458, Kluwer Academic Publishers, Netherlands
2. Aruna 1996. Journal of Materials Synthesis and Processing **4**(3), 175-179.
3. U. Bach, D. Lupo, P. Comte, J.E. Moser, F. Weissortel, J. Salbeck, H. Spreitzer, and M. Gratzel, Nature **395**, 583 (1998).
4. Z. Zhang, C. Wang, R. Zakaria, and J. Ying, J. Phys. Chem. B **102**, 10871 (1998).
5. W. Li, S. Ismat Shah, C.-P. Huang, O. Jung and C. Ni, to be published in J. Appl. Phys.
6. Y. Zhou, C.Y. Wang, H.J. Liu, Y.R. Zhu, Z.Y. Chen, Materials Science and Engineering B**67**, 95 (1999).
7. Freeware form http://www.ccp14.ac.uk/tutorial/xfit-95/
8. B.D. Cullity, Elements of X-Ray Diffraction (Addison-Wesley, Menlo Park, CA 1978).
9. L.H. Edelson and A.M. Glaeser, J. Amer, Ceram. Soc. **71**, 225(1988).
10. C.D. Wagner, W.M. Riggs, L.E. Davis, J.F. Moulder, and G.E. Muilenberg (Eds), Handbook of X-ray Photoelectron Spectroscopy (Perkin-Elmer corporation, 1979).
11. S.K. Sen, J. Riga, and J. Verbist, Chem. Phys. Lett. **39**, 560 (1976).
12. R.D. Shannon, Acta Crystallogr. Sect. A **32**, 751 (1976).
13. R.D. Shannon and C.T. Prewitt, Acta Crystallogr. Sect. B **25**, 925 (1969).

Mat. Res. Soc. Symp. Proc. Vol. 703 © 2002 Materials Research Society V5.4

# Insight into the Formation of Ultrafine Nanostructures in Bulk Amorphous $Zr_{54.5}Ti_{7.5}Al_{10}Cu_{20}Ni_8$

André Heinemann[2], Helmut Hermann[1],Albrecht Wiedenmann[2], Norbert Mattern[1], Uta Kühn[1], Hans-Dietrich Bauer[1], Jürgen Eckert[1]
[1]Institut für Festkörper- und Werkstofforschung Dresden,
PF 27 00 16, D-01171 Dresden, Germany
[2]Hahn-Meitner-Institut Berlin, Glienicker Straße 100,
D-14109 Berlin, Germany

## Abstract

Bulk amorphous $Zr_{54.5}Ti_{7.5}Al_{10}Cu_{20}Ni_8$ is investigated by means of small-angle neutron scattering (SANS), differential-scanning calorimetry (DSC), high-resolution electron microscopy (HREM) and other methods. The formation of ultrafine nanostructures in the glassy phase is observed and explained by a new model. Structural fluctuations of randomly distributed partially ordered domains grow during annealing just below the glass transition temperature by local re-ordering. During annealing the DSC gives evidence for a increasing volume fraction of the locally ordered domains. At high volume fractions of impinging domains a percolation threshold on the interconnected domain boundaries occurs and enhanced diffusion becomes possible. At that stage SANS measurements lead to statistically significant scattering data. The SANS signals are analyzed in terms of a model taking into account spherical particles surrounded by diffusion zones and interparticle interference effects. The mean radius of the nanocrystalline particles is determined to 1 nm and the mean thickness of the depletion zone is 2 nm. The upper limit for the volume fraction after annealing at 653 K for 4 hours is about 20 %. Electron microscopy confirms the size and shows that the particle are crystalline.

## Introduction

The mechanisms of nanostructure formation in amorphous precursors are of much current interest. According to the variability of chemical composition, short- and medium-range order, and preparation methods of metallic glasses [1], these materials show a great variety of physical and chemical properties. One of these properties is the ability of some amorphous alloys (e.g., Finemt, see [2]) of transforming into a nanostructured state during annealing. Both from the technological and physical point of view, it is important to understand the processes responsible for the transition from the homogeneous amorphous state into the nanostructured one. Several possible mechanisms of the formation of nanoscale structures in metallic glasses have been discussed: preformation of aggregates in the liquid state [3, 4, 5, 6], extremely high nucleation rate accompanied by decreased growth rate [7, 8], spinodal decomposition [9], decomposition within the amorphous state and subsequent crystallization of at least one of the amorphous phases [8, 10], homogeneous nucleation taking into account linked stochastic fluxes of interfacial attachment and diffusion in the cluster neighborhood [11], and a model considering inhibitors accumulating at the surface of the nanocrystals to be responsible for limited growth [12]. Recently, ultrafine nanostructures have been observed in Zr-based bulk

amorphous alloys. Crystal-like clusters [13] and nanocrystals [14] with mean grain size of 2 nm were detected and analyzed by means of $X$-ray diffraction(XRD) and HREM, respectively. It was shown [15, 16, 17] that partial crystallization of such alloys on a nanometer scale may have considerable influence on mechanical properties of the material. Here we

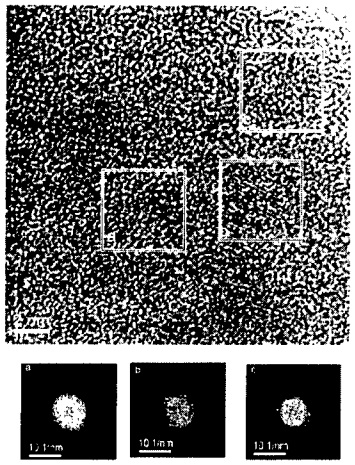

Figure 1: HREM image of the sample annealed for 240 min. at 653 K. For the marked areas *a*), *b*) and *c*) two dimensional fast fourier transformations were shown in separate pictures. In *b*) and *c*) a nanocrystal is visible.

examine the evolution of ultrafine nanostructures in bulk amorphous $Zr_{54.5}Ti_{7.5}Al_{10}Cu_{20}Ni_8$ during annealing in the glass transition range in order to find out the mechanisms of the structure formation.

## Sample preparation and thermal treatment

The samples were prepared by a single roller melt spinning technique. By rapid quenching from the melt one obtains ribbons with a width of about 5 mm and a thickness of about 50 $\mu$m). The obtained as-prepared samples are homogeneous with respect to HREM and SANS. The SANS signal of the as-quenched state which contains only statistical noise was shown in figure 6. From this material a time-series of samples was prepared by annealing at 653 K for 15 min up to 240 min. The used temperature is slightly below the glass temperature $T_g$ which is characterized by the estimates of the $T_g$(onset)= 660 K and $T_g$(inflection point)= 680 K temperatures of the glass transition region shown in figure 2. The thermal characterizations were made by using a Perkin-Elmer DSC 7 calorimeter at a heating rate of 40 K/min. The DSC plot for the as-prepared sample in a temperature range from 500 K to 850 K is shown in figure 2. Two exothermic events between 695 K and 740 K and above 740 K lead to an heat release of 19.7 J/g and 14.0 J/g, respectively. Annealing up to 873 K

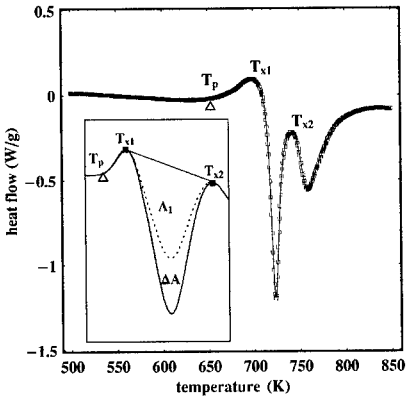


Figure 2: The heat flow measured with DSC technique. The DSC scan (40 K/min) shows two exothermic events. The total heat release between $T_{x1} = 695$ K and $T_{x2} = 740$ K is 19.7 J/g. For the second event ($T > 740$ K) one obtains 14.0 J/g. The annealing temperature of the samples was $T_p = 653$ K.

lead to a completely crystallized state with particles of about 50 $\mu$m in diameter. All the ultrafine nanostructures occur only below 740 K. The preparation temperature of 653 K was chosen because pre-experiments indicated that the time scale of transformation was good for our observations. The embedded picture in figure 2 outlines the procedure of the determination of the heat releases for the annealed samples. The difference (proportional to $\Delta A$ in the picture) between the heat release measured for the as-quenched sample (19.7 J/g) and the heat release obtained for the annealed one (proportional to $A_1$) was used to define the transformed volume fraction during this exothermic event in figure 5. The fractional heat releases for the sample series with different annealing times is used in figure 5 to describe the transformation kinetics.

## Small-angle neutron scattering

The SANS experiments were carried out at the small-angle scattering facility V4 at the Berlin Neutron Scattering Center (BENSC). To characterize the global time evolution of the SANS signal on can calculate the scattering invariant $I_2$ defined (see e.g. [18]) by

$$I_2 = \int_0^\infty dq\, q^2 \left(\frac{d\sigma}{d\Omega}\right) \sim \sum_{i=1}^{N} \Delta q_i\, q_i^2 \left(\frac{d\sigma}{d\Omega}(q_i) - \left(\frac{d\sigma}{d\Omega}\right)_\infty\right) \quad . \tag{1}$$

The result of this analysis is shown in figure 3. The error bars arise from the experimental errors of $d\sigma/d\Omega(q_i)$ and the confidence interval of the background fit $(d\sigma/d\Omega)_\infty$. For two-phase systems $I_2$ is given by $c(1-c)\,\Delta\eta^2$ where $\Delta\eta$ is the scattering length density contrast

of the two phases and c the volume fraction of one of the phases. The behavior of $I_2$ versus annealing time differs in a fundamental manner from the DSC (see figure 5) and XDR results [13]. In the bound of the errors there is no change of the invariant during the annealing procedure up to 90 min. In contrast to the evolution of the heat release shown in figure 5. After 90 min. the heat release at this stage of the annealing process reaches over 70 %. This means the transformation process responsible for the observed heat release is not detectable in SANS. Then the value of $I_2$ changes significantly for 120 min, 180 min and 240 min annealing. This gives a hint to the presumption that a new kind of transformation process was actuated. This confirms to a significant change in the behavior of the heat release curve (see figure 5) and the viscosity curve (see figure 7) at that time.

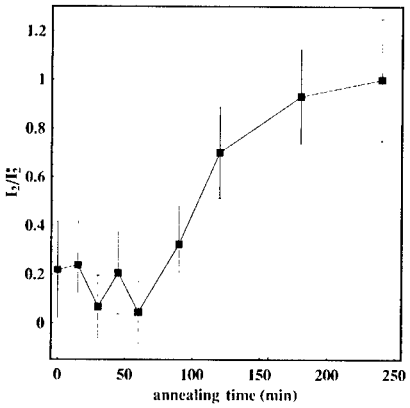


Figure 3: Evolution of the SANS scattering contrast versus annealing time. The scattering invariant $I_2^*$ is equal to $(34 \pm 9) * 10^{-10}$ nm$^{-4}$ sr$^{-1}$.

A qualitative analysis of the SANS data for the 120 min., 180 min. and 240 min. annealed samples is made with a model of polydisperse spherical particles with diffusion zones [19]. To take into account interparticle interferences we combine the Percus-Yevick approach according to [20] and our model in the following way:

$$I(q) = S(q, R_{hc}, c_p)|F(q, \mu, \sigma, l)|^2 \quad . \tag{2}$$

$|F(q, \mu, \sigma, l)|^2$ describes the contribution of the isolated gamma distributed spherical particles with diffusion zone where $\mu$ and $\sigma$ are mean value and root mean square of the gamma distribution, respectively, and $l$ characterizes the dimension of the diffusion zone (for details see [19]). $S(q, R_{hc}, c_p)$ is the contribution of the hard-core system with hard-core radius $R_{hc}$ and volume fraction $c_p$ and can be expressed in the Percus-Yevick approach as

$$S(q, R_{hc}, c_p) = \frac{c_p}{1 + c(2qR_{hc}, c_p)} \quad . \tag{3}$$

Table 1: Results of the least-square fit of the SANS data obtained from the 653 K / 240 min state. Mean values and limits of the 95% confidence intervals.

| parameter | $\mu$ (nm) | $\sigma$ (nm) | $l$ (nm) | $R_{hc}$ (nm) | $c_p$ (%) |
|---|---|---|---|---|---|
| **mean value** | **0.96** | **0.34** | **2.2** | **5.2** | **17.2** |
| lower limit | 0.85 | 0.31 | 1.6 | 3.7 | 7.0 |
| upper limit | 1.07 | 0.37 | 3.0 | 5.7 | 21.3 |

Here $c(x, c_p)$ is a function which can be calculated analytically (see e.g. [21, 22]). The experimental SANS data are fitted by equation (2) using a non-linear least-square routine. The results are given in table 1 and the quality of the fit was demonstrated in figure 6. The upper and lower bounds of the confidence intervals are not symmetric to the mean value. This is a consequence of the non-linearity of the fit. The confidence interval is chosen so that the true value of the parameter fitted can be found within this interval with a probability of 95%. The spatial distribution of the scattering length density for one particle with the Radius $\mu$ is shown in figure 4. It was shown [22] that for the samples annealed for

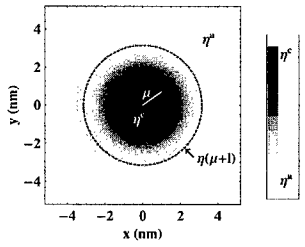


Figure 4: Radial profile of the scattering length density for a given particle.

120 min., 180 min. and 240 min. it is essential to use a model with diffusion zones to fit the data. The influence of the interparticle interferences together with a simple two-phase model (e.g. polydisperse spheres) cannot explain the SANS data. In our model this interferences permitted a estimate of the volume fraction of the particles. This estimate is crowing from about 7 % in the 120 min. case up to 17 % in the 240 min. case. The results of the particle sizes were confirmed by HREM in figure 1. The HREM images were taken with the 300 kV microscope TecnaiF30-STwin (FEI) at IFW Dresden after preparation in the Rapid Etching System RES010 (Bal-Tec) with flat striking $Ar^+$ ions. The embedded FFT pictures in figure 1 additionally shows that the particles are crystalline.

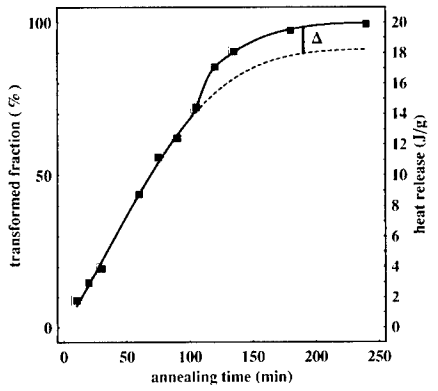


Figure 5: Time evolution of the fractional heat release during annealing. The solid line shows the theoretical curve $h_a(t) + h_b(t)$, the dashed line shows $h_a(t)$ for $t \geq h_b$.

# Results and Discussion

The different behavior for the evolution of the SANS curves versus annealing time and the DSC curves guided to a model with two different processes during nanocrystallisation. The presented interpretation is based on the idea that the structure of a supercooled liquid alloy is heterogenous. Recent experimental (see e.g. [23, 24, 25]) and theoretical (see e.g. [26, 27, 28, 29]) workings discuss the influence of this assumption to physical properties. It might be expected that the reason for the type of nanostructuring described here is related to properties of the supercooled liquid state, especially to dynamical heterogeneities. We assume that in the supercooled liquid state different local configurations exists with different local free energy and correlation length. Annealing with a proper temperature enables cluster having a suitable free energy start to grow by rearranging of atoms or atom-groups at their surfaces. We state that the heat release in the DSC measurements up to about 100 min. rises from this process. If the growing clusters are distributed randomly in the material and all clusters participate in the growing process the well known Kolmogorov-Johnson-Mehl-Avrami (KJMA) model (see [30, 31, 32]) can be used to explain the growing of the clusters. If $v_a$ is the transformed volume fraction the KJMA model predict a time evolution of this parameter to:

$$v_a = v_a^{max} \left(1 - \exp\left\{A_0(1 - (1 + \frac{v\,t}{r_0})^3)\right\}\right) \quad . \tag{4}$$

Here $1 - \exp\{-A_0\}$ is the volume fraction of the activated clusters at $t = 0$ and $r_0$ their mean radius at the beginning of growth. $v$ describes the velocity of the cluster surface propagation during growing and in a first approximation $v$ is supposed to be constant. In equation (4) it is supposed that the activated clusters have a finite size at the beginning of the growing process. If we assume, that the heat release $h_a$ is proportional to the transformed volume

fraction $v_a$ we can fit the DSC data with following equation.

$$h_a = h_a^{max}\left(1-\exp\left\{A_0(1-(1+\frac{v\,t}{r_0})^3)\right\}\right) \quad (5)$$

The result is shown in figure 5 as a dashed line.

For annealing times greater than approximately 100 min we learned from the SANS results, that a new process should occur to explain the increase of $I_2$ and the predicted particles with a mean radius of about 1 nm. The essential diffusion zone around the particles places us in the position to postulate the start of a diffusion controlled process after about 100 min. If we assume here again, that the heat release is proportional to the transformed volume fraction we can approximate its contribution to the heat release also by a KJMA expression.

$$v_b = c_b^{max}\left(1-\exp\left\{(1-a(t-t_b)^{3/2})\right\}\right) \quad \text{for} \quad t \geq t_b \quad (6)$$

$$h_b(t) = h_b^{max}\left(1-\exp\left\{(1-a(t-t_b)^{3/2})\right\}\right) \quad \text{for} \quad t \geq t_b \quad (7)$$

A least-squares fit of $h_a + h_b$ to the DSC data shown in figure 5 as a solid line. A statistical analysis reveals the parameter values $h_a^{max} = 17.7$ J/g , $h_b^{max} = 2.0$ J/g, $A_0 = 0.35$, $t_b = 96$ min, $vt_b/r_0 = 0.67$ where the 95 % confidence intervals are in the range of 10 % to 20 % of the expectation values. It is obvious that the introduction of diffusion controlled mechanism

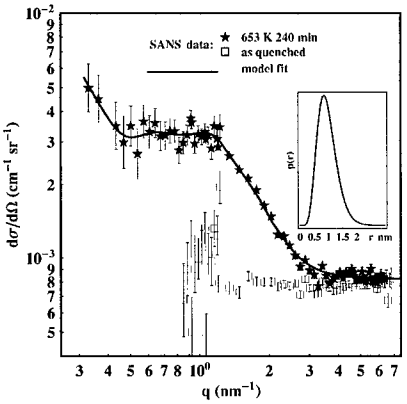


Figure 6: Sans data obtained from the as-prepared state and the annealed sample (240 min at 653 K). The solid line is a theoretical curve obtained with a model of polydisperse spherical particles with diffusion zones. The embedded picture shows the fitted probability density $p(r)$ of the particle sizes.

at a time $t_b$ can explain both the results of the DSC experiment and the results from the SANS experiment. The question of physical background of this process arises naturally. We assume

that large locally ordered clusters become unstable during the growth. This assumption is suggested by theoretical and experimental results on the stability of clusters of atoms. It has been shown that icosahedral arrangement of atoms is energetically advantageous for small clusters consisting of several hundreds of atoms whereas for larger particles crystalline order is more favorable (see e.g. [33]). It is reasonable to assume the existence of icosahedral local packing in the present metallic glass since in similar alloys such as $Zr_{65}Cu_{17.5}Ni_{10}Al_{7.5}$ the formation of icosahedral phases was observed experimentally [34, 35]. Additionally at this stage of the process the packing fraction is so high that due to diffusion processes at the impinging surfaces the transformation into the crystalline state can be promoted. The change of the local chemical composition or their local boundary conditions can than lead to the scattering contrast increase observed by SANS. The onset of diffusion and/or the formation of nanocrystallites should be visible in the behavior of the shear viscosity $\gamma$ of a sample subjected to isothermal annealing. Figure 7 shows the result of the corresponding

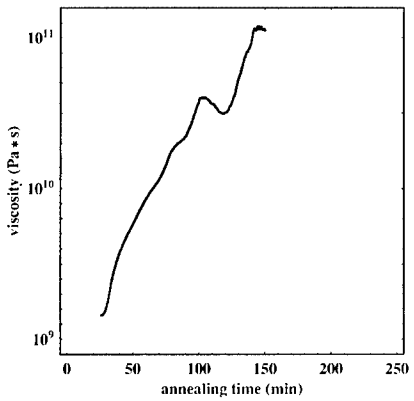


Figure 7: Evolution of the shear viscosity versus annealing time.

experiment carried at a constant uniaxial load using a Perkin-Elmer DSC 7E. There is a continuous increase of $\gamma$ from the beginning of the thermal treatment at 653 K up to about 90 min. This increase can be understood as a decrease of the mean free $\bar{v_f}$ volume according to the expression

$$\gamma(t) \propto \exp\left\{\frac{v_c}{\bar{v_f}}\right\} \quad \text{with } v_c \text{ a critical value of } \bar{v_f} \tag{8}$$

In the interval from 100 min to 130 min annealing time the curve shows a significant dip indicating a temporarily increase of the mean free volume according to equation 8. So that also the shear viscosity recorded a significant change of its behavior at the same stage as SANS and DSC do. In this model the improvement of the medium-range order during annealing in the samples at constant properties of the next-nearest neighbor shell can be understood as the increase of the correlation length of local icosahedral packing realized by re-arranging

of small icosahedral structure units at the cluster surface. This also may explain a decrease of the free volume and a increase of the shear viscosity according to equation 8. The evolution of the correlation length $r_{xrd}$ measured by XRD (see [13]) and its mean value of about 1.6 nm confirms this interpretation as well. We assume further on, that large noncrystalline clusters become unstable during their growth. Then the change of the chemical composition and/or their local boundary conditions lead to an transformation into the crystalline state. As mentioned above icosahedral arrangements of atoms are energetically advantageous for small clusters whereas for larger particles crystalline order is more favorable (see e.g. [33]). The volume fraction of locally ordered clusters at that stage of about 70 % leads to impinging of domains. An percolation threshold on the interconnected domain boundaries may occur and enhanced diffusion becomes possible. The SANS results were obtained under the assumption of a diffusion zone around spherical particles and a good evidences for its existence was found. All parameters obtained with the non-linear least-square fit are in a very good agreement with the results from HREM, DSC and XDR analysis. The methods together permit us to suggest a model with is in agreement with the data and theoretical considerations. Therewith this model is a contribution to explain the formation process of nanoscale structures in metallic glasses.

# References


[1] W. Klement, R. H. Willens, and P. Duwez, Nature **187**, 869 (1960).

[2] Y. Yoshizawa, J. Metastable Nanocryst. Mater. **1**, 51 (1999).

[3] F. Sommer, Z. Metallk. **73**, 72 (1982).

[4] E. Nold, G. Rainer-Harbach, P. Lamparter, and S. Steeb, Z. Naturforsch. **38**, 325 (1984).

[5] E. Nassif, P. Lamparter, and S. Steeb, J. Non-Cryst. Solids **61-62**, 319 (1984).

[6] F. E. Fujita, in *in Rapidly Quenched Metals* (North-Holland, Amsterdam, 1985).

[7] M. Calin and U. Köster, Mater. Sci. Forum **269-272**, 749 (1998).

[8] U. Köster, A. Rüdiger, and J. Meinhardt, J. Metastable Nanocryst. Mater. **1**, 9 (1999).

[9] S. Schneider, P. Thiyagarajan, U. Geyer, and W. L. Johnson, Physica B **241-243**, 918 (1998).

[10] J. F. Löffler and W. L. Johnson, Appl. Phys. Lett. **76**, 3394 (2000).

[11] K. F. Kelton, Phil. Mag. Lett **77**, 337 (1998).

[12] H. Hermann, A. Heinemann, N. Mattern, and A. Wiedenmann, Euro. Phys. Lett. **51**, 127 (2000).

[13] N. Mattern, U. Kühn, J. Neuefeind, and J. Eckert, Appl. Phys. Lett. **77**, 1153 (2000).

[14] C. Fan and A. Inoue, Appl. Phys. Lett. **77**, 46 (2000).

[15] C. Fan and A. Inoue, Mater. Transactions *JIM* **40**, 1376 (2000).

[16] C. Fan and A. Inoue, C. Fan and C. Li and A. Inoue and V. Haas **61**, 3761 (2000).

[17] J. G. Wang, B. W. Choi, T. G. Nieh, and C. T. Liu, J. Mater. Res. **15**, 798 (2000).

[18] G. Porod, *Small Angle X-ray Scattering* (Academic Press, London, 1982).

[19] A. Heinemann, H. Hermann, A. Wiedenman, N. Mattern, and K. Wetzig, J. Appl. Cryst. **33**, 1386 (2000).

[20] N. W. Ashcroft and J. Lekner, Phys. Rev. **145**, 83 (1966).

[21] W. K. Bertram, J. Appl. Cryst. **29**, 682 (1996).

[22] H. Hermann, A. Heinemann, H.-D. Bauer, N. Mattern, U. Kühn, and A. Wiedenmann. J. Appl. Cryst. **34**, 666 (2001).

[23] A. Heuer, M. Wilhelm, H. Zimmermann, and H. W. Spiess, Phys. Rev. Lett. **75**, 2851 (1995).

[24] R. Böhmer, G. Hinze, G. Diezemann, B. Geil, and H. Sillescu, Europhys. Lett. **36**, 55 (1996).

[25] R. Zorn, Rev. B **5**, 6249 (1997).

[26] W. Kob, C. Donati, S. J. Plimpton, P. H. Poole, and S. C. Glotzer, Phys. Rev. Lett. **79**, 2827 (1997).

[27] C. Donati, J. F. Douglas, W. Kob, S. J. Plimpton, P. H. Poole, and S. C. Glotzer, Phys. Rev. Lett. **80**, 2338 (1998).

[28] D. Caprion and H. R. Schober, Phys. Rev. Lett. **85**, 4293 (2000).

[29] C. Kaur and S. P. Das, Phys. Rev. Lett. **86**, 2062 (2001).

[30] A. N. Kolmogorov, Izv. Akad. Nauk USSR. **2**, 355 (1937).

[31] W. A. Johnson and R. Mehl. Trans. AIME **135**, 416 (1939).

[32] M. Avrami, J. Chem. Phys. **7**, 1103 (1939).

[33] D. Holland-Moritz, J. Non-Equilibrium Processing **11**, 169 (1998).

[34] U. Köster, J. Meinhardt, S. Roos, and H. Liebertz. Appl. Phys. Lett. **169**, 179 (1996).

[35] J. Eckert, N. Mattern, M. Zinkevitch, and M. Seidel, Mater. Trans. JIM **39**, 623 (1996).

Mat. Res. Soc. Symp. Proc. Vol. 703 © 2002 Materials Research Society V5.5

# Supersonic Nanocrystal Deposition for Nanostructured Materials

W.T. Nichols[1], D.T. O'Brien[2], G. Malyavanatham[3], M.F. Becker[2,3] and J.W. Keto[1,3]

[1] Department of Physics
[2] Department of Electrical and Computer Engineering,
[3] Texas Materials Institute-Materials Science and Engineering
University of Texas at Austin, Austin, TX 78712

## ABSTRACT

We experimentally demonstrate the large scale production and controlled collection of metal and semiconductor nanocrystals by laser ablation of microparticles entrained at high density in a flowing aerosol. For silver, produced nanocrystals exhibit bimodal, log-normal size distributions. Mean particle sizes are controlled from 3-16 nm by varying the type and pressure of carrier gas as well as laser fluence. For collection, a micronozzle orifice (d = 200 μm) accelerates nanocrystals through a sonic jet into a vacuum chamber for deposition onto a room temperature substrate. We describe two regimes of deposition that depend on the nanocrystal's energy per atom on impact. Soft landings ( $E << 1$ eV/ atom) preserve the individual particle properties such as size and shape. Low energy impaction is demonstrated for CdSe in an argon carrier gas. The CdSe nanoclusters remain crystalline upon deposition and display visible photoluminescence. At higher particle impaction velocities ($E \sim 0.3$ eV/atom) nanocrystals exhibit the onset of self sintering upon impact. At high number densities, adherent, conductive lines are formed from deposited silver nanocrystals. Line widths of 33 μm FWHM are directly written onto substrates using a 200 μm diameter nozzle.

## INTRODUCTION

Cluster beam methods have been gaining increasing attention for the formation of nanoscale systems.[1] These techniques have the ability to produce and deposit both individual nanocrystals as well as thin and thick films directly from the nanocrystal jet[2]. Traditionally, however, cluster beam techniques have faced a trade off between controlling the properties of the individual deposited nanoclusters or producing significant quantities of materials. Recently our group has reported a technique known as laser ablation of microparticles (LAM)[3] which is capable of controlling the size of the nanocrystals at production rates of grams per hour. Here we demonstrate the use of this system for deposition of individual nanocrystals and their assembly into nanocrystalline thick films.

Smalley and co-workers first demonstrated laser ablation followed by supersonic expansion of the vapor to form nanoclusters with controllable properties.[4] Particle deposition using an orifice as small as 200 μm was described by Hayashi and co-workers[5] for depositing metal nanoparticles. This work first demonstrated the ability of gas jet deposition for producing nanostructured patterns. Recently, supersonic deposition of nanoparticles has been developed

extensively by Girshick and co-workers.[6-7] Their technique involves the aerodynamic focusing of nanoparticles formed in a thermal plasma into a collimated beam that supersonically impacts onto a substrate. By aerodynamic focusing, they are able to deposit macroscopic quantities of nanoparticles in a controllable manner. Though their results are quite good, the production technique lacks fine nanoparticle control and the collection technique is hindered by the use of a large nozzle (~2 mm) that requires an increased pumping capacity as well as a series of aerodynamic lenses to collimate the nanoparticle beam to sub-millimeter dimensions. The LAM technique coupled with a sonic micronozzle combines the advantage of fine nanocrystal control exhibited by laser ablation with the large quantities inherent to many aerosol processes and the controllable direct deposition of sub-millimeter patterns.

This system has been tested with silver for its applicability to conductive nanostructures and CdSe for its potential as a tunable optical device element. Previous work has characterized the nanocrystals produced by ablation of silver microparticles. In addition to silver and cadmium selenide, several other materials are being tested for various applications. Functional materials such as Terfinol-D yield adherent nanostructured thick films with magnetostrictive properties. Soft impaction of silicon and gallium nitride nanocrystals are being studied for use in nonlinear optical nanocomposites.

## SOURCE NANOCRYSTALS

The LAM system consists of a generator producing an aerosol of micron sized feedstock microparticles which are ablated by a pulsed excimer laser forming an aerosol of nanocrystals.[3] Previously, we have characterized this nanocrystal generator for the production of silver nanoparticles in argon, nitrogen and helium at various pressures[8]. Pressure was found to be an excellent parameter for tuning the size distributions to a desired mean size in the range from 6-20 nm (Fig. 1a). More detailed studies of the size distributions for silver nanocrystals showed that they exhibit bimodality with a mode due to the laser induced shock wave, at small sizes (3-6 nm) and a second surface evaporation mode at larger sizes (11-16 nm)[9]. The mass in the distribution displayed a striking shift from the surface mode to the shock mode with increasing laser fluence as seen in Fig. 1b,c.

The produced nanocrystals are sonically accelerated into a vacuum chamber for deposition onto a solid substrate. In this work we have studied the collection sub-system by utilizing a micronozzle and two different carrier gases with greatly different expansion velocities. Of special note is the compatibility of the LAM process with the use of micronozzles for collection. As discussed by Di Fonzo et al.[6] micro-expansion nozzles produce narrow beams of nanoparticles, however, due to their small diameter often become clogged. Our system has not encountered this difficulty when using nozzles as small as 150 microns, even at large deposition rates. It is believed that two factors are responsible for the large, continuous throughputs. First, we use a co-axial sheath gas to reduce radial diffusion of the aerosol. A skimmer is adjusted to accept the nanoparticle flow plus a fixed amount of the sheath gas flow to buffer the nanoparticles from the walls of the expansion nozzle. Second, LAM produces nanoparticles that are charged, thus preventing coalescence of the small particles into larger agglomerates that may cause material build up around the edges of the nozzle leading to blockage of the flow.

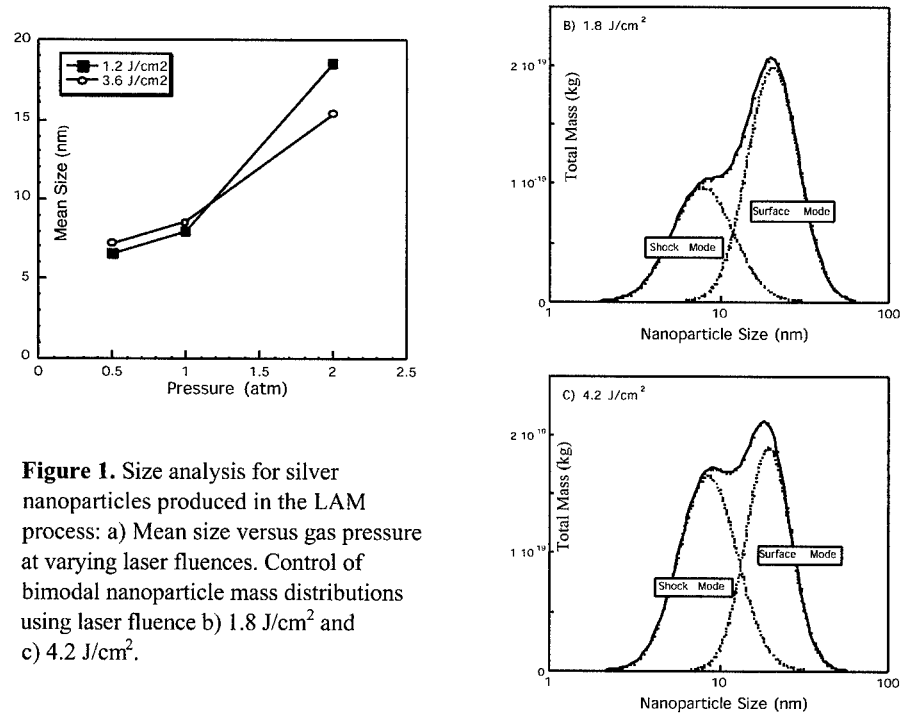


**Figure 1.** Size analysis for silver nanoparticles produced in the LAM process: a) Mean size versus gas pressure at varying laser fluences. Control of bimodal nanoparticle mass distributions using laser fluence b) 1.8 J/cm$^2$ and c) 4.2 J/cm$^2$.

## RESULTS AND DISCUSSION

### Particle Deposition

Soft landings of the produced nanocrystals are required to retain their individual properties such as size and shape. Hard impaction leads to particle agglomeration and low temperature coalescence into materials with enhanced mechanical and electrical properties due to the nano-scale grain sizes. For a given substrate and cluster type, the kinetic energy per atom determines the fate of the cluster on impact. Simulations of Hsieh et al.[10] indicate that clusters with energy much less than 1 eV per atom show little deformation on impact while near this energy significant deformation and compaction occurs.

Our nanocluster beam expands through the micro-orifice nozzle into a low pressure chamber with a pressure ratio of $10^4$. The rarefied gas flow accelerates to the limiting choked-flow velocity (He: $v_c$ = 760 m/s; Ar: $v_c$ = 240 m/s). Particles in this flow accelerate to the gas velocity within seven relaxations times[11] which corresponds to ~ 1-2 nozzle diameters for particles of 10 nm or less. The distance required for particle acceleration is less than 400 μm, well within our typical

collection distances of 1-3 mm. Therefore, we can expect the nanoclusters will impact onto the substrate surface with a kinetic energy given to good accuracy by the mass of the cluster and the velocity of the choked flow of gas through the micronozzle.

To adjust this velocity through our thin plate nozzle we have two options: increase the carrier gas stagnation temperature or use different carrier gases. Higher temperatures produce faster jets through an increase in the average kinetic energy of the gas molecules in the carrier gas. In this work we demonstrate soft and hard impaction through the use of different carrier gases. The average velocity of an ideal gas is inversely proportional to the molecular mass. A low molecular weight gas such as helium will have a high gas velocity ($v_c$ = 760 m/s) whereas heavier molecules such as argon have a lower average velocity ($v_c$ = 240 m/s). For materials like silver and cadmium selenide in argon the kinetic energy per atom is limited to 0.03 eV/atom while for helium it is up to 0.3 eV/atom. Therefore materials deposited from a helium jet have kinetic energy that is a significant fraction of the cluster binding energy and will compact on the substrate. On the other hand, materials deposited in argon are expected to land softly.

**Soft Landings (CdSe nanocrystals in Argon)**

For application as quantum dots, nanocrystals must retain their size and shape upon impaction. In addition, no defects should be generated within the nanocrystals during deposition. As discussed above, CdSe nanocrystals in an argon carrier gas impact the substrate with no more than 0.03 eV/atom, well below the binding energy of the crystal. Figure 2 demonstrates that the nanoparticles were non-agglomerated, spheroidal and remained crystalline upon impact. Note that the nanocrystal density on the surface can be controllably deposited in a fractional monolayer by adjusting the number density of feedstock in the carrier gas and the raster speed of the substrate underneath the jet. Visible luminescence was observed from CdSe nanocrystals deposited onto quartz substrates.

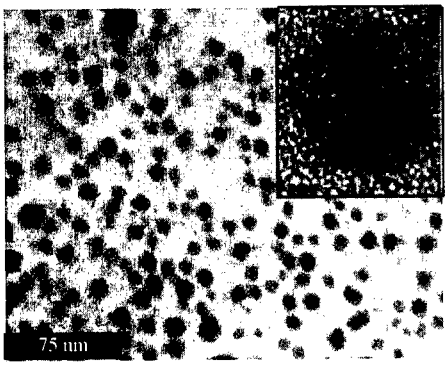


**Figure 2.** Cadmium Selenide nanocrystals deposited at low kinetic energy in argon carrier gas. The main TEM micrograph shows the overall size distribution and the inset shows a single crystalline 8 nm diameter CdSe nanocrystal.

**Hard Impacts (Ag nanocrystals in Helium)**

To demonstrate hard impaction of clusters, we ablated silver microparticles and deposited the resultant nanoclusters onto a room temperature substrate. At large velocities, the nanocrystals sintered together on the substrate as a continuous adherent film.[12] Preliminary conductivity measurements as well as cross-sectional SEM imaging of these films support the conclusion that the nanocrystals form dense, sintered compacts. By employing a micronozzle for the expansion and by using a small substrate-nozzle distance (~1mm), the width of the nanocrystal jet at the substrate can be minimized. Figure 3 shows an optical micrograph of silver nanocrystals deposited on a translated silicon wafer to controllably write lines. The height profiles of these lines can easily be made in the 10 - 100 μm range with widths of less than 80 μm FWHM. The diffuse edges of the lines are due to Brownian diffusion within the jet. To achieve sharp edged lines, a stencil mask can be used[13]. It should be noted that these lines are less than half the nozzle diameter demonstrating the effectiveness of the sheath gas both at reducing radial particle diffusion in the jet and the ability to aerodynamically focus the jet.

These films are robust and adherent when deposited on silicon wafers from a helium jet. No indication of scratch off is noted when the film is measured with the sharp profilameter scribe. This demonstrates qualitatively the onset of sintering even at room temperature. Observations of the microstructure within the deposited silver lines revealed a variation in grain structure with impaction energy. At lower cluster energies, the films were nanostructured and exhibit numerous small voids with coarsening of grains. For higher energies, better compaction was seen with fewer voids and a grain structure approaching the bulk. Films impacted from the helium jet at large deposition energies (~ 0.3 eV/atom) had improved conductivity as compared to silver films deposited in argon.

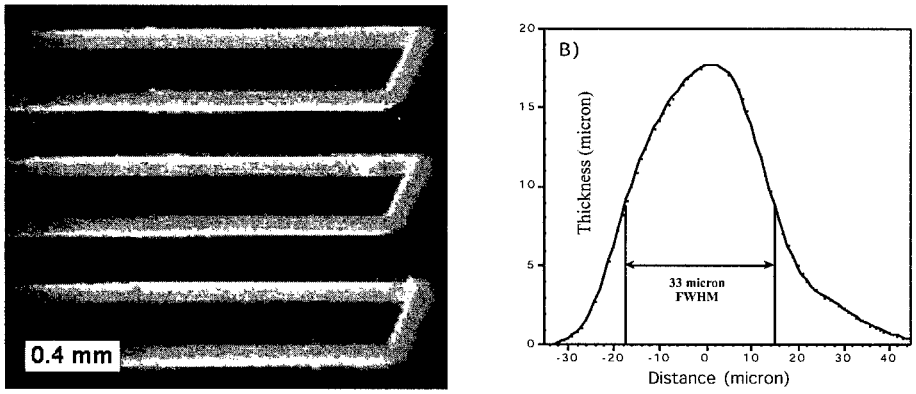


**Figure 3**. Adherent and conductive silver lines that were directly written from silver nanocrystals in a helium jet. A) Optical micrograph of a serpentine test pattern, B) Profilometer scan of a line with 33 μm FWHM and 80 μm base width.

## CONCLUSIONS AND FUTURE WORK

We have demonstrated soft impaction of CdSe nanocrystals in an argon jet and hard impaction of Ag nanocrystals in a helium jet. Aerodynamically focused silver nanoparticle jets are capable of writing patterns of narrow conductive lines with good adhesion to the substrate. Currently we are studying the variation of conductivity and film microstructure with particle kinetic energy. Luminescence studies of semiconductor nanocrystal quantum dots are underway to determine the fraction of fluorescing particles and their quantum yield. To incorporate these particles into functional optoelectronic nanocomposites, we have constructed a system with allows nanocrystal deposition as described above followed by thin film passivation with a larger band gap material by ion beam sputtering or pulsed laser deposition.

## ACKNOWLEDGMENTS

We gratefully acknowledge support from the NSF GOALI Program (grant no. CTS-9530347), the Texas Advanced Technology Program (grant no. 3658-348) and the Robert A. Welch Foundation.

## REFERENCES

1. P. Jensen, Rev. Mod. Phys., **71**, 1695 (1999) and references therein
2. For a recent review see: P. Milani and S. Iannotta, *Cluster beam synthesis of nano-structured materials*, Springer, Berlin 1999
3. W.T. Nichols, J.W. Keto, D.E. Henneke, J.R. Brock, G. Malyavanatham, M.F. Becker and H.D. Glicksman, Appl. Phys. Lett. **78**, 1128 (2001)
4. T.G. Dietz, M.A. Duncan, D.E. Powers and R.E. Smalley, J. Chem. Phys. **74**, 6511 (1981)
5. S. Kashu, E. Fuchita, T. Manabe and C. Hayashi, Japn. J. Appl. Phys., **23**, L910 (1984)
6. F. Di Fonzo, A. Gidwani, M. Fan, D. Neumann, D. Iordanoglou, J. Heberlein, P. McMurry, S. Girshick, N. Tymiak, W. Gerberich and N.P. Rao, Appl. Phys. Lett. **77**, 910 (2000)
7. N.P. Rao, N. Tymiak, J. Blum, A. Neuman, H.J. Lee, S.L. Girshick, P.H. McMurry and J. Heberlein, J. Aerosol Sci., **29**, 707 (1998)
8. W.T. Nichols, G. Malyavanatham, D.E. Henneke, J.R. Brock, M.F. Becker and J.W. Keto and H.D. Glicksman, J. Nanoparticle Res., **2**, 141 (2000)
9. W.T. Nichols, G. Malyavanatham, D.E. Henneke, D.T. O'Brien, M.F. Becker and J.W. Keto, submitted to J. Nanoparticle Res.
10. H. Hsieh, R.S. Averback, H. Sellars and C.P. Flynn, Phys. Rev. B, **45**, 4417 (1992)
11. P.C. Reist, *Aerosol Science and Technology*, 2nd ed., McGraw-Hill, New York 1993 pp.82
12. W.T. Nichols, G. Malyavanatham, M.P. Beam, D.E. Henneke, J.R. Brock, M.F. Becker and J.W. Keto, Mat. Res. Soc. Proc. **581**, 193 (2000)
13. E. Barborini, P. Piseri, A. Podesta and P. Milani, Appl. Phys. Lett. **77**, 1059 (2000)

Mat. Res. Soc. Symp. Proc. Vol. 703 © 2002 Materials Research Society V5.8

# Orientation of Aromatic Ion Exchange Diamines and the Effect on Melt Viscosity and Thermal Stability of PMR-15/ Silicate Nanocomposites

Sandi Campbell and Daniel Scheiman[1]
NASA Glenn Research Center, Cleveland, Ohio, 44135
[1]NASA contract via QSS

## Abstract

Nanocomposites of PMR-15 polyimide and a diamine modified silicate were prepared by addition of the silicate to the PMR-15 resin. The orientation of the ion exchange diamine within the silicate gallery was determined by x-ray diffraction and found to depend on the clay cation exchange capacity. The oligomer melt viscosity exhibited a dependence on the orientation of the diamine in the silicate interlayer, and in some cases, on the length of the diamine. A correlation was observed between the oligomer melt viscosity and the crosslinking enthalpy, where nanocomposites with an increased melt viscosity exhibited a decrease in enthalpy on crosslinking. After crosslinking, those nanocomposites with a high melt viscosity had poorer thermal oxidative stability compared to the less viscous systems. The melt viscosity was tailored by co-exchange of an aromatic diamine and an aliphatic amine into the silicate. Nanocomposites prepared with this silicate exhibited an increase in thermal oxidative stability compared to the neat resin.

## Introduction

The durability and reliability of materials used in aerospace components is a critical concern. Many of these applications, in particular those in propulsion components, require a high glass transition temperature ($T_g$), high temperature stability in a variety of environments, and good mechanical properties over a wide range of temperatures.[1] PMR (Polymerization of Monomer Reactants)- type polyimides are thermosetting polymers which combine excellent processability, mechanical properties, and thermal oxidative stability (TOS). PMR-15 is commercially available and prepared in two stages from three monomer reactants: 2-carbomethoxy-3-carboxy-5-norbornene (nadic ester, NE), 4,4'-methylenedianiline (MDA), and the dimethyl ester of 3,3',4,4'-benzophenonetetracarboxylic acid (BTDE). Curing under heat and pressure results in a highly crosslinked network structure.[2] There has been a significant amount of research aimed at increasing the TOS of PMR-15 by altering the structure of the diamine,[2] the dianhydride,[3] or the end-cap[4]. An alternative to modification of the polymer, as a means of increasing TOS, is the dispersion of a layered silicate in the polymer matrix.

Layered silicates have quickly become recognized as useful fillers in polymer matrix composites. Their platelet morphology and high aspect ratio results in greatly improved thermal,[5] mechanical,[6] and barrier properties.[7] A number of papers have reported improvements in the physical properties of thermoplastic polyimide nanocomposites.[8] However, the majority of work in thermosetting polymers has focused on epoxy systems.[9] The purpose of the work described in this paper was to investigate the TOS of PMR-15 nanocomposites. Specifically this research was focused on the relationship between the ion exchange diamine chain length and orientation, including its effect on the oligomer melt viscosity and the polymer crosslink density.

## Experimental

Bentonite (Bentolite-H, cation exchange capacity (CEC) = 90 meq/100g) was received from Southern Clay Products and will be referred to as SCP throughout this paper. Montmorillonite (PGV-grade, CEC = 145 meq/100g) was received from Nanocor and will be referred to as PGV.

PMR-15 resins were fabricated in several steps, as illustrated in Figure 1. The monomers were dissolved in methanol (50 wt%) followed by solvent evaporation, on a hot plate, at 60° to 70°C. B-staging the mixture at 204° to 232°C in an air circulating oven produced a mixture of low molecular weight imide oligomers. The oligomer mixture was then cured in a mold at 315°C under 2355 psi to produce the crosslinked polymer. The polymer was post cured in an air circulating oven for 16 hours at 315°C to further crosslinking. The average number of imide rings was kept constant by using a stoichiometry of 2NE/ (n+1)MDA/ nBTDE (n=2.087) corresponding to an average molecular weight of 1500.[10] The method used in the preparation of PMR-15 nanocomposites was identical to that used for the neat resin, except that the organically modified silicate (1 wt% to 7 wt%) was added to the methanol solution of the monomers.

Aromatic diamines were used for ion exchange. They included: *p*-phenylene diamine (pPDA), methylene dianiline (MDA), 4,4'(1,4-phenylene-bismethylene) bisaniline (BAX), and 4,4'-bis(4-aminobenzyl)diphenylmethane (MMM). Ion exchange of the interlayer cations of SCP and PGV clays with the protonated forms of the listed amines was performed by dissolving the amine (5mmol) in 450 mL of a 0.005M aqueous HCl solution at 60°C. In the case where the diamine did not dissolve in the aqueous solution, ethanol (25 – 50 mL) was added. The silicate (5g) was dispersed in the solution and the resultant mixture was stirred at 60°C for three hours. The solution was filtered and the clay was washed thoroughly with warm water. To maximize the amount of diamine exchanged, the procedure was repeated by addition of the organically modified silicate to a new solution of protonated amine. A total of three exchange reactions were completed for each silicate/ amine system.[11] The silicate was then dried overnight in a vacuum oven at 100°C. Throughout this paper, the clays modified with various amines will be identified by the silicate and the ion exchange amine, for example, SCP-amine or PGV-amine for the organically modified forms of SCP and PGV respectively.

The melt viscosities of B-staged nanocomposites were compared by measurement of the materials' squeeze flow index (SFI).[12] Comparison of the SFI gives a relative indication of the melt flow. The powders (0.5g) were cold pressed into a pellet. The pellet was placed between Kapton sheets in a 25 ton press and held at 315°C and 200 psi for two minutes. This process resulted in a circular "splat" of resin, due to the resin flow. The diameter of the "splat" was measured in several places and the average was used to calculate the area of resin flow. Each sample was run in triplicate.

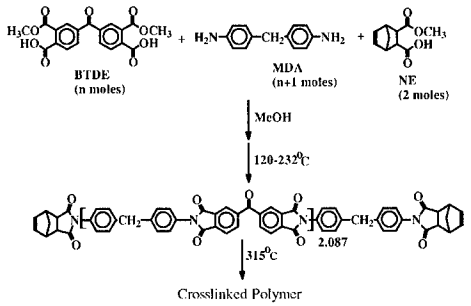


**Figure 1.** PMR-15 synthesis

## Results and Discussion

The aromatic diamines chosen as the ion exchange material were similar in chemical structure to, or the same as, the diamine found in PMR-15. Tethering one end of the diamine to the silicate leaves the second free for reaction with BTDE during PMR-15 synthesis. Wei *et al.*[8] demonstrated this as a viable method of achieving irreversible swelling of the silicate in a thermoplastic polyimide matrix.

The d-spacing of the organically modified silicates was calculated from x-ray diffraction (XRD) data. The investigated diamines and the XRD patterns of SCP exchanged with each diamine are shown in Figure 2. The $d_{001}$ peak of untreated SCP appears at $2\theta = 7.07^{\circ}$ ($d_{001}$ = 1.25 nm). Ion exchange with pPDA shifts the peak to $2\theta = 5.97^{\circ}$ ($d_{001}$ = 1.48 nm). After this initial increase in gallery height, there is little change in d-spacing as the number of phenylene linkages in the diamine increases. Unlike SCP, ion exchange in PGV produces a monotonic increase of the d-spacing with increasing diamine length.

The observed variation in d-spacing between organically modified SCP and PGV suggests that the exchange diamines may adopt a separate configuration in each silicate. Organically modified SCP shows little change in gallery height on increasing the length of the diamine, suggesting that the longer diamines adopt a folded conformation within the silicate gallery. The increase in d-spacing that is observed on ion exchange with PGV suggests the aromatic diamines are not folding, but may extend away from the silicate surface. However, the increase in gallery spacing is small and therefore the chains are likely not perpendicular to the silicate, but may lie at an inclined angle with respect to the silicate surface.

The clays differ in CEC (PGV =145 meq/100g, SCP = 90meq/100g) therefore fewer diamines can be exchanged with SCP. It has been shown that the orientation of alkyl ammonium cations within a silicate gallery is dependent on the chain length and layer charge density of the clay.[13, 14] Due to the low CEC of SCP, there is a large surface area available to the chains so that they may fold back toward the silicate sheet. As the CEC increases, the chain packing density of the exchange diamines increases and the available surface area decreases. This may prevent folding and force the diamines away from the silicate surface, resulting in the observed dependence of PGV d-spacing on the aromatic chain length.

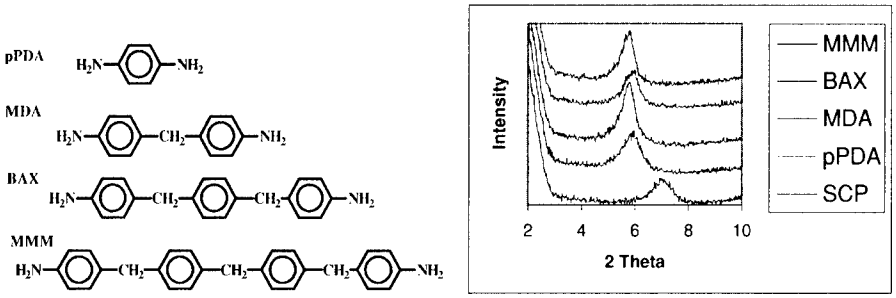


**Figure 2.** Structures of the diamines used in ion exchange and the XRD patterns of unmodified SCP (bottom pattern) and SCP organically modified with pPDA, MDA, BAX and MMM.

A comparison of the amount of exchanged diamine was made by thermogravimetric analysis (TGA).[15] Measurement of the weight loss on heating the untreated clays to 800°C gives the content of adsorbed and structural water within each clay. Heating the organically modified clays to 800°C, and subtracting out the weight loss corresponding to water content, gives an indication of the amount of diamine present. TGA measurements suggest that an average of 33% more diamine by weight was exchanged into PGV, which is consistent with the difference in the CEC of each clay. An exception is the ion exchange of pPDA, where approximately 18% by weight more diamine is exchanged into SCP.

PMR-15/ silicate nanocomposites were prepared using either modified SCP or PGV. The silicate dispersion was evaluated by XRD and transmission electron microscopy (TEM). All systems showed primarily exfoliated silicate layers with regions of intercalation evident in TEM. The SFI data shown in Table I reveals an increase in the oligomer melt viscosity of SCP nanocomposites compared to the neat resin. Nanocomposites prepared using PGV show a similar oligomer melt viscosity increase when the clay has been ion exchanged with pPDA and MDA. However, nanocomposites prepared with the longer chain diamines, PGV-BAX or PGV-MMM, show an identical or an increased SFI. This suggests a similar or even lower oligomer melt viscosity.

The energy released during endcap crosslinking was measured by high pressure differential scanning calorimetry (HP-DSC) for B-staged nanocomposites and is listed in Table 1. HP-DSC thermograms of B-staged SCP nanocomposites show a decrease in the amount of energy released during the crosslinking reaction, compared to the neat resin, with little dependence on the ion exchange diamine. In B-staged PGV nanocomposites there is an increase in the exotherm, compared to neat PMR-15, with the exception of PGV-pPDA.

The data in Table I suggests a correlation between the oligomer melt viscosity and the crosslinking enthalpy. The apparent decrease in crosslinking with increased oligomer melt viscosity suggests that polar interactions between the oligomer and the silicate surface may limit chain mobility and increase the oligomer melt viscosity, thus decreasing the number of crosslinks formed upon curing.

Typically, an advantage of polymer-clay nanocomposites is an improvement in the polymer thermal stability over that of the neat resin. However, PMR-15 is a fairly stable thermosetting polymer. Disruption of its highly crosslinked structure could lead to a reduction in the TOS. Weight loss measurements of the neat resin and the nanocomposites over 1000 hours at 288°C

show a decrease in TOS in all SCP and PGV nanocomposites, with the exception of PGV-MMM nanocomposites. This material has a weight loss approximately equal to PMR-15 and is the only nanocomposite with an oligomer melt viscosity lower than the neat resin.

Since the higher oligomer melt viscosity tends to decrease the nanocomposite TOS, decreasing the melt viscosity of the B-staged PGV-MDA nanocomposite should yield improvements in TOS. To decrease the melt viscosity of B-staged PMR-15/ PGV-MDA, PGV was ion exchanged with 50 mol% MDA and 50 mol% dodecylamine, (C12). The longer chain length of C12 compared to MDA should keep the oligomer from close contact with the silicate, but still allow reaction between the tethered diamine and BTDE.

**Table I.** SFI and DSC measurements for PMR-15 nanocomposites prepared with modified SCP and PGV clays. The clay concentration was 2 wt%.

| Sample (clay modification) | SFI ($cm^2$) (SCP) | DSC (mcal/mg) (SCP) | SFI ($cm^2$) (PGV) | DSC (mcal/mg) (PGV) |
|---|---|---|---|---|
| PMR-15 | 93.3 | 13.7 | 93.3 | 13.7 |
| PPDA | 77.0 | 12.0 | 67.83 | 11.92 |
| MDA | 78.5 | 10.3 | 82.39 | 14.5 |
| BAX | 81.7 | 10.4 | 93.3 | 14.6 |
| 4-ring | 73.9 | 10.7 | 108.7 | 15.0 |

Measurements of the melt viscosity and crosslinking enthalpy for B-staged nanocomposites prepared with the mixed amine demonstrate that the oligomer melt viscosity and crosslink density can be manipulated by introduction of a long chain alkylamine onto the silicate. Figure 3 shows the TOS of the PGV-(MDA-C12) nanocomposites, where the silicate concentration is increased from 1 wt% to 7 wt%. It should be noted that the degradation temperature of the alkylamines is near the processing temperature of PMR-15 so there is a question as to whether these materials degrade during processing. There is ongoing work to address this question. Here it is assumed that the aliphatic amine is present within the silicate during processing and is responsible for the observed decrease in oligomer melt viscosity. Unfortunately, the low molecular weight alkyl amine can act as a plasticizer in the polyimide matrix, reducing the $T_g$. The $T_g$ of neat PMR-15 as measured by DMA is 345°C. Addition of 2 wt % PGV-MDA results in a small increase to 348°C, where addition of 2 wt% PGV-C12 lowers the $T_g$ to 330°C. Co-exchange of MDA and C12 results in a $T_g$ of 340°C, which is not a significant change in the $T_g$.

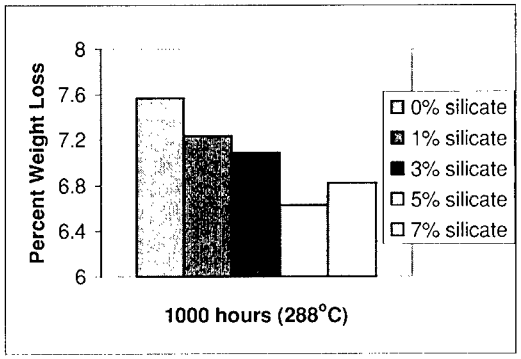


**Figure 3.** Weight loss of neat PMR-15 and nanocomposites on increasing clay concentration. The silicate is PGV modified with MDA and C12.

## Conclusions

The orientation and packing density of the aromatic diamine used to modify bentonite and montmorillonite clays affects the oligomer melt viscosity of a PMR-15/ silicate nanocomposite. An increase in oligomer melt viscosity is accompanied by a decrease in the oligomer crosslinking enthalpy, as well as a decrease in the TOS of the cured nanocomposite. The oligomer melt viscosity can be modified by co-exchange of an aromatic diamine and a long chain alkyl amine on the clay. Incorporation of PGV/( MDA-C12) into the PMR-15 matrix has little affect on $T_g$. In addition, the TOS of the nanocomposite is improved compared to the neat resin or nanocomposites prepared with clay exchanged only with the aromatic diamine. Thus, use of PMR-15/ silicate nanocomposites is a viable approach to improve high temperature stability.

## Acknowledgments

The authors would like to thank Linda Ingrahm for carrying out the TOS measurements, David Hull for TEM analysis, Ralph Garlick for XRD analysis, and Michael Faile for the preparation of the aging specimens.

## References:

1. M.A. Meador, Annu. Rev. Mater. Sci. **28,** 599 (1998).
2. P. Delvigs, D.L. Klopotek, P.J. Cavano, High Perform. Polym. **6,** 209 (1994).
3. W. Alston, High Perform. Polym. **7** (1), 93 (1995).
4. M.A.B. Meador, J.C. Johnston, A. Frimer, P. Gilinsky-Sharon, H. Gottlieb, Chem. Mater. ASAP Article, (2001).
5. H.L. Tyan, Y.C. Liu, K.H. Wei, Chem. Mater. **11,** 1942 (1999).
6. T. Lan, T. Pinnavaia, Chem. Mater. **6,** 573 (1994).
7. S. Burnside, E.P. Giannelis, E.P. Chem. Mater. **9** (7), 1597 (1995).

8. H.L. Tyan, Y.C. Liu, K.H. Wei, Chem. Mater. **11** (7), 1942 (1999).
9. T. Lan, D. Kaviratna, T. Pinnavaia, Chem. Mater. **7,** 2144 (1995).
10. T. Serafini, P. Delvigs, G. Lightsey, J. Appl. Poly. Sci. **16,** 905 (1972).
11. H. Shi, T. Lan, T.J. Pinnavaia, Chem. Mater. **8,** 1584 (1996).
12. C. Gariepy, PhD. Thesis, University of Akron, 2000.
13. T. Lan, D. Kaviratna, T. Pinnavaia, J. Phys. Chem. Solids **6-8**, 1005 (1996).
14. R. Vaia, R. Teukolsky, E.P. Giannelis, Chem. Mater. **6**, 1017 (1994).
15. A. Usuki, M. Kawasumi, Y. Kojima, A. Okada, T. Kurauchi, O. Kamigaito, J. Mater. Res. **8** (5), 1174 (1995).

Mat. Res. Soc. Symp. Proc. Vol. 703 © 2002 Materials Research Society V5.9

# PRODUCTION AND MAGNETIC PROPERTIES OF NANOCOMPOSITES MADE OF FERRITES AND CERAMIC MATRICES

H. A. CALDERON[1], A. HUERTA[1], M. UMEMOTO[2], K. CORNETT[3]
1 Depto. Ciencia de Materiales ESFM-IPN, Apdo. Postal 75-707, México D.F. 07300
2 Dept. Production Systems, Technical Univesity of Toyohashi, Japan
3 Motorola Inc. Fort Lauderdale FLA, USA.

## ABSTRACT

This investigation deals with the production of materials containing a dispersion of magnetic nanoparticles in an insulating matrix. Such a distribution of magnetic centers is expected to absorb electromagnetic radiation in a range of wavelengths. Wüstite-magnetite and magnesia-magnesioferrite nanocrystalline ceramics have been prepared by mechanical milling and spark plasma sintering. As-milled powders have a nanocrystalline structure in both systems. Low energy milling gives rise to an increasingly higher volume fraction of wüstite as a function of milling time in the $Fe_{1-x}O$-$Fe_3O_4$ system. Similar results are obtained in the MgO-$MgFe_2O_4$ system with increasingly larger amounts of $MgFe_2O_4$ produced by milling. Composites of magnetic particles ($Fe_3O_4$ or $MgFe_2O_4$) in a nonconductive matrix (FeO or MgO, respectively) are found in the sintered samples. Measurement of magnetic properties can be used to determine conclusively the nature of the developed phases and the effect of grain size.

## INTRODUCTION

Materials for absorption of electromagnetic waves can be divided into basically two types. One of them consists of pure materials such as ferrites and the other is typically a composite including a polymeric supporting phase and a magnetic material in dispersion or forming a characteristic arrangement. Ferrites have high potential for electromagnetic wave absorption since they have frequency dependent physical properties such as permittivity and permeability. There are several investigations on the frequency dispersion of complex permeability in polycrystralline ferrite [1-3]. Such properties depend on the chemical composition of the ferrite and on the postsintering density, grain size, porosity and inter or intragranular porosity [3]. On the other hand, composite wave absorbers are also commonly produced. Takada et al. [4] report the properties of a Ferrite/SiC sintered composite showing a dependence between the volume fraction of ferrite and the absorption properties. Arrangements of aligned thin magnetic metal particles in polymers have also been successfully used as electromagnetic wave absorbers [5]. Nevertheless few efforts have been made to evaluate the effect of a nanostructure (including grain size and scale of the magnetic centers) on the wave absorbing properties of this type of materials. This investigation deals with the production of a wave absorber by using mechanical milling. Such an experimental method produces nanostructured materials usually in a non stable condition but proper heat treatment can be used to achieve the desired dispersion of nanomagnetic particles in the insulating matrix. This report summarizes the production, magnetic properties and characterization of materials designed for electromagnetic wave absorption.

## EXPERIMENTAL PROCEDURE

Materials containing particles of $MgFe_2O_4$ (magnesioferrite) in a $Mg_{(1-x)}Fe_xO$ (magnesio-wustite) matrix and particles of $Fe_3O_4$ (magnetite) into $Fe_xO$ (wustite) have been produced by the mechanochemical reaction of pure components in low, high and ultrahigh energy mills (horizontal, planetary and Spex mills, respectively). All powder handling was performed in an

Ar-filled glove box with an oxygen content below 0.01 ppm. Consolidation of powders was performed by spark plasma sintering (SPS). Cylindrical solid samples of 18 mm or 13 mm in diameter and 5 mm of thickness were produced by sintering at high temperature (873 to 1273 K) and low pressure (50 MPa) or at low temperature (673, 773 K) and high pressure (100 MPa). Microstructural characterization was done by means of X-Ray diffraction (Siemens D-500, $Cu_{K\alpha}$ XRD), scanning electron microscopy (JSM-200, SEM), transmission electron microscopy (Hitachi 800, TEM) and high resolution electron microscopy (Philips CM300, HREM). Measurement of magnetic properties was made in a vibrating sample magnetometer (Riken Denshi Co., VSM). Identification of the iron containing phases was made by Mössbauer spectroscopy (Source Co-60, MöS).

## RESULTS AND DISCUSION

XRD patterns of powders in the $Fe_xO$-$Fe_3O_4$ system milled in a horizontal mill indicate a reduction of grain size and a variation of the unit cell dimensions. Fig. 1a shows the XRD of different samples milled for 1000 h. A variety of starting materials has been used, pure $Fe_3O_4$, $Fe_3O_4$ with additions of Fe or C and $Fe_2O_3$ together with Fe. The obtained XRD patterns have broad intensity maxima at similar angular positions suggesting the formation of the same phases in all cases. The angular positions expected for the pure phases are also indicated in the lower section of this figure. It can be seen that the experimental angular positions do not correspond to either of the equilibrium phases ($Fe_xO$, $Fe_2O_3$ or $Fe_3O_4$). They are close to wustite or magnetite and thus the experimental peak positions can be interpreted either as a Fe-lean non-equilibrium wüstite phase or as a Fe-rich non-equilibrium magnetite. However, consideration of the peak displacements suggests that an Fe-lean wüstite is formed during milling with some minor amounts of magnetite. The MgO-$MgFe_2O_4$ system is represented in Fig. 1b that shows XRD patterns corresponding to the sample MgO-4 cat.% Fe after different milling times. The mixture was prepared with powders of $Fe_2O_3$ and MgO as starting materials. Fig. 1b shows that low amounts of $Fe_2O_3$ can be dissolved into the MgO lattice producing lattice distortions that give rise to variation of the expected angular positionso of MgO. The displacement is always towards large lattice spacing and thus it is likely that the MgO lattice saturates with Fe and thus the as-milled microstructure is composed mostly of $Mg_{1-x}Fe_xO$. Other peaks indicate the presence of $MgFe_2O_4$, especially after long milling times. The XRD maxima in the patterns also show broadening indicating a reduction of the crystal size.

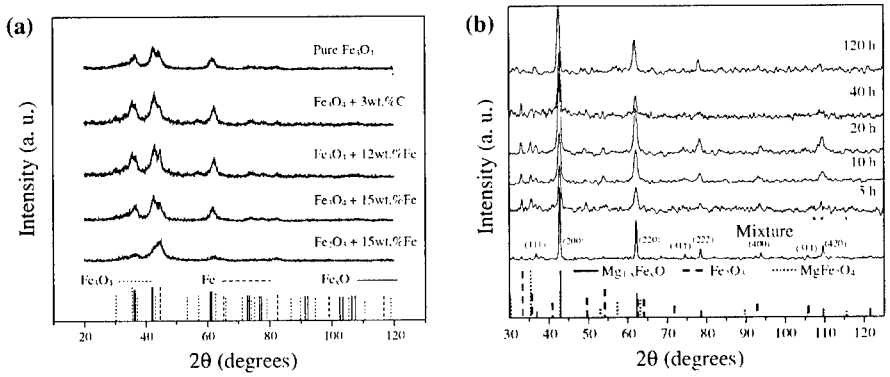


Figure 1. XRD patterns of powders after milling 1000 h in a horizontal mill from the $Fe_xO$-$Fe_3O_4$ system. (b) XRD patterns of MgO-4cat.% Fe before and after milling in a Spex mill.

Figure 2 shows a typical view of the grain structure of the as-milled powder particles. In this case the sample is $Fe_3O_4$ with addition of 12 wt.% Fe after 200 h of milling. Nanosized grains can be clearly seen with an average size of 10 ± 8 nm (Fig. 2a). The corresponding diffraction pattern is given in Fig. 2b, the somewhat diffuse rings are typical of fine grained materials and the angular positions allow identification of the phases $Fe_3O_4$ and $Fe_xO$.

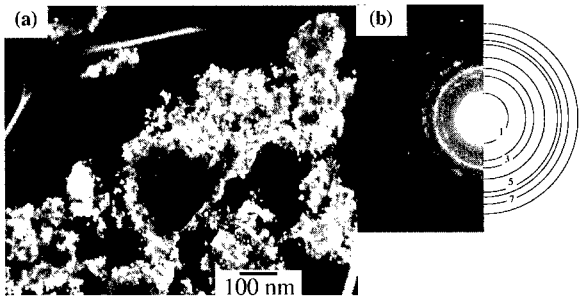


| Ring | $Fe_3O_4$ | $Fe_xO$ |
|---|---|---|
| 1 | (111) | |
| 2 | (220) | |
| 3 | (222) | (111) |
| 4 | | (200) |
| 5 | (422) | |
| 6 | (511) | |
| 7 | (440) | (220) |
| 8 | (533) | (311) |

Figure 2. (a) Dark field TEM image of sample $Fe_3O_4$+12 wt.%Fe milled in a horizontal mill for 200 h. It was taken with the overlapping reflections (222) of $Fe_3O_4$ and (111) of $Fe_xO$. (b) Diffraction pattern.

Mössbauer spectroscopy (MöS) has been used to identify the nature of the iron-containing phases. Fig. 3a shows an example that corresponds to pure $Fe_3O_4$ milled for 500 and 1000 h in a horizontal mill. They consist of two separate sextets (magnetic effect, see *i* and *ii*) and one pair of overlapping doublets (paramagnetic effect, see *I* and *II*). Thus only two phases can be identified i.e., magnetite and wüstite. The spectra exhibit a magnetic relaxation as a function of the milling time i. e., the intensity of the sextets (magnetite phase) is smaller for the sample milled for 1000 h and therefore the amount of $Fe_{1-x}O$ increases with longer milling times. Quantitative evaluation shows an increase from 66.6 % to 74 % for 500 and 1000 h of milling. In addition, the spectra present a strong absorption asymmetry, which can be related to disordered phases or nanosized grains. These results suggest that during milling magnetite transforms into wustite. The same tendency, i.e. formation of a solid solution, is found for the other investigated mixtures. Figure 3b shows the MöS spectra of MgO - 4 cat.% Fe milled for 40 and 120 h in a Spex mill. The spectrum of the sample milled for 40 h consists of two sextets (magnetic effect, see *i*) and two doublets (paramagnetic effect, see *ii*). The magnesiowüstite ($Mg_{1-x}Fe_xO$) phase produces the two doublets and the magnesioferrite ($MgFe_2O_4$) the two sextets in the MöS spectrum. Quantitative evaluation shows that the as-milled powders are rich in magnesioferrite (75% refered to the total amount of Fe-containing phases) with low amounts of magnesiowüstite. On the other hand, the spectrum of the sample milled for 120 h consists of one sextet (see *I*), two doublets (see *II*) and one singlet (see *III*). The doublets are related to magnesiowüstite (a total content of 80 %) and the sextet is due to pure iron (20 %). These results suggest that the mechanochemical reaction between MgO and $Fe_2O_3$ ends before 120 h of milling and also that the magnesioferrite formed at shorter milling times (40 h) transforms into magnesiowüstite if milling is continued further. Measurement of magnetic properties of as-milled powders also indicates the formation of a new magnetic phase during milling i.e., magnesioferrite. Thus a similar transformation sequence is observed in this system in that the spinel oxide precedes the formation of the solid solution i.e., $MgO+Fe_2O_3 \rightarrow MgO+MgFe_2O_4 \rightarrow Mg_{(1-X)}Fe_XO$.

Figure 4 shows measurements of magnetization (M) as a function of applied field (H) in the wüstite-magnetite system after mechanical milling in a horizontal mill. Measurements of samples

containing magnetite as starting material show a decrease of saturation magnetization $M_s$ as a function of milling time. A different behavior is observed in the sample prepared with hematite as shown in Fig. 4a ($Fe_2O_3$ + 15 wt.% Fe), where Ms shows a fluctuation in value. The monotonic

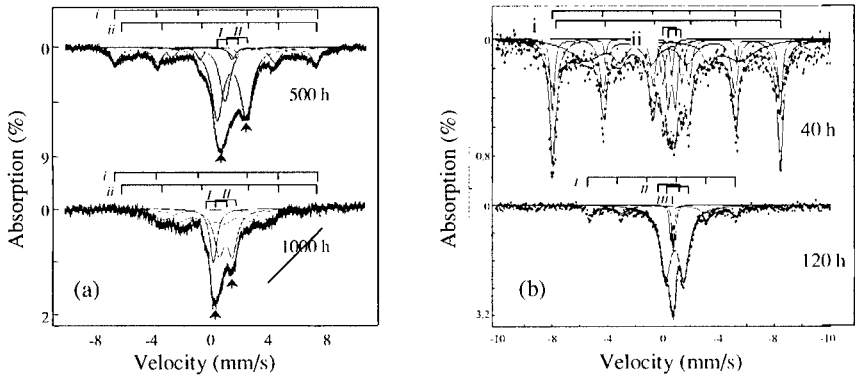


Figure 3. MöS spectra. (a) Pure $Fe_3O_4$ milled 500 and 1000 h in a horizontal mill. (b) MgO-4 cat.% Fe powders milled 40 and 120 h in a Spex mill.

reduction in $M_s$ can be seen in Fig. 4b ($M_s$ Vs milling time) that shows a summary of results for the as-milled powders. Such a trend can be explained by the transformation of magnetic phases into non-magnetic phases i.e., magnetite and/or iron into wüstite. A net reduction of approximately 50% in Ms is seen when comparing $M_s$ values after 50 and 1000 h of milling. However, the transformation of magnetic phase into paramagnetic wüstite is not complete even after 1000 h of milling due to the applied low energy processing. A different behavior is seen for the sample prepared with $Fe_2O_3$ as starting material. There is an increase of the $M_s$ value for milling times up to 500 h. Additional milling promotes $M_s$ values similar to those found for other samples. Apparently $Fe_2O_3$ first transforms into $Fe_3O_4$ upon milling and then to $Fe_xO$. Therefore the decomposition sequence appears to be $Fe+Fe_2O_3 \rightarrow Fe_3O_4 \rightarrow Fe_xO$. This can also be predicted from the relative values of the oxides free energy of formation [6]. Thus the initial components have a definite influence on formation of phases during milling. On the other hand, the central sections of the hysteresis loops are magnified and shown in the insert of Fig. 4a. This can be used to evaluate the coercivity of the as-milled powders (half width of hysteresis loop with no induced field, M). As seen in Fig. 4a, the coercivity remains constant in this sample as a function of milling time, indicating that the size of the magnetic domains is independent of such a variable.

Figure 5 shows representative measurements of magnetic properties in sintered samples. Fig. 5 corresponds to pure $Fe_3O_4$ milled for 500 and 1000 h and sintered at 1073 and 1173 K. Lower saturation magnetization values are achieved in these samples with respect to the as-milled powders (see Fig. 4b). This suggests that a phase transformation takes place during the sintering process, most likely a transformation to oversaturated wüstite (paramagnetic) which represents the solid solution of Fe and O. This phase can still transform upon aging to wüstite and magnetite in metastable equilibrium as shown in [7] for materials prepared by conventional melting techniques. In addition the relative differences among the curves shown in Fig. 5 can be explained on the basis of two effects i.e., the magnetic domain size ($s_m$) and the volume fraction of magnetite ($f_v$). A higher $f_v$ of magnetite produces a higher $M_s$ value while a smaller $s_m$ gives rise to a higher coercivity. The central sections of the hysteresis loops have been magnified and are shown in the insert in to to depict the differences in coercivity.

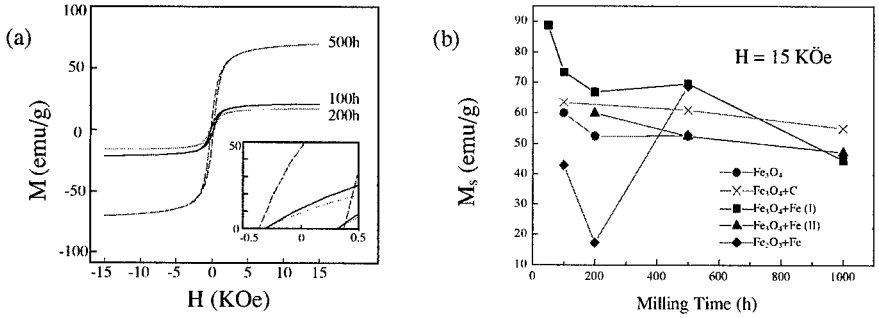


Figure 4. Magnetization curves of wüstite magnetite system after milling in a horizontal mill. (a) $Fe_2O_3$ + 15 wt.% Fe. (b) Saturation magnetization ($M_s$) as a function of the milling time.

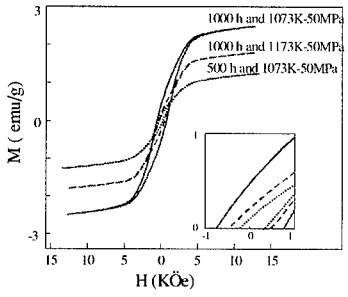


Fig. 5. Magnetization curves of sintered $Fe_3O_4$ samples.

Thus for example the sample milled for 1000 h and sintered at 1073 K contains a finer distribution of magnetic particles in the paramagnetic $Fe_xO$ matrix. However in all cases in Fig. 5, the formation of a fine dispersion of magnetic particles in a matrix of $Fe_xO$ is evident. Therefore it is possible to control the magnetic behavior by controlling the milling time and the sintering temperature.

The final microstructure after SPS depends on the sintering conditions. Low sintering temperatures produce microstructures composed of fine nanograins around 30 nm in average size and very similar to the microstructures of as-milled powders. SPS at 1073 K gives rise to equilibrium phases in most cases. In addition, the grain size depends on the processing temperature. For example powders of pure $Fe_3O_4$ milled for 1000 h produce an average size of 230 ± 120 nm if sintered at 1173 K while a value of 150 ± 70 nm is found for sintering at 1073 K. In general sintering below 1073 K allows retention of the nanocrystalline grain structure.

As sintered samples have a characteristic dispersion of phases. Fig. 6 shows darks field images and diffraction patterns of some grains in a sample sintered at 1273 K after 500 h of milling with a nominal composition of $Fe_3O_4$ with 15 wt.% Fe. The images have been obtained in dark field by using the satellite reflections of the diffraction patterns. The modulated microstructures are typical of an spinodal decomposition process (see arrows). Nucleation by an spinodal mechanism is rarely seen in ceramic phases and it can appear in this wustite – magnetite system among other factors because of the close structural similarities between the two lattices. The oxygen sublattice is common in the two lattices giving a perfect coherency between the two phases and only the Fe content changes to produce the typical composition modulation on the spinodal decomposition. The microstructure formed during sintering has been also observed by means of HREM. Fig. 7 shows experimental and processed images of the sample $Fe_3O_4$-15wt. % Fe milled for 200 h and sintered at 1173 K. Two different orientations are given in this figure i.e., [100] and [110] as shown in the inserted diffraction patterns obtained from a Fourier transform of the experimental image. The experimental images (Figs. 7a and 7c) show the presence of domains where different spacings of the structural lattice are apparent. Such domains can be seen more easily in the

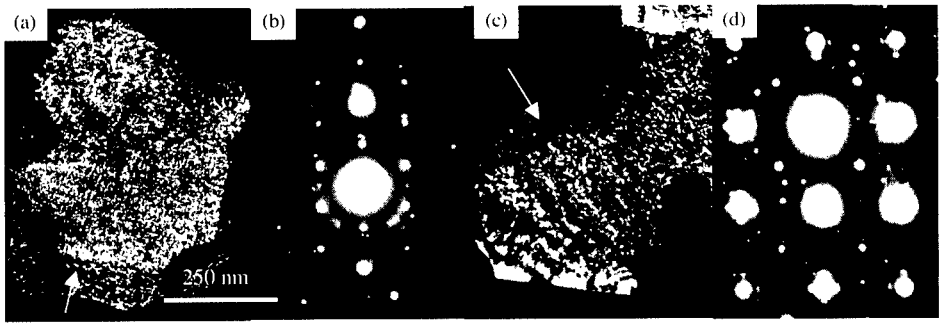


Figure 6. TEM images from $Fe_3O_4$-15wt.% Fe milled for 500 h and sintered at 1273 K. (a) and (c) Dark field images form [200] reflections. (b) and (d) Electron diffraction patters showing satellite reflections.

processed images. The processing consists in creating a Moire pattern with a selected reflection from the diffraction pattern. The differences (if any) in the periodic distribution created by domains nucleated independently as in the case of an spinodal decomposition can then be more easily observed.

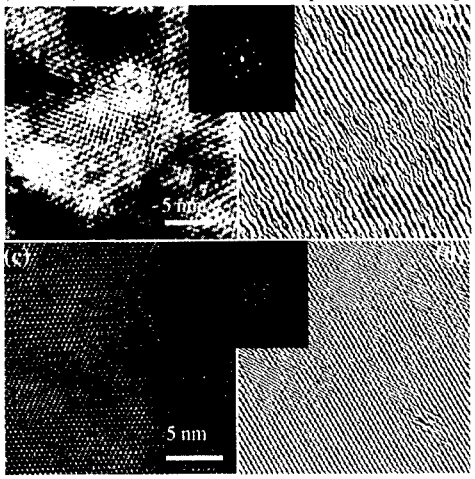


Figure 7. $Fe_3O_4$-15wt. % Fe milled for 200 h and sintered at 1173 K. (a) HREM image with B = [100]. (b) Moire pattern of image a. (c) HREM image with B = [110]. (d) Moirè pattern of image c.

## CONCLUDING REMARKS

A fine distribution of magnetic particles in a nonconductive matrix can be produced by mechanical milling and sintering in the systems $Fe_xO$-$Fe_3O_4$ and MgO-$MgFe_2O_4$. It is noticed that phase formation is related to the relative values of the energy of formation. The spinel phase precedes the formation of the oxygen solid solution in both systems under investigation.

## ACKNOWLEDGEMENTS

AH acknowledges financial support from CONA CYT and TUT. HAC acknowledges support from CONACYT (Project 28925 U), Motorola Inc. and COFFA-IPN. NCEM-LBNL is gratefully acknowledged for the use of HREM equipment.

## REFERENCES

1. G.T. Rado, Rev. Mod. Phys. 25, 81 (1953).
2. D. Polder and J. Smit, Rev. Mods. Phys. 25, 89 (1953).
3. T. Nakamura, J. Appl. Phys. 88, 348 (2000).
4. J. Takada, M. Nakanishi, M. Yoshino, T. Fuji, M. Fukuhara, A. Doi, Y. Kusano, Adv. Powder Metal. and Part. Mats, Pub. by Metal Powder Ind. Fed., Part 12, p. 11 (1999).
5. M. Matsumoto and Y. Miyata, IEEE Trans. on Mag., 33 (1997) 4459.
6. C.H.P. Lupis, *Chemical Thermodynamics of Materials*, Prentice-Hall Inc. A Simon and Schuster Company, Englewood Cliffs, New Jersey, (1983).
7. M. E. Fine, American Ceramic Society Bulletin, 51 (1972) 510-15.

# Nanophase and Nanocomposite Materials II

Mat. Res. Soc. Symp. Proc. Vol. 703 © 2002 Materials Research Society V6.2

# Crystalline-Amorphous Interface: Molecular Dynamics Simulation of Thermal Conductivity

**Sebastian von Alfthan, Antti Kuronen, Kimmo Kaski**
Helsinki University of Technology, Laboratory of Computational Engineering
P.O.Box 9400, FIN-02015 HUT, FINLAND

## ABSTRACT

Effect of a crystalline-amorphous interface on heat conduction has been studied using atomistic simulations of a silicon system. System with amorphous silicon was created using the bond-switching Monte Carlo simulation method and heat conduction near room temperature was studied by molecular dynamics simulations of this system.

## INTRODUCTION

As the sizes of electronic devices decrease an increasing amount of heat has to be dissipated by ever decreasing volume of the device material. The details of device structures, namely interfaces, surfaces and defects in them affect the heat conduction, which can give rise to behavior that differs drastically from behavior in bulk materials [1, 2].

In addition to the interest in improving the heat dissipation from electronic components, different nanostructures can be utilized to decrease heat conduction where it is not desired. One example of this are the new thermoelectric devices where thermal conduction is reduced by ultra-short-period superlattices [3]. When the dimensions of nanostructures become comparable to the phonon mean free path in the material the Fourier law describing thermal conduction in macroscopic systems becomes inapplicable. Heat conduction is influenced – among other things – by phonon scattering from interfaces, by phonon interference and the modification of the phonon dispersion relation due to small dimensions of the device. These events can be included in kinetic theories of heat conduction [4] in an approximate way. However, in order to get a reliable estimate how the *atomic* level structure of the device influences the heat conduction, atomic level studies are needed.

In this work we study heat conduction through an interface between crystalline (c) and amorphous (a) material. We use molecular dynamics (MD) method to study the effect of the crystalline silicon and amorphous silicon (c-Si/a-Si) interface on the heat conduction near room temperature. We have chosen this particular system with only structural (not chemical) differences in order to study the basic effects of the interface. This study – which is interesting on own right – serves as a necessary but yet insufficiently explored precursor for investigating perhaps the most important interface in electronics; namely an interface between crystalline silicon and amorphous silicon dioxide.

## COMPUTATIONAL DETAILS

Our simulation system consisted of a layer of a-Si between slabs of c-Si (see Fig. 3). In order to avoid complication with open surfaces periodic boundary conditions were applied in all three dimensions. However, this means that the system is effectively a superlattice. Three systems (denoted **A**, **B**, and **C**) with different sizes were studied (see Fig. 3):

**A**: $L_c = 296$ Å, $L_a = 100$ Å, $d = 32$ Å, 20736 atoms

**B**: $L_c = 187$ Å, $L_a = 38$ Å, $d = 16$ Å, 2952 atoms

**C**: $L_c = 187$ Å, $L_a = 38$ Å, $d = 32$ Å, 11808 atoms

Initially the amorphous part of the system was prepared by using the bond-switching Monte Carlo algorithm [5, 6]. In this method a continuous random network (CRN) of atoms is constructed starting from a perfect diamond lattice by introducing disorder through switching bonds between neighboring atoms (see Fig. 1). In this way, four-fold coordination of each atom is preserved but long-range order is destroyed. In the beginning of the simulation the system was mixed by applying bond-switching moves without rejection on the average two times for each atom in the system. After this bond switching moves were continued but this time the move was accepted by using the standard Metropolis algorithm. Moreover, all the atomic positions were relaxed in order to calculate the potential energy of the proposed state. This relaxation was performed by simulated annealing method, which is known to give very good 'optimization' results, quite slowly. The system with a c-Si/a-Si interface was created by applying the bond switches only to the center part of the system that was required to be amorphous.

The bond-switching method requires a potential model that uses explicit bonding information. Therefore, we chose a Keating-type valence force field (VFF) potential model [7, 8] for Si:

$$E = \sum_i k_b (b_i - b_0)^2 + \frac{1}{2} \sum_{i \neq j} k_\theta (\cos\theta_{ij} - \cos\theta_0)^2 \qquad (1)$$

where the sums run over the *bonds* in the system and $b_i$ is the length of the bond $i$ and $\cos\theta_{ij}$ is the angle between bonds $i$ and $j$ originating from the same atom. Values for the constants $k_b$, $b_0$, $k_\theta$, and $\cos\theta_0$ were taken from Ref. [8]. In addition to the VFF potential a repulsive potential was applied between those atoms that were not the nearest or next nearest neighbors according to the bonding information used to calculate the VFF potential. This prevented atoms that were not bonded to come too near to each other.

The system created using the bond-switching method was relaxed with the Stillinger-Weber [9] potential and the heat conduction through the interface was studied by using this potential and the method proposed in Ref. [10]. This is particularly suitable to study heat conduction through interfaces, because it does not require a homogeneous system. Moreover, it is compatible with periodic boundary conditions and a rapidly convergent quantity

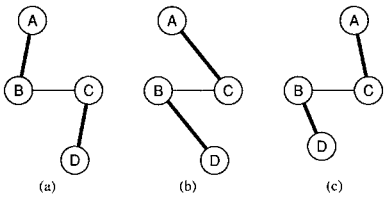


***Figure 1.*** *Principle of the bond-switching algorithm. (a) Initial configuration. (b) Configuration after bond switching. (c) Configuration after energy minimization.*

– i.e. temperature gradient – is calculated. In this method the desired heat flux $\mathbf{J}$ is generated into the system by exchanging velocities in the 'hot' and 'cool' parts of the system. This creates a temperature gradient $\nabla T$. The thermal conductivity $k$ is calculated based on the macroscopic definition

$$\mathbf{J} = -k\nabla T. \tag{2}$$

In the simulations a slab with width of 8 Å at the center of the amorphous region was assigned as the hot part and slabs with widths of 4 Å at the both ends of the system were assigned as cool parts (see Fig. 3). In this case temperature in the system depends only on one coordinate, namely $x$, and the problem reduces to one-dimensional: $J = -kdT/dx$. In a homogeneous system the temperature profile should be linear and the thermal conductivity can be obtained by fitting a line to the profile. Conductivities in the amorphous and crystalline parts of the system were calculated this way. Temperature profiles were calculated as averages of data obtained from simulation times between 200–500 ps.
The amount of heat flux can be adjusted by varying the interval between velocity exchanges. In our simulations we used a flux of $J = 3 \times 10^9$ W/m$^2$.

## RESULTS AND DISCUSSION

In Fig. 2 we show the radial distribution function of the amorphous part of the system along with the recent experimental data [11]. The simulated curve is convoluted with a Gaussian in order to make it comparable with the experimental data. The width of the Gaussian was chosen such that the width of the first peak in $T(r)$ is the same for the experimental and simulated curves. As can be seen, results of the current simulation are in agreement with the experimental data. Also shown in Fig. 2 is the bond angle distribution which is in reasonable agreement with other simulation studies [12]. The final potential energy – given by the VFF potential – of the amorphous part of the system was 0.74 eV/atom. Note that the VFF potential has zero potential energy for the equilibrium diamond structure of silicon. In Fig. 3 we show an example of the configuration created using the bond-switching simulation. It should be noted that not all the crystalline material is shown: some additional crystalline material are added on both sides of the system.

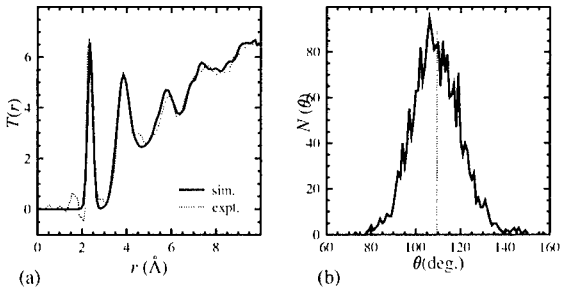


***Figure 2.*** *(a) Radial distribution function of amorphous silicon. Solid line is the result of the bond-switching simulation (convoluted with a Gaussian) and dotted line is experimental data from Ref. [11]. (b) Bond angle distribution of simulated amorphous silicon. Dashed line denotes the tetrahedral angle of the perfect diamond lattice.*

Simulations of the interface systems yielded the following values for the thermal conductivity in the amorphous ($k_a$) and crystalline ($k_c$) regions: system **A**, $k_a = 0.93$ W/mK, $k_c = 13$ W/mK; system **B**, $k_a = 0.85$ W/mK, $k_c = 9$ W/mK; system **C**, $k_a = 0.80$ W/mK, $k_c = 15$ W/mK. Uncertainties due to fitting procedure are approximately 5% and 20% for the amorphous and crystalline values, respectively. For an amorphous silicon system without crystalline parts and with a size of $215 \times 42 \times 46$ Å$^3$ (20480 atoms) thermal conductivity of $k = 1.11 \pm 0.04$ W/mK was obtained.

Result for the amorphous system without interfaces are in agreement with theoretical and experimental data presented in Ref. [13]. Values of the thermal conductivity for the amorphous regions in the interface systems are not very far from that of the pure amorphous system. Moreover, the dependence on system size is not very strong, indicating that even a moderate size simulation systems are sufficient in describing thermal conduction realistically in amorphous materials. However, the values for the crystalline regions are at least order of magnitude lower than experimental values for bulk silicon (160 W/mK at room temperature) and the calculated values depend on the system size. This is expected since the mean free path of the heat carriers – i.e. phonons – in crystalline silicon at room temperature is of the order of 1000 Å. In addition, the statistical errors in the curves for crystalline regions in Fig. 4 are larger than for the amorphous parts. Finite size of the simulation system is manifested in the bending of the temperature profiles at the ends of the samples. This gives additional uncertainty to the results for the crystalline regions. In order to draw quantitative conclusions from the size dependence of the thermal conductivity more extensive simulations are needed.

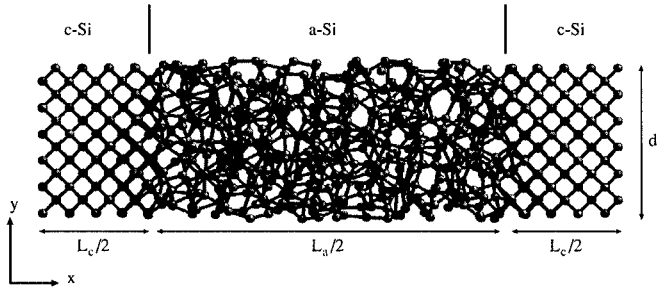


***Figure 3.*** *Example of a configuration of a simulation system containing crystalline-amorphous interface.*

No thermal boundary resistance could be observed in the simulation data. This probably partly due to the statistical noise in the data and partly due to the fact that the two materials are not very different as far as phonon properties are concerned.

## CONCLUSIONS

We have studied heat conduction through an interface between crystalline and amorphous silicon. The effect of the interface can be seen clearly in the temperature profiles. Results for the amorphous regions indicate that even for very thin layers conductivity values turned out to be near the bulk values. Values obtained for the crystalline regions show larger size dependence. Due to the statistical noise in the data and the fact that the two materials are not very different no thermal boundary resistance was observed. This study is currently being extended to investigate the thermal properties of an interface between crystalline silicon and amorphous silicon dioxide.

## ACKNOWLEDGMENTS

This work is supported by the Academy of Finland, Research Centre for Computational Science and Engineering, project no. 44897 (Finnish Centre of Excellence Programme 2000-2005).

## REFERENCES

1. K. E. Goodson and Y. S. Ju, *Ann. Rev. Mater. Sci.* **29**, 261 (1999).
2. G. Chen, *Journal of Nanoparticle Research* **2**, 199 (2000).
3. R. Venkatasubramanian, E. Siivola, T. Colpitts, and B. O'Quinn, *Nature* **413**, 597 (2001).
4. G. P. Srivastava, *The Physics of Phonons* (Adam Hilger, Bristol, 1990).
5. F. Wooten, K. Winer, and D. Weaire, *Phys. Rev. Lett.* **54**, 1392 (1985).

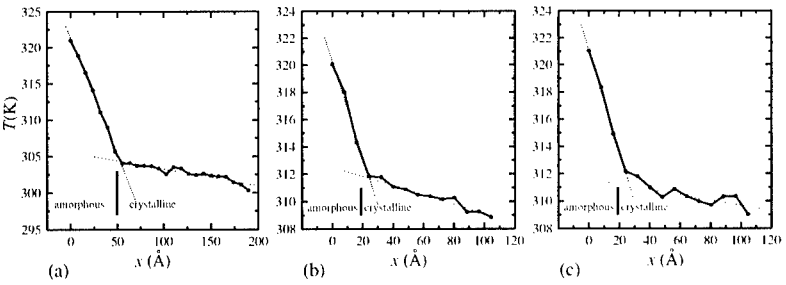


***Figure 4.*** *Temperature profiles for the simulation systems* ***A*** *(a),* ***B*** *(b), and* ***C*** *(c). Straight lines are fits to the amorphous and crystalline parts of the curves. Thick vertical lines show the position of the interface. Origin is in the center of the amorphous region (see Figure 3). Curves are averages of the profiles of the left and right parts of the system.*


6. Y. Tu, J. Tersoff, G. Grinstein, and D. Vanderbilt, *Phys. Rev. Lett.* **81**, 4899 (1998).
7. P. N. Keating, *Phys. Rev.* **145**, 637 (1966).
8. Y. Tu and J. Tersoff, *Phys. Rev. Lett.* **84**, 4393 (2000).
9. F. H. Stillinger and T. A. Weber, *Phys. Rev. B* **31**, 5262 (1985).
10. F. Müller-Plathe, *J. Chem. Phys.* **106**, 6082 (1997).
11. S. Kugler, G. Molnár, G. Petö, E. Zsoldos, L. Rosta, A. Menelle, and R. Bellissent, *Phys. Rev. B* **40**, 8030 (1989).
12. G. T. Barkema and N. Mousseau, *Phys. Rev. B* **62**, 4985 (2000).
13. J. L. Feldman, M. D. Kluge, P. B. Allen, and F. Wooten, *Phys. Rev. B* **48**, 12589 (1993).

Mat. Res. Soc. Symp. Proc. Vol. 703 © 2002 Materials Research Society V6.3

# $Fe/SiO_2$ Nanocomposite Soft Magnetic Materials

S. Hui[1], Y. D. Zhang[1], T. D. Xiao[1], Mingzhong Wu[2], Shihui Ge[2], W. A. Hines[2], J. I. Budnick[2], M. J. Yacaman[3], and H. E. Troiani[4]
[1]Inframat Corporation, 74 Batterson Park Road, Farmington, CT 06032
[2]Physics Department and Institute of Materials Science, University of Connecticut, Storrs, CT 06269
[3]Department of Chemical Engineering, University of Texas, Austin, TX 78712
[4]CNM and Texas Materials Institute, University of Texas, Austin, TX 78712

## ABSTRACT

In an effort to explore new highly resistive soft magnetic materials, $Fe/SiO_2$ nanocomposite materials have been synthesized using a wet chemical reaction approach in which the precursor complex was annealed at various temperatures. The crystallographic structure, nanostructure, morphology, and magnetic properties of the synthetic $Fe/SiO_2$ particles were studied by x-ray diffraction, transmission electron microscopy, and magnetic measurements. The experimental results show that for this approach, the α-Fe particles are coated with amorphous silica. The progress of the reaction, the purity of $Fe/SiO_2$ in the synthetic powder, and the Fe particle size are highly dependent on the annealing temperature. By adjusting the annealing temperature, the particle size can be controlled from approximately 20 nm to 70 nm. For the synthetic nanopowder obtained by $H_2$ reduction at 400 °C, there exists a superparamagnetic behavior below room temperature; while for the nanopowders obtained by reduction at higher temperatures, the ferromagnetic behavior is dominant. Based on these studies, optimum synthesis conditions for $Fe/SiO_2$ nanocomposites is determined.

## INTRODUCTION

The application of soft magnetic materials in AC electrical and electronic devices can be divided into two categories. One is the low power application, such as magnetic cores in inductors. In this case, the material works in its initial (linear) magnetization region; the frequency range can be from 100 Hz to 10 GHz. The other is the high power application, such as magnetic cores of transformers or chokes. In this case, the material works in a high magnetization region (over 50% of its saturation magnetization). Both applications require soft magnetic core materials which possess high resistivity, high saturation magnetization, high Curie temperature, high initial permeability, low eddy current loss, low hysteresis loss, low residual loss, and low dielectric loss. The advances in electronic equipment technology are in the direction of increasing the operating frequency, which creates a large demand for high frequency magnetic core materials.

Originally, metallic alloys possessed the best soft magnetic properties among all of the soft magnetic materials, but their extremely low resistivity ($10^{-6}$ Ω cm) make them inapplicable for slightly elevated frequency (> 50 kHz), even in thin ribbon form. To overcome this problem, two types of highly resistive magnetic materials have been developed: ferrites and powder materials. However, ferrites possess low saturation magnetization and low Curie temperature, while the demagnetizing factor makes the permeability of powder materials very low.

Nanocomposite processing has resulted in new opportunities to develop novel magnetic materials. For instance, in a metal/insulator nanocomposite, resistivity, which is the major concern at high frequencies, can be dramatically increased, leading to significantly reduced eddy current loss. Meanwhile, the exchange coupling between neighboring magnetic nanoparticles can overcome the anisotropy and demagnetizing effects, resulting in better soft magnetic properties than conventional materials [1]. Based on this idea, nanocomposite thin films with significantly improved high frequency properties have been developed [2,3]. However, the thin film techniques cannot be used to produce bulk components. In an earlier report, a study was presented which concerned $Co/SiO_2$ nanocomposite high frequency soft magnetic materials. These materials were fabricated using chemical synthesis and powder processing, suitable for mass production of bulk size magnetic components [4]. In addition, the $Fe/SiO_2$ nanocomposite system has also been developed. Here, the structural and magnetic property studies on the synthetic $Fe/SiO_2$ nanoparticles are presented.

## EXPERIMENTAL

$Fe/SiO_2$ nanocomposites were synthesized using a wet chemical solution technique [5]. Solutions of Fe- and Si-containing precursors were prepared separately in alcohol with controlled pH, reaction time, and temperature, to form precomposite precipitates in solution. The precipitated nanoparticle suspensions were dried in an oven to obtain a precomposite powder, which was then transferred to a high-temperature crucible in an environmental furnace. The precomposite powder was then thermochemically converted into a metal-ceramic $Fe/SiO_2$ nanocomposite powder in the presence of a reducing agent at temperatures from 400 °C to 900 °C. The nanocomposites were passivated in oil to prevent oxidation. The oil was finally washed away by an organic solvent.

Characterization of the crystal structure and particle size of the synthetic powders were carried out using x-ray diffraction (XRD) with Cu $K\alpha_1$ radiation. The nanostructure of the $Fe/SiO_2$ particles was also examined using high-resolution transmission electron microscopy (HRTEM) and Mossbauer effect (ME) experiments. Static magnetic properties of the synthetic $NiFe_2O_4$ nanoparticles were measured using a Quantum Design SQUID magnetometer at temperatures between 10 K and 300K.

## RESULTS AND DISCUSSION

### Structure

In the synthesis procedures of the $Fe/SiO_2$ nanoparticles, the $H_2$ reduction treatment of the precursor is the most critical step. In a previous paper, it was mentioned that the precursor consisted of ferrihydrite ($5Fe_2O_3 \bullet 9H_2O$) and $Fe_2SiO_4$ [6]. By annealing the precursor in $H_2$ at different temperatures, they gradually convert into bcc $\alpha$-Fe. We refer the reader to Ref. [6] for a detailed discussion of the ferrihydrite-to-Fe conversion. Here, we focus on the crystal structure and morphology of these $(Fe)_v/(SiO_2)_{1-v}$ nanoparticles, where v represents volume percentage. Figure 1 shows the XRD patterns of the synthetic $(Fe)_{50}/(SiO_2)_{50}$ powder samples obtained by reducing the precursor in hydrogen at 400, 600, and 900 °C for 3 hours. For comparison, the figure also includes the XRD pattern of a bulk-size conventional Fe sample. The XRD results indicate that all of the synthetic $(Fe)_{50}/(SiO_2)_{50}$ powders have the same bcc structure. Chemical

analysis was performed for the nanoparticles as synthesized, and the content for $SiO_2$ is 48.7% in volume for $(Fe)_{50}/(SiO_2)_{50}$ sample. As shown in the figure, there is no trace of any $SiO_2$ XRD lines, implying that the $SiO_2$ is in an amorphous state. From the linewidth of the main peak at 44.6° the mean particle size for the Fe nanoparticles was calculated according to the Scherrer equation [6]. Our results show that the Fe particle size increases with increasing $H_2$ reduction temperature in general; however, other processing parameters affect the particle size as well. For example, at the same H reduction temperature of 600 °C, the resultant Fe particle size can vary between 20 nm to 70 nm.

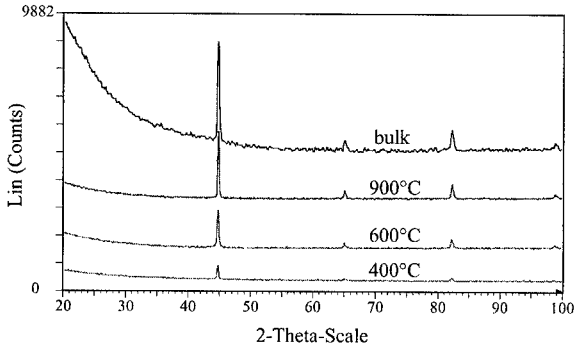


**Figure 1.** XRD patterns for $Fe/SiO_2$ nanoparticles and microsized (bulk) Fe particle.

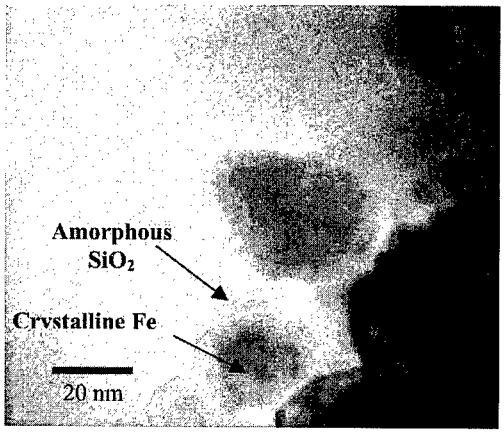


**Figure 2.** A typical TEM image showing the morphology of $Fe/SiO_2$ nanoparticles.

High-resolution transmission electron microscopy experiments were used to study the nanostructure of the synthetic $Fe/SiO_2$. Bright field images, electron diffraction, and lattice images were carried out. A typical HRTEM image showing the morphologies of the $Fe_{50}/(SiO_2)_{50}$ nanoparticle materials is presented in Figure 2. This image shows a nanoparticle

where the inner Fe core and the outer $SiO_2$ cover are distinguished. Transmission electron microscopy observations clearly show that the outer $SiO_2$ cover is amorphous. Another interesting result obtained from TEM is that the outer cover and the inner Fe core are in close contact all around the interface.

## Static magnetic properties

Figure 3 shows typical magnetization curves measured at 10 K and 300 K for $Fe_{50}/(SiO_2)_{50}$ powder sample reduced in $H_2$ at 700°C. It can be seen from the figure that the magnetization curve is close to saturation in a field of 6 kOe. The saturation magnetization of the powder is obtained to be 7095 G. Figure 4 shows the saturation magnetization as a function of the $H_2$ reduction temperature. Starting from 400°C, reducing at an elevated temperature makes the ferrihydrite and $Fe_2SiO_4$ phases more completely converted to bcc α-Fe, thus the saturation magnetization increases with increasing reduction temperature.

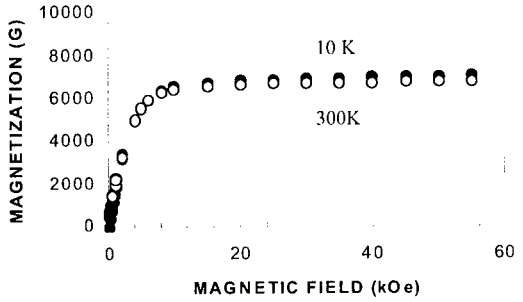


**Figure 3.** Magnetization curves of the 400°C reduced $Fe_{50}/(SiO_2)_{50}$ nanopowder sample measured at 10 K and 300 K.

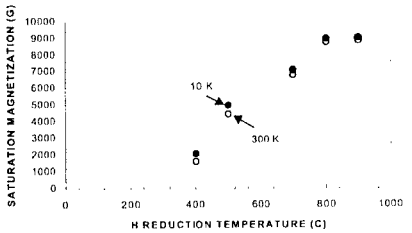


**Figure 4.** The variation of saturation magnetization with $H_2$ reduction temperature for $Fe_{50}/(SiO_2)_{50}$ nanopowder samples measured at 10 K and 300 K.

As shown in Figure 3, the magnetization curves measured at 10 K and 300 K for the 700°C annealed $Fe_{50}/(SiO_2)_{50}$ sample are very close. This is due to the high Curie temperature of α-Fe

(> 700 °C). However, for the 400°C annealed sample, its magnetization curves shown in Figure 5 are quite different; a significant decrease in saturation magnetization occurs going from 10 K to 300 K. In order to gain additional information, a low field measurement of the magnetization temperature dependence was carried out. In this measurement, the sample was cooled from room temperature to 4.2 K in a zero magnetic field (ZFC), and then a 100 Oe field was applied. The magnetization variation was measured with increasing temperature up to 360 K, followed by decreasing temperature (FC) to 10 K. The results are plotted in Figure 6. The curve shows a superparamagnetic relaxation behavior with a rather broad blocking temperature distribution.

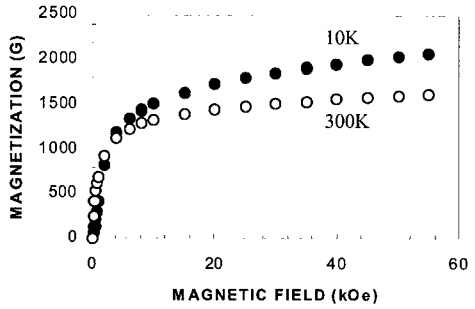


**Figure 5.** Magnetization curves of the 700°C reduced $Fe_{50}/(SiO_2)_{50}$ nanopowder sample measured at 10 K and 300 K.

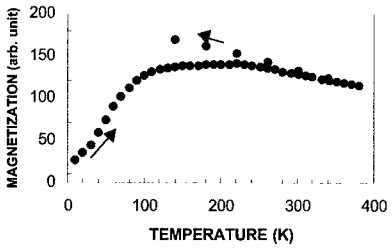


**Figure 6.** Magnetization as a function of temperature for the $Fe_{50}/(SiO_2)_{50}$ nanopowder reduced in $H_2$ at 400 °C. The arrows indicate the direction of the temperature variation.

## CONCLUSION

A wet chemical approach is developed for synthesizing $Fe/SiO_2$ nanoparticles. By reducing the precursor with a controlled $H_2$ atmosphere, temperature and time period, the conversion into α-Fe can be completed and the particle size can be controlled. In this $Fe/SiO_2$ nanocomposite, the $SiO_2$ is in an amorphous state which plays as a network coating the Fe nanoparticles.

## ACKNOWLEDGMENTS

The work is supported by NSF Grant No.DMI-0060158.

## REFERENCES

1. G. Herzer, in *Handbook of Magnetic Materials, Vol. 10*, edited by K. H. J. Buschow, (Elsevier, Netherlands, 1997) p. 415.
2. Y. Hayakawa, A. Makino, H. Fujimori, and A. Inoue, J. Appl. Phys. **81**, 3747 (1997).
3. H. Fujimori, Sripta Met. Mat. **33**, 1625 (1995).
4. Y.D. Zhang, S. H. Wang, T. D. Xiao, J.I. Budnick, and W.A. Hines, IEEE Trans. Mag. **37**, 2275 (2001).
5. Y.D. Zhang, S.H. Wang, and T.D. Xiao, U.S. Patent Appl. No. 60/243,649 (October 26, 2000).
6. D. P. Yang, Y. D. Zhang, and S. Hui, submitted to the 2001 MMM Conference, Seattle, CA, 2001.

Mat. Res. Soc. Symp. Proc. Vol. 703 © 2002 Materials Research Society V6.4

# Preparation of Optically Transparent Films of Poly(methyl methacrylate) (PMMA) and Montmorillonite

Elena Vasiliu[1], Chyi-Shan Wang[1,2], and Richard A. Vaia[3]
[1]Department of Chemical and Materials Engineering, University of Dayton, Dayton OH 45469
[2]University of Dayton Research Institute, Dayton OH 45469
[3]Air Force Research Laboratory, Wright-Patterson Air Force Base, OH 45433

## ABSTRACT

Transparent polymeric material with enhanced thermal, mechanical and barrier properties are of special interest for advanced structural, optical and photonic applications. The present paper reports a novel solution processing scheme for fabricating optically transparent polymer nanocomposites involving organophilic layered silicates. It is shown that the nanocomposite material prepared with PMMA and an organically modified montmorrilonite maintains the excellent optical transparency of PMMA. Small-angle x-ray scattering of the polymer nanocomposite material does not show any Bragg's reflection of the organophilic layered silicate. The optical transparency of the nanocomposite material is attributed to a high degree of exfoliation of the montmorrilonite in the polymer matrix.

## INTRODUCTION

Organic and inorganic fillers are commonly used to enhance polymer performance. Among the various inorganic fillers, nanoscale layered silicates, which have a sheet-like structure and an extremely large surface area (700 $m^2/g$ vs. 150 $m^2/g$ for carbon black) [1], are especially attractive for conferring thermal, mechanical and barrier properties to polymeric materials for specific applications. The organic affinity of the nanophase fillers can be modified by cation exchange with organic salts to tailor the structure and properties of the resulting polymer composite material. Individual platelets of nanoscale layered silicates have a length scale smaller than the wavelength of visible light. As a result, they may be used to reinforce organic polymers such as PMMA and polycarbonate without significantly degrading their optical clarity. The transparent polymer nanocomposite material has potential for advanced applications in protective coatings, windows, and integrated optical devices [2].

In order to achieve the maximum reinforcement of the layered silicates, their unit layers must be uniformly dispersed in the polymer matrix and have strong interaction with the polymer [3]. Various methods, such as solution mixing [4,5], melt mixing [6,7], and in-situ polymerization [8,9], have been used to disperse layered silicates into organic polymers. However, except a very few cases [9,10], results are usually a composite material containing both intercalated and exfoliated layered silicates. Normally, such a phase-separated composite material does not lead to significant improvement in thermal, mechanical and barrier properties over its host polymer. The only system that exhibits dramatic property improvement is the nylon 6-montmorrilonite nanocomposites obtained by in-situ polymerization. This composite material contains highly exfoliated montmorrilonite unit layers that are uniformly dispersed in the polymer matrix. As the in-situ polymerization of nylon 6 from caprolactam is initiated by the amino acid counter ions on the surface of the montmorrilonite, it is believed that the interfacial nylon molecules are tethered to the layered silicate through the organic salt.

In the present study, a novel solution processing scheme is devised to produce optically transparent PMMA-montmorrilonite nanocomposites. The nanodispersion of an organically modified montmorrilonite (OMM) in PMMA is achieved by mixing in a common solvent with ultrasonic agitation. The composite solution is sprayed into a fine mist to result in a rapid removal of the solvent and thereby, to obtain the nanodispersion of the OMM in the polymer matrix. The x-ray scattering patterns and optical transmission spectra of the sprayed polymer composite films are compared with those obtained from the composite films prepared by the conventional solution casting method.

## EXPERIMENTAL

### Materials

The OMM used in this study is Cloisite 6A (C6A) from Southern Clay products, Inc. This montmorrilonite is cation-exchanged with 1.40 meq/g of dimethyl dehydrogenated tallow ammonium from a sodium montmorillonite, Cloisite $Na^+$ (CNa). Since the cation-exchange capacity of CNa is 0.92 – 0.95 meq/g, therefore the C6A unit layers are covered with about 50% excess of the surfactant. The characteristic d-spacing of C6A is 36.4 Å. The PMMA was obtained from Scientific Polymer Products. It has a weight-average molecular weight of 63,000 g/mol and a polydispersity of 1.7. The solvent used is xylene from Aldrich Chemicals.

### Sample Preparation

In this study, composite solutions of PMMA and C6A were prepared by adding PMMA to a 2% C6A solution in xylene. The final solutions had a concentration of approximately 12 wt% solid content. Two mixing methods, i.e., mechanical stirring and ultrasonic agitation, were applied to preparing the solutions and the detailed processing conditions are provided in Table 1. The ultrasonic agitation vessel was immersed in an ice water bath to control the temperature. The solutions were immediately used after mixing for preparing the polymer composite films by a spraying or a casting method. The spraying was carried out using a Paasche single action-gravity feed airbrush with a 0.635mm diameter nozzle under a pressure of 20 psi. The films were sprayed on a glass substrate from a distance of 15 cm. The various polymer composite samples prepared are denoted by their solution preparation and film forming methods. For example, a D-C film indicates the sample prepared from solution D, followed by the solution casting method. All the polymer composite films characterized had been vacuum dried at 80°C overnight.

### Characterization

Small-angle x-ray scattering (SAXS) was used to probe the dispersion of C6A in the polymer composites. It was performed using an Ultrax 18 rotating anode generator equipped with a Statton camera. $CuK_\alpha$ radiation ($\lambda$ = 1.5418 Å) with a graphite monochromator was used at an accelerating voltage of 50kV/150mA. The x-ray scattering patterns were recorded on phosphor image plates. UV-visible spectra of the polymer composite films were measured over a wavelength range from 200 to 1000 nm with a Hewlett Packard 8453 spectrophotometer at ambient conditions.

**Table 1.** Composite solution preparation conditions

| Solution | C6A/xylene | PMMA/C6A/xylene |
|---|---|---|
| A | Mechanical stirring/1 hr | Mechanical stirring/1 hr |
| B | Mechanical/1 hr + Ultrasonic/3 hrs | Mechanical stirring/1 hr |
| C | Mechanical/1 hr + Ultrasonic/3 hrs | Ultrasonic agitation/1 hr |
| D | Mechanical/1 hr + Ultrasonic/3 hrs | Ultrasonic agitation/3 hrs |
| E | Ultrasonic agitation/1 hr | Ultrasonic agitation/1 hr |
| F | Mechanical stirring/1 hr | Ultrasonic agitation/3 hrs |

## RESULTS AND DISCUSSION

Small-angle x-ray scattering was used to probe the nanodispersion of C6A in both sprayed and cast composite films. The as received C6A has a d-spacing of 36.4 Å, which decreases to 34Å after C6A is vacuum dried at 80°C. However, after C6A is dissolved in xylene and then vacuum dried at 80°C, it shows a d-spacing of 31.6Å. It suggests that once C6A is dissolved in xylene, some dimethyl dehydrogenated tallow ammonium is removed from the C6A surface resulting in the smaller d-spacing. Figure 1 shows the x-ray scattering pattern of a D-C composite film. The film exhibits a basal spacing of 38.2Å, indicating PMMA molecules have migrated into the C6A gallery and formed an intercalated polymer composite material. The flat-view scattering pattern of the polymer composite suggests that the intercalated C6A platelets are uniformly dispersed in the film, while the edge-view pattern indicates that the C6A platelets are oriented to some degree in the plane of the film, giving rise to stronger scattering intensity in equatorial direction.

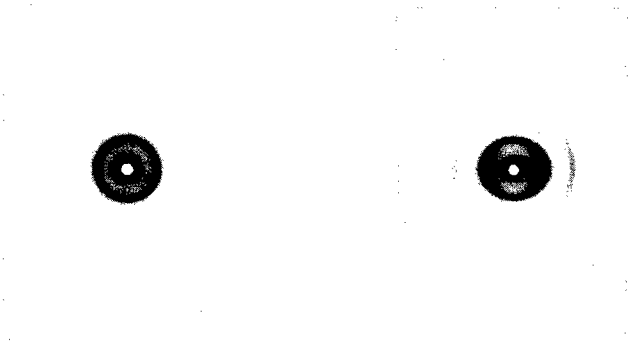

(a) (b)

**Figure 1.** X-ray scattering pattern of a D-C composite film: (a) flat-view and (b) edge-view.

The D-S composite film did not show an x-ray scattering pattern of significant intensity in either flat-view or edge-view test configuration. Figure 2 compares the intensity scan in equatorial direction of the flat view scattering pattern of a D-C composite film with that of a D-S composite film. The sprayed composite film shows minimal scattering intensity due to Bragg's reflection from the basal spacing of the layered silicate. It suggests that the OMM was exfoliated

in the D-S composite film. Since the D-C and the D-S composite films were prepared from the same solution, the distinct morphologies of the two films must arise from the different film forming processes. In order to cast optically clear and surface-smooth polymer composite films, solvent evaporation was controlled at a considerably slow rate. Previously, it was found that when the solvent of a polymer composite solution of layered silicates is removed to a certain extent, the solution forms a gel-like structure. This gel-like structure gradually builds up as the layered silicate platelets orient themselves towards a position of minimum free energy under the influence of Brownian motion [11]. Upon coalescing of the platelets, polymer chains are entrapped in between platelets resulting in a basal spacing of 38-40Å. In the sprayed films, the solvent was removed so rapidly that the system did not have an opportunity to reach the equilibrium state. As a result the composite film retained the nanodispersion of the layered silicate platelets in the polymer matrix as that in the composite solution.

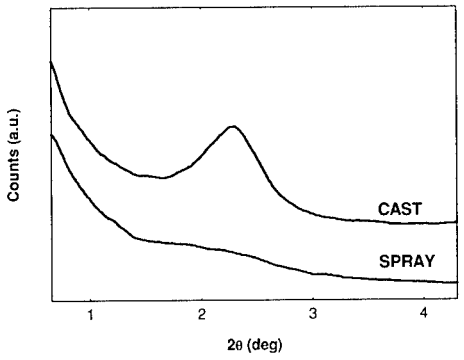


**Figure 2.** X-ray intensity scan of a sprayed and a cast composite film prepared from solution D (intensity vertically shifted for clarity).

A series of composite films were prepared by the spray method from the various composite solutions. Their x-ray intensity scan in equatorial direction of the flat-view scattering pattern is shown in Figure 3. It indicates that A-S composite film sprayed from solution A had the characteristic basal reflection of intercalated structure. Since the same spray method was used to prepare A-S as well as D-S composite film, the difference in the morphology must originated from their composite solutions. This points out that mechanical stirring alone is insufficient to exfoliate C6A into individual unit layers in the composite solution. The films that showed the highest decrease in the degree of coherent layer stacking were those sprayed from solutions D and F, which had experienced the longest ultrasonic agitation after the addition of the layered silicate. The initial ultrasonic agitation of C6A/xylene solution did not seem to facilitate the subsequent exfoliation of the layered silicate in the composite solution, which may be due to a poor chemical affinity between PMMA and C6A. When the composite solution is under ultrasonic agitation, high intensity energy is introduced into the solution keeping the layered silicate platelets in constant motion and dissociated from one another. The lack of basal reflection in D-S composite film pattern suggests that using ultrasonic agitation to disperse layered silicates in polymer solutions achieves exfoliation even when the silicate concentration is moderately high (20% wt).

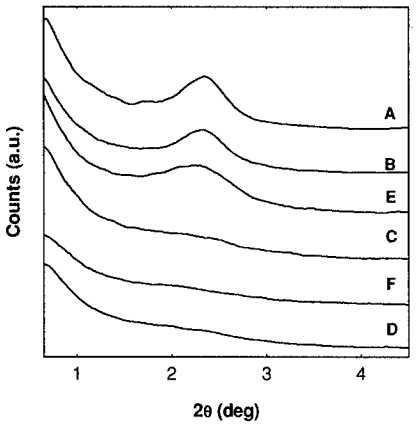


**Figure 3.** X-ray intensity scan of various sprayed composite films (vertically shifted for clarity).

The optical transmittance of several sprayed and cast composite films is shown in Figure 4. The transmittance was measured with a UV-Vis spectrometer over a wavelength range from 200 to 1000 nm. Figure 4 shows that the most optically clear composite films have a transmission between 80 and 90% in the visible light region. However, the optical transmission of the cast composite films was relatively poor, especially in the low wavelength region. This indicates that the cast films contain layered silicate particles that are large enough to scatter the visible light. The result suggests that the present processing scheme may open new windows for achieving nanodispersion of layered silicates in organic polymers, even when the polymer is incompatible with the layered silicate.

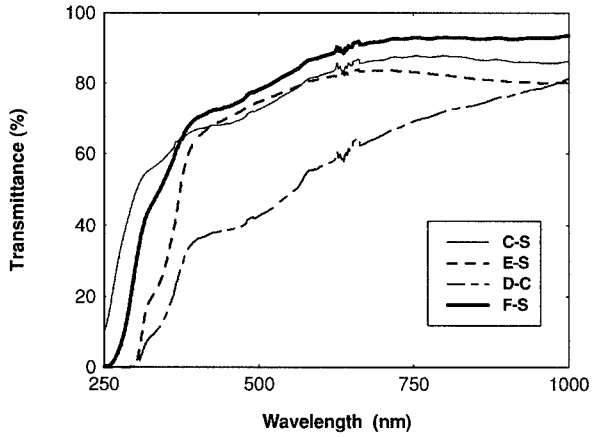


**Figure 4.** Optical transmittance of sprayed and cast PMMA/C6A composite films.

## CONCLUSIONS

A novel solution processing scheme was devised to produce optically transparent polymer nanocomposites of layered silicates. In the processing scheme, ultrasonic agitation is utilized to achieve nanodispersion of an organophilic layered silicate in the composite solution of a choice polymer. Then the solvent is rapidly removed by spraying the composite solution into a fine mist. This rapid solvent removal greatly curtails the phase separation kinetics of the layered silicates, even though it may be thermodynamically favored. It is shown that PMMA/C6A nanocomposites (20 wt% of the layered silicate) prepared by the present processing scheme have an optical transmission greater than 80% in the visible light region. This processing scheme opens new processing windows for achieving polymer/layered silicate nanocomposites even if the polymer may not be compatible with the layered silicate.

## ACKNOWLEDGMENTS

This research was supported in part by the U.S. Air Force under contract No. F33615-00-D-5008. One of the authors (EV) was supported by a Fellowship from Delphi Automotive Systems.

## REFERENCES

1. Olphen, H. V. *An introduction to clay colloids chemistry*; Wiley: New York, 1977.
2. Carotenuto, G.; Nicolais, L.; Kuang, X. *Appl. Composite Matls.* **1996**, *3*, 103-116.
3. LeBaron, P. C.; Wang, Z.; Pinnavaia, T. J. *Appl. Clay Sci.* **1999**, *15*, 11-29.
4. Gao, Z.; Xie, W.; Hwu, J. M.; Wells, L.; Pan, W.-P. *J. Thermal Anal. Calorim.* **2001**, *64*, 467- 475.
5. Lemmon, J. P.; Wu, J.; Oriakhi, C.; M.Lerner, M. *Electrochimica Acta* **1995**, *40*, 2245-2249.
6. Alexandre, M.; Beyer, G.; Henrist, C.; Cloots, R.; Rulmont, A.; Jérôme, R.; Dubois, P. *Macromol. Rapid Commun.* **2001**, *22*, 643-646.
7. Vaia, R. A.; Jandt, K. D.; Kramer, E. J.; Giannelis, E. P. *Chem. Mater.* **1996**, *8*, 2628-2635.
8. Messersmith, P. B.; Giannelis, E. P. *Chem. Mater.* **1994**, *6*, 1719-1725.
9. Lincoln, D. M.; Vaia, R. A.; Wang, Z.-G.; Hsiao, B. S. *Polymer* **2001**, *42*, 1621-1631.
10. Chen, G.; Ma, Y.; Qi, Z. *Scripta Materialia* **2001**, *44*, 125-128.
11. Luckham, P. F.; Rossi, S. *Adv. Colloid Interface Sci.* **1999**, *82*, 43-92.

Mat. Res. Soc. Symp. Proc. Vol. 703 © 2002 Materials Research Society V6.6

# Characterization of the Morphology of Faceted Particles by Transmission Electron Microscopy

Shirley Turner, David S. Bright
Chemical Science and Technology Laboratory, National Institute of Standards and Technology, Gaithersburg, MD 20899-8371

## ABSTRACT

Faceting in a polyhedral rutile particle was modeled from transmission electron microscopy images. A double-tilt, rotate transmission electron microscope (TEM) sample holder was used to manipulate the particle. Using this holder, it was possible to align the c axis of the particle along one of the axes of the sample holder. This alignment allowed images to be obtained of the particle in several orientations around its c axis. Assuming symmetrical growth perpendicular to the c axis of the rutile particle, comparison of dimensions and angles obtained to those obtained for hypothetical models of the particle gives information about its likely prismatic and pyramidal faceting. This approach to facet modeling in combination with thickness information should be useful for more complete determination of the faceting in individual euhedral particles using transmission electron microscopy.

## INTRODUCTION

Identification of the faceting in polyhedral particles is important in many applications. For example, different facets in catalysts have different efficiencies for promoting reactions. In pigment particles, certain morphologies are more desirable for durability of paint. Characterizing the morphology of particles with transmission electron microscopy is challenging because a TEM image is a two-dimensional (2D) projection of the material. In the biological field, 3D reconstruction techniques have long been used to derive 3D models of cellular and other biological structures from 2D TEM images. Recently, there have been several efforts to apply similar reconstruction techniques in the material science field [1-4]. The techniques have been applied to deriving the distribution of metal particles on silicates [1,2], channels in zeolites [1], and particles in nanocomposites [4].

The 3D reconstruction techniques have not yet been used to derive information about the faceting of particles. At present, such faceting information is typically derived by examining oriented crystallites and measuring angles between linear features in the outline of the 2D projections. If several crystallites are found in different orientations, a 3D model for the typical particle can be derived. Such a 3D model is an average of information from different particles and is not particle specific. In this work, a double-tilt, rotate (2TR) holder is used to orient and tilt a particle to derive information for comparison with morphological models. The 2TR holder has three degrees of freedom theoretically allowing the TEM operator to align a crystallographic direction of interest along one of the tilt axes. This alignment is not possible with conventional double-tilt or rotate-tilt holders unless serendipity leads to a suitably oriented particle. When a crystallographic direction of interest is suitably oriented, tilting of the particle around that direction can allow for measurement of dimensions and comparison to models of crystallite faceting. In this initial study, four-fold symmetrical growth perpendicular to the c axis of the particle was assumed.

## EXPERIMENTAL

The material examined was rutile ($TiO_2$) used in paint pigment. The material was dry mounted onto a carbon film grid. It was studied in an FEI CM30 TEM operated at 300 kV[1]. A Gatan Model 679 CCD camera was used to record images of the particle. A Gatan Model 925 TEM sample holder was used in the study (note: in this work, the tilt axis along the rod length is referred to as the x axis; the tilt axis perpendicular to the x axis is referred to as the y axis). The tilt range around the x axis is limited by the objective pole piece ($\pm 45^{\circ}$ in this work) and tilt around the y axis is $\pm 24^{\circ}$. Measurement of particle width and length was done using tools in Lispix, a public domain image analysis program for Windows [5,6]. The particle was highlighted using a threshholding tool and the maximum and minimum diameters determined automatically using a caliper tool. Two sets of measurements were made. Particle modeling was aided by use of Shape software [7].

## RESULTS

For this initial study, a euhedral rutile particle approximately 200 nm in width and 500 nm in length was chosen. The particle was oriented down [110] using the double-tilt x and y axes of the sample holder. The particle was then rotated around [110] so that the c axis of the particle was aligned along the x axis of the sample holder (Fig. 1a). The particle was then tilted around its c axis (Figs. 1a-f). The alignment of the c axis of the particle and the x axis of the sample holder is confirmed by the acquisition of several diffraction patterns containing [001]* including those in Figs. 1b, d, and f.

### Prismatic faceting

For the 2D projection given in Figure 1a, there are several possible prismatic facets including those commonly found for rutile - {110}, {230}, {120}, {130}, {140}, {170} and {100}[8]. It is not possible to readily distinguish between these forms using the single image of Figure 1a. However, the good alignment of the c axis of the particle to the x axis of the sample holder allows for deductions to be made about the prismatic faceting based on measurement of the particle width and its variation with tilt angle. Images were collected in intervals of $3^{\circ}$ tilt around the particle c axis with the [110] orientation at $0^{\circ}$ tilt. The width of the particle at each tilt was measured. Slight curvature of the particle sides was noted at higher angles of tilt. For this initial study, the largest width was measured. For comparison purposes, the width at each orientation was then normalized to the width of the particle in the [110] orientation.

Subsequently, the projected widths for hypothetical particles with the common rutile forms were calculated at $3^{\circ}$ intervals from the [110] orientation. As done for the rutile particle, each width was then divided by the width of the particle in the [110] orientation. Plots of the width ratios vs. tilt angle for the actual particle and the models are given in Figure 2. The width ratios for the particle do not exactly match any of those for the common single forms. It is therefore postulated that the prismatic facets consist of a combination of forms. We note from

[1] Certain commercial equipment, instruments, or materials are identified in this paper to specify adequately the experimental procedure. Such identification does not imply recommendation or endorsement by the National Institute of Standards and Technology, nor does it imply that the materials or equipment are necessarily the best available for the purpose.

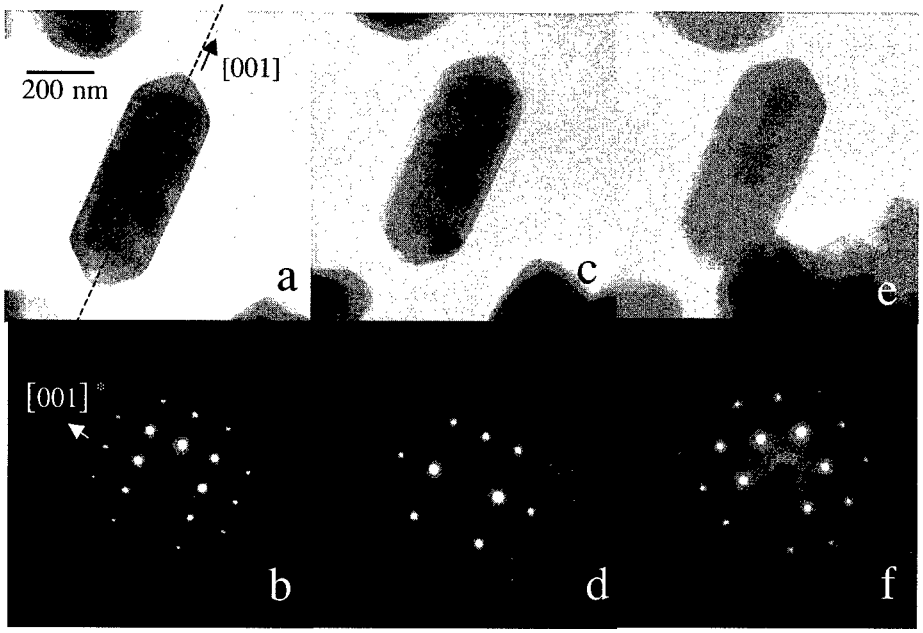


Figure 1. Images and diffraction patterns of a rutile particle. The particle is oriented down [110] so that the c axis of the particle is aligned along the x axis of the sample holder (projection of x axis indicated by dashed line in Fig 1a). The particle is rotated around the holder x axis. Diffraction patterns containing [001]* are obtained (b) [110], (d) [210], and (f) [100].

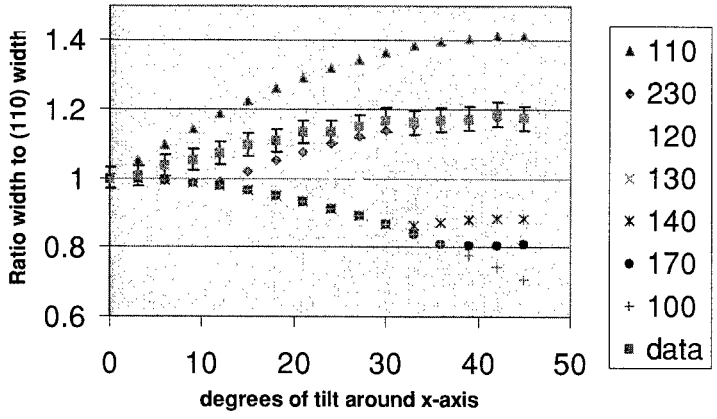


Figure 2. Plots of the ratio of particle width to particle width in [110] orientation vs. degrees tilt for various prismatic forms of rutile and for particle data.

Figure 2 that the width ratios for the particle increase for increasing tilt angle whereas there is an initial decrease in width ratios for {230}, {120}, {130}, {140}, {170} and {100}. It is therefore postulated that {110} is a major facet since it is the only form for which the width ratio consistently increases with tilt angle.

Possible combinations of common forms include {110} with {120}, {130}, {140}, {170} or {100}. Models of three of these combinations are shown in Figure 3 a-c. Width ratios for the five possible combinations were determined for different orientations for the models rotated around the c axis at 3° intervals (plots for three of the models are given in Figs. 3d-f). A comparison of the data and plots for the five cases shows that the {120} modification is not a good match to the data; the other models show a fairly good match. Given the uncertainties in measurements in the present work, it is not possible to distinguish between the {110} form modified by {130}, {140}, {170} or {100}.

Pyramidal faceting

Pyramidal facets can be modeled directly from the projected angles (Figs. 4a, b). The average measured pyramidal angles in the [110] orientation is ~ 95 ± 2° and in the [100] orientation is ~ 114 ± 2°. These values can be compared to those expected from pyramidal facets commonly found in rutile (Table 1) [8]. Projected angles were determined from Shape software.

Table 1. Projected angles for common pyramidal facets of rutile

| Pyramidal form | Projected angle [110] | Projected angle [100] |
|---|---|---|
| {101} | 131.02° | 114.42° |
| {111} | 95.38 | 114.42 |
| {301} | 72.39 | 54.72 |
| {501} | 47.41 | 34.5 |
| {221} | 57.52 | 75.63 |
| {133} | 117.46 | 114.42 |
| {131} | 57.52 | 54.72 |
| {233} | 105.59 | 114.42 |
| {231} | 47.41 | 54.72 |

Projected angles for {111} most closely match the angles in experimental images in both [110] and [100] orientations. Note that for both the [110] and [100] orientation there are forms with the same projected angles. Acquisition of angles in two orientations is helpful in making an unambiguous identification.

Model for faceting of the particle

A basic model for faceting of the particle consists of {110} prismatic facets with {111} pyramidal facets. The corners of the {110} facets are truncated. A working model of the faceting is shown in Figure 5 in the [110] and [100] orientation. The modification of {110} is represented as {hk0}. The model is an approximation to the particle shape as there is slight curvature of the crystallite edges and rounding of facet corners in some projections.

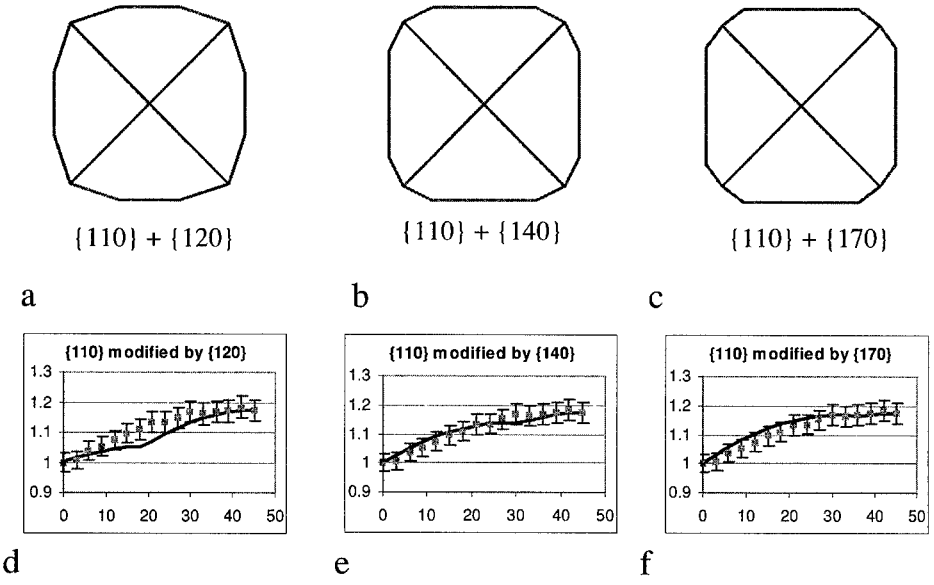


Figure 3. (a-c) Examples of three possible combinations of common prismatic rutile forms. The models are viewed down [001]. The dimensions of the facets fit the width ratios for data collected from the particle in the [110] and [100] orientations. (d-f) Plots of projected width ratio (y axis of plot) vs. tilt angle (x axis) for tilting of each model above. The lines on the plots correspond to the width ratio for the model; the markers correspond to data from the particle.

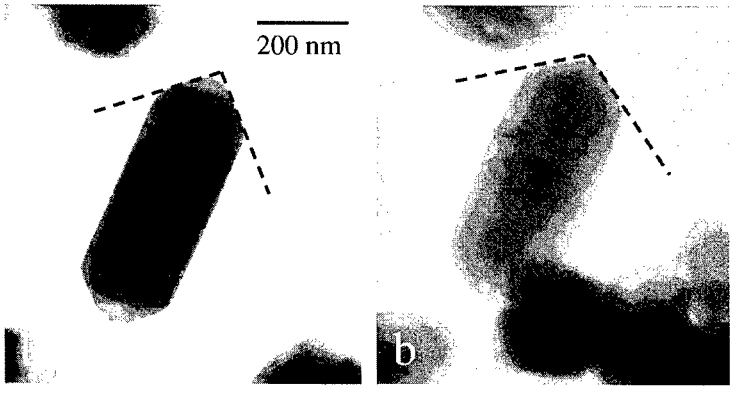


Figure 4. Projected pyramidal angles (dashed lines) of rutile particle in (a) [110] orientation and (b) [100] orientation.

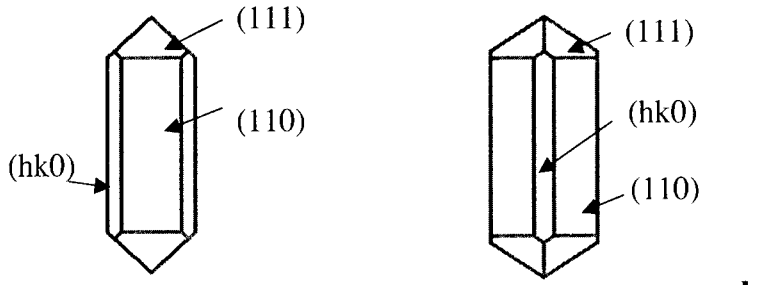


Figure 5. Model for faceting of rutile particle shown in (a) [110] and (b) [100] orientations.

## SUMMARY

This work has shown that the 2TR holder allows for alignment of crystallographic directions of interest along holder axes. Measurement of changes in crystal width and angles in a range of known orientations can therefore be compared to changes in widths and angles expected from possible models of crystal faceting in the same orientations. In this initial study of a rutile particle, four-fold symmetrical growth perpendicular to the c axis was assumed. Measurement of width ratios indicates that {110} is the likely predominant prismatic facet and that the {110} faceting is further modified although the uncertainty in the measurement does not allow distinction between several facet models. Measurement of projected angles of the particle in two orientations indicates that {111} is the predominant pyramidal facet. The faceting model derived in this study provides basic information about the particle shape but is only an approximation to it and is based on the assumption of symmetrical growth perpendicular to the particle c axis. It is expected that this approach to facet modeling in combination with thickness determination and 3D reconstruction techniques will be a useful method for more complete characterization of faceted, euhedral particles.

## REFERENCES

1. A.J. Koster, U. Ziese, A.J. Verkleij, A.H. Janssen, and K.P. De Jong, J. Phys. Chem. B, **104** (40), 9368 (2000).
2. M. Weyland, P.A. Midgley, and J.M. Thomas, J. Phys. Chem. B. **105** (33), 7882 (2001).
3. P.A. Midgley, M. Weyland, J.M. Thomas and B.F.G. Johnson, Chem. Commun., **2001**, 907 (2001).
4. G. Mobus and B.J. Inkson, Appl. Phys. Let. **79** (9), 1369 (2001).
5. D.S. Bright, Microbeam Analysis **4,** 151 (1995).
6. www.nist.gov/lispix/[2]
7. www.shapesoftware.com
8. C. Palache, H. Berman and C. Frondel, *Dana's System of Mineralogy*, Vol. 1, (John Wiley and Sons, New York, 1944).

[2] At the time this paper was written, URLs referenced herein were deemed to be useful supplementary material for this paper. Neither the authors nor the Materials Research Society warrants or assumes responsibility for the content or availability of URLs referenced in this paper.

Mat. Res. Soc. Symp. Proc. Vol. 703 © 2002 Materials Research Society V6.9

# Preparation of Copper Aluminium Oxide by Spray Pyrolysis

Ji Youn Rim, Shin Ae Song and Seung Bin Park
Korea Advanced Institute of Science and Technology, Dept. of Chemical Engineering,
373-1, Guseong-dong, Yuseong-gu, Daejeon, 305-701, Republic of Korea

## ABSTRACT

Copper aluminium oxide($CuAlO_2$) particles, a promissing p-type TCO(transparent conducting oxide), were prepared by spray pyrolysis. Delafossite phase of $CuAlO_2$ was obtained when copper nitrate, copper acetate and copper sulfate, divalent copper precursors, were used as copper precursor and aluminium nitrate as aluminium precursors. However, when copper chloride (CuCl, a monovalent copper precursor) was used, the delafossite phase was not obtained regardless of the type of aluminium precursor. The $O_2$-doped $CuAlO_2$ was obtained by using oxygen as carrier gas.

## INTRODUCTION

The $CuAlO_2$ particles are prepared by solid-state reactions of $Cu_2O$ and $Al_2O_3$.[1] Solid-state reaction method is cheap and oxide precursors are readily available. But this method needs repeated milling and calcination, and the prepared particles have irregular morphology and large size. The spray pyrolysis has some advantages in comparison to the solid-state reaction method. Spray pyrolysis is simple and has the ability to produce chemically homogeneous multi-metal oxides[2]. A wide variety of reactants can be used as long as they have proper solvent. This flexibility allows the use of inexpensive reactants such as metal nitrates, chlorides, fluorides, etc.

In this work, copper aluminium oxide particles with delafossite were prepared by the spray pyrolysis for the first time. Various metal salts were used as precursors, and their effects on the crystal structure were investigated. The bulk conductivity of $CuAlO_2$ is known to be $1.7\times10^{-3}$ S/cm [3] and the origin of positive hole in $CuAlO_2$ is not clear but may be excess oxygen[4]. To obtain higher conductivity, M. S. Lee et al. annealed $CuAlO_2$ pellet at 943 K under $O_2$ atmosphere for $O_2$ doping to $CuAlO_2$. However, the doping process decomposed $CuAlO_2$ into CuO and $CuAl_2O_4$[5]. Therefore, the particles were prepared by using oxygen as carrier gas to prepare $O_2$ doped $CuAlO_2$

## EXPERIMENTAL DETAILS

The spray pyrolysis system consisted of an ultrasonic nebulizer and a reaction furnace. The stock solution was atomized with a sonicator equipped with 1.7 MHz resonator. Copper nitrate, copper acetate, copper sulfate ( divalent copper precursors) and copper chloride (a monovlent copper precursor) were tested as copper precursors and aluminium nitrate, aluminium chloride and aluminium sulfate were tested as aluminium precursors. Stock solutions of 0.5 M were prepared by dissolving copper and aluminium precursors into two different solvents. Copper chloride was dissolved into 15 wt.% HCl because of its low solubility in pure water and the other precursors were dissolved in distilled water. The reactor temperature was fixed at 973 K. The flow rate of carrier gas was 4 L/min. Air, $N_2$ and $O_2$ were used as carrier gas. The as-prepared

particles were annealed at 1073, 1373 and 1573 K for 3 hours for crystallization. The crystalline structure was characterized by x-ray diffraction(XRD). The conductivity was measured by the 4-probe method at room temperature. For measurement of conductivity, pellets of 13mm in diameter and 0.2mm in thickness were fabricated by pressing at 3000 psia. As a reference, conductivity of particles which were prepared by solid-state reaction at 1373K for 10hr was measured by the same method.

## RESULTS AND DISCUSSION

Figure 1 shows the XRD spectra of particles prepared from copper nitrate and aluminium nitrate. The particles had different peaks depending on annealing temperatures. Before annealing, they had only CuO peaks. The particles annealed at 973 K had peaks of CuO and $CuAlO_2$ which was not a TCO(transparent conducting oxide). After annealing at 1373 K, they were converted to $CuAlO_2$ of delafossite structure. Being annealed at 1573 K, the particles had peaks corresponding to CuO, $Cu_2O$ and $Al_2O_3$. It is clear that there exists an optimum post-treatment temperature. In this experiment, samples treated at 1373 K, give the delafossite structure.

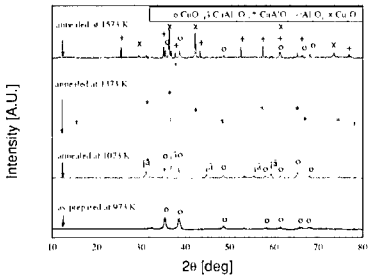


**Figure 1**. The XRD spectra of particles prepared from starting solution of $Cu(NO_3)_2$ and $Al(NO_3)_3$ after annealing at 973, 1373 and 1573 K. [carrier gas : air]

Figure 2 shows the effect of the types of copper and aluminium precursor. Figure 2(a) is the XRD pattern of particles prepared from aluminium nitrate. When copper nitrate, copper acetate and copper sulfate were used as copper precursor, the particles had delafossite phase. The particles prepared from copper chloride(CuCl) which was a monovalent copper precursor had not only delafossites ($CuAlO_2$) but also spinel phase($CuAl_2O_4$). But spinel peaks were stronger than delafossite peaks. Therefore, copper chloride was not a suitable copper precursor. The result is contradictory to the solid state reaction in which only monovalent copper precursor is suitable for the formation of delafossite phase.

Figure 2(b) is the XRD patterns of particles prepared by using aluminium chloride. In this case, the delafossite phase was obtained from copper nitrate and copper sulfate. But they had spinel phase, too. The particles prepared from copper acetate and copper chloride had peaks of $CuAl_2O_4$ and $Al_2O_3$. Therefore, aluminium chloride is not suitable for preparing pure delafossite phase

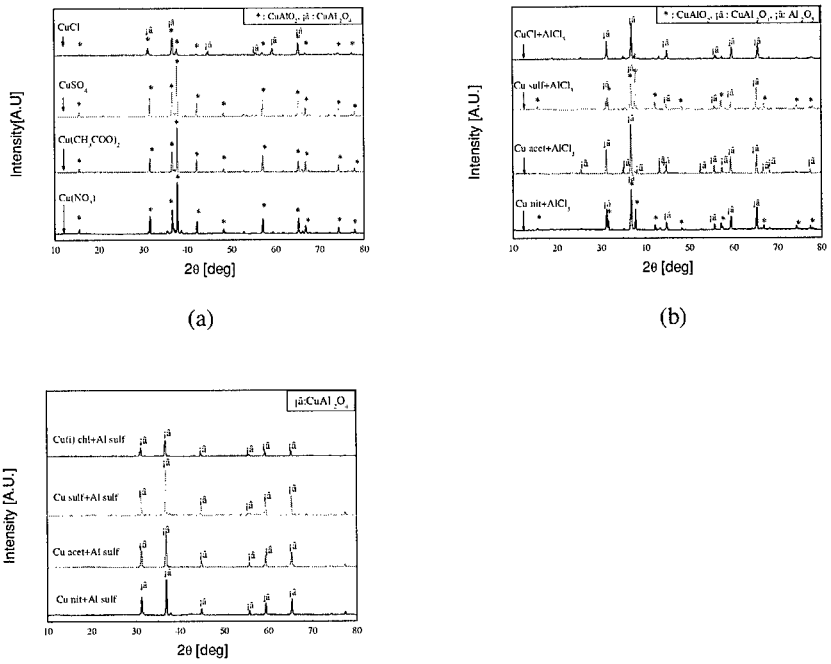


**Figure 2.** The XRD spectra of particles prepared from aluminium nitrate(a), aluminium chloride(b) and aluminium sulfate(c) after annealing at 1373K.[carrier gas : air]

Figure 2(c) is the XRD spectra of particles prepared from aluminium sulfate. The particles prepared by using aluminium sulfate had not delafossite structure but spinel phase of $CuAl_2O_4$ regardless of the types of copper precursors.

Figure 3 shows that the kind of carrier gas did not affect crystal structure of particles. The particles were prepared from stock solution of copper nitrate and aluminium nitrate and had delafossite structure after annealing at 1373K regardless of carrier gas. The conductivity was affected by carrier gas. The conductivities of particles are in table 1. The pellet of the particles prepared by using $O_2$ as carrier gas had the highest conductivity. It shows that using $O_2$ as carrier gas help to prepare $O_2$ doped copper aluminate.

**Table 1.** Conductivities of particles.

| Precursors | Cu nit + Al nit | | | Cu acet+Al nit | Cu sulf+Al nit | Solid-state reaction |
|---|---|---|---|---|---|---|
| Carrier gas | $N_2$ | Air | $O_2$ | Air | Air | |
| Conductivity[S/cm] | 0.205 | 0.157 | 0.589 | 0.138 | 0.015 | 0.376 |

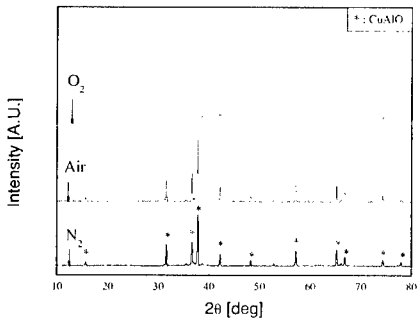


**Figure 3.** The XRD spectra of particles prepare by using $O_2$, air and $N_2$ as carrier gas and annealed at 1373 K. [ copper precursor : $Cu(NO_3)_2$, aluminium precursor : $Al(NO_3)_3$]

## CONCLUSIONS.

Copper aluminium oxide particles with delafossite were prepared by spray pyrolysis for the first time. $Cu(NO_3)_2$, $Cu(CH_3COO)_2$ and $Cu(SO_4)$ can be used as copper precursor. However, only $Al(NO_3)_3$ was a proper aluminium precursor. For doping oxygen, $O_2$ had to be used as carrier gas. In the solid-state reaction, post-treatment with $O_2$ converted the $CuAlO_2$ to $CuAl_2O_4$ and CuO. Therefore, It was expected that $O_2$ doped $CuAlO_2$ was difficult to be prepared by solid-state reaction. The highest conductivity was achieved when $Cu(NO_3)_2$ and $Al(NO_3)_3$ was used as precursors, and $O_2$ as carrier gas. This value was higher than the bulk conductivity of $CuAlO_2$ prepared by solid-state reaction

## ACKNOWLEDGMENT

This work was financially supported by the Brain Korea 21 project.

## REFERENCES

[1] H. Kawazoe, M. Yasukawa, H. Hyodo, M. Kurita, H. Yanagi and H. Hosono, Nature 389, 30 (1997)
[2] Toivo T. Kodas and Mark J. Hampden-Smith, Aerosol processing of materials Wiley-VCH
[3] F. A. Benko and F. P. Koffyberg, J. Phys. Chem. Solids 45, pp 57-59 (1984)
[4] Gordon Thomas, Nature 389, pp 907-908 (1997)
[5] M. S. Lee, T. Y. Kim, and D. Kim, Applied physics letters 79, 13, pp 2028-2030 (2001)
[6] H. Yanagi, H. Kawazoe, A. Kudo, M. Yasukawa and H. Hosono, J. of Electroceramics 4:2/3, pp 407-414 (2000)

Mat. Res. Soc. Symp. Proc. Vol. 703 © 2002 Materials Research Society V6.19

# Temperature Dependence of Electroresistivity, Negative and Positive Magnetoresistivity of Graphite/Diamond Nanocomposites and Onion-Like Carbon

Anatoliy I. Romanenko[1], Olga B.Anikeeva[1], Alexander V. Okotrub[1], Vladimir L. Kuznetsov[2], Yuriy V. Butenko[2], Andrew L. Chuvilin[2], C. Dong[3], Y. Ni[3]

[1]Institute of Inorganic Chemistry SB RAS, Lavrentieva 3, Novosibirsk 630090, RUSSIA.
[2]Boreskov Institute of Catalysis SB RAS, Lavrentieva 5, Novosibirsk 630090, RUSSIA.
[3]National Laboratory for Superconductivity, Institute of Physics Chinese Academy of Science, P.O.Box 603, Beijing 100080, China

## ABSTRACT

Here we present the result of measurements of electrical resistivity and magnetoresistivity of graphite/diamond nanocomposites (GDNC) and onion-like carbon (OLC) prepared by vacuum annealing of nanodiamond (ND) at various fixed temperatures. GDNC contain particles with a diamond core covered by closed curved graphitic shells. The electrical resistivity of annealed ND is characteristic of systems with localized electrons and can be described in terms of variable hopping-length hopping conductivity (VHLHC). The magnetoresistivity of OLC is negative in the range of field $0<B<2$ T, and is positive at $B>2$ T. The conduction carrier concentration for OLC samples was estimated in the framework of the theory of negative magnetoresistance in semiconductors in the hopping conduction region. The free path length for conducting electrons at liquid helium temperature was estimated from the data on positive magnetoresistivity. The localization length of current carriers was also estimated. The determined parameters are in agreement with proposed structure model of OLC constructed using HRTEM data.

## INTRODUCTION

The study of electron transport properties of carbon materials is of interest due to wide practical applications and provides information on their structural perfection and electronic structure. The electronic properties of carbon materials vary over an enormous range due to the possibility of carbon to form different allotropes. Diamond is insulator, while graphite can be considered as a semi-metal. At the same time electronic transport and magnetic properties of graphitic materials strongly depend on their structure and the presence of defects. Thus the conduction carrier concentration ($n$) depends on the defect number and structure [1], while the electrical and magnetic properties depend on this concentration [2, 3]. Influence of defects on the properties of multiwall carbon nanotube are considered in [ 4-7]. We have developed a method for production of graphite/diamond nanocomposites (GDNC) and onion-like carbon (OLC) based on controlled vacuum annealing of ND [8, 9]. In this work we study electrical resistivity and magnetoresistivity of GDNC and OLC prepared by ND annealing at various fixed temperatures.

## EXPERIMENTAL DETAILS

ND samples with an average particle size of 4.7 nm were prepared by an explosive method and isolated from the detonation soot by the oxidative removal of nondiamond carbon with a hot mixture of concentrated $H_2SO_4$ and $HClO_4$ acids in 1:1 proportion. Annealing procedure is described elsewhere [8, 10]. The diamond weight fractions in GDNC treated at different temperatures have been previously determined by the measurements of the true densities of the samples. Surface area of samples increases with annealing temperature from 340 $m^2/g$ up to 500 $m^2/g$. Carbon black (286 $m^2/g$), graphitized soot (2700 K, 9 $m^2/g$) and POCO graphite AF (12 $m^2/g$) were used as comparison carbon samples. Micrographs of the annealed products were obtained with a JEM-2010 transmission electron microscope.

Four-probe *dc* measurements of resistivity vs. temperature $\rho$(T) at 4-300 K were performed. For details see in [10]. The samples were placed in glass tubes with a diameter $d$=2 mm and length $l$=20 mm to measure the electrical resistance. Silver wire was used to make contacts with the samples. We find that ρ(T) is highly reproducible for several measurements on different samples from the same batch.

The magnetoresistivity was measured in the field ($B$) range 0 - 5.5 T at a temperature of 4.5 K using a model MPMS-5 SQUID magnetometer.

## RESULTS

Fig.1 presents typical TEM images of ND heated at four different temperatures. The dark straight contrast lines in micrographs (a) and (b) correspond to the (111) crystallographic diamond layers. The distance between these lines is 2.06 Å. The dark curved lines in Figs.(b), (c) and (d) correspond to the (0002) crystallographic graphite layers (d ~ 3.4 Å). The TEM images of the ND heated at 1170 K show no diamond to graphite transformation (Fig. 1a). ND graphitization started after ND annealing at 1420 K leading to the formation of 2-3 graphite layers on the surface of the diamond particles. The higher degree of graphitization is achieved with increase of annealing temperature (see Fig. 1b corresponding to ND annealing at 1600 K). The graphitization of diamond particles proceeds from the diamond surface toward the particle bulk. The diamond core can be clearly observed in some particles. Fig. 1 (c) presents the micrograph of the OLC produced at 1800 K. The ND particles are almost completely converted into the onion-like carbon. Fig. 1 (d) presents the micrograph of the OLC produced at 2140 K. Heating at this temperature results in the formation of hollow onion-like carbon particles. According to the true density measurements, diamond content (x) in the samples heated at different temperatures varies with temperature: $x_{1170} > 90\%$, $x_{1420} = 0.86$, $x_{1600}=0.57$, $x_{1800}=0.15$, $x_{1900}=0.05$ and $x_{2140}=0.00$.

The ND samples heated at temperatures lower than 1170 K, which do not exhibit any surface graphitic species, have the highest resistivity values (higher $10^9$ Ω cm). As diamond graphitization occurs the resistivity of the corresponded samples drop significantly. The temperature dependencies of resistivity of ND annealing products and carbon comparison standards are presented in Fig.2. For ND annealing products treated at temperatures higher than 1600 K the values of resistivity at 300 K lie in the range 0.2-0.5 Ω·cm and are comparable to

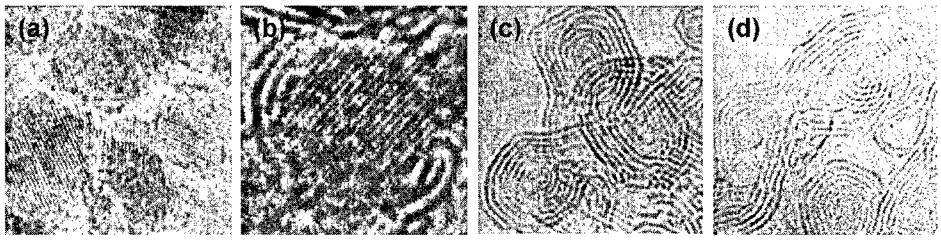


**Figure 1.** HRTEM micrographs of ND samples annealed under vacuum at (a) 1170, (b) 1600, (c) 1800, (d) 2140 K.

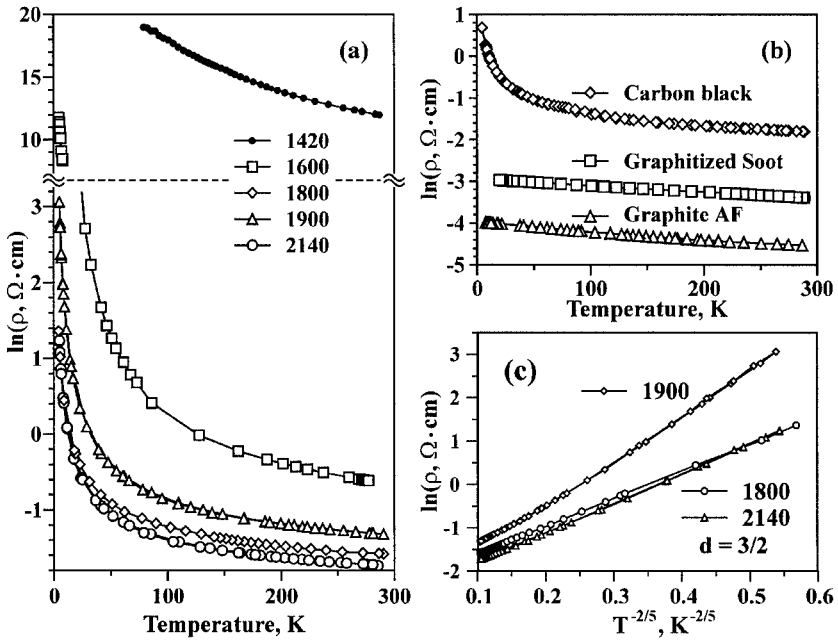


**Figure 2.** Temperature dependence of resistivity of (**a**) ND annealing products and (**b**) comparison carbon samples. (**c**) – example of data fitting in the plot of $\ln(\rho)$ versus $(1/T)^{\alpha}$, here $\alpha=2/5$ [10]. See text for a definition of *d*.

that of carbon black (Fig.2 b). It should be mentioned that despite the tendency to a decrease of resistivity with increasing annealing temperature the resistivity of the sample treated at 1900 K is higher than the resistivity of the samples treated at 1800 and 2140 K in the whole temperature region.

For all samples annealed at temperatures higher than 1170 K the electrical resistivity shows the temperature dependence typical of systems with VHLHC [11]. This dependence takes place

in strong disordering materials with a length of local disordering of about a few interatomic distances [12-14]. For these systems, the temperature dependence of resistance $\rho$(T) may be described by the equation:

$$\rho(T)= \rho_0 exp(T_0/T)^{\alpha} \qquad (1)$$

where $\rho_0$ and $T_0$ are constants. Fig. 2c shows the resistivity data of ND annealed products plotted in coordinates of $\ln\rho$ *vs* $(1/T)^{\alpha}$ where $\alpha$ is varied from 2/5 to 2/3. One can clearly see that the data of ND annealed at 1800 K, 2140 K plotted so approximate straight lines with $\alpha$ equal to 2/5. Data of OLC produced at 1900 K approximate straight lines with $\alpha$ equal to 1/2. The value of $\alpha$ correlates with dimensionality $d$ of the movement space for current carriers as $\alpha=1/(1+d)$. For CDNC prepared at 1420 and 1600 K the following values for $d$ were estimated: 1 and 0.5 respectively. For OLC (prepared at 1800, 1900 and 2140 K) dimensionality varies as 1.5, 1 and 1.5. It should be noted that for carbon black (within the interval 4–300 K) and graphitized soot (4–40 K) the resistivity data in graph of $\ln\rho$ *vs* $(1/T)^{\alpha}$ approximate a straight lines with $\alpha = -1/4$ that corresponds to a dimensionality $d$ equal to 3.

The value of $d = 1$ corresponds to the case when current carriers move along the one-dimensional chains of carbon atoms. A value of $d = 0.5$ corresponds to the case of formation of one-dimensional chains with length of chains being less then the hopping length in VHLHC. $d \geq 1.5$ corresponds to the formation of two dimensional conductive planes. For details see [10].

The dependencies of resistivity of OLC on the applied magnetic field measured at 4.2 K are presented in Fig.3. The magnetoresistivity of OLC is negative in the range of field $0<B<2$ T, and is positive at $B>2$ T. The free path length $l$ for conducting electrons at liquid helium temperature was estimated from the data on positive magnetoresistivity [15]. Fig.3a presents data plotted in coordinates of $\rho(B)/\rho(0)$ *vs* $B^2$. The solid lines are fits by equation (2) with parameters: $l\sim$ 12 Å for OLC (1800 K); $l\sim$ 18 Å for OLC (2140 K).

$$\rho(B)/\rho(0) \cong B^2(l/r_L)^2 \qquad (2)$$

The conduction carrier concentration $n$ for OLC samples was estimated in the framework of the theory of negative magnetoresisrance in semiconductors in the hopping conduction region (with the proposition $n \sim n_c$, *where* $n_c$ is the critical concentration). Fig.3b presents data plotted in coordinates of $ln[\rho(B)/\rho(0)]$ *vs* $B$ [16]. The solid lines are fits to equation (3) with parameters: $n \sim 8\cdot10^{21}$cm$^{-3}$ for OLC prepared at 1800 K and $n \sim 3\cdot10^{21}$cm$^{-3}$ for OLC prepared at 2140 K.

$$ln[\rho(T,B)/\rho(T,0)] = -A\{(eB/hc)n^{-2/3}\}ln[\rho(T)/\rho_0] \qquad (3)$$

Here $A$ is a number of the order unity. As we found the electrical conductivity of GDNC and OLC is characteristic for the systems with localized electrons and can be described within the model of VHLHC. These systems can be characterized with the value of localization length $\xi$ of current carriers, which determines the tunneling probability of conducting electrons. The $\xi$ value depends not only on the barrier height but also on the proximity to the metal-insulator transition point and can be described with equation (4) [16].

$$\xi \sim a(n_c - n)^{-1/2} \qquad (4),$$

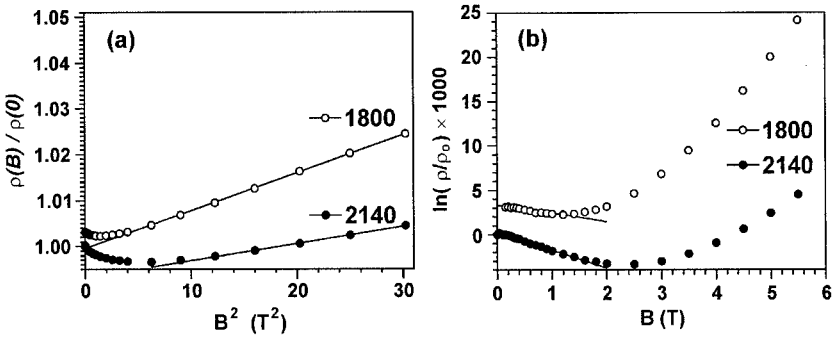


**Figure 3.** The dependencies of specific resistivity of OLC on magnetic field at 4.2 K: **a)** $\rho(B)/\rho(0)$ *vs* $B^2$; **b)** $ln[\rho(B)/\rho(0)]$ *vs* $B$.

where $n_c$ is the critical concentration and $n$ is concentration of carries ($a$~1). We have used equation (4) for a crude estimate of the minimal value of localization length $\xi$ (when $n << n_c$ ). In our case it was equal to 60-100 nm. This value is comparable with the size of OLC aggregates (0.1- 0.5 μm).

## CONCLUSIONS

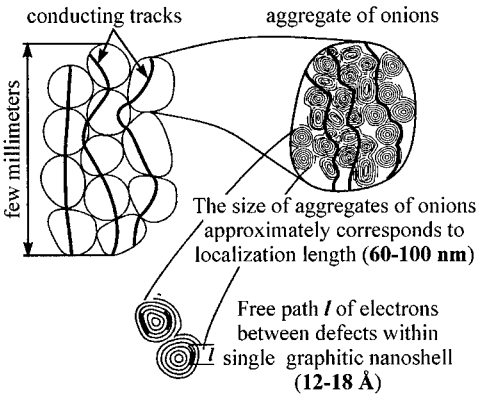


**Figure 4.** The scheme of three scales of OLC particle organization. The hard solid lines correspond to current conduction tracks.

Fig. 4 summarizes the data on the conductivity of OLC. The carbon powders obtained by annealing of ND consist of the OLC aggregates. Within the aggregates onions are linked to each other with defect graphite-like sheets and C-C bonds. Some part of the onions is presented by elongated particles with linked external graphitic layers and closed quasi-spherical shells. Study of X-ray emission spectra of OLC combined with quantum-chemical simulation for the characterization of their electronic structure led us to the conclusion that the onions produced by ND annealing at the intermediate temperature (1400–1900 K) have holed structure of internal shells [17]. The origin of such defects accompanying the OLC formation can be explained in terms of deficit of diamond carbon atoms in the diamond/graphite interface to form perfect fullerene-like shells during ND annealing [17].

The free path length of electrons within OLC particles is comparable with the size of graphitic fragments within holed structure of single onion ($l \sim 12\pm2$ Å). When their holed structure is annealed with the formation of hollow polygonized structures the free path length of the electron increases up to 18±2 Å. The size localization length of current carriers is comparable with the size aggregates of OLC particles.

## ACKNOWLEDGMENTS

The work was supported by the Russian Foundation of Basic Research (Grant No. 00-02-17987), INTAS (Project Nos. 97-1700, 01-237) and CRDF grant REC 008.

## REFERENCES

1. A. S. Kotosonov, JETP Lett. **43**, 1, 30 (1986).
2. A. S. Kotosonov, JETP **93**, 5(11), 1870 (1987).
3. A. S. Kotosonov, Solid State Phys. (Rus.) **33**, 2616 (1991).
4. A. S. Kotosonov, and S. V. Kuvshinnikov, Phys.Lett. **A230**, 377 (1997).
5. A. S. Kotosonov, and D. V. Shilo, Carbon, **36**, 1649 (1998).
6. A. S. Kotosonov, JETP Lett. **70**, 468 (1999).
7. A. S. Kotosonov, and V.V. Atrazhev, JETP Lett. **72**, 2, 76 (2000).
8. V.L.Kuznetsov, A.L. Chuvilin, Yu.V.Butenko, I.Yu. Mal'kov, V.M. Titov, *Chem. Phys. Lett.*, ***222***, 343 (1994).
9. Yu.V. Butenko, V.L.Kuznetsov, A.L. Chuvilin, V.N. Kolomiichuk, S. V. Stankus, R. A. Khairulin, B. Segall, J. Appl. Phys., **88**, 4380 (2000).
10. V.L.Kuznetsov, Yu.V.Butenko, A.L. Chuvilin, A.I.Romanenko and A.V.Okotrub, *Chem. Phys. Lett.*, **336**, 397 (2001).
11. N.F. Mott, E.A. Davis, *Electron processes in non-crystalline materials*, Clarendon Press, Oxford, 1979.
12. A.I. Romanenko, Solid State Phys. (Russian). **27**, 2526 (1985).
13. A.I.Romanenko, in: A.A. Aronov, A.I. Larkin, V.S. Lutovinov (Eds.), Progress in high temperature superconductors, World Scientific, Singapore, **32,** 72 (1992).
14. A.I. Romanenko, N.F. Zakharchuk, N.G. Naumov, V.E. Fedorov, U-Hyon Paek, Materials Research Bulletin, **32**, 1037 (1997).
15. A. A. Abrikosov, *Bases of metal theory (Rus.)*, Nauka, Moscow (1987).
16. B. L. Al'tshuler, A. G. Aronov, and D. E. Khmel'nitskii, JETP Lett. **36**, 5, 157 (1982).
17. A.V. Okotrub, L.G. Bulusheva, V.L. Kuznetsov, Yu.V. Butenko, A.L. Chuvilin, and M.I. Heggie, *J. Phys. Chem.* **A105**, 9781 (2001).

Mat. Res. Soc. Symp. Proc. Vol. 703 © 2002 Materials Research Society V6.23

# Rapid-Solidification Effect on Magnetostriction in Iron-based Ferromagnetic Shape Memory Alloy

YASUBUMI FURUYA*, TAKESHI KUBOTA*, TEIKO OKAZAKI*, MITSUTAKA SATO* and MANFRED WUTTIG**

*Fac. of Science and Technology, Hirosaki Univ., Hirosaki 036-8561, Japan

**Dept. of Materials Science and Engineering, Maryland Univ., College Park, MD 20742-2115, USA

## ABSTRACT

Fe-29.6at%Pd ferromagnetic shape memory alloy (FSMA) ribbon formed by rapidly solidified, melt-spinning methods is expected to be useful as a new type of material which shows giant magnetostriction as well as quick response. The giant magnetostriction in the rolling direction depends strongly on applied magnetic-field direction and has a maximum value of $8\times10^{-4}$ when the field is normal to the surface. This phenomenon is caused by the rearrangements of activated martensitic twin variants. The inverse phase transformation temperatures (As) obtained from Laser micrographs and magnetization vs. temperature curve are ~307 K and 400~440 K, respectively. We analyze magnetostriction, magnetic property and crystal structure of Fe-29.6at%Pd bulk sample before rapid solidification and the ribbon sample. From these results, it can be concluded that remarkable anisotropy of giant magnetostriction of ribbon sample is caused by the fine structure formed by the melt-spinning method. It may be possible to apply this method successfully to other FSMA and $Ni_2MnGa$, which is difficult to manufacture owing to its brittleness.

## INTRODUCTION

Ferromagnetic Fe-Pd shape memory alloy is useful as a micromachine and intelligent / smart material system controlled by a magnetic field. Martensitic twin's initiations and the following its movements depending on magnetic field are thought to be closely related with a new type of magnetostriction[1]. The previous studies [2,3] showed that the rapidly solidified Fe-29.6 at%Pd alloy ribbon has stronger crystal anisotropy, giant magnetostriction as well as shape memory effect. Magnetostriction is changed with temperature and has a maximum of 18 $\times10^{-4}$. However, the mechanism of magnetically induced strain has not yet been discussed. We think that a directional dependence of magnetostriction is probably caused by fine columnar microstructure formed by rapid solidification methods. To confirm this hypothesis, in the present study, at first, we analyze magnetostriction, magnetic property and crystal structure of Fe-29.6at%Pd bulk sample before rapid solidification and compare these properties with those of the ribbon sample. Next, we investigate the

relation between a phase transformation from martensite ( fct ) to austenite (fcc) to martensitic twin's mobility during magnetization process.

## EXPERIMENTAL DETAILS

The rapidly solidified Fe-29.6at%Pd 60 $\mu$ m-thin ribbon samples were prepared by originally designed electro-magnetic melt-spinning single- or twin-roll method from bulk alloy [3]. Samples were annealed at 1173 K for 0 and 0.5 h in vacuum to study the effect of heat treatments on magnetostriction. The magnetization, M vs. applied magnetic field, H loop was measured by VSM method. The magnetostriction, $\varepsilon$ was measured by strain-gauge attached on the sample which was set in a furnace between the electromagnets. The sample can be rotated in H, and the rotation axis is set to be the rolling direction (RD). H was applied perpendicular to RD and strain changes were measured along RD with increasing $\theta$ from 0° to 90° , where $\theta$ is the rotation angle ( see Fig.1(b) ). The X-ray diffraction (XRD) was obtained with Cu K $\alpha$ line for ribbon and bulk samples.

## RESULTS AND DISCUSSION

The M vs. H loops of the melt-spun ribbon prepared by single-roll method (S-0 h ribbon) are shown in Fig.1 (a). Figure 1 (b) is schematic diagram of measurement method. The loops for $\theta$ =0° and H || RD saturate at H>1 kOe and have small coercive force Hc(~25 Oe). While, the loop for $\theta$ =90° dose not saturate still at H=5 kOe because of large demagnetic field, and has large Hc(~60 Oe) because of magnetically anisotropic microstructure. The results suggest that the melt-spun Fe-29.6at%Pd thin ribbon sample has a strong crystal anisotropy in the surface direction perpendicular to RD. On the other hand, the bulk sample, which is annealed for 0.5 h at 1173K in order to take off strain caused by cutting, also shows the similar M vs. H loops but its Hc is small.

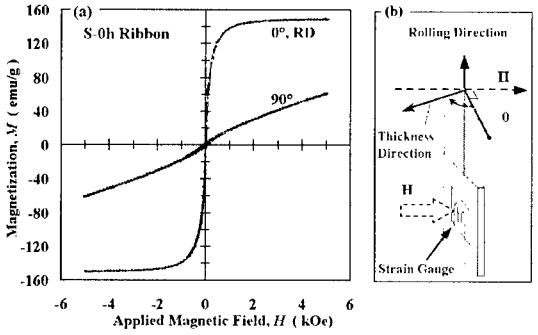


Fig.1 Direction dependence of magnetization in the ribbon sample (a), and schematic diagram of measurement method (b).

Figure 2 (a) shows the dependence of $\varepsilon$ on H of the S-0h ribbon. $\varepsilon$ depends on remarkably and has a maximum, $-8.3 \times 10^{-4}$ at $\sim 85^{\circ}$. Figure 2 (b) is the dependence of $\varepsilon$ on $\theta$ for bulk sample, where $\varepsilon$ has a maximum, $+60 \times 10^{-6}$ at $0^{\circ}$ and a minimum, $-42 \times 10^{-6}$ at $90^{\circ}$, as ordinarily expected. A comparison of direction dependence of Hc between the ribbon and bulk samples is shown in Fig. 3. The Hc of the ribbon depends on $\theta$ remarkably and has a maximum,98 Oe at $\theta = 85^{\circ}$. Similar dependency is seen for $\varepsilon$ (See Fig.2(a)). The Hc of the bulk depends hardly on $\theta$, that is magnetically isotropic texture.

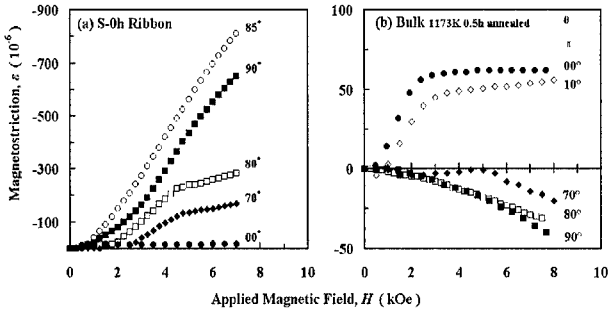


Fig.2 Direction dependence of magnetostriction measured at room temperature for (a) S-0 h ribbon sample and (b)

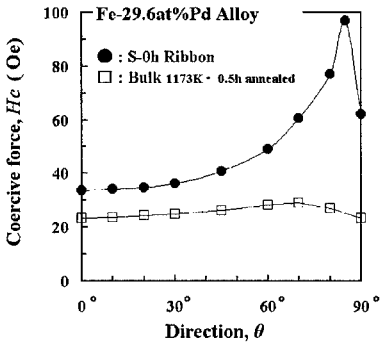


Fig.3 Comparison of direction dependence of coercive force between the ribbon and bulk samples.

Figure 4 shows magnetization dependence of the maximum magnetostriction, $\varepsilon_m$ for two different material processings. A ratio of ribbon $\varepsilon_m$ to bulk one is larger than 30. A comparison of XRD

patterns obtained for the two sample surfaces is shown in Fig.5. For bulk, there are fcc and bcc structures equally. On the other hand, for ribbon obtained after the rapidly solidification, the bcc structure decreases and martensite phase, fct structure appears. Consequently, the {200} peak at 293 K has three structures : fct (200), fcc (200) and fct (002).

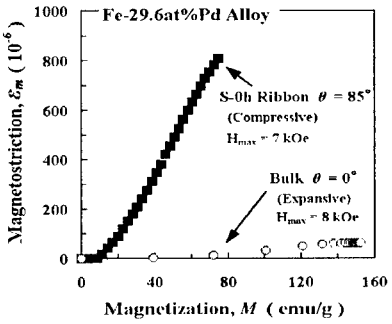


Fig.4 Magnetization dependence of the Maximum magnetostriction for two different material processings.

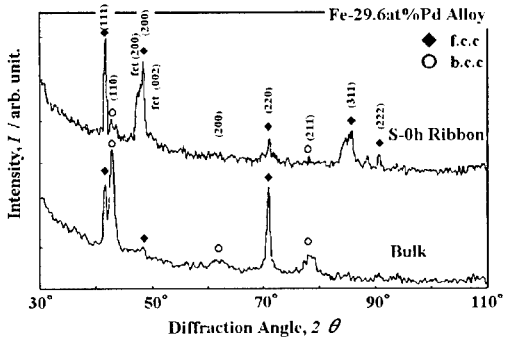


Fig.5 Comparison of X-ray diffraction pattern for two different material processings.

Figure 6 shows the temperature dependence of $\varepsilon$ at $\theta$ =80° ~85° for S-0 h ribbon and 1173 K · 0.5 h annealed ribbon which was prepared by twin- roll method ( T-0.5h ribbon). When T-0.5 h ribbon temperature increases ( see processes (1) and (1') ), $\varepsilon$ first decreases from $6.3\times10^{-4}$ to $5.2\times10^{-4}$ and then increases reaching a maximum at 400 K, and finally decreases suddenly to $1.4\times10^{-4}$ at 440 K. A jump and discrepancy from (1) to (1') was caused by the experimental discontinuity of heating procedure. Thereafter, we let the temperature down ( see process (2) ). $\varepsilon$ increases again to $3.5\times10^{-4}$ at 400 K and decreases $1.6\times10^{-4}$ at 190 K. Then, we elevate the temperature again ( see process (3) ).

$\varepsilon$ increases and goes approximately back over its way. From these results, we conclude that large magnetostrictive phenomenon was caused by rearrangements of the activated martensitic twin variants responding to H. Furthermore, it is suggested that the austenite phase starting (As) and finishing (Af) temperatures, are about 400K and 440K, respectively. Figure 6 also suggests that As and Af of S-0 h ribbon are 376K and 460K, respectively.

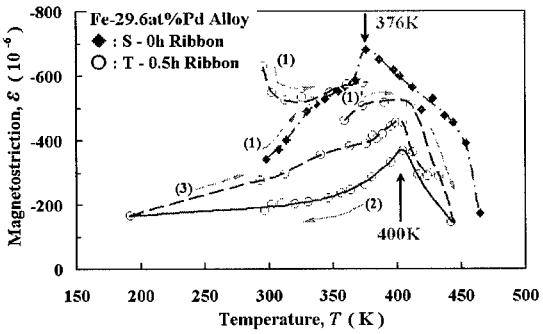


Fig.6 Maximum magnetostriction, $\varepsilon$ vs. temperature, T curves for two ribbons.

Figure 7 shows the photographs of the S-0 h ribbon surface in process of heating obtained by the Laser microscope. The martensite twin stripe-pattern observed at 303K almost disappears at 307K.

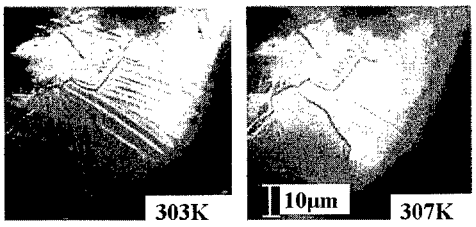


Fig.7 The photograph of martensite twin boundaries of S-0 h ribbon surface observed by the Laser microscope.

We note a discrepancy between the measured temperatures of the phase transformation. To clear the origin of the discrepancy , we investigate a shape memory effect for the S-0 h (◇) and T-0.5 h (○) ribbons, as seen in Fig. 8(a) where the shape recovery ratio, $\Phi_{T2}/\Phi_{T1}$ is shown. $\Phi_{T1}$ and $\Phi_{T2}$ are the diameters defined in (b) at $T = T_1$ and $T = T_2$, respectively. The ratios for both ribbons increase with

temperature. Especially, the ratio raises sharply in temperature ranges of 300~330 K and 380~420 K, which correspond to the As determined by microscope observation and $\varepsilon$ vs. T measurements, respectively. It can be concluded that the surface and the inner bulk of ribbons consist of different texture.

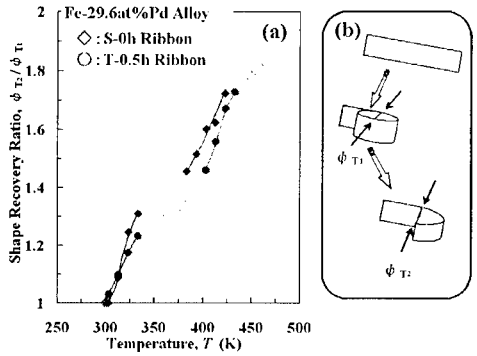


Fig.8 (a) temperature dependence of shape memory effect for the S-0 h ribbon (◇) and the T-0.5 h ribbon (○), and (b) measurement technique.

## CONCLUSION

The rapid-solidified, melt-spun Fe-29.6 at%Pd alloy ribbon has large magnetostriction of $8 \times 10^{-4}$, which is caused by rearrangements of the activated martensitic twin variants. The analysis of X-ray diffraction shows that martensite phase fct structure is created by the rapidly solidification. Two phase transformation temperatures As of ~303K and ~400K are observed for the ribbon sample. It can be considered that the surface and the inner bulk of ribbon consist of different texture.

## REFERRENCES

1. K. Ullakko, J. K. Huang, V. V. Kokorin and R.C.O. Handley : Scripta Mater., 36, 1133(1997).
2.Y. Furuya, Proceedings of 1st Japan-France Intelligent Materials and Structures Seminar, Sendai, 113(1998).
3.Y. Furuya, N. W. Hagood, H. Kimura and T. Watanabe, Mater. Trans. JLM, 39, 1248(1998).

Mat. Res. Soc. Symp. Proc. Vol. 703 © 2002 Materials Research Society V6.26

# Nanoscale compositional changes along fast ion tracks in equilibrium solid solutions: A computer simulation of ultra-fast solidification and thermomigration

Edmundo M. Lopasso, Alfredo Caro, Eduardo Ogando Arregui[1] and Magdalena Caro
Centro Atómico Bariloche - Instituto Balseiro, 8400 Bariloche, Argentina.
1 Dep. de Electricidad y Electrónica, UPV-EHU apdo. 644, 48080 Bilbao, España.

## ABSTRACT

Starting from two equilibrium solid solutions in the Au-Ni system, we analyze the change in composition due to a 400 eV/Å fast ion track simulated by molecular dynamics in the Embedded Atom approximation. We aim at determining the influence of the thermodynamic forces derived from the large thermal gradients and the rapid solidification across the *solidus* and *liquidus* on the motion of solute atoms. One dimensional gradients as well as analytic models are used to quantitatively determine the domains of influence of these forces. Evidence shows that the *liquidus* and *solidus* equilibrium solidification predicted by the phase diagram is not reached during the track. The solute concentration is mainly determined by the combined diffusion and thermomigration mechanisms in the liquid stage.

## INTRODUCTION

In the usual interpretation of radiation effects in alloys, equilibrium solid solutions are not expected to experience modification of solute distribution as a consequence of energetic collision cascades. However, the presence of huge thermal gradients and the rapid quenching across the two phase field delimited by the *solidus* and *liquidus* lines provide thermodynamic forces that may give rise to solute redistribution. In the short initial ballistic stage the atoms are displaced from their equilibrium positions, creating interstitials, vacancies and ion mixing near the cascade. The thermal stage that follows involves a liquid-like system, followed by a temperature drop that drives the system towards re-solidification; in these stages precipitation, dissolution, amorphisation, and diffusion (besides other possible transformations), influences the solute redistribution.

The diffusion mechanisms in the liquid phase are influenced by the thermomigration of solutes. The governing equation in this case is the diffusion equation with the heat of transport contribution [1]:

$$\frac{\partial C_s}{\partial t} = \nabla \cdot \left[ D \left( \nabla C_s + \frac{Q^* C_s}{kT^2} \nabla T \right) \right] \qquad (1)$$

in which $C_s$ is the solute concentration, t is the time, D is the diffusion coefficient, Q* is the heat of transport, k is the Boltzmann constant and T is the temperature. Under a thermal gradient, the thermomigration effect would drive the solute to the cold region of the sample if Q* is positive, and to the hot region of the sample if Q* is negative.

Additional effects could appear as system cools down from the liquid, and the characteristics of the phase diagram affect the final solute distribution in the solid phase. In systems with *liquidus* and *solidus* lines with negative slopes, the solute is pushed towards the liquid as the solidification interface moves on cooling. If solid diffusion is neglected due to the rapid nature of the process under consideration, the complete or partial mixing by diffusion in the liquid phase

produces a concentration profile. Standard results show that the first portion of matter that solidifies has a low solute concentration, while the last solid formed is solute enriched [2].

In a previous work [3] we determined the thermomigration effect on liquid dilute Au-Ni alloys. We found that Ni as a solute in Au has a tendency to move towards the hot core of the spike, while Au as a solute in Ni has the opposite tendency. The final solute concentrations under a fixed thermal gradient are shown in figure 1, for samples of 4.7 % initial solute content in the Au-Ni system. Figure 2 shows the Au-Ni system phase diagrams: the experimental (dotted lines) [4] and that determined in a previous publication [5], corresponding to the embedded atom potentials [6] used in this work. According to this phase diagram, during cooling from the melt the effect of the *liquidus* and *solidus* lines would drive the solute to the hot melted zone in both Ni 5% Au and Au 5% Ni systems: this would enhance (compensate) the thermomigration effect when Ni (Au) is the solute. This analysis would be correct if the solidification proceeds at thermodynamic equilibrium, a fact that we assess in the simulations reported here. Equilibrium solidification occurs when the concentration of solid and liquid phases close to the moving interface are given by the *liquidus* and *solidus* lines respectively. In this work we use molecular dynamics to study the combined effect of thermomigration and quenching during ultra-fast solidification in the Au-Ni system after a fast ion track event.

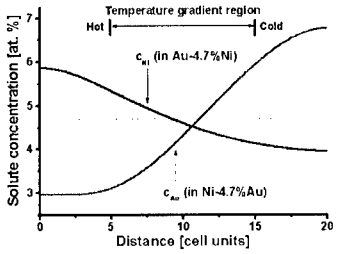


**Figure 1**: Solute distribution after 500 psec. under a fixed thermal gradient in initially 4.7% dilute alloys.

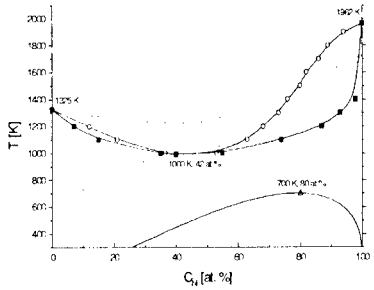


**Figure 2**: Experimental (dotted) [4] and calculated [5] Au-Ni phase diagram.

## TRACK SIMULATION

A 400 eV/Å track in the [001] direction was simulated on dilute 5% Au-Ni and Ni-Au alloys, on 64x64x16 unit cells samples. This energy deposition is in the range usually attainable by swift heavy ions.

The Ni 5% Au sample is shown in figure 3, after 1 psec. from the track event. The melted zone reaches a maximum size and then the re-solidification interface moves towards the center of the track at a variable speed, which is shown in figure 4, and is estimated from the temperature profiles shown in figure 5. These figures show that the track effect extends over roughly ten cells. After about 16 psec. the system reaches the solid phase temperature.

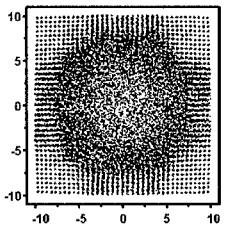

**Figure 3**: Ni 5% Au sample after 1 psec. from track event. Distances in cell units.

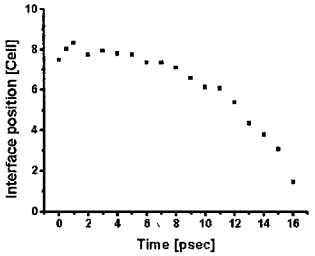


**Figure 4**: Interface position after track event in Ni 5% Au.

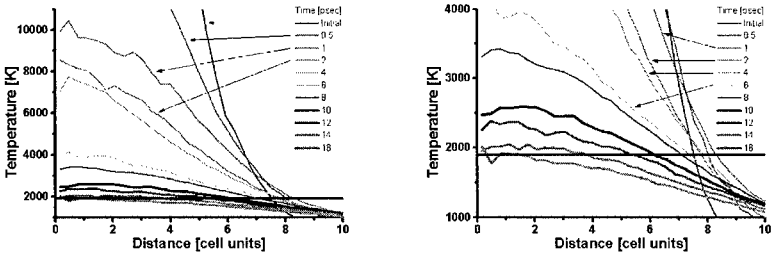


**Figure 5**: Temperature profiles after track event in Ni 5% Au.

Concentration profiles for Ni 5% Au and Au 5% Ni are shown in figure 6. From the figure it is observed that in the Ni 5% Au system the solute moves away from the center of the track, while in the Au 5% Ni system the solute moves to the track region. This observation is in agreement with the expected behavior when thermomigration is operative.

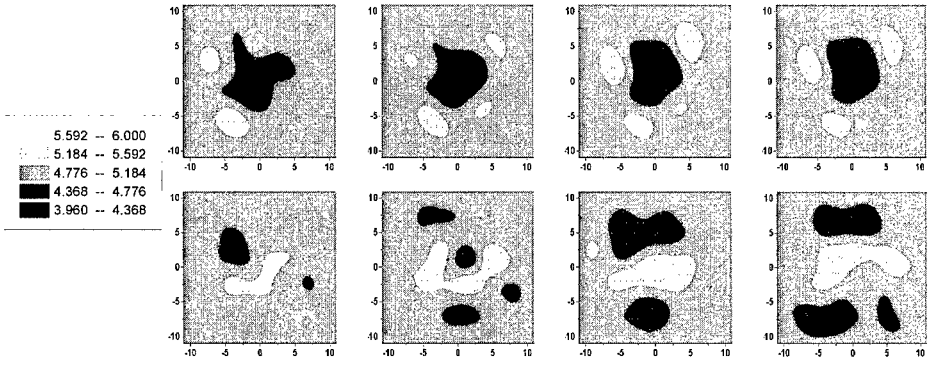


**Figure 6**: Au concentration during track cooling of Ni 5% Au system (above) and Ni concentration during track cooling of Au 5% Ni system (below). Distances in cell units. From left to right: at 2, 4, 10 and 20 psec. from track event.

From the track simulations we conclude that in the Ni 5% Au system the 20 psec. picture represents the sample back in its solid phase. In this time scale, the solidification is apparently not in equilibrium, as the thermomigration effect was not compensated by a solute enrichment in

the final liquid in the center of the sample. In the Au 5% Ni system, the picture at 20 psec. still represents a sample with a liquid track core. However, further cooling up to 50 psec. did not raise the solute concentration at the center of the sample, as would be expected if solidification occurs at thermodynamic equilibrium.

To try to understand quantitatively these results, we proceed now to the analytic modeling of the processes.

## ONE DIMENSIONAL SOLIDIFICATION MODELS

To verify the track results a molecular dynamics simulation and an analytical calculation were performed in one dimensional temperature gradient geometry under controlled temperature conditions. A thermal gradient was imposed to twenty cells long samples, with temperature control at both ends (cold ends) and at the center (hot center) and periodic boundary conditions in 3D. The cold ends were kept at 1000 K, while the hot center was initially at 11000 K and then cooled down. A fast cooling of 500 K/psec., similar to that observed during the track cooling, and a slow cooling of 10 K/psec., in an attempt to quench at thermodynamic equilibrium, are presented. The evaluation was performed in the Ni 5% Au alloy, which has a broad splitting of the two phase (liquid and solid) field and an evidence of the solidification solute redistribution is therefore expected.

### Molecular dynamics results

The concentration profiles for the fast and slow cooling conditions after the samples reached an uniform temperature (1000 K) are shown in figure 7. In both cases the thermomigration effect is present at the beginning of the run. In the fast cooling, the concentration does not vary significantly, while in the slow cooling the solute is pushed towards the hot center of the sample, compensating the thermomigration effect at the end of the run. In the slow cooling a peak moves from the cold to the hot region, suggesting that some equilibrium is achieved. The interface position shown corresponds to the approximated point at which it should be according to the imposed temperature gradient.

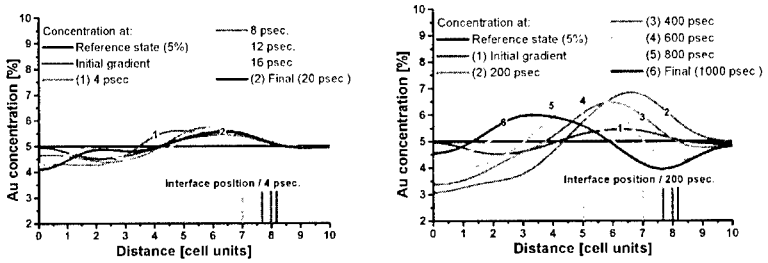


**Figure 7**: Concentration profiles for the fast (left) and slow (right) cooling down schemes. Molecular dynamics calculation in Ni 5% Au.

Figure 8 represents the sample configuration when the temperature at the center is 2000 K. The slow cooled sample is almost crystallized, while the fast cooled sample is still in a liquid like configuration. The observation is in agreement with the conclusion obtained from the

concentration profiles, and also suggests that the slow cooling allows a partial thermodynamic equilibrium, while in fast cooling the equilibrium is not reached. When the fast cooled sample was left at 1000 K for a longer period, an ordered crystal structure was obtained, and there was no changes in the concentration profile.

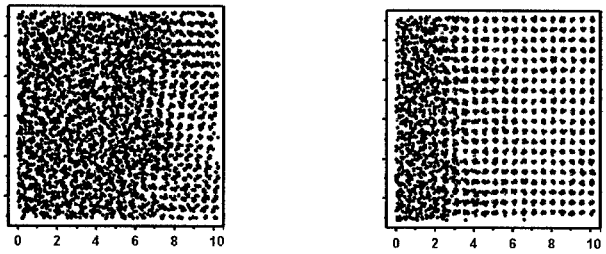


**Figure 8**: Samples obtained by molecular dynamics calculations for fast (left) and slow (right) cooling conditions in Ni 5% Au. Temperature in the center is 2000 K. The estimated interface position according to thermal gradient should be at the first cell. Distances in cell units.

## Analytic results

The analytic model assumes the system is always at equilibrium solidification, and the diffusion equation including thermomigration (1) is solved as cooling down proceeds.

The results for fast and slow cooling are shown in figure 9 for the final (left) and transient (right) concentration profiles. In spite of the concentration values, the final slow cooling profile is similar to that obtained by molecular dynamics. The fast cooling profile has a peak at the center of the sample, resulting from the impingement of solute in the final stage, which is not observed in the molecular dynamics run. An equilibrium plateau at the initial 5% concentration is observed.

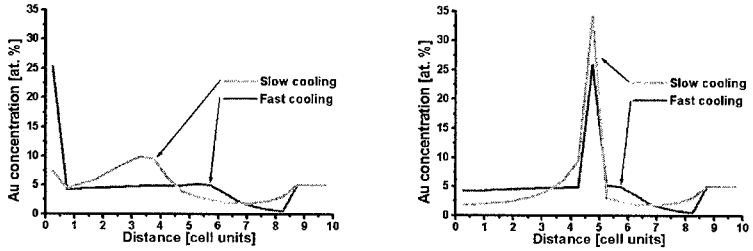


**Figure 9**: Concentration profiles from the analytical calculation, fast and slow cooling, in Ni 5% Au. Final profile (left) and transient (right).

The transient concentrations in figure 9 correspond to the same interface position for both cases. The fast cooling has a narrow concentration peak at the interface, while the slow cooling presents a diffusive profile. This allows the liquid to be enriched by solute, and as a consequence the center of the sample has an extended enriched zone in the final state. The zone of solute concentration below the initial 5% also differs. The slow cooling shows a broad zone, as the continuos build up of solute to the cold region, due to thermomigration, produces solidification at a composition close to the initial composition of the sample.

## SUMMARY AND CONCLUSIONS

The concentration profiles obtained in the simulation of the track event indicate that the thermomigration effect is the main contribution to the solute re-distribution. The very fast cooling rate observed during the simulation does not allow a thermodynamic equilibrium in the system.

The observations in the Ni 5% Au system are verified with one dimensional thermal gradients in three dimensional molecular dynamics and an analytical model which assumes equilibrium solidification during quenching. A fast cooling rate, similar to the track cooling rate, reflects differences between the analytical simulation and molecular dynamics. This implies that equilibrium is not reached in the molecular dynamics simulation. In contrast, a slow cooling rate shows similar qualitative behavior in analytical and molecular dynamics results indicating some degree of equilibrium. There are differences in the concentration values for the slow cooling simulation and the analytical calculation, which are due to the strong assumption of equilibrium solidification in the analytic model, while in molecular dynamics there is no complete equilibrium. The average interface speed during the track and the fast cooling under the one dimensional temperature gradient is estimated to be 2 Å/psec., while in the slow cooling is about 0.04 Å/psec. These values are consistent with a 0.1 Å/psec. interface speed estimated as the upper limit at which equilibrium solidification should be operative, which was obtained with molecular dynamics and analytic models not presented here.

The Au 5% Ni system cools down at a slow rate after the track. The Au 5% Ni sample shown in figure 6 is still in the liquid phase, while the Ni 5% Au sample is solid. Concentration profiles in the Au 5% Ni system in later stages after the track event do not show further modifications. This is consistent with the above conclusions since, if the phase diagram equilibrium is supposed to occur, the center of the sample should be enriched with solute. However, due to the narrow splitting of the two phase (liquid and solid) field in the Au rich zone of the phase diagram, a relevant effect would not be expected even if equilibrium occurs during cooling.

One-dimensional thermal gradients in molecular dynamics calculations, and analytical results, suggest that the cooling rate should be much slower than is the case for Ni to allow for equilibrium solidification effects to become apparent. This may occur in heavier systems. These effects depend on the sign and magnitude of the heat of transport, and on the characteristics of the phase diagram.

## REFERENCES


**1.** J.P. Stark, *Solid State Diffusion*, (John Wiley & Sons, 1976) p. 124.
**2.** D.A. Porter and K.E. Easterling, *Phase transformations in metals and alloys*, 2nd ed. (Chapman & Hall, London, 1992) pp. 208-214.
**3.** E.M. Lopasso, M. Caro and A. Caro, Phys. Rev. B **63**, 174105 (2001).
**4.** Thaddeus B. Massalski (editor), *Binary Alloy Phase Diagrams*, 2nd ed. ASM International (William W. Scott Jr., 1992) pp. 402-404.
**5.** E. Ogando Arregui, M. Caro and A. Caro: *Embedded Atom Model Prediction of the Au-Ni Phase Diagram*, submitted for publication.
**6.** S.M. Foiles, M.I. Baskes and M.S. Daw, Phys. Rev. B **33**, 7983 (1986).

Mat. Res. Soc. Symp. Proc. Vol. 703 © 2002 Materials Research Society V6.27

# Deposition of Polymer Thin Films on ZnO Nanoparticles by a Plasma Treatment

**Peng He, Jie Lian[1], L. M. Wang[1], Wim J. van Ooij, and Donglu Shi,**
Department of Materials Science and Engineering, University of Cincinnati
Cincinnati, OH 45221-0012
[1]Dept. of Nuclear Engineering and Radiological Science, University of Michigan
Ann Arbor, MI 48109

## ABSTRACT

Ultrathin acrylic acid polymer films have been deposited on the surfaces of nanoparticles of ZnO using a plasma polymerization treatment. The average size of nanoparticles is on the order of 50 nm in irregular shapes. High-resolution transmission electron microscopy (HRTEM) experiments showed that an extremely thin film of the acrylic acid layer (15 nm) was uniformly deposited on the surfaces of the nanoparticles. In particular, the particles of all sizes exhibited equally uniform ultrathin films indicating a well-dispersed nanoparticles in the fluidized bed during the plasma treatment. The deposition mechanisms and the effects of plasma treatment parameters are discussed.

## INTRODUCTION

Nanoparticles are known to have extremely high surface areas. As a result of the high surface area, the surface energy can reach the order of 100 kJ/mol for a variety of materials (1-5). Due to high surface areas, nanoparicles naturally agglomerate and can form considerable bonding between particles. If they strongly bond to each other, they cannot be easily dispersed and are referred to as an aggregate or a hard agglomerate. Therefore, for nanoscale particles, the challenge is that whether they can be well dispersed in space. Furthermore, in a well-dispersed condition, whether it is possible to coat uniformly a thin layer of foreign species on their particle surfaces. In this proposal we will address these issues and focus on the optimization of experimental procedures.

Surface coating of nanoparticles is an important area in nanomaterials synthesis. Because of their special composition, these coatings possess a unique combination of properties of the inorganic and organic components, for instance hydrophobic, hydrophilic, anti-fogging, anti-fouling, anti-adhesive and/or teflon-like properties in combination with hardness and scratch and abrasive resistance. The combination of mutually chemically interconnected organic and inorganic networks results in coatings with a very low permeability for gases and liquids. Hybrid materials are very suitable for application as coatings on a highly diverse spectrum of substrates including glasses, ceramics, plastic, wood, and metal. Before curing, the coating materials consists of a clear alcoholic solution that can easily be processed by classical application techniques such as dipping, spraying, or spin coating. However, in these previous coating processes, the coatings are quite thick up to the order of microns.

The current trend of developing nanophase materials has motivated an increased need for nanometer-scale structures in a variety of applications. Indeed, it is clear that, in order to achieve unique mechanical, physical, chemical, and biomedical properties, it is necessary to develop novel synthesis routes by which an entirely new nanostructure can

be developed. In the past, great efforts have been focused on nanoparticle synthesis, assembly, interfaces, dispersions, and functional devices (1-5). Although high volume (~80 vol.%) polymer coating of nanoparticles has been reported (6), no studies so far have shown uniform deposition of ultrathin films of the order of 10-20 Å on the surface of the nanoparticles, which is, in this letter, referred to as "nanocoating." The deposited film can also be tailored to multi-layers on a nanoparticle. Nanocoating is of particular importance in electronics, functional devices, new materials synthesis, nanobiomolecular applications, tissue engineering, and drug delivery. Using nanocoating, it is possible to alter the intrinsic properties of materials that cannot be achieved by conventional methods and materials.

For nanoscale ceramics particles, the challenge is that whether they can be well dispersed in space. Further, in a well-dispersed condition, it is possible to deposit a thin film of foreign species uniformly on the nanoparticle surfaces and thereby reduce their surface energies. In this study we will address these issues and report experimental data on the deposition of multiple layers of polymer ultrathin films on the surfaces of nanoscale alumina particles by a plasma polymerization process. The deposited thin films are plasma-polymerized pyrrole and hexamethyldidiloxane (HMDSO).

One of the possible applications of nanocoating is in ion exchange for removing metal ions from water. If on the surface of these nanoparticles, an extremely thin layer of polyacrylic film can be coated by a plasma treatment. The polyacrylic film will react with metallic ions in water. As a result of the high surface-to-volume ratio of these nanoparticles, the efficiency of ion exchange in the water flux is much higher than other types of traditional reactors. In this research we have carried out the preliminary experiments in coating nanoparticles with acrylic acid polymer films. The results have shown that, using plasma treatment, a uniform thin film of acid polymer film has been coated on the nanoparticles of ZnO.

## EXPERIMENTAL DETAILS

In this experiment, a RF-plasma reactor was used for the nanoparticle coating. We have selected nanoscale ZnO particles of 50 nm. The schematic diagram of the plasma reactor for thin film deposition of nanoparticles is shown in Figure 1. The vacuum chamber of plasma reactor consists of a long Pyrex glass column about 80 cm in height and 6 cm in internal diameter (7,8).

The nanoparticles of ZnO are vigorously stirred at the bottom of the tube and thus the surface of nanoparticles can be continuously renewed and exposed to the plasma for thin film deposition during the plasma polymerization process. A magnetic bar was used to stir the powders. The gases and monomers were introduced from the gas inlet during the plasma cleaning treatment or plasma polymerization. The system pressure was measured by a pressure gauge. A discharge by RF power of 13.56 MHz was used for the plasma film deposition. Before the plasma treatment, the basic pressure was pumped down to less than 200 mTorr and then the plasma gases or monomer vapors were introduced into the reactor chamber. The operating pressure was adjusted by the gas/monomer mass flow rate. The base pressure was less than 200 mTorr. Acrylic acid (AA) was used as a monomer for plasma polymerization. During the plasma polymerization process, the

input power was 20 W and the system pressure was 450 mTorr. The plasma treatment time was 240 min. Per batch 40 grams of powder were treated.

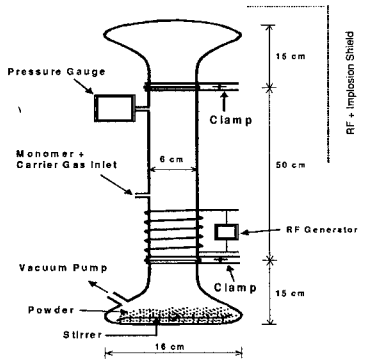


***Figure 1**. Schematic diagram of the plasma reactor for thin polymer film coating of the nano-particles.*

After the plasma treatment, the nanoparticles of ZnO were examined by using the high-resolution TEM (HRTEM) experiments performed on a JEM 2010F. In FTIR experiment, potassium bromide(KBr) of 99%+ purity was obtained from Aldrich Chemical Company Inc, Milwaukee, WI. The coated powder was mixed with KBr and pressed into small pellets for the FTIR experiment. FTIR spectra were acquired on a BIO-RAD FTS-40 FTIR spectrometer with a BIO-RAD transmittance attachment.

## RESULTS AND DISCUSSION

In transmission electron microscopy, the original and coated ZnO nanoparticles were dispersed onto the holy-carbon film supported by Cu-grids for the TEM operated at 200 kV. Figure 2 shows the transmission electron microscopy (TEM) image of the original, uncoated ZnO nanoparticles. The average particle size is about 50 nm, with the smallest particle size on the order of 15 nm. These particles also exhibit the irregular shapes for all sizes. Figure 3a is the TEM image of the coated particles. Compare to Figure 2, one can see a bright edge on the particle surfaces, which is the result of the polymer coating. Figure 3b is a high magnification image showing a uniform coating on the particle surfaces. In this figure one can see not only that acrylic acid film is uniform but the thickness of the film is also extremely thin on the order of 15 nm.

Particularly interesting, although these particles have different diameters, the coating remains the same thickness indicating the uniform distribution of polymer atoms in the plasma chamber. The coating layer is amorphous based on the HREMs of different particles. In contrast, the images of the original particles (Figure 2) do not show the amorphous layer.

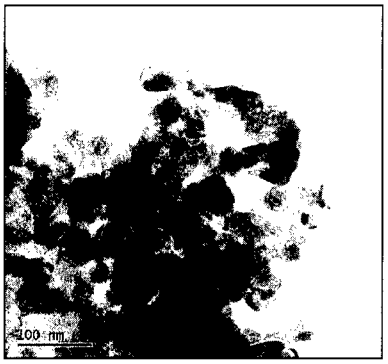


***Figure 2*** *TEM image showing the uncoated ZnO nanoparticles.*

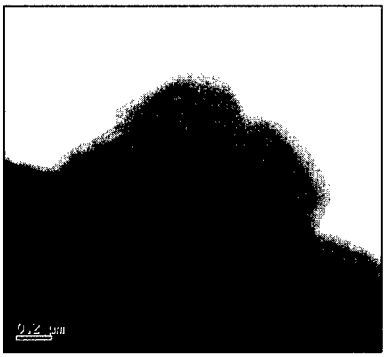

***Figure 3a.*** *TEM images showing acrylic acid coated nano ZnO particles. .*

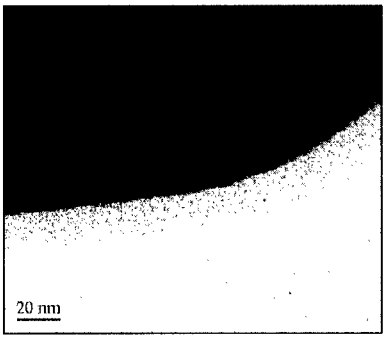


***Figure 3b.*** *The acrylic acid coating on the surface of ZnO. The film is about 15 nm think.*

Thus, we are certain that the observed layer is due to coating rather than an artifact in TEM observation.

Figure 4 shows the IR spectra of acrylic acid-coated nanoparticles of ZnO. In this figure, we can see the effect of plasma power on the coating. As the plasma power increases, the peak at about 1700 $mm^{-1}$ intensifies significantly. This peak at 1700 belongs to the function group of C=O vibration. The intensification of this peak indicates an increase of this function group C=O in the deposited films. In ion exchange, more of C=O function groups are needed in order to react with metallic ions in water. In order to investigate the film solubility in water, we immersed acrylic acid-coated nanoparticles in the $Ni^{+}$ solution at room temperature. After 1 hour, the coated nanoparticles were dried and the IR experiement was performed again on these samples. Some of the results at higher power of 60 W are shown in Figure 5. As can be seen, at higher plasma power, the acrylic acid film remains insoluable in water. However, we found that, at lower plasma powers such as 15 W and 30 W, the entire film was removed by the nickel solution indicating there were less cross-links in the polymer. At higher plasma power above 60W, the film becomes insoluble, even the polymer has very strong hydrophilic function groups of "COOH".

During coating, the polymer is introduced as a vapor and the collision frequency increases with the gas pressure. The rate of polymer condensation on the nanoparticle surfaces may be influenced by many parameters such as electron density, temperature, and energy density. Although a systematic study on the optimization of synthesis parameters has not yet been carried out, the preliminary experimental data have indicated that the coating polymer must be stable and not reactive with the substrate during coating. The gas pressure must be moderate for a low collision rate on the nanoparticle surfaces (9,10).

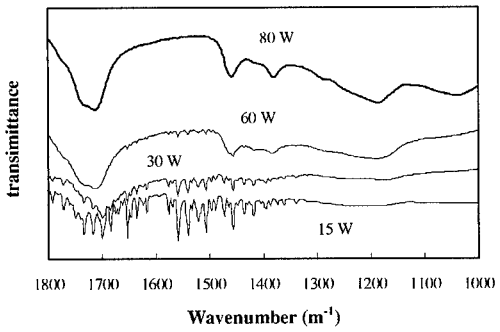


***Figure 4.*** *IR spectrum of acrylic acid -coated ZnO nanoparticles.*

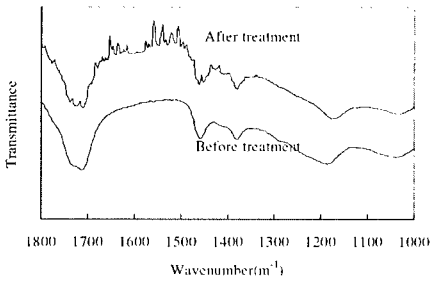


***Figure 5.*** *IR spectrum of acrylic acid -coated ZnO nanoparticles before and after water test.*

In summary, we have deposited an acrylic acid film on ZnO nanoparticles by means of a plasma polymerization treatment. The coating is not only uniform on all particle sizes, but also thin with a thickness of 15 nm. Such coating characteristics are essential in establishing unique nanostructures, tailoring unique physical properties, and pioneering novel synthesis route.

## REFERENCES


1. R. W. Siegel, Nanostructured Materials, **3**, 1-18, (1993).
2. G. C. Hadjipanayis and R. W. Siegel, "Nanophase Materials: Synthesis-Properties-Applications" Kluwer Press, Dordrecht, 1994.
3. G. M. Whitesides, J. P. Mathias, and C. T. Seto, Science, **254**, 1312-1319, (1991).
4. G. D. Stucky and J. E. MacDougall, Science, **247**, 669-678, (1990).
5. H. Gleiter, Nanostructured Materials, **6**, 3-14 (1995).
6. D. Vollath and D. V. Szabo, J. of Nanoparticle Research, **1**, 235-242, (1999).
7. W.J. van Ooij, S. Eufinger, W.J. van Ooij, and T.H. Ridgway, Journal of Appl. Pol. Sci., **61**, 1503 (1996),
8. W.J. van Ooij, S. Eufinger and T.H. Ridgway, Plasma and Polymers, **1**, 231 (1996).
9. Donglu Shi and W. J. van Ooij, "Uniform Deposition of Ultrathin Polymer Films on the Surface of Alumin Nanoparticles by a Plasma Treatment," *Appl. Phys. Lett.*, **78**, 1234 (2001).
10. Donglu Shi and W. J. van Ooij, Multi-Layer Coating of Ultrathin Polymer Films on Nanoparticles on Alumina by a Plasma Treatment, Mat. Res. Soc. Symp. Vol. **635** (2001).

Mat. Res. Soc. Symp. Proc. Vol. 703 © 2002 Materials Research Society V6.31

# Synthesis of Nanosized Lithium Manganate For Lithium-ion Secondary Batteries

Hsien-Cheng Wang, Yueh Lin, Ming-Chang Wen, and Chung-Hsin Lu
Department of Chemical Engineering, National Taiwan University.
Taipei, Taiwan

## ABSTRACT

Nanosized lithium manganate powders are successfully synthesized via a newly developed reverse-microemulsion (RμE) process. Monophasic $LiMn_2O_4$ powders are obtained after calcining the precursor powders at 700°C. The particle size of the spinel compound significantly depends on the concentration of the aqueous phase. Increasing the water-to-oil volume ratio results in an increase in the particle size. While the aqueous phase is equal to 0.5 M, the size of the obtained $LiMn_2O_4$ powder is around 60-70 nm. It is found that the specific capacity of nanosized $LiMn_2O_4$ particles is greater than that of submicron particles. The large surface area of ultrafine particles is considered to facilitate the intercalation and deintercalation of lithium ions during the cycling test.

## INTRODUCTION

Lately, lithium-ion secondary batteries have became one of the most promising candidates in the field of rechargeable batteries owing to their high working voltage, high energy density, steady discharging properties, and long cycle life. For perfecting the performance of lithium ion batteries, the electrochemical characteristics of cathode materials have been intensively investigated. A variety of lithiated transition metal oxides including $LiCoO_2$, $LiNiO_2$, and $LiMn_2O_4$ have been explored for utilizing as cathode electrodes in lithium-ion secondary batteries [1-4]. Among these cathode materials, lithium manganate with a spinel structure is of particular interest for using in the rechargeable cells because of its inexpensive material cost, acceptable environmental characteristics, and better safety compared to $LiCoO_2$. However, $LiMn_2O_4$ suffers the disadvantages of relatively low discharge capacity and serious capacity fading during the cycling process [6-8]. For optimizing the electrochemical performance of $LiMn_2O_4$, a great deal of efforts have been devoted to synthesize $LiMn_2O_4$ powders with a controlled morphology [9,10]. A new reverse-microemulsion (RμE) process was thus to control the morphology and particle size of $LiMn_2O_4$ powders,developed in this study, and the electrochemical performance of the obtained powders was also evaluated.

## EXPERIMENTAL DETAILS

Lithium nitrate ($LiNO_3$) and manganese nitrate ($Mn(NO_3)_2$) were chosen as the starting materials. The well-dispersed aqueous phase was mixed with the continuous phase that

comprised oil and surfactant. After emulsifying these starting compounds, a transparent RμE system was successfully obtained. The RμE system was heated and dried for preparing the precursors of the target spinel compound. The precursor powders were calcined in a tube furnace at 350°C with a heating rate of 10°C /min to obtain the $LiMn_2O_4$ powders. The powders prepared at the cationic concentration of 0.5 M and 2.0 M were named as sample A and B, respectively. The crystallinity of the formed products was identified via the powder X-ray diffraction (XRD) analysis. The morphology and the particle size of the obtained powders were measured with a field emission scanning electron microscopy (FESEM). The electrochemical cell was composed of the RμE- derived $LiMn_2O_4$ powders as the cathode, lithium foil as the anode, and an electrolyte of 1 M $LiPF_6$ in ethylene carbonate (EC) and 1,2-dimethyl carbonate (DMC) solution. The charge and discharge characteristics of the cathode materials were investigated using a current density of 0.23 $mA/cm^2$ in the voltage range of 3.0 and 4.3 V.

## RESULTS AND DISCUSSION

Figure 1 illustrates the XRD patterns of the RμE derived specimens heated at 700°C for 1 h. After analyzing the structural characteristics, these calcined powders were identified to be monophasic spinel $LiMn_2O_4$ with a cubic unit cell and a space group of Fd3m. All the diffraction peaks were consistent with the data in ICDD PDF No. 35-782 [11]. It is confirmed that at the cationic concentration of 0.5 and 2.0 M, pure spinel $LiMn_2O_4$ powders can be effectively synthesized using the RμE process.

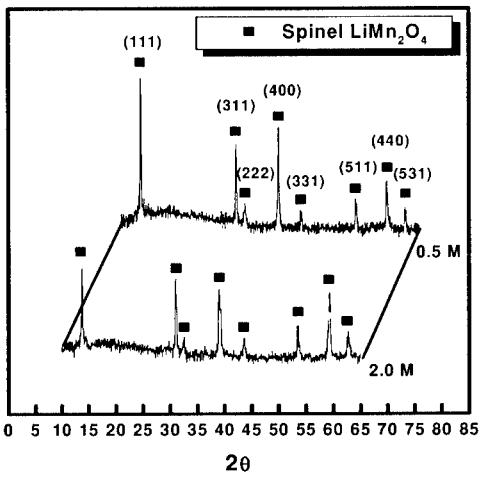


Fig. 1. XRD patterns of the RμE-derived powders.

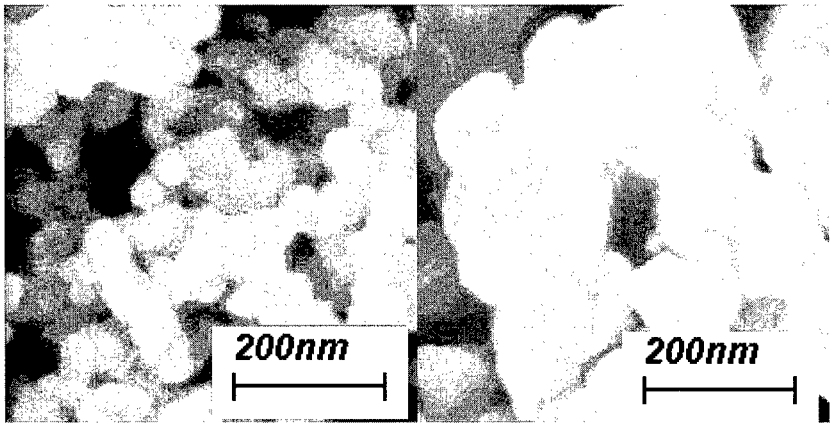


(a) (b)

Fig. 2. The FESEM photos of the RμE-derived powders (a) 0.5 M and (b) 2.0 M.

Figure 2 illustrates the field emission scanning electron microscopic photos of the pure spinel powders. Sample A has an uniform morphology and the particle sizes are around 60-70 nm with a narrow size distribution. Meanwhile, the mean particle size of sample B is 136 nm much larger than that of sample A. In comparison with previous solution methods, the RμE process significantly reduces the particle size of $LiMn_2O_4$ even down to a nanosized order. In addition, the cation concentration of the aqueous phase has a significant effect on the particle size of $LiMn_2O_4$ powders. Increasing the cation concentration will increase the particle size of $LiMn_2O_4$ powders. Adjusting the cation concentration is a critical issue for controlling the particle size of $LiMn_2O_4$.

Figure 3 shows the charge-discharge profiles for the 700℃-calcined samples cycled at 0.23 $mA/cm^2$. The cell consisting of sample A delivered the discharge capacity of 116 mAh/g in the first cycle at room temperature. After ten cycles, the discharge capacity retained 104.2 mAh/g. For the electrochemical characteristics of the sample B, the discharge capacity in the first cycle was 92.2 mAh/g, which was smaller than that of sample A. The superior performance of sample A was attributed to the larger surface area of smaller particles, which facilitated lithium ions to participate in the intercalation/deintercalation process.

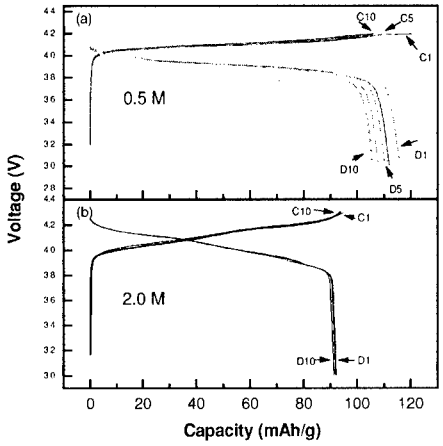


Fig. 3. Charge and discharge properties of the RμE-derived powders cycled at the ambient temperature.

In order to investigate the cycling performance of the RμE-derived powders at elevated temperatures, the electrochemical characteristics were also examined at 55℃. Figure 4 illustrates the charge and discharge profiles of the 700℃-calcined specimens. For sample A, the first-cycle discharge capacity was 98.8 mAh/g, while that of the 10th cycle was 81.0 mAh/g. As for sample B, the discharge capacities of the first and tenth cycles were 88.7 and 84.1 mAh/g, respectively. It was found that the RμE-derived powder obtained at low cationic concentration demonstrated worse capacity fading than that derived from high cationic concentration.

The cycling stability at 55℃ and the capacity retention of the RμE-derived powders are shown in Fig. 5. It was found that the capacity fading of sample B was less severe than that of sample A, indicating that high cationic concentration in the RμE system is effective in suppressing the capacity fading. Figure 5(b) depicts that the capacity retention of sample A and B after 10 cycles at this temperature were 82% and 95%, respectively. It was found that the specific capacity increased with an increase in the surface area of the obtained $LiMn_2O_4$ powders, however the capacity retention was completely opposite. The reason for better capacity retention of sample B at elevated temperature was its larger particle size. The enlargement of surface area facilitated the insertion and extraction of lithium ions, but also increased the dissolution of manganese ions into the electrolyte. For optimizing the electrochemical performance of the RμE-derived $LiMn_2O_4$ powders, the particles size should be precisely controlled.

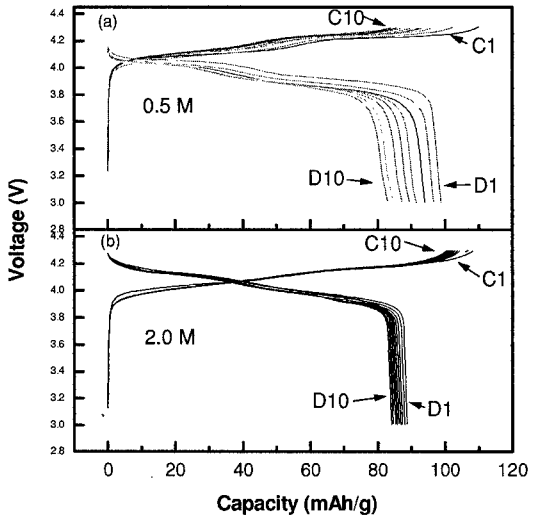


Fig. 4. Charge and discharge performance of the RμE-derived powders at 55℃. The aqueous concentration are (a) 0.5 M and (B) 2.0 M, respectively.

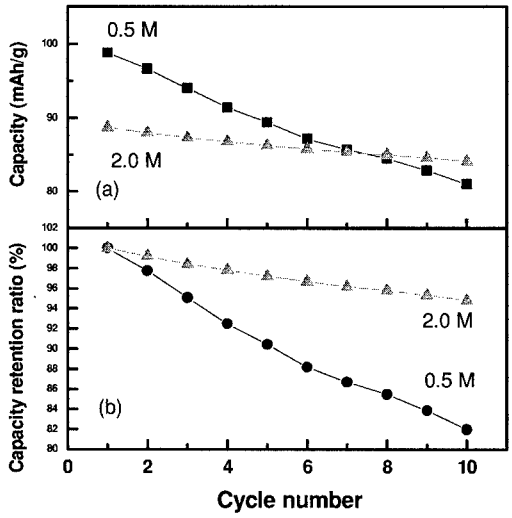


Fig. 5. Comparison of the cycling stability and the capacity retention of the RμE-derived powders at 55℃.

## CONCLUSIONS

Monophasic nanosized $LiMn_2O_4$ powders were successfully synthesized after calcining the precursor powders at 700°C for 1 h. The electrochemical performance of the obtained $LiMn_2O_4$ powders was also examined. The particle size decreased and the surface area increased with a drop in the cationic concentration. It was found that $LiMn_2O_4$ particles with larger surface area gave rise to a greater specific capacity but a worse cyclability at elevated temperatures. The first-cycle discharge capacities of the samples prepared from cationic concentrations of 0.5 M and 2.0 M were 98.8 and 88.7 mAh/g at 55°C, and the corresponding capacity retentions after ten cycles were 82% and 95%, respectively. In order to optimize the electrochemical performance of $LiMn_2O_4$, the control of particle size is necessary.

## REFERENCES


1. J. M. Tarascon, E. Wang, F. K. Shokoohi, W. R. McKinnon, S. Colson, J. Electrochem. Soc. **138**, 2859 (1991).
2. A. Momchilov, V. Manev, A. Nassalevska, J. Power Sources **41**, 305 (1993).
3. Z. Jiang, K. M. Abraham, J. Electrochem. Soc. **143**, 1591 (1996).
4. T. Ohzuku, M. Kitagawa, T. Hirai, J. Electrochem. Soc. **137**, 769 (1990).
5. X. H. Hu, X. P. Ai, H. X. Yang, Sh. X. Li, J. Power Sources **74**, 240 (1998).
6. W. Liu, G. C. Farrington, F. Chaput, B. Dunn, J. Electrochem. Soc. **143**, 879 (1996).
7. Y. H. Ikuhara, Y. Iwamoto, K. Kikuta, S. Hirano, J. Mater. Res. **14**, 3102 (1999).
8. H. J. Kweon, S. S. Kim, G. B. Kim, D. G. Park, J. Mater. Sci. Lett. **17**, 1697 (1998).
9. C. H. Lu, S. K. Saha, Mater. Sci. Eng. **B79**, 247 (2001).
10. C. H. Lu, S. W. Lin, J. Power Sources **93**, 14 (2001).
11. Powder Diffraction File, # 35-782. Joint Committee on Powder Diffraction Standards, Swarthmore, PA, USA.

# Applications and Properties I

Mat. Res. Soc. Symp. Proc. Vol. 703 © 2002 Materials Research Society V7.5

# Nanostructured Hydroxyapatite Coatings for Improved Adhesion and Corrosion Resistance for Medical Implants

Zongtao Zhang, Matthew F. Dunn, T. D. Xiao
Inframat® Corporation, 74 Batterson Park Road, CT 06032
Antoni P. Tomsia and E. Saiz
MS 62-203, Lawrence Berkeley Lab, Berkeley, CA 94720

**Abstract:** Hydroxyapetite (HA) coating on medical implant has been used in commercial application for several decades. The coating, commercially made by thermal spray method, functions as a intermediate layer between human tissues and the metal implant. The coating can speed up early stage healing after operation but the life span is much limited by low interfacial bond strength, which comes from the dissolution of amorphous HA in human body fluid during its service. This amorphous phase is formed in coating process under high temperature. To overcome these problems, we have developed a novel room temperature electrophoretic deposition process to fabricate nanostructured HA coating. This nanostructured HA coating significantly improved coating's bond strength up to 50-60 MPa, 2-3 times better than the thermal sprayed HA coating. The nanostructured HA coating also has corrosion resistance 50-100 times higher than the conventional HA coating. X-ray diffraction shows that all the HA coating is fully crystalline phase. It is expected that the implants with the nanostructured HA coating will have much longer service life. Other benefits derived from this process include room temperature deposition, the ability to control the coating microstructure and phases, and low cost for production.

## INTRODUCTION

The field of hydroxyapatite ("HA") coatings is growing very rapidly. Since the 1980's, titanium implants typically have been coated with HAP using thermal spray techniques. There are two major shortcomings associated with plasma-sprayed HAP coatings. First, due to the high temperature plasma (≥15,000°C), a large fraction of crystalline HAP turns amorphous while in transit. This phase is soluble in body fluids and results in subsequent dissolution of the material during operation. Second, while thermal spray coatings in general are characterized by strong mechanical bonds, on a relative scale, this type of bond is weak in comparison to metallurgical or chemical bonds. In the 1990's, a chemical precipitation method was used for coating porous implants. This process operated at a temperature lower than 100°C, overcoming the HA dissolution problem, but the bonding between the HA coating and substrate interface is very week. In fact, the *poor adhesion* of HA coatings to titanium substrates is *the* single most troublesome aspect of today's technologies in relation to the viability of commercial implantable products [1].

Free-standing crystalline nanostructured HA ("*n*-HA") has been synthesized by Ying *et al.* [2] using a wet chemical synthesis technique. Note that this material has not been fabricated as a coating. Powder agglomerates were consolidated into bulk form for testing of mechanical properties such as fracture toughness, and bend and compressive strength. The MIT group found that the compressive strength of bulk n-HA can be increased up to 4-fold in comparison to bone

(879 MPa *vs.* 193 MPa for compacted bone). The bend strength was found to be roughly equivalent (193 MPa *vs.* 160 MPa in bone). These impressive numbers are a good indication of what can be anticipated in electrophoretic n-HA.

Electrophoretic deposition of HA can be done at room temperature (or lower) and avoids problems related to formation of the amorphous phase. Most importantly, the nature of the bond is metallurgical rather than mechanical and is expected to result in dramatically improved bond strength in comparison to thermal spray techniques. In addition, electrophoresis enables multicomponent codeposition. However, one disadvantage is porosity, allowing body fluid to enter and cause corrosion of the titanium substrate, and delamination. High temperature sintering has been used to decrease porosity and increase the density to mitigate this problem. Unfortunately, due to a poor mismatch in thermal expansion coefficients between the HA and titanium at high temperatures (during sintering) and the large volume pore reduction, cracks result.

In contrast, for nanostructured materials, this has been found to be less of a problem [3]. It has been demonstrated that nano ceramics have thermal expansion coefficients that nearly match the metal alloys due to the large volume fraction of atoms located at the grain boundary, which improves mobility [3,4]. To date, electrophoretic deposition ("EPD") of HA has been limited to conventional materials of micron grain size [5-9]. Mechanical properties of the micron HA are limited by relatively poor bend strength, fracture toughness, and compressive strength. Also, n-HAP can be sintered at a much lower temperature, as has been demonstrated for n-$TiO_2$, which can be sintered at 1/3 of the melting point (600 °C vs 1400 °C) [4]. At lower temperatures, there is less thermal expansion. We expected that the n-HAP could be sintered at a much lower temperature (900 °C or lower with low pressure HIPing, 500 °C), as observed by Ying [2]. Finally, a dense gradient bond coat of $TiO_2$ was introduced (a few microns thick) between n-HAP and titanium, so that body fluids have no opportunity to attack and degrade the titanium substrate.

## EXPERIMENTAL PROCEDURES

Nanostructured HA powders were synthesized using a wet chemical process. This wet chemical process produced high quality n-HA particles with particle size ranging from 20 to 50 nm. The as-synthesized n-HA particles were suspended in polarized solvent. Ti6Al4V coupons with 1.0 inch diameter and 0.25 inch thickness were used as a substrate. The Ti alloy and platinum were used as cathode and anode, respectively. This process produced tenacious HA nanocoatings.

Characterization of the HA nanocoatings included interfacial bond strength using ASTM Standard F 1501-95 via tensile tester, Surface and cross-sectional microstructure and morphology using SEM, in-vitro testing of the coated coupons in simulated human body fluids, and electropolarization measurements during in-vitro tests.

## EXPERIMENTAL RESULTS AND DISCUSSION

***Microstructure and bond strength:*** The EPD process produced a high quality HA nanocoating. Both surface and cross-sectional SEM indicated that the as-produced HA nanocoatings were highly dense with few closed pores. Fig. 1 shows a typical SEM cross-sectional view of the coating. The cross-section morphology showed a very clean coating to substrate interface and

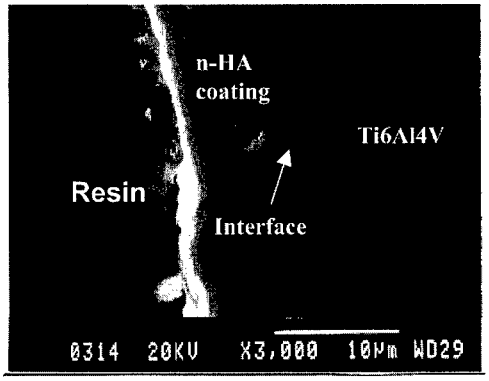


**Fig. 1.** SEM micrograph showing the cross-sectional view of nano-HA on Ti substrate. Note that the coating to substrate interface is clean, and with high bond strength.

high density. Coating to substrate adhesion evaluation using direct-pull-tests indicated that the as-fabricated nanocoatings exceed 60 MPa, exceeding the FDA required bond strength value, which is 50 MPa.

***PH Change with time.*** Fig. 2 shows the pH change with soaking time in simulated human body fluid at 37 °C. In comparison, plasma sprayed conventional micrometer sized HA coatings were also tested using the same conditions. It was found that the EPD n-HA coatings kept a constant pH value at 6.5 soaked in the simulated body fluid for more than 60 days. However, in the case of plasma sprayed HA coatings, the simulated human body fluid had a sudden pH increase up to 9.7. Two days latter, the pH reached the highest point of 10.5. After that, the pH gradually went down to 7.5 and tended to be stable within 30 days. These curves demonstrated that the EPD coated n-HA coatings were much more stable than the conventional thermal sprayed HA coating during in-vitro tests in the simulated body fluid.

***Calcium content change with time.*** Fig. 3 shows the calcium content change with soaking time of both conventional thermal sprayed ("T/S") HA coatings and EPD n-HA coatings. The calcium content release ranking can be expressed as

*Non-heat treated T/S HA coating > heat treated T/S HA coating > EPD n-HA coatings*

For the two thermal sprayed HA coatings, both exhibited high calcium release, which was caused by the dissolution of amorphous HA and other impurities of calcium phosphates of the coatings in the simulated human body fluid. In the actual experiments, we also found a white-colored

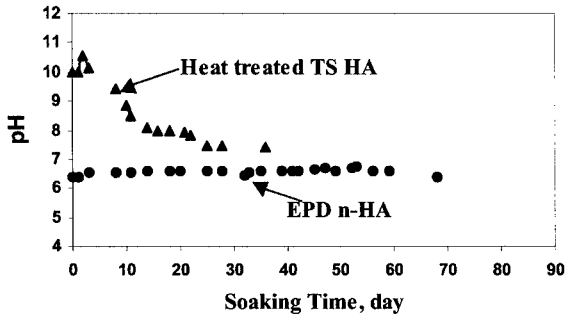


**Fig. 2.** pH plot vs. soaking time during in-vitro testing in the simulated human body fluid.

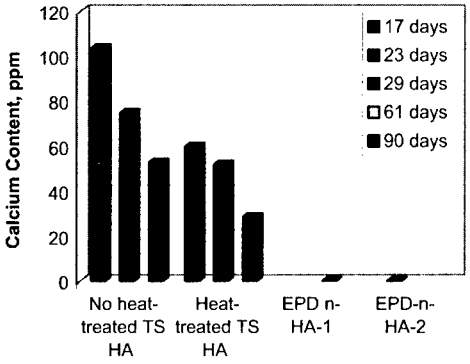


**Fig. 3.** Calcium content release into the simulated body fluid vs. different materials at 37°C for 3 months.

material, which first appeared on the thermal sprayed HA coating surface and then gradually dissolved into the solution. This phenomenon was more serious for the non-heat treated thermal sprayed HA coatings than for the heat-treated ones. It was noticed that calcium release of the thermal sprayed HA coatings decreased with the soaking time. For the heat-treated HA coating, the calcium content release was: 60.1, 52.2, and 28.8 ppm for soaking 17, 29, and 90 days in the simulated body fluid, respectively. The decrease of the calcium release could be explained by the reaction of the calcium ions with absorbed $CO_2$, which produces $CaCO_3$. When solid $CaCO_3$ formed, the $Ca^{2+}$ concentration would decline. The $CO_2$ absorption and reaction with $Ca^{2+}$ can explain pH gradually going down with soaking time in Fig. 2.

The most important finding was that, for both EPD nanocoatings, *e.g.,* n-HA-1 coatings soaked 61 days and EPD n-HA-2 for 23 days, the calcium contents in the simulated human body fluid were zero, indicating no calcium release to the simulated body fluid.

***Electrochemical Corrosion:*** The corrosion resistance results for both EPD n-HA coatings and thermal sprayed HA coatings are shown in Fig. 4, where the n-HA coating had a corrosion current 50-100 time smaller than the thermal sprayed coating in simulated human body fluid at room temperature.

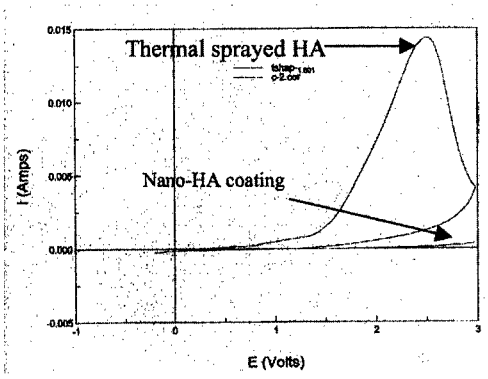


**Fig. 4.** Electro-polarization corrosion curves for both EDP n-HA coatings and thermal sprayed HA coatings.

As shown in Fig. 1, the n-HA coatings are nearly 100% dense. XRD analysis indicated 100% crystallinity of the HA nanocoatings. In the n-HA coatings, simulated human body fluid had no chance for contact with the Ti alloy surface, consequently, no corrosion occurred. In contrast, thermal sprayed HA coating had many defects associated with the as-fabricated coatings, porosity, and cracks were evident, as well as the presence of amorphous phases. The interfacial and coating cracks are usually formed during cooling down of the fabricated components in the thermal spray process, due to large thermal expansion coefficient differences between the HA coating ($\alpha_{HA}$=13.5 $\times 10^{-6}$ /°C) and the Ti substrate ($\alpha_{Ti}$=9.5 $\times 10^{-6}$ /°C).

The interfacial reaction at the interface area is divided into two steps. First, the $H^+$ produces at the interface area when corrosion occurs (eq. 1). Second, the HA material dissolves in the high $H^+$ concentration area (eq. 2). Because the $H^+$ cannot be well circulated out at interface, the local pH of the interface is extremely low. The HA dissolution automatically speeds up, so this corrosion is a self-catalytic process. Whenever the corrosion starts, it cannot stop until the entire interfacial HA material is dissolved. Since water can easily go through the connective cracks of the thermal sprayed coating, the corrosion proceeds very quickly. This is why conventional thermal sprayed HA coating always fails at the HA/Ti ally interfacial area.

$$Ti + 2H_2O = TiO_2 + 4H^+ + 4e \quad (1)$$

$$Ca_{10}(PO_4)_6(OH)_2 + 2H^+ = 10Ca^{2+} + 6(PO_4)^{-3} + H_2O \quad (2)$$

***Bond strength changes with soaking time in-vitro:*** It is seen in Fig. 5 that the EPD n-HA coatings have much higher initial tensile bond strength (50-60 MPa) than that of conventional thermal sprayed HA (30 MPa) and chemical deposited HA coatings (14 MPa) before *in-vitro* corrosion in simulated human body fluid was conducted. During the *in-vitro* testing period, e.g., 10 weeks, the bond strength of the n-HA coatings kept a constant value (60 MPa), while the plasma sprayed and chemical deposited HA coatings have a significant bond strength loss.

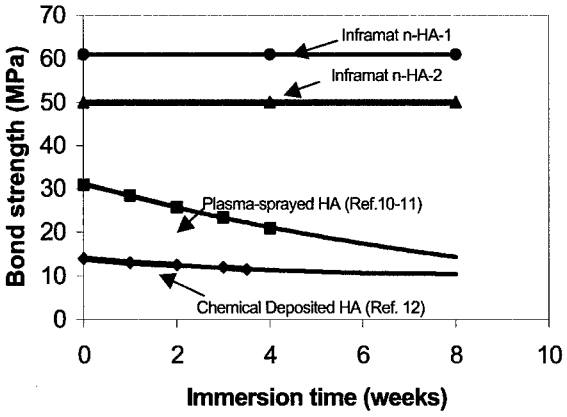


**Fig. 5.** Bond strength vs. soaking time during in-vitro test in simulated body fluid. The experimental errors are 10% of the data

## CONCLUSIONS:

1. The EPD n-HA coating has strong interfacial bonding on Ti alloy and maintained tensile bond strength 50-60 MPa after 2 month in-vitro testing, which was much better than the plasma-sprayed HA and chemical precipitated HA coating that suffered bond strength loss in vitro.
2. The electrochemical corrosion resistance of the EPD n-HA coating was 50-100 times higher than the plasma-sprayed HA coating.
3. The EPD n-HA coating did not exhibit dissolution in simulated human body fluid in 2-month *in-vitro* test.


## ACKNOWLEDGEMENT

This project was supported by the National Institute of Health, SBIR Phase I Contract, No.1R43AR47278-01.


## REFERENCES


[1]. Limin Sun, Christopher C. Berndt, Karlis A. Gross, Ahmet Kucuk, " Material Fundamentals and Clinical Performance of Plasma-Sprayed Hydroxyapatite Coatings A Review." J. Biomed. Mater.Res., Vo. 58, 570-592, 2001.

[2]. E.S. Ann, N.J. Gleason, A. Nakahira, and J.Y. Ying, "Nanostructured Processing of Hydroxyapatite-based Bioceramics," *MRS 1998 Fall Meeting*, Abstract, pp. 611, private communication, Danny Xiao and Jackie Ying 1998.

[3]. H. Gleiter, "Materials with Ultrafine Microstructures: Retrospective and Perspectives," Nanostructured Materials **1**, 1-9, 1992.

[4]. J. Eastman & R. Seigel, *Research & Development*, p.56, Jan. 1989.

[5]. P. Sarkar and P.S. Nicholson in a feature paper, "Electrophoretic Deposition (EPD): Mechanism, Kinetics, and Appl. to Ceramics, " *J. Am cerm. Soc.,79[8] 1987-2002 (1996).*

[6]. P. Ducheyne, S.Radin, M. Heughebaert, and J.C. Heughebaert, "Calcium Phosphate Ceramic Coating on porous Ti: Effect of Structure & Composition on Electrophoretic Deposition, Vacuum Sintering, and in *Vitro* Dissolution," *Biomaterials*, **11**, 244-54 (1990).

[7]. M. Nagai, K Yamashita, and T. Umegaki, "Electrophoretic Deposition, of hydroxyapatite coating," *Phosphorous Research Bullin*, Vol. 1, pp167, 1991.

[8]. K. Yamashita, E. Yongehara, X. Ding, M. Nagai, T. Umegaki, and M. Matsuda, " Electrophoretic coating of multilayered apatite composite on alumina ceramics," *J. Biomedical Mater. Res.,* Vol. 43, pp 46-53,1998.

[9]. T.V. Vijayaraghavan and A. Bensalem, "Electrodeposition of apatite coating on pure titanium and titanium alloys," *J. Mater. Sci. Lett.*, vol.13, pp. 1782-5,1994.

[10]. S.R Sousa and M.A. Barbosa, "Effect of hydroxyapatite thickness on Metal ion release from Ti6Al4V substrates, Bio materials 1996, vo.17, no.4, 397-404.)

[11]. Yang CY, Wang BC, Chang E, Wu BC. "Bond degradation at the plasma-sprayed HA coating/Ti-6Al-4V alloy interface: An in vitro study. J. Mater Sci: Mater Med 1995: 6: 258-265.

[12]. Yong Han, Tao Fu, Jian Lu, Kewei Xu, Characterization and stability of hydroxyapatite coatings prepared by an electrodeposition and alkaline-treated process." J. Medical Mater. Research." Vol.54, No.1, 96-101(2000).

Mat. Res. Soc. Symp. Proc. Vol. 703 © 2002 Materials Research Society V7.7

# Characterization of Self-Assembled $SnO_2$ Nanoparticles for Fabrication of a High Sensitivity and High Selectivity Micro-Gas Sensor

R.C.Ghan, Y. Lvov, and R.S.Besser
Louisiana Tech University
Institute for Micromanufacturing
911 Hergot Avenue,
P.O.Box 10137,
Ruston, LA, 71270.
Fax: (240) 255-4028
Email: rbesser@coes.latech.edu

## ABSTRACT

In order to refine further the material technology for tin-oxide based gas sensing we are exploring the use of precision nanoparticle deposition for the sensing layer. Layers of $SnO_2$ nanoparticles were grown on Quartz Crystal Microbalance (QCM) resonators using the layer-by-layer self-assembly technique. Scanning Electron Microscopy (SEM), Transmission Electron Microscopy (TEM), and Electron Diffraction Pattern (EDP) analyses were performed on the self-assembled layers of $SnO_2$ nanoparticles. The results showed that $SnO_2$ nanoparticle films are deposited uniformly across the substrate. The size of the nanoparticles is estimated to be about 3-5 nm. Electrical characterization was done using standard current-voltage measurement technique, which revealed that $SnO_2$ nanoparticle films exhibit ohmic behavior. Calcination experiments have also been carried out by baking the substrate (with self-assembled nanoparticles) in air at 350°C. Results show that 50%-70% of the polymer layers (which are deposited as precursor layers and also alternately in-between $SnO_2$ nanoparticle monolayers) are eliminated during the process.

## INTRODUCTION

Solid-state gas sensors find applications in automobiles, toxic and domestic environments, the chemical industry, and elsewhere. The gas-sensor market is fast burgeoning and was estimated to be about $0.9 billion at the end of the last decade [1]. Ceramic $SnO_2$ has been used extensively as a sensor element in semiconductor gas-sensors for detecting a range of gases such as carbon monoxide, oxides of nitrogen, hydrogen sulfide, freon and many others [2]. $SnO_2$ is the prime choice for semiconductor sensors because of its bulk-material stability and resistivity characteristics. Sensors with $SnO_2$ as sensing element function on the principle of surface chemical reaction between an analyte gas and the sensing element, which causes a change in the resistance of the element. Thus the sensing characteristics depend on the surface properties of the element [3]. While performing sufficiently for commercial deployment, these sensors displayed a variety of material issues including the degree of crystallinity of $SnO_2$, crystallite size, density of lattice defects, surface area, and surface structure. These issues translated to low or varying selectivity and sensitivity of the $SnO_2$ sensors. Some of the techniques that have been implemented for improving the selectivity include cyclic manipulation of the sensor temperature, doping of the $SnO_2$ with various additives like Pt and noble metals [3], surface modification of the base metal oxide with hydrophobic groups, calcium oxide, zinc oxide and sulfur [4]. The

method of fabrication is also a variant in the process to improve the performance of $SnO_2$ sensors. The different routes for fabrication adopted for metal-oxide thin film sensors are sol-gel method of deposition of $SnO_2$ thin films, reactive sputtering [5], and sintering and annealing [6]. These fabrication methodologies attempted to deposit thin films of $SnO_2$ for manifesting improved selectivity and sensitivity. Decreasing the particle size of $SnO_2$ is another factor which could contribute to improving performance. In the present study, we attempt to circumvent many of the limitations of the traditional preparation methods by depositing $SnO_2$ nanoparticles using the Layer-By-Layer (LBL) self-assembly technique which is based on alternate adsorption of oppositely charged components [7].

Nanocrystalline structure is known to impart high sensitivity and selectivity to gas-sensors [8]. Nanoparticles offer a high degree of structural control due to their well-defined size and shape, and the LBL assembly method allows them to be uniformly and precisely ordered on the substrate with the precision of a few nanometers [9]. We therefore anticipate the resulting films to possess high reproducibility of thickness, of crystallite size, and of the geometry of intergranular contact, which are known to be key factors in the gas sensing mechanism [8]. In addition, the LBL process permits the architecture of the layer to be engineered by insertion of monolayers of alternate materials (e.g. $SiO_2$ to enhance activity), doped nanoparticles, or nanoparticles of varying radius to modulate the film density [4]. We report here on the characterization of the $SnO_2$ layers formed by the LBL method. SEM, TEM, and EDP analysis were done on the nanolayers of $SnO_2$, in order to determine the size of the nanoparticles and thickness of the nanofilm. Electrical characterization was done to observe the current-voltage characteristics of the nanofilms. Calcination studies were also performed to investigate the elimination of the polymer layer, which is a by-product of the LBL process.

## EXPERIMENTAL DETAILS

$SnO_2$ nanoparticles were obtained from Nyacol® NanoTechnologies (Nyacol Colloidal Tin Oxide) as two separate samples, SN-15 (negatively charged, pH 8.0-9.0, specific gravity 1.15, viscosity 5-10 cps and counter–ion concentration of 0.5% potassium) and SN-15CG (negatively charged, pH 9.0-10.5, specific gravity 1.15, viscosity 5-10 cps and counter ion concentration of 0.23% $NH_3$). The polyions used were Polydialyldimethyldiammonium chloride (PDDA), Sodium-polystyrene sulfonate (PSS), and Polyethyleneimine (PEI) of 2 mg/mL in aqueous solution (all Sigma-Aldrich. [9]. The initial characterization of the $SnO_2$ was carried out on a quartz crystal microbalance (QCM, USI-System, Japan) resonator in order to monitor the film growth during each step in the process. The technique initially involves layer-by-layer electrostatic assembly of several pairs of oppositely charged polyion layers as the precursor layers to promote the structural stability of the subsequently assembled nanoparticles. The outermost precursor polyion layer is oppositely charged (positive) with respect to the anionic nanoparticles. Then the nanoparticles and the complimentary polyion layer are alternately self-assembled as shown in Figure 2.

Self-assembly was tried first with PEI/PSS/$(PEI/SnO_2)_7$ and then with PDDA/PSS/$(PDDA/SnO_2)_{7\text{-}16}$. The latter sequence was found to result in more reproducible growth of $SnO_2$ nanoparticle multilayers. Thereafter all self-assembly experiments were done with the same sequence, i.e., PDDA/PSS/$(PDDA/SnO_2)_7$. In order to assess whether steady-state conditions had been reached during the adsorption process, the time of retention of the QCM resonator in the $SnO_2$ colloidal solution was varied and the results were obtained as change in

frequency plotted against the number of monolayers assembled. The self-assembled samples were sent to RIKEN Frontier Research System, Topochemical Design Laboratory in Japan for SEM analysis. For TEM analysis for nanoparticle size measurement, EDP, and High Resolution TEM of nanoparticle grain structure, the samples were sent to Material Characterization Lab at Louisiana State University.

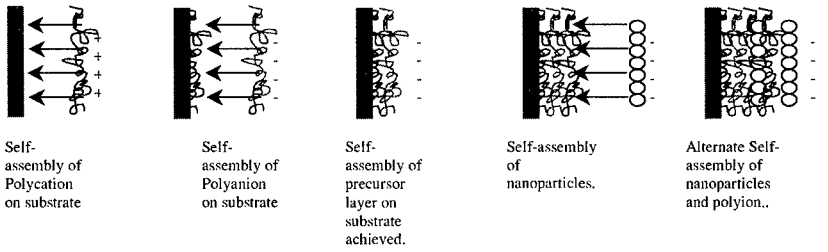


**Figure 1**: Schematic of the Layer-By-Layer process used for self-assembly of $SnO_2$ nanoparticles.

I-V characteristics were studied using a standard electrical characterization set-up. The samples were prepared as 2.75cm x 3.5cm coupons of Pyrex glass. $SnO_2$ nanoparticles were self-assembled on the glass substrate. Electrical contact patterns were designed using LEDIT® software. The pattern was transferred onto Mylar® sheets, and cut out to form electrical contact patterns. Patterns for both two-point and four-point tests were created. Using these patterns, Pt contacts were sputter deposited onto the self-assembled glass samples. The samples were then tested for their I-V characteristics.

Calcination studies were carried out by baking a blank silver electrode resonator (resonator with no self-assembled layers), and another with 20 self-assembled layers of $SnO_2$ in a Thermolyne® Furnace at 350°C for 4 hours in one-hour intervals. The frequency readings for both the resonators were taken after each hour interval.

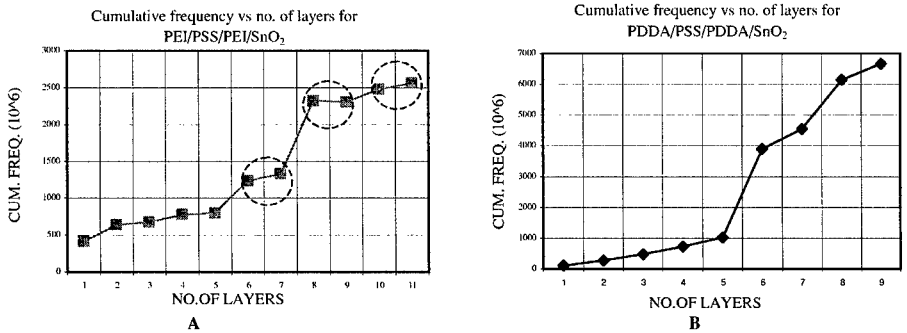


**Figure 2**: Graphs for cumulative delta F (Hz.) for (A) [PEI/PSS/PEI/$SnO_2$] and (B) [PDDA/PSS/PDDA/$SnO_2$].

## RESULTS AND DISCUSSION

### Self-Assembly of $SnO_2$ Nanoparticle Multilayers and Characterization

$SnO_2$ nanoparticles were self-assembled on a QCM resonator using two alternative sequences: 1) PDDA/PSS/ $(PDDA/SnO_2)_n$ and 2) PEI/PSS/$(PEI/SnO_2)_n$, where n = 5-16. After every adsorption cycle, a sample was dried, and the QCM frequency was measured. The frequency shifts ($\Delta F$) characterized the mass adsorbed on resonator, and an increase of the film thickness [3].

As seen in the Figure 2 (A), the three-circled areas represent poor or irreproducible uptake of the PEI layer. This irreproducibility led to non-uniform deposition of subsequently self-assembled $SnO_2$ nanoparticle layers. No such phenomenon is observed in the sequence PDDA/PSS/PDDA/$SnO_2$. Therefore it was concluded that the second sequence was better suited for self-assembly of $SnO_2$ nanoparticles as it exhibited sound linearity in growth characteristic. Further experiments were carried out with the sequence PDDA/PSS/PDDA/$SnO_2$ and the time of immersion in the $SnO_2$ colloidal nanoparticle solution was varied from 20 minutes, 10 minutes, and 15 minutes down to 5 minutes. Figure 3 shows that the self-assembly of $SnO_2$ follows an approximately time-independent behavior i.e. addition of nanoparticles is essentially complete in less than 5 minutes of immersion time. This behavior yields a high precision of thickness control in the growth process. The anomalous behavior in the 18$^{th}$ growth layer of the 20-minute immersion film can be attributed to manual errors in handling the resonator while transferring it from one solution to another and/or handling while drying.

High-resolution imaging reveals that the particle size is approximately in the range of 3-5 nm. The thickness of the film deposited was calculated to be 490 nm using the QCM frequency data and the relation $\Delta t = -0.016*\Delta F$ [9] and the results obtained from the SEM analysis show that the thickness of the self-assembled films of eight $SnO_2$ monolayers is approximately 300-400 nm.

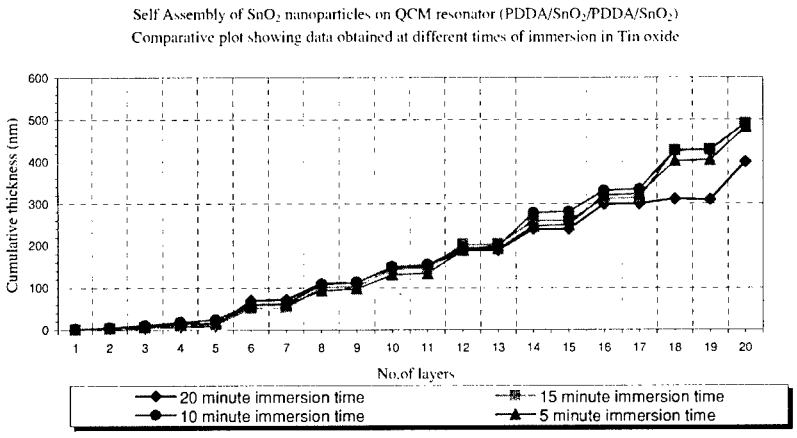


**Figure 3:** Comparative plot showing data obtained at different times of immersion in tin-oxide colloidal nanoparticle solution.

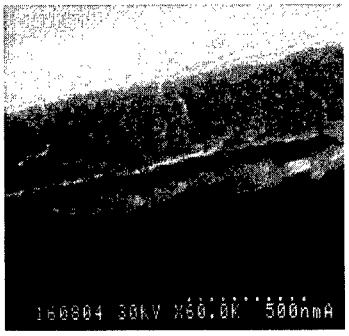


**Figure 4:** SEM image of cross-section of QCM resonator with self-assembled $SnO_2$ nanoparticles.

**Electrical Characterization**

Coupons of Pyrex glass of the same dimensions as the electrical patterns were prepared and Pt contacts 2000Å were sputter coated onto the coupons. One coupon was calcined for 1 hour to eliminate interlayer polyions. Two-point I-V results showed linear (ohmic) behavior of the deposited $SnO_2$ layers (Figure 5) for the calcined sample. The I-V characteristics for the uncalcined sample showed several spurious readings which are linked to the presence of the polyion layers in between the $SnO_2$ nanoparticle layers. We believe polyion layers impose regions of parallel conductance that undergo electrical breakdown to a high-impedance state thereby resulting in what appears to be a I-V characteristic superimposed with noise. Measured resistivities were 0.18 ohm-cm for the uncalcined sample, and 0.63 ohm-cm for the calcined sample.

**Calcination**

Calcination effectively eliminates the spurious points and also results in a higher net resistivity corresponding to the substantial reduction in polyion conductivity contribution .In the first calcination experiment, a self-assembled QCM resonator with 8 layers of $SnO_2$ (and total of 20 layers including the polyion layers), and a blank resonator control were used for

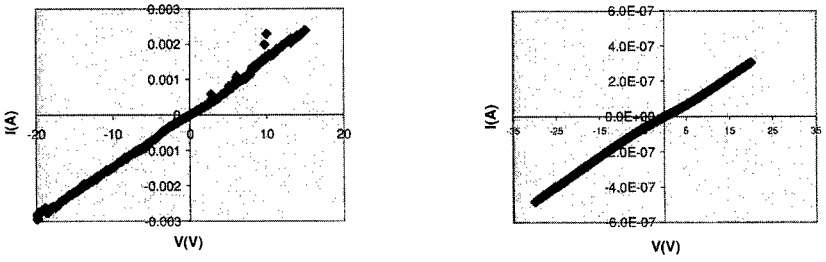


**Figure 5:** I-V characteristics for uncalcined (left) and calcined (right) samples.

calcination studies. Both the resonators were calcined for 4 hours and frequency measurements were recorded after every 1-hour interval. The initial frequency was measured for both the resonators before calcination. After every 1 hour, frequency deviation was recorded for both the resonators. Mass change was calculated using the relation [3]:

$$\Delta m(ng) = -0.87 \cdot \Delta F(Hz) \quad (1)$$

The self-assembled resonator lost approximately 2000 ng in the first hour, and less than 300 ng thereafter. The initial loss corresponded to 50% loss of total polyion deposited by self-assembly.

These results are in agreement with earlier study of temperature decomposition of the linear polycation / polyanion multilayers [10] which have shown that calcinations at 350° C for three hours is necessary to eliminate these films.

## CONCLUSION

We have demonstrated self-assembly of $SnO_2$ nanoparticles on QCM resonator and glass substrates. SEM, TEM, and HRTEM analysis have been performed which give an estimate of the $SnO_2$ nanoparticle size, which is approximately 3-5 nm. The $SnO_2$ nanoparticle films deposited by LBL process are uniformly deposited across the substrate and the thickness of these films can be precisely controlled. Electrical characterization of self-assembled $SnO_2$ substrates has been performed and results show that self-assembled samples, which are calcined, show smoother ohmic behavior as compared to self-assembled samples, which are not calcined. Preliminary calcination studies show that approximately 55% to 70% of polyion mass is eliminated in the process.

## ACKNOWLEDGMENTS

We are grateful to Dr. Izumi Ichinose, of RIKEN-Frontier Research System, Japan for making the SEM micrograph of the film cross-sections. This work was partially funded by NSF-EPSCoR research infrastructure grant "Chemical and Biochemical Micro- and Nanosytems."

## REFERENCES

1) M. Madou, "Fundamentals of Microfabrication," (CRC press, 1997), pp. 495-500.
2) B. Hoffheins, "Resistive gas sensors," *Chemical and Biological Sensors*, ed. R.F Taylor, J.S Schultz, (IOP publishing Ltd., 1996) pp. 371-377.
3) S. Morrison, "Chemical Sensors," *Semiconductor Sensors*, ed. S. M. Sze, (John Wiley & Sons, Inc., 1994), pp. 383-412.
4) K. Ihokura, J. Watson, "Stannic Oxide Gas Sensor," (CRC press Inc., 1994) pp. 1-5.
5) S. Davis, A. Wilson, J. Wright, *IEE Proc.- Circuits Devices Syst.*, **145** (5), pp.379, (1998).
6) M. Ippommatsu, H. Ohnishi, H. Sasaki, T. Matsumoto, *J. App.Phys.* , **69**, pp.8368, (1991).
7) G. Decher, *Science*, **277**, 1232, (1997).
8) M. S. Hettenbach, "$SnO_2$ (110) and Nano-$SnO_2$: Characterization by Surface Analytical Techniques," pp. 18-20, 2000.
9) Y. Lvov, K. Ariga, I. Ichinose, T. Kunitake, *Langmuir*, **13**, 6195 (1997).
10) T. Farhat, G. Yassin, S. Dubas, J. Schlenoff, *Langmuir*, **15**, 6621 (1999).
11) R.C.Hughes, A.J.Ricco, M.A.Butler, S.J. Martin, *Science*, **6**, 74, (1991).

Mat. Res. Soc. Symp. Proc. Vol. 703 © 2002 Materials Research Society V7.8

# Fluorescence from Coated Oxide Nanoparticles

D. Vollath, I. Lamparth, D. V. Szabó
Forschungszentrum Karlsruhe, Institut fuer Materialforschung III
P.O.Box 3640, D-76021 Karlsruhe, Germany

## ABSTRACT

In many cases, coated nanoparticles behave like isolated ones. Using the microwave plasma process, it is possible to produce oxide nanoparticles with ceramic or polymer coating. Coating the particles has the additional advantage that by proper selection of the coating it is possible to suspend the particles in distilled water without using any colloid stabilizer. From quantum dots made of sulfides or selenides, it is well known from literature that fluorescence depends strongly on the coating of the kernels. In the case of CdSe, the kernels are coated with CdS. Within this study, similar phenomena are found with coated oxide nanoparticles having sizes of ca. 6 nm exhibiting a very narrow particle size distribution. The coating consists of a second ceramic phase or a polymer one, each one influencing fluorescence differently. Obviously, the type of coating is a tool to modify fluorescence. This behavior is demonstrated on kernels made of $Al_2O_3$, $ZrO_2$, $HfO_2$, ZnO etc. PMMA, PTFE, or $Al_2O_3$ were used as coating material. In most cases, the fluorescence spectra showed broad bands. In some cases, such as ZnO, additionally, a sharp emission line in the UV appears. It is interesting to note that coatings made of fluorine containing polymer materials did not lead to fluorescence intensities comparable with PMMA coatings. The observed spectra are equivalent whether the powder is in aqueous suspensions or dry on a quartz glass carrier. The experimental results in this study indicate that the combination of non-fluorescent oxide core with a non-fluorescent polymer coating may lead to a nanocomposite with strong fluorescence. This is a phenomenon not described in literature until now.

## INTRODUCTION

Many applications of nanoparticles use fluorescence properties, e.g. in medical, biological, or pharmaceutical area. [1-7] Usually, fluorescence is a property of organic molecules or single isolated nanoparticles. Therefore, in most cases, fluorescence is determined in suspensions. Best fluorescence efficiency is obtained with semiconductor nanoparticles and semiconductor quantum dots based on sulfides, selenides, or tellurides. [8, 9] The best-described fluorescent nanoparticles are GaN [10, 11], doped ZnS [12], or doped CdSe. [13] All of these particles have the disadvantage of being as well poisonous as carcinogenic. Additionally, these particles show a very limited thermodynamic stability against oxidation. Therefore, research in the direction of fluorescent oxide nanoparticles is under way. [14-16] In most cases, fluorescence is obtained by doping with small amounts of rare earth ions. [17] In many cases, electron excitation of the fluorescent material led to the best results.

The Karlsruhe Microwave Plasma Process is capable to synthesize ceramic nanoparticles coated with a second ceramic layer [18,19] or a polymer. [20] In situ coating of each single particle is possible, because the particles leave the plasma zone, where the reaction occurs, with electric charges of equal sign. Therefore, the particles repel each other. This avoids agglomeration and makes it possible to coat the particles in a second step. The coating is performed in a

second step of a cascaded process of synthesis. The coating may consist of a ceramic or a polymer layer.

The availability of non-agglomerated coated nanoparticles is the basis for a new class of fluorescent nanoparticles based on non-toxic oxides. This study describes the fluorescence behavior of isolated respectively separated nanoparticles in suspension or as a powder. As particle cores $Al_2O_3$, $ZrO_2$, $HfO_2$, $TiO_2$, $SnO_2$, $WO_x$, and ZnO were selected. Coating material was $Al_2O_3$, PMMA, or PTFE, respectively. Electron microscopy revealed that the particle size of the different cores was in the range between 5 and 10 nm. The thickness of the coating was in the range from 0.5 to 2 nm for alumina and 2 to 5 nm for the polymer coatings.

## EXPERIMENTAL

As mentioned above, the oxide nanoparticles were synthesized using the Karlsruhe Microwave Plasma Process. Except for zinc, chlorides or carbonyls were used as precursor compounds. For zinc, di-ethyl zinc was applied. PMMA coating was made using the monomer as precursor; PTFE like coating was obtained using $C_{20}F_4$. Figure 1a and 1b depict typical electron micrographs of the material. Figure 1a shows crystallized $HfO_2$ coated with amorphous $Al_2O_3$. Polymer coated material is shown in figure 1b. To obtain good contrast for printing, PMMA coated $Fe_2O_3$ was selected as example.

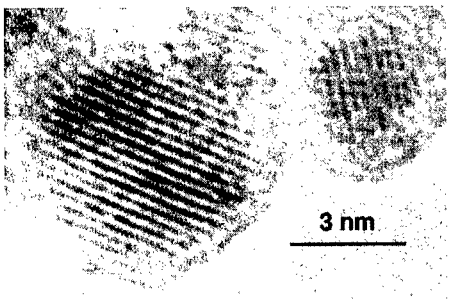


**Figure 1a:** Hafnia nanoparticles coated with alumina. The lattice fringes are belonging to $HfO_2$; the $Al_2O_3$ coating is amorphous.

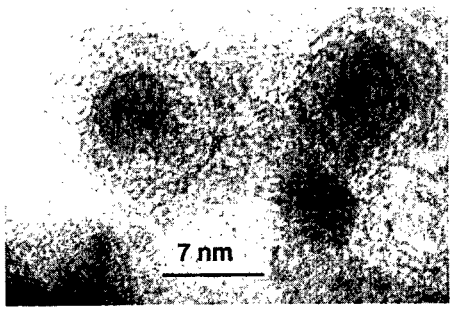


**Figure 1b:** Polymer (PMMA) coated ceramic nanoparticles. To obtain good visibility of the two phases, in this example, $Fe_2O_3$ was selected as kernel material

The fluorescence spectra were measured with a system using a Czeney-Turner monochromator. For illumination a HeCd (325 nm) or a xenon lamp were applied. The fluorescence signal was detected using a photomultiplier tube.

Figure 2 displays the fluorescence spectrum of pure alumina nanoparticles in comparison to the spectra of PMMA or PTFE coated alumina nanoparticles. Besides the fluorescence emission bands, the graph shows the exciting wavelength in first (325 nm) and second (650 nm) order. From this figure, it is obvious that PMMA coating enhances fluorescence and - most important – narrows the emission band.

Figure 2 leads to the assumption that the coating is an essential element of the fluorescent particle design. It is obvious that PMMA coating results in a maximum gain of the fluorescence. The effect of PTFE coating is significantly smaller, whereas the fluorescence of pure alumina is

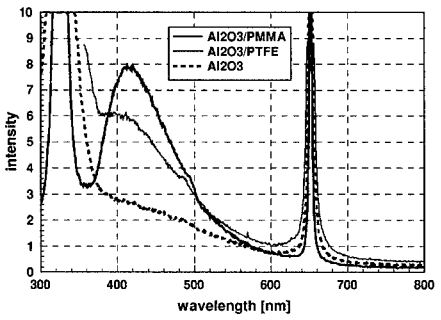


**Figure 2:** Fluorescence spectra of bare and polymer coated alumina nanoparticles

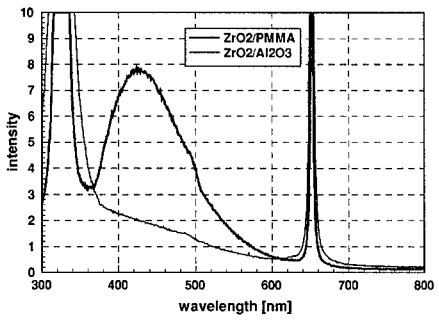


**Figure 3:** Comparison of the fluorescence spectra of alumina and PMMA coated zirconia nanoparticles.

nearly negligible. The figure 3 depicting the fluorescence behavior of zirconia with alumina or PMMA coating supports this assumption. Both figures clearly show the amplification of fluorescence by coating. Obviously, polymer coatings are more effective than coating with $Al_2O_3$. Comparing the spectrum of alumina coated $ZrO_2$ with the one of bare $Al_2O_3$ particles, one may assume that the small fluorescence observed in this case stems from the alumina. In this context, the question arises whether it is possible to stimulate fluorescence with any oxide kernel that is coated with PMMA.

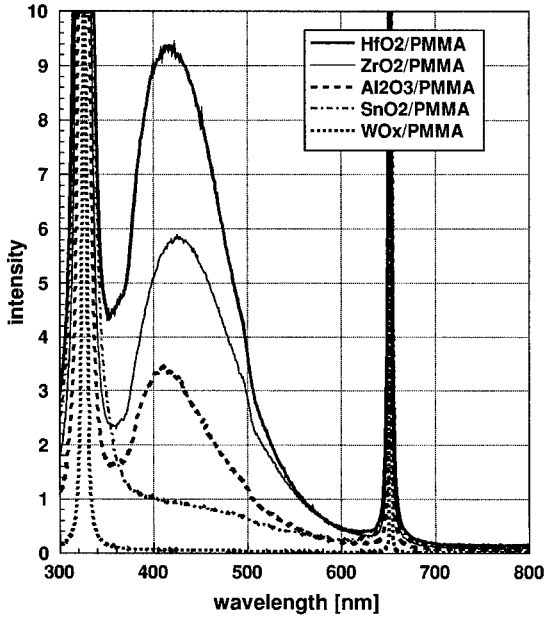


**Figure 4:** Fluorescence spectra of different oxide nanoparticles coated with PMMA.

Figure 4 summarizes of fluorescence spectra of different oxide kernels coated with PMMA. This figure demonstrates that polymer coating obviously enhances fluorescence, provided the kernel itself promotes fluorescence. The graph depicts drastically that the fluorescence intensity varies strongly with the oxide core. In the selected example, $HfO_2$ coated with PMMA has the highest fluorescence intensity, whereas $WO_x$ is not fluorescing at all. This product is amorphous and has a deep blue color. Most probably it is one of the mixed $W^{4+}$ / $W^{6+}$ oxides. On the other hand, it is interesting to note that the intensity maximum of the emission is not significantly dependent on the composition of the kernel. The small shift visible for the different oxide particles may be an artifact due to wavelength dependent self-absorption in the oxide cores. The similarity of the emission bands depicted for different oxide kernels with PMMA coating proposes an interpretation of these lines as Raman scattering or a related phenomenon. To clarify this point, the experiments were repeated with wavelengths of 250 and 350 nm. One of these results, depicted in figure 5, obtained with PMMA coated $ZrO_2$ shows clearly that the position of this emission band is independent of the exciting wavelength.

The fluorescence behavior of ZnO coated with PMMA is different (Figure 6). This nanocomposite exhibits the broad emission band with a maximum around 567 nm and additionally, a relatively sharp line emission with a maximum around 379 nm and 20 nm FWHM. Especially in aqueous suspensions, the intensity ratio of these two emission lines depends strongly on the concentration of the particles in the suspension. This is due to self-absorption phenomena.

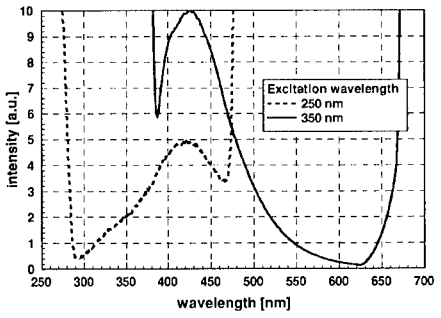


**Figure 5:** Fluorescence spectra of PMMA coated $ZrO_2$ dispersed in water as a function of the excitation wavelength. The intensity of the emission at 250 nm was multiplied by a factor of 20 to make the fluorescence visible for comparison.

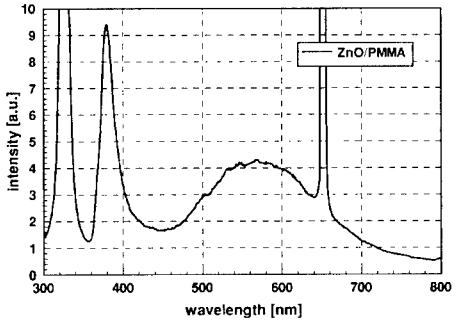


**Figure 6:** Fluorescence spectrum of ZnO/PMMA nanocomposites

## DISCUSSION

Figures 2 and 3 clearly show that the fluorescence phenomena described in this paper are strongly dependent on the coating of the nanoparticles. Despite the different coatings on the oxide kernels, PMMA, or PTFE, in figure 2, the position of the fluorescence maximum is quite similar and in any case stronger than the fluorescence of the pure ceramic kernels. This may lead to the assumption that the fluorescence phenomena described in these figures are ones re-

lated to the interaction between ceramic kernel and polymer coating. This assumption is strongly supported by the results depicted in figure 4. In this figure, one realizes an astonishing similar fluorescence emission for the oxides $HfO_2$, $ZrO_2$, and $Al_2O_3$. This is insofar strange as the electronic structure and the crystallization of these three compounds is very different. As nanoparticle, hafnia crystallizes monoclinic, zirconia cubic and alumina remains amorphous. Looking at the fluorescence spectra obtained with PMMA coated kernels of $SnO_2$ and $WO_x$ one realizes that not every combination of an oxide core with PMMA leads to a light emitting system. This, in combination with the fluorescence results obtained at different wave length, as it is depicted in figure 5 using $ZrO_2$/PMMA as an example, makes clear that the emission peak around 420 nm cannot be attributed to Raman scattering or a related phenomenon. The phenomena lose even more systematic adding the results obtained with ZnO/PMMA composites. In this case, a strong fluorescence peak at 379 nm is observed. This peak may be attributed to the ZnO ceramic core, as it was also found by A. Mitra and R. K. Thareja in pressed and sintered pure ZnO powder with grain size significantly larger than 20 nm. [21] These authors report, for the material in use, the maximum of the emission around 395 nm. This is compatible with the blue shift of the emission of quantum dots, as the material used in this study had a grain size in the range of 5 – 10 nm. On the other hand, L. Guo et al. show that the intensity of this peak depends strongly on the amount of PVP in a ZnO/PVP mixture. It is of special importance that this peak was not found in the case of pure ZnO. [16] The broad peak, in this study observed with a maximum at 567 nm, was observed in other studies too. Depending on the environment, the maximum is at 500 nm [15], 520 nm [16] or 605 nm [22]. The reason for the difference between the composite ZnO/PMMA and the other oxide core/PMMA composites is not clear. IR spectra of the coated particles reveal that the polymer molecules at the surface undergo partial loss of ester groups under formation of carboxylate bonds to the particle surface. [23] Even when the amount of carboxylates formed is different, this may not explain the difference in the spectra between the ZnO/PMMA and the other equivalent nanocomposites.

The experimental results concerning the effect of a ceramic coating is not clear. It can not be excluded that the fluorescence found in composites with alumina coating is just the fluorescence of the alumina.

## CONCLUSIONS

Nanocomposite particles consisting of an oxide ceramic core and a ceramic or polymer coating may exhibit fluorescence. Coated particles of this type can be synthesized using the Karlsruhe Microwave Plasma Process. The experimental results indicate that the fluorescence phenomena observed are directly related to the interface between kernel and coating. The important point is that polymer coatings are promoting fluorescence more strongly than ceramic coatings. The fluorescence observed can not be attributed to Raman scattering related phenomena.

It is important to mention that the oxide/PMMA nanoparticles are neither toxic nor carcinogenic.

## REFERENCES

1. T. Soukka, J. Paukkunen, H. Harma, S. Lonnberg, H. Lindroos, T. Lovgren, Clinical Chemistry 47, 1269 (2001).

2. M. Bruchez Jr., M. Moronne, P. Gin, S. Weiss, A. P. Alivsatos, Science 281, 2013 (1998).
3. D. Gerion et al., J. Phys. Chem. B 105, 8861 (2001).
4. W. C. W. Chan, S. Nie, Science 281, 2016 (1998).
5. S. Schaertl, F. J. Meyer-Almez, E. Lopez-Calle, A. Siemers, J. Kramer, J. of Biomol. Screening 5, 227 (2000).
6. J. R. Taylor, M. M. Fang, S. M. Nie, Anal. Chem. 72, 1979 (2000).
7. I. de Miguel, L. Imbertie, V. Rieumajou, M. Major, R. Kravtzoff, D. Betbederm Pharmaceutical Res. 17, 817 (2000).
8. Y. Tien, T. Newton, N. A. Kotov, D. M. Guldi, J. H. Fendler, J. Phys. Chem. 100, 8927 (1996).
9. H. E. Porteanu, E. Lifshitz, M. Pflughoefft, A. Eychmüller, H. Weller, Phys. Stat. Sol. B 226, 219 (2001).
10. Y. Yang, V. J. Leppert, S. H. Risbud, B. Twamely, P. P. Power, H. W. H. Lee, Appl. Phys. Lett. 74, 2262 (1999).
11. Y. G. Cao, X. L. Chen, J. Y. Li, Y. C. Lan, J. K. Liang, Appl. Phys. A 71, 229 (2000).
12. P. Yang, M. Lu, D. Xu, D. Yuan, G. Zhou, Appl. Phys. A 73, 455 (2001).
13. F. V. Mikulec, M. Kuno, M. Bennati, D. A. Hall, R. G. Griffin, M. G. Bawendi, J. Am. Chem. Soc. 122, 2532 (2000).
14. Y. Chen, Y. Cao, Y. Bai, W. Yang, J. Yang, H. Jin, T. Li, J. Vac. Sci. Technol. B 15, 1442 (1997).
15. S. Monticone, R. Tufeu, A. V. Kanaev, J. Phys. Chem. B 102, 2854 (1998).
16. L. Guo, S. Yang, C. Yang, P. Yu, J. Wang, W. Ge, G. K. L. Wang, Chem. Mater. 12 2268 (2000).
17. Y. Wang, H. Cheng, L. Zhang, Y. Hao, J. Ma, B. Xu, W. Li, J. Mol. Catal. A 151, 205 (2000).
18. D. Vollath, German Patent G9403581.4 (1994).
19. D. Vollath, D. V. Szabó, Nanostr. Mater. 4, 927 (1994).
20. D. Vollath, D. V. Szabó, B. Seith, German Patent DE19638601C1 (1998).
21. A. Mitra, R. K. Thareja, Modern Phys. Letters B, 13, 1075 (1999)
22. H. Cao, J. Y. Xu, S.-H. Chang, S. T. Ho, Phys. Rev. E, 61, 1985 (2000)
23. I. Lamparth, D. V. Szabó, D. Vollath, Macromolecular Symposia, in the print

Mat. Res. Soc. Symp. Proc. Vol. 703 © 2002 Materials Research Society V7.9

# Nanocomposite Electrodes for Advanced Lithium Batteries: The $LiFePO_4$ Cathode

Shoufeng Yang, Yanning Song, Peter Y. Zavalij and M. Stanley Whittingham*
Institute for Materials Research, Binghamton University,
Binghamton, NY 13902-1600, U.S.A.

## ABSTRACT

$LiFePO_4$ was successfully synthesized by high temperature and hydrothermal synthesis. A nanocomposite was formed by carbon coating this material; initial electrochemical results showed that up to 70% capacity could be obtained at 1.0 $mA/cm^2$ current density. In contrast, the hydrothermally prepared $LiFePO_4$ showed a lower capacity even at lower discharge rates due to a partial occupation of lithium sites by iron. This occupation, identified by Rietveld X-ray refinement, decreased both the rate and degree of intercalation and de-intercalation of lithium; chemical reaction with butyl lithium and bromine confirmed the electrochemical behavior. This investigation showed that the cathode could be prepared by high temperature synthesis, followed by a carbon black coating to achieve high capacity at high current density.

## INTRODUCTION

$LiFePO_4$ has been of much interest recently [1-3] due to its low cost, high performance and stability. Its theoretical capacity is 170 mAh/g, 40% more than that of the $Li_xCoO_2$ presently used in commercial batteries, where $\Delta x \approx 0.6$. The discharge voltage is about 3.4 V, high enough for large-scale application, but not high enough to decompose the electrolyte during recharge. However, the low electronic conductivity results in low kinetics and hence small current densities. This can be partially overcome by increasing the temperature, but this might increase electrolyte decomposition. The low kinetics and their improvement at elevated temperature have been discussed previously [4,5]. Ravet et al [6] showed that with a conductive carbon coating, full capacity could be attained at 80°C at C/1 current density.

We demonstrated the possibility of synthesizing $LiFePO_4$ via hydrothermal synthesis in just a few hours [7,8]. When this hydrothermal material was coated with sucrose following the Ravet method [9], good cycling behavior was observed at 60% capacity and a current density of 0.14 $mA/cm^2$. However, a recent study showed that the in the hydrothermal material there is some disorder of the lithium and iron atoms resulting in poor behavior of the as-synthesized material [10].

Nazar's group [11] used a carbon gel technology to optimize $LiFePO_4$ and showed that it could be cycled with 80% capacity at a 2C current density at ambient temperature. We have reproduced their results [10]. Dominko [12] recently showed that with a novel carbon coating by aqueous gelatin solution, $LiMn_2O_4$ and $LiCoO_2$ had better performance, and the polarization was reduced. Here we used the same technology for $LiFePO_4$ and demonstrated that 70% capacity was available at 1.0 $mA/cm^2$ density.

* Contact author, stanwhit@binghamton.edu

## EXPERIMENTAL

$LiFePO_4$ was prepared hydrothermally as previously reported by us [7] (material A), the sample was then coated with carbon [7] (material B). In order to prepare $LiFePO_4$ (material C) by high temperature, $NH_4H_2PO_4$ (Alfa-Aesar) was ground, mixed stoichiometrically with $CH_3COOLi$ (Aldrich) and $FeC_2O_4 \bullet 2H_2O$ (Aldrich), ground for 10 min, then pressed into pellets and heated at 350°C in a tube furnace in flowing helium gas for 4 h. After slowly cooling to room temperature, the gray soft pellets were reground for 10 min, pressed into pellets again, heated slowly to 700°C, and kept there for 10 h. The sample was ground after cooling to room temperature before use.

In order to remove the moisture from material A, it was heated in a tube furnace in flowing helium at 350°C for 4 h. Material C was used as prepared. Both materials were reacted with bromine (Fisher) in acetonitrile solution for up to 5 d. The final compound was washed with acetonitrile several times to remove the impurities, then dried in a vacuum oven overnight at 100°C. The materials were analyzed using XRD on a Scintag diffractometer to identify the phases present.

Carbon Coating: 17 mg and 9 mg gelatin (Type A, Aldrich) were dissolved in 30 ml and 10 ml water respectively and 2 drops of 0.05 M LiOH solution were added to the 30 ml solution resulting in a pH of 8.85. 1.02 g $LiFePO_4$, 82 mg carbon black and 2 ml 0.05 M LiCl were added to this solution with stirring. Then the 10 ml solution was added and the beaker was put on a hot plate with spinning bar until almost all the water was gone. The sample was dried in a vacuum oven at 100°C overnight.

The electrodes were prepared by mixing the $LiFePO_4$ composite formed above with carbon black, and Teflon in the weight ratio 85:10:5 and grinding the slurry with 2 drops of hexane in a mortar. A thin film was made, which was hot pressed into an Exmet grid at a typical loading of 15 mg/cm$^2$. The electrolyte was a 1M solution of $LiPF_6$ in a 1:1 volume ratio of dimethylcarbonate and ethylenecarbonate (EM. Industries). Only the weight of the $LiFePO_4$ was included for calculating the capacity. All of the data were collected on a MacPile system at ambient temperature (25°C).

## DISCUSSION

Rietveld structure refinements were performed on materials A, B and C. The refiments reveals the presence of iron in the lithium sites, for which Fe/Li ratio was refined as shown in Table I. The $FePO_4$ was prepared by the bromine delithiation of material C.

**Table I.** Rietveld refinements for $LiFePO_4$ materials A, B, C and $FePO_4$.

| | $LiFePO_4$ (A) | $LiFePO_4$ (B) | $LiFePO_4$ (C) | $FePO_4$ |
|---|---|---|---|---|
| **a (Å)** | 10.381 | 10.351 | 10.333 | 9.837 |
| **b (Å)** | 6.013 | 6.018 | 6.011 | 5.799 |
| **c (Å)** | 4.716 | 4.713 | 4.696 | 4.790 |
| **Fe on Li site** | 0.08 | 0.05 | 0.0 | 0.0 |
| **$R_I$** | 3.4% | 2.8% | 2.7% | 3.9% |
| **$R_P$** | 10.21% | 8.94% | 8.65% | 9.19% |

DCP-AES for material A showed that the Li, Fe, P atomic ratios are 0.83:1.07:1. This 7% excess iron is consistent with the Rietveld determination of 7-8% iron on the lithium sites.

The X-ray parameters of material C are consistent with the results reported by Thomas [13]. The mechanism for the iron substitution in materials A and B is not known. Because the size of $Fe^{2+}$ (0.78 Å) is larger than $Li^{+}$ (0.60 Å), when lithium is partly substituted by iron, the lattice is larger. The ordering of the Li and Fe in the high temperature synthesized $LiFePO_4$ is essentially perfect with no disorder detected by the Rietveld analysis. For materials A and B, the iron on the lithium sites probably partially blocks the pathway for the diffusion of lithium, even during the oxidation by liquid bromine. Figure 1 shows the XRD for $LiFePO_4$ (A and C) after reaction with bromine.

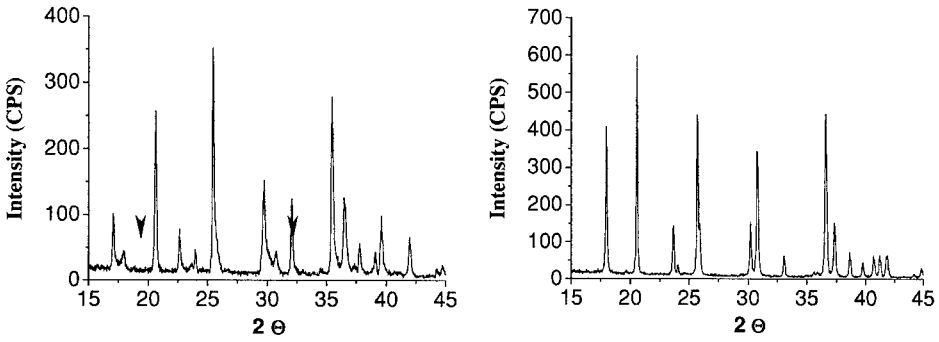


**Figure 1.** XRD of materials A and C after reaction with $Br_2$, arrows show the $FePO_4$ phase in material A.

Material C was converted to $FePO_4$ easily and no $LiFePO_4$ was observed in the XRD, but for material A, even after 5 d, the major phase was still $LiFePO_4$, with a small amount of $FePO_4$. This difference can be explained if the iron atoms block the diffusion of lithium during the oxidation.

The electrochemistry of the hydrothermal $LiFePO_4$ carbon coated using sucrose (material B) is shown in figure 2. Here the capacity was only about 60% of the theoretical value even at low current density. And the profile shifted to the left, probably as more lithium was removed from the sample. During the first recharge, much of the lithium removal occurs at elevated potentials; as this behavior is not observed on subsequent cycles some atomic re-organization may be occurring. The flat recharge/discharge curve after the initial recharge is typical of a two-phase system. The maximum capacity of under 80% is related to the maximum lithium content of around 0.8 per phosphorus, due to the excess iron atoms on the lithium sites.

The electrochemistry of material A is lower than that of material B, even at current density as low as 0.03 $mA/cm^2$, with only 40-45% capacity could be obtained and both the discharge and recharge curves were sloped following the first cycle with large polarization.

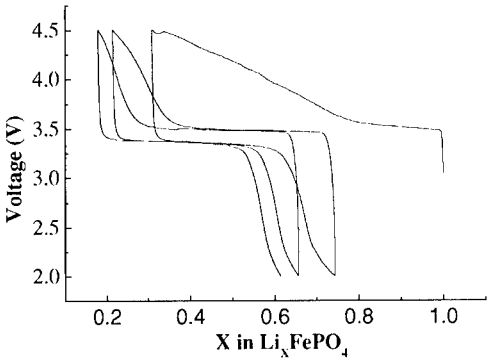


**Figure 2.** The first three cycles of $LiFePO_4$ at current density 0.14 mA/cm$^2$, after [7].

Figure 3 shows the electrochemistry of $LiFePO_4$ with the carbon black coating. At a high current density of 1 mA/cm$^2$, 80% of the lithium is removed on the first charge, and 0.7 Li are subsequently cycled giving a capacity of 120 mAh/g. The high current leads to a large polarization. In contrast to the iron rich material shown in Figure 2, the sloping potential on the first charge is much reduced. This is probably related to the perfect ordering of the Fe and Li ions. The 0.7 Li cycling capacity can be increased by reducing the current density. This is consistent with the data from SONY that showed only a 3% capacity loss for a current density of 0.12 mA/cm$^2$ in a button cell configuration [2].

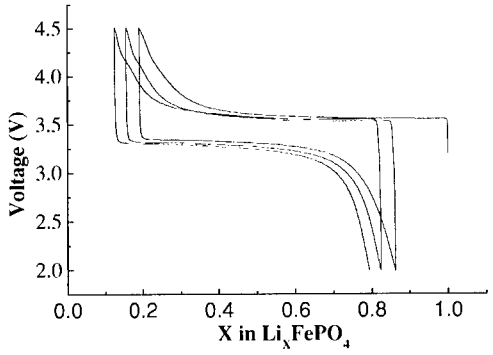


**Figure 3.** The first three cycles of $LiFePO_4$/C at current density 1.0 mA/cm$^2$.

The good performance of this system was achieved with a 15% carbon in the cathode structure. We are currently working on optimizing the carbon content by understanding its nano-structure so that minimum quantities can be used.

## CONCLUSIONS

The very good electrochemical behavior of $LiFePO_4$, which combined with its low cost, makes it an excellent candidate for an intermediate capacity cathode replacement for $LiCoO_2$ until cathodes with capacities over 200 mAh/g are developed. Hydrothermal synthesis leads to iron disorder and excess iron in the structure, which degrades its electrochemical performance relative to high temperature formed materials. This may be partially corrected by a subsequent high temperature heating with carbon. High temperature formed $LiFePO_4$, carbon coated from gelatin, demonstrated more than 70% capacity even at current densities of 1 $mA/cm^2$.

## ACKNOWLEDGMENTS

We thank the US Department of Energy, Office of Transportation Technologies, for support of this work through the BATT program at Lawrence Berkley National Laboratory. We also thank Professor Dick Naslund for DCP-AES. Initial results of this work have been reported in the cognizant DOE reports.

## REFERENCES

1. A. K. Padhi, K. S. Nanjundaswamy, C. Masquelier and J. B. Goodenough, *J. Electrochem. Soc.* **144**, 1609 (1997).
2. A. Yamada, S. C. Chung and K. Hinokuma, *J. Electrochem. Soc.* **148**, A224 (2001).
3. P. P. Prosini, D. Zane and M. Pasquali, *Electrochim. Acta.* **46**, 3517 (2001).
4. A. K. Padhi, K. S. Nanjundaswamy, C. Masquelier and J. B. Goodenough, *J. Electrochem. Soc.* **144**, 1188 (1997).
5. A. S. Andersson, J. O. Thomas, B. Kalska and L. Häggström, *Electrochem. Solid-State Lett.* **3**, 66 (2000).
6. N. Ravet, J. B. Goodenough, S. Besner, M. Simoneau, P. Hovington and M. Armand, *Electrochem. Soc. Abstracts*, **99-2**, 127 (1999).
7. S. Yang, P. Y. Zavalij and M. S. Whittingham, *Electrochem. Commun.* **3**, 505 (2001).
8. M. S. Whittingham, S. Yang, K. Ngala, and P.Y. Zavalij, *Electrochem. Soc. Abstracts*, **2001-2**, 191 (2001).
9. N. Ravet, S. Besner, et al., *European Patent* 1 049 182 A2.
10. S. Yang, Y. Song, P. Y. Zavalij and M. S. Whittingham, *Electrochem. Commun.* in Press.
11. H. Huang, S. C. Yin and L. F. Nazar, *Electrochem. Solid-State Lett.* **4**, A170 (2001).
12. R. Dominko, M. Gaberšček, J. Drofenik, M. Bele and S. Pejovnik, *Electrochem. Solid State Lett.* **4**, A187 (2001).
13. A. S. Andersson, B. Kalska, L. Häggström and J. O. Thomas, *Solid State Ionics.* **130**, 41 (2000).

# Applications and Properties II

Mat. Res. Soc. Symp. Proc. Vol. 703 © 2002 Materials Research Society V8.1

# NANOCOMPOSITE COATINGS – APPLICATIONS AND PROPERTIES

Roger H. Cayton and R. W. Brotzman, Jr.
Nanophase Technologies Corporation
Romeoville, IL 60446, U.S.A.

## ABSTRACT

Nanocomposite coatings were made by incorporating nano-sized and micron-sized alumina into aqueous and non-aqueous polymer systems. At approximately 50wt% nano-sized alumina a synergistic effect was observed in coating hardness with no degradation in optical properties.

## INTRODUCTION

Nano-sized materials produced by gas phase condensation have novel characteristics including chemical reactivity, composition, morphology, and processing advantages. These materials are commercially available and are being engineered for nanocomposite coating applications.

The structure of nanocomposites is important because often multiple physical properties are desired, i.e., electrical conductivity or abrasion resistance with transparency. In effect, the composite structure is selected for the desired physical property – from uniform surface distribution of nanoparticles for abrasion resistance to connected nanoparticle structures for electrical conductivity.

### Nanomaterial production

Nanophase Technologies Corporation (NTC) produces nanocrystalline metal oxide powders by a patented Physical-Vapor Synthesis (PVS) process. The process involves vaporizing a metallic or metal oxide precursor in a plasma, followed by rapid quenching to induce condensation and formation of extremely small metal oxide crystallites. The size of the crystalline particles is controlled by the condensation rate and the particle concentration in the quench zone. The discrete metal oxide nanocrystalline particles form loose aggregates that are collected as a dry powder. The loose aggregates can be dispersed in solution to provide stable suspensions of the individual particles.

The PVS process uses metal or metal oxide precursors and avoids product contamination that may result from solvent or solvated precursor materials. The resulting purity of the metal oxide nanoparticles, in both the bulk phase and on the surface, is maintained at a very high level. The PVS process has been scaled to provide production rates of tons/year. Examples of nanocrystalline oxides currently produced at bulk scale at NTC include alumina, ceria, titania, zinc oxide, iron oxide, antimony/tin oxide, and indium/tin oxide. Numerous other pure oxides and mixed metal oxides can be produced with the PVS process.

Metal oxides prepared by the PVS process are crystalline, equiaxed, nonporous, discrete particles with mean diameters in the 10 – 50 nm range, and have surface areas of 15-90 $m^2/g$.

## Particle surface treatment

In most nanocomposite coating systems, the nanocrystalline metal oxide powders require surface treatment to enable dispersion into the matrix coating materials. NTC has developed proprietary surface treatment processes for metal oxide nanoparticles, each designed to provide one or more of the following properties:

- dispersion into fluids (aqueous, alcohol, and hydrocarbons),
- prevention of particle agglomeration,
- compatibility with polymer matrix materials,
- chemical fuctionalization of the nanopowder surface with reactive groups, and
- passivation of the nanopowder surface chemistry.

As produced, the metal oxide powders disperse well in aqueous systems wherein hydrogen bonding disrupts the loose agglomerates and provides stable dispersions of the primary crystalline particles. The affinity of nanocrystalline powders for aqueous environments is often sufficient to allow the powders to be used in many water-borne coating formulations. However, because the powders do not disperse well in non-aqueous media, specialized surface treatments have been developed to enable compatibility of the particles with the organic fluids and resins to reduce particle agglomerates and yield stable dispersions. These treatments also prevent re-agglomeration and enable the oxides to be used in a wide variety of solvent-borne coatings.

In some instances, the surface treatment process incorporates functional groups onto the oxide particles, allowing for direct interaction with resin polymers. Finally, the nanocrystalline oxide surface is very reactive, and in some coating systems this necessitates a surface treatment process to passivate this reactivity to prevent interference with film curing.

## Abrasion-resistant coatings

Conventional abrasion resistant coatings often feature particles incorporated within the resin to suppress marring, scratching, or abrading of the coating. Alumina is a preferred oxide for this purpose due to its extreme hardness (9 on the Mohs scale) and relatively low cost. The drawback to such alumina-containing films is that, although abrasion resistance is often improved, the transparency of resulting coatings is compromised due to light scattering from the micron-sized alumina particles. However, using nanometer-sized alumina in coatings offers a solution to this problem because these particles are less than 100 nm in diameter and greatly reduce light scattering. Additionally, alumina produced by PVS is spherical which when combined with a small particle size yields a smooth film surface that further enhance coating scratch resistance.

## EXPERIMENTAL DETAILS

The abrasion resistance of nanocomposite coatings was evaluated by incorporating alumina into aqueous and non-aqueous cross-linked resins. Melamine-formaldehyde (M-F) and urethane (PU) were evaluated as aqueous and non-aqueous resins, respectively. Both resins are transparent, very hard and find commercial application as protective coatings on non-flexible surfaces such as furniture and flooring.

**Aqueous composite system**

NTC NanoTek® nanocrystalline alumina (average particle size of 30-40 nm) and conventional alumina were dispersed and surface treated in water to prevent particle agglomeration during the film curing process. The treated alumina particles were blended with the M-F resin (BTL Melamine Resin, BTLM 817) at the desired concentration. Films were drawn down on glass substrates at 1-mil wet thickness and cured by heating at 150°C for 15 minutes. The cured film thickness was about 10 μm.

**Non-aqueous composite system**

NTC NanoTek® nanocrystalline alumina and conventional alumina were dispersed and surface treated in xylene. The treated alumina particles were blended with a commercial polyurethane (Minwax, oil-based high-gloss polyurethane, 45.5 wt% solids) at the desired concentration. Films were drawn down on glass substrates at 1-mil wet thickness and cured by drying at room temperature for 24 hours. The cured film thickness was about 10 μm.

**Measurement of coating properties**

Haze and transmittance of the coatings on glass were measured using ASTM-1003 and ASTM-1044 protocols with a BYK Gardner haze-gard plus. Hardness of the coatings on glass is measured by determining the least weight necessary to cause a scratch for specified pencil leads using ASTM D-3353. Hardness is reported as a ratio of a coating's value with respect to an unfilled coating at equal pencil hardness.

## DISCUSION

**M-F nanocomposite coating**

The effect of NTC NanoTek® nanocrystalline alumina and conventional alumina loading on transmitted haze in M-F coatings is shown in Figure 1. The incorporation of NTC NanoTek® alumina improves the scratch resistance of M-F coatings, while only slightly increasing haze. For example, inclusion of 20 wt% NTC alumina in an M-F film yielded up to 3.5 times the scratch resistance of neat M-F resin, and only increased the haze from 0.23% to 0.77%. By comparison, a larger alumina (A-16, Alcoa, average particle size of 500 nm) provides even greater scratch resistance (up to 8x that of neat MF resin at 20 wt% alumina), but at the expense of higher haze (18.9%).

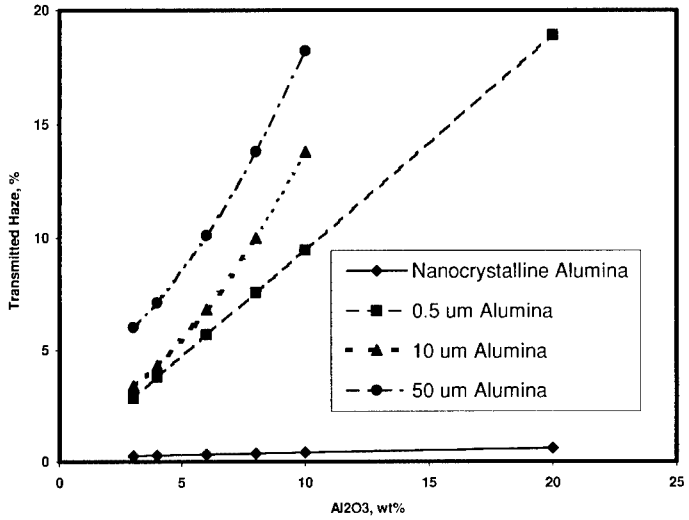


**Figure 1.** Effect of Alumina on Transmitted Haze in Melamine-Formaldehyde Coatings.

However the combination of NTC alumina and A-16 alumina in M-F coatings provided the most interesting results. Haze of alumina composite blends showed linear additive behavior, indicating that each alumina component acts independently with respect to its haze contribution. But a synergistic effect was observed with respect to the hardness of M-F nanocomposite coatings containing blends of NTC and A-16 aluminas. This synergistic effect was evaluated over the experimental range: total alumina – 0 to 20 wt%, NTC alumina with respect to total alumina – 0 to 100 wt%, and surface treatment – 0 to 10 wt% with respect to alumina.

Haze results as a function of total alumina wt% and % nano-sized alumina (indicated as % small), are presented in a 2D plot in Figure 2. Haze displays linear additive behavior. Coating hardness is presented in a 2D plot as a function of total alumina wt% and % nano-sized alumina for H pencil hardness levels in Figure 3.

## PU nanocomposite coatings

A synergistic effect was observed between nano-sized NTC NanoTek[5] alumina and micron-sized alumina on the mechanical properties of a water-soluble M-F system. Is this synergistic effect observed in organic systems as well?

PU coatings were evaluated over the experimental range: total alumina; 0 to 5 wt%, NTC alumina with respect to total alumina; 0 to 100 wt%, and surface treatment; 0 to 10 wt% with respect to alumina. Haze displays linear additive behavior and the synergistic effect observed in the M-F resin system is also observed in the PU system (see Figure 4).

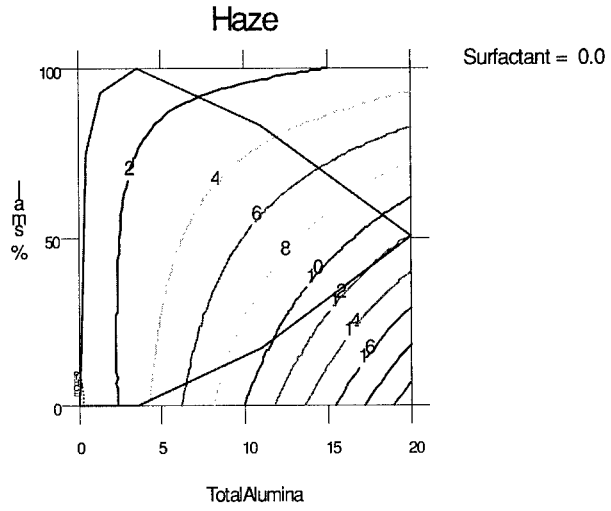


**Figure 2.** Haze as a function of total alumina and wt% nano-sized alumina in M-F coatings.

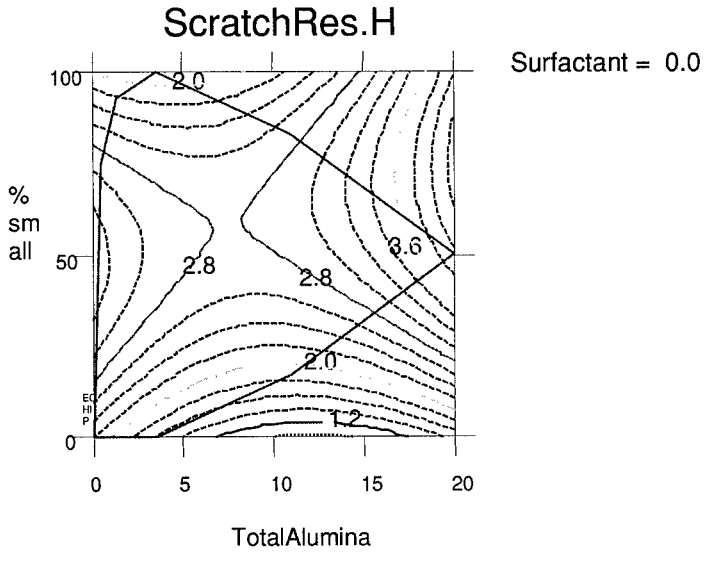


**Figure 3.** Hardness as a function of total alumina and wt% nano-sized alumina for H pencil hardness level in M-F coatings.

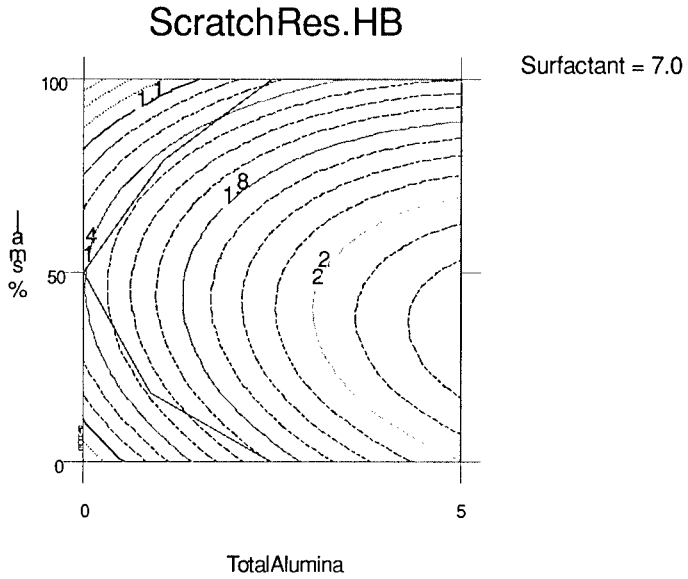


**Figure 4.** Hardness as a function of total alumina and wt% nano-sized alumina for HB pencil hardness level in polyurethane (PU) coatings.

## CONCLUSIONS

The combination of high crystallinity and extremely small particle size of NTC alumina produced by the PVS process positions this material to be uniquely suited to coating applications where high transparency and high abrasion resistance is required.

- Coatings containing both nano-sized and micron-sized fillers display a maximum in hardness with respect to the percent nano-sized filler (synergistic behavior).
- The location of the maximum is approximately 50wt% nano-sized filler.
- Approximately 2x to 3x the hardness is imparted to the coating with respect to the unfilled coating at the maximum for 5wt% total alumina in the systems studied.
- Nanostructured coatings provide significant economic advantage.
  - The physical properties of coatings may be significantly increased with no detrimental effects on optical quality.
  - Less expensive micron-sized fillers may be combined with nano-sized fillers to achieve superior mechanical and optical properties.

Nanocrystalline alumina, available in comercial quantities from Nanophase Technologies, has been formulated into several commercial abrasion-resistant coating products with numerous other potential applications currently under development.

Mat. Res. Soc. Symp. Proc. Vol. 703 © 2002 Materials Research Society V8.3

# Vanadium Oxide Nanotubes: Characterization and Electrochemical Behavior

Samuel T. Lutta, Arthur Dobley, Katana Ngala, Shoufeng Yang, Peter Y. Zavalij, and M. Stanley Whittingham*

Chemistry Department and the Institute for Materials Research,
State University of NewYork at Binghamton,
Binghamton, NewYork 13902-6016, U.S.A.

## ABSTRACT

Vanadium oxide nanotubes (VONT) were formed from vanadium (V) oxide and the dodecylamine templating agent by a sol-gel reaction and subsequent hydrothermal treatment. The nanotubes were characterized by transmission electron microscopy (TEM), electron diffraction, thermogravimetric analysis (TGA), infrared spectroscopy and powder X-ray diffraction (XRD). The nanotubes consist of $VO_{2.4}$ $[C_{12}H_{28}N]_{0.27}$ and range in diameter from 100 nm to150 nm. The study further reveals that the compound maintained the tubular morphology when heated at 430° C in an inert atmosphere. However, the tubular morphology is destroyed when the compound is heated at about 130° C in oxygen.

Organic free manganese intercalated vanadium oxide nanotubes (MnVONT) were synthesized by an ion exchange reaction. The previously mentioned techniques were used to characterize MnVONT. $Mn_{0.86}V_7O_{16+\delta}\cdot nH_2O$ layers have 2D tetragonal cell with a=6.157(3) Å, while interlayer spacing is 10.52 (3) Å. VONT, heated VONT and $Mn_{0.86}V_7O_{16+\delta}\cdot nH_2O$ are redox – active and can insert lithium reversibly. This study reveals that the electrochemical performance of VONT is enhanced by removing the organic template by heating in an inert atmosphere or exchanging with $Mn^{2+}$ ions.

## INTRODUCTION

In the course of the present efforts towards miniaturization of electronic and mechanical devices, structures with a size in the nanometer region have stimulated intensive research activities as evidenced in increase in volume of publications in recent past. Among such nanostructures are materials with tubular morphology.

Recently transition metal compounds, mainly oxides with two dimensional and three dimensional open structures, have been studied and developed for use as cathode materials in rechargeable secondary lithium battery in our research laboratory [1-3]. Our interest has focused on materials with one-dimensional structures for which the nanotubes are very promising candidates. The tubes attract much scientific interest for electrochemical insertion mainly for two reasons. One, they offer four different contact regions, namely, the inner and outer wall surfaces as well as the tube ends. Secondly, they can provide electrolyte-filled channels for faster transport of the ions to the insertion sites [4]. This study for the first time shows how the electrochemical behavior of the nanotubes can be improved by removing the organic templates by heating under inert atmosphere.

* Contact author; stanwhit@binghamton.edu

## EXPERIMENTAL DETAILS

The vanadium oxide nanotubes were prepared according to literature method with modifications where necessary [5]. Vanadium (V) oxide and dodecylamine were mixed in the molar ratio 1:1 in ethanol and the mixture stirred for 3 hours in air. The mixture was then hydrolyzed under vigorous stirring followed by aging, which led to the formation of a yellow suspension. Subsequent hydrothermal treatment for 7 days resulted into a black powder. The product was washed with ethanol, diethylether and water to remove excess dodecylamine and any decomposed products. It was then dried under a vacuum at 80° C for 12 hours.

Substitution of the organic template for $Mn^{2+}$ ions was done by stirring a mixture of VONT and $MnCl_2$ (molar ratio 1:4) for 2 hours in ethanol/water mixture 4:1 (v/v) (200ml/g of VONT). The resulting mixture was centrifuged and washed with water, ethanol and diethyl ether. The product was then dried in the vacuum at 80° C for 12 hours.

The morphology and the structure of the nanotubes were investigated by using XRD and TEM. Thermal stability of the nanotubes was investigated using TGA in oxygen and nitrogen. In an oxygen atmosphere structure collapse at about 130° C. By heating the compound in helium at 430° C for 1 hour the organic portion in the VONT was removed but the tubular morphology was maintained.

The performance of these compounds as positive electrode was tested by galvanostastic cycling in the potential range 1.4-3.9 V vs $Li/Li^+$. In all cases the sample was prepared by mixing the nanotubes with equal weight of Teflonized carbon black (25 wt.% polytetrafluoroethylene and 75 wt.% acetylene black). The cathode material was then hot pressed onto a stainless steel Exment ™ grid at 110° C to dehydrate the sample. Metallic lithium served as counter and reference electrodes.

## DISCUSSION

The product was obtained as black powder suggesting that the vanadium be in mixed oxidation state +4 and +5 because mixed-valent vanadium oxides are generally black e.g. $V_6O_{13}$. In fact, the compound reduces standard cerium (IV) sulphate. Quantitative analysis indicates that about 46% of the vanadium ions are in oxidation state +4. In the exchange reaction, all of the organic was replaced with metal cations as explained in later sections of this paper. Attempts to replace the organic with lithium ions and other organic molecules are being made.

### Thermogravimetric analysis

This study showed the presence of the dodecylamine template in VONT is about 33% by weight. Thermoanalysis of $Mn_{0.86}V_7O_{16+\delta}.nH_2O$ shows that it is possible to replace the entire templating organic agent with $Mn^{2+}$ cations.

### Fourier transformed infrared spectroscopy

FTIR confirmed the presence of the organic template in VONT from C-H vibrations at 2900 $cm^{-1}$and 1460 $cm^{-1}$, which are absent in heated VONT and MnVONT. The V-O bonds were assigned to vibrations at 635 $cm^{-1}$, 903 $cm^{-1}$ and 948 $cm^{-1}$ [6] were assigned to V-O bonds.

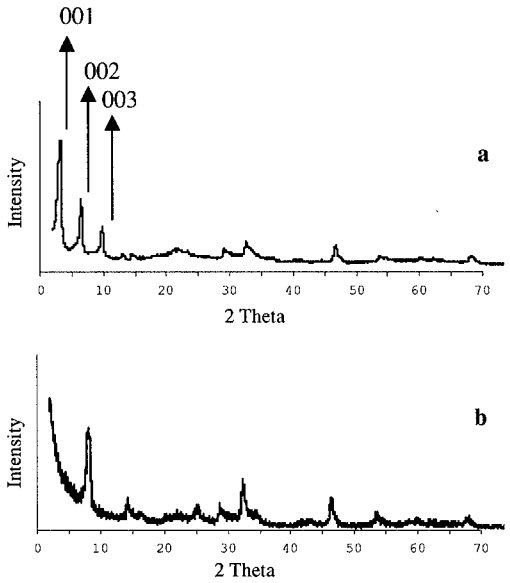


**Figure 1**. XRD patterns of a) VONT and b) MnVONT showing substantial decrease in interlayer spacing (*001* reflections shift towards higher angles) while *hk0* are at the same positions in both patterns (after [7].

X-ray diffraction

X-ray diffraction pattern of the vanadium oxide nanotubes (VONT) with dodecylamine displays three strong peaks at 20.720 Å (001), 12.59 Å (002) and 10.23 Å (003). Replacing the organic template with the cations results in drastic reduction of the d-spacing to 9.3 Å [7]. Further evidence for this was shifting of 00l reflections due to interlayer Vanadium oxide sheets to large scattering angle as shown in Figure 1. The hk0 reflections due to the vanadium oxide sheets remain at the same positions showing that the structure of the layers remains the same [8].

Transmission electron microscopy

TEM shows that VONT consists of tubes with outer diameter ranging from 100 nm –130 nm, while their length vary from 500 nm to a maximum of 1500 nm. Closer look at the image shows reveals scroll-like tubes with open ends (Figure 2). Layers or the strides on the walls confirm that vanadium and the organic template molecules distribution occur in distinctly alternating regions in the wall regimes. In contrast, some walls of the $Mn^{2+}$ ions exchanged nanotubes had no distinct alternating regions confirming the incorporations of the metal ions in the layers (Figure 3). Since Vanadium and manganese ions have similar scattering factors, it is difficult to distinguish their sites.

TEM also confirmed that it is possible to remove the organic by heating VONT in helium at 430° C but preserve the tubular morphology. TEM image shows the sites previously occupied by the organic molecules in VONT are empty after heating.

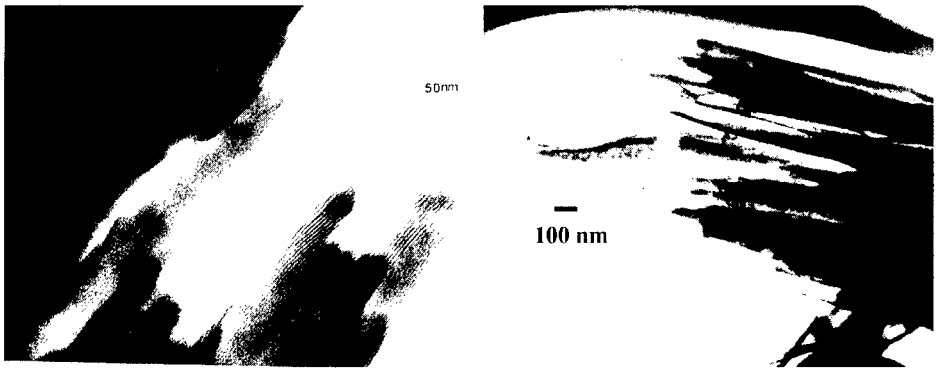


**Figure 2.** Typical TEM images of VONT (left) showing open ends and MnVONT (right) (product of $MnCl_2$ treatment). The layered structure inside the VONT walls appears as alternating narrow dark lines and broad bright lines.

X-ray diffraction however shows that the structure of the compound changes after heating. In oxygen, the tubular morphology is destroyed when the material is heated at about 130°C.

Electrochemistry

The cell performance of compounds as it was shown closely depends on the electrolyte salt used. Cells were made in $LiClO_4$ and $LiPF_6$ as the electrolyte salt; the solvent used was propylene carbonate (PC). The electrochemistry of MnVONT was investigated in $LiAsF_6$ (Figure 3). The compound intercalates 0.5 mole $Li^+$ ions per one mole of vanadium. Capacity of heated VONT was over 100 mAh/g for at least 40 cycles in the two salts. However, the capacity of VONT drops after the second cycle but remains constant at 46 mAh/g after the eighth cycle (Figure 4). Effect of electrolyte salt on the performance of these compounds has been reported elsewhere [9]. Maximum specific charge in mAh/g for each material is given in the table below.

| Material | in $LiClO_4$ | in $LiPF_6$ |
|---|---|---|
| VONT- $VO_{2.4}[C_{12}H_{28}N]_{0.27}$ | 60 | 180 |
| heated-VONT | 120 | 220 |
| $Mn_{0.86}V_7O_{16+\delta}.nH_2O$ | 140 | 240 |

It appears that heating VONT and replacing part of the organic molecules with metal ions enhance its electrochemical performance as cathode material for lithium battery. We propose that removal of the organic allows for insertion of more lithium ions hence improving its electrochemical behavior.

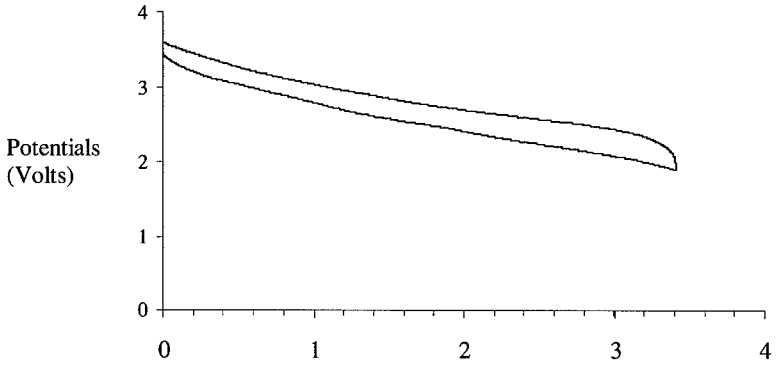


**Figure 3.** First electrochemical cycle of MnVONT in $LiAsF_6$ salt. About 3.4 moles of $Li^+$ ions were reversibly intercalated into the compound, after [7].

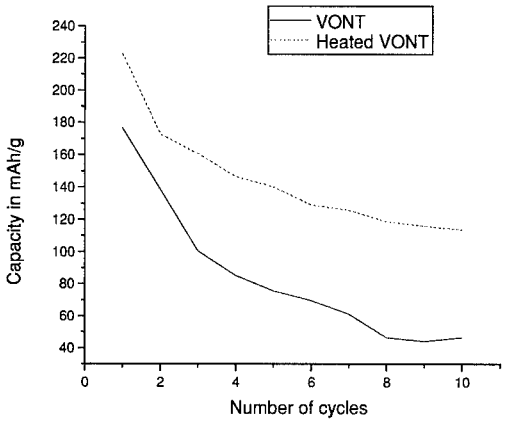


**Figure 4.** Capacity of VONT and heated VONT for the first 10 cycles with $LiPF_6$ as salt in propylene carbonate. The electrode material contained 50 wt% teflonized carbon.

## CONCLUSIONS

For the first time it was shown that the tubular morphology of vanadium oxide can be preserved if the organic template is removed by heating the material in an inert atmosphere. The present study shows that the performance of the nanotubes as cathode materials can be enhanced by removing the organic template by heating or by substituting it with $Mn^{2+}$ ions.

## ACKNOWLEDGEMENTS

The authors would like to thank National Science Foundation for support of this work through grant DMR-9810198. We also thank Henry Eichelberger for help with the TEM experiments.

References:
1. T.A. Chirayil, P.Y. Zavalij, and M. S. Whittingham, *Chem. Mater.* **10**, 2629 (1998).
2. R. Chen, and M.S. Whittingham, *J. Electrochem. Soc.* **144**, L64 (1997).
3. F. Zhang, P.Y. Zavalij, and M.S. Whittingham, *J. Mater. Chem.* **9**, 3137 (1999).
4. M.E. Spahr, P. Stoschitzki-Bitterli, R. Nesper, O. Haas, and P. Novak, *J. Electrochem. Soc.* **146** , 2780 (1999).
5. J.M. Reinoso, H.J. Muhr, F. Krumeich, F. Bieri, and R. Nesper, *Helvetica Chimica Acta.* **83**, 1724 (2000).
6. R.T. Conley, *Infrared Spectroscopy*; Allyn and Bacon Inc., Boston, 1996.
7. A. Dobley, K. Ngala, S. Yang, P.Y. Zavalij, and M.S. Whittingham, *Chem. Mater.***13,** 4382 (2001).
8. F. Krumeich, H.J. Muhr, M. Niderberger, F. Bieri, B. Schnyder, and R. Nesper, *J. Am. Chem. Soc.* **121**, 8324 (1999).
9. K. Edström, T. Gustafsson and S. Nordlinder, *Electrochemical and Solid State Letters*, **4**, A129 (2001).

# Nanophase and Nanocomposite Materials III

Mat. Res. Soc. Symp. Proc. Vol. 703 © 2002 Materials Research Society V9.4

# Controlling the Microstructure and Magnetic Properties of Ferromagnetic Nanocrystals Produced by Ion Implantation.

K.S. Beaty,[1] A. Meldrum,[1] J.P. Franck,[1] K. Sorge,[2] J. R. Thompson,[2] C.W. White,[3] R.A. Zuhr,[3] L.A. Boatner,[3] S. Honda[3]
[1] The University of Alberta, Edmonton, AB
[2] The University of Tennessee, Knoxville, TN
[3] Oak Ridge National Laboratory, Oak Ridge, TN

## ABSTRACT

Ion implantation coupled with annealing is a versatile and flexible approach to creating ferromagnetic near-surface nanocomposites that represent a wide range of particle/host combinations. We have used ion implantation and thermal processing to create a layer of Co nanoparticles in a sapphire host that was subsequently irradiated with Xe, Pt, or Pb in order to systematically modify the magnetic properties of the composite. Transmission electron microscopy (reported in an accompanying paper in this volume) was used to carry out a detailed characterization of the microstructure of the resulting near-surface composites whose magnetic properties were determined using SQUID magnetometry or magnetic circular dichroism. These composites exhibit magnetic hysteresis with coercivities ranging from near zero (i.e., superparamagnetism) up to 1.2 kG – depending on the composition and microstructure. We also present the results of preliminary experiments in which we attempt to control the spatial distribution of magnetic elements within ion-implanted ferromagnetic nanocomposites. The results demonstrate methods for tailoring the magnetic properties of nanocomposites produced by ion implantation for specific applications.

## INTRODUCTION

Ion implantation was first used to create embedded magnetic nanoclusters over a decade ago [e.g., see Ref. 1]. By injecting varying concentrations of Fe, Co, or Ni into dielectric hosts such as crystalline $Al_2O_3$ and fused $SiO_2$, relatively soft magnetic composites were created with low coercivities and a magnetic moment per atom similar to that of bulk magnetic material. Room-temperature superparamagnetism is often reported, due to particle sizes well below that needed to prevent random thermal reorientation of the particle magnetization. Blocking temperatures have been calculated from the precipitate sizes and anisotropy constants, and seem to agree reasonably well with experimentally observed blocking temperatures obtained from field-cooled and zero-field-cooled measurements of the magnetization. Nevertheless, a range of particle sizes is often reported, and the thermal blocking temperature is accordingly distributed over a range of temperatures. Furthermore, the effects of the dielectric host material on the magnetic properties of the composite are only rarely investigated or reported.

In previous ion implantation work, single-element nanoparticles (and in some cases, oxide particles) of Fe, Ni, or Co have been produced in either $SiO_2$ glass or crystalline sapphire wafers [1]. More recently, additional motivation for research in this area has been provided by the potential for creating new materials with possible applications as magnetic recording media. Single-nanocrystal-per-bit data recording would represent an important advance in the information storage capacity of such media [2]. Nevertheless, several quite stringent

requirements must be met in order to achieve device-quality performance. For single-particle bits to be written individually, the precipitates must be discrete, magnetically isolated, ferromagnetic nanoparticles that are larger than the superparamagnetic limit and whose coercivity, size, orientation, and position can be controlled. Ferromagnetic nanoclusters produced by ion implantation can be formed as single domain particles that are larger than the superparamagnetic limit. The crystallographic orientation (and therefore, the magnetic anisotropy directions) can also be controlled by using single-crystal hosts [3,4 ]. However, the question of magnetic isolation is still problematic [5], size distributions are relatively wide, and there has been no effective in-plane control over the spatial distribution of the magnetic nanoclusters.

Here, we describe recent progress in exercising additional control over the magnetic properties of ferromagnetic nanocluster composites, and we discuss our initial attempts to control the in-plane spatial distribution of the magnetic nanoclusters. The present investigations focus on the magnetic characteristics of Co nanoclusters formed by ion implantation and annealing of a single-crystal sapphire wafer, and we explore the magnetic properties of $Al_2O_3$-Co nanocomposites irradiated with either Xe, Pt, or Pb ions. Ion irradiation of pre-existing nanoclusters dramatically modifies the magnetic characteristics [3] and establishes a means for tailoring the materials properties. Finally, we report on the initial results of micron- and sub-micron-scale ion-beam patterning using ion implantation.

## EXPERIMENTAL

In the ion implantation technique, high-energy ions are injected into a selected host material, producing a supersaturation of implanted material in the near-surface region. During a subsequent thermal processing step, the implanted material nucleates as discrete nanoscale precipitates embedded below the surface of the host. In our experiments, high-purity single-crystal sapphire wafers were implanted at room temperature with 140 keV $Co^+$ to an ion fluence of $8 \times 10^{16}$ ions/cm$^2$. In order to induce precipitate formation, the specimens were subsequently annealed in a quartz tube furnace for 2 hours at 1100 °C under Ar+4% $H_2$ atmosphere. The specimens were retracted out of the hot-zone in order to cool rapidly to room temperature. X-ray and electron diffraction measurements were used to determine the structure and orientation of the resulting precipitates. In order to investigate the effects of ion irradiation on the Co nanoparticles, the specimens were subsequently irradiated with either 244 keV Xe or 320 keV Pt ions. These ions were chosen to create maximum displacement damage in the Co-nanoparticle layer, while either minimizing (Xe) or intentionally inducing (Pt) chemical effects due to the implanted impurities. Ion energies were selected to give a similar projected range for both species. Magnetic measurements were done using a SQUID magnetometer or by magnetic circular diochroism.

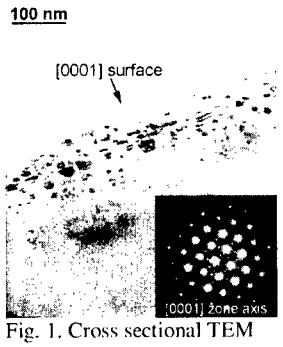

Fig. 1. Cross sectional TEM image if the Co nanocrystals in $Al_2O_3$. An electron diffraction pattern is shown in the inset.

## RESULTS AND DISCUSSION

### Control over the magnetic properties

Figure 1 shows a cross-sectional image of a sapphire wafer implanted with $8 \times 10^{16}$ ions/cm$^2$ $Co^+$ at room

temperature and subsequently annealed for two hours at 1100°C followed by a rapid cool-down. The resulting nanocrystals extend to a depth of ~120 nm in the host sapphire. The nanoparticles are either rounded or faceted, depending on their depth below the surface. This depth dependence of the precipitate morphology is discussed in more detail in a TEM investigation in an accompanying paper in this volume [6]. The precipitates are crystallographically aligned with the sapphire, as demonstrated by the double-diffraction spots in the electron diffraction pattern in Fig. 1. X-ray diffraction results (not shown here) showed that both the hexagonal and cubic phases of cobalt are present in roughly equal amounts.

Magnetic hysteresis measurements for this specimen are shown in Figure 2. These data, obtained by SQUID magnetometry, were corrected to eliminate the effect of the diamagnetic sapphire host. The coercivity of the Co nanoparticles for an applied field perpendicular to the specimen surface is approximately 150 G and the saturation moment is ~2.3 x $10^4$ G/cm$^3$. These values are slightly lower when the field is applied parallel to the specimen surface. After implantation with 320 keV $Pt^+$ to a fluence of 6.4 x $10^{15}$ ions/cm$^2$, the field-perpendicular hysteresis loop broadened considerably (Fig. 3). The saturation magnetization decreased to ~2.0 x $10^4$ G/cm$^3$, but the coercivity increased from 150 G to 1.14 kG. A TEM investigation of this specimen [6], shows that Pt irradiation amorphizes the host sapphire, but that the Co precipitates remain crystalline and do not lose their original crystallographic alignment.

In Figure 4, we compare the effects of 244 keV Xe and 320 keV Pt irradiation on the field-perpendicular coercivity of the Co nanoclusters for varying ion doses. For the Xe irradiation, the coercivity of the Co-sapphire nanocomposite increases rapidly at first, but then levels off at ~500 G. For the Pt-irradiated sample, the coercivity saturates at ~1.2 kG.

There are several possible reasons for the magnetic hardening observed with increasing radiation dose. First, defects and defect clusters may pin the magnetization of the particles, as has been observed in magnetic thin film materials [e.g., Ref. 7]. This pinning effect could inhibit the reorientation of the magnetization, thereby increasing the coercive field. Radiation-damage investigations show damage saturation at some level that

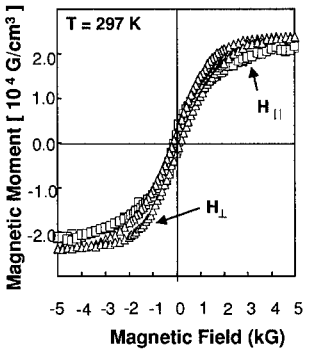


Fig. 2. Magnetic hysteresis measurements for magnetic field parallel or perpendicular to the plane of Co precipitates.

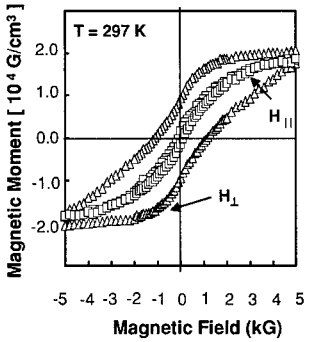


Fig. 3. Same as Fig. 2, after a subsequent implantation Pt to a fluence of 6.4 x $10^{15}$ ions/cm$^2$.

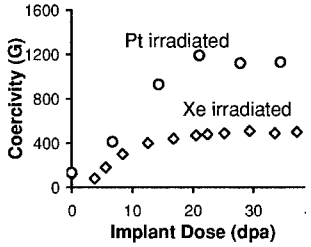


Fig. 4. MCD measurements of the coercive field as a function of dose for the $Al_2O_3$-Co specimen implanted with Xe or Pt.

depends on the kinetics of defect production and recombination [e.g., Ref. 8]. This saturation may be reflected in the "leveling off" of the coercive field at high ion doses. An additional factor may be due to the amorphization of the host sapphire. Sapphire undergoes a volume expansion during the crystalline-amorphous transition, which may place the precipitates under a directional stress. We have found that specimens irradiated at 100 °C to high doses with Pb, as opposed to the RT implants done here, show little increase in the coercivity and the $Al_2O_3$ is not amorphized. The atomic-scale processes responsible for the large increase in the coercivity of the Pt-irradiate specimens, as compared to the Xe-irradiated case, is still under investigation. If the injected Pt reacts with the Co, atomic-scale domains of a CoPt alloy - a magnetic material with high coercivity - may exist within the nanocrystals.

These results suggest means by which the magnetic properties of ferromagnetic nanocomposites produced by ion implantation can be precisely controlled, and hard magnetic materials with high coercivities can be readily obtained. It is possible to create a Co-nanocluster composite whose magnetic coercivity, for example, can be tailored between 150 and 1,120 G. We also have found that even higher coercivities can be obtained by annealing to form CoPt alloy particles.

Fine spatial control of the magnetic properties

One of the outstanding drawbacks of the ion implantation technique is the lack of adequate spatial control over the nanoparticle location. Focused ion beams have some promise for patterning with "manufacturer-claimed" beam diameters of < 10 nm at the specimen surface. Focused ion beam devices currently available, however, have been developed mainly as cutting or thinning tools and are very limited in both source type (mainly Ga) and energy range (< 35 kV). At this low energy, sputtering processes dominate [1]. An alternate method that is currently being explored is the patterning of implanted materials through lithographic masking. This is a method that has been extensively used in the microelectronics industry for spatial selection of regions to be doped using ion implantation [9], and it has recently been applied to the patterning of the magnetic properties of Co/Pt magnetic multilayers through ion irradiation [10].

For these initial investigations, fused $SiO_2$ was selected as the host and Fe as the implant material. Fe was selected because the microstructural properties of implanted Fe have been well studied [e.g., 4,11,12]. Additionally, our work on Co precipitates shows that the nanoparticles have different crystal structures, complicating the interpretation of the magnetic results. The first step in the masking/implanting procedure is to create a patterned mask on top of the host material ($SiO_2$). The masking material must have a high stopping power, adhere well to the substrate, be easily removed from the substrate after implantation, and have low sputtering yield. It must also withstand high-dose ion implantation without significant physical degradation. Based on these requirements, we grew sputter-deposited films of Cr and Mo directly on the $SiO_2$ wafers (Fig. 5). In general, the Cr films oxidized quickly and gave less consistent lithographic patterns. Standard deep UV lithography was used to transfer the pattern from a specially designed mask with features ranging from 10.0 to 0.5 microns, followed by wet chemical etching and removal of photoresist.

The masked substrates were then implanted with 80 keV $Fe^+$ to fluences of either $1.5 \times 10^{17}$ ions/cm$^2$ or $5 \times 10^{16}$ ions/cm$^2$. Scanning electron microscopy (SEM) images of a representative mask before and after implantation are shown in Figs. 6 and 7. The implantation

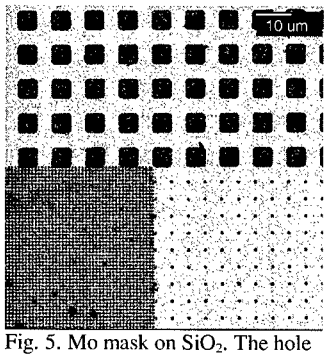


Fig. 5. Mo mask on $SiO_2$. The hole sizes range from almost 10 um to less than 1 um across.

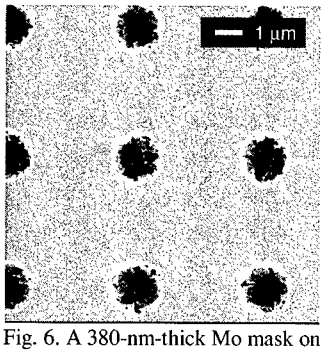


Fig. 6. A 380-nm-thick Mo mask on $SiO_2$. The hole-bottoms contain residual material.

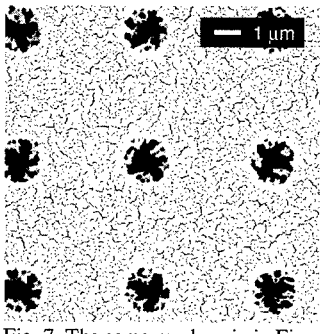


Fig. 7. The same mask as in in Fig. 6, after implantation with 5 x $10^{16}$ ions/$cm^2$ $Fe^+$ at 80 keV. Compared to Fig. 6, the hole bottoms are cleaner.

process had little obvious impact on the mask. In fact, mask sputtering tends to clean the bottoms of holes in the mask that were incompletely etched before implantation. The overall structure of the mask, however, remains intact. This ion-cleaning cleaning effect is illustrated in Figure 7, where there is relatively little residual material in the mask holes.

Optical microscopy of the Fe implanted samples was done after chemical removal of the mask (Fig. 7). The features transferred quite well and are readily apparent under standard viewing conditions. Current experiments using oil immersion optical microscopy show that even the 0.5-micron structures are well preserved in the implanted $SiO_2$ wafer. We are currently investigating the optimal thermal processing parameters to produce "digital block arrays" of Fe nanocrystals. Magnetic and magneto-optic investigations of the patterned specimens are ongoing.

These initial results show that the combination of ion implantation and lithographic masking has promise for extending experimental control into the sub-micron spatial domain. Patterning at smaller scales, however, will present special challenges. Other forms of lithography will be needed to create features smaller than 0.5 microns in diameter, and anisotropic etching techniques will have to be employed to improve the aspect ratio of the mask hole walls. Also, the mask thickness will have to be reduced. Ion-beam scattering effects (both within the mask and within the host material) may become a technical problem at the smallest feature sizes. Nevertheless, these initial results are encouraging, and if the associated materials-related challenges can be met, it may be possible to create patterned arrays of single embedded nanoparticles with controlled size and shape.

## CONCLUSIONS

Two main goals of our work on ferromagnetic nanocluster composites are to obtain fine-scale control over the magnetic properties, and to achieve sub-micron spatial control over the location of these properties. Progress toward achieving these goals has been made in the work presented here, although considerable materials-characterization and theoretical work on the magnetic properties remains to be done. Extensive future and

ongoing work will be required to fine-tune both the spatial and magnetic control aspects of the research in order to obtain implantation-produced nanocomposites that can meet the requirements of specific device-related applications.

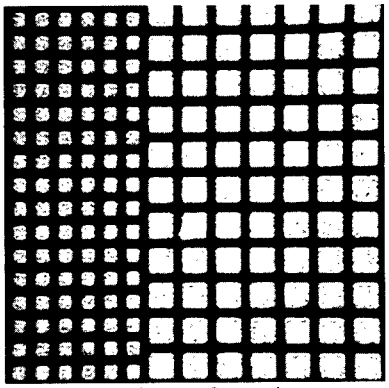

Fig. 8. Optical image of a specimen implanted with 1.5 x $10^{17}$ ions/cm$^2$ of Fe. The mask has been removed and the bright regions correspond to the implanted area. The edge length of the large squares is 12 um.

ACKNOWLEDGEMENTS

The authors wish to thank D. Mullen and G. Braybrook for technical support. This research was supported by NSERC. Oak Ridge National Laboratory is managed by UT-Battelle, LLC, for the U.S. Department of Energy under Contract No. DE-AC05-00OR22725

REFERENCES

1. C. W. White, C. J. McHargue, P. S. Sklad, L. A. Boatner, and G. C. Farlow, Materials Science Reports **4**, 41-146 (1989). For a recent review see: A. Meldrum, R.F. Haglund, L.A. Boatner, and C.W. White, Adv. Mater. **13**, 1431 (2001).
2. D.N. Lambeth, E.M.T. Velu, G.H. Bellesis, L.L. Lee, and D.E. Laughlin, J. Appl. Phys. **79** (1996) 4496.
3 S. Honda, F. A. Modine, T.E. Haynes, A. Meldrum, J.D. Budai, K. J. Song, J.R. Thompson, and L.A. Boatner, Mat. Res. Symp. Proc. **581**, 71-76 (2000).
4 S. Honda, F.A. Modine, A. Meldrum, J.D. Budai, T.E. Haynes, L.A. Boatner, and L.A. Gea, Mat. Res. Symp. Proc **540**, 225-230 (1999).
5. T.C. Schulthess, M. Benakli, P.B. Visscher, K.D. Sorge, J.R. Thompson, F.A. Modine, T.E. Haynes, L.A. Boatner, G.M. Stocks, W.H. Butler, J. Appl. Phys. **89**, 7594 (2001).
6. A. Meldrum, K.S. Beaty, M. Lam, C.W. White, R.A. Zuhr, and L.A. Boatner (these proceedings).
7. N.M. Dempsey, X.L. Rao, J.M.D. Coey, J.P. Nozieres, M. Ghidini, B. Gervais, J. Appl. Phys. **83**, 6902 (1998).
8. W. J. Weber, Nucl. Instr. Meth. **166**, 98 (2000).
9. J. W. Mayer, L. Eriksson, and J. A. Davies, Ion Implantation in Semiconductors Academic Press, New York (1970).
10. C. Chappert, H. Bernas, J. Ferre, V. Kottler, J.-P. Jamet, Y. Chen, E. Cambril, T. Devolder, F. Rousseaux, V. Mathet, H. Lanois, *Science* **280**, 1919 (1998).
11. S. Honda, F. A. Modine, A. Meldrum, J.D. Budai, T. E. Hayes, and L. A. Boatner, *Appl. Phys. Let.* **77**, 711 (2000).
12. E. Alves, C. MacHargue, R. C. Silva, C. Jesus, O. Conde, M.F. da Silva, and J. C. Soares, *Surf. Coat. Tech.* **128-129**, 434 (2000).

Mat. Res. Soc. Symp. Proc. Vol. 703 © 2002 Materials Research Society V9.7

# Innovative And Cost-Effective Microfabrication Of Nanoceramic Components

Balakrishnan G. Nair
Ceramatec Inc.
Salt Lake City, UT 84119

## ABSTRACT

An innovative and cost-effective processing technique has been developed at Ceramatec Inc for the microfabrication of ceramic components requiring very high dimensional tolerance. The materials system is a proprietary nanophase composition called CERCANAM (CERamatec CAstable NAno Material). Scanning electron microscopy revealed that CERCANAM components can be fabricated with dimensional tolerance as high as $\pm$ 2 μm for surface features on the die that have dimensions about 1 mm. The process can also be modified to fabricate nanoporous ceramic components with very high surface areas. Components with retained surface areas as high as 67-82% of the starting powder were fabricated. The fabrication process does not involve a high-temperature sintering step, which eliminates the loss of surface area from high temperature sintering. It is anticipated that microcomponents fabricated with specific microstructures and properties will have applications in the optical fiber industry as interconnects, in the electronic packaging industry and the chemical industry.

## INTRODUCTION

Conventional micro-machining techniques to form high-precision components (e.g. wet and dry etching) are very slow and expensive processes, and often do not meet the desired production rates and cost criteria required for bulk production of components. Further, most of these processes are specific for silicon, which has a relatively low fracture-toughness (0.7-0.8 $MPa.m^{1/2}$)[1] and is subject to severe corrosion in the high-temperature oxidizing conditions[2] typical of industrial chemical processes employing microchannel devices. Ceramic materials have excellent corrosion and mechanical properties that make them very attractive for high-temperature applications. However, most current processing techniques for micro-devices made of ceramics are even more expensive than silicon technology. Most of these processes require sintering/pyrolysis at high-temperature that result in at least 10-20% shrinkage.[3] Such shrinkage is very difficult to accurately model, and therefore the component dimensions are difficult to control to required tolerances.

## MATERIALS AND METHODS

Our process involves a novel casting technique to form net-shape components made of a reaction-bonded nano-ceramic material, which we will refer to henceforth as CERCANAM (for CERamatec CAstable NAno Material). This material was developed as a result of an internally funded research project at Ceramatec, Inc, in Salt Lake City, UT. The specific composition of CERCANAM and the processing technique are considered proprietary and are not relevant to the technical content of this manuscript. The idea of using reaction-bonded nano-ceramics like CERCANAM to fabricate micro components is novel.

Firing temperatures to form the finished component are usually as low as 200-600°C, although it can be as high as 1000°C if necessary. These temperatures are well below sintering temperatures of the ceramic materials that form the primary phase, and therefore there is no loss of dimensional accuracy due to sintering. Figure 1 shows the various processing alternatives for microfabrication of ceramic components using CERCANAM. The ceramic powder, composed either entirely or with a majority phase of sub-micron or nano-sized particulates is mixed with the appropriate reagent and stirred until gellation occurs and water separates out. The gel is collected and a green body is formed by one of the techniques shown in Figure 1, namely slip casting, tape casting, gel casting or extrusion. The casting technique is followed by punching the necessary design using a reusable die that has the "negative" of the required pattern. The die can be fabricated either from conventional materials like silicon using wet or dry etching, or using a photoresist material for use in a lost-mold technique, where the polymer is decomposed or vaporized completely during heat-treatment to form the finished component.[4]

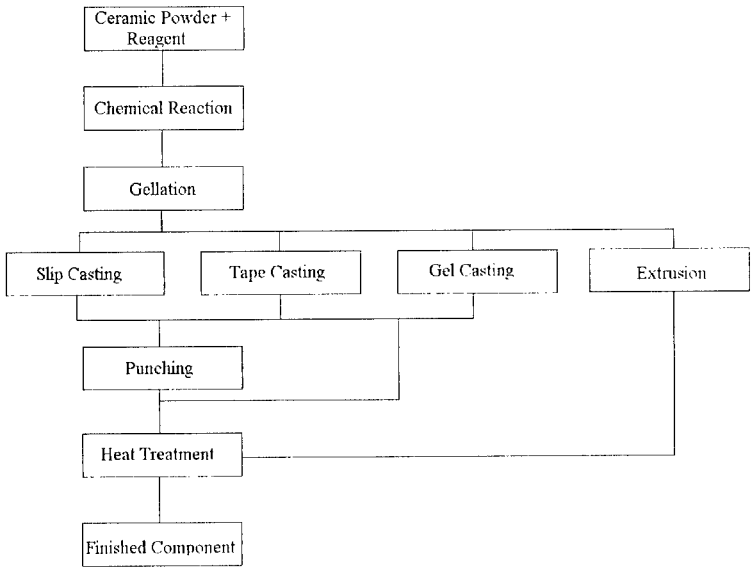


**Figure 1** Processing routes for micro-fabrication of ceramic components with CERCANAM

## RESULTS AND DISCUSSION

Micro-features on CERCANAM components have been shown to have very high dimensional accuracy with respect to features on the die. Figure 2(a) shows optical micrographs of a copper penny and the impression obtained by the penny on a post-fired CERCANAM specimen (firing temperature: 200°C); figure 2(b) shows SEM micrographs of the same. Digital analysis of the micrographs using image analysis software shows that dimensional accuracies of ± 3 μm over

distances of 2mm have been achieved on the CERCANAM specimen with respect to features on the copper penny. Features as small as 20 μm have been accurately imprinted.

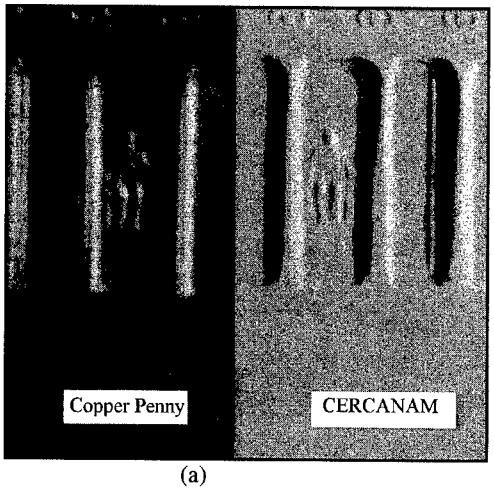


(a)

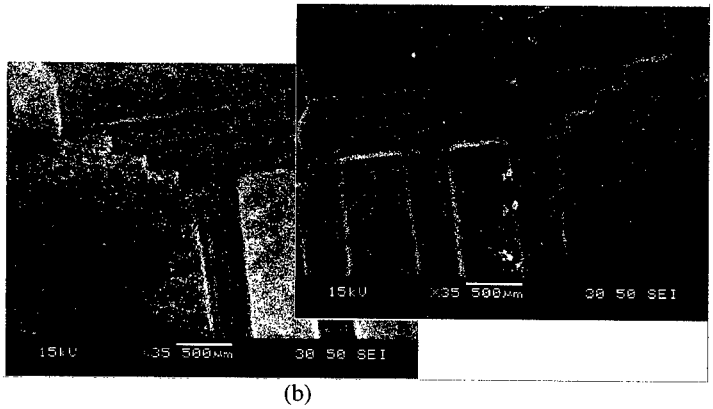


(b)

**Figure 2** Comparison of features obtained on a post-fired CERCANAM specimen imprinted with a copper penny (right) with respect to features on the penny (left): (a) optical micrographs; (b) SEM micrographs.

Figure 3(b) shows a microfabricated, post-fired CERCANAM component (firing temperature: 600°C) with a design imprinted from an etched silicon wafer with 100 μm × 100 μm etch pits, which is shown in figure 3(a). The bases of the pyramids obtained on post-fired CERCANAM specimens have been measured to be 100 μm ± 1 μm. The attainment of such high dimensional

tolerances illustrates the significant potential of CERCANAM materials for high-precision applications such as optical fiber interconnects, MEMS, etc. However, the fact that the processing technique is very inexpensive relative to other ceramic microfabrication techniques should make it attractive even for other microfabricated components such as microchannel devices and high-power/high temperature electronic packaging, where the attainment of sub-micron dimensional tolerances are not as critical.

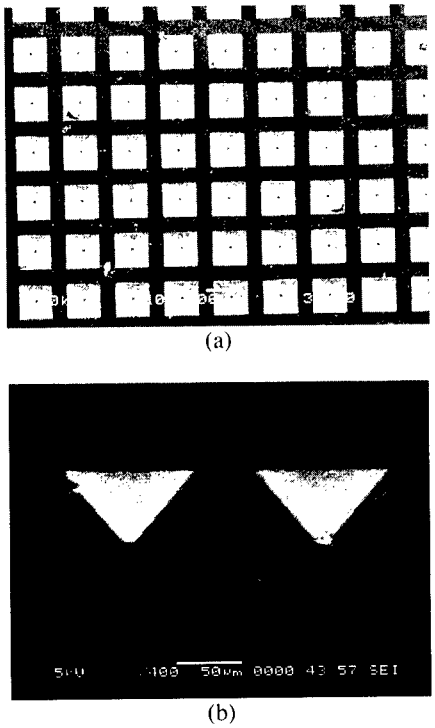


(a)

(b)

**Figure 3** (a) 100 µm × 100 µm etch pits on a silicon wafer used as a die for fabricating a slip-cast CERCANAM specimen; (b) pyramids of base dimensions 100 µm × 100 µm formed on the post-fired CERCANAM specimen. The tolerances on the base of the pyramids are estimated to be ±1 µm.

Another advantage of this processing technique is that high-surface area CERCANAM compacts can be obtained by relatively minor changes in the processing technique. The only modification is the addition of a pore-forming phase that can be removed at relatively low temperatures, and the use of a high surface area powder as the primary ceramic phase. Since the material is reaction bonded, and final firing temperatures are well below sintering temperatures, a very high proportion of the surface area (67-82%) of the starting powder can be retained by controlling the

volume fraction of the binding phase through control of processing parameters such as concentration of the reagent and time of reaction. This property of CERCANAM makes it a good choice in certain microchannel devices where a high-surface area ceramic is required as a support for particles of a catalytic or adsorbent phase that can be dispersed in the fine pores of the support.

## CONCLUSIONS

Microfabrication of CERCANAM components offers a technologically simple, one-step alternative for complex geometries that would require multiple-step processing with silicon technology. This material/process is expected to have significantly lower processing costs and production times for complex geometries, and can be scaled to large volume output with very high component production rates. Further, CERCANAM materials, due to their inherent thermochemical/thermomechanical stability are attractive for applications where microfabricated components are subjected to high temperatures (600-1000°C) and corrosive environments (e.g high-temperature gas sensing, high-temperature, high-power electronic packaging).

## REFERENCES


1 Chen, C. P. and M. H. Leipold, "Fracture toughness of silicon," *Am. Ceram. Soc. Bull.* **59**[4] 469-72 (1980).

2 Declerck, G. J., "Silicon oxidation," *Microelectron. Mater. Processes* **164** 79-132 (1989).

3 L-A. Liew, W. Zhang, L. An, S. Shah, R. Luo, Y. Liu, T. Cross, M. L. Dunn, V. Bright, J. W. Daily and R. Raj, "Ceramic MEMS: New Materials, Innovative Processing and Future Applications," *Am. Ceram. Soc. Bull.* **80** [5] 25-30 (2000).

4 U. P. Schonholzer, R. Hummel, Rene and L. J. Gauckler, "Microfabrication of ceramics by filling of photoresist molds," Adv. Mater., **12** [17] 1261-1263 (2000).

Mat. Res. Soc. Symp. Proc. Vol. 703 © 2002 Materials Research Society V9.10

# PROCESSING EFFECTS ON THE MORPHOLOGY OF HYDROTHERMALLY DERIVED NANOCRYSTALLINE LEAD TITANATE.

Zhiyuan Ye, Elliott B. Slamovich, and Alexander H. King
School of Materials Engineering, Purdue University,
West Lafayette, IN 47906, U.S.A.

## ABSTRACT

Nanocrystalline lead titanate was synthesized by reacting nanocrystalline titanium oxide in aqueous solutions of potassium hydroxide and lead acetate at 200 degrees C. X-ray diffraction (XRD) and TEM studies suggest that the initial KOH concentration influenced the nucleation and growth behavior of the lead titanate nanoparticles. Powders were processed in aqueous solutions containing 0.10 M lead acetate and a Pb:Ti ratio of 1, with varying concentrations of KOH. Powders processed in 0.01 M KOH were composed of irregularly shaped particles with 50-100 nm in size, processing in 0.10 M KOH produced particles with finger-like morphology and broader particle size distribution, and processing in 1.0 M KOH resulted in anisometric plates with (001) facets, and 100-200 nm in size. XRD studies have shown systematic variations in the position and symmetry of reflections with a l component as a function of particle size. This indicates that the c/a ratio of lead titanate increases with decreasing nanoparticle size

## INTRODUCTION

Hydrothermal processing, which involves reaction of aqueous solutions or suspensions of precursor and precipitation of complex oxides at elevated temperatures and pressures, has been widely applied in producing multicomponent metal oxide ceramic powders and thin films [1]. The $ABO_3$ peroveskites, such as barium titanate and lead titanate, have been successfully fabricated by hydrothermal technique under various conditions [2-6]. Hydrothermal synthesis of high phase purity, ultrafine, crystalline $PbTiO_3$ has been demonstrated by several groups at temperatures lower than 200 °C.[7-10] Compared to other processing methods such as solid-state reaction, sol-gel and coprecipitation, hydrothermal processing does not require going through a high temperature calcinations step, which causes particle coarsening and agglomeration [1]. Lower processing temperatures mean reduced energy budget. In the case of $PbTiO_3$, elimination of calcinations step also avoids lead volatilization [11]. Furthermore, by varying the processing parameters like temperature, pH, and the reagent concentrations, it is possible to control the size distribution and the morphology of final products [1,9].

Hydrothermal synthesis of $PbTiO_3$ has been extensively investigated experimentally and theoretically [3,4,7,10,11]. Thermodynamic calculations and experiments by Lencka and Riman [4] revealed the phase stability diagram under hydrothermal conditions. The phase stability diagram provided profound information about optimal process setup. However, the detail particle nucleation and coarsening mechanism remained unknown. Morphology studies not only were important for application, but also could provide more insight of the mechanism. Vast literatures have been devoted to the morphology [2,3,6,7,9]. High pH generally resulted in faster reaction rate and cuboidal morphology, while low pH could result in acicular or platelet morphology. In this paper, the influence of the concentration of mineralizer KOH, in turn the pH in starting suspensions on the resulting morphology will be presented. A possible mechanism of morphological evolvement under different initial KOH concentration is proposed to explain the observations.

## EXPERIMENTAL PROCEDURE

Hydrothermal $PbTiO_3$ nanoparticles were processed by mixing nanocrystalline $TiO_2$ (P25, Degussa, Dublin, OH) with lead acetate trihydrate ($Pb(CH_3COO)_2 \cdot 3H_2O$, Aldrich, 99+% purity) at a 1:1 molar ratio, then suspended in aqueous KOH in a Teflon lined autoclave (Model No. 4748, Parr Instrument Co., Moline, IL). The KOH solution was prepared by dissolving KOH (Mallinckrodt, 85% KOH, ≈15% $H_2O$) in boiling $CO_2$–free deionized water. The autoclave was then placed into a preheated force-air oven, holding at 200°C for reaction under autogenous conditions. After reaction, the autoclave was force-air cooled to room temperature. The suspension was vacuum filtered, repeatedly washing with $CO_2$–free deionized water. The collected powders were dried overnight at 90°C. $PbTiO_3$ nanoparticles were examined by X-ray diffraction (XRD) (Siemens D500 diffractometer) using Cu$K\alpha$ radiation. Particle size and morphology were characterized by transmission electron microscopy (TEM) (JEOL 2000FX).

The processing parameters were varied systematically to examine effects on particle morphology. The feedstock of every run maintained a lead concentration of 0.1M with [Pb]/[Ti] =1.0. KOH concentrations of 0.01M, 0.1M and 1M, with processing time from 6hrs to 12hrs to 24hrs, were investigated.

## RESULTS AND DISCUSSIONS

### X-ray diffraction (XRD) observations

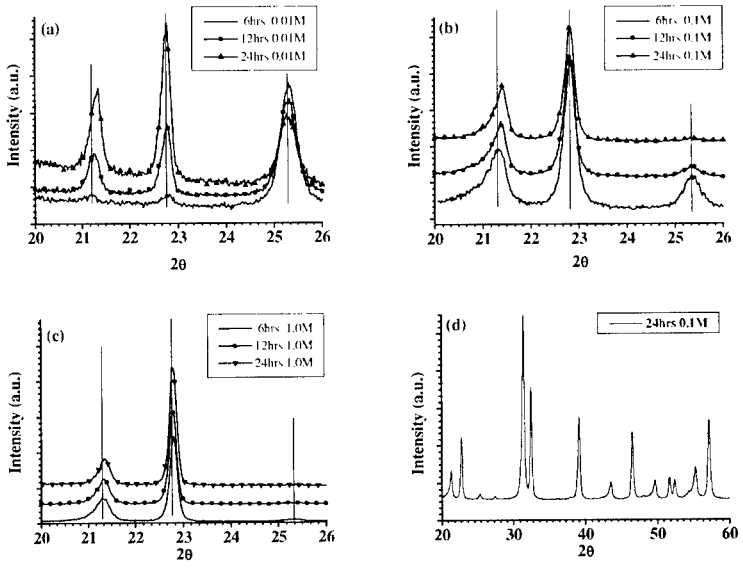


**Figure 1.** XRD patterns of $PbTiO_3$ nanoparticles processed at 200°C with [Pb]=[Ti]=0.1M. Initial KOH concentrations and processing time of (a),(b) and (c) are as indicated in legends. Vertical lines are guides for eyes. (001) peak (≈21.4°) and (100) peak (≈22.8°) of $PbTiO_3$ and peak for $TiO_2$ (anatase, ≈25.4°) are shown. (d) is a typical $PbTiO_3$ XRD pattern with 2θ from 20° to 60°.

XRD patterns of the collected powders prepared under different conditions show that the powders are composed of either pure $PbTiO_3$ or mixture of $PbTiO_3$ and unreacted $TiO_2$. This indicates that, under the processing conditions, $PbTiO_3$ is the only reaction product, which agrees with the majority of the literature (Figure 1).

The significant changes of relative intensities between $PbTiO_3$ and $TiO_2$ in Figure 1 (a), (b) and (c) along with time reflect the progress of reaction. The initial KOH concentration, or the pH has great influence on reaction rate. At 1.0M KOH, the residual $TiO_2$ is not detectable via XRD within 12 hours, while it takes 24 hours for process with 0.1M KOH to reach similar point. Further experiments show that, significant amount of $TiO_2$ remains even after 96 hours of processing. The reaction driving force strongly depends on the pH of the starting suspension.

Figure 1. (a), (b) and (c) all show that (001) peak of $PbTiO_3$ systematically shift toward high $2\theta$ as processing time increases. This indicates a decrease of lattice constant c as particle size increases (due to longer process time). This result is in line with a previous work of one of the authors.[9] The size effect on lattice of $PbTiO_3$ nanoparticles prepared by sol-gel technique has been studied theoretically and experimentally [12,13]. However, the reported relation was opposite to our observations [12]. This discrepancy may be attributed to slightly different stoichiometry and different morphology. Further investigation will be necessary to clarify this problem.

The (001) peaks in Figure 1. (b) show stronger asymmetric shape than those in (a) and (c). This might be also attributed to size effect on lattice constant. If this were the case, the particles from 0.1M KOH would have a broader size distribution. Our TEM observations have supported this conclusion.

## Transmission electron microscopy studies

There is a significant presence of tiny spherical shaped $TiO_2$ nanoparticles in TEM photographs of the powders from 0.01M KOH and 0.1M KOH (6 hours and 12 hours) (Figure 2). This is consistent with XRD observations, indicating that higher [KOH] will provide higher driving force, hence a faster reaction rate. TEM observations also demonstrate that the initial [KOH] has stronger effect on the $PbTiO_3$ morphologies than the processing time. The change of [KOH] not only affected the reaction rate, but also altered the crystal growth mechanism and anisotropy. At 0.01M KOH, the crystal growth did not strongly depend on growth direction, resulting in irregular, rounded shaped morphology. The large particle size, slow consumption rate of $TiO_2$ and relatively narrower size distribution indicate that the nucleation rate in 0.01M KOH suspension was very low, and the reaction was dominated by coarsening of the particles. The mechanism might involve dissolution of $TiO_2$ and precipitation of $PbTiO_3$ on the particle surface. At [KOH] of 1.0M, the particle growth was highly anisotropic, resulting in rectangular shaped, (001) faceted, platelet morphology. At 0.1M KOH, TEM photographs revealed a "finger like" morphology, characterized by several columnar structures ~25nm in width, ~150nm in length, parallely growing on a substrate. Strong evidence of secondary nucleation can be observed. The surface roughness change due to secondary nucleation might change the local reagent distribution, resulting in 1-D preferential crystal growth.

The influence of [KOH] on nucleation and grain growth was different. At low pH, the concentration of reagents could hardly initiate nuclei, resulting in a very low nucleation density. The transformation of feedstock to $PbTiO_3$ would be dominated by continuous coarsening of the existed particles. At high [KOH], the strong supersaturation could cause a homogeneous nucleation inside the suspension, majority of the feedstock would be consumed in this stage and therefore inhibit further nucleation. The higher solubility of $PbTiO_3$ at high

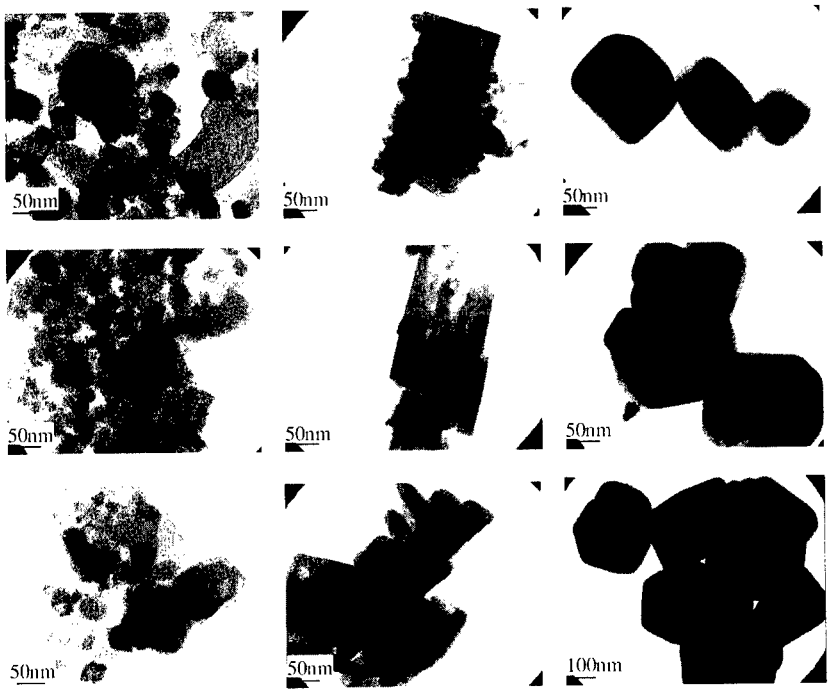


**Figure 2.** Morphology evolvement as a function of processing time and initial KOH concentrations. From top to bottom, the processing time is 6 hours, 12 hours and 24 hours, respectively. From left to right, the initial [KOH] is 0.01M, 0.1M and 1.0M respectively. The spherical shaped particles with size ~25nm are residual $TiO_2$, which is the most visible in first column.

pH could effectively prompt the dissolution-precipitation process, which might dominate the coarsening in this case. At intermediate [KOH], nucleation and grain growth could occur spontaneously, resulting in a high possibility of secondary nucleation and a broader size distribution.

## CONCLUSIONS

The initial concentration of KOH has strong influence on the morphology of hydrothermally derived $PbTiO_3$ nanoparticles. Low [KOH] revealed rounded particles while high [KOH] resulted in faceted platelet structure. Both low and high [KOH] give narrower size distribution than the intermediate [KOH]. Particles from intermediate [KOH] show a characteristic "finger like" morphology. The observations have been explained with a nucleation-growth competition mechanism.

## ACKNOWLEDGMENTS

This work was partly supported by the National science Foundation grant # DMR 0096147. Z. Ye is grateful for support from the Purdue Electron Microscopy Consortium.

## REFERENCES


1. W.J. Dawson, *Ceram. Bull.* **67**, 1673 (1988).
2. H. Cheng, J. Ma, Z. Zhao, and D. Qiang, *J. Am. Ceram. Soc.* **75**, 1123 (1992).
3. G.A. Rossetti Jr., D.J. Waston, R.E. Newnham, and J.H. Adair, *J. Crystal Growth 116*, 251 (1992).
4. M.M. Lencka and R.E. Riman, *J. Am. Ceram. Soc.* **76**, 2649 (1993).
5. J.O. Eckert Jr., C.C. Hung-Huston, B.L. Gersten, M.M. Lencka, and R.E. Riman, *J. Am. Ceram. Soc.* **79**, 2929 (1996).
6. E.B. Slamovich and I.A. Aksay, *J. Am. Ceram. Soc.* **79**, 239 (1996).
7. A.T. Chien, J. Sachleben, J.H. Kim, J.S. Speak, and F.F. Lange, *J. Mater. Res.* **14**, 3303, (1999).
8. C.R. Peterson and E.B. Slamovich, *J. Am. Ceram. Soc.* **82**, 241 (1999).
9. C.R. Peterson and E.B. Slamovich, *J. Am. Ceram. Soc.* **82**, 1702 (1999).
10. M.C. Gelabert, B.L. Gersten, and R.E. Riman, *J. Crystal Growth* **211**, 497 (2000).
11. M.C. Gelabert, R.A. Laudise, R.E. Riman, *J. Crystal Growth* **197**, 195 (1999).
12. B. Jiang, J.L. Peng, L.A. Bursill and W.L. Zhong, *J. Appl. Phys.* **87**, 3462 (2000).
13. B. Jiang and L. A. Bursill, *Phys. Rev. B* **60**, 9978 (1999).

Mat. Res. Soc. Symp. Proc. Vol. 703 © 2002 Materials Research Society V9.11

# Nanocomposite based on semiconductor oxides $SnO_2/WO_3$

M.N.Rumyntseva, M.N.Boulova, D.A.Chareev, L.I.Ryabova, B.A.Akimov[1], A.M.Gaskov
Chemistry Faculty, Moscow State University, Moscow 119899, Russia
[1]Low Temperature Physics Department, Moscow State University, Moscow 119899, Russia

## ABSTRACT

Nanocrystalline $SnO_2$ and $WO_3$ and nanocomposite with Sn:W ratio 1:9, 1:1, 9:1 were prepared by co-precipitation of α-stannic and tungstic acids. Phase composition and average crystallite size were determined from XRD data. Presence of the second component results in the reduction of the crystallites growth rate, giving rise to the enhancement of thermal stability of nano-scaled system. TGA data allowed to estimate the concentration $\nu_{H2O}$ of water adsorbed on nanocomposite effective surface. Maximal $\nu_{H2O}$ value and the highest resistance were observed for nanocomposite with Sn:W = 1:1. The temperature dependence of resistance R reveals its activation character. The current-voltage curves are interpreted in terms of electrochemical capacitor recharge.

## INTRODUCTION

Metal oxides $SnO_2$, ZnO, $In_2O_3$ in ultradispersed form are widely used as resistive type gas sensors. High values of gas sensitivity may be regarded as their main advantage, while microstructure stability being their main deficiency. The stability of the ultradispersed systems is heightened in more complicated materials containing an additional phase and characterized by non-homogeneous structure and composition: nanoheterogeneous materials or nanocomposites [1-3]. The reduction of the total area of the crystallite surface contacts for each of the ultradispersed phases slows down the growth of the grains. If the grain size of the oxides is comparable with the Debye length the introduction of new phases may also result in qualitative modification of material properties. Nanocomposites based on semiconductor metal oxides $Me_1O$-$Me_2O$ with low mutual solubility are of a special interest as gas sensing materials. The present work deals with the synthesis, structure characterization and electric properties of $SnO_2$ - $WO_3$ nanocomposites. The influence of the high temperature anneal together with the composition variation on the grain size in each phase is studied. The charge transport is found to involve ionic component, the conductivity activation energy is estimated.

## EXPERIMENTAL

Nanocrystalline $SnO_2$, $WO_3$ and nanocomposite with Sn:W ratio 1:9, 1:1, 9:1 (samples $Sn_1W_9$, $Sn_1W_1$ and $Sn_9W_1$ respectively) were prepared by co-precipitation of α-stannic and tungstic acids. α-stannic acid was prepared by conventional hydrolysis of $SnCl_4$ in ammonia water solution. Tungstic acid was obtained by hydrolysis of $(NH_4)_{10}W_{12}O_{41}$ in HCl water solution. Gels of the acids mentioned above were co-precipitated from the solution containing $(NH_4)_{10}W_{12}O_{41}$ and $Na_2[Sn(OH)_6]$ prepared by reaction of α-stannic acid with 1 M NaOH. The precipitates were

centrifuged, washed with deionized water until the absence of chloride ion ($AgNO_3$ test) and dried at 80° C for 24 h.

Thermal anneals have been undertaken to study the microstructure stability of the individual nanocrystalline oxides and nanocomposites. The samples were annealed at T=80, 150, 300, 600, 800 C during 24 h. After the annealing procedure the samples color varied from white to yellow depending on the composition and annealing temperature.

Phase composition and microstructure of the powders were studied by X-ray diffraction (XRD) (STOE) with use of $Cu(K_\alpha)$ radiation. The average grain size of $SnO_2$ and $WO_3$ was estimated from diffraction patterns using the Sherrer's equation.

Mass loss during the annealing procedure was studied by means of thermogravimetry (TGA-7, Perkin-Elmer) in air, the temperature was varied from 35 up to 900 C with the heating rate of 10 °/min.

Electrophysical properties were measured for ceramic pellets of 6 mm in diameter and 1.5 mm thick prepared by pressing at 700 MPa with subsequent annealing in air at 600 C for 24 h. The golden contacts were deposited on the pellet surface by thermal evaporation technique. The distance between the contacts was 2 mm. The resistance of the samples was studied in static electric fields up to 10 V in temperature interval 200 -300 K.

## RESULTS AND DISCUSSION

Phase composition of the investigated samples determined from the diffraction XRD patterns is given in the Table. The following phases are found: $SnO_2$, $WO_3*H_2O$ and $WO_3$. Phases of ternary compounds were not observed. In the samples $SnO_2$ and $Sn_9W_1$ annealed at T≥150 C the cassiterite ($SnO_2$) phase alone was found. The degree of crystallization rises with the annealing temperature increase. For $WO_3$ and $Sn_1W_9$ samples the increase of the annealing temperature results in the change of phase composition. At low annealing temperatures 80 and 150 C $WO_3*H_2O$ phase is observed, at T≥300 C this phase falls down and at the same time $WO_3$ phase appears. In diffraction patterns of the $Sn_1W_1$ nanocomposite the reflexes corresponding to both the phases of $SnO_2$ and $WO_3$ exist. However, the interpretation of the XRD spectra and quantitative calculations of the peaks positions are complicated due to the superposition of triplet peaks of $WO_3$ ($2\theta$ = 26.49, 26.62, 26.84)and $SnO_2$ peak ($2\theta$ = 26.61), and the group of lines $WO_3$ ($2\theta$ = 33.00, 33.58, 33.92, 34.11, 34.49) and $SnO_2$ peak ($2\theta$ = 33.89).

**Table.** Phase composition of $SnO_2$-$WO_3$ nanocomposites

| **Sample** | **W:Sn ratio** | **Annealing temperature, T (C)** | | | | | **$E_a$, eV** |
|---|---|---|---|---|---|---|---|
| | | 80 | 150 | 300 | 600 | 800 | |
| ***$WO_3$*** | 1:0 | $WO_3*H_2O$ | $WO_3*H_2O$ | $WO_3$ | $WO_3$ | $WO_3$ | 0.12-0.14 |
| ***$Sn_1W_9$*** | 9:1 | $WO_3*H_2O$ | $WO_3*H_2O$ | $WO_3$ | $WO_3$ | $WO_3$ | 0.15-0.18 |
| ***$Sn_1W_1$*** | 1:1 | Amorph. | Amorph. | $SnO_2$ | $WO_3$+$SnO_2$ | $WO_3$+$SnO_2$ | |
| ***$Sn_9W_1$*** | 1:9 | $SnO_2$ | $SnO_2$ | $SnO_2$ | $SnO_2$ | $SnO_2$ | |
| ***$SnO_2$*** | 0:1 | $SnO_2$ | $SnO_2$ | $SnO_2$ | $SnO_2$ | $SnO_2$ | 0.035 |

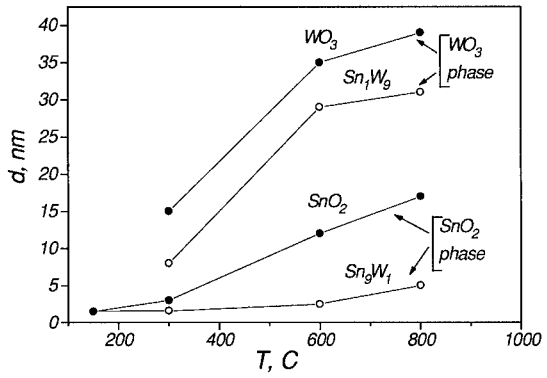


**Figure 1.** Crystallite size of $SnO_2$ and $WO_3$ phases in nanocomposites vs annealing temperature.

In contrast with the data for $WO_3$ and $Sn_1W_9$ samples the crystallization of tungstic acid was not observed in $Sn_1W_1$ nanocomposite. Comparison of the XRD patterns for all the investigated samples annealed at 600 C shows that in nanocomposites the degree of crystallization of the individual oxides reduces. The annealing temperature increase leads to the grain size growth for both the $SnO_2$ and $WO_3$ phases (Fig.1). $WO_3$ crystallites are of 10-50 nm that significantly exceeds the size of $SnO_2$ crystallites (2-15 nm) at the same annealing temperature. It is important that the introduction of an additional component results in the reduction of the crystallite growth rates for both the phases.

The thermogravimetry (TGA) analysis data are in good accordance with the XRD results. For the samples $SnO_2$ and $Sn_9W_1$ two characteristic temperature regions may be regarded: 35 - 175 C and 175 - 800 C. Low temperature region is characterized by a pronounced peak at the DTG curves at 90 C. This peak may be attributed to surface water desorption. High temperature region is smooth and the mass loss for this case may be due to a gradual water removal during the transformation of α-stannic acid into β-form.

Therefore it may be concluded that up to the temperatures ~800 C tin dioxide exists in partially hydrated state. For the samples $WO_3$ and $Sn_1W_9$ TG curves also may be characterized by two temperature regions of mass loss. The low temperature region (35 - 150 C) with a peak at 50 C corresponds to desorption of water molecules slightly bonded at the surface by physical adsorption mechanism. Another peak at 250 C corresponds to transformation of tungstic acid into tungsten oxide. The mass loss at this temperature range equals to 6.75% for $WO_3$ sample that corresponds to removal of 0.96 mole of $H_2O$ from 1 mole of $WO_3$. At the DTG curve for $Sn_1W_1$ high temperature peak was not observed in agreement with XRD data since the crystallization of tungstic acid was not found. The low temperature region of the DTG curve for this sample is characterized by mass loss significantly exceeding the values obtained for all other samples. The estimation of the adsorbed water quantity $\nu_{H2O}$ (mole per 1 mole of the nanocomposite) as a function of $SnO_2$ mole fraction in the nanocomposite is shown in Fig.2. The non-linear character

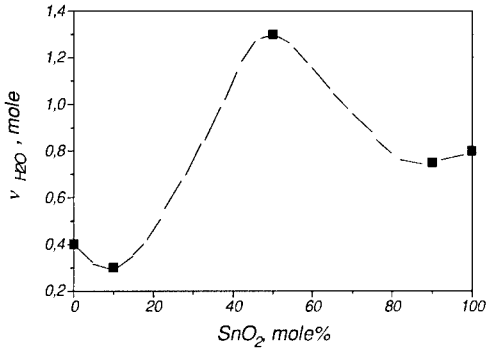


**Figure 2.** Calculated quantity of surface adsorbed $H_2O$ as a function of sample composition. Line is a quide for eye.

of this dependence may be attributed to grain size reduction and possible increase of effective surface in nanocomposites compared to individual oxides.

The charge transport is characterized by electric current instabilities for all investigated samples. A typical current –voltage (I-U) curve is shown in Fig.3 for $Sn_1W_1$ sample. The arrows indicate the order of voltage switching. In low fields U<1 V current is unstable reducing down to values, which registration is eliminated by the devise sensitivity ($10^{-3}$ μA). Thus current values at low fields may be considered as some effective data taken at a gradual field switching. At U>3 V the current stabilizes and I-U curve transforms into a linear one. The current was stable while the sample was kept under U=5 V for 5 minutes. After what the field was gradually switched off.

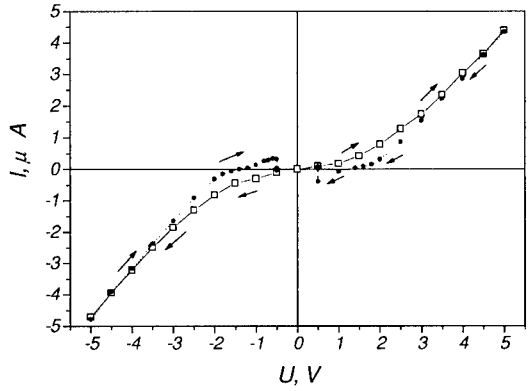


**Figure 3.** Current - voltage characteristic of $Sn_1W_1$ nanocomposite.

The hysteresis at I-U curve appears at U ≤ 3 V, and at U=1.4 V current reaches zero and then changes the sign. At the same time the current instabilities appear. To illustrate the relaxation process the sample was kept under the fixed voltage U=0.5 V. In 5 minutes I relaxes to a value shown on Fig.3 as a rhombus. In the field of opposite direction the picture is the same. The observed peculiarities of the I-U curves may be explained in terms of electrochemical capacitor. Charge accumulation on the capacitors electrodes may be associated with ionic component in charge transport. It involves the dissociated water and, possibly, $Na^+$ and $Cl^-$ ions, which presence is related to the synthesis methods. Charge accumulation process in the nanocomposite seems to be of special interest, since the voltage corresponding to the change of current sign is high enough.

Strongly identical conditions were chosen to estimate and compare the conductivity of the samples with different composition. The measurements were performed in the dry helium atmosphere. The voltage U=0.5 V was applied to the samples contacts. Two current values were registered: immediately after the field switching on and 5 minutes later. Resistance R was calculated for both current values, the results are shown in Fig4. Solid line corresponds to the values taken at the first moment after field switching, dotted line - to the data obtained 5 minutes later. The resistance measured at the first moment seems to be closer to the electronic component of conductivity. After some time passes the external field is reduced by the ions accumulated on the electrodes (the charging of electrochemical capacitor). Though the data shown in Fig.4 are only an estimation, the uncertainty in determination of R is significantly less than resistance change under composition variation. Maximal ability for charge accumulation (and maximal resistance value) is observed in nanocomposite with Sn:W = 1:1 ratio. That may be related at least to two self-consistent factors: maximal water adsorption ability and minimal grain size. It should be mentioned that for nanocrystalline $SnO_2$ films according to [4] the reduction of grain

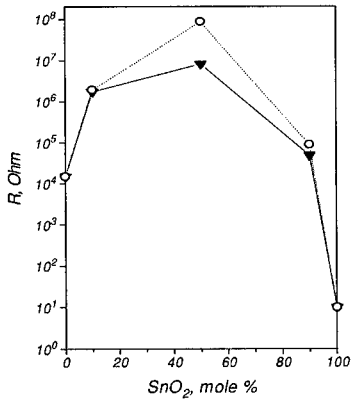


**Figure 4**. Resistance R as a function of sample composition. Solid line corresponds to the values taken at the first moment after field switching, dotted line - to the data obtained 5 minutes later.

size from 10 down to 6 nm results in resistance growth from 2 $10^4$ up to 6 $10^4$ Ohm at the room temperature. Under cooling this difference increases and at T=77 K reaches 8 $10^4$ and 3 $10^6$ Ohm respectively.

The temperature dependence of the resistance R have been measured only for the samples, where current instabilities may be neglected at a first approximation. The dependencies R(T) were taken in dry helium atmosphere under a fixed voltage U=1 V. The criterion of the measurements trust-worth was the coinciding of the curves taken during the temperature cycling from cooling to heating. All the plots lnR-1/T demonstrate the linear behavior. The activation energies $E_a$ were calculated with use of the equation R~ exp($E_a$/kT) (see Table). The activation character of the conductivity process reveals the barrier mechanism, the barrier height $E_a$ rises with the resistance increase.

## CONCLUSIONS

The presented results confirm the possibility to obtain more stable microstructure in nano-scaled systems. Introduction of an additional component whether to $WO_3$ or to $SnO_2$ results in slowing down of the crystallite growth rates. Microstructure of investigated nanocomposites practically does not change under thermal annealing in temperature interval 100-600 C. Just this range is important in gas sensor applications. Water adsorption ability, grain size and electrical properties correlate and depend on the composition of the samples. Nanocomposite with metals ratio 1:1 is of special interest as the most stable and possessing the highest adsorption ability.

## ACKNOWLEDGEMENTS

This work was supported by INTAS program (grant N2000-0066) and RFBR (grant N01-03-32728).

## REFERENCES

1. H.Gleiter, Acta Mater. **48**, 1 (2000).
2. G. Martinelli, M. C. Carotta, E. Traversa, G. Ghiotti, Mat.Res.Soc.Bull. **24**, 30 (1999).
3. Q. Yitai, H. Yuan, W. Chengyun, C. Zuyao, L. Bing, F. Chengao, J. Nanostructered Mater. **1**, 347 (1992).
4. M. N. Rumyantseva, A. M. Gaskov, L. I.Ryabova, J. P. Senateur, B. Chenevier, M. Labeau, Mater.Sci.Eng.B, **41**, 333 (1996).

Mat. Res. Soc. Symp. Proc. Vol. 703 © 2002 Materials Research Society V9.12

# NICKEL NANOCOMPOSITE THIN FILMS

Honghui Zhou, A. Kvit, D. Kumar, and J. Narayan
Department of Materials Science and Engineering and NSF Center for Advanced Materials and Smart Structures.
North Carolina State University, Raleigh, NC 27695-7916, U.S.A.

## ABSTRACT

Nickel was deposited on epitaxial TiN matrix layer grown on Si (100) substrate by pulsed laser deposition process (PLD). Transmission electron microscopy (TEM) study shows that nanoparticles formed are single crystals with two kinds of epitaxial relationship with respect to matrix TiN. One is cube on cube, where (200) Ni // (200) TiN // (200) Si and (02 $\bar{2}$) Ni // (02 $\bar{2}$) TiN // (02 $\bar{2}$) Si. The particles grown in this orientation have a trapezoidal morphology in [011] projection. The other involves a 90 ° rotation with respect to [011] direction of TiN matrix (zone axis), where (0 $\bar{2}$2) Ni // (200) TiN // (200) Si and (200) Ni // (02 $\bar{2}$) TiN // (02 $\bar{2}$) Si. The particles grown in this rotated orientation have a triangular morphology in [011] projection and a smaller lattice constant compared with that of pure nickel. The possible mechanism of forming these two epitaxial orientations is discussed. Superconducting quantum interference device (SQUID) magnetometer was used for magnetic measurements. In order to investigate the effect of texturing on magnetic properties of nanoparticles, results were compared with those obtained from Ni nanoparticles grown on amorphous $Al_2O_3$ matrix layer in previous research. It was found that both blocking temperature and coercivity of Ni nanoparticles grown on epitaxial TiN matrix are significantly higher than that of Ni grown on amorphous $Al_2O_3$. The higher value of coercivity is possibly associated with the stronger tendency of crystallographically oriented particles to retain their magnetic moments in the presence of reversing magnetic field.

## INTRODUCTION

Nanomagnetic materials have drawn significant attention in recent years due to their dramatically improved physical properties critical for enhancing the magnetic device performance, such as giant magnetoresistance, superparamagnetism, large coercivities, high Curie temperature, and low saturation magnetization [1-7]. Magnetic properties of the nanomagnetic materials are closely related to the magnetic anisotropy of the material, which depends not only on the size, shape and strain state of the particles, but also on their crystal structure and orientation. However, so far, most studies in this area have been focused on the dependence of magnetic properties on the particle size and separation. It is expected that further improvement in these properties could be realized by texturing the magnetic particles along their easy axis. In the present study, epitaxial Ni nanoparticles were grown on TiN thin-film matrix by pulsed laser deposition (PLD) technique. The crystalline quality of the particles was investigated by conventional and high-resolution transmission electron microscopy (TEM and HRTEM). In order to investigate the effect of texturing of magnetic particles on their magnetic properties, superconducting quantum interference device (SQUID) magnetometer was used to measure the particle magnetic properties and the results were compared with that of randomly oriented Ni particles of similar size obtained in previous research [8].

## EXPERIMENTAL DETAILS

Ni nanoparticles and their matrix layer TiN and $Al_2O_3$ were deposited by ablating a pure nickel target and hot pressed TiN and $Al_2O_3$ target, respectively, in a pulsed laser deposition (PLD) system. Si (100) was used as the substrate. Before deposition, the silicon substrates were ultrasonically degreased and cleaned in acetone and methanol for 5 ~ 10 minutes, which was followed by 1-minute etching in 49 % hydrofluoric acid solution so that the surface silicon dioxide layer could be removed. The main deposition parameters are as follows: vacuum $5 \times 10^{-7}$ Torr; substrate temperature 600° C; laser energy density 2 J/cm$^2$; laser frequency 10 Hz. In order to get sufficient signal during the investigation, three kinds of sample with different particle sizes (by controlling Ni deposition time) and numbers of particle layers were made: sample #1 (45 seconds and 1 layer Ni); sample #2 (30 seconds and 1 layer Ni); sample #3 (30 seconds and 5 layer of Ni separated by TiN). Particle morphology, size distribution and the crystalline quality information of both Ni particles and matrix layer were obtained through conventional and high-resolution transmission electron microscopy (TEM and HRTEM) study by JEOL 2010F and TOPCON 002B microscopes with point-point resolution of 0.18 nm. Magnetic properties of the sample were measured using superconducting quantum interference device (SQUID) magnetometer. In order to get sufficient signal, samples containing five layers of nickel separated by TiN or $Al_2O_3$ layer were used. Details of the measurements were published in our previous paper [8].

## RESULTS AND DISCUSSION

Transmission electron microscopy study

Shown in Fig. 1 (a) is a bright filed cross-sectional image of a Ni/TiN/Si sample (#1) taken from Si [011] zone axis. As seen, uniform-sized faceted Ni nanoparticles were formed on the top of TiN matrix layer. Two distinct morphologies were found, which correspond to two different epitaxial orientation relationships and will be discussed later. Fig. 1 (b) is the corresponding selected area diffraction (SAD) pattern of Fig. 1 (a). It is easily seen that TiN was epitaxially grown on Si (100) substrate with an orientation relationship (200) TiN // (200) Si and (02 $\bar{2}$) TiN // (02 $\bar{2}$) Si. Two sets of diffraction pattern related to Ni were found: (1) cube-on-cube orientation with (200) Ni // (200) TiN and (02 $\bar{2}$) Ni // (02 $\bar{2}$) TiN; (2) (0 $\bar{2}$2) Ni // (200) TiN and (200) Ni // (02 $\bar{2}$) TiN, which is a result of 90 ° rotation with respect to the TiN [011] (zone axis). Fig. 1 (c) is a centered dark-field image formed with the circled diffraction spot in the rotated pattern of Fig.1 (b). The dark-field image study shows that the particles with a triangular morphology in [011] projection grown in the 90 ° rotated epitaxial orientation while the particles grown in cube-on-cube epitaxial relationship have a trapezoidal morphology. It was also found that some particles, like the one shown in the left side of the image, contain both orientations.

The two different epitaxial orientations corresponding to the two distinct morphologies were also found in high-resolution electron microscopy study. Fig. 2 (a) and Fig. 2 (c) are high-resolution transmission electron microscopy (HRTEM) images of nanoparticles (sample #1 and #2, respectively) taken along Si [011] zone axis. Again, the trapezoidal and triangular morphologies are clearly seen. In sample #2 the particle size is smaller than that of sample #1 due to the reduced deposition time and no particle coalescence occurred. Also shown in Fig. 2

are corresponding Fast Fourier Transform (FFT) of the two HRTEM images (Fig. 2 (b) and Fig. (d)), which confirm the above-mentioned two distinct epitaxial orientations.

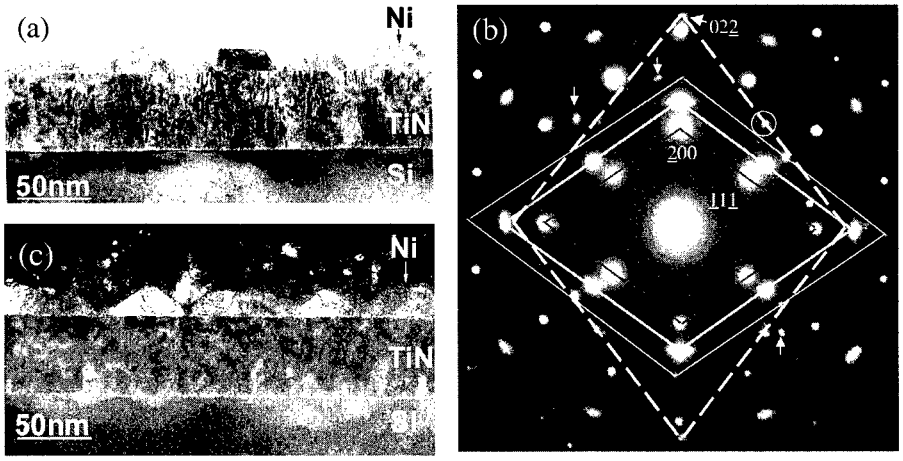


**Fig.1 (a)** BF image of Ni/TiN/Si sample (#1) taken from Si <011> zone axis; **(b)** The corresponding SAD pattern from the same area. Rhombus with dark, bright-wide- and bright-narrow-solid lines correspond to Si, TiN and Ni cube-on-cube epitaxial relationships, respectively. Rhombus with dashed line corresponds to 90º rotation epitaxial relationship. Note that lattice parameters calculated from the pattern corresponding to 90° rotation are slightly smaller than that of pure Ni. Arrows indicate double diffraction reflexes; **(c)** CDF image of the same area taken from the diffraction spot circled on the SAD pattern corresponding to 90º rotation (Fig.1 (b)).

Usually, in epitaxial growth, the lattice mismatch induced strain energy as well as the interfacial or chemical energy determine the orientation relationship and the epitaxial layer always orients itself in such a way that the lattice mismatch is reduced and the anisotropy interfacial energy is lowered [9]. The lattice constant of two kinds of particles could be estimated from their corresponding SAD pattern. It was found that the lattice constant of the particles grown by cube-on-cube orientation is very close to that of Ni, but the lattice constant of particles from rotated growth is apparently smaller that of pure Ni. We think that this rotated epitaxial growth was probably due to the fact that the particle formed is not pure nickel. This Ni-enriched phase was formed as a result of diffusion of foreign atoms, such as titanium. The excess titanium atoms in the TiN film would tend to diffuse to the interface and alloy during the particle growth. TiN, seen from SAD pattern and HRTEM images, is cube-on-cube epitaxially grown on Si substrate with some area of small angle misorientation. These regions could have possibly provided the diffusion path. This also could explain that in the observed area, particles with trapezoidal morphology tend to have "triangular" particles as neighbors so that particles of two morphologies are mixed. In order to explain exactly the mechanism of this rotated epitaxial

growth, future studies, such as electron energy loss spectrum (EELS) and high resolution atomic contrast imaging still need to be conducted.

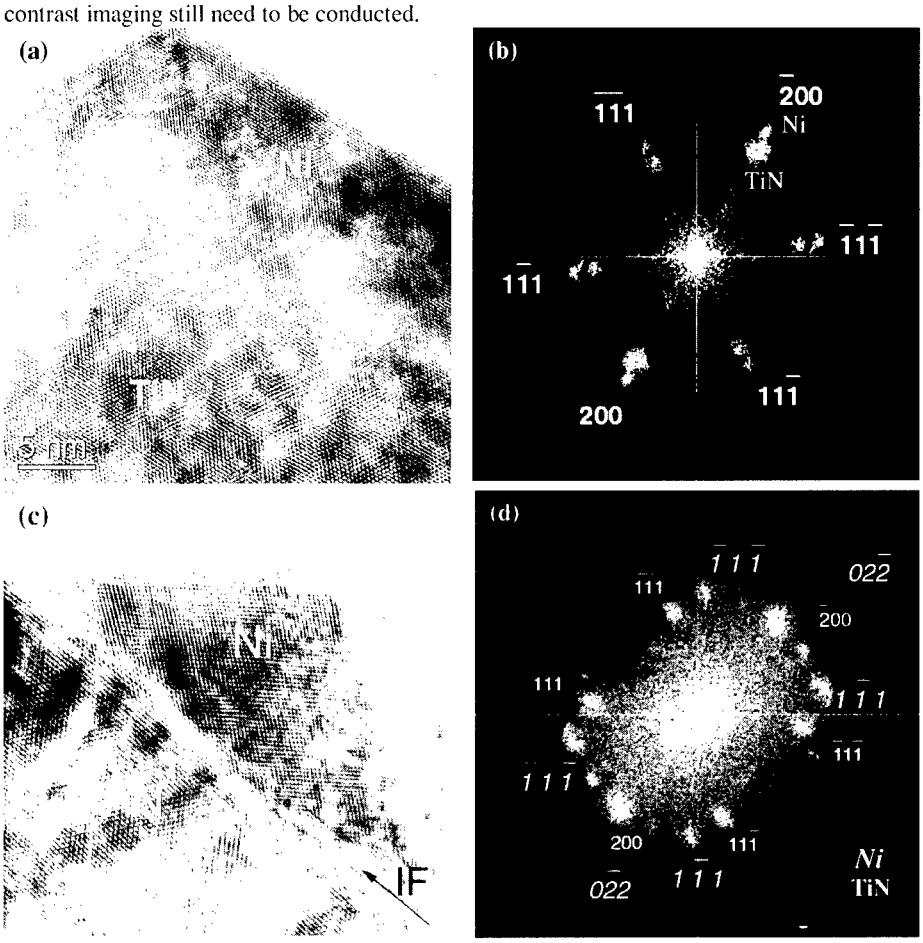


**Fig.2 (a)** High-resolution TEM image of a trapezoidal particle (sample #1) taken from Si <011> zone axis; **(b)** The corresponding FFT picture of (a) indicating Ni cube-on-cube epitaxial growth; **(c)** High-resolution TEM image of a triangular particle (sample #2) taken from Si <011> zone axis; **(d)** The corresponding FFT picture of (c) indicating the particle 90° rotation epitaxial growth Indexes in smaller regular numbers and bigger oblique numbers correspond to the reflections of TiN and Ni-related particle, respectively.

Magnetic measurements

Shown in Fig. 3 (a) and (b) are the ZFC and FC magnetization data as a function of temperature for $Ni/Al_2O_3$ sample and Ni/TiN sample (#3). The average size of Ni particles was similar in both cases. As seen, in both cases ZFC and FC curves diverge from each other at a

certain temperature, below which, ZFC curve in both cases reaches a maximum. The temperature at which this maximum occurs is known as the blocking temperature $T_B$. The temperature where the irreversibility sets in for two samples is quite different: 100 K for $Ni/AL_2O_3$ and 275 K for Ni/TiN, so is the blocking temperature. The blocking temperature for Ni on TiN matrix is around 190 K, much higher than that of Ni on $Al_2O_3$ matrix, which is around 30 K. Ideally, the blocking temperature and the temperature at which the irreversibility sets in ZFC and FC magnetization should be the same [6,7]. The difference in the two temperatures observed in the experiment is attributed to the size distribution of magnetic particles having different $T_B$ [6,7].

The higher value of $T_B$ in Ni/TiN sample with respect to that in $Ni/Al_2O_3$ sample is believed to be associated primarily with the texturing of Ni particles, which influences the anisotropy energy of the system. Blocking temperature is a characteristic temperature for single domain material. Below this temperature, the material shows ferromagnetic properties. As temperature increases to a certain value, the magnetic anisotropy energy, which poses the barrier for the single domain to change the magnetic orientation (magnetization vector reversal), will be overcome by thermal energy and the magnetic moments would fluctuate rapidly and freely as if a paramagnetic system, a phenomenon called superparamagnetism [10]. Above the blocking temperature the material magnetization is unstable and the sample loses any hysteric responses in the magnetization versus field measurements. The Ni particles in Ni/TiN sample grow epitaxialy via domain match on epitaxial TiN matrix [11], while the Ni particles in $Ni/Al_2O_3$ sample are randomly oriented due to the amorphous nature of alumina matrix. The textured nanoparticles are expected to have higher anisotropy energy. Therefore, the thermal energy required to reverse the magnetization vectors, and as a result, the blocking temperature will be higher for textured magnetic nanoparticles.

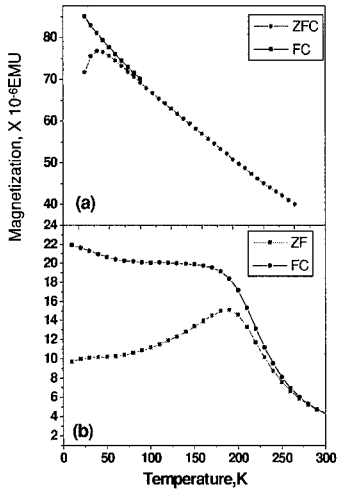


Fig. 3. ZFC and FC magnetization data as a function of temperature for (a) Ni/Al2O3 and (b) Ni/TiN samples.

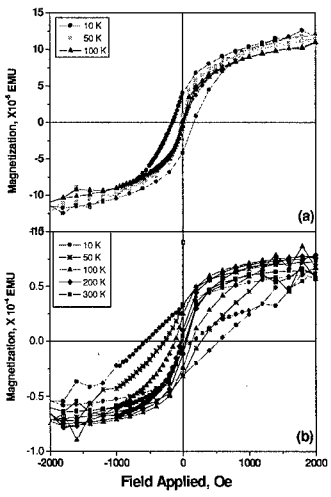


Fig. 4. Magnetization versus field curves for (a) $Ni/Al_2O_3$ and (b) Ni/TiN samples.

Fig. 4 shows the magnetization versus field curves for the $Ni/Al_2O_3$ and Ni/TiN samples. The values of $H_c$ are found to be 25, 45, 125, 270, and 550 Oe at 300, 200, 50 and 10 K, respectively for Ni/TiN sample. The $Ni/Al_2O_3$ sample exhibits a coercivity ~ 150 Oe at 10 K and it is almost superparamagnetic at temperature higher than 100 K, which is in accordance with blocking temperature of $Ni/Al_2O_3$ sample measured form M-T plot. A comparison of the coercivity values of the two samples under several temperatures indicates that epitaxial Ni particles exhibit significantly higher coercivity than randomly oriented Ni particles. The high value of $H_c$ of epitaxial Ni nanoparticles is envisaged to be associated with the stronger tendency of crystallographically oriented particles to retain its magnetic moments than that of randomly oriented particles under a reversing magnetic field.

## CONCLUSIONS

In summary, we have fabricated textured and polycrystalline Ni nanoparticles on epitaxial TiN and amorphous $Al_2O_3$ matrix, respectively. The Ni particles in a Ni/TiN sample grow epitaxially because the TiN matrix layer, which grows epitaxially on Si substrate by domain match, acted as the template whereas the growth of Ni particles in $Al_2O_3$ matrix is polycrystalline due to the amorphous nature of alumina. Two kinds of orientation relationships related to Ni grown on TiN were found. One is cube on cube, where (200) Ni // (200) TiN // (200) Si and (02 $\bar{2}$) Ni // (02 $\bar{2}$) TiN // (02 $\bar{2}$) Si and the particles grown in this orientation have a trapezoidal morphology in the [011] projection. The other involves a 90 ° degree rotation with respect to [011] direction of TiN matrix, where (0 $\bar{2}$2) Ni // (200) TiN // (200) Si and (200) Ni // (02 $\bar{2}$) TiN // (02 $\bar{2}$) Si. The particles grown in this orientation have a triangular morphology in the [011] projection and a smaller lattice constant compared to that of pure nickel. The blocking temperature of the Ni/TiN sample (~190 K) is significantly higher than that of $Ni/Al_2O_3$ sample (~30 K) with similar size of embedded magnetic particles. A comparison of the values of coercivity ($H_c$) of the two samples has shown that epitaxial Ni particles also exhibit significantly higher coercivity than polycrystalline randomly oriented Ni particles.

## ACKNOWLEDGMENTS

This research was supported by the US National Science Foundation Center for Advanced Materials and Smart Structures.

## REFERENCES

1. A.P. Alivisatos, Science **271,** 933 (1996).
2. C. B. Murry, C. R. Kagan and M. G. Bawendi, Science **270**, 1335 (1995).
3. V. F. Puntes, K. M. Krishnan and A.P. Alivisatos, Appl. Phys. Lett. **78**, 2187 (2001).
4. J. L. Dorman, D. Fiorani and E. Tronc, Adv. Chem. Phys. **98**, 283 (1997).
5. A. S. Edelstein and R. C. Cammarata, *Nanomaterials: Synthesis, Properties and Applications* (IOP, Bristol, 1998).
6. W. Luo, S. R. Nagel, T. F.Rosenbaum, and R. E. Rosensweig, Phys. Rev. Lett. **67**, 2721 (1991).
7. R. W. Chantrell, N. S. Walmsey, J. Gore and M. Maylin, Appl. Phys. Lett. **85**, 4320 (1999).
8. D. Kumar, H. Zhou, T. K. Nath, A. Kvit and J. Narayan, Appl. Phys. Lett. **79**, 2817 (2001).

9. T. Zheleva, K. Jagannadham and J. Narayan, J. Appl. Phys.**75**, 860 (1994).
10. C. L. Chien, Nanostructured Materials **1**, 179 (1992).
11. J. Narayan, US Patent No. 5,406,123 (11 April, 1995).

Mat. Res. Soc. Symp. Proc. Vol. 703 © 2002 Materials Research Society V9.16

# Thermal and Structural Characterization of Nanocomposite Iron Nitride - Alumina and Iron Nitride - Silica Particles

Ann M. Viano[1] and Sanjay R. Mishra[2]
[1]Department of Physics, Rhodes College, 2000 North Parkway
Memphis, TN 38112, U.S.A.
[2]Department of Physics, The University of Memphis,
Memphis, TN 38152, U.S.A.

## ABSTRACT

Nanocomposite iron nitride based powders are known to have enhanced magnetic and other physical properties. To further explore their potential for application in various fields, we have performed a systematic study of the iron nitride - alumina and iron nitride - silica systems. Iron nitride powder of composition $Fe_xN$ ($2 < x < 4$), containing both $Fe_3N$ and $Fe_4N$ phases, was mechanically milled with $Al_2O_3$ or $SiO_2$ powder for 4, 8, 16, 32, and 64 hours at the following compositions; $(Fe_xN)_{0.2}(Al_2O_3)_{0.8}$, $(Fe_xN)_{0.6}(Al_2O_3)_{0.4}$, $(Fe_xN)_{0.2}(SiO_2)_{0.8}$, and $(Fe_xN)_{0.6}(SiO_2)_{0.4}$. Differential thermal analysis and X-ray diffraction were performed to investigate thermal and structural transitions as a function of milling time. As the milling time is increased, the thermal peak corresponding to $Fe_4N$ is diminished, while the one corresponding to $Fe_3N$ is enhanced. These transitions are correlated with X-ray diffraction patterns. All XRD peaks broaden as a function of milling time, corresponding to smaller particle size. Transmission electron microscopy also reveals a decrease in particle size as the milling time in increased.

## INTRODUCTION

Small magnetic particles are important in many practical applications for their superior magnetic properties such as high saturation magnetization and high coercive field. Improvements in these properties have been obtained through sputtering [1,2] and mechanical alloying [3] of iron particles with alumina or silica, an improvement which has been correlated with a reduction in particle size. Metal-metalloids, such as $Fe_xN$, have these desirable magnetic properties, but conventional techniques used to produce small particles often lead to oxidation and the formation of an iron oxynitride surface layer, which is ferromagnetically coupled to the core of a particle. Surface oxidation may be avoidable by embedding single domain $Fe_xN$ particles in an insulating matrix such as $Al_2O_3$ or $SiO_2$. In fact, iron particles dispersed in such an insulating matrix have shown enhanced magnetic and mechanical properties [3-5]. In this work, small $Fe_xN$ particles are embedded in an insulating matrix through mechanical ball-milling. The resulting particles should have the advantageous properties of both small particle size and metal-metalloid composition. To fully understand the mechanisms producing these particles, structural and thermal studies are performed in this study to evaluate the phase formation as a function of milling time.

## EXPERIMENTAL DETAILS

Samples of iron nitride - alumina or iron nitride - silica were formed by mechanically milling powder of $Fe_xN$ ($2<x<4$) with $Al_2O_3$ or $SiO_2$ powder for 4, 8, 16, 32, or 48 hours in a Fritsch planetary ball mill. The 325 mesh powders were 99.9% pure. Oxidation during milling was prevented by milling in the presence of ethyl alcohol. The mixture of $Fe_xN$ powder to $Al_2O_3$ or $SiO_2$ powder was varied so that samples at each milling time were obtained for $(Fe_xN)_y(Al_2O_3)_z$ and $(Fe_xN)_y(SiO_2)_z$ with y = 0.2 and 0.8 (z = 0.8 and 0.2, respectively).

Thermal analysis was performed using an Instrument Specialists differential thermal analyzer with Pt/PtRd thermocouples and alumina sample and reference cups. $Al_2O_3$ powder was used as the reference material and scans were carried out with a heating / cooling rate of 10° / minute. Powder X-ray diffraction data was obtained with a Philips PC-APD3520 diffractometer using Cu $K_\alpha$ radiation. Samples were prepared for transmission electron microscopy (TEM) by sonicating the powder in methanol and then placing a few drops of the solution onto a holey-carbon coated grid. TEM was performed on a JEOL 1200 EX. TEM negatives were scanned at 1200dpi and then analyzed using the National Institute of Health's (NIH) Image software to measure particle size.

## RESULTS AND DISCUSSION

Figure 1 shows XRD plots for the milled compounds with y = 0.2 (z = 0.8) and the pure $Fe_xN$ powder. The starting $Fe_xN$ powder ($2 < x < 4$) is a mixture of $Fe_3N$ (ε phase) and $Fe_4N$ (γ').

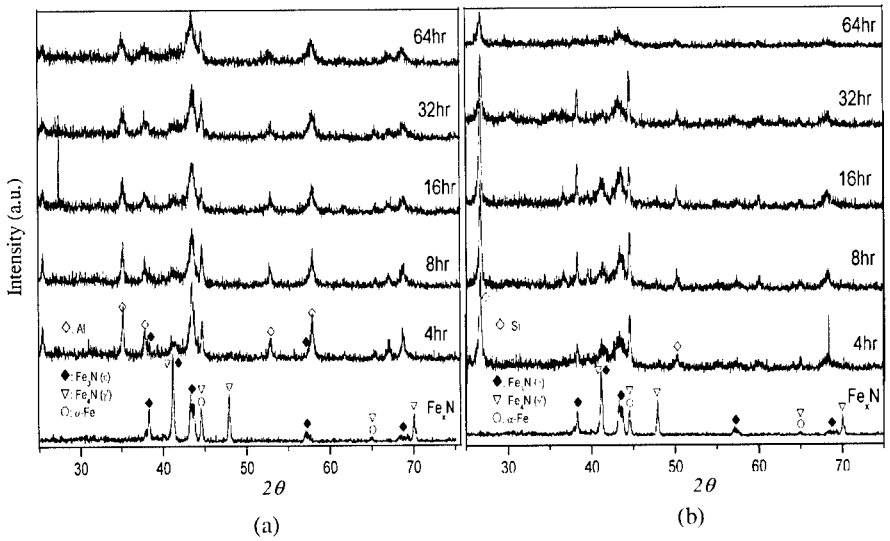


**Figure 1**: XRD patterns for (a) $(Fe_xN)_{0.2}(Al_2O_3)_{0.8}$ and (b) $(Fe_xN)_{0.2}(SiO_2)_{0.8}$ for the various milling times and for the starting $Fe_xN$ powder.

The peaks at 44.5° and 65.0° could be either α-Fe or γ' –$Fe_4N$. For the $Al_2O_3$ series (figure 1a), it is clear that peaks corresponding to $Fe_4N$ decrease in intensity with milling time. In particular, the $Fe_4N$ peaks at 48° and 70° completely disappear at even short milling times. An increase in milling time also correlates with an increase in the intensity of the $Fe_3N$ peaks, particularly those at 43.3° and 69°. This suggests that milling induces a transition from $Fe_4N$ to $Fe_3N$. Thus, there is an excess of Fe, which is evidenced by the enhancement of α-Fe peaks at 44.5° and 65°. The peak at 41° (γ' and ε) grows on high side with milling time, which indexes more to the $Fe_3N$ phase. A similar trend is seen for the $SiO_2$ series (figure 1b). The $Fe_3N$ peaks increase in intensity while the peaks corresponding to the γ' phase decrease. Again, the persistence of the peak at 44° suggests a growth of α-Fe due to excess Fe coming from the $Fe_4N$ to $Fe_3N$ transition. Similar results were obtained for the higher Fe composition samples; $(Fe_xN)_{0.6}(Al_2O_3)_{0.4}$ and $(Fe_xN)_{0.6}(SiO_2)_{0.4}$. All of the XRD peaks broaden as milling time increases, indicates a decrease in particle size.

Figure 2 displays the DTA traces for both series as well as the curve for the starting $Fe_xN$ powder. The ε phase ($Fe_3N$) has a wide range of solubility and its decomposition temperature at 25% N (atomic percent) occurs over a range of temperatures, but is less than 680°C for bulk material. $Fe_4N$, with a much narrower range of solubility, decomposes at 680°C for bulk material [6]. For small particles, these decompositions occur at lower temperatures. Decomposition temperatures of 570°C have been reported for 10μm $Fe_3N$ particles [7], and 410°C-582°C has been reported for 0.3-5μm $Fe_3N$ particles [8]. Table I displays our average

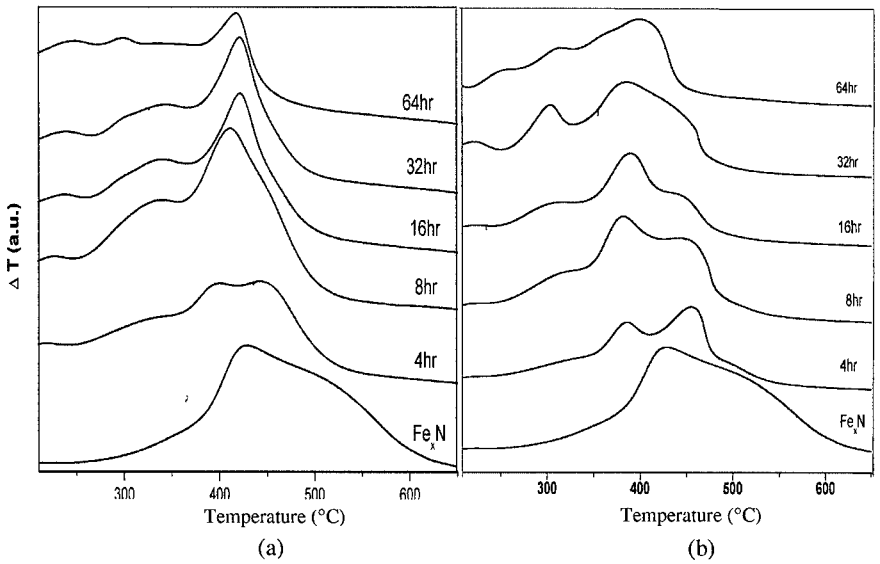


**Figure 2**: DTA curves for (a) the $(Fe_xN)_{0.2}(Al_2O_3)_{0.8}$ series and (b) the $(Fe_xN)_{0.6}(Al_2O_3)_{0.4}$ series. The y-axis is ΔT in °C, but normalized to show multiple curves on one graph. The peaks shown covered a range in ΔT of 20°C.

**Table I** Average particle size as measured by TEM studies for the $Al_2O_3$ samples.

| Milling Time (hr) | Average Particle Size (nm) | |
|---|---|---|
| | $(Fe_xN)_{0.2}(Al_2O_3)_{0.8}$ | $(Fe_xN)_{0.6}(Al_2O_3)_{0.4}$ |
| 4 | 376 | 516 |
| 8 | 278 | 340 |
| 16 | 172 | 232 |
| 32 | 159 | 200 |
| 64 | 64 | 110 |

particle sizes for the $Al_2O_3$ samples as measured by TEM. Since our particle sizes are all less than 0.5μm, the decomposition of the nitride phases will occur at lower temperatures. For the starting powder, which is a mixture of $Fe_3N$ (ε) and $Fe_4N$ (γ'), two exothermic peaks appear in range for nitride decomposition (400-600°C). The prominent peak at 425°C likely represents $Fe_3N$ decomposition, and the peak nested in its high temperature shoulder represents the decomposition of $Fe_4N$.

For the $Al_2O_3$ samples, the $Fe_3N$ peak becomes more prominent with milling time. This peak also shifts to slightly lower temperature, which correlates with the decrease in particle size upon increased milling time. This shows, as did the XRD data, the $Fe_4N$ being converted to $Fe_3N$ upon increased milling time. The DTA curves also show the growth of a peak between 300°C and 350°C as milling time increases. If the excess Fe is going into the α phase, as suggested by the XRD, this peak could correspond to a transition from γ' to α-Fe as N is liberated. Both of these phases have a wide range of solubility for N below 590°C. These lowest temperature peaks could also be due to adsorbed water or the presence of hydrocarbons in the samples, which were milled in ethyl alcohol to prevent oxidation. The two nitride phase peaks are most prominent in the samples with lower milling time (see the 4, 8, 16hr samples for $(Fe_xN)_{0.6}(Al_2O_3)_{0.4}$, figure 2b). As the milling time increases, the lower temperature peak is more prominent. The shift to lower temperature for the $Fe_3N$ peak is also most prominent in the $(Fe_xN)_{0.6}(Al_2O_3)_{0.4}$ series, although these particles are larger on average than those in the $(FexN)_{0.2}(Al_2O_3)_{0.8}$ samples. The higher concentration of $Al_2O_3$ is therefore partly responsible for the decomposition of the nitride phases.

A similar trend is seen for the $SiO_2$ samples (figure 3). For the $(Fe_xN)_{0.2}(SiO_2)_{0.8}$ (figure 3a) series, it is clear that the peak corresponding to $Fe_3N$ (400-450°C) grows with increasing milling time, indicating the presence of more $Fe_3N$ phase. This trend is also see for the $(Fe_xN)_{0.4}(SiO_2)_{0.4}$ series (figure 3b), with the exception of the 64hr and perhaps the 4hr sample. In these two cases, the $Fe_4N$ peak is more prominent. The three prominent peaks between 200°C and 375°C for the 64hr sample suggest that it may have oxidized or otherwise been contaminated. More studies should be performed to verify this suggestion.

## CONCLUSIONS

We have explored ball milling of $Fe_xN$ and an insulating component (alumina or silica) as a means of producing ultrafine $Fe_xN$ particles. A reduction of the $Fe_xN$ particle size is seen as

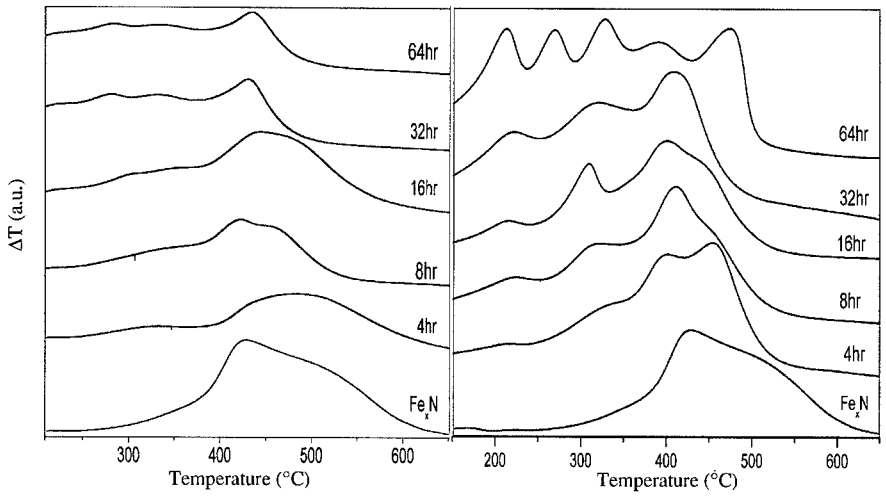


**Figure 3**: DTA curves for (a) the $(Fe_xN)_{0.2}(SiO_2)_{0.8}$ series and (b) the $(Fe_xN)_{0.4}(SiO_2)_{0.6}$ series. The y-axis is $\Delta T$ in °C, but normalized to show multiple curves on one graph. The peaks shown covered a range in $\Delta T$ of 20°C.

milling time increases, and this is accompanied by a transition from $Fe_4N$ to $Fe_3N$. Both structural and thermal characterization show that there is an increase of the ε $Fe_3N$ phase as milling time is increased. This decrease in size causes the decomposition of the $Fe_3N$ phase to shift to a lower temperature, and a broadening of lines in the XRD spectra. Studies of the magnetic properties of these ultrafine particles have been completed [9] and suggest that ball milling iron nitride particles is a viable technique to produce small particles with desirable magnetic properties.

## ACKNOWLEDGEMENTS

The authors would like to acknowledge Ms. Sharon Frase for her assistance with the electron microscopy performed in this study.

## REFERENCENES

1. C. L. Chien in *Science and Technology of Nanostructured Magnetic Materials*, edited by G. C. Hadjipanayis and G. A Prinz, (Plenum, New York, 1991) p. 32.
2. B. Abeles in *Applied Solid State Science: Advances in Materials and Devices Research*, edited by R. Wolfe, (Academic, New York, 1976) p. 1.
3. A. Gavrin and C. L. Chien, *J. Appl. Phys.* **67**, 938 (1990).

4. A. K. Giri, C. De Julian, and J. M. Gonzalez, *J. Appl. Phys.* **76**, 6573 (1994).
5. T. E. Schlesinger, R. C. Cammarata, A. Gavrin, C. L. Chien, M. F. Ferber, and C. Hayzelden, *J. Appl. Phys.* **70**, 3275 (1992).
6. K. H. Jack, *J. Appl. Phys.* **76**, 6620 (1994).
7. G. M. Wang, S. J. Campbell, and W. A. Kaczmarek, *Mat. Sci. Forum* **235-238**, 433 (1997).
8. W. A. Kaczmarek and B. W. Ninham, *J. Mat. Sci.* **30**, 5514 (1995).
9. S. R. Mishra, G. J. Long, F. Grandjean, R. P. Hermann, S. Roy, N. Ali, and A. Viano, *J. Appl. Phys.* (in press).

Mat. Res. Soc. Symp. Proc. Vol. 703 © 2002 Materials Research Society V9.19

# Structure and Nanocrystallites of Ni and NiO Three Dimensional Ordered Macromeshes

W.L. Zhou[a], L. Xu[a], A.A. Zakhidov[b], R.H. Baughman[b], and J.B. Wiley[a]
[a]Advanced Materials Research Institute, Department of Chemistry, University of New Orleans, LA 70148
[b]Honeywell Int., Corporate Technology, Morristown, NJ 07962
E-mail: wzhou@uno.edu

## ABSTRACT

Three dimensional Ni and NiO inverse opal macromeshes were characterized by scanning electron microscope (SEM) and transmission electron microscope (SEM). The octahedral cubes of the macroporous Ni were found mostly grown as single crystals with staking faults and microtwins. There was no preferential growth of these cubes as determined by selected area diffraction pattern (SADP). Some NiO nanocrystals with size of about 5 nm were formed on the surface of inverse Ni opal membrane during etching away of silica spheres. The oxidation of Ni mesh turned it into NiO macromesh with grain size of about 20 nm at 550°C. The nanocrystalline NiO mesh is suitable for further fabrication of three dimensional nanobeads. By annealing the meshes at 650°C, the NiO nanograins grew to a size of over 50 nm . This three dimensional ordered macroporous structure with higher temperature treatment is considered as stable and important for further application.

## INTRODUCTION

Recently we reported on the use of inverse opals as the templates to generate three dimensionally ordered nanobeads from various functional materials such as metals [1,2]. Therefore it is important to study the structure and nanocrystallites in such inverse metal membranes to understand its growth mechanism for future application. The fabrication of macromeshes of metal and polymer have been reported by several groups[3-7]. The potential applications of these three dimensional macroporous structure will be in photonic, catalysis and magnetics. The detailed study of the nanostructure and nanocrystallites could possibly improve the fabrication of three dimensional free standing macromesh for various purposes.

## EXPERIMENTAL

The opal template used here was composed of 290 nm silica spheres. The fabrication of macroprous Ni was done by electrochemical deposition, which was reported elsewhere[1]. The advantage of electrodeposition method is that one is able to control the filling depth by controlling the deposition time. Secondly it is easier to obtain homogenerous large scale free standing three dimensional macroporous structure for further application. Ni mesh was obtained by etching away silica beads using 2% HF. The NiO macromesh was obtained by slowly oxidizing the Ni mesh in open air by

heating to 550°C at 1°C/min. Scanning electron microscopy was performed using a JEOL 5410 SEM. Transmission electron microscopy investigation was carried out with a JEOL 2010 at 200kV. The TEM samples were prepared by putting small pieces of mesh on TEM copper grid and directly loaded in TEM for observation.

## RESULTS AND DISCUSSION

As-deposited opal sample was broken into small pieces and directly put in SEM for observation. Figure 1a is a SEM cross-sectional micrograph of the sample near the electrode side (Au film side). The Ni appeared as ordered white dots on the opal surface and was also confirmed by electron energy dispersive (EDS) analysis. It seems that the Ni infiltration was a bit uneven at the top area as shown in figure 1b. The white ordered dots among the spherical silica beads are Ni metal. It was hard to estimate the Ni deposition thickness under SEM.

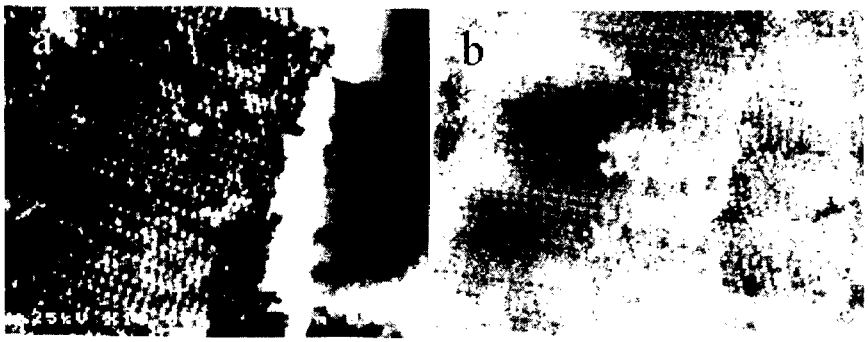


Figure 1. Cross-sectional SEM images of (a) nickel metal infiltrated near the Au film (b) nickel metal deposited at the top area of the opal.

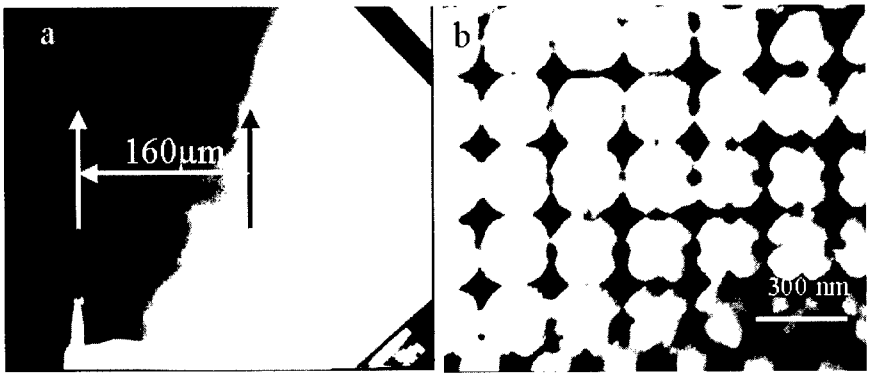


Figure 2. Cross-sectional TEM images of (a) thickness of infiltrated Ni in opal (b) the black nickel octahedral cubes infiltrated in the opal interstices.

In order to know the exact thickness of as-deposited Ni samples, a cross-sectional sample was prepared by gluing the sample between two silicon pallets and cutting into slices. The sample was then ground, polished and ion milled until transparency for electron beam. The thickness of the electrodeposited Ni could be clearly determined along the edge of the sample by TEM. In our case the thickness of the deposited Ni is around 160 um as shown in figure 2a. Figure 2b is (001) monolayer opal with the Ni (black contrast) infiltrated in the opal interstices. By putting the metal-opal into 2% HF solution for about 24 hours, we could etch away the colloidal silica and obtain the free standing rigid inverse Ni macromesh. Figure 3a is a SEM image observed from [001] direction. The square features are essentially cubes with concave sides that arise from filling the octahedral sites in the close packed structure. Each cube is connected to eight other cubes through its vertices via tetrahedra [2]. We can also see the second layer Ni cubes through the first layer Ni pores. The inset is the higher resolution SEM image which clearly shows the connections of octahedral and tetrahedral nickel cubes forming rigid Ni membrane. By loading a small piece of the inverse Ni macromesh on a TEM copper grid, the two dimensional projection of Ni network can be seen as shown in figure 3b. Microtwins and stacking faults were found as shown in the left inset by

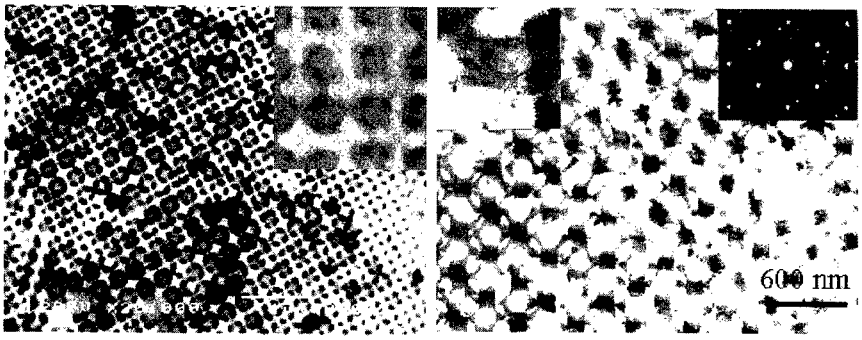


Figure 3 (a) (100) inverse nickel macroprorous. The inset is the higher resolution of connections of octahedral and tetrahedral nickel cubes. (b) TEM micrograph of inverse Ni frame. The inset on the left is a single octahedral cube and the left is the SADP of the cube.

carefully investigating a single cube, which can be also determined from the <011> SADP as shown in the right side inset. The streaks and twin diffraction spots can be clearly seen. By doing SADPs of many nickel octahedra, we found that most of the octahedral cubes formed single crystals during the electrodeposition. The reason for forming such unique structure is that the octahedral interstices have bigger space and gave enough time for Ni cubes to crystallize and grow into homogeneous structure. The connections of the macromesh were composed of nanograins. The narrow space of connections and large silica surface provide a rapid quenching environment for forming Ni nanograins. Even though the single crystal octahedral Ni cubes were formed, it was hard to find any preferential growth of these nanocubes by doing SADP. The SADP

showed polycrystalline feature with homogenous diffraction rings. The nanograins of the connections were composed of Ni nanocrystallites with size ranging from 20-50 nm. Additionally, some small nanocrystals with size about 5 nm was often found sticking to the surface of the Ni membrane after etching away silica beads as shown in figure 4a. By doing EDS analysis, these nanoparticles were contained Ni and oxygen, which was confirmed as NiO nanocrystals by doing SADP. Figure 4b is the high resolution image of these nanocrystals. Similar phenomena was also observed by Blanford *et al.*[9]. When they removed the template in an oxygen containing atmosphere, any metal form

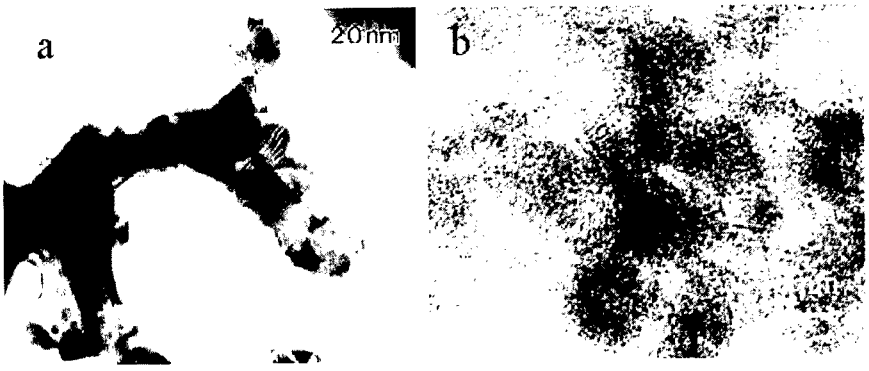


Figure 4 (a) some nanoparticles stick on the surface of the Ni macromesh. (b) HREM images of NiO nanocrystals.

was immediately oxidized forming metal oxide. In our case, when the silica beads were etched away, the fresh Ni surface was exposed to air and easily oxidized and formed NiO nanocrystals. In addition, the feature of Ni and NiO macromeshes are quite different from those prepared by chemical synthesis method reported by Yang *et al* [10]. In their samples Ni or NiO walls of macromeshes were composed of fused nanograins with size of about 50 nm and 6 nm, respectively. The NiO phase was found by them was hexagonal structure. In our case the nanocrystals of the NiO on the surface of the Ni membrane is of cubic structure with size about 5 nm.

By annealing the Ni membrane in air, the NiO semiconductor macromesh was obtained as shown in SEM image in figure 5a. The size of the pores became smaller due to the oxidation of Ni macromesh. The macromesh is quite uniform and good for further fabrication [2]. The annealing process turned the Ni membrane completely into a mesh consisted of NiO nanograins. Figure 5b is the (011) TEM image of the macromesh. All of the macromesh now was composed of fused NiO nanograins with an average diameter of 20 nm. The inset is the SADP of the NiO membrane with fcc structure. Further annealing of the NiO membrane at 650°C induced the NiO nanograins to grow bigger. TEM picture as shown in figure 6a shows that NiO nanograins grew into a size of 50-80 nm. By using the NiO macromesh as a template as shown in figure 6a, three dimensional ordered Au nanobeads were successfully fabricated. The higher temperature treatment made NiO membrane more stable for further application. Experiments are continuing for fabrication of metal nanobeads using NiO macromesh treated at 650°C.

## CONCLUSIONS

Three dimensional Ni and NiO membrane prepared by electrodeposition were studied by SEM and TEM, respectively. The octahedral cubes of Ni membrane were grown mostly as single crystals with stacking faults and microtwins. The connections of the membrane were composed of Ni nanograins with a size of about 10-50 nm. Small nanocrystals with size of about 5 nm were found on the surface of Ni membrane after etching away silica beads. The fresh Ni macromesh is air sensitive. By annealing the Ni mesh at 550°C, the membrane completely turned into a macromesh fused by 20 nm NiO nanograins. The template is good for fabrication of three dimensional ordered metal nanobeads. By annealing the NiO macromesh at 650°C, the NiO nanograins grew into bigger nanograins with a size over 50 nm. This membrane has potential applications.

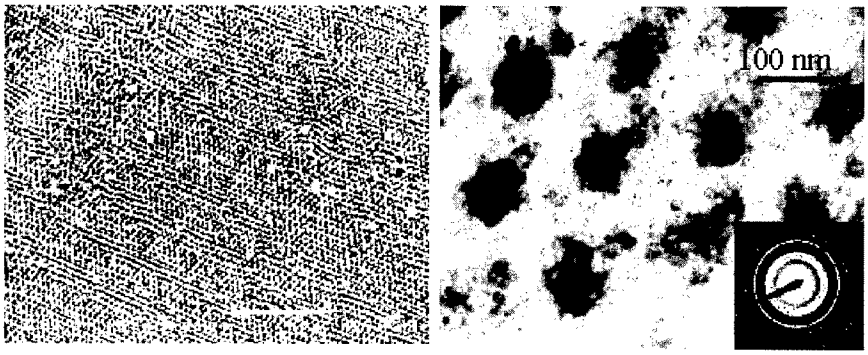


Figure 5 (a) SEM image of NiO macromesh after annealing Ni mesh at 550°C. (b) (011) TEM image of the NiO mesh composed of 20 nm nanograins. The inset is the SADP.

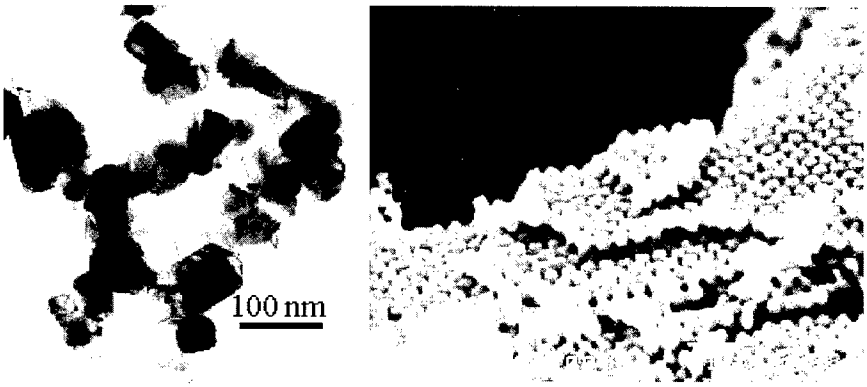


Figure 6 (a) 650°C heat treatment NiO membrane. (b) three dimensional ordered Au nanobeads.

## ACKNOWLEDGMENTS

This work is supported by the Department of Defense (DARPA MDA 972-97-1-0003 and DAAB07-97-C-J036).

## REFERENCES

1. L. Xu, W.L. Zhou, C. Frommen, R.H. Baughman, A.A. Zakhidov, L. Malkinski, J.-Q. Wang, and J.B. Wiley, *Chem. Commun.*, 997 (2000).
2. L.Xu, W.L. Zhuo, M.E. Kozlov, I.I. Khayrullin, I. Udod, A.A. Zakhidov, R.H. Baughman, and J.B. Wiley, *J. Am. Chem.Soc.* **123**, 763 (2001).
3. B.T. Holland, C.F. Blanford, and A. Stein, Science **281**, 538 (1998).
4. O.D. Velev, P.M. Tessier, A.M. Lenhoff, and E.W. Kaner, Nature **401**, 548 (1999).
5. S.A. Johnson, P.J. Ollivier, and T.E. Mallouk, *Science* **283**, 963 (1999)
6. A.A. Zakhidov, R.H. Baughman, I.I. Khayrullin, I. Udod, M. Kozlov, N. Eradat, V. Z. Vardeny, M. Sigalas, and R. Biswas, *Synth, Metals* **116**, 419 (2001).
7. R. Rengarajan, P. Jiang, V.Colvin, and D. Mittleman, *Appl. Phys. Lett.* **77**, 3517 (2000).
8. (a) N.D. Deniskina, D.V. Kalinin, and L.K. Kazantseva, *Gem Quality Opals: Syntheic and Nature Genesis,* Nauka, Novosibirsk, 1988 (in Russian); A.P. Philips, *J. Mater. Sci. Lett.* **8**, 1371; and (c) P.J. Darragh, A.J. Gaskin, and J.V. Sanders, *Scient. Amer.* **234**, 84 (1976).
9. C.F. Blanford, H. Yan, R.C. Schroden, M. Al-Daous, and A. Stein, *Advanced Materials* **13**, 401 (2001).
10. H. Yan, C.F. Blanford, B.T. Holland, M. Parent, W.H. Smyrl, and A. Stein, *Advanced Materials* **11,** 751 (1999).

Mat. Res. Soc. Symp. Proc. Vol. 703 © 2002 Materials Research Society V9.20

# Substrate Dependence in the Growth of Three-Dimensional Gold Nanoparticle Superlattices

S. Sato, N. Yamamoto, H. Yao and K. Kimura
Department of Material Science, Himeji Institute of Technology,
3-2-1 Koto, Kamigori-cho, Ako-gun, Hyogo 678-1297 JAPAN

## ABSTRACT

Three-dimensional superlattices consisting of gold nanoparticles were grown at air/suspension or suspension/solid interfaces. The growth of superlattices was found to be strongly dependent on substrate materials: Micrometer-sized superlattices were grown at air/suspension interfaces and upon silver substrates, whereas no growth was observed on silicon, silicon oxide, or amorphous carbon substrates. To explain the observed substrate dependence, Lifshitz theory was used to calculate the Hamaker constants between gold nanoparticle assemblies and substrates through the suspension. Van der Waals interactions estimated from this calculation fully explain the experimental results.

## INTRODUCTION

Three-dimensional (3D) superlattices of nanoparticles represent a class of promising new electronic materials whose band structures may be engineered through control of core sizes, of surface coverage thicknesses, and of packing arrangements for the nanoparticles. Recently, high-quality superlattices have been synthesized using the self-assembly process of nanoparticles in liquid phases [1-4]. For superlattices to be introduced into industrial applications, they need to be grown at gas/solution or solution/solid interfaces. However, there have been no reports focusing on superlattice growth at various interfaces. Recently, we have found that gold (Au) nanoparticles, whose surfaces are modified with hydrophilic surfactants, are good components for 3D superlattices since the assembly rate of Au nanoparticles (i.e., the growth rate of superlattices) is widely tunable through pH control [5,6]. By enforcing an extremely slow growth rate (i.e., equilibrium growth), Au nanoparticles self-assemble into high-quality lattice arrangements. In this communication, we report substrate dependence in the growth of Au nanoparticle superlattices in aqueous suspensions.

## EXPERIMENTAL

The preparation of Au nanoparticles is outlined as follows. 4.1 ml of an aqueous solution of 0.12 M hydrogen tetrachloroaurate tetrahydrate ($HAu(III)Cl_4 \cdot 4H_2O$) was mixed with 100 ml of methanol containing 1.5 mM of mercaptosuccinic acid (MSA). 25 ml of an aqueous solution of 0.2 M sodium borohydride ($NaBH_4$) was then added under vigorous stirring. After the reaction, Au nanocrystals were obtained whose surfaces were modified with MSA. The solvent was decanted after centrifugation at 9840×g, which corresponds to 10,000 rpm for the Kubota 1720 centrifuge. Samples were then washed twice with a 20 % (v/v) water-methanol solution by repeating re-suspension with a sonicator and re-centrifugation, and finally dialyzed to remove inorganic (Na, Cl, and B) and organic impurities.

The surfactant affects the dispersion of Au nanoparticles in aqueous suspensions at low ion concentrations. After the Au nanoparticles were dispersed in distilled water, hydrochloric acid (HCl) was then added into the suspension. This process induced self-assembly of the nanoparticles. This is a

result of the added protons suppressing ionization of the surfactants and hence, weakening repulsive interactions among the nanoparticles. Silver (Ag), silicon (Si), Si oxide, or amorphous carbon (a-C) substrates were immersed in the suspension, and samples were stored in a closed glass bottle to prevent solvent evaporation. Prior to the experiment, the surface oxide of Si substrates was removed by dipping into a 47 wt. % HF solution.

The obtained superlattices were examined with a transmission electron microscope (TEM: Hitachi H −8100) operated at 200 kV, and a scanning electron microscope (SEM: Philips XL-20LaB6) operated at 9 kV.

## RESULTS

### Growth at air/suspension interfaces

With an appropriate amount of HCl, superlattices appeared at the air/suspension interface within 4 - 10 days. Figure 1 shows TEM images of (a) the overall shapes of the superlattices and (b) an edge of one of the superlattices. Superlattices achieved widths of several micrometers and formed faceted structures as shown in image (a). This indicates that they were grown under equilibrium conditions [7,6]. Image (b) shows that Au nanoparticles form a close-packed arrangement in the superlattices. The diameters of the component nanoparticles are 4.9 nm: The core diameters of the component nanoparticles are 3.5 nm, and the thickness of the surfactants is 0.7 nm.

### Growth at suspension/substrate interfaces

After the addition of an appropriate amount of HCl into the suspension, superlattices were grown on

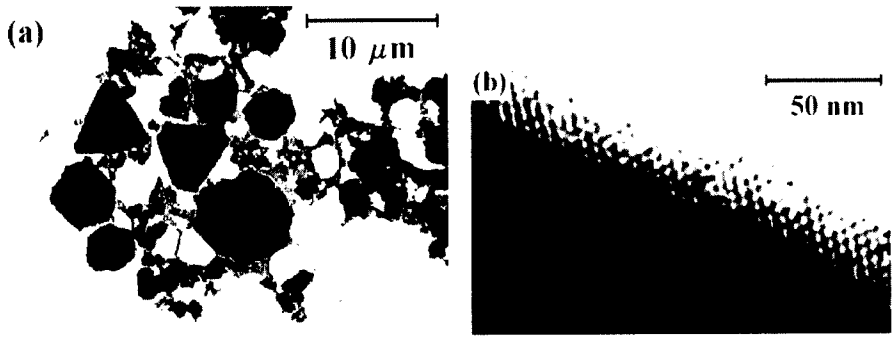


**Figure 1.** TEM images of superlattices grown at the air/suspension interface: (a) a low magnification image, and (b) a typical image of an edge of the superlattice. The superlattices were prepared with an HCl concentration of $3.6\times10^{-1}$ M.

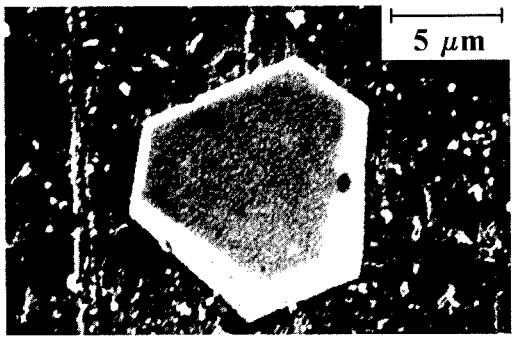


**Figure 2.** A typical SEM image of a superlattice grown on an Ag substrate. The sample was prepared with an HCl concentration of $3.6\times10^{-2}$ M.

Ag substrates, however, no growth was observed on Si, Si oxide, or a-C substrates. A typical SEM image of a superlattice grown on an Ag substrate is shown in Fig. 2. After sufficient growth, the superlattices spanned several micrometers, and they formed clear facets, indicating formation of the desired superlattices.

## DISCUSSION

Throughout this discussion, we will consider interactions between Au nanoparticle assemblies and substrates to determine the observed substrate dependence. Interactions between two materials consist of (1) surface interactions such as Coulombic and hydrophobic interactions; and (2) volume interactions such as the van der Waals interaction [8]. In general, surface interactions are dominant in nanostructured materials as the number of atoms at the surface is significant relative to the volume. However, our experimental results are not fully explained by surface interactions. The attractive interaction between air and the Au nanoparticle assemblies cannot be explained solely by Coulombic interactions. Although this attractive interaction can be explained by hydrophobic interactions, it conflicts with the experimental observation that assemblies are not attracted to other hydrophobic materials, such as hydrogen-terminated Si or a-C. It appears that a volume interaction needs to be taken into account for complete understanding of the observed substrate dependency.

To consider volume interactions, we calculate the Hamaker constants between the Au nanoparticle assemblies and various substrates across water, which describe the attractive or repulsive magnitude of the van der Waals interaction. In Lifshitz theory [8], the Hamaker constant between material 1 and material 2 across medium 3 is given by

$$A \approx \frac{3}{4}kT\left(\frac{\varepsilon_1-\varepsilon_3}{\varepsilon_1+\varepsilon_3}\right)\left(\frac{\varepsilon_2-\varepsilon_3}{\varepsilon_2+\varepsilon_3}\right)+\frac{3h}{4\pi}\int_{\nu_1}^{\infty}\left(\frac{\varepsilon_1(i\nu)-\varepsilon_3(i\nu)}{\varepsilon_1(i\nu)+\varepsilon_3(i\nu)}\right)\left(\frac{\varepsilon_2(i\nu)-\varepsilon_3(i\nu)}{\varepsilon_2(i\nu)+\varepsilon_3(i\nu)}\right)d\nu, \qquad (1)$$

where $\varepsilon_1$, $\varepsilon_2$, and $\varepsilon_3$ are the static dielectric constants of the three materials, $\varepsilon(i\nu)$ are the values of $\varepsilon$ at imaginary frequencies, and $\nu_1$ is $2\pi kT/h$. Using appropriate forms of $\varepsilon(i\nu)$ is the key for successful estimation of the Hamaker constants in the present calculation.

Let us consider what form of $\varepsilon(i\nu)$ is suitable for Au nanoparticle assemblies. We will begin by assuming Au nanoparticles as artificial atoms. The conduction electrons in a metal nanoparticle behave not as a relaxator system, but as an oscillator system with an eigenfrequency equal to the surface plasmon frequency of the metal [9]. This means that Au nanoparticles can be likened to atoms of the Thomson model. The number of valence electrons in this artificial atom corresponds to the number of conduction electrons in an Au core: $N_v = (4/3)\pi R^3 n_{Au}$, where $R$ is the radius of the Au core and $n_{Au}$ is the conduction electron density of bulk Au ($5.9\times10^{28}$ m$^{-3}$). Since MSA is an insulator, the contribution of conduction electrons from MSA to the artificial atom is neglected. Au nanoparticle assemblies are, therefore, likened to virtual dielectrics consisting of those artificial atoms. Assuming that the artificial atoms are simple harmonic oscillators with the eigenfrequency $\nu_0$, the function $\varepsilon(i\nu)$ of the virtual dielectrics is

$$\varepsilon(i\nu) = 1 + \frac{n_a N_v e^2}{4\pi^2 \varepsilon_0 m} \cdot \frac{1}{\nu_0^2 + \nu^2 + \nu\Gamma/(2\pi)}, \qquad (2)$$

where $n_a$ is the number density of the artificial atoms in a virtual dielectric and $\Gamma$ is the damping factor. We set the number density, $n_a$, to the value at which nanoparticles form closest-packing arrangements. From optical studies of our superlattices [10], the surface plasmon frequency $\nu_0$, the damping factor $\Gamma$, and the optical mass $m$ were estimated to be $4.6\times10^{14}$ sec$^{-1}$, $1.4\times10^{15}$ sec$^{-1}$, and 2.5 $m_e$ ($m_e$: mass of free electrons), respectively. The static dielectric constant of the virtual dielectric was estimated by substituting 0 for $\nu$ in Eq. 2. For $\varepsilon(i\nu)$ of Ag, Si, $SiO_2$, and a-C substrates and water, we used the equations shown in Ref. 8. In addition to those substrates, we also analyzed AgCl substrates since the surface of our Ag substrates may be chloridized as a result of the HCl addition. Physical parameters to construct $\varepsilon(i\nu)$ of $SiO_2$ and water are listed in Ref. 8. For other substrates, the following parameters are used, the static dielectric constant, the refractive index, and the main electronic absorption frequency of Si are 12, 3.5, and $1.0\times10^{15}$ sec$^{-1}$, respectively [11], and those of AgCl are 11, 2.1, and $1.2\times10^{15}$ sec$^{-1}$, respectively [12, 13]; The volume plasmon frequency of Ag is $9.1\times10^{14}$ sec$^{-1}$ [14], and that of a-C is $6.3\times10^{15}$ sec$^{-1}$ [14].

Using all of the above equations and parameters, interactions between the virtual dielectrics, which represent Au nanoparticle assemblies, and the substrates were calculated. Figure 3 shows the calculated Hamaker constants as a function of the diameters of component nanoparticles. The positive and negative values correspond to attractive and repulsive interactions, respectively. The Hamaker constants at the diameter of the component particles, 4.9 nm, predict the following interactions. Au nanoparticle assemblies are attracted to the air and Ag substrates, but repulsed from $SiO_2$, Si and a-C substrates. These results perfectly explain the experimental results. The interaction between Au nanoparticle assemblies and AgCl is almost neutral at 4.9 nm. Thus, even if an AgCl layer is grown on the Ag surface, the layer does not inhibit the attractive interaction between Au nanoparticle assemblies and Ag substrates.

It is quite surprising that the experimental results are fully explained without the consideration of surface interactions. This may indicate that our proton density in the aqueous suspensions was appropriate for neutralizing hydrophilicity/hydrophobicity as well as suppressing Coulombic interactions. In the present experiment, an extremely slow growth rate for the superlattices was tuned by adjusting the HCl concentration. Thus, the proton density was adjusted to balance attractive and

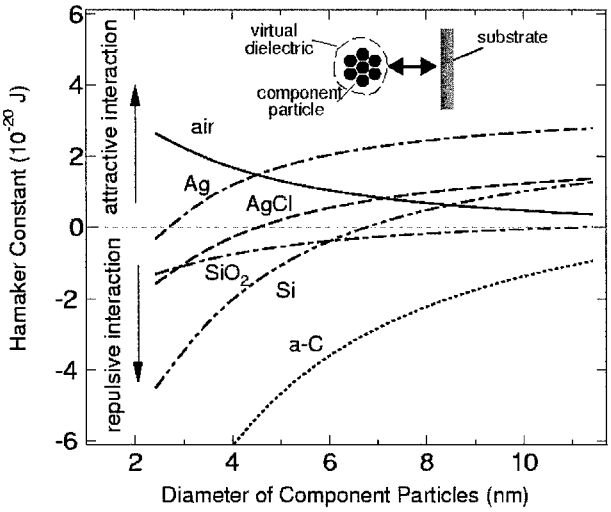


**Figure 3.** Substrate dependency of the Hamaker constants between the virtual dielectrics and various substrates through water as a function of the diameters of component nanoparticles. The virtual dielectrics represent the close-packing assemblies of Au nanoparticles.

repulsive interactions between the nanoparticles. This adjustment may prove to be a general procedure by which the surface interactions of MSA monolayers become insignificant. To verify this hypothesis, an investigation of the pH dependence of surface forces of MSA monolayers is currently underway.

## CONCLUSIONS

We investigated substrate dependence in the growth of Au nanoparticle superlattices in aqueous suspension. Superlattice growth proceeded at the air/suspension interface and the suspension/Ag interface. After sufficient growth, the superlattices reached widths of several micrometers and formed clear facets. In contrast, no growth was observed on Si, $SiO_2$, and a-C substrates. The observed substrate dependency was not explained by surface interactions but by the van der Waals interaction. The Hamaker constants between Au nanoparticle assemblies and substrates through water were calculated using the Lifshitz theory. In the calculation, Au nanoparticle assemblies were assumed as virtual dielectrics consisting of artificial atoms of Thomson model. The calculation results well explained the experimental observations.

## ACKNOWLEDGEMENTS

This study was supported by the Hosokawa Powder Technology Foundation, the Mitsubishi Research Institute, and the Japan Space Utilization Promotion Center.

## REFERENCES

1. A. Taleb, C. Petit and P. Pileni, Chem. Mater. **9**, 950 (1997).
2. S. A. Harfenist, Z. L. Wang, M. M. Alvarez, I. Vezmar and R. L. Whetten, J. Phys. Chem. **100**, 13904 (1996).
3. C. B. Murray, C. R. Kagan and M. G. Bawendi, Annu. Rev. Mater. Sci. **30**, 545 (2000).
4. C. P. Collier, T. Vossmeyer and J. R. Heath, Annu. Rev. Phys. Chem. **49**, 371 (1998).
5. K. Kimura, S. Sato and H. Yao, Chem. Lett. 372 (2001).
6. S. Sato, N. Yamamoto, H. Yao and K. Kimura, (to be published).
7. A. Zangwill, *Physics at Surfaces* (Cambridge University Press, Cambridge, 1988) pp. 12 - 15.
8. J. Israelachvili, *Intermolecular and Surface Forces* (Academic Press, London, 1992).
9. U. Kreibig, and M. Vollmer, *Optical Properties of Metal Clusters* (Springer-Verlag, Berlin, 1995) pp. 23 - 25.
10. S. Sato, H. Yao and K. Kimura, (to be published).
11. S. Adachi, *Optical Constants of Crystalline and Amorphous Semiconductors* (Kluwer Academic Publishers, Boston, 1999) pp. 18 – 32.
12. D. R. Lide, *CRC Handbook of Chemistry and Physics*, 77th ed. (CRC press, Boca Raton, 1996) p. **12**-45.
13. H. Kanzaki, Photo. Sci. Eng., **24**, 219 (1980).
14. H. Raether, *Excitation of Plasmons and Interband Transitions by Electrons* (Springer-Verlag, Berlin, 1980) pp. 51 - 52.

Mat. Res. Soc. Symp. Proc. Vol. 703 © 2002 Materials Research Society V9.22

# Topology and Electronic Structure of Onion-Like Carbon and Graphite/Diamond Nanocomposites.

Lyubov G. Bulusheva[1], Alexander V. Okotrub[1], Vladimir L. Kuznetsov[2], Andrew L. Chuvilin[2], Yuriy V. Butenko[2], Malcolm I. Heggie[3]
[1]Institute of Inorganic Chemistry SB RAS, Novosibirsk, RUSSIA.
[2]Boreskov Institute of Catalysis SB RAS, Novosibirsk, RUSSIA.
[3]School of Chemistry, Physics and Environmental Science, University of Sussex at Brighton, UK.

## ABSTRACT

Annealing of nanodiamond at moderate temperature makes it possible to produce structures being intermediate in the carbon transformation from $sp^3$- to $sp^2$-state (graphite/diamond nanocomposites) and onion-like carbon (OLC). Electron microscopy shows such structures involve cage shells with spacing close to graphite. X-ray emission spectroscopy has been applied to examine the electronic structure of OLC and graphite/diamond nanocomposites. The CKα-spectra of OLC produced in the temperature range of 1600-1900 K were found to be markedly different from the spectrum of particles formed at 2140 K and characterized by better ordering of graphitic shells. The latter spectrum was shown to be very similar to the CKα-spectrum of polycrystalline graphite, while the former ones exhibited a significant increase of high-energy maximum that might be caused by the holed defect structure of graphitic networks forming at the intermediate annealing temperatures. To interpret experimental spectra, the quantum-chemical semiempirical AM1 calculation of icosahedral $C_{540}$ cage and that with holed defects was carried out. The lack of at least 22% atoms in an internal carbon cage was found to be essential to provide an increase of density of high-energy electronic states similar to that observed in the spectrum of OLC produced at 1900 K.

## INTRODUCTION

Onion like carbon (OLC) is one of the nanostructured forms of carbon consisting of fullerene like shells enclosed each into another. It can be formed via two principally different approaches. First approach uses a condensation of carbon atoms or small clusters in gas phase during an electric arc discharge [1] or in metal matrix [2]. Another approach is based on the transformation of condensed carbon under high-energy treatment. So Ugarte has found the curling and closure of graphitic networks of carbon soot into OLC particles under electron beam irradiation [3]. Later we developed technique, which allows producing hundreds of grams OLC by heat treatment of nanodiamond (ND) [4]. Two different types of OLC carbon can be produced by these mentioned methods, one contains spherical shells another one consists of polygonized shells. The latter contains fullerene like spheres with twelve pentagons, which preferentially responsible for the formation of polygonized structure. It should be mentioned that

polygonized OLC is usually formed after heat treatment of carbon soot [5] or spherical OLC [4] at the temperature higher than 2000 K.

To explain the sphericity of onions formed under electron beam irradiation of carbon [6] the structural models including combinations of pentagons and octagons have been proposed by Terrones [7]. Recently, we proposed that the sphericity of onions produced by ND annealing at the intermediate temperature (1400–1900 K) can be explained by the formation of holed structure of onion shells [8]. Here we used a combination of X-ray fluorescence spectroscopy and quantum-chemical simulation for the characterization of the electronic structure of OLC and graphite/diamond nanocomposites produced via the controlled annealing of ND.

## EXPERIMENTAL AND CALCULATION DETAILS

In this work we used ND powders with average particle sizes of 4.7 nm, obtained by explosion of TNT/RDX mixture [9]. Non-diamond forms of carbon were removed by boiling the sample in a 1:1 mixture of concentrated $H_2SO_4$ and $HClO_4$ at 130-200°C [10]. The annealing of ND samples was performed in a high vacuum chamber at temperatures 1170, 1600, 1900, and 2140 K (samples I, II, III, and IV respectively). The micrographs of the products were obtained with a JEM-2010 transmission electron microscope.

X-ray fluorescence spectra of ND and ND annealing products and non-textured polycrystalline graphite (CKα spectra) were recorded with X-ray spectrometer "Stearat" using a crystal-analyzer from ammonium biphtalate [11]. The samples were deposited on copper supports and cooled down to liquid nitrogen temperature in the vacuum chamber of the X-ray tube operating with copper anode (U=6 kV, I=0.5 A). Determination of X-ray band energy was accurate to ±0.15 eV with spectral resolution of ~0.5 eV.

The quantum-chemical calculations of carbon cages were carried out using semiempirical AM1 method [12]. The fullerene molecule $C_{540}$ being a third inner shell of ideal spherical onion [13] was chosen as a model of a closed graphitic cage. The cages $C_{456}$ and $C_{420}$ were obtained by removing all pentagonal rings and respectively two or five neighboring atoms from the $I_h$ $C_{540}$. Theoretical CKα spectra were built in the framework of the frozen orbital approximation (Koopman's theorem) on the basis of calculation of the ground state of compound. X-ray transition intensity was calculated by summing the squared coefficients for carbon 2p atomic orbitals (AOs) in the real occupied molecular orbital (MO). The energy location of intensity corresponded to the MO eigenvalue. Intensities so obtained were normalized by maximal value and broadened by convolution with Lorentzian functions of 0.6 eV half width at half maximum (HWHM).

## RESULTS AND DISCUSSION

CKα-spectra of the ND and its annealing products are presented in figure 1 together with high-resolution transmission electron microscopy (HRTEM) images of the samples. The CKα-spectrum of sample I exhibits one broad maximum around 279 eV and is almost coincident with

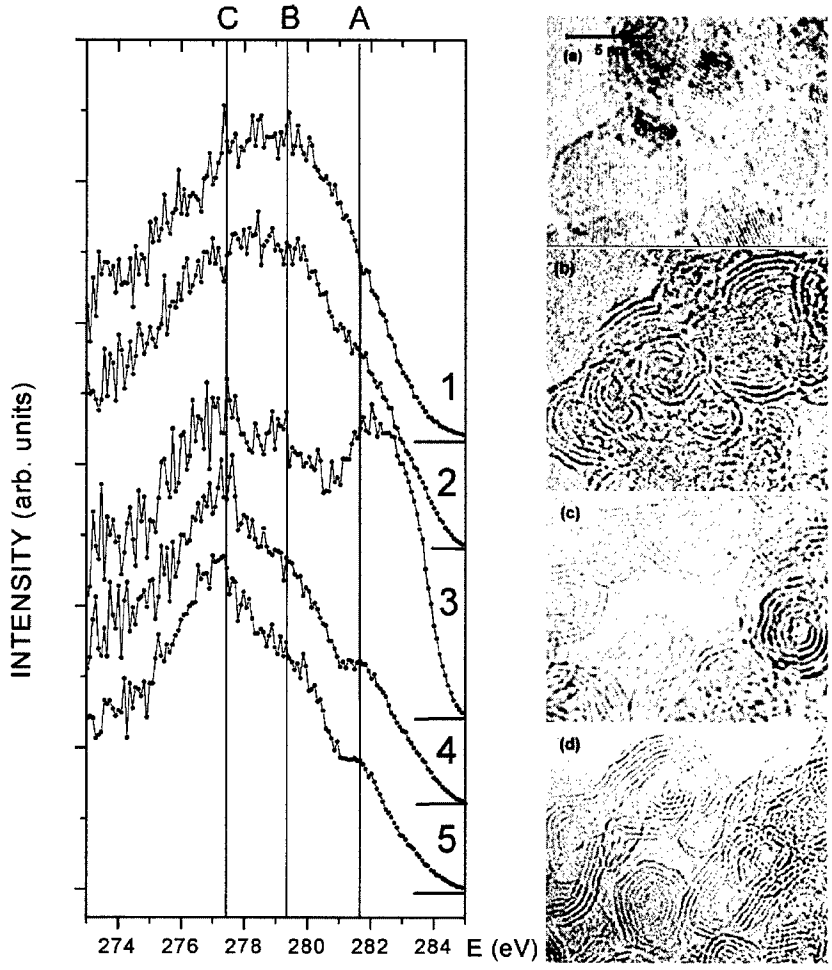


**Figure 1.** CKα-spectra of the samples produced at 1170 K (1), 1600 K (2), 1900 K (3), and 2140 K (4), and of non-textured polycrystalline graphite (5). HRTEM images of measured samples: (a) – sample I, the dark contrast lines in micrographs indicate the (111) crystallographic diamond layers, which are separated by 0.206 nm; (b) – sample II, (c) – sample III, and (d) – sample IV. The dark contrast closed circles lines in micrographs (b), (c) and (d) correspond to graphite-like sheets. The distance between these sheets (~0.35 nm) is closed to that of graphite (0.34 nm).

the spectrum of diamond single crystal [14]. A presence of interference fringes spaced by 2.06 A (figure 1(a)) is evidence for the diamond particles in this sample. The CKα-spectrum of sample II is slightly different from the former spectrum by somewhat more pronounced high-energy shoulder A. The image of the sample II demonstrates the rearrangement of ND surface into graphite layers with the retention of a portion of diamond particles (figure 1(b)). As CKα-spectrum measures the density of 2p-occupied states for all carbon atoms in a sample, the enhanced intensity of the shoulder A in the spectrum of sample II is caused by the atoms forming graphitic layers. The CKα-spectrum of sample III consisted of OLC (figure 1(c)) exhibits three maxima at 277.5, 279 and 282 eV. The further heating of ND above 2140 K led to the polyhedral hollow OLC particles (sample IV depicted in figure 1(d)). The CKα-spectrum of this sample has the main maximum C around 277.5 eV, the high-energy shoulder B around 279.2 eV, and the short-wave maximum A at 281.6 eV and it is in good agreement with the spectrum of polycrystalline graphite (figure 1). Some variation in the location of the main maximum and in the relative intensities for the former spectrum may be attributed to the contribution of the edge states of polyhedral particles.

Inspection of the spectra indicated the electronic state of carbon particles produced at the initial and final stage of ND annealing mainly corresponds to that characteristic of diamond and graphite respectively. Although the sample of OLC (sample III) is intermediate product in the transformation from ND particles to polyhedral graphitic particles, its spectrum is considerably different from another measured spectra. Maximum A in the CKα-spectrum of sample III is comparable with main maximum C by intensity. Furthermore, this maximum is shifted by 0.4 eV toward the high-energy spectral region relative to the position of maximum A in the graphite spectrum. These two effects indicate the enhanced localization of weakly bonding electrons in OLC. The localization might result from defects in the curved graphitic networks, namely, the dandling bonds. The origin of such defects accompanying of the OLC formation can be explained in terms of deficit of diamond carbon atoms in the graphite/diamond interface to form perfect fullerene-like shells [8]. When the temperature of ND treatment reaches about 2100 K and mobility of carbon atoms increases the defects in OLC anneal out.

To reveal the effect of a portion of dandling bonds on the density of occupied 2p-electronic states the quantum-chemical calculations of carbon cages (figure 2) were performed using AM1 method. The theoretical spectrum of icosahedral $C_{540}$ has three features A, B, and C, which intensity and energetic separation are in good agreement with corresponding values in the CKα-spectrum of sample IV. The maxima C and A correspond to σ- and π- like MOs, while the shoulder B is formed by both types of orbitals. The spectra of cages $C_{456}$ and $C_{420}$ show a sequential increasing of the maximum A relative to that in the $C_{540}$ spectrum.

Formation of the holes causes a disruption of joint π-system in $C_{540}$ and, hence, π-electron localization. This localization however cannot provide the increase of density of weekly bonding states observed in the experiment. It is evident that the electrons of dangling bonds contribute to the maximum A of spectra of the holed cages. The localization of electron density on the zigzag sites of graphitic edges was found in [15,16]. The edges of holes in the $C_{456}$ cage are actually zigzag-like, while those in the $C_{420}$ cage are armchair-like. Considerable increasing of the maximum A in the $C_{420}$ spectrum compared to that in the $C_{456}$ one indicates that the shape of boundary of a hole is not important. The governing factor is a portion of the dangling bonds, that is about 15% and 22% in the cages $C_{456}$ and $C_{420}$ relative to the perfect $C_{540}$ shell.

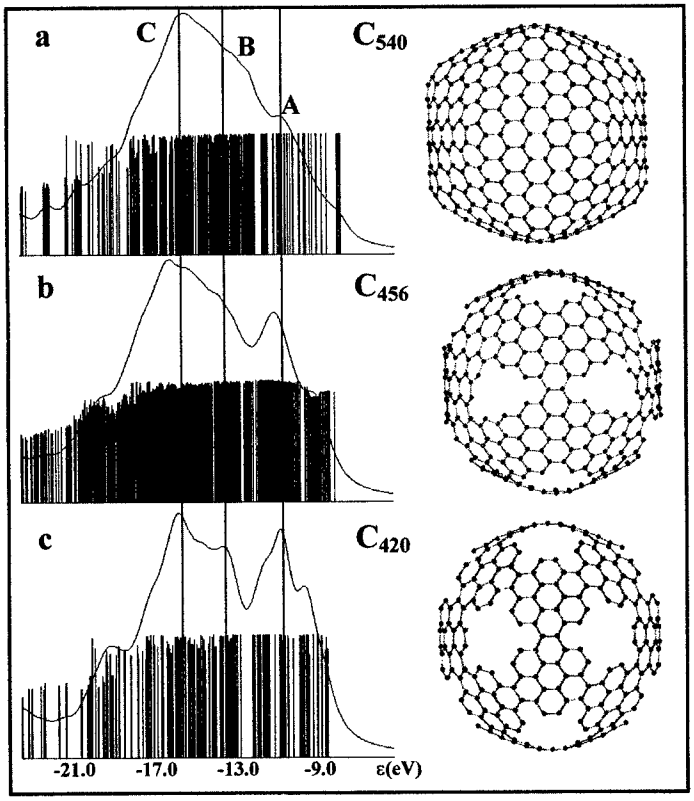


**Figure 2.** Theoretical CKα-spectra plotted by the result of AM1 calculation on the carbon cages $C_{540}$ (a), $C_{456}$ (b), and $C_{420}$ (c).

Accidental near degeneracy in energy of the localized π-states and electron states of the dangling bonds provides the high total density observed in the high-energy region of the holed carbon cages (figure 2). At the same time one can observe increasing of the density of states around –9.0 eV that is in the correspondence with the detected shifting of the maximum A in the CKα-spectrum of sample III. The changes found from the comparison between the spectra of $C_{540}$ and $C_{420}$ cage are similar to those observed in the CKα-spectra of polyhedral particles (sample IV) and OLC (sample III). We suggest the network of OLC prepared by ND annealing incorporates the dandling bonds in an internal carbon cage, which portion is about 22% or some more.

## CONCLUSION

X-ray fluorescence spectroscopy investigation of OLC and graphite/diamond nanocomposites produced at various temperatures of ND annealing detected the enhanced density of weekly bonding states in the former material. Quantum-chemical calculations on the carbon cages showed such enhancement is more likely explained by the occurrence of dandling bonds in an internal carbon cage, which may significantly modify the chemical and physical properties of OLC compared to the polyhedral graphitic particles prepared on the final stage of ND annealing. The holes in OLC may cause unusual effects in its transport, magnetic and optic properties [17].


## ACKNOLEDGEMENTS

Research was supported by the INTAS (Project Nos. 97-1700, 01-237), the Russian Foundation for Basic Research (Project Nos. 00-03-32463a, 00-03-32510a), CRDF grant REC 008, and the Royal Society via a Joint Project grant.


## REFERENCES


1. S. Iijima, *J. Cryst. Growth* **50**, 675 (1980).
2. T. Cabioc'h, J.C. Girard, M. Jaouen, M.F. Denanot; and G. Hug, *Europhys. Lett.* **38**, 471 (1997).
3. D. Ugarte, *Nature* (London) **359**, 707 (1992).
4. V.L. Kuznetsov, A.L. Chuvilin, Yu.V. Butenko, I.Yu. Mal'kov, and V.M. Titov, *Chem. Phys. Lett.* **222**, 343 (1994).
5. W.A. de Heer and D. Ugarte, *Chem. Phys. Lett.* **207**, 480 (1993).
6. F. Banhart, T.Fuller, Ph. Redlich, and P.M. Ajayan, *Chem. Phys. Lett.* **269**, 349 (1997).
7. M. Terrones and H. Terrones, *Fullerene Sci. Technol.* **4**, 517 (1996).
8. A.V. Okotrub, L.G. Bulusheva, V.L. Kuznetsov, Yu.V. Butenko, A.L. Chuvilin, and M.I. Heggie, *J. Phys. Chem.* **A105**, 9781 (2001).
9. V.L. Kuznetsov, I.Yu. Malkov, A.L. Chuvilin, E.M. Moroz, V.N. Kolomiichuk, Sh.K. Shaichutdinov, and Yu.V. Butenko, *Carbon* **32**, 873 (1994).
10. Aleksandrov, I.V. Zagoruiko, A.L. Chuvilin, E.M. Moroz, V.N. Kolomiichuk, and V.A. Sakovitch, *Carbon* **29**, 665 (1991).
11. V.D. Yumatov, A.V. Okotrub and L.N. Mazalov, *Zh. Struktur. Khim.* **26**, 59 (1985).
12. M.J.S. Dewar, E.S. Zoebisch, E.F. Healy, and J.J.P. Stewart, *J. Am. Chem. Soc.* **107**, 3902 (1985).
13. J.P. Lu and W. Jang, *Phys. Rev.* **B49**, 11421 (1994).
14. E.Z. Kurmaev, S.N. Shamin, K.M. Kolobova, and S.V. Shulepov, *Carbon* **24**, 249 (1986).
15. K. Nakada, M. Fujita, G. Dresselhaus, M.S. Dresselhaus, *Phys. Rev.* **B54**, 17954 (1996).
16. L.G. Bulusheva, A.V. Okotrub, D.A. Romanov, D. Tomanek, *Phys. Low-Dim. Struct. 3/4*, 107 (1998).
17. A.I. Romanenko, O.B. Anikeeva, A.V. Okotrub, V.L. Kuznetsov, Yu.V. Butenko, A.L. Chuvilin. MRS Fall meeting 2001, paper V 6.19.

Mat. Res. Soc. Symp. Proc. Vol. 703 © 2002 Materials Research Society V9.23

# Mechanical Properties of Unsaturated Polyester / Montmorillonite Composites

A. Baran Inceoglu and Ulku Yilmazer
Middle East Technical University,
Chemical Engineering Department,
06531, Ankara, TURKEY

## ABSTRACT

Nanocomposites composed of unsaturated polyester matrix and organically modified clay filler were prepared. After the synthesis, XRD patterns showed that the interlayer spacing expanded from 1.25 nm to 4.5 nm. The mechanical properties of the nanocomposites were determined and it was found that adding only 3 w/w % organically modified clay improved the flexural modulus of unsaturated polyester by 35%. From DSC diagrams, it was found that $T_g$ values of the nanocomposites also increased with the clay content. It is concluded that partially exfoliated / intercalated nanocomposites were formed at relatively low clay contents.

## INTRODUCTION

Nanocomposites with thermoplastic matrices have been synthesized and characterized [1-4]. Several studies have also been reported on nanocomposites with thermoset matrices. Lee and Jang [5] reported the characterisation of epoxy-clay hybrid composites prepared by emulsion polymerization. The effects of promoter and curing process on exfoliation behavior of epoxy/clay nanocomposites were studied by Ke, Lü, Yi, Zhao and Qi [6]. Kornmann, Linberg and Berlung [7] synthesized epoxy clay nanocomposites and analysed the nature of the curing agent on structure. Kornmann, Berglund and Giannelis [8] studied nanocomposites based on montmorillonite modified with silane coupling agent and unsaturated polyester. In the present study, the type and content of the montmorillonite (MMT) on mechanical and thermal properties are investigated using an unsaturated polyester (UP) matrix.

## EXPERIMENTAL

Organically treated montmorillonite (Cloisite® 30B from Southern Clay Products, USA) and non-treated Na-montmorillonite (Cloisite® $Na^+$ from Southern Clay Products, USA) were used as the filler. Ortho-phthalic-general purpose unsaturated polyester (Neoxil C-92 N 8 from Camelyaf, Turkey) was used as the matrix. The resin and the matrix were first mixed mechanically for 3 hours at 50°C followed by ultrasonic mixing for better dispersion. 0.9 phr of methyl ethyl ketone peroxide (MEK-P) and 0.2 phr of cobalt naphthanate (as 8 % solution) were used as the catalyst and accelerator respectively.

Flexural tests were performed according to the Test Method-I Procedure A of ASTM D790-92 using Lloyd 30k Universal Testing Machine with a crosshead speed of 2.8 mm / min. Pendulum Charpy Impact Tests were done according to the Test Method-I Procedure A in ASTM D256-91a using a Coesfeld Material device. In order to evaluate changes in $T_g$ with increasing clay content, differential scanning calorimeter analyses were carried out using General

V4.1C DuPont 2000. Fracture surfaces were investigated by using JEOL JSM-6400 Scanning Electron Microscope (SEM). The fracture surfaces of pure UP and specimens containing MMT were compared. X-Ray diffraction patterns were recorded by monitoring the diffraction angle 2θ from 1° to 10° using a Rigaku Geigerflex diffractometer.

## RESULTS AND DISCUSSION

Figure 1 shows the XRD pattern of organoclay Cloisite® 30B. The diffraction peak appears at 2θ = 4.4°, with basal spacing of 1.97 nm. The original $Na^+$-montmorillonite gives basal spacing of 1.25 nm. [4]. In Figure 2, it can be seen that the peak corresponding to the basal spacing of organoclay has disappeared. It is clearly shown that for all the samples with Cloisite® 30B a new diffraction peak appeared at 2θ = 2° with a basal spacing of 4.5 nm. However, if the organoclay loading is greater than 3%, the hybrids also show a small peak at 2θ = 4.93° (d = 1.93 nm), which is the main peak of the organoclay, suggesting that a small part of organoclay is not dispersed at the molecular level.

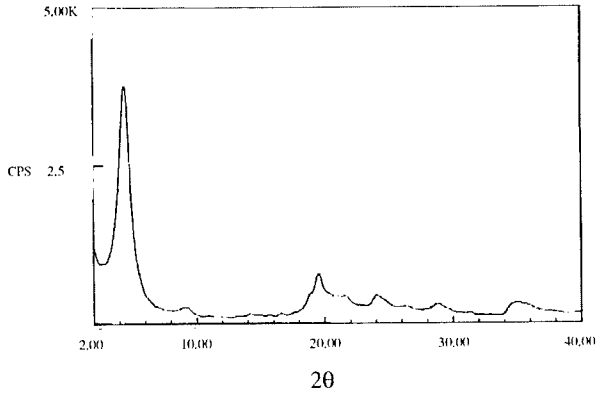


**Figure 1:** X-Ray pattern of Cloisite® 30B

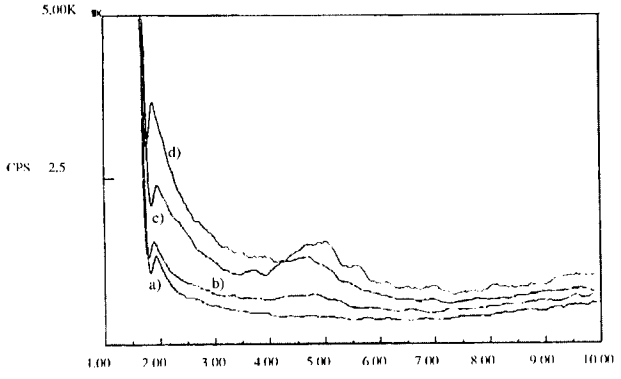


**Figure 2:** X-Ray patterns of nanocomposites a) 3%, b) 5%, c) 7%, d) 10% filler

Figure 3 shows the effect of the clay content on the $T_g$. Since the glass transition process is related to the molecular motion, the increase in the $T_g$ of the nanocomposites, in comparison with the original unsaturated polyester, can be attributed to high degree of adhesion between the polymer and the layered silicate surfaces. The nanometer size restricts segmental motion near the organic-inorganic interface. However, the clay particles also consume free radicals that are formed during curing, thus the cross-link density might decrease at high clay contents suggesting that the glass transition might also decrease at high clay contents.

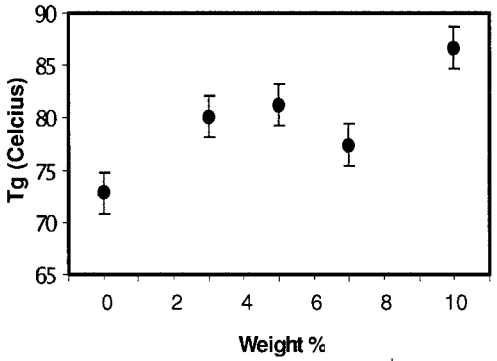


**Figure 3:** $T_g$ results of samples with Cloisite® 30B or $Na^+$

As can be seen from Figure 4, flexural modulus increases and makes a peak at 3% loading of Cloisite® 30B. With respect to the clay content, the increase in flexural modulus is more than the increase in tensile modulus (not shown here). The tensile modulus of unsaturated polyester was improved by 17% at 5% of Cloisite® 30B. The orientation of the clay particles may be substantially parallel to the mold surface and this leads to high flexural modulus values. After 7% of loading, there is a decrease in the modulus. At high loading levels, polymer-clay interactions are lower and agglomeration of the clay particles results in lower modulus. The cross-link density might also be lower at high clay contents as discussed earlier, leading to lower modulus. In Cloisite® $Na^+$ samples, the increase in flexural modulus is not significant owing to lack of intercalation of the polymer chains in between the clay layers.

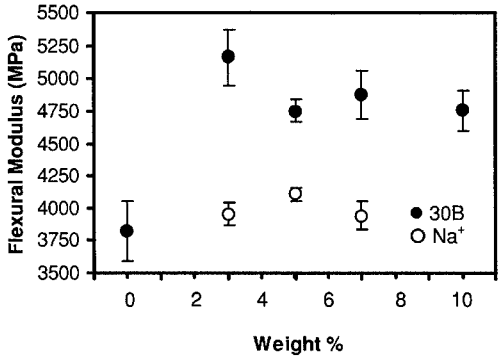


**Figure 4:** Flexural modulus versus weight % values of Cloisite 30B and $Na^+$ samples

As can be seen from Figure 5, at high Cloisite® 30B content, flexural strength of the specimens decrease, since the clay particles act as stress concentrators and intercalation is poor at high filler contents. The flexural strength of Cloisite® $Na^+$ samples also decreases. In this case, the clay particles, which are in the agglomerate form, act as stress concentrators and tend to decrease the flexural strength of the specimens.

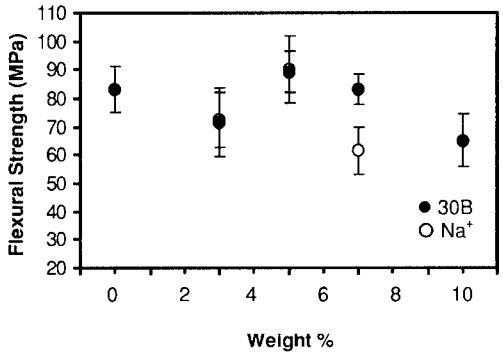


**Figure 5:** Flexural strength versus weight % values of Cloisite 30B and $Na^+$ samples

The strain at break values decrease for both types of samples with respect to the clay content, since the elongation is born by the decreasing quantity of matrix at high filler contents (Figure 6).

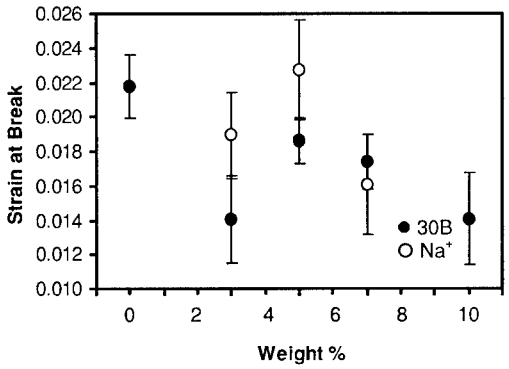


**Figure 6:** Strain at Break versus weight % values of Cloisite 30B and $Na^+$ samples

As far as the impact behavior is concerned (Figure 7), clay particles act as a crack initiator, but at high clay contents the particles also act as crack stoppers. Impact values of Cloisite® $Na^+$ show that unmodified clay particles have no positive effect on the composite, because the narrow d-spacing of the clay, do not permit the polymer to enter between the galleries leading to agglomeration of the particles and lower impact strength values.

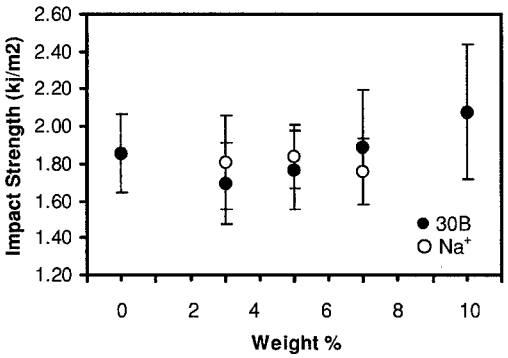


**Figure 7:** Impact strength values of Cloisite® 30B and $Na^+$ samples

As can be seen from Figures 8 and 9, the size of the agglomerates found in the samples containing Cloisite® $Na^+$ are larger then the samples containing Cloisite® 30B. In Figure 9, it is seen that the quantity of the agglomerates is higher, and the impact energy is lower owing to the higher quantity of particles.

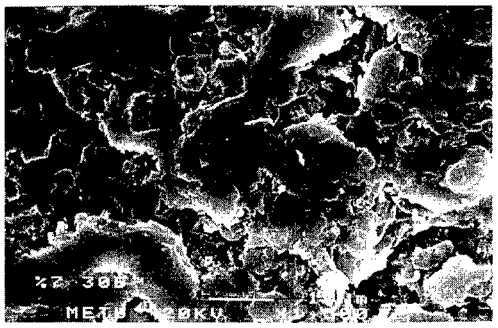

**Figure 8:** Impact surface of 7 % Cloisite® 30B sample at x1500 magnification

**Figure 9:** Impact surface of 7 % Cloisite® $Na^+$ sample at x1500 magnification

## CONCLUSIONS

Addition of an organoclay (Cloisite® 30B) in relatively low ratios, to an unsaturated polyester resin resulted in partially exfoliated nanocomposites. From XRD patterns, it is concluded that the d-spacing of the organoclay expanded from 1.97 nm to 4.5 nm in all samples with Cloisite® 30B. $T_g$ values of the samples containing Cloisite® 30B increased from 72°C, in unfilled unsaturated polyester, to 86°C in 10% Cloisite® 30B loaded unsaturated polyester.

The flexural modulus of the samples containing Cloisite® 30B increased by 35% at 3% clay loading. Flexural strength decreased at high clay contents and the strain at break values changed in the opposite manner to the flexural modulus. The flexural modulus of specimens containing Cloisite® $Na^+$ exhibit a maximum of 3829 MPa at 5% clay loading, resulting in an increase of only 7%. The impact values of the samples containing Cloisite® 30B first decreased and then, started to increase. However, in samples containing Cloisite® $Na^+$, the values of the impact strength showed continual decrease with respect to clay content.

From Scanning Electron Microscope, it was seen that there are large agglomerates in the samples containing Cloisite® $Na^+$ type of clay leading to poor mechanical properties. With the help of the X-Ray analysis, it is concluded that the dispersion of the Cloisite® 30B montmorillonite particles is good and the silicate particles near the primary particles are exfoliated.

## REFERENCES


[1] A. Okada, M Kawasumi, Ausuki, Y. Kojima, T. Kurauchi, and O. Kamgaito, "Nylon 6-clay Hybrid", *Mater. Res. Soc. Proc., 171, 45-50* (1990)

[2] Richard A. Vaia, Klaus D. Jandt, Edward J. Kramerand E. P. Giannelis, "Kinetics of Polymer Melt Intercalation", *Macromolecules, 28, 8080-8085* (1995)

[3] X. Fu, Squtubuddin, "Polymer-clay Nanocomposites: Exfoliation of Organophilic Montmorillonite Nanolayers in Polystyrene", *Polymer, 42, p: 807-813* (2001)

[4] T. Agag, T. Koga, T. Takeichi, "Studies on Thermal and Mechanical Properties of Polyimide-clay Nanocomposites", *Polymer, 42, p: 3399-3408* (2001)

[5] Dong Choo Lee, Lee Wook Jang, "Characterization of Epoxy-clay Hybrid Composite Prepared by Emulsion Polymerization", *Journal of Applied Polymer Science, Vol. 68, 1997-2005* (1998)

[6] Y. Ke, Jiankun Lü, X. Yi, J. Zhao, Z. Qi, "The Effects of Promoter and Curing Process on Exfoliation Behavior of Epoxy/clay Nanocomposites", *Journal of Applied Polymer Science, Vol. 78, 808-815* (2000)

[7] X. Kornmann, H. Lindberg, L. A. Berglund, "Synthesis of Epoxy-clay Nanocomposites. Influence of the Nature of the Curing Agent on Structure", *Polymer, 42, p: 4493-99* (2001)

[8] X. Kornman, L. A. Berglund, J. Sterte and E. P. Giannelis, "Nanocomposites Based on Montmorillonite and Unsaturated Polyester", *Polymer Engineering and Science, V38 No:8 p: 1351–1358* (1998)

Mat. Res. Soc. Symp. Proc. Vol. 703 © 2002 Materials Research Society V9.25

# Microwave Plasma CVD of Silicon Nanocrystalline and Amorphous Silicon as a Function of Deposition Conditions

J-H Jeung, Hak-Gue Lee, Lihong Teng and W.A. Anderson,
SUNY at Buffalo, Electrical Engineering, 208 Bonner Hall, Buffalo, NY, 14260.

## Abstract

Using ECR-CVD (electron cyclotron resonance-chemical vapor deposition) , we can make amorphous-silicon (a-Si) and nanocrystalline (nc-Si) thin films. We are looking forward to improve the photo/dark conductivity ratio ($\sigma_p / \sigma_d$) by measuring the photo and dark current-voltage (I-V). In the ECR deposition, there are several factors which we can control and adjust for improved results, such as the amounts of silane and argon, the vacuum, and the temperature of the substrate. These become the critical factors for ECR deposition in order to make better films. Input gases consist of Ar, 2%$SiH_4$ in He and $H_2$. In the process, $SiH_4$ is decomposed into $SiH_x$. A residual gas analyzer (RGA) gives composition in the plasma. Because Ar possibly etches the substrate and Si is to be deposited, the best RGA signal is obtained with low Ar content. This work serves to correlate process conditions, RGA signals and electrical data. The best RGA signal occurs for 5 mTorr Ar, 60 mTorr $SiH_4$:He, and power of 600 W. Best value of dark conductivity ($\sigma_d$) was 1.53 x $10^{-9}$ S/cm and1.58x $10^{-5}$ S/cm for photo conductivity ($\sigma_p$). High value of $\sigma_p$ and low value of $\sigma_d$ indicate material with fewer defects. Adding extra $H_2$ improves the photo-conductivity ($\sigma_p$). Applications of these films are heterojunction solar cells and thin film transistors. The heterojunction solar cell had a structure of metal grid/ 500°A of a-Si:H/p-Si wafer/Ohmic contact. These cells gave an open circuit voltage ($V_{oc}$) = 0.51 (V) and short circuit current density ($J_{sc}$) = 5.5 mA/cm$^2$ under 50mW/cm$^2$ tungsten halogen lamp. Thin film transistors using nc-Si, with gate length/width (L/W) =450/65 gave field effect mobility of 18 cm$^2$/V-s, and Ion/Ioff of 1.25x$10^5$.

## Introduction

ECR plasma deposition can control the properties of the plasma so that it can be applied to deposit nanocrystalline silicon (nc-Si) thin films or amorphous silicon (a-Si) for thin film transistors (TFT's) and solar cells [1]. With ECR deposition, ion bombardment and etching during growth can be controlled. Also, low pressures can minimize the radical-radical reactions. Other benefits of rf- generated plasma processing includes high fraction of ionization and dissociation, high electron kinetic temperature, and no need for an electrode inside the chamber which can reduce the contamination of samples [2].

In-situ mass spectroscopy [3] is used in the analysis of the plasma during the deposition. In the ECR process, we need to induce a good argon plasma and also reduce the defects from argon ions. Therefore, before beginning the deposition, it is helpful to check the RGA (residual gas analyzer) signals and try to obtain a good signal from the RGA. By using excess hydrogen, we can reduce dangling bonds that are present in the a-Si. This produces a-Si:H. It can improve the characteristics of the photo-conductivity and the properties needed for applications [4].

## EXPERIMENT

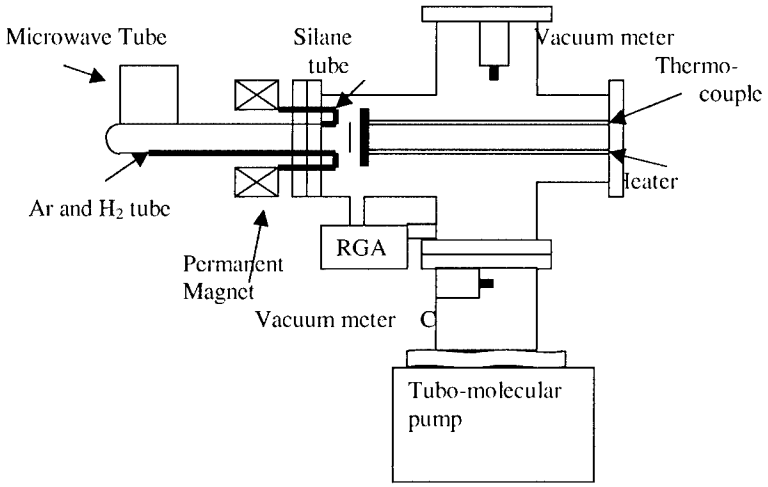


Fig 1. ECR chamber geometry.

The ECR-CVD geometry is shown in Fig.1 above. The filament of the RGA (SRS CIR200) in placed just below the plasma coming out of the quartz-tube near the substrate. Ar + $H_2$ and 2%$SiH_4$ in He are introduced through the gas feed tubes. 2%$SiH_4$ in He is decomposed due to the Ar plasma. Angle of the substrate is 90 degrees and the distance from the tube is ¾ inches. Two permanent magnets reside to control the plasma. The substrate holder is heated to 250 °C for a-Si and 400 °C for nc-Si. Microwave power is 600 Watts. Current-voltage (I-V) is measured to obtain the dark conductivity ( $\sigma_P$ ) and photo-conductivity ( $\sigma_d$ ) under an AM1.0 spectrum of 100cmW/cm$^2$ from a tungsten halogen lamp.

### Data and Results

Before the ECR-CVD deposition, the proper conditions of deposition are confirmed using the RGA. Standard conditions were 5 mTorr of Ar and 52 mTorr to 64 mTorr of 2% $SiH_4$ in He.

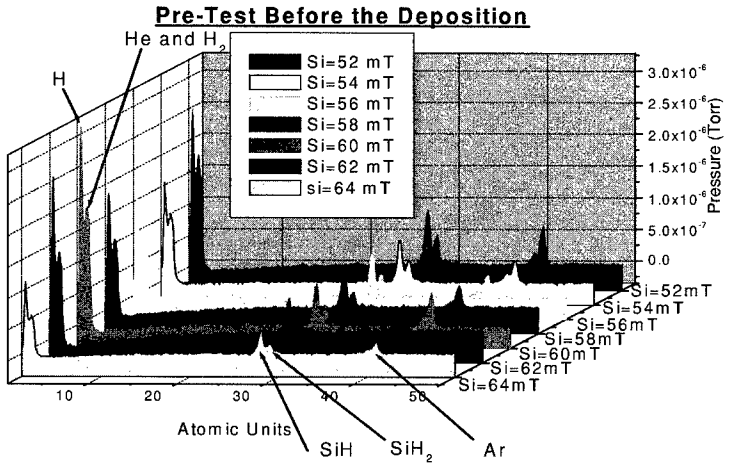


Fig. 2 RGA signal of the pre-test with changing amount of $SiH_4$

In Fig. 2, the RGA signals show the atomic units and the pressure of each gas. $SiH_4$ is decomposed into SiH, $SiH_2$, $SiH_3$, H and $H_2$. At 60 mTorr of $SiH_4$, the high peaks of H, SiH and $SiH_2$ are seen, indicating good decomposition. The result of the photo and dark conductivity ratio is below in Fig.3.

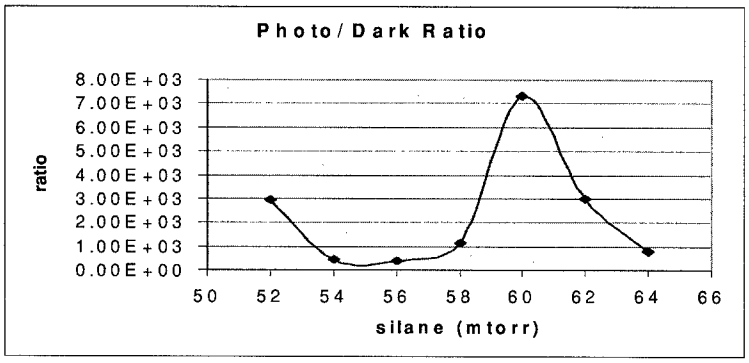


Fig. 3 The photo and dark conductivity ratio

The best conductivity ratio result was achieved at 60 mTorr of silane and 5 mTorr of Ar from Fig.3. The photo-conductivity is $1.58 \times 10^{-5}$ S/cm, and the dark-conductivity is $2.16 \times 10^{-9}$ S/cm at 60 mTorr of silane. In most of the cases, dark conductivities are similar, but improved photo-conductivity leads to the higher conductivity ratio of the samples.

Too much or too little silane is a disadvantage. In order to obtain better photo-conductivity, hydrogen was added during depositon. $H_2$ was changed from 0.5 mTorr to 3 mTorr. More than 4 mTorr of hydrogen did not give a good RGA signal. Amount of silane was changed from 52 mTorr to 68 mTorr. Since hydrogen can reduce the dangling bonds of $SiH_x$ more effectively, the ratio of photo and dark conductivity was improved. The ratio results are in the Fig. 4.

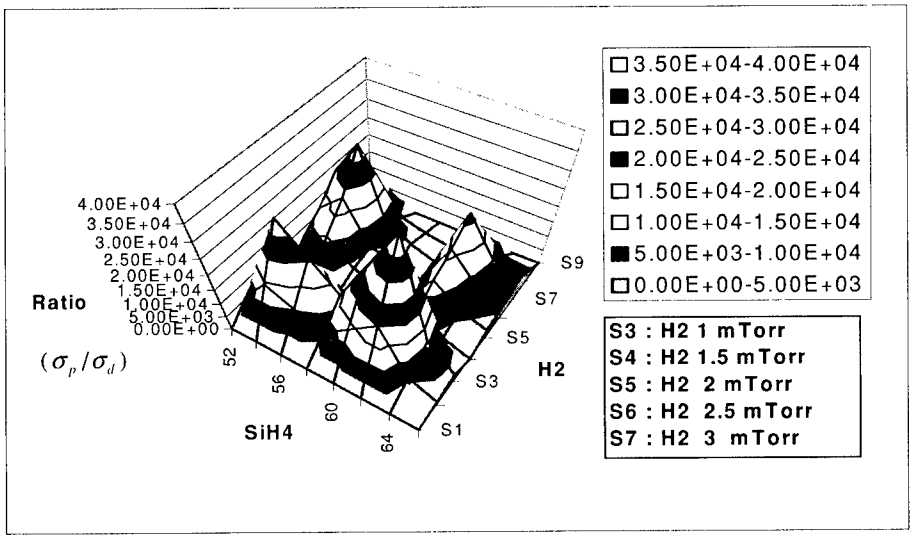


Fig. 4 The photo & dark conductivity ratio variation with $SiH_4$ and $H_2$

The best photo and dark conductivity ratio was 4.0 x $10^4$ S/cm at 62 mTorr of silane, 1 mTorr of $H_2$, and 4 mTorr of Ar. The photo-conductivity was 1.12 x $10^{-4}$ S/cm, and the dark conductivity was 2.8 x $10^{-9}$ S/cm

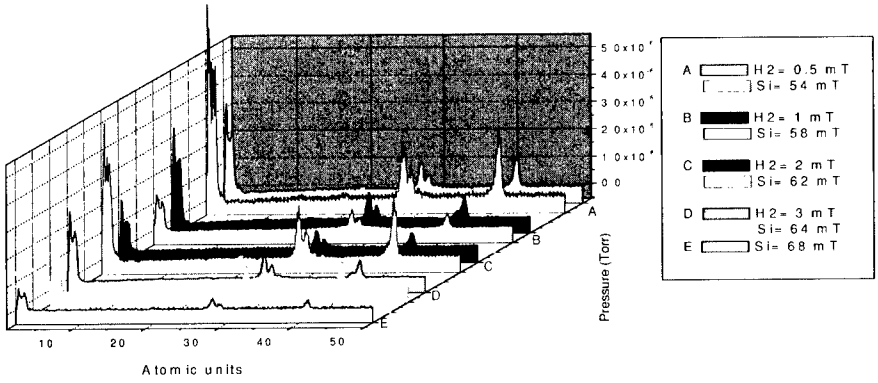


Fig. 5 Signal change with variation in $H_2$(filled box) or Silane (clear box)

The high peak H, $H_2$ and $SiH_x$ are at 62 mTorr of silane. The RGA signals of the result is in Fig.5 . It proved the ratio related with gas decomposition. In this condition, TFT and solar cell sample current and voltage curves are in Fig. 6 and Fig.7.

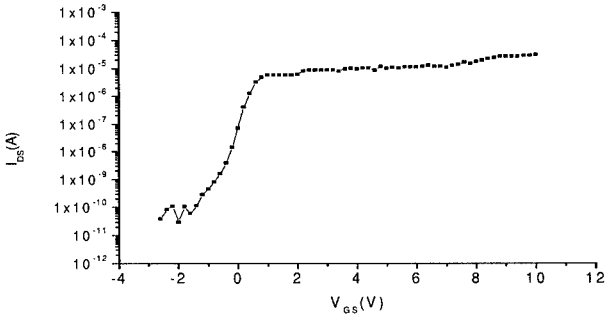


Fig. 6 TFT data for a transistor made form nc-Si

For the TFT of Fig.6, an inverted staggered structure was used with a gate oxide of thickness 100-200 nm deposited by PECVD. The gate length / width ratio is (W/L) = 450/85, and at the $V_{DS}$ = 1 (V), field effect mobility was 18 $cm^2$/V-s. Turn-on and off current were $I_{on}$ = 2.5 x $10^{-5}$ A and $I_{off}$ = 2.0 x $10^{-10}$ A.

Solar cells with an area of 1$cm^2$ were fabricated with the back side having an Al Ohmic contact of 1000 A°. a-Si was deposited with 250 °C substrate temperature for an a-Si solar cell and 400°C for a nc-Si solar cell with a thickness of 500 A° . On the top, the grid line was 200-300 A° Mg/ 800-1000 A° Al. The current–voltage curve is below in Fig.7.

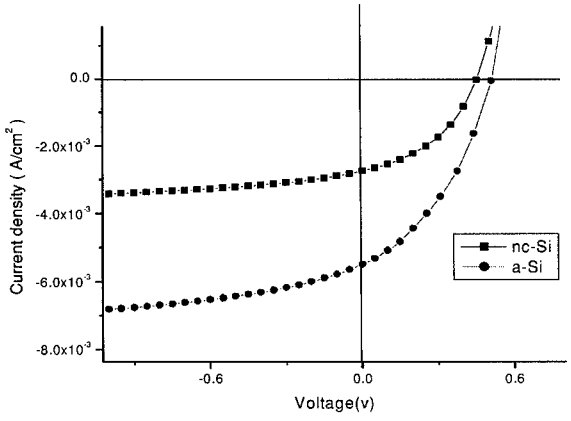


Fig. 7 nc-Si and u-Si solar cell J-V curve under 50 mW/$cm^2$ light.

The nc-Si solar cell has $V_{oc}$=0.45 (V) and current density ,$J_{sc}$ = 2.8 mA/cm$^2$ under 50 mW/cm$^2$. The a-Si solar cell has $V_{oc}$= 0.51 (V) and $J_{sc}$ = 5.5 mA/cm$^2$ under 50 mW/cm$^2$. The a-Si solar cell shows the better results.

## Conclusion

The conditions of ECR-CVD deposition are very critical factors. Best conditions for a-Si:H deposition were 4 mTorr of Ar , 62 mTorr of $SiH_4$: He and 1 mTorr of $H_2$ with 250°C substrate temperature.
The nc-Si was obtained using the same conditions of gases with substrate temperature of 400°C. Proper combination of each gas is one of the important conditions in order to obtain a good ratio, however, pumping pressure and power are adjusted for inducing a good plasma.
The films were useful for producing solar cells and thin film transistors.

## Acknowledgment

Research was sponsored by NSF, grant number ECS9902437, under Dr. Usha Varshney.

## References

[1] W. A. Anderson, B. Jagannathan and E. Klementieva, Progress in Photovoltaics **5**, 433 (1997)

[2] J. Reece Roth, Industrial plasma Engineering Vol. 1. (Institute of Physics Publishing, Bristol and Philadelphia, 1995)

[3] A.Matsuda and K. Tanaka, Thin Solid Films **92**, 171 (1981)

[4] Y.J. Song, E. Guliants,H.Lee, and W.A.Anderson. Proc. Of Mater. Res. Soc.Symp. April 2000.

Mat. Res. Soc. Symp. Proc. Vol. 703 © 2002 Materials Research Society V9.26

# Dispersion of Functionalized Nanoclay Platelets in an Amine-Cured Epoxy Resin System

D. Raghavan, E. Feresenbet, D. Yebassa, A. Emekalam, and G. Holmes[1]
Polymer Division, Department of Chemistry, Howard University, Washington DC 20059.
[1]G. Holmes, Polymer Division, National Institute of Standards & Technology, Gaitherburg, MD 20899.

## ABSTRACT

Nanocomposites are a relatively new class of materials obtained by dispersing montmorillonite clay in a polymer matrix. Evidences from literature suggest that clay platelet dispersion during nanocomposite preparation and clay-matrix adhesion are major technical issues that need to be addressed in order to achieve the desired property enhancements in polymer-clay hybrid nanocomposites. We have studied the interaction of the organically functionalized clay with the epoxy resin by including along the chain structure functional groups that will facilitate interaction with the resin. Through conventional routes, functional molecules have been synthesized and deposited on to the clay surface. Both the functionalized and nonfunctionalized clay has been analyzed using thermal gravimetric analysis (TGA), and Fourier transform infrared spectroscopy (FTIR). The exfoliation of nanoclay platelets in amine cured epoxy system has been studied using X-ray diffraction (XRD) and transmission electron microscopy (TEM).

## INTRODUCTION

Aromatic amine cured epoxy resins, where the diglycidyl ether of bisphenol-A (DGEBA) resin cured with meta-phenylene diamine (MPDA) is a representative member, are the most widely used matrix materials for preparing conventional composites. Resins of this class are brittle and their ability to absorb energy during failure is limited. The successful use of nanoclay reinforcement technology to improve the performance of epoxy resin would represent a major technical achievement in the development of high-temperature and tough advanced structural materials. Nanoclays are inexpensive relative to traditional reinforcing materials, thermally inert, and environmentally friendly. The use of nanoclay hybrid polymer composites in structural parts is expected to improve environmental and moisture stability and increase energy efficiency in the transportation sector through weight reduction [1].

Evidences from literature suggest that exfoliation and dispersion of clay platelets during nanocomposite preparation and clay-matrix adhesion are major issues that needs to be addressed in order to achieve the desired property enhancements in polymer-clay nanocomposites [2-7]. In recent years, efforts have focussed on understanding the nature and mechanism of the exfoliation process of the surface treated clay in the polymer network structure. For example, Messersmith and Giannelis [2] achieved a significant increase in stiffness of epoxy nanocomposite by using organoclays modified with bis(2-hydroxyethyl) methyl tallow-alkyl ammonium chloride at a mass fraction of 4 %. The

role of the organic chain on alkyl ammonium chloride is primarily to facilitate the intercalation of the clay by organic molecules (e.g., DGEBA). These researchers found that curing of a DGEBA/clay mixture with primary and secondary amines resulted in an immediate clouding of the resin. It has been suggested that the bridging of the silicate layers by the bifunctional polar amines prevented the extensive layer separation. In recent years, several researchers [2-7] have studied amine-cured epoxy clay composites to show that exfoliation of nanocomposite depends on the following parameters:

(1) Alkyl ammonium ion type (e.g. primary, secondary or tertiary)
   a. affects intra-gallery polymerization rates and clay-matrix dispersion
(2) Length of the alkyl chain
   a. impacts swelling of clay by epoxy monomer
   b. controls intra-gallery diffusion
(3) Curing agent type (e.g. aromatic diamines, aliphatic diamines, anhydrides, and homopolymerization agents)
   a. affects resin glass transition temperature
(4) Curing conditions
   a. affects intra- and extra-gallery polymerization rates and resin Tg
(5) Charge density of the clay
   a. impacts swelling of clay by epoxy monomer

The focus of this research is to investigate the influence of modified clay with functional groups on the miscibility of monomer with organically modified nanoclay platelets. In this research, the sodium ions in the clay are exchanged with an alkylammonium salt of suitable chain length followed by adsorption of ω-epoxy carboxylic acid of suitable chain length on the clay surface. The epoxy groups of ω-epoxy carboxylic acid are expected to facilitate the miscibility of DGEBA monomer with the clay platelets. In this study we investigate how the type of organophilic groups intercalated between the clay layers, influences the structure of the resulting nanocomposites. In particular, we compare the effect of the two nanoclays (functional and non-functional clay) on the exfoliation process and the final structure of epoxy-based nanocomposites. For the synthesis of functional clay, we use clay treated with C18 quaternary ammonium salts (C18 clay) as the base structure. The C18 clay is then mixed with *functional oleochemicals* to form functional clays. The functional oleochemicals are synthesized from vernonia oil (see Figure 1). The nanostructure of the epoxy clay composite was characterized by X-ray diffraction (XRD) and transmission electron microscopy (TEM).

## EXPERIMENTAL

### (A) Synthesis of C18 Clay

7.5 g of purified Na clay from Southern Clay Products[1] was dispersed into 600 ml of distilled water at 80 °C. 3.0 g of octadecylammonium chloride in 300 ml distilled

[1] Certain commercial materials and equipment are identified in this paper in order to specify adequately the experimental procedure. In no case does such identification imply recommendation or endorsement by the National Institute of Standards and Technology, nor does it imply necessarily that the items are best suited for the purpose.

water was poured in the hot clay/water suspension and stirred vigorously for 1 h at 80 °C. The mixture was then filtered and the solid washed several times with ethanol/hot water mixture (for 3 h) to remove free chloride ions. The washing was continued until the solid was verified for absence of chloride ions, by checking the filtrate solution with $AgNO_3$ solution. The attachment of long alkyl groups to clay surfaces facilitates clay sheet separation and makes it possible to introduce functional molecules in the interlayer space.

**(B) Synthesis of Vernolic acid:**

Vernonia oil (VO) was refluxed with base/methanol mixture for 2 h and transferred to a beaker containing ice/water. The solid compound was recovered by filtration and acid treated to convert the acid salt (soap) to vernolic acid. Vernolic acid was purified by adopting solvent exchange procedure and freeze drying techniques. Figure 1 describes the reaction scheme used to synthesize vernolic acid. The purified compound was FTIR characterized and compared to the literature reporting for epoxy fatty acid [8].

**(C) Synthesis of Vernolic Acid Mixed C18 Clay:**

1.25 g of C18 clay was suspended in 0.5 g of vernolic acid dissolved in 30 ml of hexane and the solution was stirred under nitrogen gas for 48 h and the product was filtered. Fresh hexane was added to the solid product and attempts were made to free the solid product of residual vernolic acid. The C18 clay containing vernolic acid was allowed to air dry and is termed as the *vernolic acid mixed C18 clay*. The product was characterized by FTIR and TGA technique.

**(D) Synthesis of Epoxy Nanocomposite:**

We have selected the model resin system DGEBA (provided by Dow Chemical) and MPDA for the current study. DGEBA resin was kept in a vacuum oven at 75 °C for 3 h. The clay-epoxy mixture was prepared by dispersing a mass fraction of 2.5 % of C18 clay in hot DGEBA with stirring, followed by sonication for about 2 h and degassing in vacuum for 2 h. 14.5 phr MPDA (melted at 60 °C) was then added to the clay-epoxy mixture at 60 °C under vacuum. The DGEBA/clay/MPDA mixture was heated for 2 h at 80 °C and post cured for another 2 h at 125 °C. The same curing procedure was applied to vernolic acid mixed C18 clay.

**(E) FTIR and TGA Analysis of Nanoclay Powder**

FTIR analyses were performed on the Na clay, C18 clay, and vernolic acid mixed C18 clay. Each sample was mixed with KBr and vacuum packed to obtain pellets of the material. The pellets were analyzed using a Nicolet Magna IR 560 (the standard instrument uncertainty in measuring wave number is ± 0.01 $cm^{-1}$, the $cm^{-1}$ were rounded off to the nearest 1 $cm^{-1}$) spectrophotometer.

TGA analysis was performed on the Na clay, C18 clay, and vernolic acid mixed C18 clay using a Perkin Elmer 7 Series system (the standard instrument uncertainty in

measuring a temperature is ± 1 °C) in a nitrogen atmosphere, by placing 25 mg of sample in a crucible and heating it from 30 °C to 900 °C at a heating rate of 20 °C /min. Nitrogen gas was allowed to flow at a sweep rate of 5 ml/min.

### (F) XRD and TEM Analysis of Epoxy Nanocomposites

XRD analyses were performed using a Scintag Inc. XRG 3000 diffractometer with Cu radiation (40 KV, 35 mA). The scanning speed and the step size were 0.01 °/min and 0.04 °, respectively. The nanocomposite dogbone produced during the moulding process has a fairly smooth surface. The dogbone specimens were cut to size and analyzed by XRD.

TEM specimens were cut from dogbone using an ultramicrotome, equipped with a diamond knife. They were collected in a trough filled with water and lifted out of water using 200 mesh copper grids. Electron micrographs were taken with a Philips EM400C at an accelerating voltage of 120 KV.

## RESULTS AND DISCUSSION

### A. Characterization of Nanoclay Powder

The FTIR spectra of the neat Na clay, C18 clay and vernolic acid mixed C18 clay in the region (4000 to 500) $cm^{-1}$ are shown in Figure 2. Both the vernolic acid mixed C18 clay and C18 clay display sharp methylene-stretching modes at 2920 $cm^{-1}$ and 2860 $cm^{-1}$, that is characteristic of organophilic groups on clay surfaces. The spectra of C18 and vernolic acid mixed C18 clay also show a distinct peak at 1600 $cm^{-1}$ that can be assigned to the quaternary ammonium salt in modified clay. In addition, the vernolic acid mixed C18 clay contains bands at 1710 $cm^{-1}$ and 1759 $cm^{-1}$ suggesting that the vernolic acid is present in the clay matrix. Vernolic acid present in the interlayer space is trapped in the matrix, while vernolic acid present at the edges in a limited amount is involved in physico-chemical interactions with hydroxyl groups on clay edges. This is because, plate-like clay surfaces have hydroxyl groups at low content at edges of individual particles.

Thermogravimetric analysis was used to examine the stability of organophilic groups on nanoclay. The thermograms of the Na clay, C18 clay, and vernolic acid mixed C18 clay are shown in Figure 3. The peak at 100 °C corresponds to the loss of surface water molecule from the clay platelets. We see the onset of decomposition peak (i.e. release of functional onium ion and vernolic acid molecule) at above 200°C in both C18 and vernolic acid mixed C18 clay. The peak at 650 °C is the irreversible dehydroxylation peak for clay. As expected, the peak at 650°C for Na clay is significantly larger than that of vernolic acid mixed C18 clay.

### B. Characterization of Epoxy Clay Nanocomposites

Both the uncured and cured epoxy were studied by XRD for layer separation. The X-ray diffraction results of C18 clay and vernolic acid mixed C18 clay showed a sharp X-ray diffraction peak that corresponds to a layer separation of about (22 ± 3) Å, where the number after ± is one standard deviation from the mean. After the C18 clay was

sonicated in epoxy mixture for 2 h, X-ray diffraction was recorded for the uncured sample. The interlayer spacing increased to (37 ± 3) Å. However, when the clay was allowed to swell for several hours in hot epoxy resin, the sharp peak diminished. Instead a shoulder was noticed for both C18 clay and mixed nanoclay. Figure 4 shows a comparison of the C18 clay and vernolic acid mixed C18 clay epoxy nanocomposite. The appearance of a shoulder at approximately 2.3° (2θ) suggests that nanoclay platelets are partially exfoliated. It has been reported recently that epoxy infiltration into nanoclay platelets can be achieved by prolonged swelling of clay in uncured epoxy [10].

To verify our results, we performed TEM studies on C18 clay and vernolic acid mixed C18 clay nanocomposites. Figure 5 shows bright field transmission electron micrograph of epoxy- (a) C18 clay and (b) vernolic acid mixed C18 clay nanocomposite. Detailed TEM verified the intercalated structure of epoxy C18 clay nanocomposite and partially exfoliated epoxy vernolic acid mixed C18 clay nanocomposite. There were regions in the vernolic acid mixed C18 clay epoxy nanocomposite where the nanoclay platelets were intercalated (regular arrangement of clay platelets) and other regions where platelets were exfoliated (randomly arranged and well separated platelets). One would expect that the addition of vernolic acid to C18 clay should result in intercalated epoxy nanocomposite because of crowding of functional groups on clay edges. However, our preliminary results indicate that the addition of vernolic acid to C18 clay has improved exfoliation of nanoclay platelets to a limited extent in epoxy matrix. We believe that the epoxy groups of ω-epoxy vernolic acid sorbed on clay edges may facilitate the miscibility of DGEBA monomer with the clay platelets and infiltration of epoxy resin. This aspect requires further investigation. Studies are also underway to obtain information about the clay dispersability in epoxy matrix (using NMR technique).

## ACKNOWLEDGMENTS

The authors thank the AFOSR, for providing financial support, Steve Hudson of NIST for the transmission electron microscope studies of morphology, and Maureen Williams of NIST for assistance with XRD studies.

## REFERENCES

1. J. M. Garces, D. J. Moll, J. Bicerano, R. Fibiger, and D. G. McLeod, Adv. Mat., 12, 1835(2000).
2. P. B. Messersmith, E. P. Giannelis, Chem. Mater. 5, 1064(1993).
3. H. Shi, T. Lan, and T. J. Pinnavaia, Chem. Mater. 8, 2216(1996).
4. I. J. Chin, T. Thurn-Albrecht, H. C. Kim, T. P. Russell, Polymer, 42, 5947 (2001).
5. J. M. Brown, D. Curliss, and R. A. Vaia, Chem. Mater. 12(11), 3376(2000).
6. C. Zilg, R. Thomann, J. Finter, and R. Mulhaupt, Macromol. Mater. Eng. 280, 41(2000).
7. X. Fu and S. Qutubuddin, Polymer, 42(4), 807(2001).
8. F. O. Ayorinde, E. Y. Nana, P. D. Nicely, A. S. Woods, E. O. Price, and C. P. Nwanicha, J. Am. Oil Chem. Soc., 74, 531(1997).
9. K. Song and G. Sandi, Clay and Clay Minerals, 49, 119(2001).
10. X. Kornmann, H. Lindberg and L. A. Berglund, Polymer, 42(4), 1303(2001).

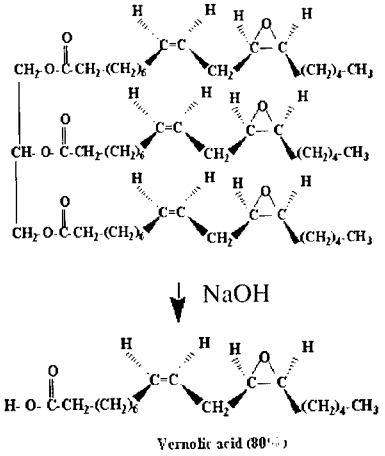


Figure 1. Reaction scheme for vernolic acid

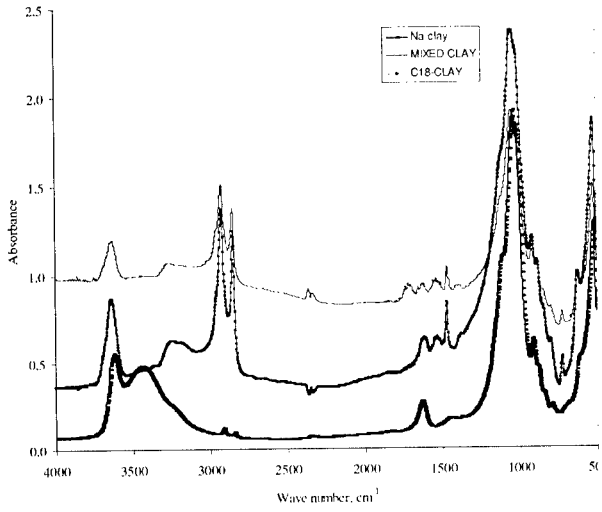


Figure 2. FTIR spectrum of Na-clay, C18 clay and vernolic acid mixed C18 clay powders.

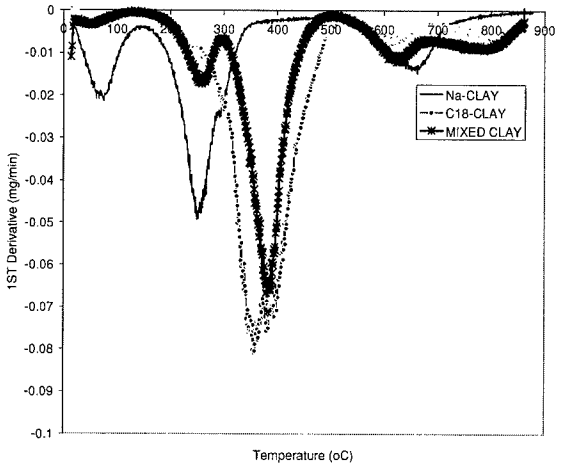


Figure 3 TGA of Na clay, C18 clay and vernolic acid mixed C18 clay powders.

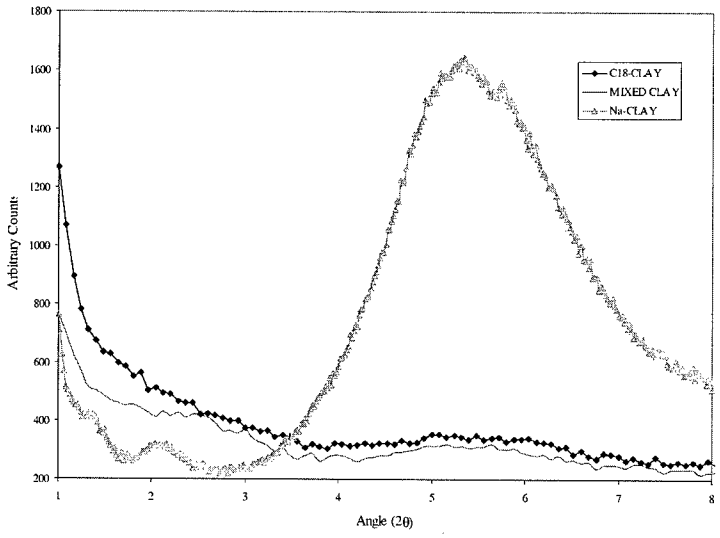


Figure 4. XRD of Na clay, C18 clay and vernolic acid mixed C18 clay nanocomposite.

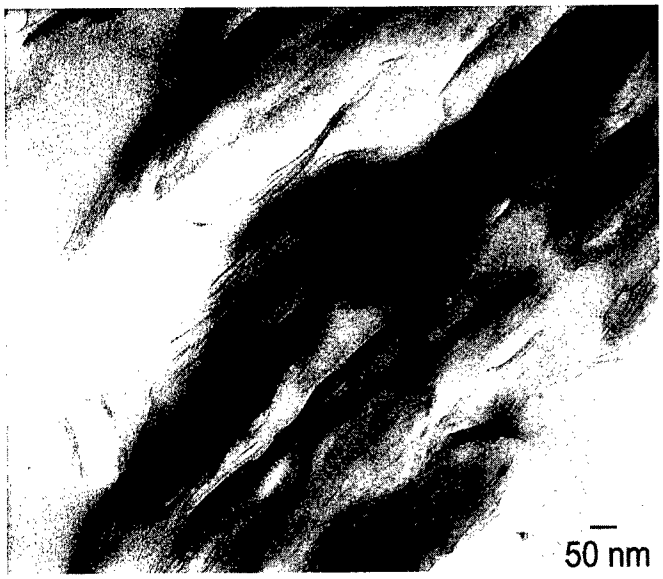


a

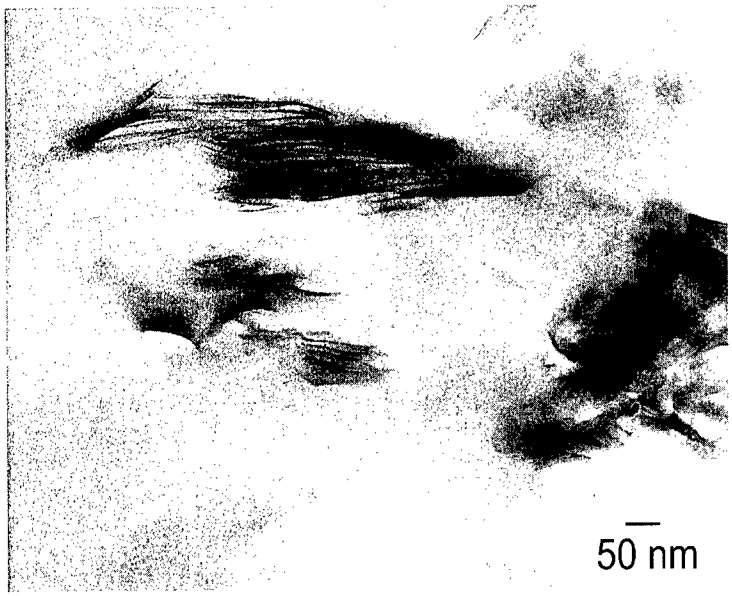


b

Figure 5. TEM of (a) vernolic acid mixed C18 clay and (b) C18 clay nanocomposite (the standard uncertianty of magnification is 3 %).

Mat. Res. Soc. Symp. Proc. Vol. 703 © 2002 Materials Research Society V9.31

# Single-Wall Carbon Nanotubes Synthesis by Means of UV Laser Vaporization: Effects of the Furnace Temperature and the Laser Intensity Processing Parameters

N. Braidy[1], M.A. El Khakani[1], G.A. Botton[2]
[1]Institut National de la Recherche Scientifique, INRS-Énergie et Matériaux, 1650 Lionel-Boulet, Varennes, PQ, J3X 1S2, Canada.
[2]Materials Technology Laboratory, CANMET, 568 Booth Street, Ottawa, ON, K1A 0G1, Canada.

## ABSTRACT

Carbon single-wall nanotubes (SWNTs) have been successfully synthesized by means of KrF laser vaporization of a Co-Ni-doped graphite pellet in a flowing argon atmosphere. The effects of two key processing parameters, namely the furnace temperature (in the 25-1150 °C range) and the laser intensity (in the 0.8-4.4 x $10^8$ W/cm$^2$ range), on the yield and the structural characteristics of the carbon SWNTs were investigated. By characterizing the obtained deposits by means of transmission electron microscopy and micro-Raman spectroscopy techniques, we were able to identify a threshold temperature as low as ~550 °C, below which no carbon SWNTs can be grown. The increase of the furnace temperature from 550 to 1150 °C was found to lead not only to a significant increase in the SWNTs yield but also to the formation of larger SWNTs bundles. Raman analysis have also revealed that the diameter distribution peak shifts from ~1.05 to ~1.22 nm as the temperature is raised from 550 to 1150 °C. At the highest furnace temperature of 1150 °C, we also found that a minimum laser intensity of about 1.6 x $10^8$ W/cm$^2$ is required to grow carbon SWNTs by means of the KrF laser. Higher laser intensities have resulted in a higher yield of SWNTs with relatively thicker bundles. Moreover, the increase of the laser intensity was found to promote the growth of 1.22 nm-diameter nanotubes to the detriment of thinner carbon nanotubes (1.05 and 1.13 nm-diameters).

## INTRODUCTION

Since the first demonstration in 1995 of the use of a Q-switch Nd:YAG laser as a new alternative to synthesize single-wall carbon nanotubes [1], the field of laser synthesis of carbon nanotubes continues to attract great interest for either fundamental or applications purposes. Indeed, the laser vaporization technique stands out by its capacity to produce exclusively single-wall nanotubes (SWNTs) at the highest yield ever reported (~80 %) [2]. Focus has been put on the study of the effect of many processing parameters in order to optimize the technique. For example, the influence of the furnace temperature was investigated for dual pulse Nd:YAG laser [3] and pulsed $CO_2$ laser [4] to conclude that a higher furnace temperature leads not only to the production of a higher fraction of SWNTs (against other carbonaceous species) but also to a preferential growth of SWNTs of larger diameters. Other studies have reported on the influence of laser intensity for single and/or dual pulse Nd:YAG laser and established the existence of an optimal laser intensity at which SWNTs are preferentially grown [5, 6]. On the other hand, all the research reported to date on the laser synthesis of SWNTs was carried out using lasers emitting in the visible and/or infrared (from 532 nm to 10,6 μm) part of the spectrum. The growth of carbon nanotubes by using lasers emitting in the UV domain remains unexplored.

In this paper, we report on the successful synthesis of SWNTs by means of UV laser vaporization. We will focus here on the study of the influence of two processing parameters, namely the furnace temperature and the laser intensity, on the growth of SWNTs. In particular, it is found that carbon SWNTs can be grown by means of KrF laser vaporization at a temperature (550 °C) lower than the lowest temperature (850 °C) required when using Nd:YAG lasers.

## EXPERIMENTAL

Carbon SWNTs were produced by ablating a Co-Ni-doped graphite pellet by means of a pulsed KrF excimer laser (wavelength = 248 nm; pulse duration = 15 ns; repetition rate = 30 Hz). The target was fabricated by pressing a mixture of a graphite powder (-325 mesh), a carbon cement and Co-Ni powder catalyst (0.6% at.) at a pressure of 5 kPsi. The obtained pellet is cured at 800°C for 8h, heated at 1150 °C for 12h in a flowing argon atmosphere and then placed in a quartz tube in the center of the furnace. During synthesis, the laser beam was rastered over the target surface in order to ensure a uniform ablation. KrF laser vaporization was carried out in a flowing argon atmosphere (300 SCCM, 500 Torr) at different furnace temperatures ranging from room temperature (RT) to 1150 °C an with various on-target laser intensities in the (0.8-4.4) x $10^8$ W/cm$^2$ range. The laser vaporized species were carried by the flowing argon gas towards a water-cooled copper collector, located at the exit end of the furnace, on which the nanotubes were collected.

The as-produced carbon deposits (no purification processing was used) were systematically characterized as a function of the processing parameters by means of : (i) transmission electron microscopy (TEM) (FEG Philips CM20 microscope, acceleration voltage of 200kV), (ii) high-resolution TEM (HRTEM) imaging (Gatan image filter multiscan camera) and (iii) micro-Raman spectroscopy (Renishaw Imaging Microscope Wire$^{PM}$, argon ion excitation with $\lambda_{exc}$= 514.5 nm).

## RESULTS AND DISCUSSION

Figure 1 shows the Raman spectra of the samples produced at various furnace temperatures ranging from RT to 1150°C with a KrF laser intensity of 3.5 x $10^8$ W/cm$^2$. The Raman peaks in the low frequency region (100-300 cm$^{-1}$) are due to the radial breathing modes (RBM) of the nanotubes, and their position ($\omega$ in cm$^{-1}$) can be directly related to the nanotube diameter ($d$ in nm) by using the relation ($d = 223.75/\omega$) proposed by Bandow *et al.* [3]. For furnace temperatures < 550 °C, the absence of RBM peaks in the low-frequency part of the Raman spectra clearly indicates that no nanotubes were formed at these low temperatures. In contrast, the strong scattering RBM peaks observed for temperatures ≥ 550 °C are a typical signature of SWNT containing samples. Indeed, the main peaks (centered around 183, 198 and 213 cm$^{-1}$) that compose the RBM band are due to carbon SWNTs having diameters of 1.22, 1.13 and 1.05 nm, respectively. As the furnace temperature is raised from 550 to 1150 °C, the RBM peak assigned to the 1.22 nm nanotubes becomes more intense to the detriment of the 1.05 and 1.13 nm-diameter nanotubes. This shift of the maximum of the nanotube diameter distribution (from 1.05 to 1.22 nm) suggests that the furnace temperature increase favors the growth of thicker nanotubes. The increase of the nanotube diameter with the growth temperature has been also observed for SWNTs produced by means of dual pulse Nd:YAG laser configuration [3].

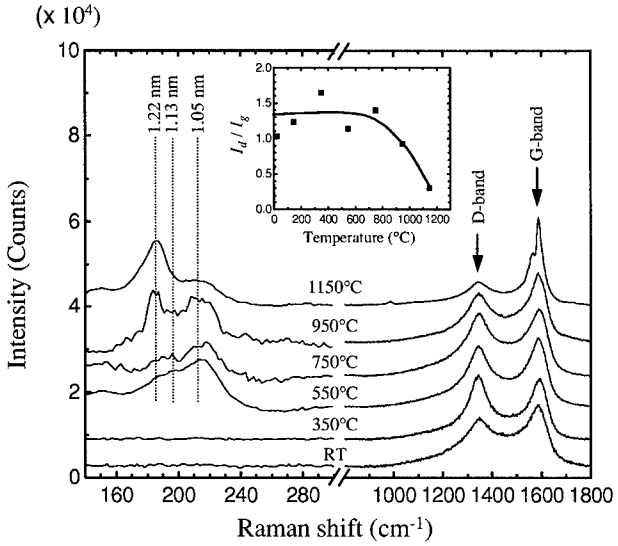


**Figure 1.** Raman spectra of the UV laser produced deposits at various furnace temperatures ranging from RT to 1150 °C. The RBM Raman peaks are identified (dashed vertical lines) along with their corresponding carbon SWNT diameters in nm. The inset shows the variation of the $I_d/I_g$ ratio of the deposits as a function of the furnace temperature.

The high-frequency G and D Raman bands are due to the graphitic $E_{2g}$ tangential acoustic mode of the SWNTs and to disordered $sp^2$ carbon, respectively [7]. The ratio of the intensities of the D-band to the G-band ($I_d/I_g$) is proportional to the relative amount of amorphous carbon or other disordered $sp^2$ carbon species [7]. The inset of figure 1 shows that the $I_d/I_g$ ratio oscillates around an average value of ~ 1.3±0.3 for furnace temperatures ≤ 750 °C, and then steadily decreases for higher temperatures to reach a value of ~0.3 at 1150 °C. This indicates that high processing temperatures lead to a lower fraction of disordered carbon in the deposits. The resonant enhancement of the G-band (which is a consequence of the high yield of SWNTs observed at high temperatures) may also contribute to the observed lowering of the $I_d/I_g$ ratio.

Figure 2 shows the typical TEM micrographs of the deposits at selected furnaces temperatures. At a furnace temperature of 350 °C, an extensive search failed to uncover any SWNT in the deposit (this is consistent with the absence of the RBM band in the corresponding Raman spectrum). The carbon soot was rather composed of graphitic cages having a concentric layer morphology and an average diameter in the 5-10 nm range (inset of Fig. 2a). At a temperature of 550 °C, bundles of SWNTs having diameters ranging from 10 to 15 nm were found in low yield. Figure 2b is a typical TEM image of the deposits synthesized at 550 °C where a loop-like bundle having 14 nm in diameter and ~1.4 μm in length is clearly observed (The HRTEM micrograph shown in the inset of Fig. 2b confirms the typical internal structure of a SWNT bundle). In addition to the nanotubes, the carbon nanostructures that compose also the deposit at 550°C were found to consist of interconnected fullerene-like structures [8]. When the furnace temperature is raised to 1150°C, the deposit was found to contain a significantly higher fraction of SWNTs (Fig. 2c) self-organized in larger bundles (15-20 nm-diameter). Moreover, the average diameter of the SWNTs was found to be 1.2±0.3 nm, as deduced from HRTEM micrographs using direct lattice images of nanotubes bundles lying parallel to the microscope focal plane [2]. At 1150°C, the carbon nanoparticles co-produced with the SWNTs were found

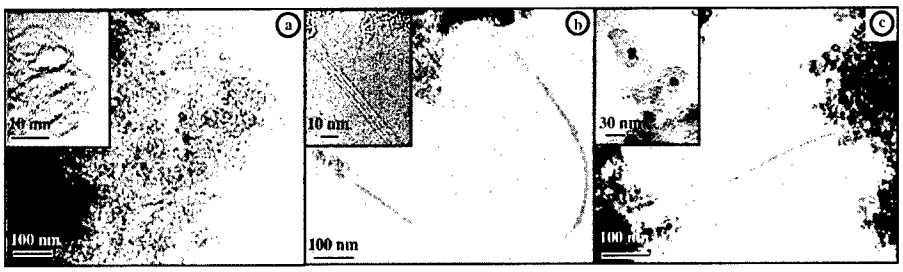


**Figure 2.** TEM micrographs of the deposits grown at (a) 350 °C, (b) 550 °C and (c) 1150 °C furnace temperatures.

to have a diameter in the 30-50 nm range and were most often constituted of amorphous carbon surrounding catalyst nanoclusters (see inset of Fig. 2c).

At the highest furnace temperature of 1150 °C, the effect of the laser intensity on the growth of SWNTs was investigated over the 0.8-4.4 x $10^8$ W/cm$^2$ range. A laser intensity of 1.6 x $10^8$ W/cm$^2$ was identified as the lowest value that produces sufficient amount of SWNTs containing soot that permits subsequent characterizations. Figure 3 displays the Raman spectra of the SWNT samples produced at increasing laser intensities. The RBM band clearly indicates the presence of carbon nanotubes having diameters in the (1.05- 1.50) nm range. One can note that as the laser intensity is increased, the 1.22 nm-diameter peak becomes sharper and more intense to the detriment of the other components. A tendency to favor the formation of nanotubes with larger diameters as the laser intensity is increased have been also reported when Nd:YAG lasers were used [6,9].

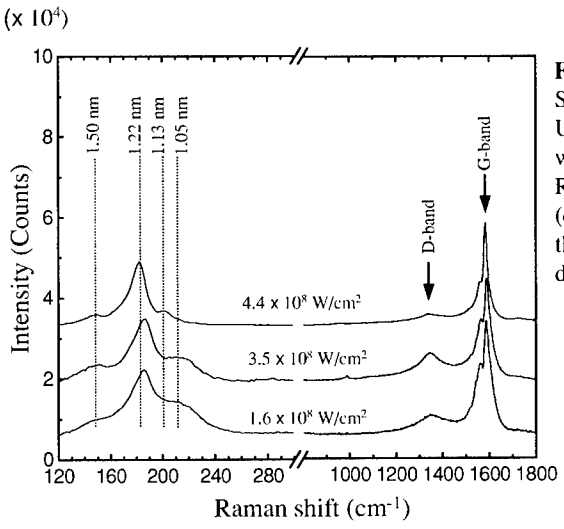


**Figure 3.** Raman spectra of the SWNTs synthesized by means of UV laser vaporization at 1150 °C with various laser intensities. The RBM Raman peaks are identified (dashed vertical lines) along with their corresponding carbon SWNT diameters in nm.

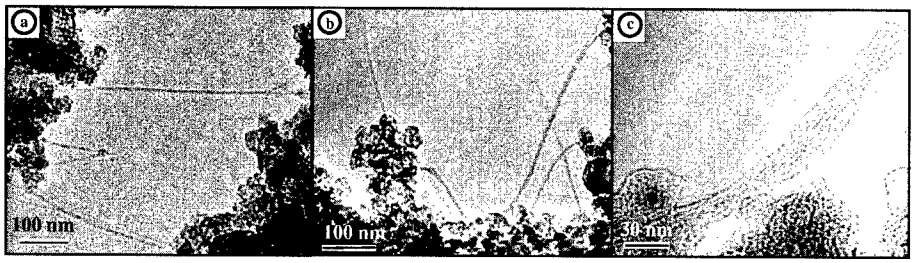


**Figure 4.** TEM micrographs of SWNT samples produced at 1150 °C with various KrF laser intensities: (a) 2.7 x $10^8$ W/cm$^2$, (b) 3.5 x $10^8$ W/cm$^2$ and (c) 4.4 x $10^8$ W/cm$^2$.

Figure 4 shows TEM micrographs taken from SWNT samples produced at different laser intensities. At low laser intensities (1.6-2.7 x $10^8$ W/cm$^2$), the deposit is constituted of SWNT bundles having an average diameter of 12 nm along with catalyst nanoclusters embedded within a-carbon nanoparticles (30-50 nm-diameter). The morphology and the diameter of these particles were found to remain insensitive to the laser intensity over all the investigated range. However, the fraction of nanotubes in the deposits was found to increase as the laser intensity is raised to 3.5 and 4.4 x $10^8$ W/cm$^2$. The diameter of the SWNT bundles also increases with the laser intensity. SWNT bundles having a diameter of up to ~30 nm were observed at the highest laser intensity investigated here (see Fig. 4c).

## CONCLUSION

The synthesis of single-wall carbon nanotubes by means of KrF laser vaporization is demonstrated. It is shown that SWNTs can be grown at a temperature as low as 550 °C. At a furnace temperature of 1150 °C, it is found that a minimum laser intensity of about 1.6 x $10^8$ W/cm$^2$ is required to produce carbon SWNTs. The obtained results show that the increase of the furnace temperature leads to a higher yield of SWNTs and favors the growth of larger SWNTs organized in thicker bundles. Similar effects, but at a lesser degree, were also observed with the increase of the laser intensity. Such a similarity could be explained by considering that an increase of the laser intensity would lead to an enhancement of the temperature of the surface target during laser vaporization. Indeed, for the relatively low laser intensities investigated here, a major part of the laser energy is expected to be absorbed at the target near-surface, acting thereby as a local furnace. Finally, the extension of the useful laser wavelengths to the UV domain not only offers a new alternative to produce efficiently SWNTs, but might also open new prospects in the fundamental and/or application aspects of laser synthesized nanotubes.

## ACKNOWLEDGMENTS

This work was financially supported by Natural Science and Engineering Research Council (NSERC) of Canada. The authors would like to thank E. Charette, P.P. Mercier and C. Sirois for their technical assistance and M. Charest for assistance during TEM observations.

## REFERENCES


1. T. Guo, P. Nikolaev, A. Thess, D.T. Colbert, and R.E. Smalley, *Chem. Phys. Lett.* **243**, (1995) 49.
2. A. Thess, R. Lee, P. Nikolaev, H. Dai, P. Petit, J. Robert, C. Xu, Y.H. Lee, S.G. Kim, A.G. Rinzler, D.T. Colbert, G.E. Scuseria, D. Tománek, J.E. Fischer, and R.E. Smalley, *Science* **273**, 483 (1996).
3. S. Bandow, S. Asaka, Y. Saito, A.M. Rao, L. Grigorian, E. Richter, and P.C. Eklund, *Phys. Rev. Lett.* **80**, 3779 (1998).
4. F. Kokai, K. Takahashi, M. Yudasaka, R. Yamada, T. Ichihashi, and S. Iijima, *J. Phys. Chem. B* **103**, 4346 (1999).
5. M. Yudasaka, T. Ichihashi, and S. Iijima, *J. Phys. Chem. B* **102**, 10201 (1998).
6. N. Braidy, M.A. El Khakani, and G.A. Botton, submitted to *Carbon* (2001).
7. J.M. Holden, P. Zhou, X.X. Bi, P.C. Eklund, S. Bandow, R.A. Jishi, K. Das Chowdhury, G. Dresselhaus, and M.S. Dresselhaus, *Chem. Phys. Lett.* **220**, 186 (1994).
8. S. Iijima, T. Wakabayashi, and Y. Achiba, *J. Phys. Chem.* **100**, 5839 (1996).
9. M. Yudasaka, T. Komatsu, T. Ichihashi, and S. Iijima, *Chem. Phys. Lett.* **278**, 102 (1997).

Mat. Res. Soc. Symp. Proc. Vol. 703 © 2002 Materials Research Society V9.38

# Using Ion Beams to Modify Nanocrystalline Composites: Co Nanoparticles in Sapphire

A. Meldrum,[1] K.S. Beaty,[1] M. Lam,[1] C.W. White,[2] R.A. Zuhr,[2] L.A. Boatner[2]
[1] Dept. of Physics, University of Alberta, Edmonton, AB, CANADA
[2] Solid State Division, Oak Ridge National Laboratory, Oak Ridge, TN, USA

## ABSTRACT

Ion implantation and thermal processing were used to create a layer of Co nanoclusters embedded in the near-surface region of single-crystal sapphire. The Co nanoparticles ranged in size from 2-20 nm and were crystallographically aligned with the host sapphire. Specimens were irradiated with Xe and Pt ions, and the microstructural evolution of the nanoclusters was investigated by transmission electron microscopy. With increasing Pt or Xe ion dose, the Co nanoparticles lost their initially excellent faceting, although they remained crystalline. The host $Al_2O_3$ became amorphous and the resulting microstructure consisted of a buried amorphous layer containing the still-crystalline Co nanoparticles. EDS mapping and electron diffraction were used to determine the distribution of the implanted species, and the magnetic properties of the composite were measured with a SQUID magnetometer. The results show that ion beams can be applied to modify and control the properties of ferromagnetic nanocomposites, and, combined with lithographic techniques, will find applications in exercising fine-scale spatial control over the properties of magnetic materials.

## INTRODUCTION

Ion irradiation is an established and widely used technique for modifying and controlling the microstructural and electronic properties of thin films. Frequently, the injected ions pass through the film, creating displacement defects and ion mixing effects, but no intrinsic chemical changes. In recent years, several investigations have used ion irradiation as a means of controlling or patterning film properties. For example, the magnetic exchange bias of ferromagnetic-antiferromagnetic thin film multilayers can be modified and controlled by ion irradiation [1]. Ion irradiation has also been used to alter magnetic hysteresis behavior, and it has been possible to use lithographic masking combined with He-ion irradiation to pattern the magnetic properties of thin film materials [2].

In contrast, the effects of ion irradiation on nanocrystalline composites have not been extensively investigated despite over 50 years of radiation damage studies on bulk materials. As is the case for thin films, ion irradiation is expected to radically alter the microstructural and electronic properties, physical strength, and hardness of nanocomposites. These effects may be particularly important where nanocrystalline materials are to be used in high-flux environments (e.g., space flight). Furthermore, ion irradiation offers an excellent opportunity to create or pattern materials with novel properties.

The profusion of unique and/or novel properties displayed by nanocomposites produced by ion implantation suggests many applications [3]. However, one difficulty has been the fine-scale control of opto-electronic and magnetic effects. For example, Co particles produced by ion implantation into sapphire or other substrates show relatively low coercivities – regardless of the implant dose and post specimen processing (e.g., see Refs. 3,4). Using ion irradiation, it is possible, however, to increase the coercivity of Co-nanocomposite-based magnetic materials –

due to at least partly to radiation-induced amorphization of the host material. The optical properties of semiconductor nanoparticles may also be controlled or otherwise modified. New studies have recently shown that the characteristic red luminescence of Si nanoclusters embedded in $SiO_2$ can be strongly reduced, or even shifted in wavelength [e.g., Refs. 5,6,7]. These investigations have suggested the utility of ion irradiation for modifying opto-electronic properties of interest. In the present work, we focus on the results of experiments in which ion beams are used to modify the microstructural and magnetic properties of embedded Co nanocluster composites.

## EXPERIMENTAL

High-purity sapphire wafers were implanted with 140 keV $Co^+$ to a dose of 8 x $10^{16}$ ions/cm$^2$ at room temperature. Thermal treatment was carried out for two hours at 1100°C under flowing Ar + 4%$H_2$. After 120 minutes, the specimen was retracted from the hot zone and allowed to cool. X-ray diffraction and transmission electron microscopy were used to determine the structure and orientation of the resulting Co nanoparticles. The Co-sapphire nanocomposite was then irradiated at room temperature with either 244 keV Xe or 320 keV Pt ions to varying ion fluences. The corresponding dose was calculated by using the Monte Carlo computer code SRIM-2000 [8] in the full cascade mode to obtain the number of displacements per ion per nm, using displacement energies for Al and O of 20 and 50 eV, respectively. Since the ion dose varies as a function of depth, for simplicity we will refer to the dose at a depth of 60 nm (corresponding to the observed center of the Co-nanoparticle profile). Samples were prepared for TEM by conventional thinning and polishing methods. *Ex-situ* cross-sectional and plan-view electron microscopy was used to investigate the resulting particle microstructure. Cross-sectional TEM was also done in the scanning mode to determine the chemical distribution of implanted elements. *In-situ* ion irradiation experiments using 1.0 MeV $Xe^{2+}$ were conducted directly in an electron microscope at the IVEM Facility (Argonne National Laboratory). The room-temperature magnetic properties of the bulk specimens were measured using a SQUID magnetometer or by magnetic circular dichroism (MCD).

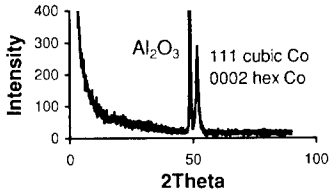

Fig. 1. X-ray diffraction results.

## RESULTS AND DISCUSSION

Figure 1 shows the X-ray diffraction results from Co-implanted and annealed sapphire. A single peak due either to the [0002] axis of hexagonal Co or to the [111] axis of cubic Co was observed. We have previously used four-circle diffraction techniques to show that a mixture of the hexagonal and cubic phases is present [4]. Plan view and cross sectional TEM images are given in Fig. 2. In plan view, most of the nanocrystals appear well faceted, having triangular or hexagonal shapes with edges parallel to the in-plane crystallographic axes of the sapphire. In cross section, there is a distinct boundary at a depth of ~55 nm in the sapphire, below which the nanocrystals are more-or-less rounded, and above which they show good crystal facets. The well-faceted particles are somewhat elongated parallel to the specimen surface. The 55-nm

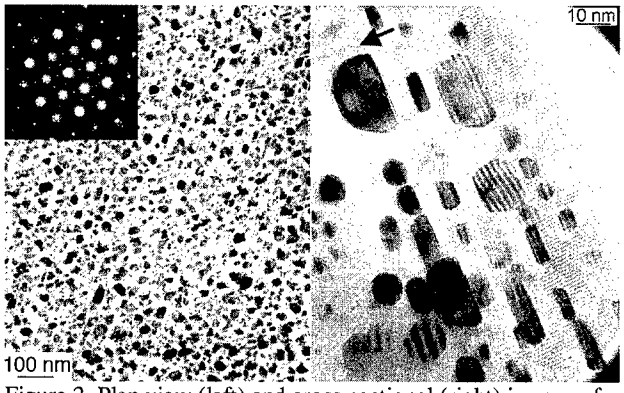

Figure 2. Plan view (left) and cross-sectional (right) images of the Co-implanted and annealed $Al_2O_3$ wafer. The arrow marks the depth above which the Co precipitates are well faceted.

boundary corresponds to the approximate depth at which the sapphire becomes amorphous during the room-temperature Co ion implantation. When the sapphire recrystallizes during thermal processing, the nanoclusters forming in the initially amorphous regions become well faceted, although the exact diffusion-related mechanism for this process remains to be investigated. The precipitates range in size from 2 to 20 nm (long axis). An [0001] zone axis electron diffraction pattern is shown as an inset to Fig. 2. There is a complex arrangement of double diffraction spots that are due to both the cubic and hexagonal Co, as well as top-bottom effects (the rings of double diffracted spots immediately surrounding the main sapphire maxima are due to the effects of the electron beam passing first through a Co precipitate and then through sapphire, and vice-versa).

Figure 3 shows the microstructural effects of 244 keV Xe irradiation. With increasing ion dose, the faceting gradually disappeared and all the particles were rounded, with some mottled internal contrast. Dark-field imaging suggested the presence of dislocation defects and possibly void or bubble-like structures within the particles. The sapphire was highly damaged, but the Co nanoparticles remained crystalline and relatively well aligned, although with poor or absent faceting. In the *in-situ* experiments, the host sapphire gradually became amorphous, and the loss of precipitate faceting was also observed. Amorphization of sapphire has not previously been reported in *in-situ* ambient-temperature irradiation experiments. Here, we irradiated to doses exceeding 10 dpa and used a low ion energy (200 keV) in order to mimic both the displacement damage and chemical effects occurring in bulk implanted specimens.

Co-sapphire nanocomposite specimens were also implanted with Pt, and both cross-sectional and plan-view electron microscopy was used to investigate the microstructure (Fig. 4). The Pt ion fluence was selected to give approximately the same displacement dose as for the 244 keV Xe irradiation. Compared to Fig. 2, the Co nanoparticles are again poorly faceted although they are still crystalline, and they are embedded within a buried amorphous layer formed in the sapphire. Overall, the effects of Xe

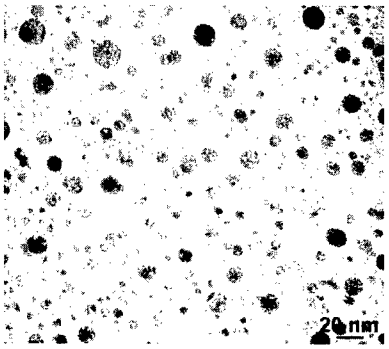

Fig. 3. Co-sapphire specimen in Fig. 2 irradiated with 244 keV Xe to a dose of ~17 dpa.

and Pt irradiation on the particle microstructure were similar: in both cases the precipitate faceting disappeared; and although the particles remained crystalline, and the sapphire host material was damaged or amorphized.

EDS mapping was used to investigate the location and distribution of the implanted material. Particularly in the case of the Pt-implanted Co nanocomposite, it is important to know whether the Pt is preferentially attracted to the pre-existing Co nanoparticles (e.g., to produce a Co-Pt alloy). Figure 5 shows a set of EDS maps for Co and Pt. The Co particles appear clearly in the Co map, but the Pt retains its implant distribution and is not preferentially located within the pre-existing Co particles. There was also no evidence of a Co-Pt alloy in the electron diffraction patterns. Therefore, the observed *microstructural* changes are probably due largely to the effects of radiation damage and less to any chemical reaction between the Co and the Pt.

The magnetic measurements were done using magnetic circular diochroism (e.g., see Ref. 4). The magnetic coercivity of the annealed Co-sapphire composite is ~50 G and the saturation magnetization is 0.014 MCD units. After Xe irradiation to a fluence of 9 x $10^{15}$ ions/cm$^2$, the coercivity increased to 464 G and the saturation MCD signal was 0.0071 units. The Pt-irradiated sample had the highest coercivity (1,500 G) and the saturation magnetization was 0.0081 units. For both Xe and Pt irradiated samples, the coercivity increases rapidly at first, but then reaches a saturation value at approximately 20 dpa (Fig. 6).

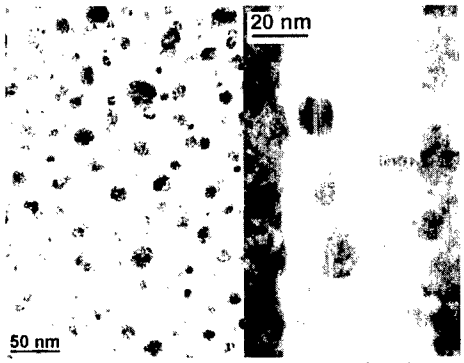

Fig. 4. Plan view (left) and cross-sectional images for Pt-irradiated Co nanocrystals in sapphire (dose = 14.4 dpa). The light band in the cross-sectional image is amorphous sapphire and the darker bands are still-crystalline sapphire. The surface was to the right of the cross sectional image.

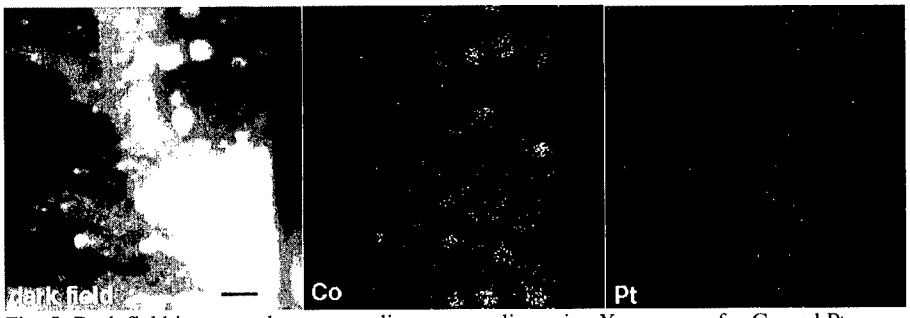

Fig. 5. Dark field image and corresponding energy-dispersive X-ray maps for Co and Pt. Scale bar is 20 nm.

Pt implantation increases the coercivity of the Co-sapphire composite by a factor of 2-3 more than the Xe implantation, for similar displacement doses. However, the EDS mapping and

electron diffraction do not suggest alloy formation in the Pt-implanted substrate on a scale larger than ~2 nm. Since the Pt implant has a greater effect on the coercive field than the Xe implant for the same ion dose, a chemical effect of some type must be involved. In initial work, we have found that nanocrystals of tetragonal CoPt alloy formed by co-implantation and annealing of sapphire have coercivities ranging up to several kG. If atomic-scale domains of this phase form within the pre-existing Co precipitates, the magnetic hardness could increase more than it would due to radiation damage alone. Further high-resolution electron microscopy will provide more information on the atomic-level structure of these particles.

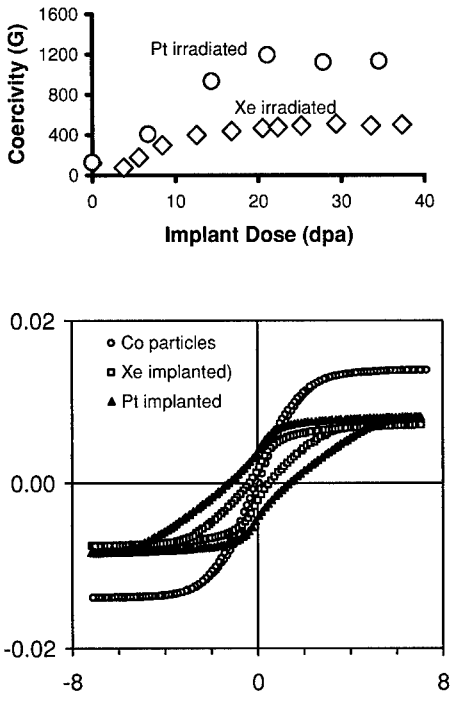


Fig. 6. Top: Coercive field as a function of implant dose for Xe- and Pt-irradiated Co nanocrystals in sapphire. Bottom: hysteresis loops for the 3 samples shown in Figs. 2-4. The abscissa is the applied field in kG and the ordinate is the magnetic circular dichroism (arbitrary units)

These results suggest that ion irradiation has a considerable effect on the microstructural and magnetic properties of magnetic nanocluster composites. Careful selection of the irradiation conditions can be used to control or tailor the coercivity and saturation magnetization. Control over the lateral distribution of irradiated material would, for the first time, provide spatial control over the magnetic properties of magnetic nanocomposites formed by ion implantation. To this end, we have recently begun experiments employing lithographic masking techniques to control the distribution of the implanted material and to radiation-pattern the resulting composite. Figure 7 shows a preliminary result, where the letters "U of A" are written as conglomerates of embedded nanoscale precipitates formed by implantation of iron into an $SiO_2$ wafer. Experiments are ongoing [9].

## CONCLUSION

This work describes ion irradiation effects on the microstructural and magnetic properties of Co-sapphire nanocomposites confirming that the magnetic properties of Co particles can be modified and controlled by ion bombardment. However, considerable work remains to be done

in order to obtain a complete understanding of both irradiated and unirradiated Co-sapphire nanocomposites. While ion irradiation can clearly be used in controlling the microstructure and magnetic properties of Co-nanocluster composites, the technique can also be used to modify other materials of interest (examples include the absorption and emission characteristics of semiconductor nanocrystals). Our ongoing ion-beam patterning experiments will permit fine-scale spatial control over the properties of interest, and we have also recently demonstrated that unusual microstructural effects can occur during irradiation of embedded nanocrystals [10]. Despite recent funding cuts at several American ion-beam laboratories, we believe that some of the most interesting times for implanted nanoparticle research are just beginning.

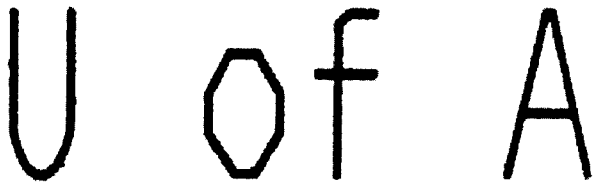


Fig. 7. Optical image showing "letters" written with Fe nanoclusters implanted into fused silica. The letters are 68 microns high and 5 microns wide.

ACKNOWLEDGMENTS

Work at the University of Alberta is supported by NSERC. Oak Ridge National Laboratory is managed by UT-Battelle, LLC, for the U.S. Department of Energy under Contract No. DE-AC05-00OR22725

REFERENCES

1 T. Mewes, R. Lopusnik, B. Hillebrands, M. Jung, D. Engel, A. Ehresmann, and H. Schmoranzer, Appl. Phys. Lett. **76**, 1057 (2000).
2 T. Devolder, C. Chappert, V. Mathet, H. Bernas, Y. Chen, J. P. Janet, and J. Ferré, *J. Appl. Phys.* **87**, 8671 (2000).
3 A. Meldrum, R.F. Haglund, L.A. Boatner, and C.W. White, Adv. Mater. **13**, 1431 (2001).
4. S. Honda, F.A. Modine, A. Meldrum, J.D. Budai, T.E. Haynes, and L.A. Boatner, Appl. Phys. Lett. **77**, (2000).
5. D.I. Tetelbaum, S.A. Trushin, Z.F. Krasil'nik, D.M. Gaponova, A.N. Mikhailov, Optical Materials **17**, 57 (2001).
6. S. Cheylan, N. Langford, and R.G. Elliman, Nucl. Instr. Meth. **166**, 851 (2000).
7. G.A. Kachurin, S.G. Yanovskaya, K.S. Zhuravlev, M.O. Ruault, Semiconductors **35**, 1182 (2001).
8. J. F. Ziegler, SRIM 2000, IBM-Research, Yorktown, NY (2000).
9 K.S. Beaty, A. Meldrum, J.P. Franck, K. Sorge, J. R. Thompson, C.W. White, R.A. Zuhr, L.A. Boatner, S. Honda (these proceedings).
10. A. Meldrum, L.A. Boatner, and R.C. Ewing, Phys. Rev. Lett. (accepted).

# Self Assembly of Nanophase and Nanocomposite Materials

Mat. Res. Soc. Symp. Proc. Vol. 703 © 2002 Materials Research Society V10.2

# Silver-Polyimide Nanocomposite Films Yielding Highly Reflective Surfaces

Robin E. Southward,[1] C. J. Dean,[2] J. L. Scott,[2] S. T. Broadwater,[2] and D. W. Thompson[2]
[1]Structure and Materials Competency, NASA, Langley Research Center, Hampton, VA 23681
[2]Department of Chemistry, College of William and Mary, Williamsburg, VA 23187

## ABSTRACT

Highly reflective surface-metallized flexible polyimide films have been prepared by the incorporation of the soluble silver ion complex (1,1,1-trifluoroacetylacetonato)silver(I) into dimethylacetamide solutions of the poly(amic acid) prepared from 2,2-bis(3,4-dicarboxyphenyl)-hexafluoropropane dianhydride (6FDA) and 2,2-bis[4-(4-aminophenoxy)phenyl]hexafluoro-propane (4-BDAF). Thermal curing of solution cast silver(I)-poly(amic acid) films leads to cycloimidization of the amic acid with concommitant silver(I) reduction and formation of a reflective surface-silvered film at 8 and 13 weight percent silver. The metallized films are thermally stable and flexible with mechanical properties similar to those of the parent polyimide. TEM reveals that the bulk (interior) of the polyimide composite films have 5-20 nanometer-sized silver particles with a surface layer of silver metal ca. 80 nm thick. Neither the bulk nor the surface of the films is electrically conductive. Adhesion of the surface metal to polyimide is excellent.

## INTRODUCTION

The fabrication of specularly reflective and electrically conductive surface metallized polyimide films is of enormous interest as reviewed by Matienzo and Unertl [1]. Applications are numerous including: anti-infective coatings, contacts and circuit lines in microelectronics, enhancement of thermal conductivity, flexible surface conductive tapes, patternable conductive surfaces on dielectric bases, the terrestrial concentration of solar radiation for power generation, and gas permeability barriers. Of particular interest to us are space applications of metallized polyimides. These include highly reflective thin film reflectors and concentrators in space environments for solar thermal propulsion [2] and solar dynamic power generation [3,4], reflectors for flat panel solar power arrays for satellites [5], large scale radiofrequency antennas for the management of EM signals [6], solar sails [7,8], and sunshields to control device temperatures for projects such as the Next Generation Space Telescope. Polymeric supports offer advantages in weight, flexibility, elasticity, fragility, and deployability relative to inorganic supports such as glass and ceramics.

Southward et al. [9] and Taylor et al. [10] have have been successful in preparing surface-metallized, in particular silver-metallized, polyimide films by a novel single-stage, internal metallization technique which leads to flexible films with excellent specular reflectivity and/or electrical conductivity. "Single-stage" denotes the fabrication in one step of metallized films from a homogeneous solution of a positive valent metal precursor and a poly(amic acid). In contrast to traditional metallized film preparation protocols, in the present work the polyimide film is not prepared in a first stage and subsequently coated with metal (vapor deposition, sputtering, etc.) in a discrete second stage. "Internal metallization" refers to a film that is cast as a homogeneous silver ion-doped poly(amic acid) solution and then thermally treated to induce metal ion reduction to give the metallized surface with concomitant cycloimidization of the amic

acid to the final polyimide. During the thermal cycle a portion of metal atoms and small clusters formed in the polyimide film aggregate at the surface to give a 50-200 nm metallic layer. Silver is the metal of interest since it has exceptional reflectivity and conductivity [11]. Polyimides were chosen as substrates owing to their excellent thermal-oxidative stability and film-forming properties [12,13].

The synthetic protocol with respect to the system reported herein is illustrated in Figure 1. Silver(I) acetate and trifluoroacetylacetone (TFAH) are allowed to react in the solvent dimethylacetamide (DMAc) to give an *in situ* solution of the (trifluoroacetylacetonato)silver(I) complex, AgTFA. A DMAc solution of the poly(amic acid) form of 6FDA/4-BDAF is added to the DMAc solution of AgTFA. A colorless homogeneous solution results. A film is then cast. Thermal curing of the Ag(I)-poly(amic acid) film effects reduction of Ag(I) to native metal and ring closure to the imide. During the cure silver atoms/clusters aggregate in part at the surface to give reflective films, usually with excellent adhesion of metal to polyimide.

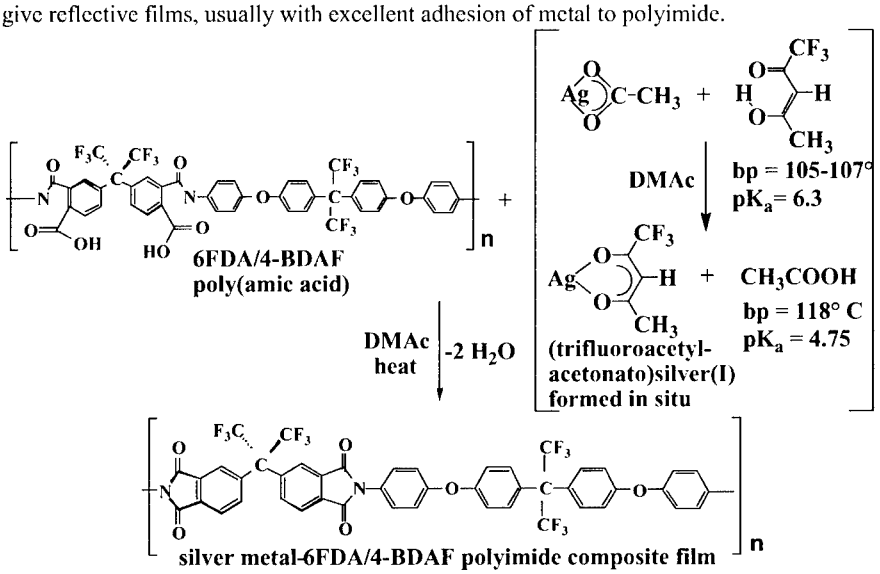


**Figure 1.** Synthetic route to a polyimide metallized film.

For present study described herein we chose the 6FDA/4-BDAF polymer because it has been reported to have high thermal stability, radiation resistance, and low absorption in the visible [14]. The low color of this polyimide is of importance since in previous studies of metallized polyimides exhibit a thin polyimide overlayer or significant polyimide at the surface. Since tradition polyimides such as PMDA/ODA, BTDA/ODA, BPDA/ODA, etc. absorb strongly in the visible, some of the loss of reflectivity has been due to surface polymer absorption.

## EXPERIMENTAL DETAILS

**Materials.** All chemicals were obtained from commercial sources. 6FDA/4-BDAF poly(amic acid) solution was prepared with a 0.5% offset of dianhydride at 15% solids (w/w) in DMAc. The resin was stirred for 5 h. The inherent viscosity was 1.2 dL/g at 35° C.

**Preparation of BTDA/4,4′-ODA metallized films.** Ag(I)-containing solutions were prepared by first dissolving silver(I) acetate in DMAc containing trifluoroacetylacetone. The 15% poly(amic acid) solution was then added to give the desired Ag to polymer ratio. Doped poly(amic acid) solutions were cast as films onto glass plates using a doctor blade set at 500-650 μm to obtain cured films 20-25 μm thick. After remaining in an atmosphere of slowly flowing dry air for 18 h, the films were cured in a forced air oven. The cure cycle involved heating over 20 min to 135 °C and holding for 1 h, heating to 300 °C over 4 h, and holding at 300 °C varying times.

## RESULTS AND DISCUSSION

As seen in Figure 2, poly(amic acid)-DMAc or diglyme (2-methoxyethyl ether) films retain a substantial portion of solvent which cannot is not lost by evaporation at 25 °C. Thus, thermal cure of Ag ion-doped films occurs in a solvent rich state; the solvent then may play a role in metal ion reduction and also serve as a plasticizing agent. Figure 3 shows the development of reflectivity as a function of time/temperature for 8 and 13 wt% silver-6FDA/4-BDAF polyimide films. For the 8% film maximum reflectivity is observed after 2 h at 300 °C. The 13% film achieves maximum reflectivity after only 1 h at 300 after which the reflectivity diminishes dramatically due to metal promoted oxidative degradation of the polyimide. The observed reflectivities (relative to an optical Al mirror) are high and do not show a strong concentration dependence (8 versus 13%). The metal is firmly adhered to the polyimide and cannot be removed by adhesive tape test protocols.

Figure 4 displays TEM data for the 13% film. The surface silver is ca. 80 nm thick and composed of particles of globular shape. The bulk of the film contains silver particle with sizes in the 5-20 nm range. Thus, only a limited quantity of the original silver appears at the surface. While the 8 and 13% films have excellent reflectivity, neither is electrically conductive. The SEM for the 13% film (Figure 5) shows the globular form of the silver particles and reveals that the particles do not form a continuous network. Intervening polyimide keeps the nanoparticles effectively isolated.

While significant reflectivity for the two films is not observed until 300 °C, X-ray data shown in Figure 6 for the 13% films make clear that reduction to silver metal is occurring at temperatures as low as 175 °C. Thus, sufficient silver aggregation at the surface to form a mirror is much slower than silver(I) reduction. Interestingly, the early low temperature silver reflections are significantly broadened which is consistent with Scherrer broadening due to very small nanometer-sized particles. As curing temperature and time increase the reflections narrow with the larger particle sizes seen in the TEM and SEM at 300 °C for 1 h.

The metallized exhibited tensile moduli and strength which are not significantly different from those of the parent polyimide. This is consistent with the relatively low concentration of silver metal and with the fact that silver is a passive metal which does not interact strongly with polyimide functional groups. Thus, the metallic silver particles appear to behave as a inert nano-filler in the polymer. The glass transition temperature in the metallized films is unchanged from that of the parent. However, while thermal stability remains high, the temperature at which there is 10% weight loss in air is *ca.* 125 °C lower than for the parent polyimide. In nitrogen the thermal stability is the same as the parent indicating that silver metal, as expected, catalyzes polyimide degradation at higher temperatures.

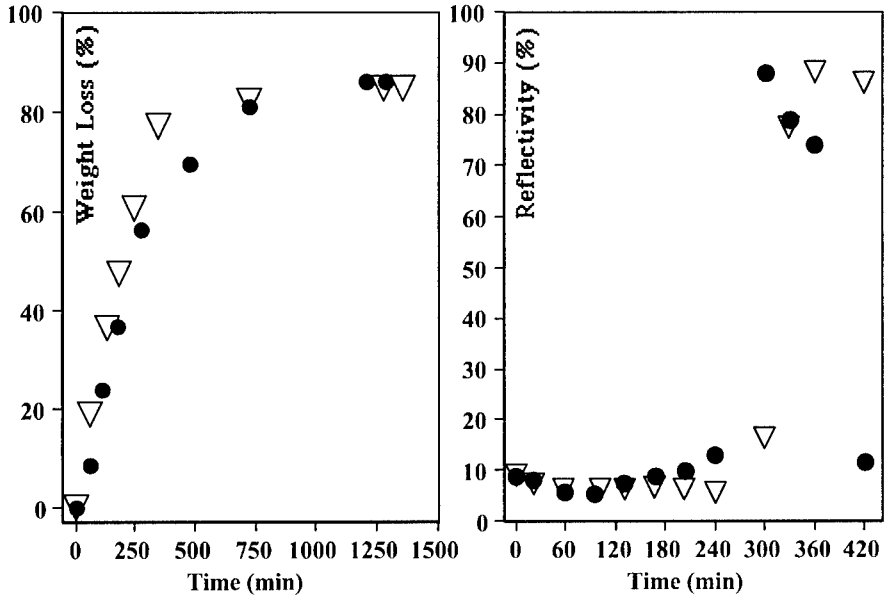


**Figure 2.** (Left) Evaporative solvent loss (DMAc-circle and diglyme-triangle) as a function of time under slowly flowing dry air.
**Figure 3.** (Right) Specular reflectivity as a function of time and temperature for 8% (triangle) and 13% (circle) silver-6FFDA/4-BDAF films

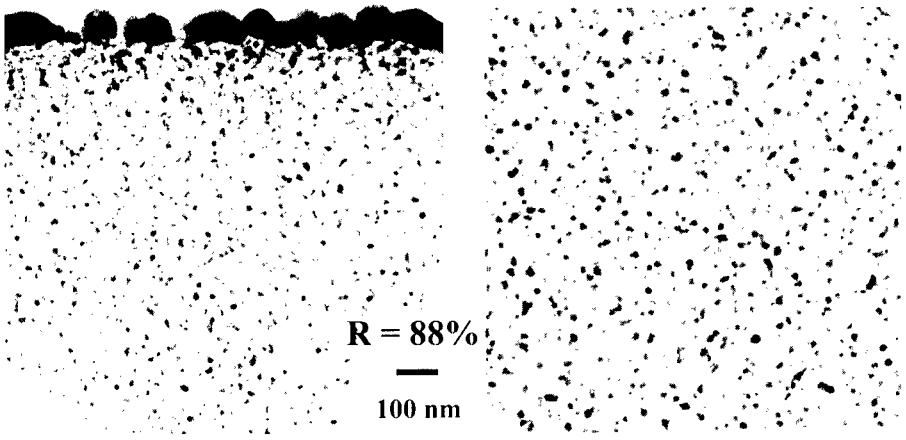


**Figure 4.** TEM micrographs for the 13% silver-6FDA/4-BDAF film cured to 300 °C for 1 h. Left - surface view; Right - bulk view.

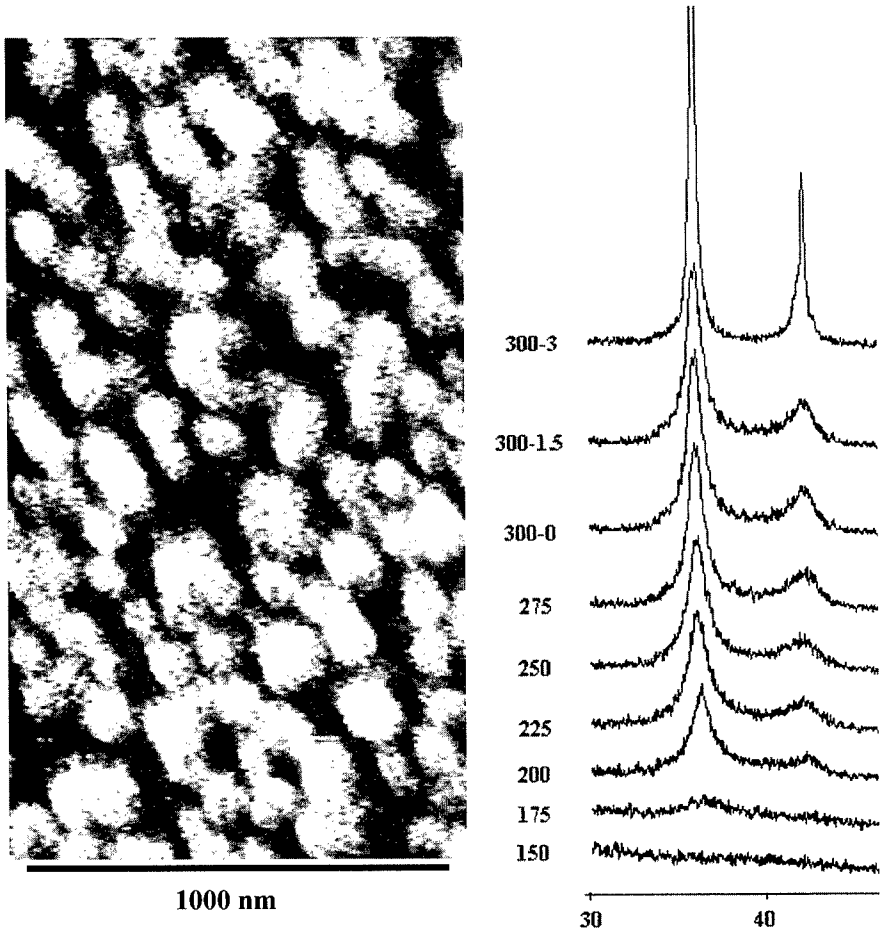


**Figure 5. (Left)** SEM micrograph for the 13% silver-6FDA/4-BDAF metallized film cured to 300 °C for 1 h.

**Figure 6. (Right)** X-ray reflections for a series of 13% silver-6FDA/4-BDAF metallized films as a function of cure temperature and time. The abscissa is in units of two theta; the ordinate is the temperature in °C at which the sample was withdrawn from the oven; at 300 °C samples where withdrawn after 0, 1.5, and 3 h. (See experimental section for cure cycle details.)

## CONCLUSIONS

Silver surface-metallized films with high reflectivities can be prepared from AgTFA with the fluorinated polyimide 6FDA/4-BDAF in a thermally promoted single-stage process. These

metallized films are not electrically conductive. Metal-polyimide adhesion is excellent, and thermal and mechanical properties of the composite films remain near those of the parent polymide.


## ACKNOWLEDGMENT

The authors thank the Petroleum Research Fund administered by the American Chemical Society for partial support of this work.


## REFERENCES


1. Matienzo, L. J.; Unertl, W. N. "Adhesion of Metal Films to Polyimides,"in *Polyimides: Fundamental and Applications*, ed. Ghosh, M. K.; Mittal, K. L., Marcel Dekker, New York, 1996. pp. 629-696.
2. Gierow, P. A. in *Proceedings of the ASME-JSME-JSES Solar Energy Conference*: Reno, NV, 1991; pp 1-7.
3. Ehricke, K. in *Meeting of the American Rocket Society*: Cleveland, OH, June 18-20,1956; pp ARS paper 310-56.
4. Gulino, D. A.; Egger, R. A.; Bauholzer, W. F. *NASA Technical Memorandum 88865*, **1986**.
5. Naval Research Laboratory, "Solarcon - Concentrator Reflector System," described online: code8200.nrl.navy.mil/solarcon.html.
6. Freeland, R. E.; Bilyou, G. in *43rd Congress of the International Astronautical Federation, IAF-92-0301*: Washington, D.C., 1992
7. McInnes, C. R. *Solar Sailing Technology: Dynamics and Mission Applications*, Springer-Verlag, London, 1999.
8. Garner, C.; Diedeich, B.; Leipold, M. A Summary of Solar Sail Technology Developments, *AIAA/ASME/SAE/ASEE, 35th Joint Propulsion Conference and Exhibit*, Los Angeles, CA, June 21-23, 1999. Available online: techreports.jpl.nasa.gov
9. Southward, R. E.; Stoakley, D. M. *Progress in Organic Coatings*, **2001**, *41*, 99-119 and references therein.
10. Rubira, A. F.; Rancourt, J. D.; Taylor, L. T.; Stoakley, D. M.; St. Clair, A. K. *J. Macromolecular Sci., Pure and Applied Chemistry* **1998**, *A35*, 621-636 and references therein.
11. Jorgensen, G.; Schissel, P. in *Metallized Plastics*; Mittal, K. L.; Susko, J. R., eds.; Plenum: New York, 1989; Vol. 2, pp 79-92.
12. Bower, G. M.; Frost, L.W. *J. Polym. Sci., A* **1963,** *1*, 3135.
13. Sroog, C. E.; Endrey, A. L.; Abramo, S. V.; Berr, C. E.' Edwards, W. M.; Olivier, K. L. *J. Polym. Sci., A*, **1965**, *3*, 1373.
14. Clair, A. K. S.; Clair, T. L. S.; Slemp, W. S. "Optically Transparent/Colorless Polyimides:" in *Recent Advances in Polyimide Science and Technology*; Weber, W. D., Gupta, M. R., eds.; Society of Plastic Engineers, Mid-Hudson Section: Poughkeepsie, 1987, pp.16-34.

Mat. Res. Soc. Symp. Proc. Vol. 703 © 2002 Materials Research Society V10.6

# Investigating Catalytic Properties of Composite Nanoparticle Assemblies

M.M. MAYE, J. LUO, Y. LOU, N. K. LY, W.-B. CHAN, E. PHILLIP,
M. HEPEL[a], C.J. ZHONG*
Department of Chemistry, State University of New York at Binghamton, Binghamton, NY 13902. [(a)] Department of Chemistry, State University of New York at Potsdam, Potsdam, NY 13676. [(*)] cjzhong@binghmaton.edu

## ABSTRACT

We present herein recent findings of an investigation of catalyst assembly and activation using metallic nanoparticles encapsulated with organic monolayers. Gold nanocrystals (2~5 nm) encapsulated with thiolate monolayers assembled on electrode surfaces, were found to be catalytically active towards electrooxidation of CO and MeOH upon activation. The activation involved partial removal of the encapsulating thiolates and the formation of surface oxygenated species. A polymeric film was also used as a substrate for the assembly of the nanoparticle catalysts. When the polymer matrix was doped with small amounts of Pt, a remarkable catalytic activity was observed. These catalysts were characterized utilizing cyclic voltammetry and atomic force microscopy.

## INTRODUCTION

The pioneer work of two-phase synthesis of gold nanoparticles with a few nm core size stabilized by alkanethiolate monolayers has led to increasing research and development interest in the field of composite nanomaterials [1]. The possibility of further processing of these particles into highly monodispersed, larger sized, and stable nanoparticles has enabled the ability to probe size-dependent reactivity, as recently demonstrated in our laboratory [2]. These nanoparticles can be effectively linked to form thin films using molecular crosslinking agents. There are several routes reported for crosslinking. One involves a stepwise "layer-by-layer" assembly method [3], and another involves one step "exchange-crosslinking-precipitation" route developed recently in our laboratory [4]. The nanostructured thin films have potential applications in microelectronics, optics, biomimetics, molecular recognition, drug delivery, chemical and environmental sensing, and catalysis [5,6,7].

Gold is traditionally considered as catalytically inert. The recent finding by Haruta and co-workers [8] demonstrated that the catalytic ability for gold increases as the size is reduced to nanometer scales [9]. Gold nanoparticles supported on oxides show high catalytic activity to CO oxidation. Although the idea of using small sized particles as catalysts has been known for a long time, problems faced when using bare nanoparticles include aggregation, short life times, and propensity of poisoning. We recently hypothesized that the core-shell nanoparticles (CSNs) could be used to solve some of these problems. Part of the concept is related to the high stability and the reactivity of CSNs by which they can be assembled in a controllable way. While the use of surface protected nanoparticles as catalysts has the effect of preventing particles from aggregation, catalytic activity may become hindered due to possible inhibiting surface

materials. To demonstrate the viability of the CSN based catalysis, we recently explored pathways that take advantage of the CSNs solubilities and functionalities to assemble thin films, and the controllable activation by core-shell surface re-constitution. The formation of surface oxygenated species is found to play an important role in the effective catalytic abilities of such thin film catalysts. In this paper, our latest results of an investigation of issues related to the catalytic activation are described.

## EXPERIMENT

*Synthesis.* The 2-nm gold nanoparticles ($Au_{2\text{-nm}}$), and 2.5 nm Au/Pt nanoparticles ($(Au/Pt)_{2.5\text{-nm}}$), were encapsulated with alkanethiolate monolayer shells were synthesized by the standard two-phase method [10]. Briefly, $AuCl_4^-$, or $AuCl_4^-$ + $PtCl_6^{2-}$ (5:1 feed ratio), was transferred to organic solvent by phase transfer agent (tetraoctylammonium chloride), and reduced by sodium borohydride in the presence of decanethiols (DT). The reaction was allowed to proceed under stirring at room temperature for 4 hours, producing a dark-brown solution of DT-encapsulated nanoparticles that was then cleaned in ethanol or used in the heating treatment.

*Processing.* Highly-monodispersed Au particles (5.3 ±0.3 nm) were prepared by thermally activated treatment of the pre-synthesized 2-nm Au nanoparticles [2]. Briefly, the 2 nm particles were pre-concentrated by a factor of ~15, heated to 140 $^0$C, and annealed at 100 $^0$C for ~2 hours. The resulting red nanoparticle solution was then cleaned in ethanol.

*Thin film Assembly.* The nanoparticles were assembled as thin films on electrode surfaces using molecular linkers via one-step exchange-crosslinking-precipitation route [4]. In a typical experiment, 1,9-nonanedithiols (NDT) were mixed in a hexane solution with DT-encapsulated nanoparticles (0.1~10 μM) and NDT (0.5~5.0 mM). The film thickness was controlled by immersion time. The films were thoroughly rinsed with pure solvent before characterizations.

*Pt impregnation in Conducting Polymer Matrix.* Polyaniline films with Pt loading were prepared by electrochemical method as reported by Lamy and co-workers [11]. Briefly, 0.1 M aniline was dissolved in 0.5 M $H_2SO_4$ solution. The polyaniline film was deposited by cyclic potential sweeping between –200 and +1000 mV at 50 mV/s. Polymerization was terminated when the oxidation peak current of ~7 mA/cm$^{-2}$ was achieved. Pt was then deposited into the film at a potential of –200 mV (vs. Ag|AgCl|Sat'd KCl) for 5 minutes in a $10^{-4}$ M $K_2PtCl_6$ solution. The activation of the film involved thermal activation at 300 $^0$C (instead of electrochemical polarization), details of which will be reported elsewhere.

*Measurements.* Electrochemical measurements (EG&G Potentiostat/Galvanostat 273A) were performed in a standard 3-electrode system using Ag|AgCl|Sat'd KCl as reference electrode, Pt as counter electrode and thin film coated glassy carbon (GC) as working electrode (0.5cm$^2$). Cyclic voltammetry was performed for characterizing the electrooxidation of both methanol (MeOH, Aldrich) and carbon monoxide (CO, Linde Gas) in alkaline electrolyte (0.5M KOH) with scan rate 50 mV/s. Atomic Force Microscopic (AFM) images were acquired using a Nanoscope IIIa (Digital Instruments).

## RESULTS AND DISCUSSION

The existence of thiolate encapsulation and NDT-linkage in the nanoparticle films has been characterized in recent publications [1-2,4]. Figure 1 shows a representative tapping-mode AFM image for a NDT-$Au_{2\text{-nm}}$ thin film assembled on GC. The particle size and distribution are relatively uniform. The assembled nanoparticles appear to be individually-isolated. The existence of nanoporosity is also evident. The particles appear somewhat larger than the core-shell particle size due to tip-sample convolution, but a cross-section view reveals an average height as expected for the particle size. Similar morphology has also been observed for NDT-$Au_{5\text{-nm}}$ film.

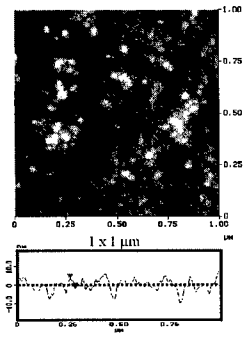


**Figure 1.** AFM image of NDT-linked $Au_{2\text{-nm}}$ film.

Figure 2 shows a typical set of cyclic voltammetric curves for NDT-$Au_{5\text{-nm}}$ thin film electrode in 0.5 M KOH in the presence of CO (saturated). The catalytic activity is dependent on the activation of the film. The thin film shows a featureless characteristic when it is cycled between -400 and +400 mV (A). In contrast, the film becomes catalytically active to CO oxidation when the electrode is subject to a positive polarization to ~ +700 mV. Following the large oxidation current, a large anodic wave is observed in the negative sweep (B). This wave is attributed to CO electrooxidation to $CO_3^{2-}$ in the alkaline condition. This wave was found to be proportional to both scan rate and CO concentration [12]. The need for a positive potential polarization is believed to be associated with the participation for oxygen species near the catalytic sites at the Au nanocrystal surface. The polarization therefore likely results in the formation of gold oxide species ($AuO_x$) and a partial removal of the organic shell molecules. These surface species or sites may be operative in catalysis in two ways. First, they reduce the barrier nature of the shell component and increase the conductivity of the thin films. Secondly, the reconstituted shell may preserve the nanocrystal core size.

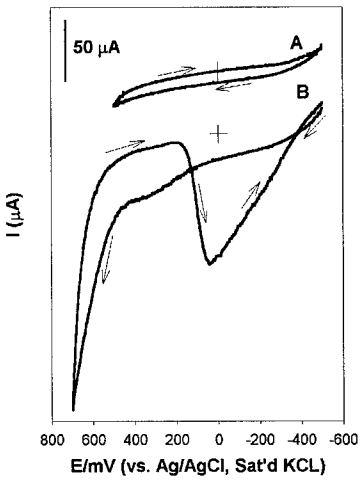


**Figure 2:** Cyclic Voltammograms of NDT-$Au_{5\text{-nm}}$ /GC; (a) unactivated, (b) activated. Electrolyte: 0.5 M KOH, sat'd CO, Electrode area: 0.5 $cm^2$ (50mv/s).

The electrocatalytic activity of the film towards methanol oxidation was examined. Figure 3 shows a representative set of CV curves for a NDT-$(Au/Pt)_{2.5\text{-nm}}$ thin film in the presence of 5 M MeOH in 0.5 M KOH. A similar effect of catalytic activation is observed. In the absence of activation (A), the voltammetric curve displays featureless characteristic. Upon

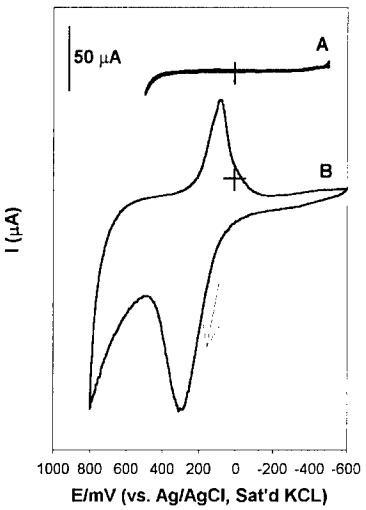


**Figure 3:** Cyclic Voltammograms of NDT-$(Au/Pt)_{2.5\text{-}nm}$/GC; (a) unactivated, (b) activated. Electrolyte: 0.5 M KOH + 5.0 M MeOH, Electrode area: 0.5$cm^2$ (50 mv/s).

electrochemical activation of the film to a positive polarization potential (+800 mV), a large anodic wave is evident at +300 mV. The peak potential closely matches the potential for Au oxide formation, suggestive of the participation of Au oxide in the overall catalytic oxidation mechanism. An integration of the charge from the cathodic wave translates to ~$9x10^{-9}$ moles/$cm^2$ for the amount of reactive Au. An estimate of the catalytic peak current and the quantity of metals yields ~5 mA/mg. Through a systematic study of the concentration and scan rate dependencies, we found two remarkable voltammetric features [13]. First, the anodic peak current increases with increasing methanol concentration, exhibiting a linear relationship. Second, in contrast to the trend for the anodic wave, the peak current for the cathodic wave decreases with increasing methanol concentration, which also exhibits a linear relationship [13]. These two features form an important set of evidence demonstrating that methanol is oxidized at the nanostructured Au catalyst. The opposite trend between the oxidation and the reduction peak currents as a function of methanol concentration is suggestive of a catalytic mediation mechanism involving redox of the surface Au oxide species. Contribution from Pt oxide may be minimum because its redox potential is more positive than Au oxide and the alloyed Pt is a very small fraction (~5%). The shell encapsulation may become partially open as a result of either the surface oxide formation or a change in shell packing due to possible thiolate desorption or reorganization. The participation of surface oxide species in the above reactions is supported both by the occurrence of the oxidation wave at the potential of gold oxidation and the suppression of the gold oxide reduction wave [12,13a], and by our recent electrochemical quartz-crystal microbalance detection of mass increase in the oxidation process [13b].

It has been demonstrated that the oxidation of MeOH often involves CO as an intermediate species. The CO intermediates are often the cause of poisoning of the Pt-group catalyst. It appears that for our catalyst films the catalytic activity is relatively stable over repetitive cycling up to 50 cycles in the presence of methanol or CO. This finding is consistent with the high catalytic activity of CO oxidation observed on bare gold nanoparticles supported on oxides [8]. While a detailed investigation of the reconstituted surface species in the activation and oxidation processes is in progress, we believe that the assembled gold nanoparticles are effective catalysts for both CO and MeOH oxidation in alkaline solution. This assessment may prove extremely important as

we develop high performance fuel cell catalysts that have a long lifetime. A further assessment of possible changes of the catalyst morphology due to the activation and the formation of oxygenated species is under way with the aid of in-situ AFM technique [14].

In view of the high catalytic activity of Pt in methanol oxidation [14], we examined a different approach to incorporate Pt component in the catalytic film. In this approach, we first prepared a polyaniline thin film that was loaded with Pt. The Pt loading was accomplished via electrochemical deposition from $PtCl_6^{-2}$ anions in solution into the conductive polymer by reducing $Pt^{IV}$ into $Pt^0$ particles. The NDT-$Au_{2\text{-nm}}$ film was then assembled on the surface of the polymer thin film. Figure 4 shows a preliminary set of CV data for this "layered" nanoparticle thin film in 2.5 M MeOH + 0.5 M KOH electrolyte. In the absence of activation, the voltammetric characteristic is basically silent, similar to the observation for NDT-$Au_{2\text{-nm}}$ film. Upon thermal activation, the film shows a large oxidation wave at a potential of -180 mV, much more negative than those observed earlier. We attribute the shift of the oxidation wave to the catalytic oxidation of methanol on Pt particles. While this peak potential corresponds closely to that of bulk platinum in alkaline solutions, the oxidation wave traditionally observed for the Pt catalyst on the return negative sweeping is largely absent, even after ~50 cycles. This may suggest that the traditional poisoning effect may be suppressed by the presence of gold nanoparticles. It is also possible that the intermediate CO species is oxidized by gold nanoparticles. In fact a small anodic wave is identifiable at ~+300 mV, corresponding to methanol oxidation at gold nanoparticle sites.

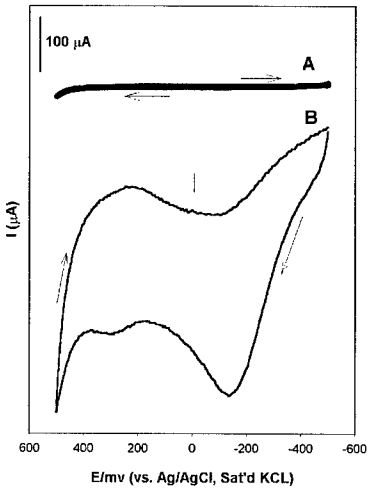


**Figure 4**: Cyclic Voltammograms of NDT-$Au_{2\text{-nm}}$ + PANI (Pt) thin film at a GC electrode; (a) unactivated, (b) thermally activated. Electrolyte: 2.5 M KOH + 2.5 M MeOH; Electrode area: 0.5 $cm^2$ (50 mv/s).

An estimate of the catalytic current vs. the quantity of metals yields ~4 mA/mg, (based on quantities of Pt and Au deposited in the film). This is qualitatively consistent with observations reported for Pt-Ru catalysts loaded in polyaniline film [11], where a ~3 mA/mg current density was found under the condition of controlled potential electrolysis. The two-component system using different approaches is another viable pathway towards the development of a poison-free catalyst.

## CONCLUSION

In conclusion, the catalytic activity of the nanostructured catalyst materials was found to be tailorable by three types of interfacial chemistries. First, the utilization of functional shell of the CSNs system is important for the assembly of nanostructures that

protect particles form aggregation. The second finding for these systems reinforces the belief that the CSNs catalytic activity can be activated by activation strategies that involve reconstitution of the core-shell structure and composition. Thirdly, the Au-Pt two-component system can effectively increase the catalytic activity. The role of the organic encapsulation is important in two aspects. First, it allows controllable fine-tuning of the core size and composition via synthesis and processing. Secondly, it allows thin film assembly at any substrates. How does the shell and network encapsulation evolve and reconstitute during the catalytic activation and oxidation is a subject of our on-going investigations.

## ACKNOWLEDGMENTS

Financial support of this work is gratefully acknowledged from the ACS Petroleum Research Foundation and 3M Corporation.

## REFERENCES

1. M. Brust; M. Walker; D. Bethell; D. J. Schiffrin, R. Whyman, *Chem. Commun.*, 801, (1994).
2. (a) M. M. Maye; W. X. Zheng; F. L. Leibowitz; N. K. Ly; C. J. Zhong, *Langmuir*, , **16**, 490, (2000) (b) M. M. Maye; C. J. Zhong, *J. Mater. Chem.*, **10**, 1895. (2000).
3. (a) D. Bethell, M. Brust, D.J. Schiffrin, C. Kiely, *J. Electroanal. Chem.* **409**, 137, (1996). (b) J.K.N. Mbindyo; B.D. Reiss; B.R. Martin; C.D. Keating; M.J. Natan; T.E. Mallouk, *Adv. Mater.*, **13**, 249. (2001).
4. F. L. Leibowitz; W. X. Zheng; M. M. Maye; C. J. Zhong, *Anal. Chem.*, **71**, 5076, (1999).
5. A. C. Templeton; W. P. Wuelfing, R. W. Murray; *Acc. Chem. Res.* **33,** 27; (2000) and references therein.
6. F. Caruso, *Adv. Mater*, **13**, 11; (2001), and references therein.
7. (a) J. J. Storhoff; C. Mirkin, *Chem. Rev.* , **99** , 1849, (1999). (b) S. Mann; W. Shenton; M. Li; S. Connolly; D. Fitzmaurice, *Adv. Mater.*,**12**, 147 (2000).
8. (a) M. Haruta, *Catalysis Today*, , **36**, 153. (1997) (b) P. C. Biswas; Y. Nodasaka; M. Enyo; M. Haruta, *J. Electroanal. Chem.*, **381**, 167. (1995).
9. (a) G. C. Bond and D. T. Thompson, *Catal. Rev.*,**41,** 319 (1999). (b) G. C. Bond, D. T. Thompson, *Gold Bulletin*, **33**, 41 (2000).
10. (a) M. J. Hostetler; J. E. Wingate; C. J. Zhong; J. E. Harris; R. W. Vachet; M. R. Clark; J. D. Londono; S. J. Green; J. J. Stokes; G. D. Wignall; G. L. Glish; M. D. Porter; N.D. Evans; R. W. Murray, *Langmuir*, ***14***, 17. (1998).
11. A. Lima, C. Coutanceau, J.-M. Leger, C. Lamy; *J. Appl. Electrochem.*, **31**, 379, (2001)
12. M. M. Maye; Y. Lou; C. J. Zhong, *Langmuir*, **16**, 7520. (2000).
13. (a) Y. Lou; M. M. Maye; L. Han; J. Luo; C. J. Zhong, *Chem. Comm.*, 473, (2001). (b) J. Luo; Y. Lou; M. M. Maye; C. J. Zhong; M. Hepel, *Electrochemistry Communications*, , **3**, 172. (2001).
14. M. M. Maye, J. Luo, L. Han, C.J. Zhong; *Nano Letts.*, **1**,10, 575, (2001).

Mat. Res. Soc. Symp. Proc. Vol. 703 © 2002 Materials Research Society V10.7

# Surfactant Templated Assembly of Hexagonal Mesostructured Semiconductors Based on $[Ge_4Q_{10}]^{4-}$ (Q=S, Se) and $Pd^{2+}$ and $Pt^{2+}$ ions.

Pantelis N. Trikalitis, Krishnaswamy K. Rangan and Mercouri G. Kanatzidis*
*Department of Chemistry, Michigan State University, East Lansing, MI 48824.*

## ABSTRACT

Mesostructured semiconducting non-oxidic materials were prepared by linking $[Ge_4Q_{10}]^{4-}$ (Q=S, Se) clusters with the square planar noble metal cations of $Pd^{2+}$ and $Pt^{2+}$ in the presence of cetylpyridinium surfactant molecules. The use of $Pt^{2+}$ afforded materials with exceptionally high hexagonal pore order similar to those of high quality silica MCM-41. These materials are semiconductors with energy band gap in the range $1.8<E_g<2.5$ eV.

## INTRODUCTION

The emergence of the family MCM-X of surfactant templated silica mesoporous molecular sieves with regular pore shape and adjustable pore size a decade ago sparked a flurry of activity worldwide that resulted in an abundance of oxidic mesoporous solids with promising technological properties (*1*). Whereas these materials will impact catalytic, separation and adsorption applications, they lack interesting electronic properties. Bulk materials that combine mesoscale features and electronic properties are envisioned for novel applications in quantum electronics (*2*), photonics (*3*) and non-linear optics (*4*) among others. Such characteristics may be expected in non-oxidic materials such as the chalcogenides (*5*). A suitable method for the construction of semiconducting mesostructured materials utilizes a self-assembly process between chalcogenido building blocks and metal cations in the presence of surfactant molecules acting as templates (*6*). However outstanding issues as to how these systems form remain. The mesostuctured chalcogenides reported todate mainly were synthesized by linking adamantane $[Ge_4Q_{10}]^{4-}$ (Q=S, Se) clusters (see scheme 1) with first row transition and main-group ions such as Mn, Co, Ni, Zn, Cd, In and Ga, whose coordination preference is mainly tetrahedral. In the exploration of the role of the linkage metal in the assembly process we decided to use noble metal $Pd^{2+}$ and $Pt^{2+}$ ions because of the strong square-planar coordination preference. Moreover these ions are less kinetically labile than the first-row transition metals and therefore may slow down the self-assembly reaction thus achieving a more ordered structure. In this work we employed the clusters $[Ge_4Q_{10}]^{4-}$ (Q=S, Se) with $Pt^{2+}$ and $Pd^{2+}$ in the presence of cetylpyridinium ($C_{16}PyBr$) surfactant molecules. We find that these two similar metal ions behave very differently. In the case of $Pt^{2+}$ the materials show remarkable hexagonal pore order similar to those of high quality silica MCM-41 whereas in the case of $Pd^{2+}$ the solids are significantly less ordered.

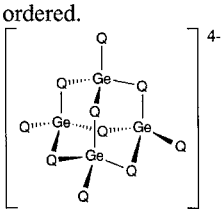


Scheme 1. Chalcogenido adamantane-type $[Ge_4Q_{10}]^{4-}$ (Q=S, Se) cluster.

## EXPERIMENTAL

The syntheses of the materials were carried out as follows: 1 mmol of $TMA_4[Ge_4Q_{10}]$ (TMA=tetramethylammonium; Q=S, Se) was dissolved in 20 ml of formamide at 80 $^0$C. To this clear solution 10 mmol of surfactant $C_{16}PyBr$ was added and the mixture stirred at 80 $^0$C until a clear solution formed. In a flask 1 mmol $K_2MCl_4$ (M=Pt, Pd) was dissolved in 10 ml of formamide and added to the surfactant/$[Ge_4Q_{10}]$ solution dropwise using a pipet. The mixture was aged overnight under stirring and the product was isolated with suction filtration, washed with warm formamide and water and dried under vacuum. The yield was >80 % and the solids were in the form of light powder.

## RESULTS AND DISCUSSION

The mesostructured materials are denoted as $C_{16}PyMGeQ$ were M=Pt, Pd. Unlike in previous cases (*6*) with other, kinetically labile linkage metals, we observe a considerable slower reaction upon addition of the $Pt^{2+}$ metal ions. That is when the $K_2PtCl_4$/FM solution was added to the $C_{16}Py/[Ge_4Q_{10}]^{4-}$ solution, instantaneous precipitation did not take place. The deposition of the mesophase began 1-1.5 min after and was completed in approximately 10-15 min. As we discuss below the platinum containing mesophases exhibit remarkably good hexagonal mesoscopic order. In contrast $Pd^{2+}$ ions, react much more rapidly giving mesophases that exhibit high degree of disorder. Figure 1 shows powder X-ray diffraction patterns of $C_{16}PyMGeQ$ materials. The platinum products show three or four well defined Bragg reflections in the $2^o<2\theta<7^o$ region, characteristic of mesostructured materials with regular hexagonal pore arrangement. Accordingly these reflections are indexed to a hexagonal *p6m* mesophase, see Figure 1. The intense, sharp, well-defined high order reflection (110) and (200) as well as the observation of the fourth (210) reflection, betray a high degree of hexagonal order in these materials as observed directly by transmission electron microscopy (TEM) (see below). In the case of palladium however, the (100) reflection is clearly broader and the high order reflections (110) and (200) are not well resolved, indicating the formation of less ordered mesostructured phases.

Samples of the mesostructured $C_{16}PyMGeQ$ were examined by TEM. Figure 2a shows a characteristic image of $C_{16}PyPtGeSe$ looking down the pore channel axis ([100] direction) where a remarkably uniform hexagonal order is clearly visible. Figure 2b shows a view of $C_{16}PyPtGeSe$ perpendicular to the pore channel axis ([110] direction). The long, straight parallel tunnels are apparent in this image and the observed interpore distances are in good agreement with those obtained from the X-ray diffraction patterns. Similar images were observed in $C_{16}PyPtGeS$ material. Figure 2c,d shows a characteristic image of $C_{16}PyPdGeS$ were the presence of local hexagonal pore arrangement along with disordered regions is evident, as indicated by the X-ray powder patterns. The quality of $C_{16}PyPtGeQ$ solids as judged by the degree of hexagonal order, is comparable to those of high quality silica MCM-41 (*7*). Figure 3 shows a TEM image of a large $C_{16}PyPtGeSe$ particle where the size of coherent, hexagonally organized domain is >500 nm.

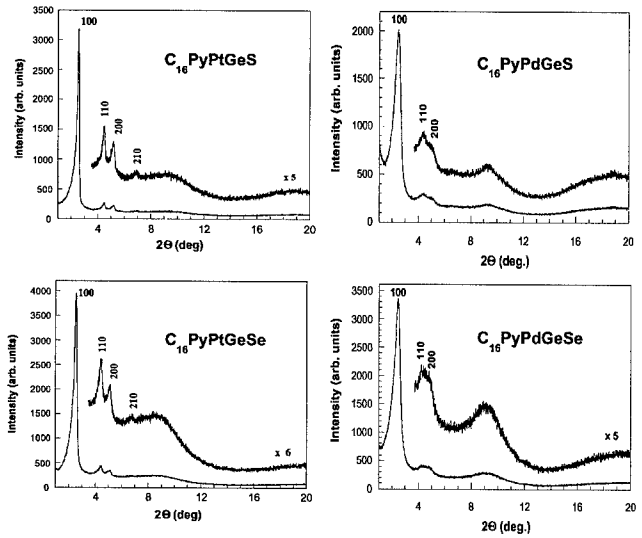


**Figure 1.** Powder X-ray diffraction patterns of mesostructured noble-metal chalcogenides (CuKα radiation).

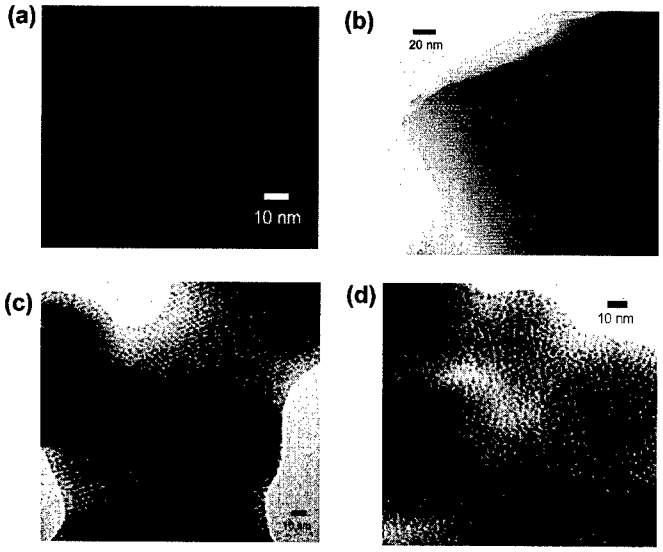


**Figure 2.** Representative TEM images of $C_{16}$PyMGeQ materials. (a) $C_{16}$PyPtGeSe down to [100] direction, (b) $C_{16}$PyPtGeSe down to [110] direction, (c) $C_{16}$PyPdGeS down to [100] direction and (d) highly disordered region of $C_{16}$PyPdGeS.

**Figure 3.** Representative image of a large particle of $C_{16}$PyPtGeSe showing the hexagonal organization extending over its full body. Particle length >500 nm.

Undoubtedly the quality of the hexagonal pore order in the platinum germanium chalcogenide materials is significantly higher than in palladium analogs. Since the synthesis of $C_{16}$PyPtGeQ is based on simple metathesis reactions according to (1),

$$K_2MCl_4 + TMA_4[Ge_4Q_{10}] + C_{16}PyBr \longrightarrow C_{16}PyMGeQ + TMA\text{-}Cl + KBr \quad (1)$$

it is natural to expect that ligand substitution kinetics and coordination preference of the linkage metal ions will affect the quality of the final product. However noble metal ions $Pd^{2+}$ and $Pt^{2+}$ exhibit strong square planar coordination geometry. Therefore the striking difference found between $C_{16}$PyPtGeQ and $C_{16}$PyPdGeQ materials in terms of long range hexagonal pore order, is attributed to the slower reaction observed in the former. In that case, the reactants have more time to react and reach equilibrium thus leading to considerably higher quality hexagonal mesostructured phases.

Infrared (IR) and Raman spectroscopy was used to examine the inorganic framework and also confirm the presence of the surfactant molecules in these materials. In the mid-IR region we observed the characteristic absorption bands of cetylpyridinium cations. Shown in Figure 4a is typical far-IR spectrum from $C_{16}$PyPtGeS together with the corresponding spectrum from the free adamantane cluster for comparison. The spectrum of $C_{16}$PyPtGeS shows characteristic peaks in the same range as the free adamantane cluster, however, the peaks are much broader indicating possible different bonding environments present.

FT-Raman spectra were collected for the mesostructured $C_{16}$PyPtGeS while for the other materials spectra could not be obtained as they decomposed under the laser beam. We observe several vibrational modes attributed to Ge-S and Pt-S stretching modes, see Figure 4b. By comparison with previous Raman studies (*6*), the sharp peak centered at 376 $cm^{-1}$ can be assigned to the totally symmetric breathing mode of the "$Ge_4S_6$" cage, while the peak at 441 $cm^{-1}$ to terminal Ge-$S_t$ stretching mode. The peak at 340 $cm^{-1}$ can be assigned to the Pt-S vibration, according to the spectroscopic analysis of Raman spectrum of PtS.

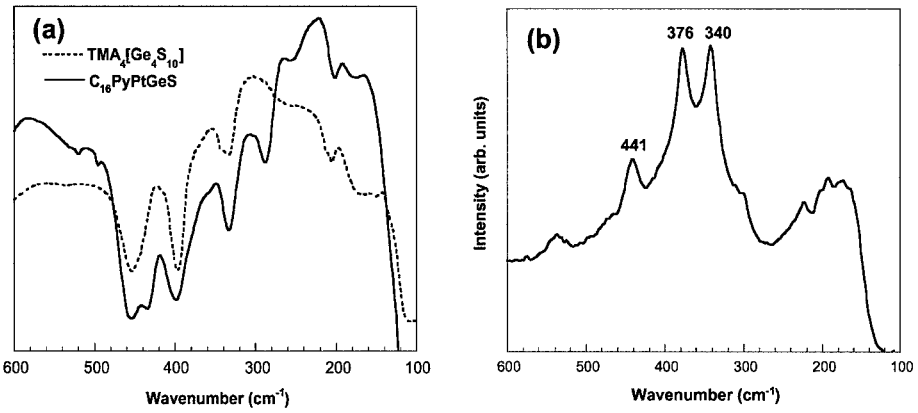


**Figure 4.** (a) Far-IR and (b) FT-Raman spectrum of $C_{16}$PyPtGeS.

The optical absorption properties of the $C_{16}$PyMGeQ mesostructured materials were investigated with solid state diffuse reflectance UV-vis/Near IR spectroscopy. All solids posses well-defined, sharp optical absorptions associated with bandgap transitions in the energy range $1.8<E_g<2.5$ eV, see Figure 5. The bandgap narrows in going from the lighter $C_{16}$PyMGeS (Pd:2.5 eV, Pt:2.3 eV) to the heavier $C_{16}$PyMGeSe (Pd:2.0 eV, Pt: 1.8 eV). Moreover the effect on the bandgap in going from $C_{16}$PyMGeS to $C_{16}$PyMGeSe is greater (0.5 eV) rather than in going from $C_{16}$PyPdGeQ to $C_{16}$PyPtGeQ (0.2 eV) suggesting a more dominant role of the chalcogenide element in the valence and conduction band of the materials.

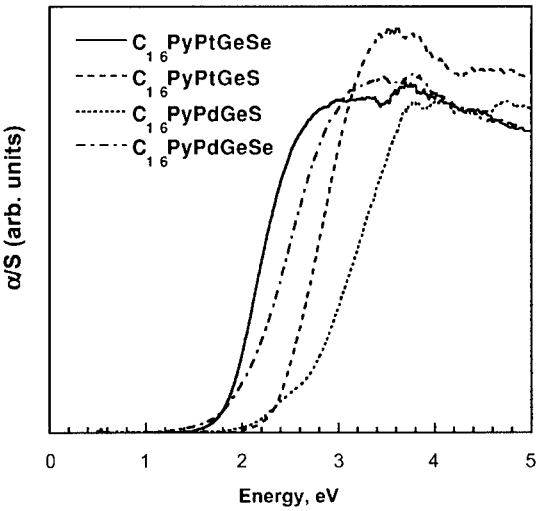


**Figure 5.** Solid state UV-vis absorption spectra of $C_{16}$PyMGeQ materials.

## CONCLUSIONS

The use of $Pd^{2+}$ and $Pt^{2+}$ as linkage metal ions in a supramolecular assembly of adamantane $[Ge_4Q_{10}]^{4-}$ clusters leads to a new class of non-oxide mesostructure materials with noble metal ions as part of the framework. In the case of platinum the solids show exceptionally high hexagonal order similar to those in silica MCM-41, whereas in the case of Pd such high order was not observed. This suggests that slower reaction kinetics of framework assembly is an important factor. The materials posses optical bandgaps, ranging between $1.8<E_g<2.5$ eV. The bandgap narrows with the incorporation of heavier elements in the framework.

**ACKNOWLEDGEMENTS** The support of this research by NSF-CRG grant CHE 99-03706 is gratefully acknowledged. This work made use of the SEM and TEM facilities of the Center of Advanced Microscopy at MSU.

## REFERENCES

1. C. T. Kresge, M. E. Leonowicz, W. J. Roth, J. C. Vartuli, J. S. Beck, *Nature* **359**, 710 (1992); Y. Ma, W. Tong, H. Zhou, S. L. Suib, *Microporous Mesoporous Mater.* **37**, 243 (2000); A. Corma, *Chem. Rev.* **97**, 2373 (1997); A. Sayari, P. Liu, *Microporous Mater.* **12**, 149 (1997).
2. P. V. Braun, P. Osenar, S. I. Stupp, *Nature* **380**, 325 (1996).
3. D. J. Norris, Y. A. Vlasov, *Adv. Mater.* **13**, 371 (2001).
4. G. A. Ozin, *Supramol. Chem.* **6**, 125 (1995).
5. H. L. Li, A. Laine, M. O'Keeffe, O. M. Yaghi, *Science* **283** 1145 (1999).
6. K. K. Rangan, P. N. Trikalitis, M. G. Kanatzidis, *J. Am. Chem. Soc.* **122**, 10230 (2000); K. K. Rangan, P. N. Trikalitis, T. Bakas, M. G. Kanatzidis, *Chem. Commun.*, 809 (2001); P. N. Trikalitis, K. K. Rangan, T. Bakas, M. G. Kanatzidis, *Nature* **410**, 671 (2001); M. J. MacLachlan, N. Coombs, G. A. Ozin, *Nature* **397**, 681 (1999).
7. Q. S. Huo, D. I. Margolese, G. D. Stucky, *Chem. Mater.* **8**, 1147 (1996).

Mat. Res. Soc. Symp. Proc. Vol. 703 © 2002 Materials Research Society V10.9

# Studies of Intersubband Transitions in Arrays of Bi Nanowire Samples Using Optical Transmission

M. R. Black[a)], K. R. Maskaly[b)], O. Rabin[c)], Y. M. Lin[a)], S. B. Cronin[d)], M. Padi[d)], Y. Fink[b)], M. S. Dresselhaus[a,d)]
[a]Department of EECS, Massachusetts Institute of Technology, Cambridge, MA
[b]Department of Material Science and Engineering, Massachusetts Institute of Technology, Cambridge, MA
[c]Department of Chemistry, Massachusetts Institute of Technology, Cambridge, MA
[d]Department of Physics, Massachusetts Institute of Technology, Cambridge, MA

## Abstract

This paper reports the fabrication of large diameter pores (> 150 nm) in anodic alumina that can be used to create wire arrays with significant surface effects, but without significant quantum confinement. These wires, therefore, allow us to distinguish between optical absorption spectra features originating from quantum effects and those from surface effects. The paper presents techniques towards fabricating these bismuth wire arrays, and presents optical absorption data from two bismuth nanowire arrays in the semimetal-semiconductor transition diameter regime. The results from previous publications are summarized and future directions are outlined.

## Introduction

We are no longer completely limited to the constraints on the properties of 3D bulk materials. By utilizing quantum confinement, we have learned how to engineer the band gap of a material. As a result we can tailor the properties of a material to conform to a desired application. Once the effects of quantum confinement are fully understood, the size of the quantum confined dimension(s) can be selected to achieve the degree of quantum confinement and surface effects desired.

Bismuth nanowires exhibit a transition from a semimetal with a small band overlap (38 meV at 0 K) to a semiconductor, as the wire diameter becomes small enough to support significant quantum confinement effects, as shown in Fig. 1. This transition occurs in Bi nanowires at relatively large wire diameters because of its small effective masses and small band overlap. For example, this semimetal-semiconductor transition is predicted to occur at a wire diameter of 16 nm in the (012) direction (the growth direction of our nanowires) at room temperature, and at 47 nm at 77K, Fig. 1. The change from a semimetal to a semiconductor has significant effects on the electronic and optical properties of bismuth, which may be desirable for some applications, such as thermoelectricity.[1, 2]

We are working towards measuring the optical properties of bismuth wires in three different size regimes: large wire diameters ($\sim$ 200 nm) which are semimetals, small wire diameters ($\sim$ 15 nm) which are semiconductors, and an intermediate wire diameter size ($\sim$ 40 nm) where the wires are a semimetal at room temperature and a semiconductor at low temperatures. Well ordered arrays of 45 nm pores in alumina have been fabricated and filled with bismuth to create wires in the intermediate diameter regime. These wires are near the semimetal-semiconductor transition at 77K. The 45 nm wires absorb in the far infrared.

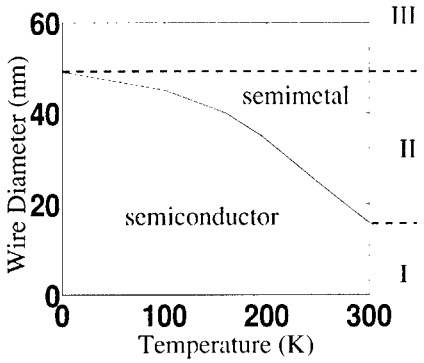


Figure 1: The phase diagram of the semimetal to semiconductor transition in bismuth nanowires is shown as a function of temperature and wire diameter. Depending on the wire diameter, a nanowire is either a semimetal (III), a semiconductor(I), or switches from a semimetal to a semiconductor as the temperature is decreased(II).

This optical absorption is attributed to intersubband transitions.[3] Well ordered arrays of small pore alumina templates (15 nm) have also been fabricated successfully. However, the liquid phase injection technique used to fill the alumina with bismuth is ineffective in filling these small diameter pores. We are therefore developing an electro-chemical method for filling small pores in anodic alumina with bismuth.[4] The process to fabricate the large pore alumina templates (> 55 nm) proved to be the most difficult to develop due to the fact that the process requires a higher voltage and many highly sensitive process parameters needed to be optimized. Optical absorption measurements, like those already reported for 45 nm wires, for both the semiconducting and semimetallic wires will help us better understand the observed absorption spectra. We therefore seek to perform measurements over the whole diameter range to gain a better understanding of the quantum confinement characteristics of the Bi nanowires.

## Fabrication and Experimental Details

Since aluminum can be anodized to form an alumina layer with an ordered array of pores[5], all the bismuth nanowires in this work were fabricated by filling porous anodic alumina. Several theories have been presented to explain the formation of the porous alumina, such as Refs. [5] and [6]. In addition, several theories have been recently proposed to explain the ordering of the pores into a hexagonal pattern when very specific conditions for the anodization are used.[7, 8] Many papers present excellent experimental results documenting conditions at which the anodization forms ordered pores and those at which the pores are irregular and not ordered.[9, 10, 11] However, to our knowledge, no complete theory exists to predict the optimal acid type, concentration, and temperature that should be used to obtain well-ordered arrays with a uniform pore diameter for a given anodization voltage and corresponding pore diameter. Therefore, whenever the desired pore size has not yet been well studied, many attempts of trial and error are required to establish the recipe for well-ordered

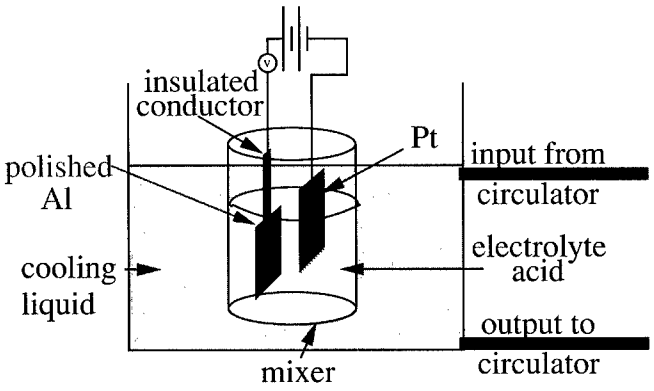


Figure 2: The anodization setup for high voltage anodization. The automatic cooling system, the high cooling liquid level, and the insulated conductor, all prevent breakdown during the anodization process.

pores. To minimize the trial and error required to find the ideal anodization conditions for large diameter pores (> 80 nm), we sought to reproduce the well-ordered arrays with a pore size of 200 nm diameter reported in Ref. [7]. However, when repeating their conditions of 160 V anodization voltage in 10 % phosphoric acid at 3°C, the anodization current became unstable. The current increased during the anodization, increasing the temperature of the acid. The rise in temperature in turn further increased the current, until the reaction became uncontrollable. This rapid rise in acid temperature and anodization current is called "breakdown" in the literature. [8]

In our samples, in addition to the increase in current at breakdown, sizzling occurred at the air/acid interface where the aluminum was exposed to air. Furthermore, the onset of this phenomenon was correlated with the ambient air temperature. This suggests that the sizzling is caused by the higher temperature of the sample at the surface (surface heating). We therefore implemented three techniques to reduce surface heating and the likelihood of breakdown, (see Fig. 2). When all three techniques are used, sizzling under our anodization conditions is eliminated. The first improvement was an automatic cooling system. A refrigerated recirculator is used to keep the cooling liquid at $-1.5 \pm 0.05\,^{\circ}\mathrm{C}$. In addition, the acid level is kept below that of the cooling liquid. This helps cool the air around the acid-air interface. Thirdly, the aluminum electrode is completely submerged in the chilled acid. In order to prevent shorting of the contact to the acid, an insulated conductor is used to make contact with the Al sheet inside the acid. The aluminum is anodized using this method for about 3 hours. The alumina is then etched off and the remaining aluminum then undergoes a second anodization for about 4 hours. The pores from a 40 V and a 160 V anodization are shown in Fig. 3 A and B, respectively.

The pores in the alumina are filled with Bi using a pressure injection technique.[12] The alumina template is then etched off using a selective etch, leaving only bismuth wires

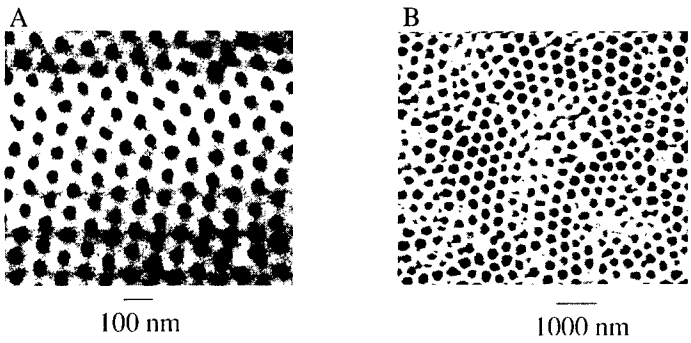


Figure 3: Scanning electron micrographs of anodic alumina anodized at (A) 40 V and (B) 160 V with pore diameters around 40 and 200 nm, respectively.

behind. Using the micro-FTIR (Fourier Transform Infrared Technique), the reflection and transmission were measured from free-standing Bi nanowires with a bismuth oxide coating around the nanowires and a thin Bi film holding them together. A schematic diagram of the sample is shown in Fig. 4(C). Bismuth nanowires protrude out of the bismuth film, which is balanced on the edge of a glass slide. Light is transmitted through the sample in the direction of the wires so that the electric field of the incident light is always perpendicular to the wire axis. Since the transmission is proportional to $e^{-Kx}$, where $K$ is the infrared absorption coefficient and $x$ is the sample thickness, the negative log of the transmission is proportional to the absorption coefficient. This is used to find the absorption spectra of the wires.

## Results and Discussion

The absorption coefficients (times the sample thickness) as a function of wavenumber, obtained by taking the negative log of the transmission intensity of $\sim 45\,\text{nm}$ and $\sim 30\,\text{nm}$ diameter free-standing bismuth nanowires are shown in Fig. 4(A). For comparison, Fig. 4(A) also shows the absorption coefficient of a film of bismuth. The two arrays of wires used for the free-standing nanowire measurements had diameters of 60 nm and 45 nm before the alumina template surrounding the wires was etched away. Since a $\sim$ 7 nm oxide grows on the free-standing wires after the alumina is selectively etched away [13], the inner bismuth portion of the free-standing wires is expected to have a diameter of around 45 nm and 30 nm. Since the thickness of the thin bismuth film holding the bismuth nanowires and the thickness of the nanowire array are not known, arbitrary units of absorption are used.

The absorption spectra of the nanowire arrays show many more features than that of the bismuth film. The absorption features are predominant for wavenumbers less than $1300\,cm^{-1}$. Simulations show that intersubband absorption tails off for $\omega > 1300\,cm^{-1}$ in bismuth nanowires, because of a fall off in the coupling between the initial and the final states.[14] Figure 4(A and B) also shows that the absorption spectra between the two wire arrays differ significantly. The absorption of each sample was taken several times and found

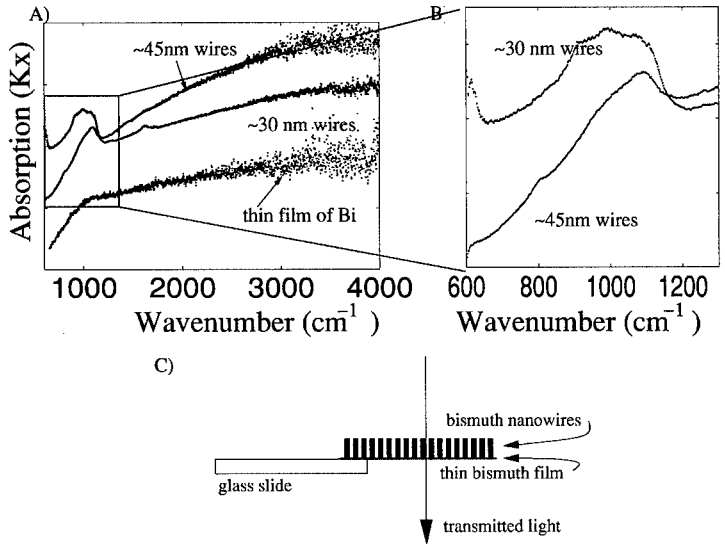


Figure 4: The dependence of the absorption coefficient on wavenumber, found by taking the negative log of the transmission of free-standing bismuth nanowires with diameters around 45 and 30 nm as well as the absorption on a thin piece of bismuth is shown in A) and B). C) shows a schematic of the experimental setup to measure absorption.

to be reproducible. The differences in the absorption spectra for wavenumbers less than $1300\,cm^{-1}$ are attributed to differences in the subband energies involved in intersubband absorption.[14]

Previous work on the optical properties of bismuth nanowire arrays inside the alumina template report a sharp absorption feature at about $1000\,cm^{-1}$.[3] The shape of the absorption peak, the frequency of observed absorption, the qualitative dependence on wire diameter, and the polarization of this absorption all indicate that intersubband transitions are the likely cause of the observed absorption.[3] In addition, a model for intersubband transitions in bismuth nanowires predicts peaks in the absorption spectra at energies that are in agreement with those observed in optical measurements of free standing wire arrays.[14] However, some aspects of the absorption curve remain unexplained. Firstly, although the energy of the absorption peak at around $1000\,cm^{-1}$ increases with decreasing wire diameter, as expected for intersubband transitions, it does not increase as rapidly as expected. Secondly, the relative intensities of the absorption peaks in the free standing wires are different from those predicted by theory.[14] In particular, the absorption peak at around $1000\,cm^{-1}$ is much more intense in the experimentally measured absorption than in the simulated intersubband absorption.[14] In this paper we report optical absorption measurements on $\sim$ 30 nm wires as well as the fabrication of ordered 200 nm pores in alumina. With the newly developed ability to fabricate well ordered 200 nm wire arrays and with the currently developing ability

to electro-chemically fill the 20 nm arrays, we hope to develop a better understanding of the observed absorption mechanisms in bismuth nanowire arrays.

## Acknowledgements

The authors gratefully acknowledge the valuable discussions with of Prof. Jackie Ying and Dr. Gene Dresselhaus. The authors also gratefully acknowledge MURI subcontract 0205-G-BB953, NSF grant DMR-0116042, and US Navy contract N00167-98-0024 for support. This work made use of MRSEC Shared Facilities supported by the National Science Foundation contract DMR-9400334.

## References

[1] Z. Zhang, X. Sun, M. S. Dresselhaus, J. Y. Ying, and J. Heremans, Phys. Rev. B **61**, 4850–4861 (2000).

[2] X. Sun, Z. Zhang, and M. S. Dresselhaus, Appl. Phys. Lett. **74**, 4005–4007 (1999).

[3] M. R. Black, M. Padi, S. B. Cronin, Y.-M. Lin, O. Rabin, T. McClure, G. Dresselhaus, P. L. Hagelstein, and M. S. Dresselhaus, Appl. Phys. Lett. **77**, 4142–4144 (2000).

[4] O. Rabin, Y. Lin, S. Cronin, and M. S. Dresselhaus. to be published.

[5] J. P. Sullivan and G. C. Wood, Proc. Roy Soc. Lond. A. **317**, 511–543 (1970).

[6] Feiyue Li, Lan Zhang, and Robert M. Metzger, Chem. Mater. **10**, 2470–2480 (1998).

[7] A. P. Li, F. Muller, A. Birner, K. Nielsch, and U. Gosele, Journal of Applied Physics **84**, 6023–6026 (1998).

[8] A. Jagminas, D. Bigelience, I. Mikulskas, and R. Tomasiunas, Journal of Crystal Growth **223**, 591–598 (2001).

[9] Hideki Masuda and Kenji Fukuda, Science **268**, 1466–1468 (1995).

[10] Y. Li, E. R. Holland, and P. R. Wilshaw, J. Vac. Sci. Technol. B. **18**, 994–996 (2000).

[11] T. E. Huber, M. J. Graf, C. A. Foss Jr., and P. Constant, J. Mater Res. **15**, 1816–1821 (2000).

[12] Z. Zhang, J. Ying, and M. Dresselhaus, J. Mater. Res. **13**, 1745–1748 (1998).

[13] S. B. Cronin, Y.-M. Lin, P. L. Gai, O. Rabin, M. R. Black, G. Dresselhaus, and M. S. Dresselhaus. In *Anisotropic Nanoparticles: Synthesis, Characterization and Applications: MRS Symposium Proceedings, Boston, December 2000*, edited by S. Stranick, P. C. Searson, L. A. Lyon, and C. Keating, pages C571–C576, Materials Research Society Press, Pittsburgh, PA, 2001. pdf.

[14] M. R. Black, Y. M. Lin, S. B. Cronin, O. Rabin, and M. S. Dresselhaus, unpublished.

Mat. Res. Soc. Symp. Proc. Vol. 703 © 2002 Materials Research Society V10.12

# The role of the interfaces in the optical effects of large-sized $SiC_xO_{1-x}N$ nanocrystallites

**K.J. Plucinski, H. Kaddouri[1], I.V. Kityk[2]**
Military University of Technology, Dept of Electronics, Warsaw, POLAND
[1] Universite du Perpignan, Lab. LP2A, Perpignan, FRANCE
[2]Institute of Physics WSP, Częstochowa, POLAND

## ABSTRACT

The band energy structure of large-sized (10-25) nm nanocrystallites (NC) of $SiC_xO_{1-x}N$ ($0.96<x<1.06$) was investigated using different band energy approaches, as well as modified Car Parinello molecular dynamics simulations of interfaces. A thin carbon sheet (of about 1 nm) appears, covering the crystallites. This sheet leads to substantial reconstruction of the near-the-interface $SiC_xO_{1-x}N$ crystalline layers. Numerical modeling shows that these NC may be treated as quantum dot-like $SiC_xO_{1-x}N$ reconstructed crystalline surfaces, covering the appropriate crystallites. All band energy calculation approaches (semi-empirical pseudopotential, fully augmented plane waves and norm-conserving self-consistent pseudopotential approaches) predicted the experimental spectroscopic data. In particular, it was shown that the near-the-surface carbon sheet plays a dominant role in the behavior of the reconstructed band energy structure. Independent evidence for the important role of the dot-like crystalline layers are the excitonic-like states, which are not dependent on the particular structure of the SiC, but are sensitive to the thickness of the carbon layer.

## INTRODUCTION

There has recently been increased interest in the possibility of using nano-technologies as materials for optics and electronics, the main reason being the size-dependent electronic and optical properties of these materials [1-4]. The properties of large-size nanocrystallites (larger than 10 nm) were treated as the so-called superposition of the NC and other structures [5-8]. One can predict that the latter will be directly dependent on the relative sizes of particular crystallites and the surrounding interface environment. Depending on these parameters, we will obtain different excitonic states which define the behavior of the interface band energy gradients. The coexistence of bulk-like and quantum confinement states presents the possibility of working with electron energy dispersion within the same crystallites contrary to the thin $SiC_xO_{1-x}N$ films deposited on the $SiC_xO_{1-x}N$ crystalline surfaces.

Among the many possible NC materials, $SiC_xO_{1-x}N$ crystallites were chosen because the technology for their manufacture with the sizes needed is well developed, the energy gap of $SiC_xO_{1-x}N$ may be manipulated within the large spectral ranges (2 – 4.5 eV), depending on polytype kinds, and because $SiC_xO_{1-x}N$ is substantially more stable than other SiON materials, when external mechanical and thermo-treatments are applied.

The main goal of the present work was to study the optical properties of $SiC_xO_{1-x}N$ NC, both experimentally, as well as theoretically. In particular, we investigated the influence of nanocrystallite size and carbon excess on the optical absorption of the $SiC_xO_{1-x}N$ nanocrystallites, the contribution of the reconstructed near-interface states to the visible absorption of the NC and the contribution of the carbon sheet interfaces to the absorption spectra observed.

The nanopowders were synthesized by $CO_2$ laser pyrolysis of silane and acetylene gaseous mixtures. The reactant fluxes monitored the ratio C/O and induced a carbon or silicon-rich network in the outer-most SiC nanoparticle surfaces.
Size-dependent effects are usually studied for NC with sizes below 8 - 10 nm, where clear size-confined effects are observed. In such cases, **k**- space bulk-like dispersion disappears and

discrete excitonic-like levels in the energy gaps appear. However, interface (reconstructed) dot-like states corresponding to an intermediate level, with both bulk-like, as well as dot-like quantised excitonic, properties can be promising in detecting experimentally obtained optical phenomena. These interface sheets are formed by reconstructed $SiC_xO_{1-x}N$ crystalline films separating the bulk-like and thin carbon layers.

On the basis of the relative presence of quantum dot states, one can estimate the relative contributions of reconstructed $SiC_xO_{1-x}N$ near-the–interface structural fragments to the band energy (BE) dispersion, as well as that of the excitonic state to the optical absorption [9-12] (being directly connected to the imaginary part of the dielectric susceptibilities).

## RESULTS AND DISCUSSION

The SiCON nanocrystallite specimens were monitored using TEM, NMR, Raman and IR methods. Optical absorption caused both by band energy reconstruction, as well as by excitonic effects, is analyzed. The role of carbon excess was demonstrated experimentally by increasing the C/O ration over the C-rich particle surfaces.

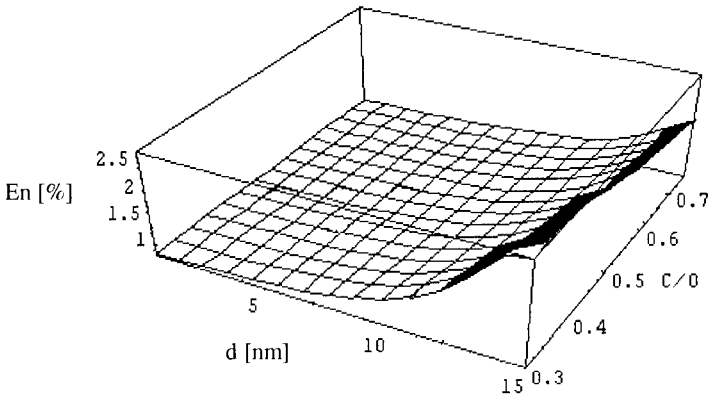


**Figure 1.** The relative contribution of the interfaces to the energy gap is presented dependent on the crystallite sizes d and ratio of the C/O.

In Fig. 2 the band energy dispersion for the interfaces in the case of the x=1.02 are presented. One can see substantial reconstruction of the band energy dispersion near the interfaces. Moreover the energy dispersion derivative is varied. This fact is caused by the reconstruction of the near-the surface states [13-16].

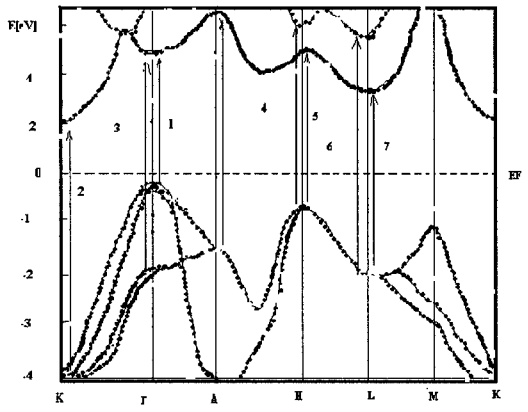


**Figure 2.** Band structure of the $SiC_xO_{1-x}N$ for the x=1.02. The points indicate the bands corresponding to the reconstructed surfaces.

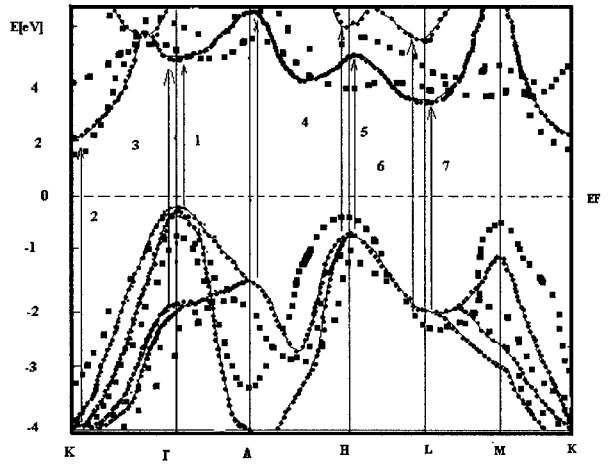


**Figure 3.** Band structure of the $SiC_xO_{1-x}N$ assuming an interface thickness of about 0.6 nm.

Fig. 3 shows additional band structure reconstruction when we undergo to the bands more close to the interfaces. This correlates well with the charge density distributions near the interfaces (see Fig. 4). One can see that a shift toward the deep interface levels stimulates additional charge density re-distribution.

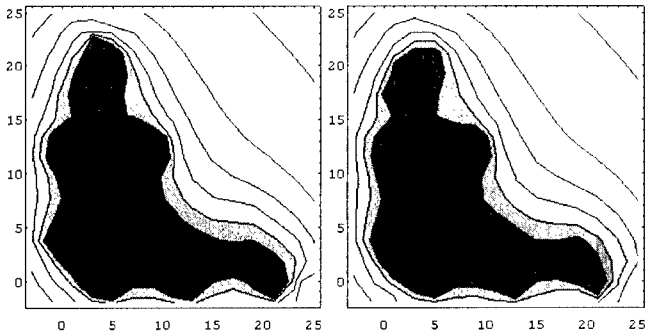


$d_{eff}$ =0.6 nm; $d_{eff}$=1.1. nm

**Figure 4.** Reconstruction of the near-the-interface charge density distribution.

This fact confirms the layered dot-like structure of the investigated nanocrystallites. Our investigations have shown that the dominant role in the optical spectra observed is played by the dot-like near-the–surface states which form strong sharp-like absorption excitonic

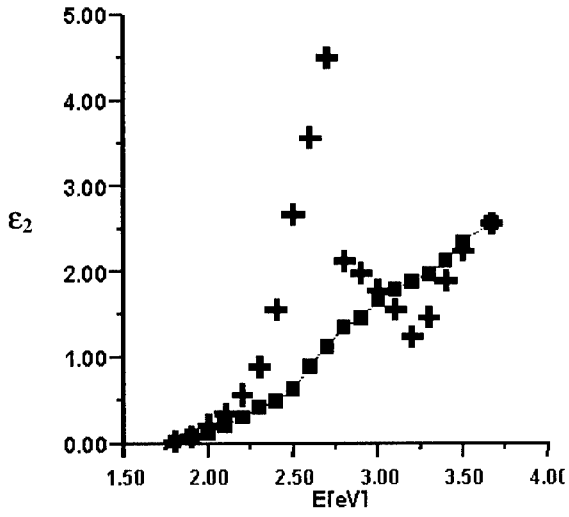


**Figure 5 .** Excitonic spectra at LHeT - + and RT - ■.

spectra (Fig. 5). From Fig. 5 one can see an occurrence of the dot-like excitons playing a key role in the observed spectra.

The connected with the measured behaviours the dependencies of the transparency T versus the film thickness and O/C ratio at LHeT are presented in the Fig. 6.

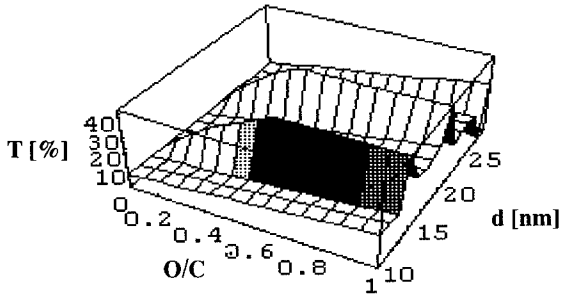


**Figure 6.** Typical dependencies of the transparency versus the O/C ratio and film thickness.

One can see that T possess modulated-like dependence versus the thickness d. This reflects an increase of competition between the long-range ordering and short-range disordering.

## CONCLUSIONS

1. Our investigations have shown that the materials investigated have interface thin layers with thickness of about 1.5 nm. This layer may be considered as a reconstructed surface of the Si by the covered films.
2. The obtained results present new opportunities in semiconductor electronics, making it possible, for example, to receive 3D memory for computers on the trapping levels.
3. The calculations we made using the *ab initio* Car-Parinello method are an additional confirmation of the new type of the interfaces that will shortly find application in the electronic technique.
4. The simulations carried out predict the modulated-like features of the transparency versus the film thickness and O/C ratio.

## ACKNOWLEDGMENTS

The study was supported by the Polish State Committee for Scientific research through grant No KBN-7-T11B 011 20.

## REFERENCES

1. *Microcrystalline and Nanocrystalline Semiconductor*s, edited by R. W. Collins, C. C. Tsai, M. Hiros, F. Koch, and L. E. Brus, MRS Symposium Proceedings No. 358, MaterialsResearch Society, Boston, 1994.
2. *Light Emission from Novel Silicon Material*s, edited by Y. Kane-mitsu, M. Kondo, and K. Takeda, The Physical Society of Japan, Tokyo, 1994.
3. L. W. Wang and A. Zunger, in *Nanocrystalline Semiconductor Material*s, edited by P. V. Kamat and D. Meisel, Elsevier Science, Amsterdam, (1996); A. D. Yoffe, *Adv. Phys.* **42**, 173 (1993); K.D.Hirschman, L.Tsybeskov, S.P.Duttagupta, P.M.Fauchet, Nature (London) **384** (1996) 338; M.C.Schlamp, X.Peng, and A.P.Alivisatos, *J.Appl.Phys.* **82** (1997) 5837.
4. F. Buda, J. Kohanoff, and M. Parrinello, *Phys. Rev. Lett.* **69**, 1272 (1992).

5. Y.S.Park, SiC *Materials and Devices, Semiconductors and Semimetals*, Academic Press, London, UK, 1998; M.B.Yu, S.F.Rusli, S.F.Yoon, S.J.Xu, K.Chew, J.Cui, J.Ahn, and Q.Zhang, *Thin Solid Films* **177**, 377-378 (2000).
6. I.V.Kityk, M.Makowska-Janusik, A.Kassiba, and K.Plucinski, *Optical Materials* **13,** 449 (2000).
7. J.A.Stroscio and D.M.Eigler, *Science* **254**, 1319 (1991).
8. V.Derycke, *Phys. Rev. Lett.* **81**, 5868 (1998).
9. V.M.Bermudez, *Phys. Stat. Solidi* **B202**, 447 (1997).
10. V.I.Gavrilenko, S.I.Frolov, and N.I.Klyui, *Physica* **B185**, 394 (1993).
11. S.Albercht, L.Reining, R.Del Sole, and G.Onida, *Phys. Rev.* **B37**, 7486 (1999).
12. G.Galli, R.M.Martin, R.Car, and M.Parinello, *Phys. Rev.* **B42**, 7470(1990).
13. B.M.Bylander, and L.Kleinman, *Phys. Rev.* **B41**, 7868 (1990).
14. P.-A.Glans and L.I.Johansson, *Surf. Sci.* **465**, L759 (2000); P.-A.Glans, T. Balasubramanian, M.Syvajori, B.Yakimava, L.I.Johansson, *Surf. Science* **470,** 284 (2001).
15. N.Troullier, and J.L.Martins, *Phys. Rev.* **B43**, 8861 (1991).
16. C.Persson and U.Lindefelt, *J.Appl.Phys.* **82**, 5496 (1997).

# Synthesis, Modeling and Theory

Mat. Res. Soc. Symp. Proc. Vol. 703 © 2002 Materials Research Society V11.1

# Intercalative Route to Heterostructured Nanohybirds

Jin-Ho Choy
National Nanohybrid Materials Laboratory
School of Chemistry and Molecular Engineering,
Seoul National University, Seoul 151-747, KOREA

## ABSTRACT

We have successfully synthesized organic-inorganic and bio-inorganic nanohybrids by applying an intercalation technique systematically to Bi-based cuprate superconductors, $Bi_2Sr_2Ca_{m-1}Cu_mO_y$ (m = 1, 2, and 3; BSCCO), and to layered double hydroxides(LDHs), those which are of high importance in terms of basic understanding of intercalation reactions and of their practical applications. The organic-inorganic hybrids were achieved via intercalative complexation of iodine intercalated BSCOO with organic salt of Py-$C_nH_{2n+1}I$ (Py = pyridine). The high-$T_c$ superconducting intercalate with its remarkable lattice expansion can be applied as a precursor for superconducting colloids when dispersed in an appropriate solvent. We were also able to demonstrate that the biomolecules stabilized in the interlayer space of LDH retain their chemical and biological integrity. If necessary, LDH, as a reservoir, can be intentionally removed by dissolving it in an acidic media or interlayer biomolecules in LDH can be released via ion-exchange reaction in electrolyte. It is, therefore, concluded that the inorganic LDH can play a role as a good host lattice for gene reservoir or carrier.

## INTRODUCTION

Recently, inorganic/inorganic[1], organic/inorganic[2], and bio-inorganic[3] heterostructured nanohybrids have attracted considerable research interests, due to their unusual physicochemical properties, which cannot be achieved by conventional solid state reactions. In order to develop new hybrid materials, various synthetic approaches, such as vacuum deposition, Langmuir-Blodgett technique, self-assembly, and intercalation method have been explored. Among them, the intercalation reaction technique—that is, the reversible insertion of guest species into two-dimensional host lattice—is expected to be one of the most effective tools for preparing new layered heterostructures because this process can provide a soft chemical way of hybridizing inorganic/inorganic, organic/inorganic, and biological/inorganic compounds. This field appears to be very creative giving the opportunity to invent an almost unlimited set of new compounds (hybrid compounds) with a large spectrum of known or unknown properties. As a consequence of the dual functionality of hybrid materials, this area is also a good field for scouting smart materials. For example, we were able to realize a new inorganic/organic hybrid system with high-$T_c$ superconducting properties. It is well known that the intercalation reaction occurs in highly anisotropic lamellar structures in which the interlayer binding forces are fairly weak,

compared with the strong ionocovalent intralayer ones. The control of the strength of interlayer interactions makes it possible to probe the relation between interlayer coupling and superconductivity.

The layered double hydroxides (LDHs), so-called "anionic clays", have also received considerable attention due to their technological importance in catalysis, separation technology, optics, medical sciences, and nanocomposite materials engineering. LDHs consist of positively charged metal hydroxide, in which the interlayer anions (along with water) are stabilized in order to compensate the positive layer charges. The composition can be generally represented as $[M^{2+}_{1-x}M^{3+}_{x}(OH)_2][A^{n-}]_{x/n}mH_2O$, where $M^{2+}$ is a divalent cation ($Mg^{2+}$, $Ni^{2+}$, $Cu^{2+}$, and $Zn^{2+}$), $M^{3+}$ is a trivalent one ($Al^{3+}$, $Cr^{3+}$, $Fe^{3+}$, $V^{3+}$, and $Ga^{3+}$) and $A_{x/n}^{n-}$ is an exchangeable anion with charge n. The unique anion exchange capability of LDHs meets the first requirement as inorganic matrices for encapsulating functional biomolecules with negative charge in aqueous media. In this study, we present that the high-$T_c$ superconducting intercalate with its remarkable lattice expansion can be applied as a precursor for superconducting colloids when dispersed in an appropriate solvent[2], also that biomolecules, such as DNA, ATP and antisenses etc. can be incorporated between hydroxide layers by a simple ion-exchange reaction to form bio-LDH nanohybrids. Moreover, the hydroxide layers can play the role not only as reservoir to protect intercalated DNA, but also as nonviral vector to transfer gene or drug to the cell.

## EXPERIMENTAL DETAILS.

### *Organic-inorganic Nanohybrids*

The pristine $Bi_2Sr_2Ca_{m-1}Cu_mO_y$ (m = 1 and 2) compounds were synthesized by conventional solid state reaction with nominal compositions of $Bi_2Sr_{1.6}La_{0.4}CuO_x$ (Bi2201) for m = 1 and $Bi_2Sr_{1.5}Ca_{1.5}Cu_2O_y$ (Bi2212) for m = 2, where the Sr ion is partially substituted by the La ion or Ca one to obtain single-phase samples. The intercalation of an organic chain into the pristine material was achieved with the following stepwise synthesis. First, the $HgI_2$-intercalated $Bi_2Sr_2Ca_{m-1}Cu_mO_y$ (m = 1 and 2; $HgI_2$-Bi2201 and $HgI_2$-Bi2212) compounds were prepared by heating the guest $HgI_2$ and the pristine materials in a vacuum-sealed Pyrex tube, as reported previously. Then, the intercalation of organic chain molecular was carried out by the solvent-mediated reaction between $HgI_2$ intercalates and alkylpyridinium iodide. The reactants of Py-$C_nH_{2n+1}I$ (n = 1, 2, 4, 6, 8, 10, and 12) were obtained by reacting alkyliodide with 1 M equivalent of pyridine in diethyl-ether solvent. The $HgI_2$ intercalates were mixed with two excess reactants of Py-$C_nH_{2n+1}I$, to which a small amount of dried acetone was added. Each solvent-containing mixture was reacted in a closed ampoule at 40 °C for 6 hours and washed with a solvent blend of acetone and diethylether (1:1 volumetric ratio) to remove the excess reactant of Py-$C_nH_{2n+1}I$. And finally the resulting products were dried in vacuum[2]. The superconducting colloidal suspension could be obtained by sonicating the organic-salt intercalates in acetone solvent[4], which was then deposited on a film by electrophoretic deposition(EPD) technique and subsequent heating.

***Bio-inorganic Nanohybrids.***

The pristine $Mg_2Al$-$NO_3$-LDH was simply prepared by coprecipitation from aqueous solutions containing metal ions ($Mg(NO_3)_2{\cdot}6H_2O$ and $Al(NO_3)_3{\cdot}9H_2O$; 2:1 molar ratio) with dropwise titration of a base (NaOH) under nitrogen atmosphere. During the titration, the solution pH and temperature were adjusted to 10 ± 0.2 and 60 °C, respectively. The resulting white precipitate was further aged for 24 hrs, then collected by centrifugation and washed thoroughly with decarbonated water. The biomolecule–LDH hybrids were then prepared by ion–exchanging the interlayer nitrate ions in the pristine LDH with various biomolecules such as adenosine–5'–triphosphate (ATP), herring testis DNA, fluorescein 5-isothiocyanate (FITC) or c-*myc* antisense oligonucleotide (As-*myc*; 5' d (AACGTTGAGGG GCAT) 3') at pH =7. Prior to intercalation, the protein free DNA was extracted from the crude materials and then sheared off to the size of 500–1000 base pairs as described in the literature [5]. The pristine LDH was dispersed in a deaerated aqueous solution containing an excess of dissolved, ATP, FITC, DNA, and As-*myc* and reacted for 48 h with a constant stirring. The reaction products were then isolated and washed as described above. The cellular uptake experiments were carried out for FITC-LDH and As-*myc*-LDH hybrid. The 1 μM and 3 μM of FITC-LDH hybrids were added to the $6 \times 10^4$ NIH3T3 cells and incubated for 1, 2, 4, 6, and 8 hrs, respectively. All the samples washed with PBS buffer, and fixed with 3.7 % formaldehyde were observed with a laser scanning confocal microscope (Carl Zeiss LSM 410). HL-60 cells were also used to prove that the LDH could act as a drug delivery vector in gene therapy. HL-60 cells were exposed to As-myc or As-*myc*-LDH hybrid at a final concentration of 5, 10, 20 $\mu$M, respectively. Cell viability was estimated by spectrophotometry measurement of the samples treated with MTT assay. MTT assay is a colorimetric assay that measures the reduction of 3-(4,5-dimethylthiazol-2-yl)-2,5-diphenyl tetrazolium bromide (MTT reagent) by mitochondrial succinate dehydrogenase. Since the reduction of MTT can only occur in metabolically active cells, the level of activity is a measure of the viability of the cells.

## DISCUSSION

***Organic-inorganic Nanohybrids.***

We have successfully synthesized organic-inorganic nanohybrids by applying an intercalation technique systematically to Bi-based cuprate superconductors, $Bi_2Sr_2Ca_{m-1}Cu_mO_y$ (m =1, 2, and 3; BSCCO). The synthetic strategy for the organic-inorganic hybrids is based on HSAB (hard-soft-acid-base) interaction between organic guest molecules and inorganic host lattice, which is illustrated in figure 1.

From the particle-size analyses and transmission electron microscopy(TEM) measurement, it is found that the plate-like particles are in the range of 50 – 200 nm(Figure 2). The electron diffraction (ED) pattern for colloidal particle exhibits characteristic pattern of the pristine Bi2212 lattice as shown in Figure 2. All the diffraction patterns can be indexed as *hl* reflections for two-dimensional pseudotetragonal lattice of 5.4 × 5.4 Å, which is consistent with the host structure of

Bi2212. According to the AFM height profiles [6], the vertical distance for the delaminated Bi2212 sheets was determined to be ~20 Å, which is comparable to the thickness of unit building block of the pristine Bi2212. Such a finding can be regarded as an evidence of effective exfoliation of host lattice.

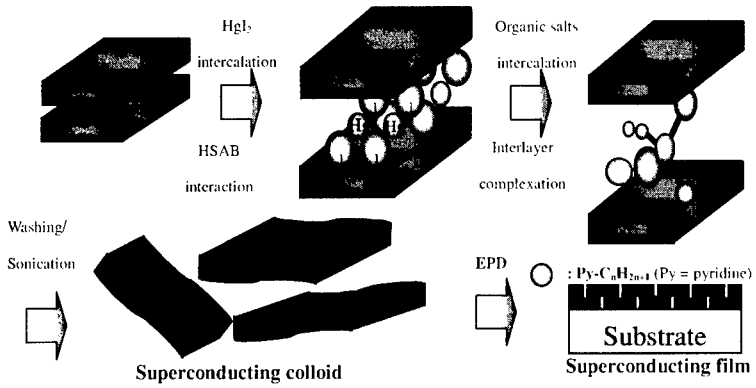


**Figure 1**. Schematic illustration of synthesis of the organic salt intercalate and superconducting film.

The film morphology plays an important role in determining the superconducting property such as critical current density ($J_c$). Especially, in order to attain a high $J_c$, it is important to suppress the volume fraction and grain growth of second phases such as Bi-free phases and Cu-free phases, because such impurity phases can diminish a portion of superconductor and disturb the aligned grain growth of Bi-based superconductor. Therefore, the morphology of representative films was examined by using scanning electron microscopy (SEM). As shown in Figure 3 a, no impurity phases could be seen on the film heat-treated at 850 °C for 5 h. The most important problem in achieving high $J_c$ film is the c-axis orientation, since the c-axis tilt and twist boundaries could act as weak links [7-8]. According to the cross-sectional view of Bi2212 film, we found that the Bi2212 film is highly textured grain along c-axis. Such a result indicates that delaminated Bi2212 nanosheets are expected to be excellent precursor for fabricating the superconducting thin or thick film and wire.

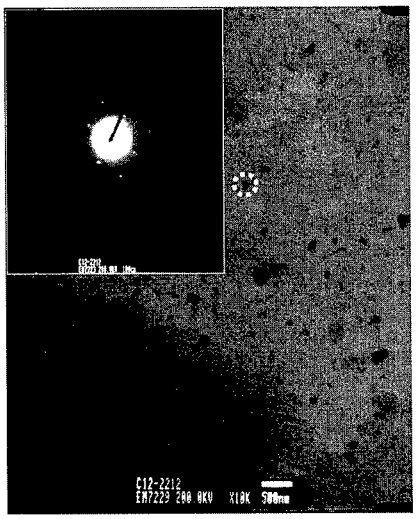

**Figure 2.** TEM and ED pattern of superconducting colloidal particles.

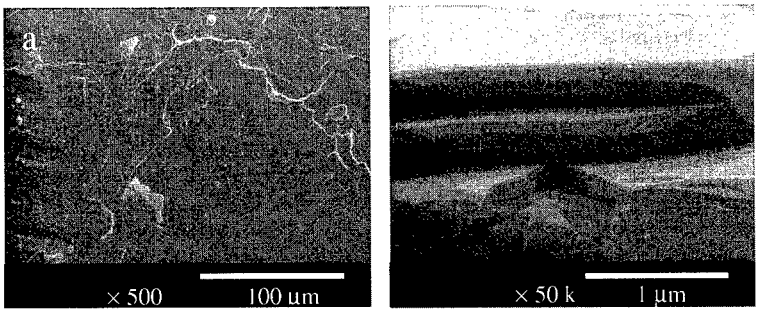


**Figure 3.** The SEM surface morphology and cross-sectional view of the fabricated superconducting film by electrophoretic deposition.

***Bio-inorganic Nanohybrids***

The purpose of this study is not only to prepare new bio-inorganic nanohybrids but also to present biotechnological applications of inorganic materials, such as inorganic gene reservoirs or nonviral drug delivery carriers.

Nano-sized inorganic clay, layered double hydroxide (LDH), has been demonstrated as an excellent reservoir and delivery carrier for genes and drugs by hybridizing with adenosine triphosphate(ATP), DNA and antisense oligonucleotide (As-*myc*), and also with fluoresceine 5-isothiocyanate (FITC). According to X-ray diffraction pattern, the interlayer distance of LDH increases from 0.87 nm (for $NO_3^-$) to 2.39 nm (DNA), 1.94 nm (ATP), 1.88 nm (FITC), and 1.71 nm (As-myc), respectively, upon intercalating of biomolecules into hydroxide layers. (Figure. 1)

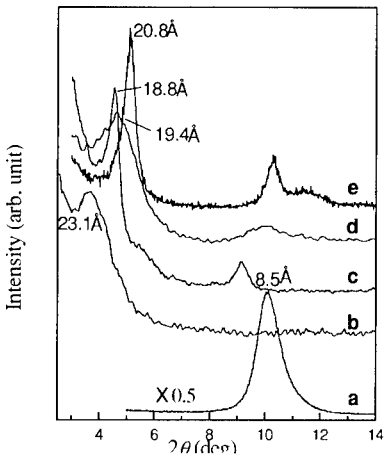


**Figure 1.** Powder X-ray diffractions for (a) the pristine LDH, (b) DNA-LDH, (c) ATP-LDH, (d) FITC-LDH, and (e) As-myc-LDH.

In the case of DNA-LDH hybrid, it was found that the hybrid has the gallery height of 19.1Å, which is consistent with the thickness of a DNA molecule (~20 Å) in a double helical conformation, with the interlayer DNA molecules arranged parallel to the basal plane of hydroxide layers. From the CD (cyclodichroism) analysis, the CD band of DNA-LDH hybrid was observed at the same wavelength compared with the band of ordinary B-form DNA, which means that the intercalated DNA is stable between the hydroxide layers. Figure 2 represents the electrophoretic analysis of DNA-LDH hybrid, which shows that the DNA-LDH hybrid has pH dependent property. There are no DNA bands beyond pH $\cong$ 3, indicating that the DNA molecules in hybrid system are quite stable even in weak acidic atmosphere. However, the DNA bands appeared when the hybrids are treated in a strong acidic media below pH $\cong$ 2, since the hydroxide layers are dissolved in such acidic condition (lane 1-10). From the DNA elution as shown in lane 11 and 12, it can be deduced that the DNA-LDH hybrid can protect DNA from DNase I enzyme. Consequently, the electrophoretic analysis reveals that the DNA-LDH hybrid plays a role as a gene reservoir.

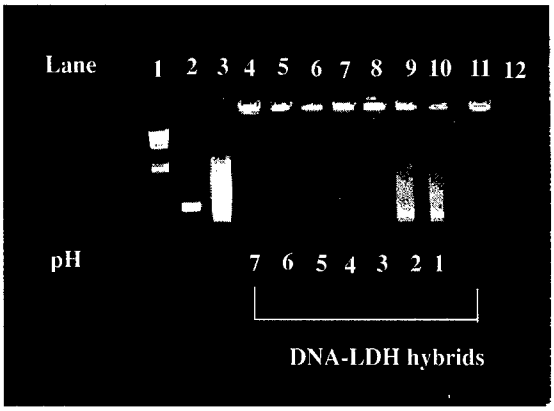


**Figure 2.** Electrophoresis analyses for the DNA–LDH hybrids with respect to pH. The pH of the solution dispersed with hybrid was adjusted to 7.5, 6.0, 5.0,4.0, 3.0, 2.0 and 1.0, respectively, by adding 1M HCl. Lane 1; λ / Hind III cut DNA marker (descent to 23.1, 9.4, 6.5, 4.3, 2.3, 2.0 kbp), lane 2; 500 bp DNA marker, lane 3; DNA and lane 4-10; DNA–LDH hybrids at pH 7.5, 6, 5, 4, 3, 2, and 1, respectively. lane 11 ; DNA-LDH hybrid treated with DNase I and DNA recovered by acid treatment. Lane 12; DNA only treated with DNase I.

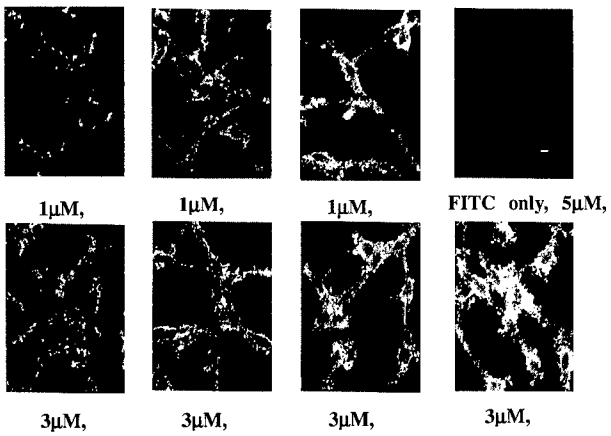


**Figure 3.** Laser confocal fluorescence microscopy of fluorophore in NIH3T3 cells. $6\times10^4$cells/well were incubated with (a)1 μM of FITC-LDH for 1, 4, and 8 hrs respectively. (b) with 3 μM FITC-LDH for 1, 2, 6, and 8 hrs respectively. The FITC only fluorescence microphotograph was obtained with 5 μM FITC only. The bar is 10 μm.

Figure 3 represents the cellular uptake experiments of FITC-LDH hybrid, which is compared

with FITC only. The amount of FITC transferred into NIN3T3 cells is measured directly from laser scanning confocal microscopy [9-11]. It is found that the cellular uptake rate increases with respect to the incubation time and the concentration of FITC-LDH hybrid, although FITC itself can not be transferred into the cells. This is evidence that the FITC-LDH hybrid has an advantage in the cellular uptake, which is thought to be influenced by the charge of transferring species. The neutralized FITC-LDH hybrid nanoparticles can be transferred into the cell more effectively than the charged FITC molecules through phagocytosis or endocytosis. So it is obvious that FITC-LDH hybrid can play a role as a nonviral delivery vector.

We also carried out experiments on the suppression of cancer cell division assuming that the biomolecule-LDH hybrid can be utilized in gene therapy. Figure 4 shows the effect of As-myc-LDH hybrid on the growth of cancer cell such as HL-60. The sequence of As-*myc* is 5' d (AACGTTGAGGGGCAT) 3', complementary to the initiation codon and the next four codons of c-*myc* mRNA, which can act as inhibitor for cancer cell. HL-60 cells treated with As-*myc*-LDH hybrids exhibit time-dependent inhibition on cell proliferation, indicating nearly 65 % of inhibition on the growth compared to the untreated cells, after 4 days. In other words, the growth of HL-60 cells treated with As-*myc* hybrid is only about 35 % compared with those treated with As-myc only.

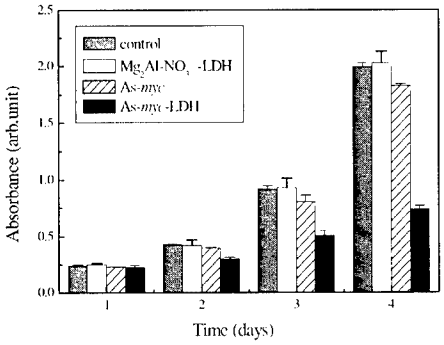


**Figure 4.** Effect of A-myc-LDH hybrids and As-myc only on the growth of HL-60 cells. Controlled cells are incubated without any treatment. The final concentration of each material was 20μM.

Since Figure 4 reveals that LDH itself does not inhibit the growth of HL-60 cells, the suppression effect of cancer cell is purely affected by As-myc-LDH. These imply that As-*myc*s are incorporated into cells and eventually inhibit the growth of cancer cells thanks to the

hybridization. It was also reported that the growth inhibition effect is time and dose dependent[12]. It is concluded that LDH can protect and deliver the intercalated oligonucleotide, and that interlayer As-myc can be effectively released from the hydroxide layer into cell fluids under physiological salt condition. Based on these findings, it is proved that LDHs can act as a new inorganic carrier in gene therapy that is completely different from existing nonviral vectors.

## CONCULSION

New classes of inorganic/inorganic and organic/inorganic heterostructures with high-Tc superconductivity can be synthesized by hybridizing metal halides or organic salts with Bi-based cuprates. These compounds are believed to be promising precursor materials for superconducting nanoparticles, thin or thick films, and wires. And also, we are able to demonstrate that the biomolecules can be intercalated into LDH via ion-exchange reaction to construct bio-inorganic nanohybrid and that inorganic supramolecules, such as the LDHs with nanometer size, can play excellent roles as reservoir for biomolecules and as delivery carrier for gene and drugs.

## ACKNOWLDGEMENT

The author for the expresses his thanks to the Korean Ministry of Science and Technology for the National Research Laboratory Project `99, and to Prof. J. S. Park and Dr. Y. J. Jeong for their helps in biochemical experiments.

## REFERENCES

1. J. H. Choy, N. G. Park, S. J. Hwang, D. H. Kim, N. H. Hur, *J. Am. Chem. Soc.* **116**, 11564–11565 (1994).

2. J. H. Choy, S. J. Kwon, G. S. Park, *Science.* **280**, 1589–1592 (1998).

3. J. H. Choy, S. Y. Kwak, J. S. Park, Y. J. Jeong, J. Portier, *J. Am. Chem. Soc.* **121**, 1399-1400 (1999).

4. J. H. Choy, S. J. Kwon, S. H. Hwang, Y. I. Kim, W. Lee, *J. Mater. Chem.* **9**, 129 (1999).

5. J. Sambrook, E. F. Firsch, T. Maniatis, "In Molecular Cloning, A Laboratory Manual. 2nd ed.", Cold Spring Harbor Laboratory Press: Plainview, NY, (1989) B.15.

6. J. H. Choy, S. J. Kwon, S. H. Hwang, E. S. Jang, *MRS Bull.* **25(9),** 32 (2000).

7 L. N. Bulaevskii, L. L. Daemen, M. P. Maley, J. Y. Coulter, *Phys. Rev. B.* **48**, 13798(1993).

8 B. Hensel, G. Grasso, R. Flükiger, *Phys. Rev. B.* **51**, 15456 (1995).

9 R. J. Lee and P. S. Low, *J .Biol .Chem.* **269**, 3198-3204 (1997).

10. Z. W. Lee, *Ibid.* **273**,12710-12715 (1998).

11. K. Vogel, S. Wang, R. J. Lee, J. Chemielewski, P. S. Low, *J. Am. Chem. Soc.* **118**, 1581-1586 (1996).

12. J. H. Choy, S. Y. Kwak, Y. J. Jeong, and J. S. Park, *Angew. Chem. Int. Ed.* **39(22)**, 4042-4045 (2000).

Mat. Res. Soc. Symp. Proc. Vol. 703 © 2002 Materials Research Society V11.2

# What Xe Nanocrystals in Al Can Teach Us in Materials Science

C. W. Allen, R. C. Birtcher, U. Dahmen[1], K. Furuya[2], M. Song[2] and S. E. Donnelly[3]
Materials Science Division, Argonne National Laboratory,
Argonne, IL 60439, USA.
[1]National Center for Electron Microscopy, Lawrence Berkeley National Laboratory,
Berkeley, CA 94720, USA.
[2]National Institute for Materials Science,
Tsukuba, Ibaraki 305-0003, Japan
[3]Joule Laboratory, University of Salford,
Manchester, M5 4WT, UK.

## ABSTRACT

Noble gases are generally very insoluble in solids. For example, Xe implanted into Al at 300 K forms a fine dispersion of crystalline precipitates and, at large enough fluence, fluid precipitates, both of which are stabilized, relative to the gas phase, by the Laplace pressure due to precipitate/matrix interface tensions. High resolution electron microscopy has been performed to determine the largest Xe nanocrystalline precipitate in local equilibrium with fluid Xe precipitates within the Al matrix. From the shape and size of the largest crystal and the Laplace pressure associated with its interface, we show that the interface tensions can be derived by setting the Laplace pressure equal to the pressure for solid/fluid Xe equilibrium derived from bulk Xe compression isotherms at the temperature of equilibration and observation. The Xe/Al interface tensions thus derived are in the range of accepted values of surface tensions for the Al matrix. Furthermore, it is suggested that this same technique may be employed to estimate unknown surface tensions of a solid matrix from the size and shape of maximal nanocrystals of a noble gas element, which have been equilibrated in that matrix at the temperature of observation.

## INTRODUCTION

The existence of nanometer-sized crystals of noble gas atoms was first recognized in 1984 in specimens of Al into which Kr had been implanted [1]. The phenomenon has now been studied for various noble gases including Ne, Ar, Kr and Xe in a number of metallic and non-metallic matrices, a good review of which is that by Templier [2]. More recently with the emergence of high resolution transmission electron microscopy (HREM) as an analytical tool during in situ experiments, we have studied the behavior of Xe nanoprecipitates in Al with emphasis on electron irradiation effects that result in dynamic shape changes, faulting, migration and coalescence of the Xe precipitates [3–6]. In this contribution, we will demonstrate that the upper limit in size of a Xe nanocrystal in Al at 300 K is consistent with the pressure for solid/fluid equilibrium determined from published bulk isothermal compression data for Xe. Generalizing this result, we then will suggest that the surface tensions of any host matrix can be estimated experimentally by locally establishing solid/fluid equilibrium at any temperature for which appropriate bulk isothermal compression data have been established and then measuring the size of the largest solid nanoprecipitate. From the dimensions of the largest solid particle an estimate of the surface tensions of the corresponding facets may then be determined. The major assumption is that the

surface tensions of the matrix phase are well approximated by the noble gas/matrix interface tensions.

The largest Xe nanocrystal in Al has been estimated previously [7] from the largest observed nanocrystal when fluid precipitates are also present to be about 5 nm in diameter. The surface tension of Al would then be deduced to be about 0.5 J $m^{-2}$; the actual value is closer to 1 J $m^{-2}$. In this case, however, the specimen was heated to several hundred deg C, followed by cooling to 300 K for TEM observation. Because of the large thermal expansion coefficient difference between solid or fluid Xe and Al, the Laplace pressure at the lower temperature would no longer be the equilibrium pressure for the Xe precipitates, and the precipitates are in effect under-pressurized relative to equilibrium. Thus the largest observed nanocrystal is then not the largest such precipitate which can exist at 300 K. The difficulty therefore is to locally equilibrate the system at the temperature of observation. We have done this at 300 K using a low flux electron beam in a 1 MeV high voltage TEM (HVEM) in which the observations were subsequently made at high resolution.

**Laplace pressure**

Laplace pressure P may be defined by the principle of virtual work which relates work done in enlarging a volume V and that in enlarging the surface S associated with that volume. In variational form the principle of virtual work may be written $P\delta V = \Gamma\delta S$ where $\Gamma$ is surface tension. For a spherical bubble of radius R, this yields the familiar relation, $P = 2\Gamma/R$. For a bubble in a matrix, P is the Laplace pressure and $\Gamma$, the interfacial tension. Because the surface tension of Al is not isotropic, voids in Al and hence Xe nanoprecipitates in Al are faceted, assuming the shape of cuboctahedra (or more properly tetrakaidecahedra) defined by {111} planes truncated by {200} facets, as illustrated in Fig. 1a. Again the Laplace pressure can be derived for this geometry. The reality of the Laplace pressure is manifested by the fact that the lattice parameter of a Xe nanocrystal in Al, typically a few nanometers across, is measurably smaller the smaller the crystal.

Xe precipitates in Al are cuboctahedral, and the two relevant surface tensions are $\Gamma^{111}$ and $\Gamma^{200}$. It is convenient to derive the Laplace pressure for this case in terms of dimensional parameters, a and h, which are easily measured from HREM micrographs in [110] orientation. These parameters are defined in Fig. 1b. Remembering that under equilibrium conditions the shape of the cavity is related to the surface tensions by the Wulff construction, it is easily shown that the following conditional test for equilibrium shape holds:

$$h/a = 1 - (\Gamma^{200}/\Gamma^{111}) \cos\theta. \qquad (1)$$

where $\theta = 54.7°$ is the angle between (111) and (200). Thus, if the quantity h/a is independent of cavity size, the system is in equilibrium. This neglects corrections to the free energies involved arising from contributions due to edges and corners of the cavity surface; such contributions are not observably significant for the relatively large sizes we are interested in here [8].

For the cuboctahedral case, the Laplace pressure (equilibrium), derived using the principle of virtual work and letting h/a = x, is given by

$$P = 2\frac{\sqrt{3}\,(1 - 3x^2)\,\Gamma^{111} + 3x^2\Gamma^{200}}{a(1-3x^3)} \qquad (2)$$

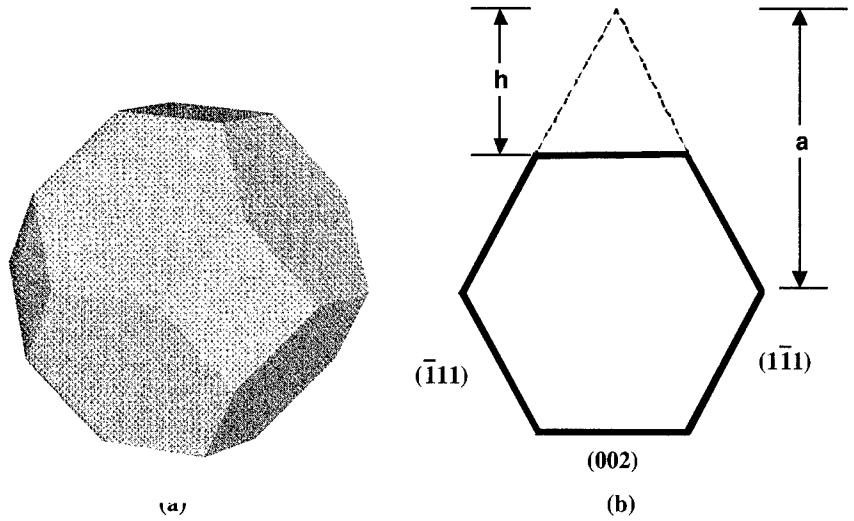


**Figure 1.** (a) Cuboctohedron. (b) Projection of cuboctohedron in <110> defining quantities a and h for equation 2 in which x = h/a.

## EXPERIMENTAL PROCEDURES

A conventional TEM specimen of annealed 5N Al was prepared by jet electropolishing followed by implantation of 35 keV Xe from one side to a relatively large fluence of $2x10^{20}$ $m^{-2}$ at 300 K. This fluence is sufficient to produce a mixture of crystalline and fluid Xe precipitates in the region of largest Xe concentration. Because the concentration of Xe is a function of depth in the Al below the surface of implantation a rather broad distribution of precipitate sizes results so that the system as a whole is far from equilibrium. Monte Carlo simulation by TRIM 95 [3] predicts the end of range of this Xe implant to be 25 nm.

As indicated above, the specimen was locally equilibrated by about 8 hours of irradiation with 1 MeV electrons at an estimated flux of $10^{23}$ –$10^{24}$ $m^{-2}$ $s^{-1}$ , corresponding to a displacement rate in the Al of about 0.006–0.06 dpa/s. This irradiation and the subsequent high resolution observation was performed in the JEOL ARM-1000 HVEM at the National Research Institute for Metals (now the National Institute for Materials Science) at Tsukuba, Japan. Details of the instrumentation and of the particular procedures involved in the high resolution observation process for these very fine precipitates have been described elsewhere [9].

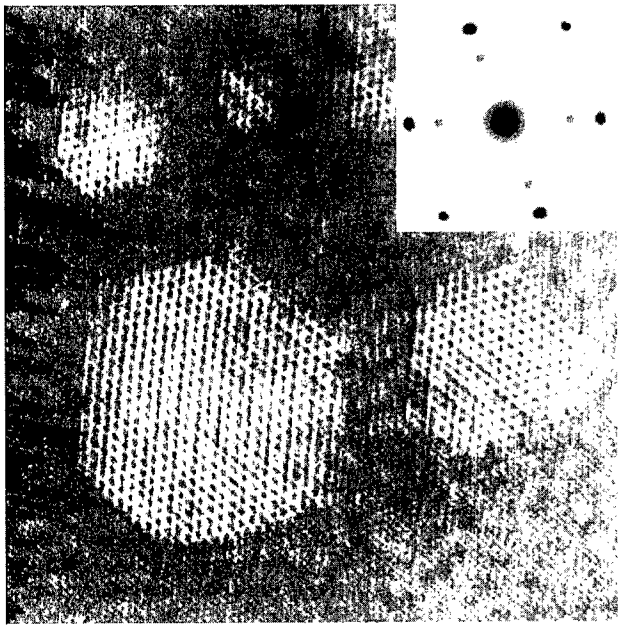

**Figure 2.** High resolution TEM micrograph of Xe-Al alloy in [110], equilibrated by 1 MeV electron irradiation at 300 K. A near-maximally sized Xe nanocrystal and corresponding selected area diffraction pattern from a larger area.

## RESULTS AND DISCUSSION

In order to determine a reliable value for the largest Xe nanocrystal in this experiment it was necessary to examine images of literally thousands of precipitate particles, in our case in more than 30 images recorded at 600–800 kX. In this population a single nanocrystal proved to be of maximum size, with more than a dozen about 0.3 nm smaller (spacing of 200 facets of the Xe nanocrystals). This largest nanocrystal is shown in Fig. 2 and has 200 facet spacing of approximately 9.85 nm (images are calibrated by the 200 Al lattice fringes). The reason for the scarcity of such maximal particles is due to the mechanism of Xe particle growth which is not a classical diffusion-dependent Ostwald ripening mechanism involving continuous size changes but rather growth by coalescence during thermal or irradiation-induced particle migration, resulting in discontinuous increases in size [3,5].

Fig. 2 is a small part of an HREM image in which two sets of 111 facets and one set of 200 facets are imaged edge-on for several Xe nanocrystals whose sizes (200 facet spacings) range from approximately 3 to 9.8 nm. If a Xe nanocrystal is in equilibrium with its immediate

neighborhood, the ratio of interface tensions $\Gamma^{200}$ and $\Gamma^{111}$ is just the ratio of the corresponding facet spacings for any sized nanocrystal (again think of the Wulff construction). For the largest Xe nanocrystal in Fig. 2 this ratio is about 1.05 (200 facet spacing divided by the average of the 111 facet spacings). This is not quite a perfect cuboctahedron as defined for equation 1. To determine the Laplace pressure for a perfect cuboctahedron with 200 facet spacing of $9.8_5$ nm, the following parameters were deduced graphically from Fig. 2: a = $8.3_2$ nm, h/a = $0.38_7$ and $\Gamma^{200}/\Gamma^{111}$ = 1.05. The pressure for solid to fluid transition of bulk Xe under isothermal compression at 293 K is 0.41 GPa [10]. From equation 2 with the Laplace pressure P = 0.41 GPa, we thus deduce $\Gamma^{111}$ to be 1.00 J $m^{-2}$ and $\Gamma^{200}$ to be 1.05 J $m^{-2}$. There are no comparable experimental values determined at such a temperature for Al. Generally, values for (isotropic) surface energies presented for 300 K are actually determined at some elevated temperature such as near or at the melting point and extrapolated to lower temperatures employing an estimate of surface entropy of the solid (for example, see [11]). Such values range from 0.98 J $m^{-2}$ [12] to 1.9 J $m^{-2}$ [11]. A value of 1.14 ± 0.2 J $m^{-2}$ was determined from void shrinkage kinetics in Al at 150–200 °C [13]. From the size of the largest Xe nanocrystal which can exist in local equilibrium, we are able to estimate the surface tensions of the matrix void facets even at temperatures for which thermal equilibration or kinetic phenomena are not achievable.

We suggest that this type of experiment involving implantation of a heavy noble gas, an insoluble solute, into a well defined matrix phase, followed by local equilibration of the system to produce the maximal solute nanocrystal may be employed to experimentally estimate unknown surface tensions for the matrix material. The equilibration step can be performed thermally provided the same temperature is employed for evaluation or by moderate flux electron irradiation provided the electron energy is above the threshold for host atom displacement. In either case, there must be no residual strain field in the matrix associated with the noble gas precipitate. The most accurate, but not necessarily the easiest way to image the precipitates for measurement is to use high resolution TEM. Other methods which are simpler but somewhat less accurate, largely because of magnification calibration errors which can be absent in the high resolution case, are dark field imaging employing 111 or 200 Xe reflections or Fresnel contrast imaging, usually underfocus, in bright field, in which case a defocus value dependent correction for the separation between the Fresnel fringes and the facet spacing should be made.

## CONCLUSIONS

Indeed, Xe nanocrystals in Al can teach us something in Materials Science, in this case something which is very difficult to determine experimentally. We have shown that one may reliably estimate the {111} and {200} surface tensions for high purity Al from high resolution TEM of an equilibrated, high dose implant of Xe at 300 K. The values determined in this way are consistent with classically accepted values, indicating that the matrix surface tensions are well approximated by the matrix/precipitate interfacial tensions. In addition to demonstrating the reality of the Laplace pressure associated with cavities in Al filled with Xe, the method suggests a new way of estimating surface tensions of a wide variety of crystalline matrix materials, including pure metals, alloy phases and ceramics.

## ACKNOWLEDGMENTS

The authors are indebted especially to several individuals at Argonne National Laboratory, Bernard Kestel, Jon Hiller, Peter Baldo and Roseann Csencsits for specimen preparation, ion implantation and preliminary observation. This work was performed under the Japan-USA Scientific Exchange Agreement. The authors are grateful to the Office of Science, US Department of Energy under Contracts No. W-31-109-Eng-38 (ANL) and No. DE-ACO3-76SFOOO98 (LBNL) and to the Science and Technology Agency of Japan for support of this work.

## REFERENCES

1. A. vom Felde, J. Fink, Th. Müller-Heinzerling, J. Pflüger, B. Scheerer and G. Linker, Phys. Rev. Lett. **53**, 922 (1984).
2. C. Templier, in *Fundamental Aspects Of Inert Gases in Solids*, edited by S. E. Donnelly and J. H. Evans (Plenum Press, New York, 1991), pp. 117–132.
3. C. W. Allen, R. C. Birtcher, S. E. Donnelly, K. Furuya, N. Ishikawa, and M. Song Appl. Phys. Lett. **74**, 2611–2613 (1999).
4. C. W. Allen, M. Song, K. Furuya, R. C. Birtcher, S. E. Donnelly, and K. Mitsuishi, J. Electron Micros. **48**, 1025–1030 (1999).
5. R. C. Birtcher, S. E. Donnelly, M. Song, K. Furuya, K. Mitsuishi, and C. W. Allen C. Phys. Rev. Lett. **83**, 1617–1620 (1999).
6. S. E. Donnelly, K. Furuya, M. Song, R. C. Birtcher, and C. W. Allen in *Proceedings of the. International Conference on the Electron*, edited by A. Kirkland and P. D. Brown.(IOM Communications Book **687**, IOM Communications Ltd, London, 1998) pp. 306–312; K. Furuya, M. Song, K. Mitsuishi, R. C. Birtcher, C. W. Allen, and S. E. Donnelly, ibid, pp. 341–347.
7. C. Templier, H. Garem, J. P. Riviere, and J. Delafond, Nucl. Instr. Meth. **B18**, 24–33 (1986).
8. E. Johnson, A. Johansen, U. Dahmen, S. Chen, T. Fujii, Mat. Sci. and Engr. **A 304-306**, 187-193 (2001).
9. K. Furuya, N. Ishikawa, and C. W. Allen, J. of Micros. **194**, 152-160 (1999).
10. P. H. Lahr P, and W. G. Eversole, J. Chem and Engr. Data **7**, 42–47 (1962).
11. W. R. Tyson and W. A. Miller, Surf. Sci. **62**, 267–276 (1977).
12. L. E. Murr, *Interfacial Phenomena in Metals and Alloys* (Addison-Wesley, Reading, MA, 1975) p. 124.
13. K. H. Westmacott, R. E. Smallman, and P. S. Dodson, Metal Sci. J. **2**, 177–181 (1968).

Mat. Res. Soc. Symp. Proc. Vol. 703 © 2002 Materials Research Society V11.3

# EXPLORING THE CONSEQUENCES OF NEGATIVE TRIPLE JUNCTION ENERGY

Gaurav K. Gupta and Alexander H. King
School of Materials Engineering, Purdue University,
West Lafayette, IN 47907-1289

## ABSTRACT
We have investigated the consequences of negative triple junction energy in grain growth. Two and three-dimensional models for total system energy, incorporating varying triple junction energy are developed. These models show that there is a decrease in overall system energy with grain size corresponding to the driving force for grain growth. Although the free energy available to drive grain growth is reduced under some conditions, it is never removed for any reasonable values of the triple junction energy.

## INTRODUCTION
Ultrafine-grained materials are characterized by a very high density of grain boundaries. Palumbo and Aust [1] have pointed out that in the nanometer grain size regime, the density of triple junctions also becomes a potentially important consideration, with the volume of triple junction material exceeding the volume of grain boundary material at a grain size of about 3 nanometers. If triple junctions have properties that differ from those of the grain boundaries [2] then they may exert a powerful influence upon materials behavior in nanostructured materials.
Srinivasan, Cahn and Kalonji [3] have suggested that triple junctions may have "negative" energy and this would certainly be expected to result in unusual behaviors wherever there is a large concentration of triple junctions in a material. In fact, "negative" triple junction energy corresponds to an energy that is lower than that of the adjacent grain boundaries, but is still greater than the energy of the corresponding crystalline material. Even with this understanding, its existence remains somewhat controversial [4].
The purpose of this paper is to investigate the possible effects of reduced triple junction energy on the overall driving force for grain growth, to see if it can contribute to the stabilization of ultrafine microstructures. At its most basic level, the driving force for grain growth is the reduction of interfacial energy that accompanies increasing grain size, and we compute this overall interfacial energy taking account of grain boundaries, triple junctions and quadruple points as potentially different components of the microstructure. The computations are performed for model microstructures corresponding to columnar-grained thin films, and equiaxed bulk polycrystals.

## 2-D MODEL
We consider a microstructure comprising uniformly sized regular, hexagonal grains with edge length '$a$' and a grain boundary thickness '$\delta$'. The grain boundaries (GBs) are rectangular slabs and the triple junctions (TJ's) are equilateral triangular prisms as shown in Fig.1. There are no quadruple points. The energy of the system depends on the amounts of the various features present in it, which vary with the grain size. Fig.2 shows a plot of the cumulative volume fractions of the various features with varying equivalent cylindrical grain diameter. Assigning reasonable

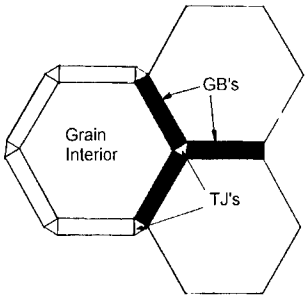


**Fig.1**: Regular hexagonal grains showing GB's and TJ's.

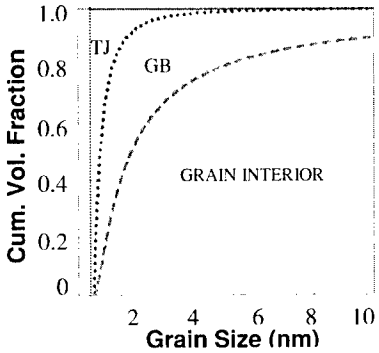


**Fig.2**: Cumulative volume fractions of different components as a function of the grain size, for a GB thickness=0.5nm, for the 2-D model. At a grain size of 2nm, the solid comprises of 54.4% Grain Interiors, an additional 38.7% of GB material, and 6.8% of TJ material.

values to the GB and TJ energies we examine the behavior of the system energy. No variation of energy among the GBs or the TJs is considered, *i.e.* we adopt a "uniform boundary" model, and we assume that no interaction energies exist among the various defects in the system, so the energies of the individual components can be straightforwardly summed. The energies assigned to the defects were:

GB energy = 1 J/m$^2$, corresponding to an energy density of 1/$\delta$ J/m$^3$
TJ energy density varying between 90% and 10% of the GB energy density.

corresponding to a range of modest through extreme cases of "negative" TJ energy. These are all excess Gibbs free energies associated with the defects. The energy of the grain interior is the ground state for the system, and is arbitrarily set to zero. Fig.3 shows the corresponding system energy as function of the grain size, in the nanometer range. In order to account for the possibility that the grain boundary structure (and hence energy) also varies with grain size [5] we have investigated a model in which the GB width varies inversely with grain size. For modeling purposes we choose the following variation:

| | |
|---|---|
| $\delta$ = 1nm | for d $\leq$ 1nm |
| $\delta$ = (9.5 – 0.5d)/9 | for 1 $\leq$ d $\leq$ 10nm |
| $\delta$ = 0.5nm | for d $\geq$ 10nm |

The results for the above variation are shown in Figs.4 and 5.

**3-D MODEL**

As a model three-dimensional case we adopt a structure comprising regular Tetrakaidecahedron-shaped (TKD) grains with edge length '*a*' and GB thickness $\delta$ as shown in Fig.6. The TKD is a 14-sided figure with 8 hexagonal and 6 square sides, that is frequently used as an approximant

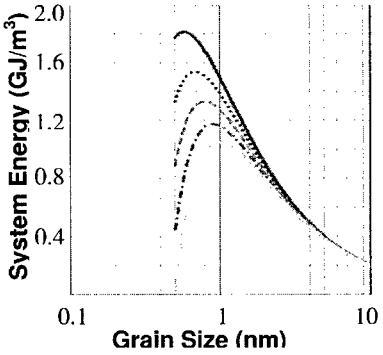


**Fig.3**: Variation of system energy with grain size, for GB thickness=0.5nm, for the 2-D model.

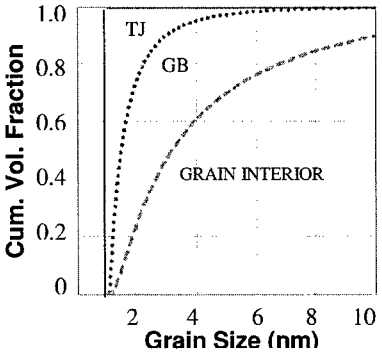


**Fig.4**: Variation of cumulative volume fraction with grain size, for variable GB thickness, for the 2-D model.

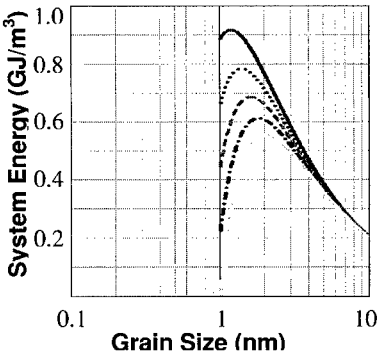


**Fig.5**: Variation of system energy with grain size, for variable GB thickness, for the 2-D model.

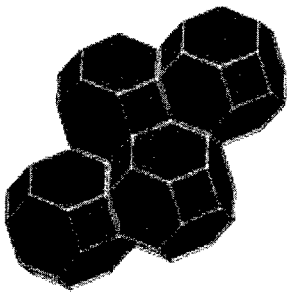

**Fig.6**: A few TKD's stacked in space.

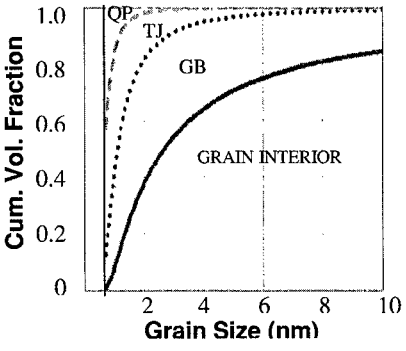


**Fig.7**: Variation of cumulative volume fraction with grain size, GB thickness=0.5nm, for the 3-D model.

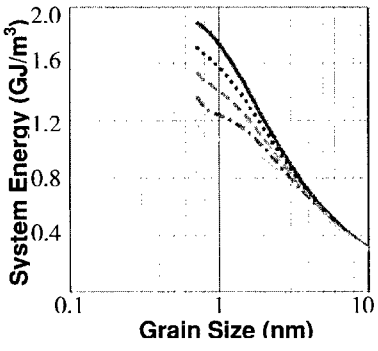


**Fig.8**: Variation of system energy with grain size, for GB thickness=0.5nm, for the 3-D model. QPE=GBE.

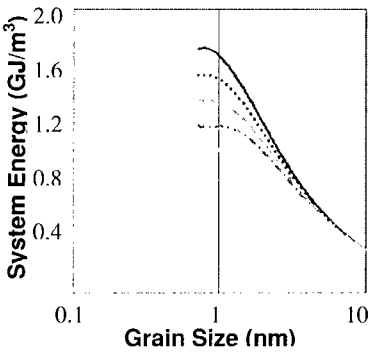


**Fig.9**: Variation of system energy with grain size for GB thickness=0.5nm, for the 3-D model. QPE=80%GBE.

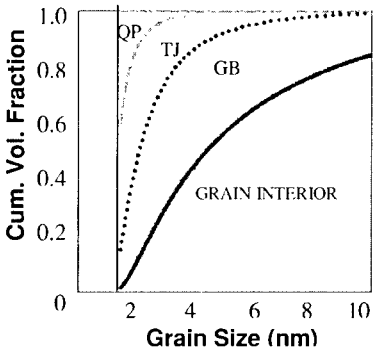


**Fig.10**: Variation of cumulative volume fraction with grain size, with varying GB thickness, for the 3-D model. The variation of GB thickness, to model varying GB properties at small grain size, is described in the text

to the shape of a three-dimensional grain, because it can fill space without leaving any voids and it preserves the topology and proper connectivity of all significant features (GBs, TJs and QPs). For any fixed grain boundary thickness, the triple junctions are polyhedra with uniform, isosceles triangular cross section (since the sides of the TKD do not meet at 120°). The quadruple points (QPs) are tetrahedra with four equal faces in the shape of isosceles triangles. The grain interior becomes an irregular TKD when the interfacial thickness is considered. The cumulative volume fractions of the various features vary with grain size, as shown in Fig.7. Assigning reasonable values to the QP, TJ and GB energies we can study the variation of the system energy with grain size, which is characterized as the equivalent sphere diameter. The energy values chosen are:

| | | | |
|---|---|---|---|
| Case 1: | GB: 1J/m$^2$; | [TJ]: 90% - 10% [GB]; | [QP] = [GB] |
| Case 2: | GB: 1J/m$^2$; | [TJ]: 90% - 10% [GB]; | [QP] = 80% [GB] |

Where [xx] = Energy density. Figs. 8 and 9 show the corresponding system energy as a function of the grain size, in the nanometer range. Now we vary the GB width with grain size in a fashion similar to that done in the 2-D model, and see how the volume fractions and the system energy change. The results for the above variation are shown in Figs.10, 11and 12.

## DISCUSSION

In our models, the volume fractions of the various features (grain interiors, GBs, TJs) are calculated as a function of the grain size, using simple geometry, and elementary simplifying assumptions. Any possible effect of grain size on grain boundary structure or energy is included by allowing the grain boundary width to vary at the smallest grain diameters. Interfacial material is an increasingly dominant fraction of the solid volume as grain size decreases, and at extremely small grain sizes, the grain junctions (TJs and QPs) can occupy as much volume as the grain boundaries themselves.

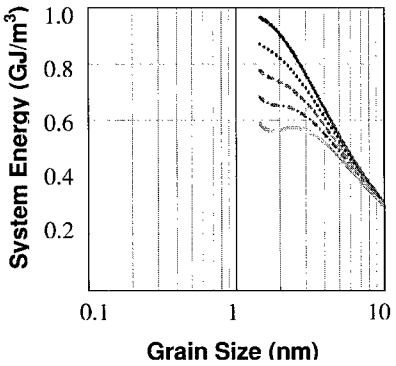


**Fig.11**: Variation of system energy with grain size, for variable GB thickness, for the 3-D model. QPE=GBE

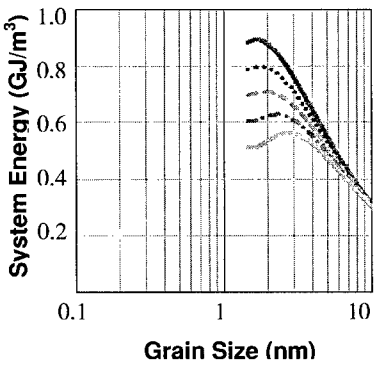


**Fig.12**: Variation of system energy with grain size for variable GB thickness, for the 3-D model. QPE=80%GBE.

A negative derivative of the system energy with respect to grain size represents the global driving force for grain growth, although local topological effects are not considered in this model. In a few of our calculations we find cases where the curve has a minimum and the derivative becomes positive over some range of grain sizes. The energy minimum would correspond to a stable grain size, in the absence of any local topological effects. All minima discovered in this work, however, occur for extreme cases of negative TJ energy, and at unphysically small grain sizes, for which the volume of grain interior material is smaller than the volume of interfacial material. Based on the observed variability of TJ properties [6], we believe that it is extremely unlikely that all of the TJs in the polycrystal would have the same energy, and it is even more unlikely that it would be as low as necessary to stabilize the microstructure, on the basis of the removal of driving force alone. At the most, "negative" TJ energy might be expected to slow grain growth at nanocrystalline grain sizes, relative to the expected high rates, but it does not provide a mechanism for halting it. Observations of reduced grain growth rates have been reported for nanocrystalline Fe [7] but the effect is maximized at a grain diameter somewhere between 20 and 30nm – about an order of magnitude greater than the grain size at which any effect of "negative" TJ energy could be expected. Although varying grain boundary width can move the energy minimum to slightly higher grain sizes, it is doubtful that any systematic change of grain boundary properties with grain size would allow it to reach 20nm, for any reasonable value of TJ energy. We believe that the observed retardation of grain growth is due to impurity-induced pinning, or triple-junction drag [8].

A curious, and possibly unphysical feature of our computations occurs at extremely small grain sizes – typically below one nanometer, depending on the exact choice of TJ energy. At these grain sizes, the TJ volume fraction is comparable to the GB volume fraction and the increasing volume of low-energy TJ material, as grain size shrinks, produces a positive derivative of energy with respect to grain size. This corresponds to a global driving force for grain *shrinkage*, below some critical grain size. If grain shrinkage really does occur, then the result might be the spontaneous amorphization of the material, once the grain size is reduced below the critical, metastable value. Amorphization of various materials has been achieved by ball milling, which first reduces the

grain size [9, 10]. Models for this effect based upon strain energy accumulation [9] could easily be re-cast as effects of strain energy on the relative energies of the intercrystalline components.

## CONCLUSIONS

At ultrafine grain sizes the volume fraction of the intercrystalline region becomes dominant and as the grain size decreases into the nanometer scale, TJ's and QP's account for an increasing fraction of the Intercrystalline region and of the overall microstructure. The negative slope of the total system energy with respect to grain size represents the global driving force for grain growth. It is possible for the system energy to exhibit minima, representing locally stable microstructures, for certain energy configurations. However, the grain sizes in question are unphysically small and carry no significance. "Negative" junction energy on its own cannot be responsible for microstructural stabilization.

## ACKNOWLEDGEMENT

We are grateful to Jon Hilden for help with Surface Evolver (the program used for representing the TKD) and in 3D geometry and visualization of the TKD. This work was supported by the National Science Foundation, Grant # DMR 0096147.

## REFERENCES

1. G. Palumbo, S.J. Thorpe, and K.T. Aust, *Scripta Metall. et Mater.*, **24**, 1347-50 (1990).
2. A.H. King, *Interface Science*, **7**, 251-71 (1999).
3. S.G. Srinivasan, J.W. Cahn, H. Jonsson, and G. Kalonji, *Acta Mater.*, **47**, 2821- 29 (1999).
4. J.E.Taylor, *Interface Science*, **7**, 243-49 (1999).
5. H. Gleiter, *Adv. Mater.* **4**, 474-481 (1992).
6. K.M. Yin, A.H. King, T.E. Hsieh, F.R. Chen and L. Chang, *Microsc. & Microanalysis*, **3**, 417-422 (1997).
7. T.P. Malow and C.C. Koch, *Acta Mater.* **45**, 2177-2186 (1997).
8. G. Gottstein, A.H. King and L.S. Shvindlerman, *Acta Mater.* **48**, 397-403 (2000).
9. C.C. Koch, *Scripta Mater.* **34**, 21-27 (1996).
10. G.F. Zhou and H. Bakker, *Scripta Mater.* **34**, 29-35 (1996).

Mat. Res. Soc. Symp. Proc. Vol. 703 © 2002 Materials Research Society V11.4

# MAGIC FAMILY OF DISCRETLY SIZED ULTRABRIGHT SI NANOPARTICLES

G. BELOMOIN, J. THERRIEN, A. SMITH, S. RAO, R. TWESTEN, S. CHAIEB[b)], AND M. H. NAYFEH
Department of Physics and Department of Theoretical and Applied Mechanics[b)], University of Illinois at Urbana-Champaign, 1110 W. Green Street, Urbana, Illinois 61801 USA

L. WAGNER, AND L. MITAS
Department of Physics, North Carolina State University, 127 Stinson Rd., Raleigh, NC 27695

## ABSTRACT

We describe a procedure for dispersion bulk Si into a family discretely sized ultrasmall ultrabright nanoparticles. We demonstrate that electrochemically etched, hydrogen capped $Si_nH_x$ clusters with n larger than 20 are obtained within a family of discrete sizes. These sizes are 1.0 ($Si_{29}$), 1.67 ($Si_{123}$), 2.15, 2.9, and 3.7 nm diameter. We characterize the particles via direct electron imaging, excitation and emission optical spectroscopy, chromatography, and colloidal crystallization. The band gaps and emission bands are measured. The smallest four are ultrabright blue, green, yellow, and red luminescent particles. The availability of discrete sizes and distinct emission in the red, green and blue range is useful for biomedical tagging, RGB displays, and flash memories.

## INTRODUCTION

Semiconductor clusters, especially silicon clusters, is currently one of the most active frontiers in physics and chemistry **[1-20]**. Their unique structures, stability, and optical and electronic and chemical reactivity, both in free space and on surface have been examined **[3].** Fabricating size-, shape-, and orientation-controlled fluorescent Si nanoparticles in the range 1-3 nm (30-1000 atoms), with reproducibility would be critical to the understanding of nanostructures and would be of significant interest to the microelectronics, optoelectonics and biomedical industries. Averaging over size or shape inhomogeneously masks spectroscopic properties, hindering testing of theory. Size uniformity is important for applications that require superlattices, high quality films, or single nanoparticle-based devices, such as fluorescent imaging and tagging. The availability of discrete sizes with distinct emission in the red, green and blue range is useful for biomedical tagging and in RGB display applications. In flash memory, nanoparticles are embedded in a MOSFET as floating gates to store electric charge. Since the shift in the device's threshold depends on the particle size, a wide size distribution would wash the operating threshold. Several efforts have been directed to develop procedures to control the size, and shape of Si nanoparticles. Only recently progress towards control over the crystallography orientation has been achieved **[12]**.

Self-terminated clusters $Si_n$ **[6-8]** with $n < 10$ exhibit discrete magic numbers, whereas the abundance spectrum of clusters $Si_n$ with $n > 20$ exhibits neither special features nor discrete magic numbers **[9].** The shape of those large ones, however, changes from prolate to more spherical in the narrow range between $n = 24$ and $n = 30$ **[10]**. In the prolate regime, atoms are arranged in one-shell and form triangular surface facets, while in the spherical regime, atoms are arranged into two shells. The outer one has the topology of a fullerene cage, and the inner

shell has a high coordination number. The bonds to the inner shell saturate most of the dangling bonds of the outer shell. The dissociation energy, which is a strongly size dependent for smaller clusters, is a smooth function of n for n > 25[**11**].

Hydrogen-capped Si clusters $Si_nH_x$ with H terminating the unsaturated bonds present opportunities to magic cluster research. Stable configurations with H capping have been recently presented **[4-5]**. Moreover, in some recent electrochemical etching measurements, hydrogen-capped Si in the 1-3 nm size regime has been shown to become highly fluorescent, exceeding the brightness of dyes such as fluorescein **[13]**, and exhibits stimulated emission **[14-15]** and harmonic generation **[16]**. We recently demonstrated that, unlike uncapped $Si_n$ particles, hydrogen-capped $Si_nH_x$ particles (n > 20) exhibit magic discrete numbers **[17]**. We dispersed crystalline Si into H-terminated Si nanoparticles and used direct electron imaging, excitation and emission spectroscopy for characterization, and colloid crystallization for segregation. Transmission electron microscopy (TEM) shows that they classify into a family of discrete sizes that includes 1.0, 1.67, 2.15, 2.9, and 3.7 ±0.1 nm diameter. Excitation spectroscopy measures for the four smallest a HUMO-LUMO gap of 3.44, 2.64, 2.39, and 2.11 eV, while emission spectroscopy shows that they are ultrabright UV/blue, green, yellow, and red luminescent particles with band peaks at ~ 410, 540, 570, and 600 nm.

## SYNTHESIS

We use highly catalyzed electrochemical etching in HF and $H_2O_2$ to disperse crystalline Si into ultrasmall nanoparticles **[18, 11]**. The wafer is laterally anodized while being advanced into the etchent slowly to produce a large meniscus-like area. Because HF is highly reactive with silicon oxide, $H_2O_2$ catalyzes the etching, producing smaller particles. Moreover, the oxidative nature of the peroxides produces high- chemical and electronic quality samples. The pulverized wafer is then transferred to an ultra sound bath for a brief treatment, under which the film crumbles into colloidal suspension of ultrasmall blue particles. Larger particles are less amenable to dispersion due to stronger interconnections. We use a post HF treatment to weaken those and then an ultra sound treatment to disperse the particles. We centrifuge the mix. The resulting residue contains the largest red particles, while the suspension contains the green/yellow particles. We re-dissolve the residue and sonificate it. The red emitting particles stay in suspension. The green particles may be separated by additional sonification/ and or the addition of a drop of HF. Commercial Gel permeation chromatography may be used to separate the particles further, if necessary, or to obtain additional accuracy in separation of the other particles. The particles are separated into several vials each contains particles of uniform size, with near 90-100 % efficiency.

## ELECTRON IMAGING

We immersed a thin graphite grid in the colloid and imaged it by high-resolution TEM **[19]**. **Fig. 1 (Top)** shows that particles are nearly spherical and classify into a small number of sizes. These include 1.0 (see inset), 1.67, 2.15, 2.9, and 3.7 nm. **Fig. 1 (Bottom)** shows the atomic planes in close ups of the 1.67, 2.15, 2.9 and 3.7 nm particles.

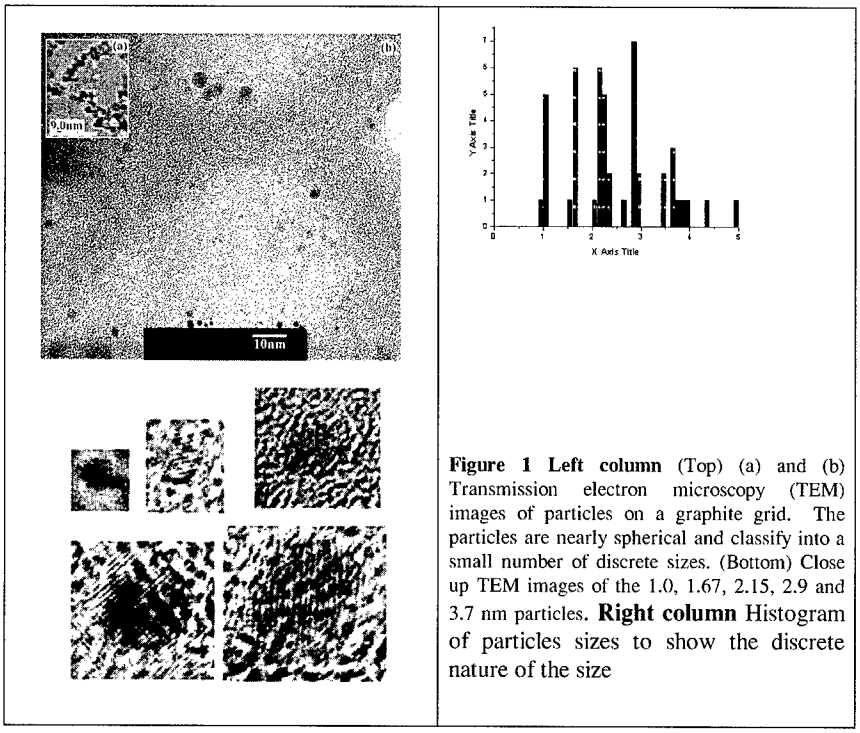


**Figure 1 Left column** (Top) (a) and (b) Transmission electron microscopy (TEM) images of particles on a graphite grid. The particles are nearly spherical and classify into a small number of discrete sizes. (Bottom) Close up TEM images of the 1.0, 1.67, 2.15, 2.9 and 3.7 nm particles. **Right column** Histogram of particles sizes to show the discrete nature of the size

OPTICAL CHARACTERIZATION OF MIXTURE

The absorption and emission gaps of the members of the family were examined. The excitation, i.e., the absorption monitored at a specific emission wavelength (product of absorption and emission) was recorded on a photon counting spectro-fluorometer with a Xe arc lamp light source and 4 nm bandpass excitation and emission monochrometers. We mapped out the excitation in the range 250 nm and 800 nm, while monitoring the emission in the range 400-700 nm. We used the mapping to identify the resonance excitation structure. **Figure 2**, which presents the excitation, shows a resonance structure at 3.44 ± 0.1, 2.64, and 2.39, and 2.11 eV. This resonance structure produces emission bands with maxima at 410, 540, 570, and 600nm respectively. We associate the resonance energies with the HUMO-LUMO edge $E_g$. According to quantum confinement, the absorption and emission photon energies correlate with the size. We pair the diameter d (in nm) with excitation resonance $E_g$ (in eV) as follows (d, $E_g$): (1.0, 3.44); (1.67, 2.64); (2.15, 2.39); and (2.9, 2.11). However, we did not record an excitation/emission resonance that can be associated with the 3.7 nm diameter particle. This may be due to low abundance or/and diminished brightness. A power law fit gives $E_g = 3.44 / d^{0.5}$.

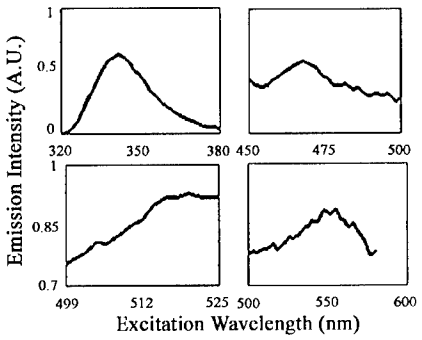


**Figure 2** The excitation spectra of the 1.0, 1.67, 2.15, and 2.9 nm in diameter particles monitored at emission wavelengths 400, 540, 570, and 600nm respectively. They show local resonance structure at 3.44, 2.64, and 2.39, and 2.11 eV respectively.

PARTICLE SEGREGATION

Size uniformity is required for organization or self-assembly. Under certain conditions, the particles segregate according to size upon crystallization. Over time, 5 to 100 μm crystals have formed in a water colloid. Colloidal crystallites were placed on glass and illuminated with light from a mercury lamp (at 360, 395, 450, 520, 560, 610 nm). Emission is detected in the backward direction and detected by an RGB filter/prism based dispersive charge coupled device (3CCD). **Figure 3** (Top Row) shows examples of blue, green, and red segregated crystals. We associate those with the particles observed in the TEM images. Recrystallization to form yellow or green crystals takes place but they are less frequent compared to the blue and red. **Figure 3** (Bottom) gives a photo of colloids of the magic sizes under the irradiation from an incoherent low intensity commercial UV lamp at 365 nm, showing the characteristic red, yellow, green, blue colors.

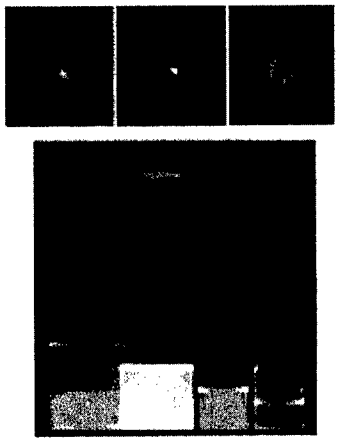

**Figure 3** (Top row) The emission from blue, green, and red colloidal crystals segregated according to the magic sizes 1.0, 1.67, and 2.9 nm in diameter. The crystals are illuminated with light from a mercury lamp. The background is due to a weak bright field. (Bottom from right to left) The emission of colloids of members of the magic family of 1.0, 1.67, 2.15, and 2.9 nm in diameter, after they have been separated, under excitation using a commercial low intensity UV source with an average wavelength of 365 nm.

## SIMULATION

We density functional with generalized gradient exchange-correlation potentials, Configuration Interaction and Monte Carlo approaches to construct structural prototype $Si_nH_x$ particles and to calculate the HOMO-LUMO bandgap **[5]**. We start from a spherical piece of a crystalline Si. The dangling bonds are saturated with hydrogen. Pairs of H from adjacent surface Si atoms are stripped (by $H_2O_2$), and replaced by reconstructed Si-Si dimers, similar to the well-known Si (001) surface 2x1 reconstruction. Reconstructed Si-Si bonds have recently been proposed as a source of novel optical activity in ultrasmall particles **[4,20]**. The resulting structure was relaxed using the Density Functional Theory (DFT) with the PW91 exchange-correlation functional. The simulation yields stable sizes, including 1.0 nm ($Si_{29}H_{24}$) and 1.6 nm ($Si_{123}H_{xx}$), with band gaps of 3.5 and 2.67 eV respectively. **Figure 4** gives the prototype of the smallest (from ref 5). It is $Si_{29}$ $H_{24}$ with five atoms constituting a tetrahedral core and 24 atoms constituting a H-terminated reconstructed Si surface. A single H atom terminates each surface Si atom. Earlier, Allan et al found that particles of 1.03 and 1.67 nm in diameters are stable with bandgaps of 3.5, and 2.67 eV, and consist of 29 and 123 Si atoms respectively **[4]**.

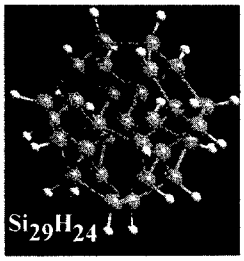


**Figure 4** Prototype structures of $Si_{29}H_{24}$. In the particle, five Si atoms (dark sphere) constitute a single tetrahedral core and 24 Si atoms (dark sphere) constitute a H-terminated (white sphere) reconstructed surface.

The dependence of the bandgap on the number of terminating H atoms is interesting. We start from bulk-like $Si_{29}$ cluster; 36 hydrogen atoms are needed to terminate the unsaturated bonds. As the number of H atoms is reduced from 36, the bandgap drops slowly. But for the number of hydrogen atoms below 24, the bandgap drops sharply, approaching a metallic zero bandgap, and requires bonding change from pure $sp^3$ tetrahedral diamond-like to a mix with $sp^2$, a configuration common in carbon but does not exist in bulk Si. The particle is a filled fullurene of a highly puckered cage and belongs to TD magic structures.

## CONCLUSION

We demonstrated that $Si_nH_x$ clusters classify into a magic discrete family of spherical size that includes ~ 1.0 ($Si_{29}$), 1.67 ($Si_{123}$), 2.15, 2.9, and 3.7 nm diameter, emitting in the UV/blue, green, yellow, and red for the smallest four particles. So far we find no stable capped particles smaller than 29 atoms. We can predominantly produce 1 nm diameter blue particles, or 2.9 nm diameter red particles. Research will be conducted to refine conditions under which the green and yellow members of the family may be predominantly prepared.

ACKNOWLEDGMENT: We acknowledge the State of Illinois Grant IDCCA No. 00-49106, the US DOE Grant DEFG02-ER9645439, NIH Grant RR03155, and US NSF grant BES-0118053.

REFERENCES

1. Physics and Chemistry of Small Clusters, edited by P. Jena, B. Rao, and S. Khanna (Plenum, New York, 1987

2. M. F. Jarold, Science 252, 1085 (1981); K. M. Ho et al., Nature (London) 392, 582 (1998); E. Kaxiras, and E. Jackson, Phys. Rev. Lett. 71, 727 (1993); J. Grossman and L. Mitas, Phys. Rev. Lett 74, 1323 (1995); L. Mitas, J. Grossman, I. Stich, and J. Tobik, Phys. Rev. Lett. 84, 1479 (2000); I. Vasiliev, S. Ogut, and J. Chelikowsky, Phys. Rev. Lett. 82, 1919 (1999)

3. I-S. Hwang, M-S Ho, and T. T Tsong, Phys. Rev. Lett. **83**, 120 (1999)

4. G. Allan, C. Delerue, and M. Lannoo, Phys. Rev. Lett. **76**, 2961 (1996)

5. L. Mitas, J. Therrien, G. Belomoin, and M. H. Nayfeh, Appl. Phys. Lett. **78**, 1918 (2001)

6. W. Brown, R. Freeman, K. Raghavachar, and M. Schulter, Science **235**, 860 (1987); L. Bloomfield, R. Freeman, and W. Brown, Phys. Rev. Lett. **54**, 2246 (1985)

7. K. Raghavachari, Phase Transitions **24-26**, 61 (1990)

8. U. Rothlisberger, W. Andreoni, and M. Parrinello, Phys. Rev. Lett. **72**, 665 (1994); W. Andreoni, and G. Pastore, Phys. Rev. B **41**, 10243 (1990); U. Rothlisberger, W. Andreoni, and P. Ginnozzi, J. Chem Phys. **96**, 1248 (1992)

9. L. Anderson, S. Muruyama, and R. Smalley, Chem. Phys. Lett. **176**, 348 (1991); H. Kroto, J. Heath, S. O'Brian, R. Curl, and R. Smalley, Nature (London) **318**, 162 (1985)

10. M. Jarrold, and V. Constant, Phys. Rev. Lett. **67**, 2994 (1991); M. Jarrold and J. Bower, J. Chem. Phys. **96**, 9180 (1992)

11. M. Jarrold and E. Honea, J. Phys. Chem. **95**, 9181 (1991)

12. G. Grom, D. Lockwood, J. McCaffrey, H. Labbe, P. Fauchet, B. White Jr., J. Dlenner, D. Kovalev, F. Koch, and L. Tsybeskov, Nature 407, 358 (2000)

13. O. Akcakir, J. Therrien, G. Belomoin, N. Barry, E. Gratton, and M. Nayfeh Appl. Phys. Lett. **76**, 1857 (2000)

14. M. H. Nayfeh, N. Barry, J. Therrien, O. Akcakir, E. Gratton, and G. Belomoin, Appl. Phys. Lett. **78**, 1131 (2001); M. Nayfeh, O. Akcakir, J. Therrien, Z. Yamani, N. Barry, W. Yu, and E. Gratton, Appl. Phys. Lett.**75**, 4112 (1999)

15. M. H. Nayfeh, S. Chaieb, S. Rao, N. Barry, J. Therrien, G. Belomoin, and A. Smith, Appl. Phys. Lett. December 24 (2001)

16. M. H. Nayfeh, O. Akcakir, G. Belomoin, N. Barry, J. Therrien, and E. Gratton, Appl. Phys. Lett. **77**, 4086 (2000)

17. G. Belomoin, J. Therrien, A. Smith, S. Rao, R. Twesten, S. Chaieb, M.H. Nayfeh, L. Wagner, and L. Mitas, Appl. Phys. Lett. (In press)

18. Zain Yamani, Howard Thompson, Laila AbuHassan, and Munir H. Nayfeh Appl. Phys. Lett. **70**, 3404 (1997); D. Andsager, J. Hilliard, J. M. Hetrick, L. H. AbuHassan, M. Plisch, and M. H. Nayfeh, J. Appl. Phys. **74**, 4783 (1993); Z. Yamani, S. Ashhab, A. Nayfeh and M. H. Nayfeh, J. Appl. Phys. **83**, 3929 (1998)

19. G. Belomoin, J. Therrien, and M. Nayfeh, Appl. Phys. Lett **77**, 779, (2000); J. Therrien, G. Belomoin, and M. Nayfeh, Appl. Phys. Lett **77**, 1668 (2000)

20. M. Nayfeh, N. Rigakis, and Z. Yamani, Phys. Rev. B **56**, 2079 (1997); MRS **486**, 243 (1998)

Mat. Res. Soc. Symp. Proc. Vol. 703 © 2002 Materials Research Society V11.9

# Optical Characterization and Modeling of Sulfur Incorporated Nanocrystalline Carbon Thin Films Deposited By Hot Filament CVD

**S. Gupta[a], B. R. Weiner[b] and G. Morell[c]**
[a]Department of Physics, University of Puerto Rico, San Juan, PO Box 23343, PR00931, USA
[b]Department of Chemistry, University of Puerto Rico, San Juan, PO Box 23346, PR00931, USA
[c]Dept. of Physical Science, University of Puerto Rico, San Juan, PO Box 23323, PR00931, USA

## ABSTRACT

Sulfur incorporated nanocrystalline carbon (n-C:S) thin films grown on molybdenum substrates by hot-filament chemical vapor deposition (HFCVD) using gas mixtures of methane, hydrogen and a range of hydrogen sulfide ($H_2S$) concentrations are optically examined using Raman spectroscopy (RS) and *ex situ* spectroscopic phase modulated ellipsometry (SPME) from near IR to near UV (1.5-5.0 eV) obtaining their vibrational frequencies and pseudodielectric function, respectively. The ellipsometry data ($\langle\varepsilon_r(E)\rangle$, $\langle\varepsilon_i(E)\rangle$) were modeled using Bruggeman effective-medium theory (BEMT) and five parameters Forouhi and Bloomer (FB) dispersion Model. A simplified two-layer model consisting of a top layer comprising an aggregate mixture of $sp^3C+sp^2C+$void and a bulk layer ($L_2$), defined as a dense amorphized FB-modeled material was found to simulate the data reasonably well. Through these simulations, it was possible to estimate the dielectric function of our n-C: S material, along with the optical bandgap ($E_g$), film thickness (d), and roughness layer ($\sigma$) as a function of [$H_2S$]. The physical interpretation(s) of the modeling parameters obtained were discussed. The Raman and ellipsometry results indicate that the average size of nanocrystallites in the sulfur-incorporated carbon thin films becomes smaller with increasing $H_2S$ concentration, consistent with AFM measurements. The bandgap was found to decrease systematically with increasing $H_2S$ concentration, indicating the enhancement of midgap states and $sp^2$ C network, in agreement with RS results. These results are compared to those obtained for the films grown without sulfur (n-C), in order to study the influence of sulfur addition to the CVD process. This analysis led to a correlation between the film microstructure and its electronic properties.

## INTRODUCTION

A great deal of attention has been given to diamond and diamond-like carbon (DLC) thin films since their advent owing to a wide range of desired and unique mechanical, optical and electronic properties (such as: high mechanical hardness, chemical inertness, negative electron affinity, and very high electron and hole mobilities) [1,2]. This combination of superlative properties paves their way to several potential and technological applications: optical coatings, wide-band IR transmissive windows, and flat panel displays (FPDs) to name a few [3]. It is also well known that the optical and electronic properties of these carbon materials are controlled by the ratio of $sp^3/sp^2$ coordinated carbon bonds [4,5]. Films having a high fraction of $sp^3$ C exhibit a higher optical band gap and hardness as compared to films rich in $sp^2$ C. A number of theoretical studies of various hypothetical phases of carbon have been carried out predicting such behavior [4,6].

The complex refractive index, $\tilde{n} = n - ik$, where n is the refractive index and k the extinction coefficient, provides information about the distribution of bonding configurations and is therefore an important parameter for designing the material for specific technological applications [7]. Among several state-of-the art techniques for optical characterization,

spectroscopic ellipsometry (SE) has proved to be very influential and advantageous for the last two decades in the thin film structural analysis because of its inherent advantages and sensitivity [4,8,9]. Recent pioneer reports on the addition of sulfur in diamond as a donor dopant, both experimental and theoretical [10,11,12], stirred great interest in the diamond community. In general, the n-type dopants of diamond (like N, P and now S) have the potential to enhance the field emission properties of disordered and nanocrystalline carbon films by providing electrons close to the conduction band [3,13]. Presently the incorporation of sulfur is not to make diamond semiconducting, but rather tailor the material as viable cold cathodes [3]. It has been previously shown that structural defects such as $sp^2$ C network yield low-field emitters [3,14], in contrast to the degradation of several other physical properties.

We have measured the dielectric function and vibrational frequencies of n-C:S thin films using SE and RS techniques as a function of [$H_2S$] in gas phase. This paper focuses on the determination of a reliable physical model to describe the optical properties of these materials. Utilizing Forouhi and Bloomer (FB) dispersion model [15], we performed multi-layer analysis to estimate the dielectric function of these n-C:S thin films. According to this five parameter model (A, B, C, n($\infty$), and $E_g$) [15], the optical absorption in the visible range is dominated by a single type of electronic transition involving states within ~ 5eV of the Fermi level and hence should involve mostly $\pi$-$\pi^*$ excitations. In order to investigate the optical absorption processes in the disordered carbon material in thin film form studied hereby, fits to the pseudodielectric SE data were performed using Levenberg-Marquardt [16] algorithm while varying all the parameters to fit simultaneously both n and k spectra. Based on this model and through RS, we explained the behavior of optical bandgap and the refractive index in terms of $sp^2$C network and the introduction of structural defect states within the bandgap (midgap states). To the best of authors' knowledge no such studies have been performed so far.

## EXPERIMENTAL PROCEDURES

The sulfur incorporated nanocrystalline carbon thin films (n-C:S) were prepared in a custom-built HFCVD reactor, described in detail elsewhere [3,17]. These thin films were prepared on Mo Substrates using a 2%$CH_4$:$H_2$ gas mixture with a total flow of 100 sccm which was directed through a Joule heated Rhenium (Re) filament. In order to incorporate sulfur (S) in the samples, $H_2S$:$H_2$ gas mixture was introduced in the chamber. Several sulfur concentrations were used, ranging from 100 ppm to 500 ppm, with an interval of 100 ppm at a fixed substrate temperature of 900 °C. The substrate was maintained at 900-930 °C during the growth process and the total gas pressure was kept at 20 Torr. Real-time SE was used to calibrate the true temperature of the substrate surface [18]. The incorporation of sulfur was quantified by X-ray photoelectron spectroscopy (XPS) and amounted to be around 0.5-1.0 at.%.

Film thicknesses were around 0.5-1.0 µm, measured mechanically using Tencor surface profilometer (Alpha Step 100). The root mean square (rms) surface roughness, average grain size and typical surface topological features were evaluated using AFM (Nanoscope IIIa, Digital Instruments Inc.). The Raman spectra were recorded using a triple monochromator (ISA Jobin-Yvon Inc. Model T64000) with around 1 $cm^{-1}$ resolution employing the 514.5 nm line of $Ar^+$ laser and a probed area of about 1-2 $\mu m^2$. The *ex situ* spectroscopic ellipsometry data were measured with a Jobin-Yvon UVISEL phase-modulated spectroscopic ellipsometer (Model DH10) from NIR (1.5 eV) to near UV (5.0 eV) with a fixed incident angle of 68.58° from the sample normal and a spot size of 3 mm. During the analysis, the bulk optical function of the

material components of the film microstructure, including diamond component ($sp^3C$) and non-diamond ($sp^2C$) as glassy carbon, were taken following Collins [18].

## RESULTS AND DISCUSSION

Figure 1 shows the Raman spectra for the n-C:S thin films grown by HFCVD as a function of [$H_2S$] in gas phase. All of the samples were grown at a fixed substrate temperature of 900 °C. The film grown with 100 ppm $H_2S$ shows the 1332 $cm^{-1}$ peak (fingerprint of diamond). Qualitative inspection of Fig. 1 also shows that the Raman spectra are dominated by broad features at 1150, 1340 and 1580 $cm^{-1}$, which are typical characteristic of nanocrystalline diamond (n-D) [19] and disordered carbon [20], the last two denoted by D and G band, respectively. These latter features predominate with respect to the increase in sulfur concentration. The film grown with 100 ppm is quite similar to intrinsic material (n-C) and one can note the disappearance of diamond peak for films grown with $H_2S$ greater than 200 ppm. The relative heights of the Raman peaks (D and G bands) differ in general. The latter features predominate at higher TS while their relative heights differ, in general. The difference among the Raman spectra can be explained by the sulfur additions. Under the specific growth conditions considered in this study, sulfur tends to introduce disorder and defects considerably, similar to nitrogen incorporation, which induces graphitization of carbon films [3,6,21,22]. Notice that the sp2 bond sites begin to diffuse and condense into clusters at high temperatures. This ability of clustering of $sp^2$ sites while keeping the $sp^3$ fraction fixed implies or indicates that these $sp^2$ sites act like defects in the $sp^3$ matrix. Predicted theoretically by Robertson *et al.* [23] that the midgap states are found for $\pi$ states on $sp^2$ sites, they cluster according to the deposition conditions, as the [$H_2S$] hereby. Changes in the surface morphological features are also apparent from AFM technique. The

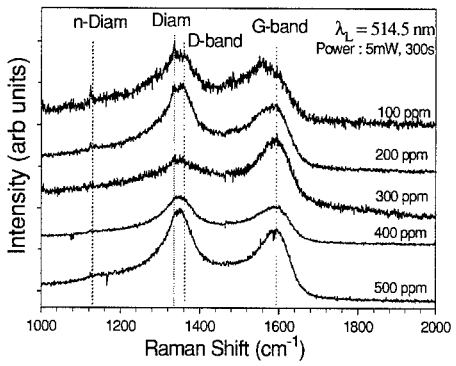


**Figure 1.** Raman spectra for S- assisted nanocrystalline carbon thin films as a function of sulfur concentration ([S]) depicting the characteristic diamond, graphitic and disordered carbon

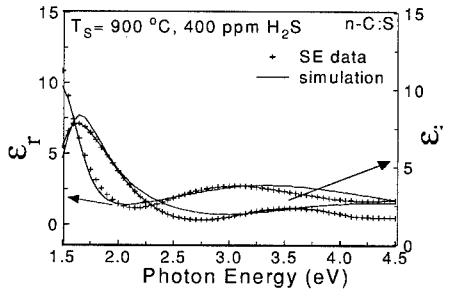


**Figure 2.** Typical *ex situ* phase modulated spectroscopic ellipsometry data for one of the sulfur-incorporated nanocrystalline carbon thin films. The crosses (+) are the raw data, while the solid line (—) is the best-fit simulation resulting from linear regression analysis (LRA) of the experimental data. The arrows indicate the two ordinates that apply to each curve.

ball-like morphology transforms to fine-grained on S-addition and the surface becomes relatively smoother (σ: 64 nm vs 25 nm). The average grain size estimated using AFM [3] becomes reduced from 60 to 20 nm with increasing sulfur addition. Moreover, the grain size distributions range from 20-60 nm to 100-150 nm for all of the samples. Since the Raman cross-section of graphitic carbon is around 50 times larger than that of diamond [19], there must be a substantial amount of microcrystalline diamond inclusions in the film. Besides, a substantial amount of threefold $sp^2$ oordinated carbon ($sp^2C$) is also present, indicated by the graphitic G-band at 1580 $cm^{-1}$. Generally speaking, the Raman band at 1360 $cm^{-1}$ has contributions from both highly defective $sp^3$ carbon (diamond-like) and disordered $sp^2$ carbon (graphitic D-band [20]).

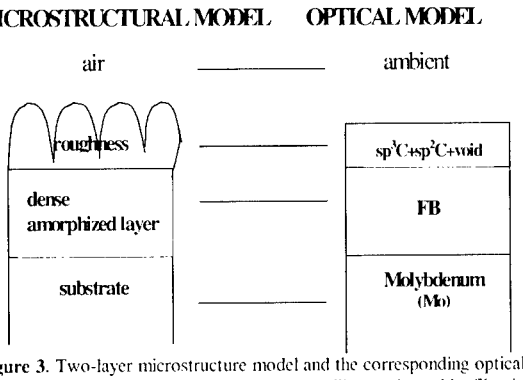


**Figure 3.** Two-layer microstructure model and the corresponding optical model to describe S-incorporated nanocrystalline carbon thin film in order to simulate the ellipsometric spectra shown in Fig. 2 for one representative sample using least-square linear regression analysis (LRA).

The experimental *ex situ* SE data and the corresponding fits of $\varepsilon_r(E)$ and $\varepsilon_i(E)$ for one of the representative sample are shown in Fig. 2. The results were fitted employing Bruggeman Effective Medium Theory (BEMT) [24] and FB dispersion model under the assumption that the film composition is an aggregate mixture of disordered $sp^3$ and $sp^2$ carbon ($sp^3$ C, $sp^2$ C). For the $sp^3$ component, the optical constants of natural type IIa diamond were adopted, while for the $sp^2$ component the optical constants of glassy carbon were used [18]. In order to find the most appropriate one, the models having a different number of layers, different composition and two dispersion models such as Tuac-Lorenz (TL) and FB within these layers were applied to ellipsometry data. The result was that a simplified two-layer model of which the microstructural and the corresponding optical model shown in Fig. 3, was required in order to simulate the data reasonably well. This model consists of a top layer (defined as a composite layer of $sp^3C+sp^2C$+voids followed by a dense amorphized FB-modeled material layer. Last is the Mo substrate, assumed to be infinite since the light does not bounce back after passing through it. This two-layer model is in contrast to the model proposed for the material grown without sulfur (n-C), whereby the top layer consists of 50%FB+50%void [17]. The degree of agreement between the model and the ellipsometry data for n-C:S material can be evaluated from Fig. 2, where the continuous line corresponds to the simulation while the crosses correspond to the measured ellipsometry data. Both $\varepsilon_r$ and $\varepsilon_i$ were simultaneously fit using regression analysis that minimizes $\chi^2$ [17].

Qualitatively, these are the best fits, while quantitative results are summarized in Table I. The overall thicknesses of the films derived from the SE model tally with those measured mechanically using a profilometer. The film thicknesses measured by these two techniques do agree reasonably well, thus giving another indication of the reliability of the model employed. On the other hand, the surface roughness measured by SE sometimes agrees with that estimated by AFM, but it is generally much lower. Results in terms of the bonding -antibonding state

**Table 1.** Summary of simulation results for the sulfur-incorporated nanocrystalline carbon thin films grown by HFCVD under several hydrogen sulfide ($H_2S$) concentrations in gas phase[a]

| Sample Growth Parameters | Thickness $L_2$ (Å) | A | B (eV) | C ($eV^2$) | n(∞) | $E_g$ (eV) | $\chi^2$ (best-fit) |
|---|---|---|---|---|---|---|---|
| No sulfur | 9819.3±19.7 | 0.190 | 4.108 | 13.916 | 1.714 | 2.701 | 0.16 |
| 100 ppm | 1600.1±21.5 | 0.27 | 4.586 | 18.73 | 1.52 | 2.18 | 0.29 |
| 200 ppm | 1530.4±12.4 | 0.25 | 3.921 | 19.30 | 1.91 | 1.15 | 0.89 |
| 300 ppm | 2300.2±36.9 | 0.60 | 3.510 | 10.71 | 2.20 | 0.92 | 0.18 |
| 400 ppm | 4613.7±29.5 | 0.94 | 3.506 | 13.36 | 2.97 | -0.70 | 0.27 |
| 500 ppm | 7100.4±112.4 | 1.16 | 3.001 | 15.00 | 3.00 | -1.28 | 1.26 |

**[a]Other deposition parameters are: [$CH_4$]= 2.0 % in high hydrogen dilution, pressure =20.0 Torr and number of deposition hours = 15-30 minutes for all of the samples.**

energy difference ($E_{\sigma\pi}$-$E_{\sigma^*}$), which is a sort of average Penn gap and excited state lifetime obtained from the B and A values respectively, are listed in Table I. The findings of the optical gap ~ -1.28-2.1 eV with decreasing sulfur concentration are in agreement with the fact that the films contain a relatively high fraction of $sp^2$ bonded carbon ($sp^2$C) with increasing [$H_2S$]. There appears to be an inverse relation between the value of n(∞) and the optical bandgap ($E_g$), in agreement with the observations made for sputtered a-C and a-C:H films studied with the same model [25]. The negative values of the $E_g$ for two of the films studied hereby seem to be unphysical but this observation is very common for these kinds of films [25] and can be overcome using modified FB model [25], which will be demonstrated in the forthcoming publication.

In the photon energy range studied hereby of 1.5-5.0 eV, the $\pi$-$\pi^*$ transitions ($sp^2$ clusters) are the predominant absorption processes involved. There are micro/nanocrystalline diamond inclusions in the film prepared with 100 ppm and, correspondingly, its bandgap is higher and the excited state lifetimes longer (smaller A) than those of the films grown with high $H_2S$ concentration. These values then change as a result of high [$H_2S$], which enhances the formation of midgap states within the band structure of the material through the formation of $sp^2$ C bonds, resulting in lower optical bandgaps ($E_g$) and shorter excited state lifetimes (larger A). These findings are in agreement with other groups concerning a-C:H deposited by PECVD with nitrogen, which leads to a strong decrease in $E_g$, because of the increase in aromatic regions [26]. The decrease in $E_g$ or $\pi$-$\pi^*$ transition energy confirms the nanocrystalline nature of the films, in agreement with RS. These results indicate similarities between n-C:S and n-C:N, rather than to n-C:O, and point at potential cold cathode applications of the material studied hereby.

## CONCLUSIONS

The optical properties of n-C:S thin films were investigated using RS and spectroscopic ellipsometry. A simplified two-layer structural model was found to be appropriate for simulating the ellipsometry spectra satisfactorily, obtained information about the electronic structure of these thin films. The reduction in the amount of ordered $sp^3$ carbon was accompanied by a reduction of the effective bandgap and of the excited state lifetimes with increasing $H_2S$ concentration in gas phase, in coordination with RS observations. Consequently, the influence of

sulfur addition to the CVD process is to increase the $sp^2$ C content and the corresponding defect states within the bandgap. This analysis led to a correlation between the film microstructure and its electronic properties.


## ACKNOWLEDGEMENTS

One of the authors (SG) acknowledges a Graduate Research Fellowship granted by the National Science Foundation (Grant No. NSF-EPS-9874782). This research work is also supported in parts by the Department of Energy (DoE Grant No. DE-FG02-99ER45796) and NASA (Grant No. NAG5-10321). We also gratefully acknowledge the use of Micro-Raman spectroscopy facility (Dr. Ram Katiyar) in the execution of this work.


## REFERENCES


1. J. C. Angus, P. Koidl, S. Domitz, in: *Plasma Deposited Thin Films*, J. Mort, F. Jansen (Eds.), CRC Press, Boca Raton, FL, 1986, p. 89 and M. N. Yoder, in: *Synthetic Diamond: Emerging CVD Science and Technology*, K. E. Spear and J. P. Dismukes editors, (Wiley, NY, 1994), p. 4.
2. J. Robertson, Adv. Phys. **35**, 317 (1986).
3. S. Gupta, B. R. Weiner, B. L. Weiss and G. Morell, Appl. Phys. Lett. **79**, 3446 (2001) and references therein.
4. D. R. Mckenzie, D. A. Muller, B. A. Paithorpe, Phy. Rev. Lett. **67**, 773 (1991); J. Hong, A. Goulet, and G. Turban, Thin Solid Films **352**, 41 (1999).
5 . J. Robertson, Philos. Mag. B **76**, 335 (1997) and references therein.
6. D. Gruen, Ann. Rev. Mater. Sci. **29**, 211 (1999).
7. Z. Yin, Z. Akkerman, B. X. Yang and F. W. Smith, Diamond & Related Mat. **6**, 153 (1997).
8. N. Savvides, E-MRS Meeting **17**, 275 (1985); N. Savvides, J. Appl. Phys. **59**, 4133 (1986).
9. R. M. A. Azzam and N. M. Bashara, in *Ellipsometry and Polarized Light* (North-Holland, Amsterdam, 1977).
10. R. Kalish, A. Reznik, C. Uzan-Saguy and C. Cytermann, Appl. Phys. Lett. **76**, 757 (2000)
11. D. S. Dandy, Thin Solid Films **381**, 1 (2001).
12. M. N. Gamo, C. Xiao, Y. Zhang, E. Yasu, Y. Kikucji, I. Sakaguchi, T. Suzuki, Y. Sato and T. Ando, Thin Solid Films **382**, 113 (2001).
13. K. Okano, S. Koizumi, S. R. P. Silva, and G. A. J. Amartunga, Nature, **381**, 140 (1996).
14. J. Robertson, Mater. Res. Soc. Symp. Proc. **509**, 83 (1998); S. Gupta, B. L. Weiss, B. R. Weiner and G. Morell, Mater. Res. Soc. Symp. Proc. **638**, (2001) (in press).
15. A. R. Forouhi and I. Bloomer, Phys. Rev. B **34,** 7018 (1986).
16. D. W. Marquardt, J. Soc. Indis. Appl. Math. **11**, 431 (1963).
17. S. Gupta, B. R. Weiner and G. Morell, Diamond and Related Materials, **10**, 1968 (2001).
18. B. Hong, J. Lee, R. W. Collins, Y. Kuang, W. Drawl, R. Messier, T. T. Tsong and Y. F. Strausser, Diamond and Related Materials, **6**, 55 (1997).
19. R. J. Nemanich, J. T. Glass, G. Luckovsky and R. E. Shroder, J. Vac. Sci. Technol. A **6**, 1783 (1988). R. C. Hyer, M. Green, and S. C. Sharma, Phys. Rev. B **49**, 14573 (1994).
20. A. C. Ferrari and J. Robertson, Phys. Rev. B **61**, 14 095 (2000).
21. S. Bhattacharyya, K. Walzer, H. Hietschold and F. Richter, J. Appl. Phys. **89**, 1619 (2001).
22. R. Haubner, S. Bohr and B. Lux, Diamond and Related Materials **8**, 171 (2000).
23. J. Robertson and E. P. O'Reilly, Phys. Rev. B **35**, 2946 (1987).
24. D. A. G. Bruggeman, *Ann. Phys. Leipzig*, **24**, 636 (1935).

25. W. A. McGahan and J. A. Wollam, Mater. Res. Soc. Symp.Proc. **349**, 453 (1994) and references therein.
26. O. Amir, and R. Kalish, J. Appl. Phys. **70**, 4958 (1991).

Mat. Res. Soc. Symp. Proc. Vol. 703 © 2002 Materials Research Society V11.10

# ANALYSIS OF THE ATOMIC-SCALE DEFECT CHEMISTRY AT INTERFACES IN FLUORITE STRUCTURED OXIDES BY ELECTRON ENERGY LOSS SPECTROSCOPY

Y. Ito, Y Lei[1], N.D. Browning[1] and T.J. Mazanec[2]

Department of Physics, Northern Illinois University, DeKalb, IL 60115
[1]Department of Physics (M/C 273), University of Illinois at Chicago, Chicago, IL 60607
[2]BP Amoco Chemicals, Naperville, IL 60566-7011

## ABSTRACT

$Gd^{3+}$ doped Ce oxides are a major candidate for use as the electrolyte in solid oxide fuel cells operating at ~500 °C. Here, the effect of the atomic structure on the local electronic properties, i.e. oxygen coordination and cation valence, at grain boundaries in the fluorite structured $Gd_{0.2}Ce_{0.8}O_{2-x}$ ceramic electrolyte is investigated by a combination of atomic resolution Z-contrast imaging and electron energy loss spectroscopy (EELS) in the scanning transmission electron microscope (STEM). In particular, EELS analyses from grain boundaries reveals a complex interaction between segregation of the dopant ($Gd^{3+}$), oxygen vacancies and the valence state of Ce. These results are similar to observations from fluorite-structured Yttria-Stabilized Zirconium (YSZ) bicrystal grain boundaries.

## INTRODUCTION

$Gd^{3+}$ doped Ce oxides are highly attractive candidates as electrolytes for solid oxide fuel cells operating at ~500 °C [1,2]. Like YSZ, the high oxygen conductivity has a structural origin, i.e. the fluorite structure has the highest capacity for oxygen vacancies while the cation sublattice holds the cubic structure of the bulk without collapsing [3]. For their successful commercial implementation, a full understanding of the defect chemistry in the bulk and at grain boundaries is essential. In particular, the contribution of the grain boundaries to the total ionic conductivity through such effects as the segregation of dopants, vacancies and impurities is of crucial importance [4].

The route to characterizing oxide materials on this level is afforded by the combination of Z-contrast imaging [4] and EELS [5] in the STEM. These correlated techniques [6] allow direct images of crystal and defect structures to be obtained, the composition to be quantified and the effect of the structures on the local electronic properties (i.e., oxygen coordination and cation valence) to be assessed [7]. Here the effect of the atomic structure on the local electronic properties, i.e. oxygen coordination and cation valence at grain boundaries of the fluorite structured $Gd_{0.2}Ce_{0.8}O_{2-x}$ ceramic membrane material is investigated by a combination of Z-contrast imaging [5] and EELS [6] in the JEOL 2010F STEM [7]. These results are compared with atomic resolution Z-contrast imaging and EELS analyses of a model symmetric [001] tilt grain boundary YSZ [8]. The use of the model system for comparison is required to obtain a detailed understanding of the atomic scale phenomena in ceramics, as the polycrystalline nature of $Gd_{0.2}Ce_{0.8}O_{2-x}$ ceramic membrane material makes it almost impossible to locate the ideal zone-axis orientation required to image the boundary plane.

## SPECIMEN

The composite membrane material consisting of polycrystalline $Gd_{0.2}Ce_{0.8}O_{2-x}$ and Pd metal grains was provided by BP Amoco Chemicals, which was sintered from high purity pre-mixed powders at high temperature with the Gd/Ce ratio of 0.2. (Pd permits the electrons to be transported). The oxygen permeation experiments were performed at 950°C where one face was in contact with air and the other was in contact with $H_2/CO_2$ with $pO_2$ = 1 x 10-15 atm ($H_2/CO_2$ = 85/15). For the present study, grain boundaries directly connected to Pd metal grains were excluded in order to characterize pure ceramic-ceramic grain boundaries (EELS and energy dispersive x-ray spectroscopy analysis confirmed the boundaries analyzed here were free from Pd). The YSZ symmetric 24° [001] tilt bicrystal stabilized in the cubic form with ~10 mol % $Y_2O_3$ doping was purchased from Shinkosha Co., Ltd. Japan. For both materials, TEM samples were prepared by standard procedures, mechanically polished and then thinned by argon ion milling to electron transparency.

## EXPERIMENTAL TECHNIQUES

The experiments were performed on a 200kV Schottky field emission JEOL 2010F STEM/TEM at the University of Illinois at Chicago, equipped with an ultra high-resolution objective lens pole piece, a JEOL annular dark field detector (ADF) for Z-contrast imaging, and a Gatan imaging filter (GIF) for EELS [7]. In this study, a probe size of 0.2 nm with a convergence angle of 13 mrad was used. The inner radius of the ADF detector was 52 mrad. Due to the dominant contribution of Rutherford scattered electrons in this imaging condition, the image contrast is approximately proportional to $Z^2$ where Z is the atomic number. Consequently, more than 95% of the intensity in the Z-contrast images from these ceramic materials is due to electrons scattered by the cations and less than 5% from oxygen.

The low-angle scattered electrons, not intercepted by the ADF detector, were used for simultaneous EELS. EELS enables us to probe atomic scale fluctuations in composition and the effect of the local atomic structure on the electronic properties (i.e. oxygen coordination and cation valence) [9]. Energy shifts and the fine structure of the ionization edges reflect the atomic arrangement and bonding effects in the specimen. Combined with Z-contrast imaging in the STEM, it is possible to obtain spectra with atomic spatial resolution [6]. The Z-contrast image can therefore be used as a map to position the probe at the specified locations in the structure to obtain atomic scale information on the composition and bonding.

Each spectrum was acquired for 4 seconds for YSZ and 3 seconds for $Gd_{0.2}Ce_{0.8}O_{2-x}$, respectively. The probe position was checked after acquisition of each spectrum to make sure that the specimen drift was minimal (< 0.1 nm). A series of spectra were acquired at every position and summed up during post-acquisition data processing. This reduces the effects of drift and allows beam damage to be monitored (no appreciable beam damage was detected.). In all the spectra, plural scattering effects were removed by deconvolution with a low-loss spectrum [5].

## RESULTS

### YSZ grain boundary

A symmetric 24° [001] tilt YSZ grain boundary was investigated as a model fluorite structure grain boundary [8]. Figure 1(a) shows an atomic resolution Z-contrast image of the grain boundary. Bright spots in the image represent the cation sub-lattice (Zr and/or Y columns).

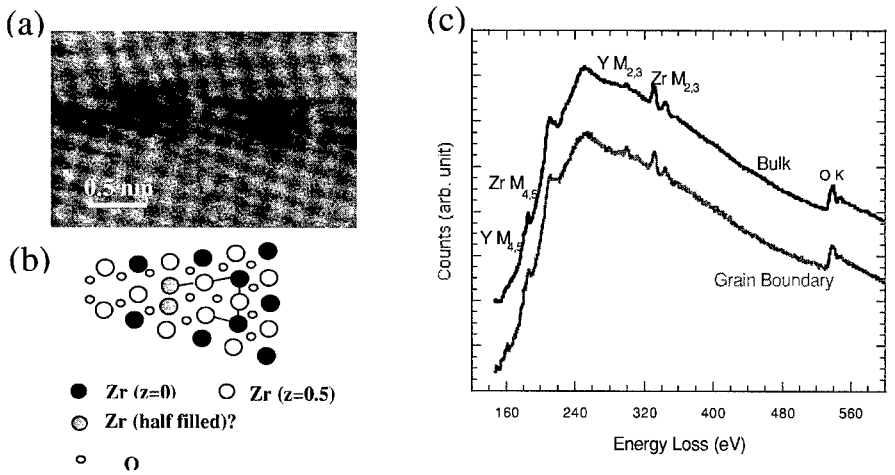


**Figure 1**: (a) Z-contrast image of a symmetric 24° [001] tilt grain boundary in YSZ. (b) a schematic of the grain boundary structure.[10] (c) EEL spectra from the bulk and grain boundary. Background before Y $M_{45}$ is removed. [8]

Based on this Z-contrast image and the bulk crystal structure of YSZ, a possible schematic of the grain boundary atomic structure is shown in figure 1(b). This structure is consistent with previous analysis by Z-contrast imaging, and contains partially occupied columns [10]. Figure 1(c) shows the EEL spectra acquired from the bulk and grain boundary of YSZ. Main differences between the two spectra include (1) a 1.5 eV shift to higher energy of the $Z_{23}$-peak at the grain boundary, and (2) a change of the O K near-edge structure (not shown) (this change in bonding character is a sign of the distortion of cubic symmetry at the grain boundary [11]). In addition, at the grain boundary there is (3) an increase of Zr and Y $M_3/M_2$ ratio, (4) an increase of the Y/Zr ratio, and (5) a decrease of O/Zr and O/Y ratios. (1) and (3) indicate an increase in the number of electrons in the boundary plane. This is consistent with the excess segregation of O vacancies (5) although it is partially compensated by the segregation of Y (4). This may cause the increase of the number of electrons in the conduction band at the boundary.

## $Gd_{0.2}Ce_{0.8}O_{2-x}$ grain boundary

Figure 2 shows typical O K- and Ce $M_{45}$-edges of bulk $Gd_{0.2}Ce_{0.8}O_{2-x}$. The principal features of the near-edge fine structure are clearly resolved. These are very similar to those of $CeO_2$ ($Ce^{4+}$)[12]. The O K-edge of $CeO_2$ is due to transitions from the 1s ground state to the p-like component of hybrid Ce 4f and O 2p energy levels (pre-edge (A)) and to the unoccupied O 2p-like states hybridized with the crystal-field split Ce d-states, i.e. $e_g$ (B) and $t_{2g}$ (C). Notice that the O K-edge of bulk YSZ does not have the pre-edge equivalent to (A). The sharp Ce $M_{45}$ peaks are due to transitions of 3d core electrons ($3d_{5/2}$ for $M_5$ and $3d_{3/2}$ for $M_4$ due to spin orbit coupling) to unoccupied states of f-like symmetry (the much weaker 3d $\rightarrow$ p edge is masked). The satellites (Y, Y') are thought to originate from transitions to 4f states in the conduction band, and these satellites have been used to estimate the degree of delocalization of the f-electrons (strong covalency hybridization between Ce 4f and O 2p).

Figure 3 shows the O K- and Ce $M_{45}$-edges across the grain boundary between Grain A and B. At the grain boundary there is, (1) a decrease of the pre-peak A and $t_{2g}$ peak C, (2) an increase of Ce $M_5/M_4$ ratio and slight broadening of the peaks, (3) a chemical shift of Ce $M_{45}$ to lower energy-loss (1.5 eV), and (4) a decrease of the satellite peaks Y and Y' of Ce $M_{45}$. (1) and (3) may indicate the reduction of O 2p-Ce d and O 2p-Ce 4f hybridization at the grain boundary, respectively. (2), (3) and (4) indicate increase of $Ce^{3+}$ at the grain boundary. This is also consistent with the change of the O 2p hybridization.

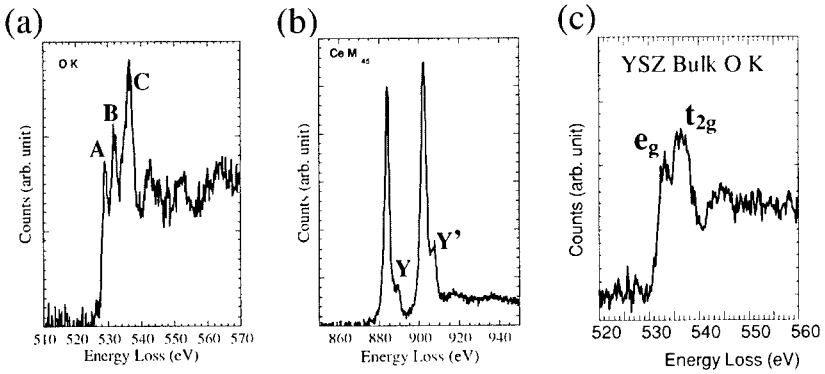


**Figure 2**: EEL spectra of bulk $Gd_{0.2}Ce_{0.8}O_{2-x}$ with high energy resolution. (a) O K-edge (b) Ce $M_{45}$-edges. (c) O K-edge of YSZ bulk for the comparison.

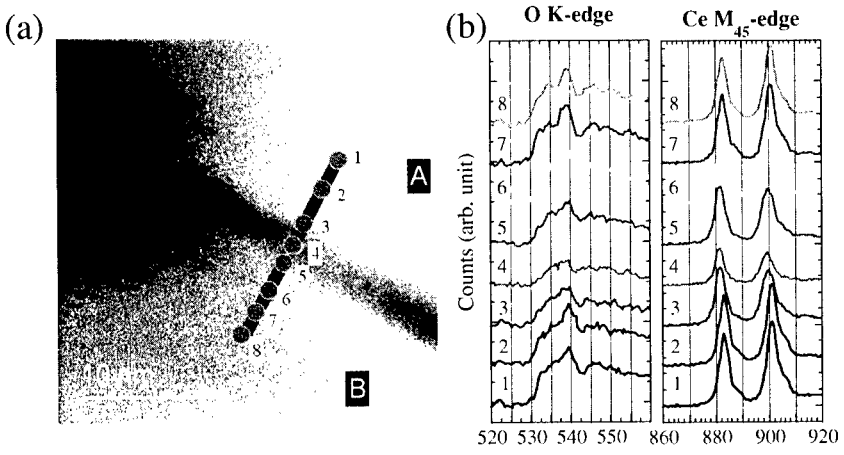


**Figure 3**: (a) Z-contrast image of a $Gd_{0.2}Ce_{0.8}O_{2-x}$ grain boundary (not aligned to a specific orientation but close to [110]). Points where EEL spectra were acquired are indicated. The numbers correspond to spectra in (b). (b) Oxygen K- and Ce $M_{45}$-EEL spectra across the grain boundary. Both O K- and Ce $M_{45}$-edges were acquired simultaneously.

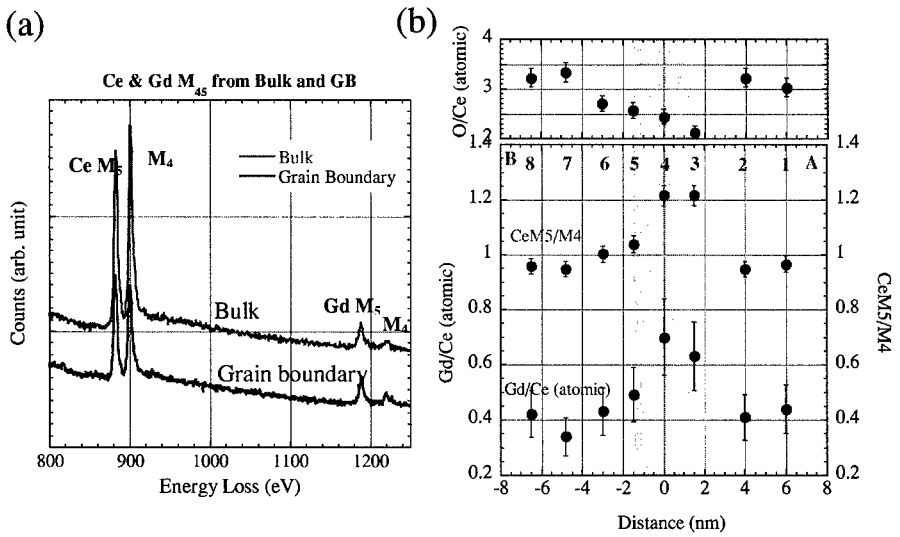


**Figure 4**: (a) Ce and Gd $M_{45}$-EEL spectra from the bulk and the grain boundary of a $Gd_{0.2}Ce_{0.8}O_{2-x}$. Both are on the same scale but shifted for the clarity. Same acquisition condition (b) The Ce $M_5/M_4$ ratio, Gd/Ce and O/Ce atomic ratios profiles across the grain boundary [8]. Numbers correspond to those in Figure 3.

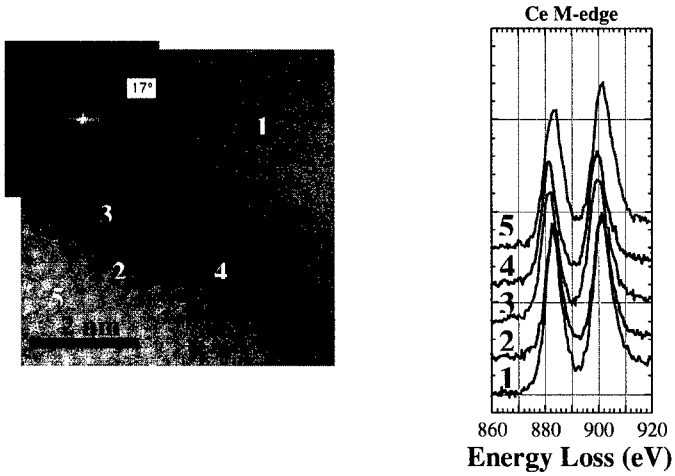


**Figure 5**: (a) Atomic resolution Z-contrast image of a $Gd_{0.2}Ce_{0.8}O_{2-x}$ grain boundary between grain A and B. (B is aligned to [110]). Points where EEL spectra were acquired are indicated. The numbers correspond to spectra in (b). The inset is a FFT of the image, indicating 17° tilt. (b) Ce $M_{45}$-EEL spectra around the grain boundary.

Figure 4 shows the segregation of the Gd and O vacancies at the grain boundaries and their close correlation with the change of the Ce $M_5/M_4$ ratio (valence state). The levels of Gd segregation and oxygen vacancies are similar to those in YSZ, and the effect on the Ce $M_{4,5}$-edge is analogous to that on the Zr $M_{2,3}$-edge. The composition at the grain boundary is calculated to be $Gd_{0.41\pm0.04}Ce_{0.59\pm0.04}O_{1.24\pm0.17}$. According to the reference of the $M_5/M_4$ values [13], the fraction of $Ce^{3+}$ at the grain boundary is estimated to be 70% by assuming a linear interpolation. Therefore, for this grain boundary, the excess of electrons near the grain boundary in this sample was derived to be $0.7 \pm 0.35$ per formula unit.

The above results are also supported by the preliminary atomic resolution EELS analysis of the same boundary (Figure 5).

## CONCLUSIONS

The interplay between oxygen vacancies, dopant distribution and valence state of Ce (Zr) at grain boundaries of the fluorite structured YSZ and $Gd_{0.2}Ce_{0.8}O_{2-x}$ ceramic electrolyte has been studied by a combination of atomic resolution Z-contrast imaging and EELS in a STEM. The majority of the grain boundaries exhibit segregation of Gd and oxygen vacancies. The Ce $M_{45}$-edge analyses indicate a decrease of the valence state. Observation of the O K-edge near-edge fine structure also indicates changes in local atomic environment between the bulk and the boundary, consistent with the change of the valence state of Ce. The results from the $Gd_{0.2}Ce_{0.8}O_{2-x}$ are consistent with those from YSZ grain boundary, implying that the present observation may be common features at the grain boundaries in many fluorite structure materials.

## ACKNOWLEDGMENTS

The authors would like to acknowledge support from BP chemicals for this work. This work was sponsored by the Department of Energy under contract number DE-FG02-96ER40512. The JEOL 2010F used to obtain the experimental results was purchased with support from the National Science Foundation under grant number NSF-DMR-9601792, and is operated by the Research Resources Center at the University of Illinois at Chicago.

## REFERENCES

[1] B. C. H. Steele, *J. Power Sources* **49,** 1 (1994).
[2] B. C. H. Steele, *Solid State Ionics* **129,** 95 (2000).
[3] Z. L. Wang and Z. C. Kang, *Functional and Smart Materials* (Plenum, 1998)
[4] S. J. Pennycook and D. E. Jesson, *Phys. Rev. Lett.* **64,** 938 (1990).
[5] R. F. Egerton, *Electron Energy Loss Spectroscopy in the Electron Microscope* (Plenum, 1996).
[6] N. D. Browning, M. F. Chisholm and S. J. Pennycook, *Nature* **366**, 143 (1993).
[7] E. M. James and N. D. Browning, *Ultramicroscopy* **78,** 125 (1999).
[8] Y. Lei, Y. Ito, N. D. Browning, T. J. Mazanec, *J. Am. Cer. Soc.* (2001) submitted.
[9] R. F. Klie and N. D. Browning, *Appl. Phys. Lett.* **77,** 3737 (2000).
[10] E. C. Dickey and X. Fan, *J. Am. Cer. Soc.* **84,** 1361 (2001).
[11] J. Yuan, T. Hirayama, Y. Ikuhara, and T. Sakuma, *Micron*, **30,** 141 (1999).
[12] L. A. J. Garvie and P. R. Buseck, *J. Phys. Chem. Solids.* **60,** 1943 (2000).
[13] J. A. Fortner and E. C. Buck, *Appl. Phys. Lett.*, **68,** 3817 (1996).

# Nanostructures II

Mat. Res. Soc. Symp. Proc. Vol. 703 © 2002 Materials Research Society V12.5

# $H_3PO_4$ / oxide nanoparticles / polymer composites as proton conducting membranes

D. Carrière, P. Barboux, M. Moreau and J.-P. Boilot.
Laboratoire de Physique de la Matière Condensée, CNRS UMR 7643C, Ecole Polytechnique, 91128 Palaiseau Cedex

## ABSTRACT

Stable sols of 60 nm colloidal zirconia have been prepared by thermolysis of zirconium acetate. The surface complexing acetate groups have been replaced by phosphoric acid groups. Phosphate grafting has been characterized by dynamic light scattering, infrared spectroscopy, $^{31}P$ nuclear magnetic resonance and impedance spectroscopy measurements. These systems give acid and proton conductive particles ($4.10^{-5}$ S.cm$^{-1}$ at 70 % relative humidity).

$H_3PO_4/ZrO_2$/PVDF-*co*-HFP composite membranes have been synthesized. Impedance spectroscopy measurements allow discrimination between proton conduction at the surface of the phosphated particles and within free $H_3PO_4$ in the polymer. For the highest $H_3PO_4/ZrO_2$ ratios, the latter phenomenon prevails, giving a proton conductivity of $6.10^{-4}$ S.cm$^{-1}$ at 70 % R.H.

## INTRODUCTION

Proton-conductive membranes may find various applications in electrochromic devices, capacitors and fuel cells. This last application requires high proton conductivity, high chemical durability and a good stability against temperature and moisture modifications. Nafion®, a purely organic acid fluoropolymer used in such devices presents a swelling effect at high humidity and temperature but also a loss of proton conductivity at low water content [1]. Dispersions of $H_3PO_4$, $H_2SO_4$ or other acids in various polymers [2] may overcome this problem. However, stability of these systems towards hydrolysis can be poor. This leads to a loss of proton carriers during fuel cell running.

An interesting alternative is dispersion of high specific surface acid oxides. Indeed, they show both good proton mobility and their acid character is stable towards hydrolysis [3]. We here present a study relative to phosphate grafting onto polycrystalline nanometric sols of $ZrO_2$, and their use in $H_3PO_4/ZrO_2$/PVDF-*co*-HFP composite membranes.

## EXPERIMENTAL

The zirconium acetate solution (Zr ~ 15-16% wt) and triethyl phosphate were purchased from Aldrich Chemicals. Acetic acid was purchased from SDS. PVDF-*co*-HFP ($M_w$ = 145000, HFP: 11% wt) has been friendly given by Atochem.

Dynamic light scattering (DLS) measurements were obtained on a Malvern 4700 photocorrelator. $^{31}P$ nuclear magnetic resonance was performed in a high-resolution liquid Bruker probe with a MSL 360 spectrometer. Impedance spectroscopy was performed with a HP4192A impedance analyzer. Silver electrodes were cast on the samples. Samples were equilibrated at 70 % relative humidity with a dilute sulfuric acid solution. X-ray powder diffraction was run with a Philips X Pert diffractometer at the CuKα wavelength. Infrared spectra were made with a Perkin Elmer 783 spectrometer on samples diluted in KBr powder.

## Zirconia sol in water

Stable aqueous sols of crystalline zirconia were prepared as described by Matchett and al. [4] as follows: 20 ml of zirconium acetate were added to a mixture of 25 ml of glacial acetic acid and 19 ml of water. The clear solution was heated at 170°C for 3 hours in a pressure vessel. The residual zirconium acetate was eliminated by successive centrifugations and redispersions until the supernatant did not precipitate upon addition of $H_3PO_4$. The solid could be then dispersed again in 30 ml of water, giving a stable sol ($ZrO_2$ content: 55 g/l i.e. 0.45 mol/l).

## $H_3PO_4$ grafted zirconia

To 30 ml of a $ZrO_2$ sol in water were added variable amounts of a 0.6 M aqueous solution of $H_3PO_4$. The mixture was stirred for 4 hours at room temperature. The solution was used as such for DLS and NMR measurements. For infrared spectra and impedance measurements, excess $H_3PO_4$ was eliminated by successive centrifugations and redispersions in water until the supernatant did not precipitate upon addition of zirconium acetate.

## $H_3PO_4$/grafted zirconia/PVDF-*co*-HFP membranes

30 ml of triethylphosphate (TEP) were added to 30 ml of zirconia sol. Water and residual acetic acid were then evaporated under vacuum at 50°C, and the solution was completed to 35 ml with triethylphosphate and 1 ml of acetic acid, giving a stable sol in TEP.

Variable amounts of the solution were added to a PVDF-*co*-HFP solution (50 g/l in TEP). The mixture was stirred for 30 min and sonified during 1 h before addition of variable amounts of $H_3PO_4$ crystals dissolved in triethylphosphate. The solution was cast in PTFE Petri dishes and dried at 100°C during 24 h, giving 50 µm to 100 µm thick membranes.

# RESULTS AND DISCUSSION

## Zirconia sol characterization

X-Ray diffraction shows the sol to be monoclinic zirconia (figure 2). The crystalline domains determined from the width of the diffraction lines are around 5 nm. DLS measurements and TEM show the $ZrO_2$ particle hydrodynamic radius to be tightly distributed around 60 nm in the initial sol (table 1 and figure 1). Thus, the colloids observed in the solution are not primary particles, but aggregates of smaller domains. This has been also confirmed by transmission electron microscopy and X-Ray small angle scattering.

The perfect stability of the sol at pH < 5 is a first evidence for an electrostatic stabilization. The low particle size results from a strong complexation of zirconium by acetic acid that limits particle growth during synthesis.

| Synthesis step | <Z> (nm) | Polydispersity |
|---|---|---|
| $ZrO_2$ sol in water after purification | 62 | 0.04 |
| $ZrO_2$ sol in TEP/acetic acid | 64 | 0.06 |
| $H_3PO_4$ grafted $ZrO_2$ (P/Zr = 1) | 79 | 0.11 |

**Table 1.** Dynamic light scattering measurements on zirconia sols in various conditions

Infrared spectra of the dried $ZrO_2$ sol (figure 1a) exhibit characteristic absorptions of surface acetate species at 1550 $cm^{-1}$ (C—O antisymmetric stretch), 1450 $cm^{-1}$ ($CH_3$ deformation) and 1420 $cm^{-1}$ (C—O symmetric stretch). The 130 $cm^{-1}$ difference between symmetric and antisymmetric C—O stretching frequencies indicates that acetates are here bidentate bridging species [5].

## Phosphate grafting

$H_3PO_4$ addition to the $ZrO_2$ sol causes an electrostatic destabilization; as a result, the hydrodynamic particle radius increases (table 1) and the solution precipitates within a few hours. Total elimination of the remaining free $H_3PO_4$ in the solution was checked by chemical analysis before recording infrared spectra. The acetate signature has nearly disappeared, while a strong absorption appears at 1050 $cm^{-1}$ that is characteristic of $PO_4^{3-}$ vibrations (figure 1b). The acetate species have been replaced by phosphates on the particle surface. The intensity of this absorption does not decrease after further rinsing in water, showing that phosphate bonding resists to hydrolysis.

The characteristic broad absorptions of the zirconium oxide network between 700 $cm^{-1}$ and 400 $cm^{-1}$ are still present after grafting. Furthermore, X-ray diffraction pattern are identical before and after grafting (figure 2). Therefore, we conclude that phosphates did not decompose the oxide particles during treatment to form bulk phosphates.

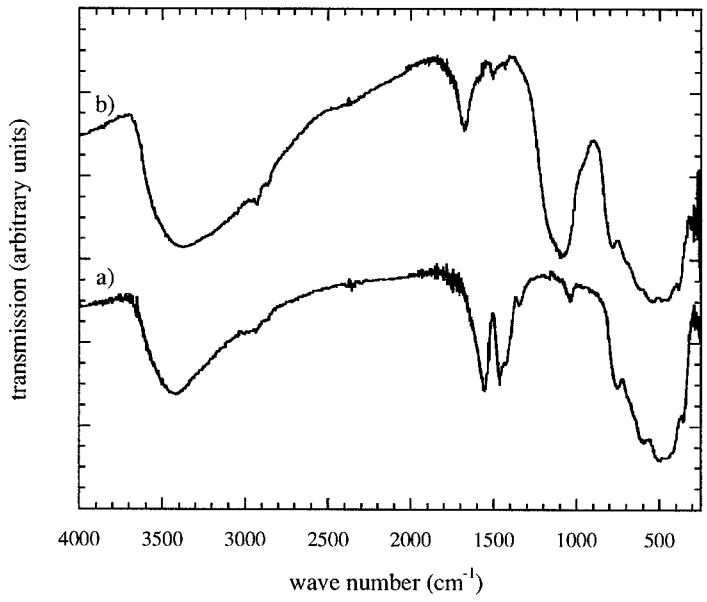


**Figure 1.** Infrared spectra of a) $ZrO_2$ sol b) $H_3PO_4$ grafted $ZrO_2$ sol.

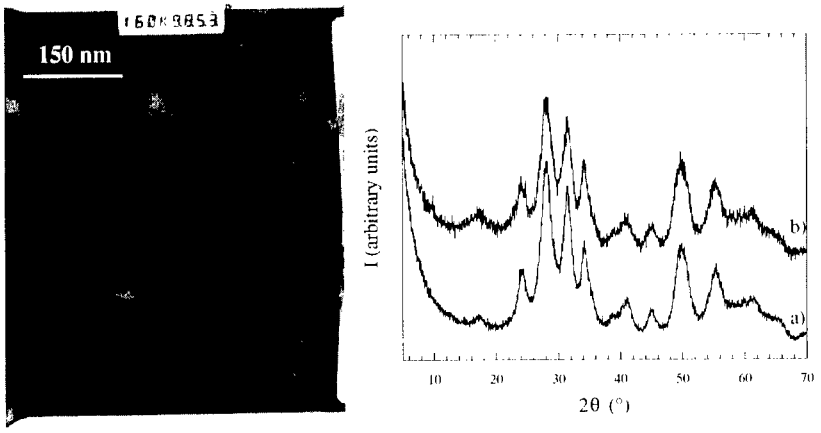


**Figure 2.** TEM of $ZrO_2$ particles and X-Ray powder diffraction of a) $ZrO_2$ particles b) $H_3PO_4$ grafted $ZrO_2$ particles

High resolution liquid state NMR $^{31}P$ spectra were performed on $H_3PO_4/ZrO_2$ mixtures with various P/Zr ratios (figure 3). For P/Zr ≤ 0.16, only a broad solid-like peak is observed, indicating that all the phosphates are bound to the zirconia particles. At a P/Zr = 0.31 ratio, free $H_3PO_4$ appears as shown by a sharp peak at 0.6 ppm.

Proton conductivity as measured by impedance spectroscopy on pressed powders of dried $ZrO_2$ sols is $10^{-8}$ $S.cm^{-1}$. After phosphate grafting, it reaches $4.10^{-5}$ $S.cm^{-1}$. This is a direct consequence of the increase in surface proton density and acidity.

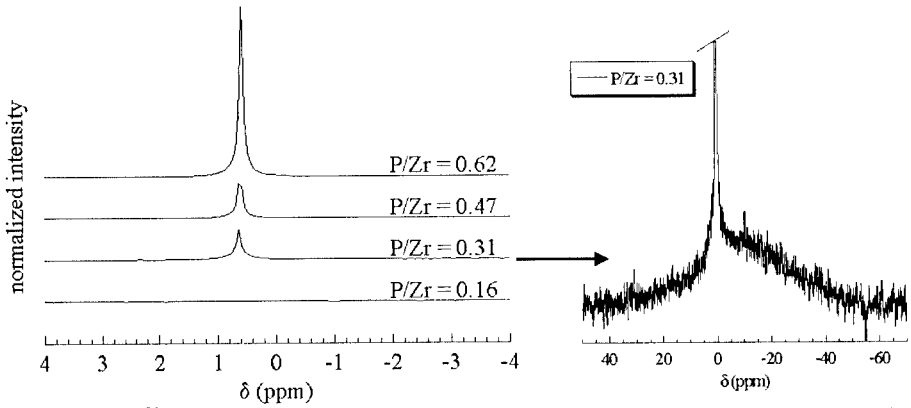


**Figure 3.** NMR $^{31}P$ spectra of $H_3PO_4/ZrO_2$ sol mixtures with variable P/Zr amounts. Chemical shifts reference: 85 % aqueous $H_3PO_4$.

## $H_3PO_4/ZrO_2$/PVDF-*co*-HFP composite membranes

The proton conductivities of $H_3PO_4/ZrO_2$/PVDF-*co*-HFP membranes have been measured by impedance spectroscopy at a 70 % relative humidity. Various $H_3PO_4/ZrO_2$ ratios were investigated. The $ZrO_2$/PVDF-*co*-HFP weight ratio was maintained to unity (figure 4). We distinguish three different domains.

$H_3PO_4/ZrO_2$ molar ratios lower than 0.26: Impedance plots show only a slightly depressed semicircle. It is interpreted as proton conductivity at the surface of grafted zirconia. This conductivity increases with the $H_3PO_4/ZrO_2$ ratio. A higher surface coverage by acid phosphate groups offers a better proton diffusion pathway on the particle.

$H_3PO_4/ZrO_2$ ratios between 0.26 and 1.1: In addition to the low-frequency impedance of the blocking electrode, the impedance plots show two depressed semicircles with different resonance frequencies (figure 5a). This is characteristic of two impedances branched in series. The high-frequency conductivity continuously increases with the P/Zr ratio, while the low-frequency conductivity is merely constant at $3.10^{-7}$ $S.cm^{-1}$.

One of the semicircle is therefore attributed to proton conduction in free $H_3PO_4$ between the zirconia grains, the other one is due to conductivity on the phosphated particles. Indeed, according to the NMR results, liquid $H_3PO_4$ is present in these systems. To verify this hypothesis, some membranes have been thoroughly washed with water to remove the free $H_3PO_4$. The low frequency impedance drastically increases and a unique semicircle is observed again (figure 5b). Therefore, impedance spectra can be understood as surface conducting grains connected through free $H_3PO_4$ in the intergranular region.

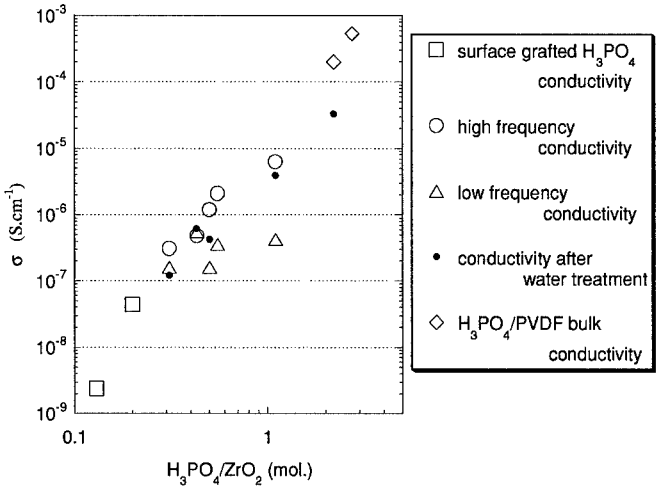


**Figure 4.** Protonic conductivities of $H_3PO_4/ZrO_2$/PVDF-co-HFP membranes as a function of $H_3PO_4/ZrO_2$ ratio at 70% relative humidity before and after water rinsing. $ZrO_2$/PVDF-co-HFP = 1 (wt).

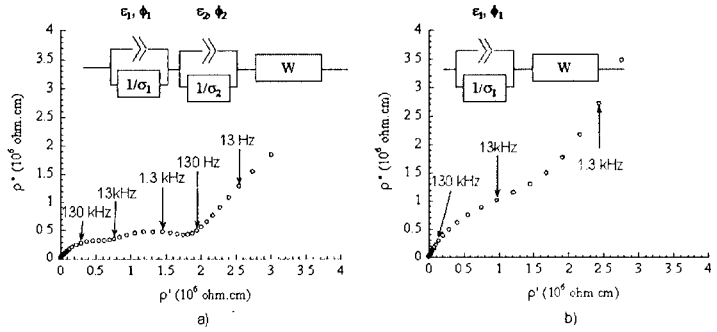


**Figure 5.** Cole-Cole diagrams and fitting circuits for $H_3PO_4/ZrO_2$/PVDF-co-HFP membranes ($ZrO_2$/PVDF = 1 (wt); $H_3PO_4/ZrO_2$ = 0.55 (mol)) **a)** before rinsing **b)** after rinsing. Frequencies are indicated. W = electrode impedance.

$H_3PO_4/ZrO_2$ ratios above 1.1: Impedance plots show a unique semicircle again. Conduction relative to free $H_3PO_4$ becomes predominant and short-circuits migration on grafted zirconia. The higher values of membrane protonic conductivity ($6.10^{-4}$ $S.cm^{-1}$) are thus attributed the bulk diffusion of protons through free phosphate species in the PVDF matrix.

## CONCLUSION

The acid functionalization of nanocrystalline $ZrO_2$ sols by $H_3PO_4$ gives proton conductive particles ($4.10^{-5}$ $S.cm^{-1}$). Infrared study shows that complexing acetate surface groups are replaced by phosphate groups stable towards hydrolysis.

In the $H_3PO_4/ZrO_2$/PVDF-*co*-HFP composite membranes, proton conduction at the surface of phosphated particles or in the $H_3PO_4$/PVDF matrix can be distinguished by impedance spectroscopy measurements. For higher $H_3PO_4/ZrO_2$ ratios, the latter phenomenon becomes predominant and short-circuits the others, giving membrane conductivities as high as $6.10^{-4}$ $S.cm^{-1}$ at room temperature and 70 % relative humidity.

## ACKNOWLEDGMENTS

The authors would like to thank Frédéric Chaput from the Laboratoire de Physique de la Matière Condensée for the transmission electronic microscopy images.

## REFERENCES

1. K.D. Kreuer, Solid State Ionics 97 (1997) 1.
2. J.C. Lassègues, in *Proton conductors: Solids, Membranes and Gels*, Ph Colomban Ed., Cambridge University Press, (1992) 311.
3. W.A. England, J.B. Goodenough, J.B. Wiseman, J. Solid State Chem. 49 (1983) 289.
4. S. A. Matchett, U.S. Patent 5,037,579.
5. N. Alcock, V. Tracy, T. Waddington, J. Chem. Soc. Dalton (1976) 2243-2246.

# Nanophase and Nanocomposite Materials IV

Mat. Res. Soc. Symp. Proc. Vol. 703 © 2002 Materials Research Society V13.4

# Soft reverse current-voltage characteristics in $V_2O_5$ nanofiber junctions

Gyu-Tae Kim, Jörg Muster, Marko Burghard, and Siegmar Roth
Max-Planck Institut für Festkörperforschung, Heisenbergstr. 1, D-70569, Stuttgart, Germany

## ABSTRACT

$V_2O_5$ nanofibers showed the rectifying current-voltage characteristics under an asymmetric contact configuration at room temperature, indicating the formation of a Schottky diode. The ideality factors as a Schottky diode were estimated to be 6.1 at the forward bias and 1.4 at the reverse bias. The larger current at the reverse bias defined by the negative voltage at the metal electrode may originate from the contribution of the tunneling via field emission or thermionic field emission. The ultimate geometric size of nanofibers enhances the influence of the tunneling mechanism and modifies the nano-scale Schottky diode, requiring more understanding in designing the nano-scale electronic devices with the metal contacts.

## INTRODUCTION

Synthetic nanofibers such as carbon nanotubes are invoking the scientific interest nowadays [1-3]. With the development of the synthesis techniques for the synthetic nanofibers, the molecular electronics based on synthetic nanofibers become more plausible by making the nano-scale electronic devices [2-7]. To achieve the realistic electronic chips, all practical issues such as electrical connection, the assembling technique and the integration processes should be considered for the new functional nano-scale devices [4,7]. Till now the electrical properties of nanofibers were investigated from the point of a field effect transistor, a rectifying diode and optoelectronic devices [3-7]. As the carbon nanotube is under the highlight because of its noble structure and outstanding electrical properties, other synthetic nanofibers are also attracting from the basic research and the application [2,3,6,7]. $V_2O_5$ nanofiber was found a century ago, and identified to have the ultimate geometric dimension with a good uniformity in the fibrous structure [8]. Recently a field effect transistor made of $V_2O_5$ nanofibers was demonstrated with a small electrical mobility of $10^{-2}$ $cm^2/V$ s owing to the hopping conduction [6]. Most of the electrical contacts defined on the $V_2O_5$ nanofibers showed the ohmic behaviors, indicating the symmetric contact in the two-probe configuration [9]. In the present study, a significant asymmetric current-voltage characteristics in a $V_2O_5$ nanofiber junction is shown and discussed by considering the influence of the tunneling mechanism through the nanofiber Schottky barrier.

## EXPERIMENT

$V_2O_5$ sols were prepared from 0.2 g ammonium(meta)vanadate ($NH_4VO_3$) and 2 g acid ion exchange resin (DOWEX 10×80) in 40 ml water. With aging for a few days, the average length of floating individual $V_2O_5$ nanofibers in the orange color solution increases up to a few μm. For the better deposition of individual $V_2O_5$ nanofibers on bare substrates, a Si substrate silanized by 3-amminopropyltriethoxysilane (3-APS) solution was dipped into a mixture of $V_2O_5$ sol/water (1:10) for 2 ~ 3 sec. Afterwards, the substrate was rinsed with water, and blown dry. Au/Pd (40%/60%) lines with a separation of 100 nm were defined on the substrate by e-beam

lithography using a two-layer resist and a modified Hitachi S2300 scanning electron microscope. Current-voltage characteristics were recorded under the low pressure of Helium atmosphere with a Keithley 617 electrometer and a Keithley 230 voltage source.

## RESULTS & DISCUSSION

Figure 1 (a) shows a scanning force microscope (SFM) image of the $V_2O_5$ nanofibers under the Au/Pd electrodes patterned by e-beam lithography. The number of the individual $V_2O_5$ nanofibers under the electrodes is 8. The $V_2O_5$ nanofibers are long enough to reach among the four successive electrodes. In Figure 1 (b), the current-voltage characteristics among the different electrode pairs are recorded at room temperature. All the two-probe pairs without the electrode 1 showed ohmic behaviors in the range of the resistance about 50 MΩ. All the pairs with the electrode 1 showed the gap feature indicating the existence of the asymmetric contact barriers at the contact 1. By the charge transfer between metal electrode and n-type $V_2O_5$ nanofibers, a Schottky barrier could be formed at the contact 1 as a depletion layer [6,10-12]. The turn-on voltages at the negative bias on the electrode 1 are lower than those at the positive bias, indicating the p-type carrier in the $V_2O_5$ nanofiber. Considering the n-type carrier in $V_2O_5$ nanofibers [6,10,11], the polarity of the forward bias contradicts, so-called soft-reverse characteristics [12,13,16,17].

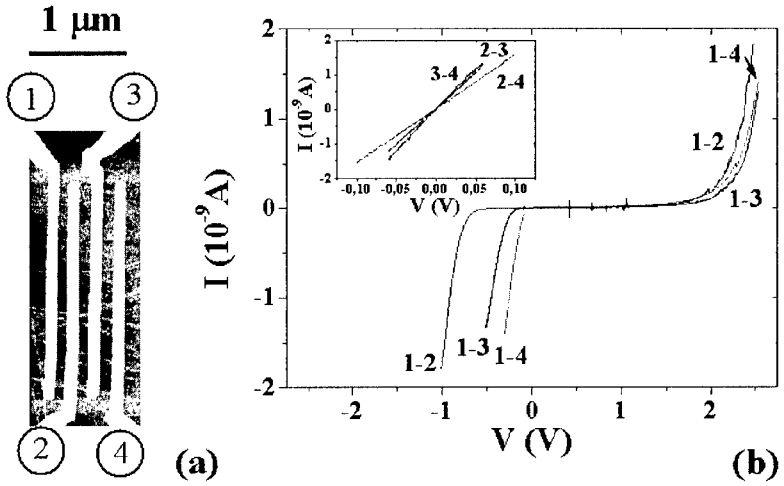


**Figure 1.** (a) Scanning force microscope image of $V_2O_5$ nanofibers below the Au/Pd electrodes with the neighboring distance, 100 nm. (b) Current-Voltage characteristics of each electrode pair at room temperature. „n-m" convention denotes the positive polarity at the electrode „n" and the negative polarity at the electrode „m". All electrode pairs including the electrode 1 show the rectifying behaviors with the asymmetric tendencies. The inset indicates the ohmic properties of the electrode pairs without the electrode 1.

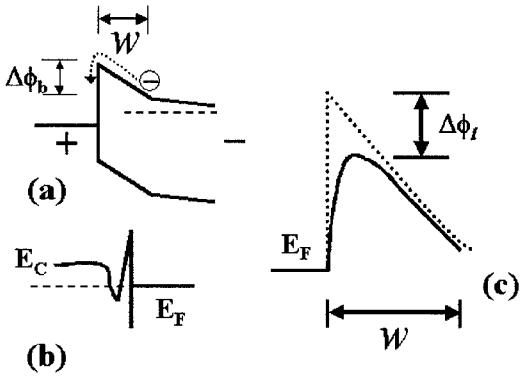


**Figure 2.** (a) Band configuration for the forward bias in a metal-n type semiconductor junction. $\Delta\phi_b$ indicates the barrier height at the normal forward bias configuration. (b) Local doping can induce a shallow tunneling barriers, resulting in an ohmic behavior. (d) Barrier lowering factors ($\Delta\phi_l$) can increase the current at the reverse bias.

By the the chemical potential alignment between the metal electrode and an n-type semiconductor as shown in Figure 2 (a), the forward bias can be defined as the positive voltage at the metal electrode [12,13]. With the negative bias at the semiconducting $V_2O_5$ nanofiber, the energy barrier ($\Delta\phi_b$) decreases because the energy of the conduction band rises. But this insight fails to explain the larger current at the negative polarity shown in Figure 1 (b). Interestingly, in the case of a carbon nanotube Schottky diode, a similar reversal behavior can be found in literature [14]. The contact barrier at the electrode 1 may lie along the surface of the $V_2O_5$ nanofibers below the electrode in a vertical configuration. The tiny pin-hole or the local doping can increase the leakage current in a $V_2O_5$ nanofiber junction as in Figure 2 (b) by the increased tunneling current, giving an ohmic behavior. The finite thickness of the $V_2O_5$ nanofiber can limit the widening or shrinking of the junction width which is different from the bulk case. According to the recent theoretical studies on the nanofiber Schottky junctions, the heavy doping can decrease the barrier width in a very narrow layer [15]. The fact that the most contacts showed the ohmic behaviors at room temperature possibly indicates the existence of a heavily doped layer as a short tunneling path. As the temperature decreases, the ohmic behavior changed to the slight non-ohmic curves but still with a symmetric tendency, indicating the existence of the symmetric thin contact barriers at the electrodes. At room temperature the ohmic transport through most of the electrodes can make it possible to assume negligible contact barriers at the electrodes except the electrode 1, which also enables the determination of the right polarity of the forward bias at the asymmetric contact barrier, the electrode 1. In the reverse bias, the equivalent circuit can be modeled by the combination of resistors and diode components as in the inset of Figure 3. Following a detailed circuit analysis, the bulk resistances in the equivalent circuit could be estimated as following ; $R_2$= 64.2 MΩ, $R_3$= 53.0 MΩ, $R_{23}$= 140.5 MΩ. According to the conventional Schottky diode, the current can be analyzed by the relation of the current, $i = i_0[\exp(qV/\eta k_B T) - 1]$, where η is ideality factor in Schottky barrier [12,13].

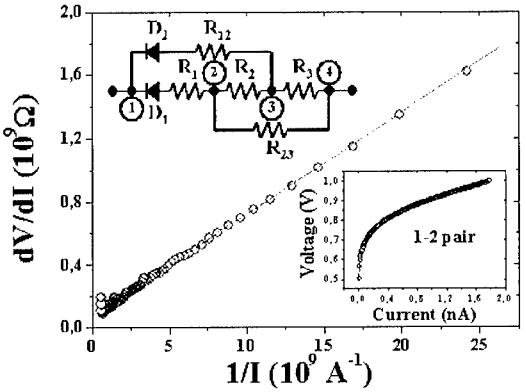


**Figure 3.** The equivalent circuit of the $V_2O_5$ nanofibers corresponding to Figure 1. At the electrode 1, the two diode components are assumed in the reverse bias configuration. The dashed lines indicate the best fitting following equation (1) and (2).

$$V = iR + \frac{\eta k_B T}{q} \ln(\frac{I}{I_0}) \qquad (1)$$

$$\frac{dV}{dI} = R + \frac{\eta k_B T}{qI} \qquad (2)$$

From the relation of the equation (1) and (2) , the linear relationship between dV/dI and 1/I can be deduced and Figure 3 shows a good agreement. By the same procedures with the different electrode pairs, $R_1$ and $R_{12}$ could be determined as $R_1$= 70.9 MΩ and $R_{12}$= 132.1 MΩ. Two diode components were resolved as $I_{D1}=2.31\times10^{-15}\exp(V/0.06435)$ and $I_{D2}=1.71\times10^{-13}$ $\exp(V/0.03636)$ with the ideality factors $\eta_1$=2.55 and $\eta_2$=1.44 in the reverse configuration. The prefactor of the current is given by the relation of $I_0=A^{**}ST^2\exp(-q\,\Delta\phi_b/k_BT)$ where $A^{**}$ is the effective Richardson constant and S the area of the junction [12,13]. The barrier heights $\Delta\phi_b$ were calculated to be 0.57 eV for $D_1$ and 0.46 eV for $D_2$ with an assumption of the junction area as 8×1.5 nm×100 nm. If the junction area is assumed as the cross-section of the $V_2O_5$ nanofibers, 8×1.5 nm×10 nm, the barrier heights are calculated to be 0.51 eV for $D_1$ and 0.40 eV for $D_2$. So the barrier height can be guessed between 0.4 eV and 0.6 eV, which is quite in the range of the energy gap of $V_2O_5$ nanofibers, $E_g$ = 2.2 eV [8-11]. Following the similar analysis, the ideality factors of $D_1$ and $D_2$ were estimated to be about 6.1 at forward bias which is quite larger than those at the reverse bias.

To explain the contradiction in the polarity of the apparent forward bias and the big differences in the ideality factors at the different bias, the tunneling contribution was considered as an origin of the soft-reverse characteristics. Assuming the high carrier concentration near the electrode contacts, the crowded electric field can enhance the tunneling probability of the carrier via the field emission or thermionic field emission [13,16,17]. These effects can be accentuated if the surface of $V_2O_5$ nanofiber is accumulated with the positive surface charges making the barrier at the edge even thinner. In the case of a gallium arsenide diode with a donor concentration of $2\times10^{18}$ $cm^{-3}$, the current at the reverse bias was known to exceed the current at the forward bias by field emission [17].

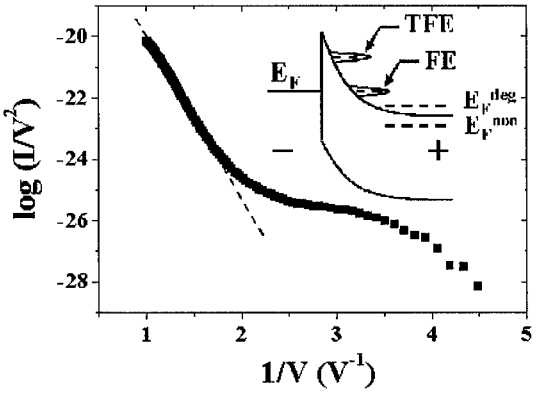


**Figure 4**. Fowler Nordheim tunneling model plot. The inset figure indicates the possible occurence of the thermoionic field emission or the field emission in the Schottky barrier.

Figure 4 shows the Fowler-Nordheim tunneling plot, which fits rather well at high electric field [12]. From the calculation of the thermoionic field emission through a Schottky barrier, the current-voltage characteristics can be characterized as the equation (3), (4) and (5) [13].

$$J = J_S \exp(V_s / E_0) \tag{3}$$

$$E_0 = E_{00} \coth(\frac{qE_{00}}{k_B T}) \tag{4}$$

$$E_{00} = \frac{\hbar}{2}[\frac{N_d}{m^* \varepsilon_s}]^{1/2} \tag{5}$$

Considering $N_d=\sigma/e\mu$ with $\sigma$=0.5 (S/cm) and $\mu=10^{-2}$ $cm^2/V$ s at room temperature [9], $N_d$ can be estimated to be $3.1\times10^{20}$ ($cm^{-3}$), which might be overestimated. $E_{00}$ was estimated to be 0.143 eV and the ideality factor was estimated to be 5.7 from the value of $E_0$, which is quite similar with our experimental ideality factor at the forward bias. Similarly, for the reverse direction in the tunneling regime, the current is given as following equation (6) and (7) [13]:

$$J = J_S \exp(V_r / E') \tag{6}$$

$$E' = E_{00}[\frac{qE_{00}}{k_B T} - \tanh(\frac{qE_{00}}{k_B T})]^{-1} \tag{7}.$$

So the ideality factor at the reverse bias can be estimated to be 1.21 from the value of $E'$, which is also quite similar with the value obtained in the measurement. So the consideration of the tunneling at the electrode 1 seems to be reasonable considering the ultra sharp shape of the metal electrode at the edge and the $V_2O_5$ thin nanofibers.

Large ideality factor was also reported in a carbon nanotube Schottky junction with a similar ideality factor, 5.8 [18]. Considering the restricted dimension, the junction property can be influenced much more than the bulk case by the enhanced electric field around the contact and

one dimensionality with the reduced screening [12]. More understanding on the physical properties of the electric contacts are still required.

## SUMMARY

We observed the rectifying current-voltage characteristics in a metal-$V_2O_5$ nanofiber junction and the larger current at the reverse bias. The ideality factors at forward bias and reverse bias were explained by introducing the tunneling, which can give the soft reverse-current voltage characteristics.

## ACKNOWLEDGMENTS

The authors are grateful to F. Schartner and U. Waizmann for technical support. G.T.K. would like to thank the support of Alexander von Humboldt Foundation. M. B. is grateful to the Deutsche Forschungsgemeinschaft (DFG) for financial support.

## REFERENCES

1. R. Saito, G. Dresselhaus, and M. S. Dresselhaus, *Physical Properties of Carbon Nanotubes*, (Imperial College Press, London, 1998).
2. J.-C. P. Gabriel, and P. Davidson, Adv. Mater. **12**, 9 (2000).
3. X. F. Duan, and C. M. Lieber, Adv. Mater. **12**, 298 (2000).
4. W. B. Choi, J. U. Chu, K. S. Jeong, E. J. Bae, J.-W. Lee, J.-J. Kim, and J.-O. Lee, Appl. Phys. Lett. **22**, 3696 (2001).
5. S. J. Tans, A. R. M. Verschueren, and C. Dekker, Nature, **393**, 49 (1998).
6. G. T. Kim, J. Muster, V. Krstic, J. G. Park, Y. W. Park, S. Roth and M. Burghard, Appl. Phys. Lett. **76**, (2000)
7. X. Duan, Y. Huang, Y. Cui, J. Wang, and C. M. Lieber, Nature, **409**, 66 (2001).
8. T. Yao, Y. Oka, and N. Yamamoto, Mat. Res. Bull. **27**, 669 (1992).
9. J. Muster, G. T. Kim, V. Krstic, J. G. Park, Y. W. Park, S. Roth and M. Burghard, Adv. Mater. **12**, 420 (2000).
10. J. Livage, Chem. Mater. **3**, 526 (1991).
11. J. Bullot, O. Gallais, M. Gauthier, and J. Livage, Appl. Phys. Lett. **36**, 986 (1980).
12. S. M. Sze, Semiconductor Devices and Physics and Technology (Wiley, New York, 1985).
13. E. H. Rhoderick, *Metal-semiconductor contacts*, (Clarendon Press, Oxford, 1978).
14. Z. Yao, H. W. Ch. Postma, L. Balents, C. Dekker, Nature, **402**, 273 (1999).
15. F. Leonard, J. Tersoff, Phys. Rev. Lett. **83**, 5174 (1999).
16. A. Y. C. Yu, Solid-St. Elect. **13**, 239 (1970).
17. F. A. Padovani, *Semiconductors and semimetals* ed. by Willardson & Beer, **6A**, Chap. 2, (Academic Press, New York, 1971).
18. P. J. de Pablo, E. Graugnard, B. Walsh, R. P. Andres, S. Datta, R. Reifenberger, Appl. Phys. Lett. **74**, 323 (1999).

Mat. Res. Soc. Symp. Proc. Vol. 703 © 2002 Materials Research Society V13.5

# GROWTH OF SOLID AND HOLLOW NANOWHISKERS FROM NANOSCALE POWDERS

R.T.Malkhasyan, R.K.Karakhanyan, M.N.Nazaryan
Scientific-Production Enterprise "ATOM", Tevosyan str. 3/1, Yerevan 375076, Armenia,
rmalkhas@aua.am

## ABSTRACT

The fast mass growth of solid and hollow nanowhiskers of $MoO_3$ and $WO_3$ is obtained owing to the heating of the nanoscale powders of these materials by means of electron beam. Based on our transmission electron microscopic observation the growth mechanism of the $MoO_3$ and $WO_3$ nanowhiskers is proposed.

## INTRODUCTION

Nanosize materials, because of their unique physical-chemical properties, have gained more importance in modern investigations [1, 2]. One of the most significant problems is to study the influence of external impact, in particular of electron irradiation, on the nanosize materials. In this connection it is necessary to mention the crystallization of amorphous materials [3], the growth of the whiskers of diamond in the chamber of electron microscope [4], the formation of the carbon onions by the electron irradiation [5-10]. The aim of this work is to obtain the $MoO_3$ and $WO_3$ solid and hollow nanowhiskers growth under the electron irradiation in the chamber of the electron microscope, as well as the study of the dynamic processes in these nanowhiskers under the influence of the electron irradiation.

## EXPERIMENTAL

The investigations were carried out on the transmission electron microscope (TEM) TESLA BS 500 at accelerating voltage of 90kV. To prepare specimens, 1-2 drops of $MoO_3$ or $WO_3$ powders suspension in hexane were drifted on the copper grid with carbon coat. For the investigation, both ordinary and treated by vibrationally excited molecules of hydrogen [11-13] the $MoO_3$ and $WO_3$ powders were used.

## RESULTS AND DISCUSSION

The transmission electron microscopic investigation showed that nanosize $MoO_3$ and $WO_3$ powders are the agglomerates of the nanoparticles (size of agglomerates is 0.4-16 μm). If the intensity of electron beam is low, the agglomerates of the $MoO_3$ and $WO_3$ nanoparticles remain stable. During the intense irradiation of the $MoO_3$ and $WO_3$ nanoparticles agglomerates, irrespective of their method of obtaining, we observed a fast mass formation of nanowhiskers of those materials (Fig.1). As seen from this micrograph, the nanowhiskers of $WO_3$ can grow separately with an arbitrary orientation as well as with formation of closely packed blocks of nanowhiskers with the same crystalline orientation. Minimal width of $MoO_3$ and $WO_3$ nanowhiskers is 8 nm, and the maximal length is 1 μm. Besides common, i.e. solid nanowhiskers, we also observed $MoO_3$ and $WO_3$ hollow nanowhiskers. The nanowhiskers of $MoO_3$ are shown in Fig. 2. The hollow nanowhiskers are indicated by arrows. The analysis of the electron diffraction patterns shows that in both cases they are growing in the direction of [001]. Such coincidence of the growth directions of $MoO_3$ and $WO_3$ nanowhiskers is caused by the well known proximity of their crystalline structure [14].

Fig. 1. Closely packed blocks of the same crystalline orientation nanowhiskers of $WO_3$.

We know three inorganic materials which form low-dimensional tube-type crystals: carbon nanotubes [15], graphite polyhedral crystals [16], cylindrical crystals of serpantine [17], hollow whiskers of aluminium borates [18]. The results of the present work allows to confirm that the nanosize powders of $MoO_3$ and $WO_3$ also refer to the above-mentioned list of materials.

As the growth of $MoO_3$ and $WO_3$ nanowhiskers passes instantaneously, it is very difficult to follow this process. The TEM investigations show that the nanowhiskers are formed on those parts where a lot of nanoparticles had been. It is seen from Fig. 3, that on the parts with a great number of long nanowhiskers, before their formation there was also a great surface density of nanoparticles. As seen from Fig. 3, by reducing the nanoparticles density (along the border of the carbon coat and on the carbon coat itself) the number and the length of the formed nanowhiskers are also reduced. Our observation revealed that when there are few nanoparticles, the nanowhiskers are not formed. Nanowhiskers can grow on the carbon coat as well as can grow aside where a carbon coat is missing, which is distinctly seen in Fig. 3.

Fig. 2. The solid and hollow nanowhiskers of $MoO_3$.

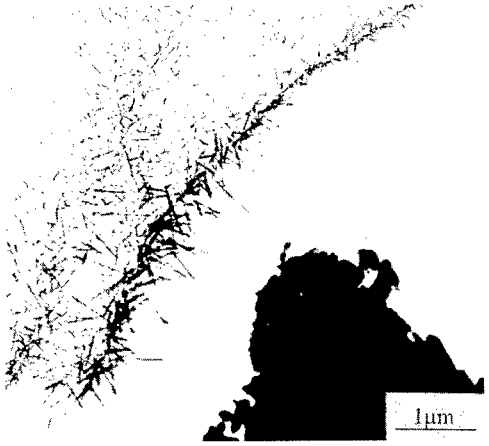


Fig. 3. Dependence of $WO_3$ nanowhiskers number and length on surface density of nanoparticles.

During the further continuous (~1min) and more intense electron irradiation, a reverse process takes place – the $MoO_3$ and $WO_3$ nanowhiskers are gradually destroyed. This destruction passes slower, than the growth of the nanowhiskers was, that allows us to have corresponding micrographs. The $WO_3$ nanowhiskers on the carbon coat are shown in Fig. 4. The nanowhiskers are in the early stage of destruction under the influence of the electron irradiation. In Fig. 5, the $WO_3$ nanowhiskers are already in a later stage of destruction. Inside the destroyed nanowhiskers separate nanoparticles obtained by the split and destruction of the initial nanowhiskers under the influence of electron irradiation are distinctly seen. The microdiffraction pattern, obtained from destroyed the $MoO_3$ and $WO_3$ nanowhiskers indicates its polycrystalline structure, in the case, that before the destruction the nanowhiskers had been single-crystalline. During the further irradiation with more intense electron beam nanowhiskers are finally destroyed and folded into clew.

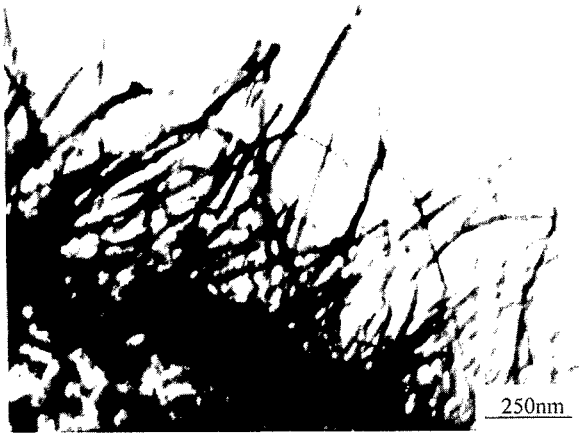


Fig. 4. The $WO_3$ nanowhiskers in the early stage of destruction.

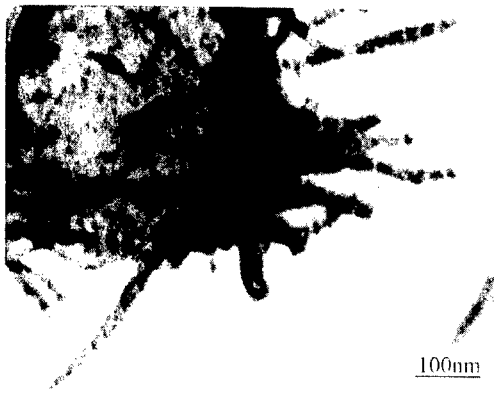


Fig. 5. The $WO_3$ nanowhiskers in the later stage of destruction.

Based on our TEM investigations, we can propose the following mechanism of the growth of $MoO_3$ and $WO_3$ nanowhiskers. In the first stage it is necessary to have individual (isolated from each other) nanoparticles, which are as a crystalline nuclei for the growth of the nanowhiskers. Next, under the influence of the electron beam by heating [19] the molecules of the $MoO_3$ and $WO_3$ from those nanoparticles are generated. As a result of a thermal movement and surface diffusion the uninterrupted migration of $MoO_3$ and $WO_3$ molecules on the carbon coat or on the agglomerate takes place. The diffused molecules interacting with a crystalline nuclei with [001] orientation, which corresponds to the maximal rate of the growth, form $MoO_3$ and $WO_3$ nanowhiskers. If the $MoO_3$ and $WO_3$ nanowhiskers grow on the borders where the carbon coat is broken or on the edges of agglomerates in aside where carbon coat is absent, diffusion of the molecules takes place on the surface of the already formed part of the nanowhiskers. Taking into account the high rate of the surface diffusion of the molecules, in our case generated by heating during the electron irradiation of isolated from each other nanoparticles, the almost instantaneous growth of the $MoO_3$ and $WO_3$ nanowhiskers becomes clear. This growth is stopped when the quantity of the individual nanoparticles is reduced. When hollow nanowhiskers are formed, it is evident that the initial crystalline nucleus has a circle-like form which is caused by the topology of a part where the given nucleus was formed. As a result, the same process as at the growth of solid nanowhiskers a further growth of hollow nanowhiskers takes place.

## CONCLUSION

At the presence of $MoO_3$ and $WO_3$ nanoparticles of definite density, irrespective of the method of their obtaining, under the influence of an intense electron irradiation owing to heating, solid and hollow $MoO_3$ and $WO_3$ nanowhiskers are grown. The formation of the hollow nanowhiskers testifies the surface nature of their growth.

## ACKNOWLEDGMENT

The authors express their gratitude to Mr. Makaryan V.K. and Mrs. Grigoryan S.L. for help in preparation of this paper. This work was partially supported by the ISTC Grant A-139.

REFERENCES


1. Metastable Phases and Microstructures, edited by R.Bormann, G.Mazzone, R.D.Shull, R.S.Averbakh and R.F.Ziolo (Mater. Res. Soc. Proc. **400,** Pittsburgh, PA, 1995) p. 368.
2. Nanophase Materials, 1994. edited by G.S. Hadjypanais and R.W.Siegel (Kluwer Academic Publishers, Dordrecht/ Boston/ London, 1994), p.808.
3. G.Schimmel, Elektronenmikroskopische Methodik, (Springer-Verlag, Berlin, Heidelberg, New York, 1969) p.250.
4. V.D. Zamojskii, and A.N.Lousin, , Dokl. AN SSSR, **224,** 369 (1975).
5. D Ugarte, Nature (London), **359**, 707 (1992).
6. W.A. de Heer and D.Ugarte, Chem.Phys. Lett., **207**, 480 (1993).
7. K.G.Mckay, H.W. Kroto and D.I.Wales, I.Chem. Soc. Faradey Trans. **88**, 2815 (1992).
8. Q.Ru, M.Okamoto, Y. Kondo and Takayanagi, Chem.Phys. Lett. **259**, 425 (1996).
9. B.S. Xu and S-I.Tanaka, Proc. Annu..Meeting Scan. Soc. Electron Microsc., **49**, 434 (1997).
10. T.Oku, T. Hirano and K.Suganuma, J. Mater. Res. **14**, 4266 (1999).
11. R.T Malkhasyan, in Metastable Phases and Microstructures, edited by R.Bormann, G.Mazzone, R.D.Shull, R.S.Averbakh and R.F.Ziolo (Mater. Res. Soc. Proc. **400,** Pittsburgh, PA, 1995)pp. 77 – 82.
12. R.T. Malkhasyan and G.H . Movsesyan, Pribory Techn. Exper. **4**, 127 (1991).
13. R.T. Malkhasyan, G.H. Movsesyan and V.K Potapov, Khim. Vysok. Energii. **26**, 63 (1992).
14. K.Schubert, Kristallstrukruren Zweikomponentiger Phase, (Springer-Verlag, Berlin, Gottingen, Heidelberg. 1964), p. 485.
15. S.Iijima, Nature, **354**, 56 (1991).
16. Y.Gogotsi, I.A. Libera, N. Kalashnikov and M.Yoshimura, Science. **290**,317 (2000).
17. E.I.W.Wittaker, Acta Cryst. **21**, 461 (19660).
18. Y.Gogotsi, V. Yaroshenko and F.Porz, J.Mater. Sci., Lett., **11**, 308 (1992).
19. L.W.Hobbs, in Introduction to Analytical Electron Microscopy, edited by Hren et al. (Plenum, N.Y.1997) p.437- 450.

Mat. Res. Soc. Symp. Proc. Vol. 703 © 2002 Materials Research Society V13.8

# The Generation of a Carbon Nanotube- Cyclodextrin Complex.

G.F. Farrell[1], G. Chambers[1,2], A.B Dalton[3], E. Cummins[1], M. McNamara[1], R.H. Baughman[3], M. in het Panhuis[2], H.J. Byrne[1].

[1]Facility for Optical Characterisation And Spectroscopy (FOCAS), DIT, Kevin Street, Dublin 08, Ireland.
[2]Trinity College Dublin, Dublin 02, Ireland/ Media Lab Europe, Sugar House Lane, Bellevue, Dublin 08, Ireland.
[3] UTD NanoTech Institute University of Texas at Dallas Richardson 75080 USA.

## ABSTRACT

In this study the intermolecular interactions of small diameter (~0.7nm) carbon nanotubes and γ-cyclodextrin were examined. Four samples of γ cyclodextrin and HiPco carbon nanotubes were prepared. The first, by grinding the tubes and the cyclodextrin (1:30 ratio) together in a dry mixture, the second was prepared in a similar fashion but was ground in the presence of water (1ml). Finally an aqueous solution of γ-cyclodextrin (0.3M) and HiPco carbon nanotubes (5mg) was prepared by refluxing for ~100 hours, forming a pale yellow solution from which a number of crystals were produced, both the solution and the recrystallised material were analysed. The samples were analysed using UV-Vis-NIR and Raman spectroscopy. The results presented are the first spectroscopic evidence of an intermolecular interaction between γ-cyclodextrin and single wall nanotubes.

## INTRODUCTION

Since the discovery [1] of carbon nanotubes there has been considerable interest in the development of fullerene based nanotechnology. Theory predicts that carbon nanotubes have extraordinary electrical properties [2] and can behave as a one-dimensional conductor making them ideal candidates for interconnects in molecular electronic devices. Experimental confirmation of these predictions however has been hampered by the difficulty in purifying, processing and manipulating the carbon nanotubes. Several methods for processing and purifying both multi-walled carbon nanotubes (MWNT) and single walled carbon nanotubes (SWNT) have been reported using conjugated polymer systems [3] and chromatographic approaches [4]. However reports on the chemical manipulation of the tubes have been slow to emerge. The recent production of small diameter (0.7-0.8nm) and high purity single walled carbon nanotubes (SWNTs) by Smalley et al. [5] using a gas-phase catalytic approach called HiPco (high pressure CO disproportionation) has resolved to some degree the question of purity, with current purities of >90% atomic percent SWNT carbon [6]. The dominant impurities begin metal catalyst particles of Iron [6]. The purity of HiPco nanotubes has aroused considerable interest in the chemistry of this unique material [7,8] and significantly the interaction of these tubes with supra-macromolcules, bio-molecules and polymeric material. Recently it has been demonstrated that SWNTs (HiPco) can be cut by simply grinding the tubes in soft organic

material such a cyclodextrins [7] (CD). The results reported on such cutting techniques however concentrated upon microscopy thereby limiting the degree of information that can be deduced about the type of interaction between the two materials.

Cyclodextrins are crystalline, water soluble, cyclic oligosaccharides built up of glucopyranose units (Glucose units) and contain a relatively hydrophobic central cavity and hydrophilic outer surface. There are three main types of cyclodextrin α-cyclodextrin, β-cyclodextrin and γ-cyclodextrin, which have inner cavity diameters of 0.47-0.53nm, 0.6-0.65nm and 0.75-0.83nm respectively [9]. One of the key chemical properties of cyclodextrins is there ability to form inclusion complexes with a wide variety of molecules that is to accommodate a guest molecule into their inner cavity. It is well know for example that $C_{60}$ can readily form an inclusion complex with γ-cyclodextrin (γ-CD) [10]. The question then is can similar electronic interactions occur with the HiPco SWNTs? It was suggested by Chen et al. [7] that it was unlikely that individual SWNTs could form inclusion complexes with γ-CD since the inner cavity size [9] is comparable to the diameter size of the HiPco tubes. Instead it was suggested that the CD is absorbed at the surface of nanotube ropes by van der Waals forces and can cut the tubes [7].

In this study UV-Vis-NIR spectroscopy and Raman microscopy have been performed upon a set of ground mixtures] of SWNTs (HiPco) and γ-Cyclodextrin to help elucidate the nature and extent of any electronic interactions between the two species. In addition an aqueous solution of γ-CD and SWNT (HiPco) refluxed together in a similar manner to early experiments with γ-CD and $C_{60}$ was also analysed.

## EXPERIMENTAL

In total there were four samples considered throughout this study. The first was a dry ground material produced by grinding in an agate mortar and pestle γ-CD and SWNT (HiPco) in a 30:1 ratio. The mixture was ground for approximately 1 hour resulting in a fine light grey powder. A second mixture again in a 30:1 ratio was then ground but this time it was ground in 1ml of deionised water resulting in a fine dark grey powder (which retained its dark grey colour after heating). The third sample was produced by refluxing a suspension of SWNTs (5mg) in an aqueous γ-CD solution (0.3M) for <100hrs at 100°C under constant stirring. It was seen that a yellow solution began to form after about ~72 hours from which a number of crystals were formed. The subsequent solution was allowed to rest for two days (allowing excess tubes to settle out) before it was decanted off and analysed. The final and fourth samples were simply the recrystallised material produce from the refluxed solution. The material, which settled out after the reflux time, was also analysed and found to be simply carbon nanotubes.

The samples were analysed using Raman microscopy and UV-Vis-NIR spectroscopy. The Raman spectra were obtained using an Instruments S.A. Labram 1B spectroscopic microscope operating at 633nm while the UV-Vis-NIR spectra were obtained using a PerkinElmer Lambda 900 spectrophotometer. All samples for the UV-Vis-NIR spectra were dissolved in de-ionised water.

## RESULTS AND DISSCUSSION

The solution produced by refluxing a suspension of SWNTs (5mg) in an aqueous γ-CD solution (0.3M) for ~100hrs at 100°C had a 'yellow' tint reminiscent of $C_{60}$-γ-CD inclusion complexes produced in a similar fashion [10]. It is unlikely however that this coloration is due to the formation of an inclusion complex between the SWNT and γ-CD a more likely explanation is the presence of dissolved $Fe^{+3}$ produced from catalytic iron particles [6]. There is evidence from the absorption spectra shown in figure 1 that the γ-CD interacts electronically with either the SWNTs or the catalyst iron particles, however identification of exactly which species it interacts with at this stage is difficult. Figure 1 (a) shows the optical absorption spectrum of the HiPco SWNTs, obtained in SDS, which agrees well with literature [6, 11] having two broad absorption peaks centered at approximately 1200nm and 1000nm. These peaks have been attributed to optical transition between mirror image spikes in density of states of semiconducting tubes [11]. In addition the peak position is also very sensitive to the tube diameter [11], allowing an estimate of the diameter distribution of the HiPco tubes used in this study to be obtained as 0.7-1.0nm. Indeed the average tube diameter obtained from TEM images was ~0.8nm. This diameter distribution further supports the notion that HiPco SWNTs and γ-CD cannot form an inclusion complex together since the diameter size of the HiPco tubes and the inner cavity size of γ-CD [9] are comparable. Spectrum (b) in figure 1 highlights the absorption spectrum of γ-CD in aqueous solution, it can be seen that this absorption has few features in the NIR region however there is a strong feature at ~260nm. By comparing the wet and dry ground sample spectra (obtained from aqueous solution) (d) and (e) respectively to the pristine samples (a) and (b) we can see a number of distinct changes.

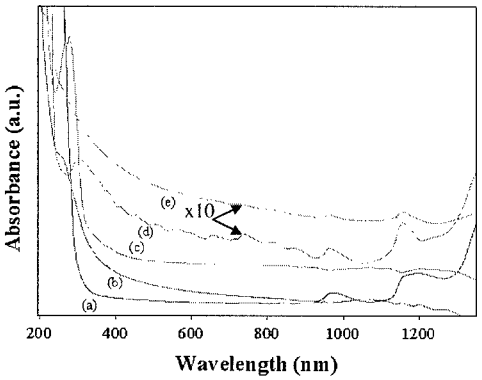


**Figure 1.** NIR-UV-Vis of (a) HiPco SWNTs raw sample in SDS solution, (b) γ-Cyclodextrin in aqueous solution, (c) aqueous solution produced from reflux. (d) wet ground miture of γ-CD and HiPco SWNTs (30:1 ratio), (e) wet ground miture of γ-CD and HiPco SWNTs (30:1 ratio). Both (d) and (e) are in aqueous solution.

Firstly the dry ground sample, spectrum (e) shows only weak SWNTs peaks in the NIR region with little or no positional changes with respect to the pristine SWNT sample. In

comparison to the γ-CD spectrum the feature at ~260nm appears to be smeared out making any conclusion about an electronic interaction difficult. However for the wet ground sample, spectrum (d) figure 1 clear differences exist. Significantly the feature at ~260nm in the absorption spectrum of the γ-CD is seen to under go a shift of ~40nm towards the red for the wet ground mixture. Indicating a change in the electronic structure of the γ-CD. Furthermore the characteristic SWNT peaks in the NIR region also appear to become more defined and sharper with peak maximum at ~960nm and ~1150nm suggesting that SWNTs of diameter ~0.76nm and 0.92nm are retained in the wet ground sample. In contrast spectrum (c) obtained for the yellow solution produced from the reflux shows no evidence of any tubes, supporting the suggestion that the yellow tint is in fact due to $Fe^{+3}$ ions. It should be noted however that the feature at 260nm for γ-CD appears to be enhanced in this solution. In general the evidence for an intermolecular interaction between the γ-CD and the HiPco SWNTs from the absorption spectra is weak.

More convincing spectroscopic evidence of an intermolecular interaction can be obtained from Raman spectroscopy. The Raman spectrum for HiPco SWNTs is shown in figure 2 (a). As in the absorption spectra the diameter distribution can be estimated from the radial breathing modes (RBMs) to be in the range 0.7nm to 1nm. Raman scattering of the RBMs (positioned between $150cm^{-1}$ and $300cm^{-1}$) and the tangential displacement mode (TDM positioned at $\sim 1580cm^{-1}$) of SWNT have been intensively studied in recent years [12,13] and are known to be sensitive to perturbations in the local environment of the tube. This is evident in the spectra shown in figure 2, which shows changes in the Raman scattering of the HiPco SWNTs as the sample preparation moves from the dry ground mixture through to the recrystallised material produced after the reflux. It is seen that the RBMs and the TDM undergo considerable changes in position and to some degree intensity.

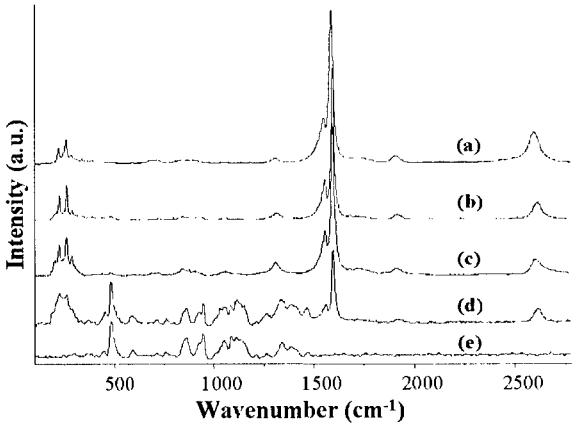


**Figure 2.** Raman spectra for (a) raw HiPco SWNTs (b) dry ground mixture, (c) wet ground mixture, (d) the recrystallised material produced from the refluxed suspension and (e) γ-CD.

Figure 3A highlights the changes observed in the RBM region of the spectrum, it can be seen that for the pristine sample the dominant RBM is positioned at $254.7cm^{-1}$ (corresponding to a tube diameter of ~0.9nm). Whereas in the ground samples (both the dry ground and the wet ground mixtures) a slight up shift in the RBMs position towards smaller diameters is observed.

In particular the dominant RBM is positioned at 257.0cm$^{-1}$ for the dry ground mixture and 257.6cm$^{-1}$ for the wet ground mixture which is a shift of 2.3cm$^{-1}$ and 2.9cm$^{-1}$ respectively from the pristine sample. Additionally a new RBMs appears for both the ground samples at ~197cm$^{-1}$ which is not descrenable in the pristine HiPco SWNTs Raman spectrum. Nevertheless the

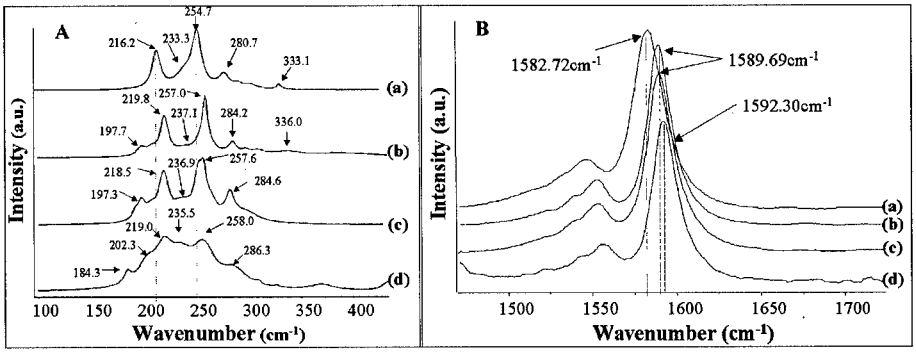


**Figure 3.** Raman spectra of (A) radial breathing modes and (B) tangential displacement mode spectra shown are (a) raw HiPco SWNTs (b) dry ground mixture, (c) wet ground mixture, and (d) the recrystallised material produced from the refluxed suspension. Peak positions were obtained from Lorentzian/Gaussian fits.

overall shape of the dry and wet ground samples are comparable to that observed for the pristine sample with only a slight shift in the main RBMs. The recrystalised material produced from the refluxed solution, however shows considerable changes in the RBMs. It can be seen from figure 3A spectrum (d), that the RBMs broaden considerably resulting in what appears to be a more even diameter distribution. This broadening may be the result of a decrease of the dominant RBMs rather then the specfic selection of larger diameter tubes. Nevertheless the changes suggest that the refluxing method results in a stronger interaction between the HiPco nanotubes and the γCD.

Further changes are obsreved for the Tangential displacement mode (TDM) poistioned at ~1580cm$^{-1}$ figure 3B. This mode involves tangential C–C bond stretching motions and stems from the $E_{2g}$ mode at 1580 cm$^{-1}$ in graphite [2]. In contrast to the RBMs the graphite-like TDM exhibits a definite upward shift of ~7cm$^{-1}$ after the nanotubes were ground with γCD and an even further up shift of ~10cm$^{-1}$ for the recrystallised material. Similar up shifts in this mode have been reported before in SWNT bundles and SWNT/expoy [12,13] composites in which it was seen that the TDM can shift up in frequency due to compressive strains induced along the length of the nanotubes. The compressive strains were attributed to van der Waals interactions between the individual SWNTs in bundles (or the epoxy and SWNTs in the composite) thereby stiffening the bond and hence constricting the molecular vibrations [12,13]. This observation of an up shift in this study may thus be due to strains induced by adsorbed cyclodextrins at the surface of nanotube ropes. Indeed Chen et.al. [7] proposed that cyclodextrins could be adsorbed onto the surface of nanotube ropes by van der Waals forces. The shifts in the TDM are thus the first spectroscopic evidence to support the notion the HiPco SWNTs can readily interact with γ cyclodextrin.

The true nature and extent of the intermolecular interaction between SWNTs and γCD however has still to be elucidated. Leaving many questions about the potential use of supramacromolecules, such as cyclodextrins, calixerines and other soft organic materials, in the development of molecular self assembly techniques.

## CONCLUSION

Reported is the first spectroscopic evidence of an intermolecular interaction between HiPco SWNTs and γ CD. It was seen that by grinding or refluxing the SWNTs with the soft organic material considerable changes to the electronic and vibrational structure of both materials can be induced. Evidence from Raman spectroscopy, in particular up shifts in the TDM at ~1580cm$^{-1}$, seem to indicate that the cyclodextrins can absorb via van der Waal forces along the length of the tube inducing a compressive strain. The interaction of SWNT with organic materials has been proposed as a possible route towards self assembly techniques, however before such techniques can be uutilised a true understanding of the nature and extent of the interaction of SWNTs with such molecules must be obtained.

## ACKNOLOGDEMENTS

The authors would like to thank Professor R. Smalley for supplying the HiPco samples Enterprise Ireland, and the Higher Education Authority of Ireland.

## REFERENCES

[1] S. Iijima, T. Ichihashi, *Nature* **363,** 603, (1993).
[2] C. N. R. Rao, B. C. Satishkumar, A. Govindaraj. M. Nath *Chemphyschem* **2,** 78, (2001)
[3] S.Curran, P.M. Ajayan. W.Blua D. Carroll, J.N. Coleman, A.B. Dalton A. Davey, A.Dury, B. McCarthy, S. Maier. *Adv. Mat.* **10,** 1091 (1998)
[4] G.S. Duesberg, W. Blau, H.J. Byrne, J. Muster, M. Burghard, S. Roth *Synth. Met.* **103**, 2484 (1999)
[5] P. Nikolaev, M.J. Bronikowski, R.K. Bradely, F. Rohmund, D.T. Colbert, K. A. Smith, R.E. Smalley, *Chem. Phys. Lett.*, **313**, 91.(1999)
[6] I. W. Chiang, B. E. Brinson, A. Y. Huang, P. A. Willis, M. J. Bronikowski, J. L. Margrave, R. E. Smalley, and R. H. Hauge *J. Phys. Chem. B* **105**, 8297, (2001)
[7] J. Chen, M. J. Dyer, and M-F. Yu *J. Am. Chem. Soc.*, **123**, 6201 (2001)
[8] M. Yudasaka, H. Kataura, T. Ichihashi, L.-C. Qin, S. Kar, and S. Iijima *Nano Letters* **1**, 487. (2001)
[9] J. Szejtli *Chem. Rev.*, **98**, 1743 (1998)
[10] S. Samal and K. E. Geckeler, *Chem. Commun.*, 1101, (2000)
[11]H. Kataura, Y. Kumazawa, Y. Maniwa. I. Umezu, S. Suzki, Y.Ohtsuka and Y. Achiba. *Synth. Met.* **103**, 2555 (1999)
[12] V. G. Hadjiev, M. N. Iliev, S. Arepalli P.B. S. Files *App. Phys. Letts.* **78**, 3193. (2001)
[13] U. D. Venkateswaran, A. M. Rao, E Richter, M. Menon, A. Rinzler, R. E. Smalley P. C. Eklund. *App. Phys. Letts.* **59**, 10928. (1999)

Mat. Res. Soc. Symp. Proc. Vol. 703 © 2002 Materials Research Society V13.20

# Optical Nonlinearity of Sputtered $Co_3O_4$-$SiO_2$-$TiO_2$ Thin Films

Hiroki Yamamoto, Takashi Naito[1] and Kazuyuki Hirao[2]
Nanotechnology Glass Project, New Glass Forum, Tsukuba Research Laboratory,
Tsukuba Research Consortium, 9-9, 5-Chome, Tokodai, Tsukuba, Ibaraki, 300-2635 Japan
[1]Hitachi Research Laboratory, Hitachi, Ltd.,
1-1, 7-Chome, Omikacho, Hitachi, Ibaraki, 319-1292 Japan
[2]Division of Material Chemistry, Graduate School of Engineering, Kyoto University
Yoshida-honmachi, Sakyou-ku, Kyoto, 606-8501 Japan

## ABSTRACT

Optical non-linearity of cobalt oxide with $SiO_2$-$TiO_2$ additives was investigated, and the change mechanism of the refractive index (n) and extinction coefficient (k), based on the relation between band structure and optical non-linearity of the thin films, was discussed. Refractive index and extinction coefficient of $Co_3O_4$ thin films in the ground state were 3.17 and 0.42, respectively. Both n and k decreased by irradiation from a pulse laser with 650 nm of wavelength (1.91eV). These values in the excited state were 2.91 and 0.41, respectively. $n_2$ estimated from the change of n and k was $-2.8 \times 10^{-11}$ $m^2/W$. The film had a band gap corresponding to 2.06eV, indicating that it was widened by the band filling effect during the laser irradiation at 1.91eV, and this led to the decrease in absorption coefficient and refractive index.

## INTRODUCTION

Spectral analyses [1-3], band structural analyses [4-6] and optical nonlinearity [7], of cobalt oxide thin films have been extensively reported. Recently, we have discovered that cobalt oxide thin films containing glass additives have remarkable optical nonlinearity, that is, their refractive index drastically changes with laser irradiation ($\lambda$=650nm, E=1.91eV) [8-11]. Therefore these films are suitable as super resolution films to reduce the spot size of the laser irradiated on optical recording media such as DVDs (digital versatile disks). Furthermore, we have reported the nano structure of some of these thin films and found they had nano-scale $Co_3O_4$ precipitated particles with an amorphous grain boundary phase of 1.0nm width [12].

Ando et al. [7] investigated the third order nonlinear optical susceptibility $\chi^{(3)}$ of thin films of transition metal oxides including $Co_3O_4$ with a phase-conjugation-type degenerate four-wave mixing (DFWM) method. They reported that thin films of transition metal oxides had large $\chi^{(3)}$ when 7ns and 35ps pulse lasers with a wavelength of 532nm were irradiated on them. $Co_3O_4$ showed significantly more nonlinearity than the other transition metal oxide films because of its high figure of merit, $\chi^{(3)}/\alpha$.

In the present study, refractive index and extinction coefficient of ground and excited states were measured by an ellipsometric method to investigate the mechanism of non-linearity of $Co_3O_4$-$SiO_2$-$TiO_2$ thin films.

## EXPERIMENTAL PROCEDURE

Thin films of $Co_3O_4$ with $SiO_2$ and $TiO_2$ additives were obtained by RF magnetron sputtering at room temperature on borosilicate glass substrates. Composition of the film was

$84Co_3O_4$-$8SiO_2$-$8TiO_2$ in molar percentage. An SPF-430H sputtering device (Anelva Co. Ltd.) was used to form the thin films. Sputtering gas was argon including 10 vol% $O_2$ and sputtering power was 600W on a 101.6 mm $\phi$ target. Thickness of each film was about 70nm. Back pressure was under $1.0 \times 10^{-4}$ Pa, and the pressure during sputtering was $6.7 \times 10^{-1}$ Pa.

Nano structure was evaluated by transmission electron microscopy (TEM; Hitachi H-9000NAR). The acceleration voltage was 300 kV. The TEM specimens were prepared by an ion milling device (Gatan Model 600 N).

We introduced a new device to measure refractive index (n) and extinction coefficient (k) in the ground and exited states. Ltd. The device had an ellipsometric optical arrangement. The ellipsometer (type DHA-NP) was designed and manufactured by Mizojiri Optical Co. The optical source was a semiconductor laser with a wavelength of 650nm. A laser driver drove the laser source and a pulse generator changed the laser power. Pulse width was 100ns. The laser beam was irradiated onto the specimen through a polarizer and focusing lens. Then the beam reflected onto the surface of the thin film specimen, and then passed through an analyzer and filter before reaching the detector. The signal was sent to a digital oscilloscope with a sampling frequency of 0.5GHz. One measurement was repeated 128 times and the average was sent to a PC, and $\Delta$, $\vartheta$, and n, k were calculated. Laser intensity (I) for measuring n and k in the ground state was under $0.13GW/m^2$ and between $1.0GW/m^2$ and $9.0GW/m^2$ for measuring them in the excited state.

Optical transmittance spectra of the films were measured by an optical spectrum analyzer (Hitachi, U-3500). Transmittance of the substrate was subtracted as the base line. Optical absorption spectra were calculated from the transmittance spectra.

## RESULTS

A high-resolution TEM image from a plane view of the $84Co_3O_4$-$8SiO_2$-$8TiO_2$ film indicated that the film consisted of nano-scale particles with a grain boundary phase. Average grain size (d) of the film was 10.7nm, and the standard deviation ($\sigma$) of the grain size of the sample was 2.14nm. The selected area diffraction images of the film corresponded to the diffraction patterns of $Co_3O_4$.

Figure 1 shows the change of n and k induced by laser pulse irradiation (wavelength, 650nm). The intensity of the pulse laser started to increase at t=0, and it rose to $9.0\ GW/m^2$. With increasing pulse laser intensity, n decreased from 3.17 to 2.91. On the other hand, k was almost constant for the duration of the pulse laser irradiation.

Laser power dependence of n and k of the thin film are shown in Figure 2. Refractive indexes decreased as a function of laser intensity. The extinction coefficient slightly decreased with increasing laser power.

We reported that n and k, estimated using optical disk style samples, decreased from 2.53 to 2.23 and from 0.66 to 0.40, respectively with increasing laser intensity [11]. Although absolute values of n and k differed between the two methods, directions and extents of the changes of n and k were similar, that is, n and k decreased with increasing laser intensity.

Next, we dealt with this phenomenon in terms of optical nonlinearity. The nonlinear refractive index is described as follows:

$$n = n_0 + n_2 I \qquad (1)$$

where $n_2$ is nonlinear refractive index, $I$ is laser power and $n_0$ is the linear refractive index when laser power is weak. In the $84Co_3O_4$-$8SiO_2$-$8TiO_2$ film, $n_0$=3.17 and n=2.91, so $n_2 I$=-0.26. Further, I=$9.0GW/m^2$, hence $n_2$ was calculated as $-2.8 \times 10^{-11}\ m^2/W$.

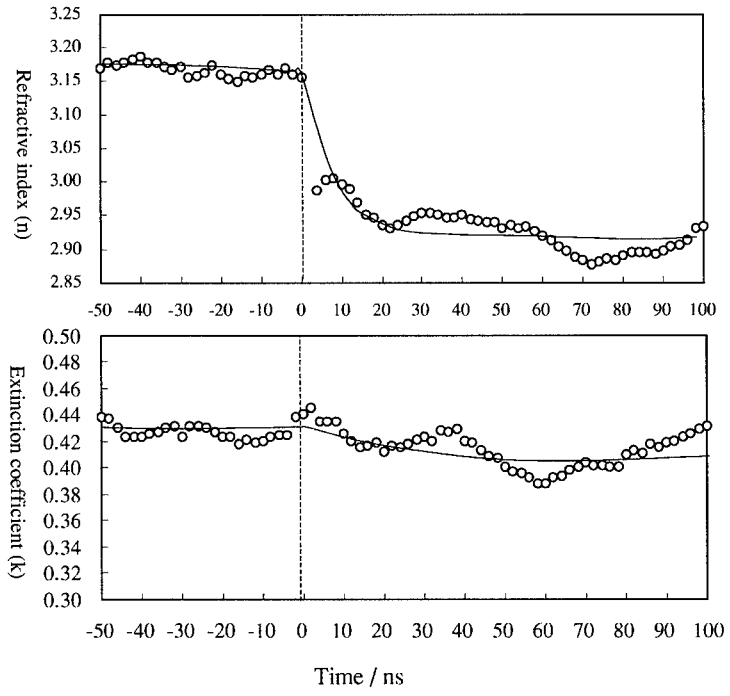


**Figure 1** Change of refractive index and extinction coefficient of $84Co_3O_4$-$8SiO_2$-$8TiO_2$ thin film by laser irradiation.

To investigate the change mechanism of the refractive index and extinction coefficient of $Co_3O_4$ films, we analyzed optical absorption spectra. Figure 3 plots $(\alpha h\nu)^2$ versus $h\nu$ of these films. Eg values were calculated in accordance with the method shown in Ref. 2. Each film had a straight line portion, and extrapolation of the line to zero absorption coefficient was close to Eg=2.0 eV. The Eg values showed good agreement with the previous findings [2].

## DISCUSSION

As we mentioned above, both n and k decreased as a function of laser pulse intensity. One of the mechanisms that can describe this phenomenon is the band filling effect in the semiconductor. The band filling effect occurs with the electron transition from the ground states to excited states induced by laser irradiation having an energy near the band gap, Eg. Excitation by electrons widen the band gap from Eg to Eg' (Eg'>Eg).

Therefore the absorption edge shifts to high energy, and then a blue shift of the absorption spectrum occurs. Consequently the absorption coefficient decreases. The refractive index also decreases in the lower energy region and it increases in the higher energy one.

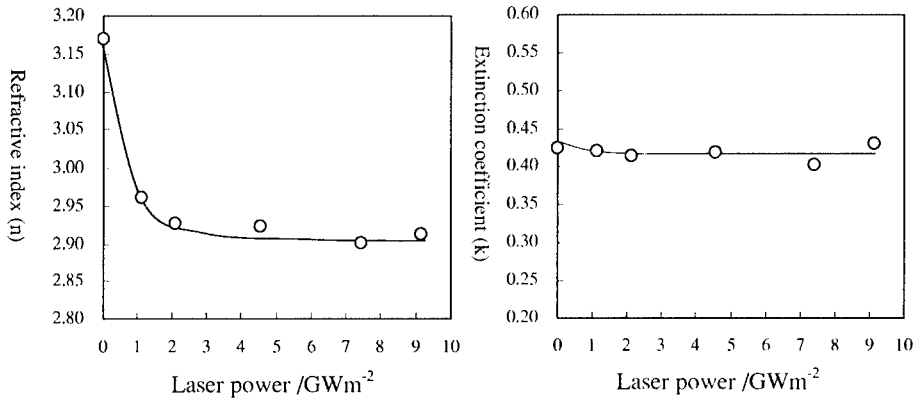


**Figure 2** Laser power dependence of refractive index and extinction coefficient of $84Co_3O_4$-$8SiO_2$-$8TiO_2$ thin film.

Since we use the laser that has a 650nm wavelength (E=1.91eV) in the present study, it is considered that the laser excited the electrons corresponding to the band gap of 2.06eV. Laser energy of 1.91eV is lower than the Eg of 2.06eV, so the refractive index also decreases.

Response time of the change of refractive index by the band filling effect was reported to be on the order of nano second in semiconductors [13]. Measured response time in the present study is also on the order of a nano second, so we have good agreement with the reported value.

Next, we consider the relation between the band structure and the reaction with the laser. $Co_3O_4$ has a spinel structure in which $Co^{2+}$ ions occupy the four-coordinate tetrahedral sites and $Co^{3+}$ ions are in the six-coordinate octahedral sites. Such a complex structure gives many localized bands, and there are several absorption peaks. The absorption band corresponding to Eg=2.06 eV is assigned as a charge transfer from $O^{2-}(\pi^*\Gamma)$ to $Co^{2+}(\sigma^*t^2)$. The laser having E=1.91eV excites this transition. Therefore we consider that $Co^{2+}$ in the $Co_3O_4$ spinel structure makes a large contribution to the optical nonlinearity.

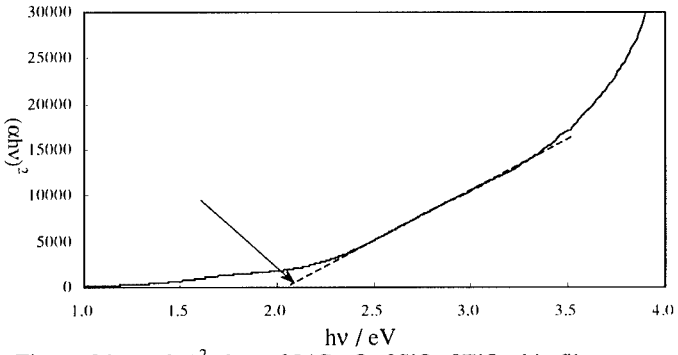


**Figure 3** hν- $(\alpha h\nu)^2$ plots of $84Co_3O_4$-$8SiO_2$-$8TiO_2$ thin film.

## CONCLUSIONS

Refractive index and extinction coefficient of $Co_3O_4$ with $SiO_2$-$TiO_2$ thin films in the ground state were 3.17 and 0.42, respectively. Both n and k decreased by irradiation of a pulse laser with 650 nm wavelength (1.91eV), and these values in the excited state were 2.91 and 0.41, respectively. $n_2$ was estimated from the change of n to be $-2.8 \times 10^{-11}$ $m^2/W$. The film had a band gap corresponding to 2.06eV, indicating that it was widened by the band filling effect during the laser irradiation at an energy of 1.91eV, and then the absorption coefficient and refractive index decreased.


## ACKNOWLEDGMENT

This work was carried out in the Nanotechnology Glass Project as part of the Nanotechnology Materials Program supported by the New Energy and Industrial Technology Development Organization (NEDO).


## REFERENCES


1. J. G. Cook, M. P. van der Meer and D. Hogg, J. Vac. Sci. Technol. A4 (3), May/June, 607-608 (1986)
2. J. G. Cook, M. P. van der Meer, *Thin Solid Films,* **144**, 165-176 (1986)
3. P. S. Patil, L. D. Kadam and C. D. Lokhande, *Thin Solid Films*, **272**, 29-32 (1996)
4. M. Lenglet and C. K. Jorgensen, *Chem. Phys. Lett.*, **229**, 616-620(1994)
5. K. M. E. Miedzinska, B. R. Hollebone and J. G. Cook, *J. Phys. Chem. Solids*, **48** [7] 649-656(1987)
6. I. D. Belova, Y. E. Roginskaya, R. R. Shifrina, S. G. Gagarin, Y. V. Plekhanov and Y. N. Venevtsev, *Solid State Commun.*, **47** [8] 577-684(1983)
7. M. Ando, K. Kadono, M. Haruta, T. Sakaguchi and M. Miya, *Nature*, **374** [13] 625-627(1995)
8. T. Shintani, K. Moritani, A. Hirotsune, M. Terao, H. Yamamoto, T. Naito, *Joint MORIS/ISOM '97 Post-deadline Papers Technical Digest*, 23, (1997)
9. T. Shintani and M. Terao, *Optical Alliance*, **9**[7], 10 (1998) (in Japanese)
10. H. Yamamoto, T. Naito, M. Terao, T. Shintani, *Digest of 11th Fall Meeting of Ceramic Society of Japan*, 243, (1998)
11. T. Shintani, M. Terao, H. Yamamoto and T. Naito, *Jpn. J. Appl. Phys.* **38**, 1656-1660 (1999)
12. H. Yamamoto, T. Naito, M. Terao, T. Shintani, *Thin Solid Films,* (manuscript submitted for publication)
13. S. Y. Auyang and P. A. Wolff, *J. Opt. Soc. Am. B,* **6** [4], 595-605 (1989)

Mat. Res. Soc. Symp. Proc. Vol. 703 © 2002 Materials Research Society V13.21

# STRUCTURE OF ZIRCONIA NANOPARTICLES USED FOR PILLARING OF CLAY

V. A. Sadykov, T. G. Kuznetsova, V. P. Doronin, T. P. Sorokina, D. I. Kochubei, B. N. Novgorodov, V. N. Kolomiichuk, E. M. Moroz, D. A. Zyuzin, E. A. Paukshtis, V. B. Fenelonov, A. Ya. Derevyankin, S. A. Beloshapkin, V. A. Matyshak*, G. A. Konin*, J. R. H. Ross**

Boreskov Institute of Catalysis, Lavrentieva, 5, Novosibirsk 630090, Russia, sadykov@catalysis.nsk.su
* - Semenov Institute of Chemical Physics, Moscow, Russia
** - Limerick University, Limerick, Ireland

## ABSTRACT

SAXS and EXAFS were applied to study genesis of polynuclear zirconium hydroxyspecies in pillaring solutions as dependent upon the zirconium concentration, addition of alkaline-earth chlorides and aging. After the montmorillonite clay pillaring, the structure of zirconium nanopillars was characterized by applying X-ray structural analysis, UV-Vis, FTIRS of adsorbed CO and nitrogen adsorption isotherms. Main pillaring species appear to be nanorods comprised of several $Zr_4$ tetramers. Basic structural features of the tetramers are preserved in zirconia nanoparticles fixed between alumosilicate layers in pillared clays. In calcined samples, those nanoparticles contain only bridging hydroxyls and/or oxygen anions responsible for bonding within pillars and between pillars and clay sheets.

## INTRODUCTION

Clays pillared by nanosize zirconia particles (Zr PILC) are promising supports and catalysts for different petrochemical processes [1-2] and selective catalytic reduction of $NO_x$ by hydrocarbons in excess oxygen [3]. Their performance strongly depends upon the size, shape and structure of nanosized zirconia pillars propping the alumosilicate layers, which are in turn determined by the properties of zirconium hydroxy polycations in pillaring solutions. The majority of published data on pillared clays synthesis mainly concerns studies of the effects of preparation procedures and properties of starting clays, while little attention has been paid to the shape and structure of pillaring species formed in solutions.

In this work, to cover this gap, SAXS and EXAFS were applied for investigation of the early stages of zirconium salts (zirconyl chloride and acetate, concentration 0.1-0.3 M) hydrolysis during aging at temperatures in the range from 25 to 80 °C. In addition, the effect of the alkaline-earth cations (Ca, Sr and Ba) on this process was considered as well. The X-ray structural analysis, UV-Vis and FTIRS of adsorbed CO were used to further characterize the zirconia nanoparticles in the calcined pillared montmorillonite clays.

## EXPERIMENTAL

Zr-containing solutions (Zr concentration 0.1-0.3 M) were prepared from recrystallized $ZrOCl_2$ 8 $H_2O$ and zirconium acetate (Aldrich 41 380-1, solution in diluted acetic acid). Those solutions were modified by adding chlorides of Ca, Sr and Ba with variation of the Zr:Me ratio in the range of 3.3-9.0. Next series of solutions were prepared and studied:

I. Zirconium salt or its mechanical mixture with Ca, Sr or Ba chlorides was dissolved in the distilled water immediately before spectra recording (Fresh).

II. 1.0 M solutions of zirconium chloride containing alkaline earth chlorides (0.1-0.3 M) were diluted and kept at a room temperature for 8 days (Aged RT).

III. Solutions of series I were aged at 55 °C for 16 h.

IV. Solutions of series II were aged at 80 °C for 3 h.

Zirconia-pillared clays were synthesized using a Ca – or Na-montmorillonite clay from the Kazakhstan deposit containing 66 wt. % $SiO_2$ and 25 wt. % $Al_2O_3$ following earlier described procedures [4] and pillaring solutions of IV series.

Solutions were studied using the X-ray Small-Angle Scattering (SAXS, a KPM-1 camera with Cu $K_\alpha$ radiation) in the range of 2θ angles 7'-4° and EXAFS (the spectra were acquired at the EXAFS station of the Siberian Center of Synchrotron Radiation, Novosibirsk) using procedures and data analysis described in details previously [5].

The size distribution of zirconium polynuclear species in solution $\mathbf{D_n(r)}$, where **r** is a characteristic size of a particles, (i.e., a sphere radius for spherical particles) was derived by using the Equation (1)

$$\mathbf{I(q) = \int D_n(r)\, m^2(r)\, i_0(qr)\, dr} \qquad (1)$$

Here, **I (q)** is the measured intensity of scattering, $\mathbf{q = 4\pi \sin\theta/\lambda}$ - amplitude of the wavevector, with $\lambda$ = 1.54 Å being the wavelength of the X-ray beam, **m (r)** –the difference between the dielectric constants of the scattering particle and surrounding media, $\mathbf{i_0(qr) = [3(\sin qr - qr\cos qr)/q^3 r^3]^2}$ – the intensity of scattering on a given spherical particle with a radius **r** [6]. The SAXS data analysis using a relation $\mathbf{\log I \sim q^2 R_g^2/3}$, where $\mathbf{R_g}$ is a gyration radius [6] was attempted as well.

The X-ray phase analysis of the initial and pillared clays was carried out using a HZG-4 (C,B) diffractometer (Cu $K_\alpha$ radiation and a flat monochromator) in the range of 2θ angles equal to 1-60°. To obtain the curves of the electronic density radial distribution, Mo $K_\alpha$ radiation and a bent graphite monochromator were applied for measurements in the 2θ range 3-140°.

Adsorption characteristics were measured on a Micromeritics ASAP-2400 installation by $N_2$ adsorption at 77 K.

UV-Vis spectra were recorded using a Shimadzu 8300 spectrometer equipped with a diffuse scattering DRS 8000 cell. Spectra were recorded in the 10000-60000 $cm^{-1}$ range with 4 $cm^{-1}$ resolution, the number of scans being equal to 50. Samples were loaded into the vacuum cells equipped with $CaF_2$ windows. To decrease the mirror reflection, a sample layer was inclined for 20-25% with respect to the horizontal plane.

The surface properties were probed by the IR spectroscopy of adsorbed CO test molecule (FTIRS, a Fourier-transform IFS 113V Bruker spectrometer).

## RESULTS

### Solutions

Fig. 1 shows typical SAXS dependencies for solutions containing 0.1 M of zirconium salts. Aging conditions very strongly affect the intensity of scattering in the range of small **q** values, while the alkaline earth cations and the nature of starting salts were mainly reflected in the high **q** part of curves. These curves contain several inflection points thus suggesting that there is a size distribution of zirconium polynuclear species. As a result, direct estimation of the gyration radius from these curves as in [6] appears to be ambiguous. The analysis of the

particle size distribution by applying the integral Equation (1) revealed that in fresh diluted solutions of pure zirconium salts polynuclear zirconium hydroxocomplexes are mainly represented by species with typical sizes in the range of 15-30 Å. They are comprised of several $Zr_4$ tetramers stacked into nanorods. The EXAFS data confirm preservation of the parent $Zr_4$ structure in those species characterized by the next typical distances and coordination numbers (CN): Zr-O - 2.21 Å (CN 7), Zr-Zr - 3.34 Å (CN 0.8), Zr-Zr - 3.67 Å (CN 1) and Zr-Zr - 4.91 Å (CN 0.8). It implies a weak interaction (mainly through the hydrogen bonds) between stacked tetramers in oligomerized zirconium hydroxycomplexes.

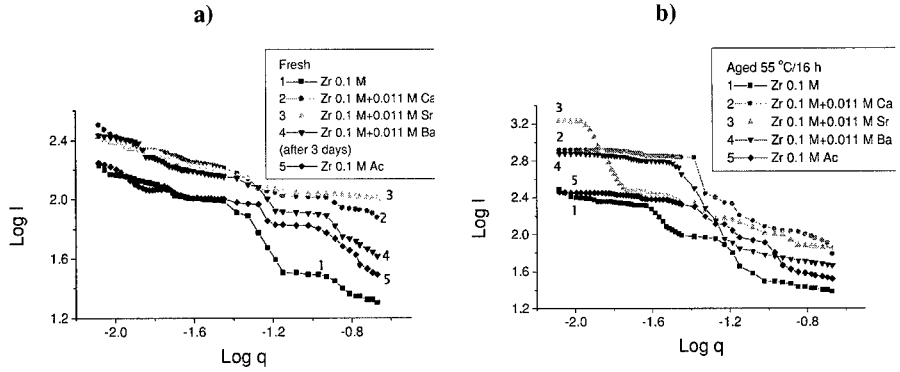


Fig. 1. SAXS intensity for fresh (**a**) and aged at 55 °C/16 h (**b**) solutions containing zirconium salts.

In aged solutions especially in those aged at 80 °C, the tetrameric units appear to be bound stronger, which is reflected in pronounced distortion of their structure. In this case, only two distances: Zr-O - 2.19 Å (CN 7) and Zr-Zr - 3.52 Å (CN 0.8) are revealed in the EXAFS spectra. These features can be tentatively explained by a structure of nanorods in which consecutively stacked $Zr_4$ units are rotated by 45 degrees relative to each other to ensure their connection by bridging OH groups formed by condensation of terminal OH groups situated at the vertexes of tetramers. The existence of sheet-like structures where disordered stacking of coplanar tetramers occurs could not be excluded as well, though formation of the latter species seems to be less probable.

In pure solutions of zirconium salts, a part of zirconium hydroxocomplexes is aggregated into large (typical diameters in the range of 60-200 Å) colloidal particles. The addition of alkaline-earth cations into solutions helps to partly suppress formation of those particles not affecting appreciably the structure of nanorods, only slightly decreasing Zr-O and Zr-Zr coordination numbers. Some increase of nanorods mean sizes (up to 45 Å) was observed as well. As alkaline-earth cations are found to be completely removed from the pillared clays at the washing stage, it suggests that in solutions, they are located at the external surface of nanorods being coordinated by terminal hydroxyls or water molecules chemically bound with Zr cations of tetramers. Such an interaction explains a higher distortion of the tetramer structure leading to decrease of EXAFS coordination numbers (in aged solutions, in the

presence of alkaline-earth cations, Zr-O CN are in the range of 6.6-6.3, while Zr-Zr CN are in the range of 0.7-0.3). The lowest coordination numbers were found for Sr-containing solutions, and the highest -for solutions with added calcium chloride. Some variation in the structure of polynuclear species in the presence of different alkaline earth cations as suggested by these results can be tentatively explained by the difference in the hydration sphere of the latter cations in water solutions [7]. Thus, for Ca the nearest sphere is comprised of regular octahedron, for Ba it is elongated octahedron, while for Sr it is a square antiprism. It can be speculated that Sr cations are included within the polynuclear species affecting the mode of their polymerization and condensation at aging.

## Clay structure and texture

In the initial clay washed by the diluted HCl solution with the pH value 2.2 equal to that in pillaring solutions and then calcined at 400 °C, the basal (001) spacing was found to be ~ 11 Å (9.6 Å being the reference value for completely dehydrated parent montmorillonite). The mean particle size in the (001) direction was around 40 Å. After pillaring, washing and calcination at 400 °C, for all samples studied here and containing ~ 20 wt.% of zirconia, the basal spacing was increased up to ~ 18 Å, while the particle size remains rather constant (~ 30 Å), suggesting that pillaring has not caused the clay exfoliation. These results imply that for all samples studied here, the mean gallery height is around 7 Å. This value corresponds to the normal orientation of tetrameric units with respect to the host layers.

In all zirconia- pillared clays studied here, any reflections which could be assigned to separate zirconia-containing phases were not observed. It means that for predominant part of pillars, their typical sizes within the basal plane are less than 25-30 Å, and that in the basal direction is less than 10 Å. The differential radial distribution curve obtained by subtracting the initial clay data from those of pillared clays was found to contain maxima at 2–2.4; 3.6; 4–4.2; 4.5–4.8; 5.6–5.9 Å, thus proving incorporation of the tetrameric units containing species into the clay structure (Fig. 2 ).

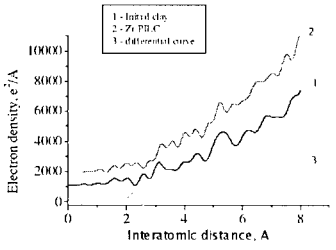


Fig. 2. Electron density radial distribution curves for the initial clay (1), Zr PILC (2) and differential (2-1) curve (3).

The negative peaks of the electron density in the differential curve show variation in the structure of a clay due to pillars incorporation. The interlayer distance between the tetrahedral $SiO_4$ layers in the alumosilicate sheets is increased up to 2.8 Å. Similarly, the distance between octahedrally coordinated cations (Me=Al, Mg) to the oxygen in the nearest tetrahedron is increased from 3.1 to 3.3 Å. These variations can be caused by strains generated by zirconia

pillars situated between the alumosilicate layers. The incorporation of a big cation (first of all, Zr) into the vacant octahedral positions could not be excluded as well.

As follows from the results of UV-Vis (Fig. 3), for Zr PILC the characteristic absorption corresponding to the anion-cation charge transfer is shifted to higher wavenumbers as compared with that for the bulk analog -highly dispersed cubic zirconia stabilized by 2 mol. % of CaO [8]. This feature can be explained by a lower O-Zr coordination number in nanosized pillars (maximum 2 for bridging oxygen anions or hydroxyls) as compared with the bulk zirconia lattice (each oxygen is surrounded by 4 Zr cations). As a result, the Zr-O bond in nanoparticles possesses a higher ionicity which is reflected in a higher energy of the charge transfer band. Decreased intensity of those bands in Zr PILCs can be related to a high disordering of the nanoparticle structure as revealed by EXAFS [8].

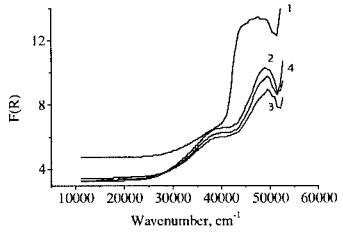


Fig. 3. UV-Vis spectra of bulk cubic zirconia stabilized by calcium (1) and zirconia-pillared clays prepared by using pillaring solutions containing Ca (2), Sr (3) and Ba (4) cations.

According to analysis of the nitrogen adsorption isotherms by using the geometric model of pillared interlayer materials [9], the specific surface area of a free space within the pillared clay galleries is in the range of 350-400 $m^2/g$. A mean diameter of pillars approximated by discs was estimated to be in the range of 15-20 Å, which agrees rather good both with the predominant sizes of pillaring species in solution and the upper limit of the size of zirconia nanoparticles as determined by XRD (vide supra).

FTIRS data of adsorbed CO and hydroxyl groups (not shown here for brevity ) indicate that on the surface of zirconia pillared clays evacuated at 400 °C, the number of coordinatively unsaturated Zr cations is much lower as compared with that for bulk highly dispersed zirconia samples [8]. Moreover, in the hydroxyls stretching regions, only bands at ~ 3650-3700 $cm^{-1}$ corresponding to bridging hydroxyls are present. It implies that the surface of zirconium nanoparticles is covered by bridging hydroxyls binding either Zr cations or Zr cations and cations in the alumosilicate layers.

## CONCLUSIONS

The structural features of zirconium polynuclear hydroxyspecies in pillaring solutions (degree of polymerization and internal arrangement) were shown to depend upon the presence of electrolytes (alkaline-earth chlorides) and aging conditions. Fixation of those species between clay sheets causes rearrangement of both the alumosilicate layers and pillars. Low Zr-O coordination numbers in zirconia nanoparticles are reflected in the high-frequency shift of the Zr-O charge transfer band indicating increased ionicity of this bond.

**ACKNOWLEDGMENTS:** This work is in part supported by INTAS project 97-11720.

## REFERENCES

1. A. Gil, L.M Gandia,. Catal. Rev-Sci. Eng., **42**, 146 ( 2000).
2. R. T. Yang, N. Trappiwattanannon, ; R.Q. Long,. Appl. Catal B: Environment., **19**, 289 (1998).
3. V. A. Sadykov, T.G.Kuznetsova et al. In: Abstracts, EUROPCAT-5, Limerick, Ireland, , Book 3, 7-O-03 (2001).
4. J. T. Kloprogge, J. Porous Mat., **5**, 5 (1998).
5. M. N. Vargaftik, I. I. Moiseev, D. I. Kochubey, K. I. Zamaraev, Faraday Discuss., **92**,.13 (1991).
6. A. Guinier, G. Fournet, Small Angle Scattering of X-rays. John Wiley. New York. 1955.
7. H.Ohtaki, T.Radnai. Chem Rev., **93**, 1157 (1993).
8. V. A. Sadykov, R. V. Bunina, G. M. Alikina, A. S. Ivanova, D. I. Kochubei, B. N. Novgorodov, E. A. Paukshtis, V. B. Fenelonov, V. I. Zaikovskii, T. G. Kuznetsova, S. A. Beloshapkin, V. N. Kolomiichuk, E. M. Moroz, V. A. Matyshak, G. A. Konin, A. Ya. Rozovskii, J. R. H. Ross, J. P. Breen. J. Cat., **200**, 117 (2001).
9. V. B. Fenelonov, A. Yu. Derevyankin, V. A. Sadykov. Micropor. Mesopor. Mater. 47, 359 (2001).

Mat. Res. Soc. Symp. Proc. Vol. 703 © 2002 Materials Research Society V13.22

# Superconductivity of embedded lead nano particles in metallic and amorphous matrices

K. Chattopadhyay[a], V. Bhattacharya[a] and A. P. Tsai[b]
[a]Indian Institute of Science, Bangalore-560 012, India
[b]National Research Institute for Metals, Tsukuba 305-0047, Japan

## ABSTRACT

Nanodispersed lead in metallic and amorphous matrices was synthesized by rapid solidification processing. The optimum microstructure was tailored to avoid percolation of the particles. With these embedded particles it is possible to study quantitatively the effect of size on the superconducting transition temperature by carrying out quantitative microstructural characterization and magnetic measurements. Our results suggest the role of the matrices in enhancement or depression of superconducting transition temperature of lead. The origin of this difference in behavior with respect to different matrices and sizes is discussed.

## INTRODUCTION

The early observations on the importance of normal-superconductor junctions were made in 1930 [1]. Since then a large body of literature are available on the subject. Intensive theoretical and experimental investigations were carried out in the sixties and seventies on granular superconductors and thin films [2,3,4]. Recently, there is a resurgence of interest due to the increasing interest in nanoscience and technology which demands understanding the behaviour of small particles [5-9]. Rapid solidification technique has been extensively used to synthesize nanoembedded particles of immiscible alloy [10]. We have successfully synthesized nanosized Pb dispersed in different matrices using this technique. In the present paper, we report the superconductive behaviour of these nanosized Pb particles embedded in Al and Al-based metallic glass matrices.

## EXPERIMENTAL PROCEDURE

Nanoembedded lead in aluminium and amophous glassy matrix was synthesized via melt spinning using 99.999%Al, Cu, V and 99.99%Pb. An optimum composition and quenching rate was chosen in order to obtain a well-dispersed microstructure. Lead is insoluble in aluminium, and in all the three elements constituting the $Al_{75}Cu_{15}V_{10}$ matrix both in the liquid state and the solid state. The processing resulted in an aluminium matrix with nanodispersions of lead, and a metallic glass matrix with nano lead dispersions. . Preliminary phase identification of the samples were carried out by X-ray diffraction (JEOL model JDX 8030 ) using Cu $K_\alpha$ radiation. Microstructural characterisation was done using a JEOL 2000 FX-II Transmission Electron Microscope (TEM) and HREM. The size distributions of particles were carried out using a

Sigma scan Pro commercial software. Magnetic measurements were carried out in a SQUID magnetometer in standard configuration. The magnetization tests were conducted under identical conditions in zero field-cooled state in order to avoid the interference of macroscopic persistent screening currents flowing in the sample. Typical fields of 20Oe & 100Oe were chosen for measurements.

## RESULTS

The composition of Pb in Al was 6.5wt% and in $Al_{75}Cu_{15}V_{10}$ was 20wt%. The detailed results of the glassy matrix has been given elsewhere [9]. Fig. 1(a) shows an electron micrograph of dispersed Pb in aluminium matrix and Fig. 1(b) shows the corresponding size distribution plot. Fig 1(c) shows the selected electron diffraction pattern from both the dispersed Pb phase and matrix confirming the cube on cube orientation relationship of Pb with Al. There exists a significant difference of lattice parameters of the two fcc cubic phases. Pb has a lattice parameter of 0.47nm while the corresponding value for Al is 0.401nm.However, no strain field could be visible around Pb particles in Al matrix. Fig 2 shows the size distribution of lead in glassy matrix obtained from high-resolution images. The Pb particle in this case is randomly oriented.

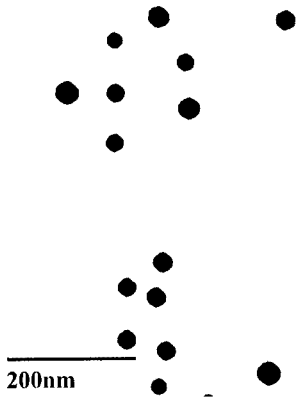


**Figure 1(a)** Electron micrograph showing nano dispersed Pb in Al

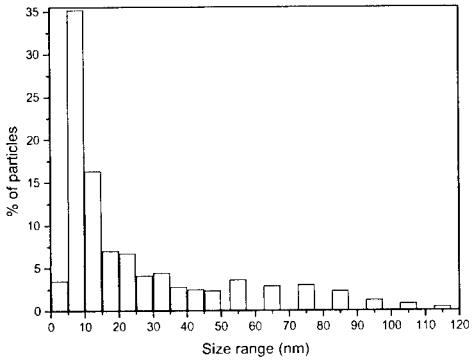


**Figure 1(b)** Size distribution showing Pb dispersoids in Al

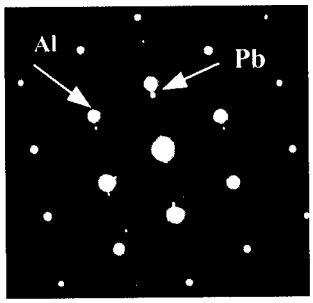


**Figure 1(c)** SADP showing Al and Pb reflections possessing cube on cube O.R

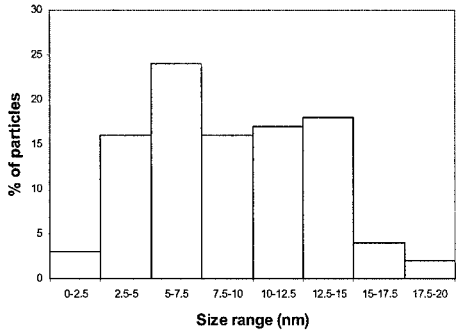


**Figure.2** Size distribution of Pb in glassy matrix

The magnetization vs temperature plots for both Pb embedded in Al-Cu-V metallic glass and Al matrices are shown in Fig. 3 and Fig.4 respectively measured at a field of 20 Oe. For comparison, measurements are also made on bulk samples of lead (see fig.3).

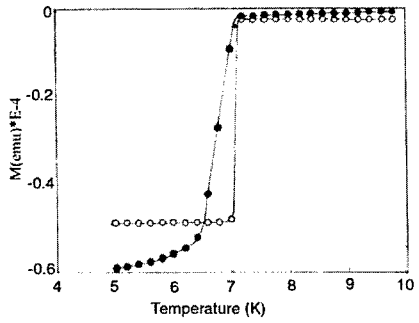


**Figure 3** Magnetization with temperature for $Al_{75}Cu_{15}V_{10}$-20wt%Pb measured with a field of 20Oe. Hollow circles represent data of bulk Pb and solid circles represent Pb in glassy matrix

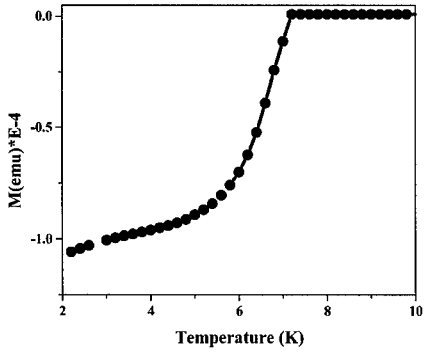


**Figure 4** Magnetization vs temperature for Al-6.5wt% Pb measured with a field of 20Oe

The transition in the bulk lead sample is sharp and the entire sample becomes superconducting at $T_c$- 7.2K.
The transition temperature of the nanodispersed lead in both the aluminium and glassy matrices occurs over a range of temperature and the magetization curve shows a sigmoidal behaviour. Fig.5 shows a typical cumulative size distribution plot obtained from the measurement of ~ 5000 particles for Pb dispersed in Al matrix. The optimum numbers of particles for measurements

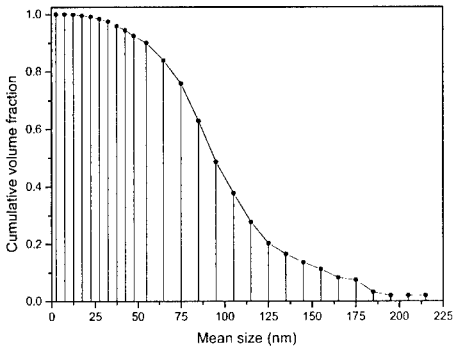


**Figure 5** Cumulative volume fraction starting from the larger particle which becomes superconducting first

were determined by ensuring that the nature of the cumulative plot does not change with increase in particle number. Assuming a spherical particle, it is possible to convert this to volume distribution of each size. The depression of the superconducting transition temperature occurs with decreasing particle size. Since, magnetization is expressed per unit volume, it is possible to map the two curves and obtain a relation between transition temperature and size. Fig.6 shows such a curve for Pb distributed in Al matrix. Fig.7 shows a comparative plot of Pb in Al and glassy $Al_{75}Cu_{15}V_{10}$ matrix.

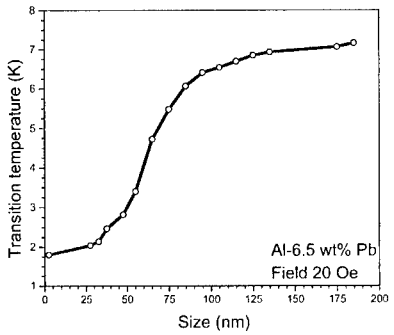


**Figure 6** Computed temperature vs size plot for Pb in Al matrix

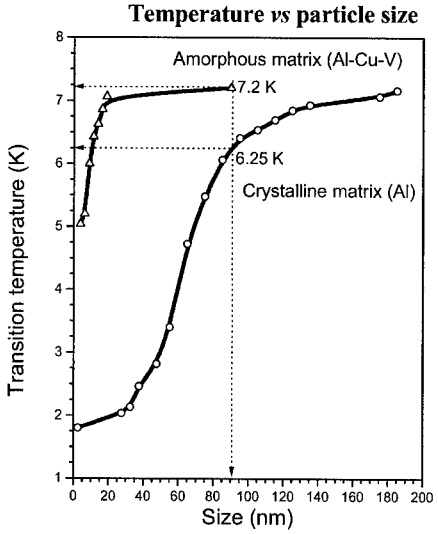


**Figure 7** Comparative transition temperature Vs size plot for Pb dispersed in Al and Al-Cu-V glassy matrix

## DISCUSSION

From our experiments, it is clear that the critical temperature of superconducting transition scales with size in a non-linear fashion. Compared to our earlier work with glassy matrix [9], the depression sets in much earlier when the particles are embedded in crystalline aluminium matrix. The effect of interface on superconductivity was studied earlier in the context of thin films [2,3,4]. These studies were conducted on evaporated layers of lead on copper and aluminium, and the layer packets produced by quench condensation at a substrate at 10K show a similar trend in transition temperature Vs thickness plot. The transition temperature of the lead layer falls rapidly as a function of thickness and drops rapidly when $D_{Pb} < 50$nm. From their plot, it is possible to extrapolate to a critical thickness of 10nm, when transition temperature approaches 1K. These results clearly revealed the depression of critical temperature as a function of film thickness. The essential difference between our situation and thin films lies in the nature of the confinement. In our case, the number of electrons in the system decreases significantly leading to discreteness of the energy levels [11]. Further, since the sizes of our particles in most cases are smaller than the coherence length in all directions, it can be considered as a zero dimensional superconductor. In such a case, the nature of the lattice of the embedding matrix is expected to play a significant role. This is clearly highlighted in the comparative plot in Fig.7. The depression in glassy matrix sets in at much smaller size range compared to the crystalline aluminium matrix. In principle, one should be able to correlate this difference with the penetration of Cooper pairs in the two normal embedding matrices. We are unable to estimate this at the present moment. We also note that $T_c$ for Pb particles having size equal to bulk coherence length is depressed for crystalline Al matrix whereas those in the glassy matrix at this size show bulk behaviour. Using the theory of superconductor of Anderson [12], Strongin et al [13] suggested the following expression for the relation between superconducting transition and energy level spacings for spherical granules:

$$\ln (T_c/T_{c0}) = \Sigma[2/(2m+1)]\times\{\tanh [ (\pi/2)((2m+1)2\pi k_b T_c/\varepsilon) ]-1\}$$

Here, $T_{c0}$ and $T_c$ is the transition temperature for the bulk and the small particles and $\varepsilon$ is the energy level spacing. According to this, for Pb, the superconductivity can be sustained up to a size of 2.2nm. In that case, both the curves in Fig. 7 should cut the y-axis at the same value. Within the experimental accuracy of our measurements, the trends of our curves seem to be different. This raises the need for more accurate experiments at small sizes. From the comparative plot it is shown that for the same size range the depression in Tc is much more for a crystalline matrix compared to the glassy matrix. Clearly, exchange of Cooper pairs and normal electrons across the interface is limited in glassy matrix compared to crystalline matrix. The data in both cases indicate a sigmoidal curve characteristic of Boltzmann distribution. It can be pointed out that the analysis of this behaviour is not possible with mean field BCS theory because of the finite number of electrons in each particle. This aspect has recently been discussed by Braun and Delft [14]. The analysis is not amenable at this stage to quantitative comparison with our experiments.

## CONCLUSION

We have established the size dependence of $T_c$ for Pb particles embedded in Al matrix. We have compared this result with that obtained for a metallic glass matrix. The results suggest a distinct difference in the behaviour of depression and indicate an important influence of the particle matrix interface in determining the depression of $T_c$.

## ACKNOWLEDGEMENT

The authors acknowledge STA, Japan and Department of Science and Technology, India for their financial support.

## REFERENCES

[1] Burton, E.F, J. O. Wilhelm and A.D. Misener: Trans. Roy. Soc. Canada, **29**(III), 5 (1934)
[2] P. Hilsch: Z. Phys. **167**, 511 (1962)
[3] G. Bergmann: Z. Phys, **187**,395 (1965)
[4] G.V. Minnigerode : Z. Phys. **192**, 379, (1966)
[5] B. Muhlschegel, D. J.Scalapino & R. Dutta, Phys.Rev.B, **6**, 5 (1972)
[6] K.A. Matven &A.I. Larkin, Phys. Rev. Letters, **78**, 19, 3749 (1997)
[7] F. Braun, J. v. Delft, D.C. Ralph & M. Tinkan, Phys. Rev. Letters, **79**, 5, 921 (1997)
[8] F. Braun& J. v. Delft, Phys Rev B, **59**,14,9527 (1999)
[9] A.P. Tsai, N. Chandrasekhar and K. Chattopadhyay, App. Phys. Lett. **75**, 11, 1527 (1999)
[10] K. Chattopadhyay, Mat. Sci. and Engg A, **226**, 1012 (1997)
[11] R. Kubo, J. Phys. Soc. Jpn **17**, 975 (1962)
[12] P. W. Anderson, J. Phys. Chem. Solids **11**, 26 (1959)
[13] M. Strongin, R. S. Thompson, O. F. Krammerer, and J. E. Crow, Phys. Rev. B **1**, 1078 (1970)
[14] F. Braun and J. v. Heft, Phys. Rev. letters, **81**, 21, 4721(1998)

Mat. Res. Soc. Symp. Proc. Vol. 703 © 2002 Materials Research Society V13.27

# Fabrication of Metal Nanostructures in Mesoporous Silicas

Kuei Jung Chao and Chia Min Yang
Department of Chemistry, National Tsinghua University
Hsinchu, 300, Taiwan

## ABSTRACT

Mesoporous silicas were used as hosts for fabrication of nanostructured metals. Due to the confinement effect, densely packed metal nanowire bundles and nano-networks or highly dispersed metal nanoparticles were prepared inside the channels of mesoporous silicas by metal incorporation/reduction processes. The structure of nanostructured metals was analyzed by TEM and PXRD, and the composition was investigated by ICP-AES, EDX and EELS.

## INTRODUCTION

Metal nanostructures have attracted growing interests recently, because of their unique physical and chemical properties of low dimensionality [1-3]. They could be synthesized within the confined space of a host material. For example, one-dimensional metal nanowire arrays have been synthesized in anodic alumina membrane with diameter of 13-100 nm [1-2,4-5]. To prepare metal nanostructures with even smaller size, ordered mesoporous silicas (*e.g.* MCM-41, MCM-48, SBA-15) with uniform pore diameters (1.5-30 nm) and tunable pore structures are considered to be promising hosts [6-8].

One advantage of mesoporous silica over other templates is the feasibility of modification of the pore walls to have desired properties [9-11]. In this report, we show that various metal nanostructures can be synthesized in the mesoporous silica hosts by following the process shown in figure 1. Preparations of various metal nanostructures including densely packed metal nanowire bundles and nano-networks or highly dispersed metal nanoparticles are demonstrated. Their structures as well as compositions were analyzed.

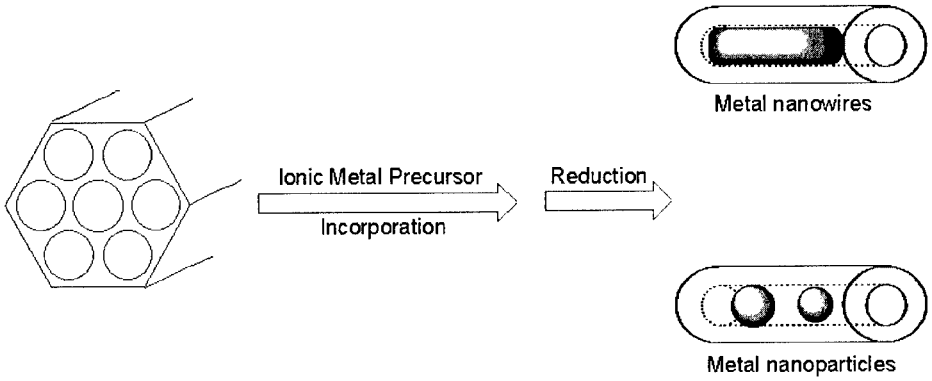


**Figure 1.** Schematic representation of fabrication of metal nanostructures in MCM-41.

## EXPERIMENTAL

Siliceous MCM-41 with one-dimensional channels and hexagonal symmetry as well as MCM-48 with bicontinuous channels and cubic symmetry were synthesized according to some known procedures [12-13]. The organic templates were removed by calcination at 813 K for 6 hours in airflow. Ionic metal precursors were incorporated on the intrachannel surface of calcined and modified mesoporous silica, and were then reduced to form metal/ silica composites in hydrogen flow at 373-573 K.

The pore diameter and the pore volume of calcined MCM-41 and MCM-48 were determined by Barrett-Joyner-Halenda (BJH) method from nitrogen sorption isotherm. The powder X-ray diffraction (PXRD) was performed to determine the structure and the periodicity of the pores in host silicas. The pore wall thickness can be deduced from the pore diameter in combination with PXRD analysis. The metal content in the reduced metal/silica composite was mainly determined by inductively coupled plasma (ICP) analysis. The peak widths of PXRD of nanostructured metals were used to estimate the average crystalline domain size of the metal in the composite by a spherical model and Scherrer's equation. The data was compared with the images from transmission electron microscope (TEM). Energy-dispersive X-ray (EDX) analysis as well as Electron energy loss spectroscopy (EELS) were also performed for compositional studies.

## RESULTS AND DISCUSSION

The Pt content of Pt/MCM-41 composite was ~40 wt% as determined by ICP analysis. The PXRD pattern of the composite indicates the existence of both the hexagonal structure of MCM-41 (small-angle region) and face-centered cubic structure of Pt metal (wide-angle region). Figure 2 shows the TEM images of the composite, which indicate that almost all the channels of MCM-41 were filled with Pt, resulting in densely packed Pt nanowire bundles with quasi-hexagonal symmetry. Few discrete Pt particles were found inside the MCM-41 due to the collapse and defects of MCM-41 formed during calcination. The diameters of Pt nanowires were uniform in size (2.1 nm), as determined by PXRD and TEM, smaller than the pore diameter of MCM-41 (2.4 nm). The lengths of Pt nanowires were several hundred nanometers in average as estimated from TEM images, occupying about 40-70% of the channel length of MCM-41as calculated from nitrogen sorption isotherm. The aspect ratio of these nanowires was generally over 100. EDX analysis of the nanowire region of Pt/MCM-41 composite revealed the Pt to Si ratio of 0.5, consisting with the result of ICP analysis. The TEM images of ultra-microtomed composites suggest that the Pt nanowires may have preferred direction of growth in the channels of MCM-41.

Alternatively, MCM-48 was used to incorporate Pt to form metal nano-networks. The

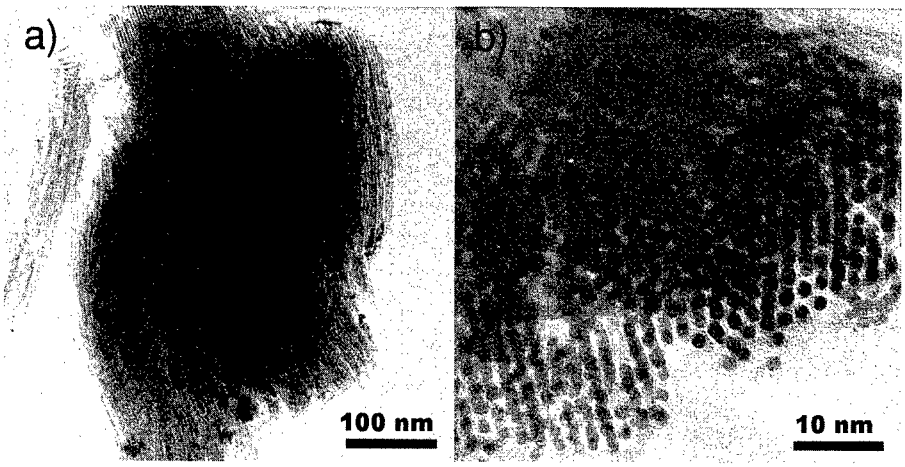


**Figure 2.** TEM images of Pt/MCM-41 composite perpendicular (a) and along (b) the hexagonal axis of MCM-41.

Pt/MCM-48 composite was filled in a capillary tube for PXRD measurements. Fig. 3a shows the PXRD ring pattern of the composite. Each diffraction ring of Pt is broad and weak in intensity, with no discernable diffraction spots in the rings. This suggests that most of Pt metals were small in size and stayed in the pores of MCM-48 after reduction. It may be due to the tortuous nature of the host MCM-48, preventing further ordered stacking in the confined space. The TEM image of Pt/MCM-48 (figure 3b) shows that all MCM-48 particles were filled with Pt metals, and the Pt nano-networks were densely packed inside the host MCM-48. The images of Pt nano-networks reflect the structure of the pore system of MCM-48 (inset of figure 3b) with Ia3d symmetry. EDX analysis revealed Pt to Si ratio similar with that of Pt/MCM-41. Because the channels of MCM-48 are bicontinuous and connected, unsupported Pt nanowire networks could be obtained after removal of the silica template by HF solution.

The same protocol can also be used to prepare other metal nanostructures. For example, palladium nanowires bundles in MCM-41 as well as gold nano-networks in MCM-48 can be prepared. In addition, our strategy to fabricate densely packed metal nanostructures can be applied to synthesize metal nanoparticles in mesoporous silicas. Uniform sized and highly dispersed Pt nanoparticles were formed in the channels of MCM-41 by controlling the loading amount of metal precursors. The Pt loading was determined by ICP analysis to be 3-11 wt%, depending on the metal loading. The supported and uniform Pt nanoparticles in MCM-41 with controlled metal loading and morphology may be useful in catalysis. By *in-situ* TEM

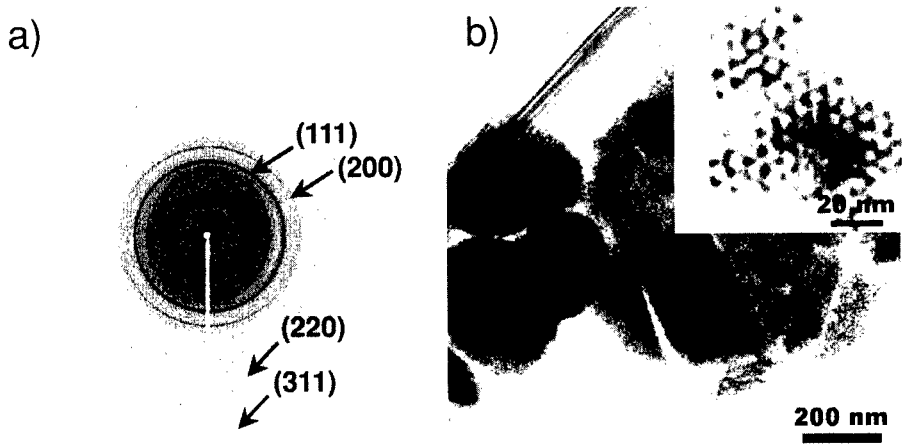


**Figure 3.** (a) PXRD ring pattern of Pt/MCM-48 composite. (b) TEM image of ultramicrotomed Pt/MCM-48 composite. The inset shows the thin edge of the composite.

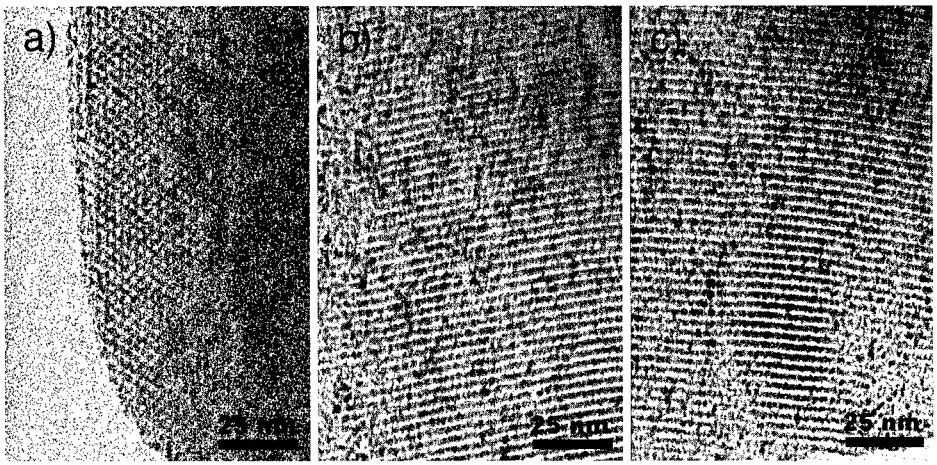


**Figure 4.** *In-situ* TEM images of Pt/MCM-41 composite at room temperature (a), 200℃ (b) and 600℃ (c).

investigation under 10 mbar hydrogen atmosphere, Pt nanoparticles formed after hydrogen reduction at 200℃ were found to be extremely stable in the confined channels. No relative movements to the host silica were observed even after heating to 600℃ (figure 4). EELS analysis showed the existence of platinum as well as trace of carbon in the composite. The unusual thermal stability of Pt nanoparticles in MCM-41 may be attributed to the host confinement effect as well as the interaction of Pt with the silica walls.

## CONCLUSIONS

In summary, the formation of metal nanostructures in mesoporous silicas has been demonstrated. The structural analyses confirm the nanocrystalline nature of the densely packed metal wire bundles and networks as well as highly dispersed metal particles. Highly dispersed Pt nanoparticles were found to have very good thermal stability inside the confined space of MCM-41.

## ACKNOWLEDGEMENTS

We wish to thank the assistance of Dr. H. S. Sheu at Synchrotron Radiation Research Center, Hsinchu, Taiwan in XRD measurements, and Dr. S. Helveg and Dr. P. L. Hansen at Haldor Topsøe A/S, Lyngby, Denmark in *in-situ* TEM investigations.

## REFERENCES

1. T. M. Whitney, J. S. Jiang, P. C. Searson, C. L. Chien, *Science* **261**, 1316 (1993).
2. Z. Zhang, J. Y. Ying, M. S. Dresselhaus, *J. Mater. Res.* **13**, 1745 (1998).
3. M. Sasaki, M. Osada, N. Sugimoto, S. Inagaki, Y. Fukushima, A. Fukuoka, M. Ichikawa, *Microporous Mesoporous Mater.* **21**, 597 (1998).
4. C. R. Martin, *Science*, **266**, 1961 (1994).
5. B. R. Martin, D. J. Dermody, B. D. Reiss, M. Fang, L. A. Lyon, M. J. Natan, T. E. Mallouk, *Adv. Mater.* **11**, 1021 (1999).
6. C. T. Kresge, M. E. Leonowicz, W. J. Roth, J. C. Vartuli, J. S. Beck, *Nature* **359**, 710 (1992).
7. Q. Huo, D. I. Margolese, U. Ciesla, P. Feng, T. E. Gier, P. Sieger, R. Leon, P. M. Petroff, F. Schüth, G. D. Stucky, *Nature* **368**, 317 (1994).
8. D. Zhao, J. Feng, Q. Huo, N. Melosh, G. H. Fredrickson, B. F. Chmelka, G. D. Stucky, *Science* **279**, 548 (1998).
9. Y. Shin, J. Liu, L. Q. Wang, Z. Nie, W. D. Samuels, G. E. Fryxell, G. J. Exarhos, *Angew. Chem. Int. Ed.* **39**, 2702 (2000).
10. H. Fan, Y. Lu, A. Stump, S. T. Reed, T. Baer, R. Schunk, V. Perez-Luna, G. P. López, C. J. Brinker, *Nature* **405**, 56 (2000).
11. A. Stein, B. J. Melde, R. C. Schroden, *Adv. Mater.* **12**, 1403 (2000).
12. Q. Cai, W. Y. Lin, F. S. Xiao, W. Q. Pang, X. H. Chen, B. S. Zou, *Microporous Mesoporous Mater.* **32**, 1 (1999).
13. R. Ryoo, S. H. Joo, J. M. Kim, *J. Phys. Chem. B* **103**, 7435 (1999).

Mat. Res. Soc. Symp. Proc. Vol. 703 © 2002 Materials Research Society V13.32

# Synthesis of Epoxy and Block Oligomer Modified Clay Nanocomposite

Kang Hung Chen and Sze Ming Yang*
Department of Chemical and Material Engineering, National Central University, Chung-Li, Taiwan 320. *To whom all correspondence should be addressed.

## ABSTRACT

Acrylic triblock ($A_xM_yB_z$) and diblock ($M_yB_z$) oligomers containing methyl methacrylate (MMA, M), methacrylic acid (MAA, A) and dimethylaminoethyl methacrylate (DMAEMA, B) groups are intercalated into the layers of montmorillonite. The results indicate that the block oligomer lay flatly between the clay layers. ICP analyses of $Na^+$ content indicate no unexchanged sodium ions are left in the intercalated clay.

Nanocomposites of epoxy and clay modified with block oligomers were synthesized. Glass transition temperature ($T_g$) of the nanocomposite is 129.6°C ($M_{18}B_{24}^{24+}$ modified clay) compared to 84.1°C for the physical mixture of epoxy and unmodified clay. $T_g$ increases with decreasing amount of modified clay. When modified clay content are below 2 phr, $T_g$ higher than 131.7 °C can be obtained. Water resistance and light transmittance of the nanocomposite is also improved over composite of epoxy and unmodified clay.

## INTRODUCTION

Clay or other inorganic materials have been added into polymer as fillers in order to improve the properties of the polymer such as dimensional stability, conductivity, mechanical, thermal and other potential properties.[1,2]. The intercalation of modified ions into the layers affects the exfoilation of the clay layer in the composite. Lan and Pinnavaia reported the enlargement of d-spacing to 18.0 Å by intercalation of onium ions [3,4]. The largest d-spacing of modified montmorillonite reaches 20.27 Å [5]. It is interesting to understand the intercalation of the clay such as montmorillonite. Acrylic block oligomers were synthesized in different chain length, hydrophobicity, sequence and charge density. Onium ions such as $[H_3N(CH_2)_{n-1}COOH]^+$, $[H_3N(CH_2)_{n-1}CH_3]^+$, $[H_3N(CH_2)_nNH_2]^+$ and $[H_3N(CH_2)_nNH_3]^{2+}$ were reported to be intercalated into the clay layers. When n>17, the compounds become too hydrophobic to be soluble enough in water. In contrast, the acrylic oligomers are soluble in water even when the atomic weight is about 7,000 Da. With these advantages, we used acrylic block oligomers as the exchanged ions to be intercalate in the layers of montmorillonite and study the effects of electron charge, charge density, hydrophobicity and block sequence on intercalation. Nanocomposites of epoxy and

acrylic block oligomers intercalated montmorillonite were synthesized. The properties of the nanocomposites including $T_g$, water resistance and light transmittance are also reported.

## EXPERIMENTAL

### Materials

$Na^+$-montmorillonite with an exchange capacity of 145 mequiv/100g (CWC) was obtained from Nanocor Inc. $Na^+$-montmorillonite with an exchange capacity of 96 mequiv/100g (CL-42) was donated by Pai Kong Ceramic Materials Co. LTD. All block copolymers were provided by Prof. Hui Chen of Department of Chemical and Material Engineering, National Central University, Taiwan.

### Intercalation of clay with oligomers

The protonated forms of block oligomers were formed by dissolving 5 mmole of the block oligomers in 400 ml of 0.01 N aqueous HCl solution at 60 ℃. The solution was adjusted to 500 ml and pH 2 with 1N HCl and deionized water. Five grams of clay was thoroughly dispersed in the solution of protonated block oligomer at 60 ℃ for three hours. Montmorillonite was separated by centrifugation and washed with deionized water.

### Synthesis of epoxy-montmorillonite nanocomposite

Intercalated clay was added with stirring to diglycidyl ether of bisphenol A and cured by addition of either nadic methyl anhydride and benzyldimethylamine. The amount of curing agent used for each formulation was as follows: 87.5 phr (per hundred epoxy resin) of NMA and 5phr of BDMA. All samples were cured at 80 ℃ for 1 hr,100 ℃ for 1 hr, 120 ℃ for 1 hr , 150 ℃ for 6 hr, and 200 ℃ for 1 hr.

## RESULTS AND DISCUSSION

### The effect of block oligomer structure on intercalation of montmorillonite

### Charge and charge density

In medium of pH 10, $A_{12}M_{12}B_{12}$ is negatively charged, and in medium of pH 2, $A_{12}M_{12}B_{12}$ is positively charged. Results in table 1 show that only cations can be intercalated into the clay layers. The influence of charge density on intercalation were also shown in table2. D-spacings of montmorillonite intercalated with MB diblock oligomers of different charge densities ($M_{18}B_n$, n=3, 18, 24, 36) are almost the same. The electrostatic interaction between MB oligomers and layer surface are too strong to yield distinct difference in d-spacing.

**Table 1**. D-spacings of various modified montmorillonites.

| Gallery cation | pH | Charge | D-spacing(Å) |
|---|---|---|---|
| $A_{12}\ M_{12}B_{12}$ | 10 | -12 | 14.5 |
| $A_{12}\ M_{12}B_{12}$ | 2 | +12 | 19.7 |
| $H^+$(0.01N) | 2 | +1 | 15.0 |
| $Na^+$(CL-42-mont.) | --- | +1 | 12.5 |

**Hydrophobicity**

The hydrophobicity of the block oligomers increases in the following order : $A_{12}M_{12}B_{12}$ > $A_{12}M_8B_{12}$ > $A_{12}M_4B_{12}$. These are confirmed by the magnitude of partition coefficient determined. According to the results in table 2, there is no relationship between d-spacing of oligomer intercalated montmorillonite and hydrophobicity of intercalated oligomer. This result further evidence that the electrostatic interaction between the positive charges of oligomers and the negative charges of the clay layers is the most important factor for intercalation.

**Table 2**. Partition coefficients of block oligomers and d-spacings of block oligomers modified montmorillonites.

| Gallery cation | Charge | D-spacing(Å) | Partition coefficient(K)* |
|---|---|---|---|
| $M_{18}\ B_3$ | +3 | 19.9 | >>1.74 |
| $M_{18}\ B_{18}$ | +18 | 19.4 | 0.69 |
| $M_{18}\ B_{24}$ | +24 | 19.9 | 0.54 |
| $M_{18}\ B_{36}$ | +36 | 19.6 | 0.41 |
| $A_{12}M_4\ B_{12}$ | +12 | 20.8 | 0.65 |
| $A_{12}M_8\ B_{12}$ | +12 | 19.1 | 0.74 |
| $A_{12}M_{12}\ B_{12}$ | +12 | 19.7 | 1.74 |

*measured in media of pH=2.

**Block sequence**

Comparison of $M_{18}B_{18}$ with different block sequence $B_9M_{18}B_9$ are shown in table 3. The oligomers showed the same molecular weight (chain length ) and charges, the change of d-spacing was caused by different block sequence. D-spacing of the $B_9M_{18}B_9^{+18}$ intercalated montmorillonite is slightly smaller than that of $M_{18}B_{18}^{+18}$ intercalated montmorillonite. This result was due to the montmorillonite is pinned at $B_9M_{18}B_9$'s two ends between layer surfaces.

**Table 3.** D-spacings and displaced percentage of $Na^+$ for $M_{18}B_{18}$ and $B_9M_{18}B_9$ modified montmorillonites.

| Gallery cation | Charge | D-spacing(Å) | Displaced $Na^+$(%) |
|---|---|---|---|
| $M_{18}\ B_{18}$ | +18 | 19.4 | 99.1±0.04 |
| $B_9M_{18}B_9$ | +18 | 19.2 | 99.4±0.03 |

**Synthesis and properties of epoxy and block oligomer modified clay nanocomposite**

TEM photographs of epoxy and modified nanocomposite are shown in fig. 1. The results indicate that the distance between clay layers in epoxy and $M_{18}B_{24}^{-24}$ modified montmorillonite (CL42) composite are larger than 200Å. The delamination of $M_{18}B_{24}^{+24}$—montmorillonite in epoxy matrix was observed.

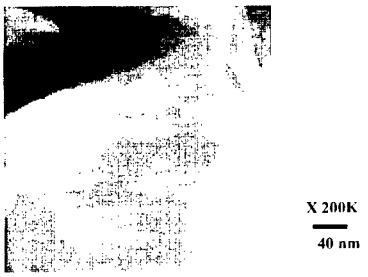


**Figure 1**. TEM photograph of nanocomposite of epoxy and $M_{18}B_{24}^{-24}$-montmorillonite(CL42).

**Glass transition temperature**

DSC results in fig. 2 showed that $T_g$ of nanocomposite formed from epoxy and modified clay(129.6 ℃) is 45.5 ℃ higher than that of composite formed from epoxy and unmodified clay(84.1 ℃). The modification of the hydrophilic montmorillonite layer surface to more hydrophobic is the main factor for the higher $T_g$ in epoxy/modified clay system. The interaction of epoxy polymer with more hydrophobic montmorillonite surface is stronger than hydrophilic montmorillonite surface, hence restrict epoxy chain movement.

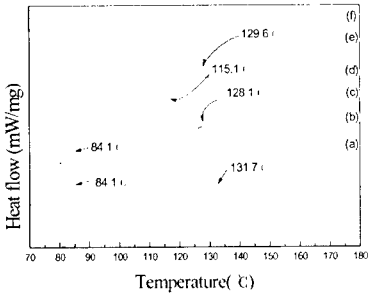


**Figure 2**. DSC curves for the $T_g$ of composites of epoxy and modified montmorillonites(CL42, 5phr). (a)Without addition of clay, (b)$Na^+$-mont(pristine), (c) $A_{12}M_8B_{12}^{12}$-mont, (d) $A_{12}M_{12}B_{12}^{+12}$-mont, (e) $M_{18}B_{18}^{+18}$-mont, (f) $M_{18}B_{24}^{-24}$-mont.

**Water resistance**

Fig. 3 shows that the water content of $M_{18}B_{24}^{+24}$-montmorillonite-epoxy nanocomposite is lower than pure epoxy after soaking in water. The results show that $M_{18}B_{24}^{+24}$-montmorillonite in nanocomposite decrease water permeability. Water resistance was strongly depends on the delamination of clay within an epoxy resin by increasing the permeant trace of water in epoxy resin. The modification by $M_{18}B_{24}^{+24}$ change the clay surface to be more hydrophobic, because the $M_{18}$ blocks of the oligomer are more hydrophobic group.

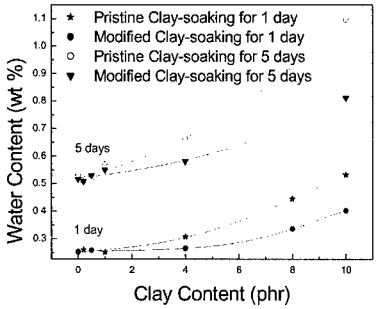


**Figure 3**. Water content of composite of epoxy and pristine or modified clay with various clay loadings after soaking in deionized water(23 ℃) for one day and five days.

**Light transmittance**

The variation of light transmittance of nanocomposite with modified clay content is shown in fig. 4. The nanocomposites with modified clay show better transmittance than that with unmodified clay.

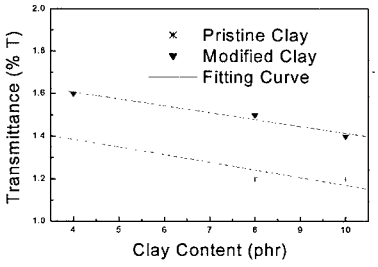


**Figure 4**. The transmittance of visible light at 550nm for composites of epoxy and modified clay ($M_{18}B_{24}^{+24}$--montmorillonite) and pristine clay($Na^{+}$--montmorillonite).

## CONCLUSIONS

The d-spacings of block oligomers modified montmorillonites are not affected by chain length of the block, hydrophobicity and charge density of the oligomers. Unlike previous experimental investigations on onium ions, the interlayer spacing depends on the chain length, functional group and charge number of alkylammonium ion. It indicates that all block oligomers lie flat in the interlayer spacing.

TEM photographs show that exfoliation of block oligomer modified clay layers in epoxy resin. The distances between clay layers are larger than 20nm. Nanocomposites of epoxy and modified clay are formed. Improvements for water resistance and transmittance of light are observed for nanocomposites. DSC results showed that the Tg of epoxy composite with modified clay(129.6 ℃) is 45.5 ℃ higher than the epoxy composite with unmodified clay(84.1 ℃). When clay content ($[B_{24}M_{18}]^{+24}$—montmorillonite(CL42) ) is lower than 2 phr, $T_g$ higher than 131.7 ℃ is obtained.

## ACKNOWLEDGE

The authors thank Dr. T. Y. Tsai of Industrial Technology Research Institute to provide the clay and valuable discussions. The authors acknowledge M. S. Lin and Prof. H. Chen in National Central University for the synthesis of the block oligomers.

## REFERENCES

1. R. A. Vaia, H. Ishii and E. P. Giannelis, Chem. Mater. **5**, 1694 (1993).
2. P. B. Messersmith and E. P. Giannelis, Chem. Mater. **6**, 1719 (1994).
3. T. Lan and T. J. Pinnavaia, Chem. Mater. **6**, 2216 (1994).
4. T.Lan, D. Kaviratna and T. J. Pinnavaia, J. Phys. Chem. Solids. **57,** 1005 (1996).
5. P. Capkova , R. A. J. Driessen, M. Numan, H. Schenk, Z. Weiss and Z. Klika, Chem Pap-Chem Zvesti **52**, 1 (1998).
6. H. L. Chen, S. F. Wang and T. L. Lin, Macromolecules **31**, 8924 (1998).
7. C. S. Tsao, T. L. Lin and M. S. Yu, Physica B **271**, 322 (1999).
8. C. S. Patrickios, PhD. Thesis, Massachusetts Institute of Technology, 1994.

Mat. Res. Soc. Symp. Proc. Vol. 703 © 2002 Materials Research Society V13.36

# Doping and Electrochemical Capacitance of Carbon Nanotube-Polypyrrole Composite Films

Mark Hughes, George Z. Chen, Milo S. P. Shaffer, Derek J. Fray and Alan H. Windle
Department of Materials Science and Metallurgy, University of Cambridge, Pembroke Street, Cambridge CB2 3QZ, UK.

## ABSTRACT

Composite films were electrochemically synthesised via the simultaneous deposition of multiwalled nanotubes and polypyrrole, a conducting polymer. Negatively charged functional groups attached to the surface of the acid treated nanotubes enables the tubes to act as a dopant for the PPy in these films. Scanning electron microscopy, cyclic voltammetry and electrochemical impedance spectroscopy revealed that the nano-porous three-dimensional arrangement of PPy coated MWNTs in these films produced specific capacitances per mass and geometric area as high as 192 F $g^{-1}$ and 1.0 F $cm^{-2}$, respectively. This value of specific capacitance per geometric area exceeds that of both component materials and other carbon nanotube-conducting polymer composites. The composite films described in this report were also able to charge and discharge more than an order of magnitude faster than similarly prepared pure PPy films. The nano-porosity and small diffusion distances within the composite films, crucial to achieving the superior capacitive performance, were found to be dependent on the concentration of nanotubes and additional dopant anions in the polymerisation electrolyte, offering possibilities for tailoring of the composite structure.

## INTRODUCTION

Growing demands in industries such as transport and communication for electrical energy storage devices that can deliver high power level pulses have prompted considerable interest in electrochemical capacitors, or supercapacitors. While carbon nanotubes and conducting polymers have separately received considerable attention as supercapacitive materials, only recently has the capacitive performance of composites made by combining these two materials been reported, revealing capacitances greater than that of either component material.[1-4] Composites of carbon nanotubes and conducting polymers such as polypyrrole, polyaniline and poly(p-phenylene vinylene) can be grown by simply mixing the polymer and nanotubes,[5-7] or using a variety of chemical[8,9] and electrochemical[4,10-12] polymerisation techniques. The superior supercapacitive performance of carbon nanotube-conducting polymer composites is attributed to their nano-porous structure which combines the three-dimension charge storage capabilities of redox active conducting polymers, with the high surface area and electrical conductivity of carbon nanotubes. Here we report the supercapacitive properties of a particular carbon nanotube-polypyrrole composite in which the conducting polymer is doped by the embedded nanotubes.

## EXPERIMENTAL DETAILS

Multi-walled carbon nanotubes (MWNTs) and polypyrrole (PPy) were simultaneously deposited onto a graphite disk working electrode (0.33 $cm^2$) using an oxidising potential of 0.7 V measured against a saturated calomel reference electrode (SCE) in a three electrode, single

compartment cell.[1,10] The aqueous polymerisation electrolyte generally consisted of 0.5 M pyrrole monomer and 0.025 wt% to 0.4 wt% MWNTs (supplied by Hyperion). The MWNTs (outer tube diameter ~ 10 nm; tube lengths from 0.2 μm to 2.5 μm) were suspended in solution using a previously described acid treatment process which attaches hydroxyl, carbonyl and carboxylic groups to the tube surface, giving the MWNTs a net negative charge and enabling them to act as both a supporting electrolyte during polymerisation, and as a dopant in the PPy deposited on the working electrode.[1,10,13] The effect of adding additional dopants such as chloride ions and dodecyl sulphate ions to the polymerisation electrolyte in 0.01 M concentrations was also examined to determine the structural and electrochemical implications of using competing dopants in MWNT-PPy composites.

Once formed, composite films of various film-formation charges (a measure of the amount of film grown) were compared to similarly prepared pure PPy films ($Cl^-$ doped) using cyclic voltammetry (CV) and electrochemical impedance spectroscopy (EIS) in an aqueous 0.5 M KCl electrolyte at potentials between –0.8 and 0.5 V vs. SCE. CV analysis was performed on a model 273A EG&G Princeton Applied Research potentiostat and EIS studies were conducted using a Solartron 1260 impedance/gain-phase analyser coupled with a Solartron 1287 electrochemical interface employing a sine-wave amplitude of 10 mV and a frequency range of $5 \times 10^5$ Hz to $1 \times 10^{-2}$ Hz.

## RESULTS AND DISCUSSION

Figures 1 and 2 compare the CV and EIS results of MWNT-PPy composite films (aqueous polymerisation electrolyte: 0.5 M pyrrole and 0.4 wt% MWNTs) with similarly prepared pure PPy films (aqueous polymerisation electrolyte: 0.5 M pyrrole and 0.5 M KCl). The cyclic voltammograms (Figure 1a) indicate several important differences between the two films. The first of these is that the peak potentials of the composite film are about 200 mV more negative than those of the pure PPy film, confirming the anionic dopant role of the MWNTs.[1,10] The second point is that the output current of the composite film is about twice that of the pure polymer. Since capacitance is given by the output current divided by the scan rate, this implies that the capacitance of the composite films is about double that of the pure polymer.

The impedance plot shown in Figure 1b can be divided into a high frequency component (inclined at about 45°) and a low frequency component (near vertical). The projected length of the high frequency Warburg-type line on the real axis (Z') characterises the slow ion migration process in the solution pores and is equal to one third the film's ionic resistance.[14] The composite and pure PPy films shown in Figure 1b had ionic resistances of 0.8 Ω and 8.2 Ω, respectively, indicating a lower barrier to ionic transport in the composite film. The superior ionic transfer of the composite films is even more exaggerated at bias potentials lower than 0.4 V.

The low frequency capacitance ($C_{lf}$) of the films produced was determined from the slope of a plot of the imaginary component of impedance (Z") at low frequency, versus the inverse of frequency ($f$) using the equation $C_{lf} = (2\pi f Z'')^{-1}$. Specific capacitances per mass and geometric area as high as 192 F $g^{-1}$ and 1.0 F $cm^{-2}$, respectively were observed for the MWNT-PPy composite films. While the capacitance per mass of composite film is quite high, it is the capacitance per area of deposition surface that draws the most interest. This value is significantly larger than that reported for supercapacitors based on conducting polymers, carbon nanotubes or other carbon nanotube-conducting polymer composites.[2-4,15]

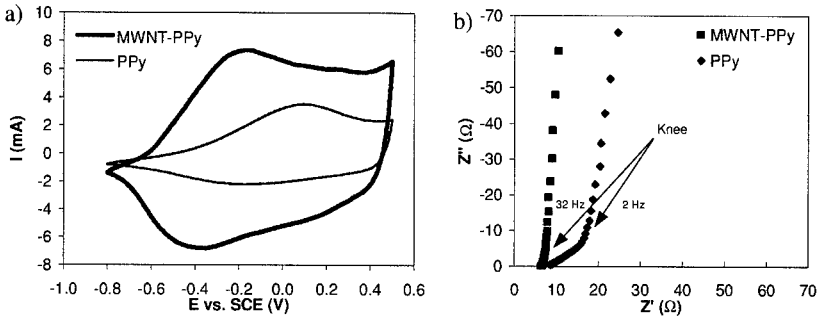


Figure 1. Comparison of MWNT-PPy composite films and pure PPy films prepared using similar conditions: a) cyclic voltammograms (film-formation charge: 1.8 C $cm^{-2}$, scan rate: 50 mV $s^{-1}$, electrolyte: 0.5 M KCl); b) complex plane impedance plots (film-formation charge: 1.0 C $cm^{-2}$, bias potential: 0.4 V vs. SCE, electrolyte: 0.5 M KCl).

Figure 2a shows how the low-frequency capacitance of the composite and pure PPy films increased with the film-formation charge. While the thickness of the composite and pure PPy films was found to increase approximately linearly with film-formation charge as expected[16] with slopes of $3.5 \times 10^{-4}$ $cm^3$ $C^{-1}$ and $1.8 \times 10^{-4}$ $cm^3$ $C^{-1}$, respectively, their capacitance deviated from its initially linear relationship for large film-formation charges (Figure 2a). This deviation is attributed to limited electrolyte access at the lower levels of thick films. As a result, ion diffusion is not able to reach all the available PPy within the time frame of the capacitive measurements, thereby restricting the amount of material that can contribute to the measured capacitance, causing it to approach an upper limit with increasing film-formation charge.

The linear regions of the capacitance versus film-formation charge plots (Figure 2a) show that for a given charge, the composite film had a capacitance that was about double that of pure PPy, supporting the capacitive results obtained from the cyclic voltammograms. The slope ($C/Q$) of these linear regions gives an indication as to the proportion of film that contributes to the capacitive performance. The superior slope of the composite films implies that more of the PPy in the film is able to access ionic charge from solution and hence contribute to the measured capacitance. The larger limiting value of capacitance apparent for the composite films indicates that their improved performance for a given polymerisation charge is not simply a result of an increase in polymerisation efficiency, which would result in the deposition of more polymer for a given polymerisation charge, relative to the pure PPy films.

The point that divides the high frequency component of the complex plane impedance plot from the low frequency component is referred to as the knee frequency[17] (Figure 1b). The knee frequency indicates the maximum frequency at which predominantly capacitive behaviour can be maintained and was more than an order of magnitude higher for the MWNT-PPy composite films than pure PPy films (Figure 2b). For low film-formation charges the knee frequency of the composite supercapacitors was as high as 200 Hz, however, as the film-formation charge was increased the knee frequency decreased rapidly as shown in Figure 2b. This performance limitation is a common phenomenon for devices based on conducting polymers and is simply related to the reduction in electrolyte access and increase in diffusion distance with film thickness.[18]

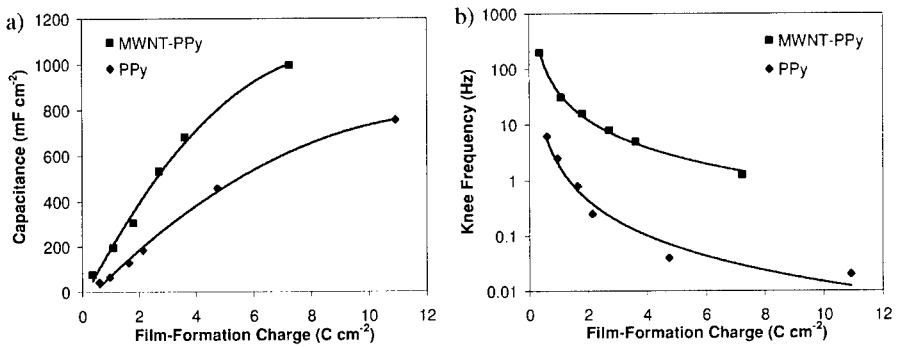


Figure 2. The relationship between film-formation charge and: a) low-frequency capacitance; b) knee frequency, for MWNT-PPy films and similarly prepared pure PPy films.

When dopant anions such as chloride ions and dodecyl sulphate ions were added to the polymerisation electrolyte, the porosity of the composite structures produced was significantly reduced as shown in Figure 3. These additional dopant ions facilitate PPy deposition in regions other than the negatively charged MWNT surfaces, enabling the PPy to fill inter-tubular voids, thereby reducing the size and number of nano-pores or eliminate them entirely. This blocking occurred both for chloride ions which are able to diffuse in and out of the PPy in response to redox cycling, and for large dodecyl sulphate ions which remain embedded in the PPy during redox cycling, necessitating the intercalation of charge balancing cations from solution. The decrease in electrolyte access and increase in diffusion distances associated with reduced nano-porosity lowered the film's capacitance by about 30% when chloride ions were added and more than 50% (to about that of pure PPy) when dodecyl sulphate ions were used, clearly illustrating the importance of the three-dimension network of nano-pores for low frequency capacitance. Additions of chloride ions and dodecyl sulphate ions were also observed to decrease the knee frequency by about 30 %. It is interesting to note that even thought the nano-pores were almost completely filled for films grown with added dodecyl sulphate, the knee frequency was still greater than that of pure PPy films, indicative of the improved ionic and electrical conductivity observed in the composite films relative to pure PPy films, particularly for low bias potentials.

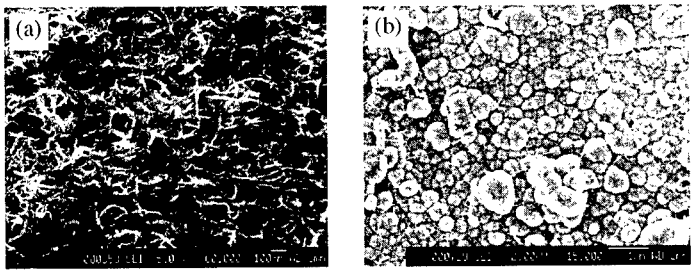


Figure 3. SEM images showing the reduction in porosity observed when using anionic dopants in addition to negatively charged MWNTs (film-formation charge: 1.8 C $cm^{-2}$): a) mobile chloride ions; b) embedded dodecyl sulphate ions.

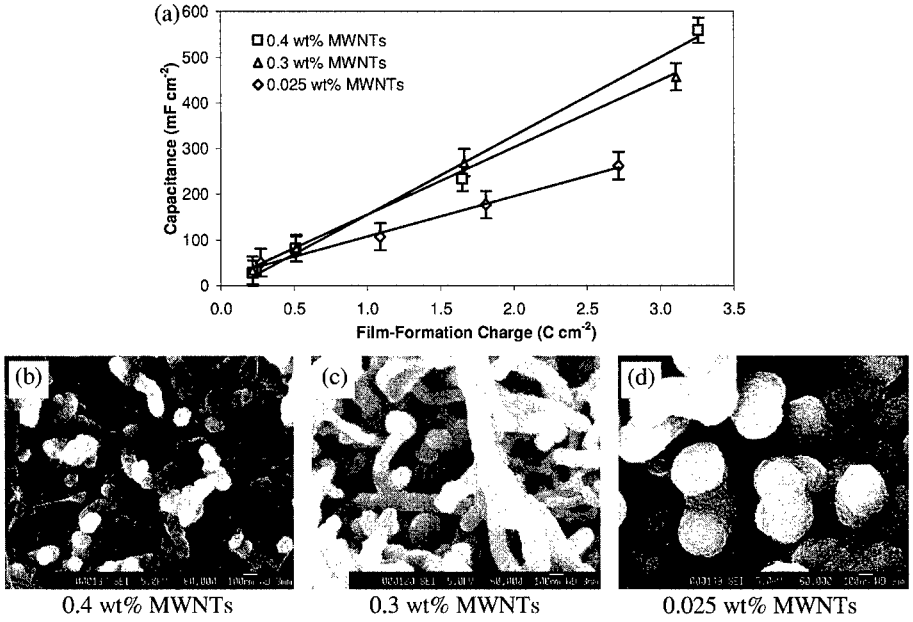


Figure 4. The effect of MWNT concentration in the polymerisation electrolyte on (a) specific capacitance (EIS electrolyte: 0.5 M KCl) and PPy coating thickness (film-formation charge < 1.8 C $cm^{-2}$): (b) 40 nm for 0.4 wt% MWNTs; (c) 60 nm for 0.3 wt% MWNTs and (d) 160 nm for 0.025 wt%.

Figure 4 shows that as the concentration of MWNTs in the polymerisation electrolyte was decreased from 0.4 wt% to 0.025 wt%, while keeping the other growth conditions constant, the thickness of PPy coated onto each nanotube increased approximately linearly from 40 nm to 160 nm. As expected, the increase in PPy thickness, and hence diffusion distance, with decreasing MWNT concentration in the polymerisation electrolyte was associated with a reduction in specific capacitance for a given film-formation charge (Figure 4a). The relationship between polymer coating thickness and specific capacitance was also approximately linear and further illustrates the importance of reduced diffusion distances in the nano-porous structure.

## CONCLUSIONS

The nano-porous composites of negatively charged MWNTs and PPy produced in this report were capable of achieving specific capacitances per mass and geometric area as high as 192 F $g^{-1}$ and 1.0 F $cm^{-2}$, respectively. This value is about double that of similarly prepared pure PPy films and is accompanied by more than an order of magnitude improvement in the rate of response relative to the pure polymer. These improvements represent a significant step towards fabrication of commercially applicable electrode materials. The superior capacitive performance of these films is closely linked with their nano-porosity and small diffusion lengths, properties that are

promoted by using high MWNT concentrations in the polymerisation electrolyte. Conversely, these structural aspects can be diminished by the introduction of additional doping anions, such as chloride and dodecyl sulphate ions. While the use of additional dopants to produce fully solid films may not be desirable for capacitor applications, these structures may find use in other devices, such as actuators, where excessive porosity may detract from the magnitude of response.

## REFERENCES


[1] M. Hughes, G. Z. Chen, M. S. P. Shaffer, D. J. Fray, A. H. Windle, *Chem. Mater.* Accepted.

[2] K. Jurewicz, S. Delpeux, V. Bertagna, F. Beguin, E. Frackowiak, *Chem. Phys. Lett.* **347**, 36, (2001).

[3] E. Frackowiak, K. Jurewicz, S. Delpeux, F. Beguin, *J. Power Sources* **97-8**, 822, (2001).

[4] C. Downs, J. Nugent, P. M. Ajayan, D. J. Duquette, S. V. Santhanam, *Adv. Mater.* **11**, 1028, (1999).

[5] J. N. Coleman, S. Curran, A. B. Dalton, A. P. Davey, B. McCarthy, W. Blau, R. C. Barklie, *Phys. Rev. B* **58**, R7492, (1998).

[6] S. A. Curran, P. M. Ajayan, W. J. Blau, D. L. Carroll, J. N. Coleman, A. B. Dalton, A. P. Davey, A. Drury, B. McCarthy, S. Maier, A. Strevens, *Adv. Mater.* **10**, 1091, (1998).

[7] K. Yoshino, H. Kajii, H. Araki, T. Sonoda, H. Take, S. Lee, *Fullerene Sci. Technol.* **7**, 695, (1999).

[8] J. H. Fan, M. X. Wan, D. B. Zhu, B. H. Chang, Z. W. Pan, S. S. Xe, *J. Appl. Polym. Sci.* **74**, 2605, (1999).

[9] E. Frackowiak, F. Beguin, *Carbon* **39**, 937, (2001).

[10] G. Z. Chen, M. S. P. Shaffer, D. Coleby, G. Dixon, W. Z. Zhou, D. J. Fray, A. H. Windle, *Adv. Mater.* **12**, 522, (2000).

[11] M. Gao, S. M. Huang, L. M. Dai, G. Wallace, R. P. Gao, Z. L. Wang, *Angew. Chem.-Int. Edit.* **39**, 3664, (2000).

[12] J. H. Chen, Z. P. Huang, D. Z. Wang, S. X. Yang, J. G. Wen, Z. R. Ren, *Appl. Phys. A-Mater. Sci. Process.* **73**, 129, (2001).

[13] M. S. P. Shaffer, X. Fan, A. H. Windle, *Carbon* **36**, 1603, (1998).

[14] W. J. Albery, Z. Chen, B. R. Horrocks, A. R. Mount, P. J. Wilson, D. Bloor, A. T. Monkman, C. M. Elliott, *Faraday Discuss.* **88**, 247, (1989).

[15] M. Mastragostino, C. Arbizzani, R. Paraventi, A. Zanelli, *J. Electrochem. Soc.* **147**, 407, (2000).

[16] E. Smela, M. Kallenbach, J. Holdenried, *J. Microelectromech. Syst.* **8**, 373, (1999).

[17] C. M. Niu, E. K. Sichel, R. Hoch, D. Moy, H. Tennent, *Appl. Phys. Lett.* **70**, 1480, (1997).

[18] A. DellaSanta, D. DeRossi, A. Mazzoldi, *Synthetic Met.* **90**, 93, (1997).

Mat. Res. Soc. Symp. Proc. Vol. 703 © 2002 Materials Research Society V13.44

# Insertion of Inorganic-Biomolecular Nanohybrid into Eucaryotic Cell

Seo-Young Kwak[1], Sung-Ho Hwang, Yong-Joo Jeong, Jong-Sang Park and Jin-Ho Choy*
School of Chemistry & Molecular Engineering, Seoul National University, Seoul 151-747, KOREA
[1] Present address: Materials Science & Engineering, University of Illinois at Urbana-Champaign, IL 61801, U.S.A.

## ABSTRACT

It has been clearly demonstrated that ATP could be intercalated into inorganic layered double hydroxide (LDH), giving rise to a biomolecular-inorganic nanohybrid with preserving its physico-chemical and biological integrity. It shows a remarkable transfer efficiency of ATP into target cells by alleviating an electrical repulsion at the cell walls due to the neutralization of negative charge of phosphates by positive hydroxide layers. From cellular uptake experiment with laser scanning confocal fluorescence microscopy, it is revealed that the FITC-LDH hybrid is effectively transferred into 293 cells. Such an unique feature of biomolecule-LDH hybrid will open a new field of reserving and delivering genes, drugs and other functional biomolecules.

## INTRODUCTION

Drug delivery system is gaining attention for life threatening diseases. For the efficient introduction of foreign gene-based therapeutics or drugs into target organ or cells, a carrier system is required. Both viral and non-viral vectors are presently under investigation. However, the conventional approaches have many problems, such as cytotoxicity, immunoreaction, low transfection, etc. Thus, there remains a need for less toxic and more efficient delivery vehicles for drug and other gene-based therapeutics.

Generally, the layered double hydroxide (LDH) consisting of magnesium and aluminum has already been used as medicine due to its applicability as an agent for treatment of peptic ulcers. An effective method for treating gastric ulcer is to inhibit the action of hydrochloric acid and pepsin in the gastric juice. $Mg_2Al(OH)_6(CO_3^{2-})$-LDH meets various requirements imposed on an antiacid, and its excellence may be attributed to its structural features. The rate of reaction of $Mg_2Al(OH)_6(CO_3^{2-})$-LDH with gastric acid is similar to that of $Mg(OH)_2$, while the buffering pH is rate-controlled by dissolution of $Al(OH)_3$ monomer, and reaches a pH value around 4, which is slightly higher than the one at which $Al(OH)_3$ is dissolved. The high antipeptic activity of LDH can be attributed both to the adsorption of negatively charged pepsin onto positively charged surface of LDH, and to buffering of the pH at about 4 for a long time. Therefore, we believe that the present LDH is quite biocompatible.

In the present study, adenosine 5-triphosphate (ATP) is selected as a guest molecule to be inserted into LDH, since it has been well known as energy carrier in biological system. But negatively charged ATP cannot be incorporated effectively into cell due to the negative cell wall. It is, therefore, thought that the encapsulated and charge neutralized ATP with LDH could enter the cell more effectively.

In this work, we were able to confirm the effective insertion of $\gamma$-$^{32}P$ labeled ATP by hybridizing with LDH. We made an effort to visualize the insertion of bio-LDH nanohybrid. The cellular uptake of fluorescein 5-isothiocyanate (FITC)-LDH hybrid was observed with laser

confocal fluorescence microscopy. From the cytotoxicity test of $Mg_2Al(OH)_6(NO_3^-)$-LDH, our primary attention was focused on verifying the possible application of bio-LDH nanohybrids as a non-viral vector by a systematic experimental approach.

## EXPERIMENTAL DETAILS

The pristine $Mg_2Al(NO_3)$–LDH was prepared by the coprecipitation under $N_2$ atmosphere following the conventional route. A mixed aqueous solution containing $Mg^{2+}$ (0.024 M, from $Mg(NO_3)_2$) and $Al^{3+}$ (0.012 M, from $Al(NO_3)_3$) was titrated dropwisely into a NaOH solution with vigorous stirring. During the titration, the solution pH was adjusted to $10 \pm 0.2$ at the room temperature. The resulting white precipitate was collected by the centrifugation and washed with decarbonated water thoroughly. The biomolecule–LDH hybrids were then prepared by ion–exchanging the interlayer nitrate ions in the pristine LDH with adenosine–5'–triphosphate (ATP, containing 40 μCi of [γ-$^{32}$P] ATP, DuPont) and fluorescein 5-isothiocyanate (FITC) at pH =7, for 48 h with a constant stirring. The reaction products were then isolated and washed as described above.[1,2]

The isotope labeled ATP-LDH hybrid and the [γ-$^{32}$P] ATP only were added to $4\times10^6$ HL-60 cells, human promyelocytic leukemia cells, in 20 ml of RPMI-1640 with 10 % heat-inactivated fetal bovine serum, and then incubated in a 5 % $CO_2$ incubator at 37 °C for 1, 2, 4, 6, 20, and 24 hours.[3] For each reaction time, 1 ml of sample was taken, centrifuged, then the separated supernatant was saved and the cell pellet was washed once with 1 ml of phosphate buffer (10 mM $Na_2HPO_4$, pH 7.4, 150 ml NaCl) and followed by sedimentation. The supernatant was again separated and saved, and the cell pellet was lysed in 200 μl of lysis buffer (10 mM Tris/Cl, pH 7.4, 150 ml NaCl, 1 % sodium dodecyl sulfate) and then extracted with 200 μl of phenol. After separating the aqueous phase, the phenol phase was extracted again with 200 μl of water. Aliquots of the combined aqueous extracts, cell walls, and culture-medium supernatant were analyzed by liquid scintillation counting. The percent of hybrid and [γ-$^{32}$P] ATP taken up by the cells was calculated by dividing the counts in the combined aqueous phases of the cell pellet extract by the total counts in the cell pellet, cell wash, and culture-medium supernatant. All the procedures were repeated 3 times to check the reproducibility.

The $2 \times 10^5$ 293 cells were grown on round cover-slips in a 24-well culture plate and cultured for a day. The 1 μM and 5 μM of FITC-LDH hybrids were added to the cells and incubated for 1, 2, 4, 6, and 8 hrs, respectively. In order to compare, control experiment was performed with only 5 μM of FITC itself under the same condition. All of the samples were washed with PBS buffer three times and fixed with 3.7 % formaldehyde in PBS. After washing again with PBS, the samples were observed with a laser scanning confocal fluorescence microscope (Carl Zeiss LSM 410). The samples were excited by a 488 nm argon laser, and the images were filtered by a longpass 515 nm filter.[4-6]

The HL-60 cells were cultured in a 24-well culture plate at an initial concentration of $5 \times 10^4$ /ml. Cells were exposed to various amounts of LDH from 1 μg/ml to 1000 μg/ml. A control experiment was performed without LDH under the same conditions. Cell viability was determined daily until the fourth day by MTT assay.[3,7]

## DISCUSSION

In a previous report,[8] we have demonstrated that the LDH could successfully encapsulate

| Time (hours) | 1 | 2 | 4 | 6 | 20 | 24 |
|---|---|---|---|---|---|---|
| Relavite uptake by cells (fold) | 21.0 | 24.0 | 11.5 | 9.3 | 4.5 | 4.0 |
| Standard deviation | 1.0 | 0.8 | 0.5 | 1.0 | 0.5 | 0.3 |

**Table I.** Relative uptake efficiency of [γ-32P] radioactive isotope labeled ATP-LDH hybrid into HL-60 cells. The uptake efficiency of ATP-LDH hybrids was normalized to that of ATP only.

biomolecules via intercalation route. According to the XRD and IR analysis, it has been concluded that the biomolecules stabilized in the interlayer space of LDH retain their chemical and biological integrities.

To elucidate the transfer efficiency, isotope-labeled [$\gamma$-$^{32}$P] ATP-LDH hybrid was prepared by ion exchange method and the uptake of such hybrids by eucaryotic cell was monitored with respect to incubation time.[3] Table 1 clearly demonstrates that the exogenously introduced ATP-LDH hybrid can enter into HL-60 cells effectively within a relatively short time. The transfer efficiency was found to be much higher, up to about 25-fold after 2 hours incubation, than that of ATP only. Whereas after 4 hours incubation, the uptake amount of the hybrids becomes lower, below 12-fold. The triphosphate group of [$\gamma$-$^{32}$P] ATP is negatively charged, which inhibits [$\gamma$-$^{32}$P] ATP to be taken up by the cell through the negatively charged cell walls. While the hybridization between ATP and LDH neutralizes the surface charge of anionic phosphate groups in ATP due to the cationic charge of LDH, which becomes favorable for endocytosis of cells, and eventually results in enhanced transfer efficiency. The longer the incubation time is in a $CO_2$ atmosphere, the more the ATP will be released from the interlayer space of hydroxide lattice. In spite of that, the transfer efficiency of the hybrid remains higher than that of ATP only, up to about 4-fold after 24 hours incubation. This result reflects that the hybridization between cationic layers and anionic biomolecules would greatly enhance the transfer efficiency of biomolecules to mammalian cells or organs. The charge neutralization through hybridization between LDH and ATP would facilitate the penetration of hybrids into cells, *via* so-called endocytosis,[9,10] because it greatly reduces the electrostatic repulsive interaction between negatively charged cell membranes and anionic biomolecules during endocytosis.

Further evidence on cellular uptake of the FITC-LDH hybrid was obtained directly from laser scanning confocal fluorescence microscopy experiments.[4-6] the 1 $\mu$M and 5 $\mu$M FITC-LDH hybrids were added to 293 cells and then incubated for 1, 2, 4, 6, and 8 hrs. Then the cells were washed with PBS, fixed with 3.7 % formaldehyde, prior to measurements. Figure 1 shows the cellular localization of the fluorophore obtained after a fixed incubation time. The fluorophores are detected in cells within an hour of incubation, and the fluorescence intensities are increased continuously up to 8 hrs. The fluorophores in the cells are distributed primarily in peripheral and cytosol parts with some in the nucleus. Moreover, the cells treated with 5 $\mu$M of FITC-LDH hybrids show more intense fluorescence than those with the 1 $\mu$M. In contrast, the cells treated with 5 $\mu$M FITC only remain dark regardless of incubation time, because cells could not take up FITC itself even with high concentration. It is obvious that LDH plays an important role in mediating the cellular uptake of FITC. All the cells can engulf the neutralized nanoparticles

through phagocytosis or endocytosis. Therefore, we conclude that the intracellular fluorescence has been created by deintercalated FITC or some by FITC-LDH hybrids in the cell.

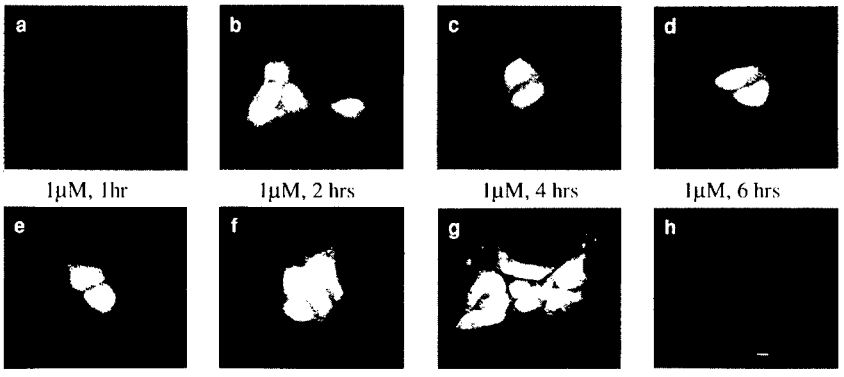


**Figure 1.** Laser confocal fluorescence microscopy of fluorophore in 293 cells. $2 \times 10^5$cells/well were incubated with 1 μM FITC-LDH for 1, 2, 4, 6, and 8 hrs and 5 μM FITC-LDH for 1 hrs, respectively. The other fluorescence microphotograph was obtained with 5 μM FITC only. The bar is 10 μm.

It is necessary to test cytotoxicity of LDHs themselves in the cells for use as gene or drug delivery carrier. In fact, one critical element for the overall transfection efficacy of gene delivery system is cytotoxicity. Cell damage resulting from a cytotoxic delivery system is deleterious because the following delivery in the cell must be capable of supporting translation and transcription. As shown in Figure 2, LDHs themselves have no effect on the viability of HL-60 cells, when administered at levels below 1000 μg/ml for up to 4 days. However, many cationic lipid complexes previously examined were bound to be toxic to cells at concentrations near their effective doses if exposure times were extended to several hours,[11] suggesting that the molecules could not easily be metabolized. For example, polylysine was the first polymer used to mediate the transfection of cells,[12] and polyethyleneimine(PEI) was of the new "proton sponge" category and was hypothesized to mediate the escape of plasmid DNA from endosomal pathway.[13,14] Though they demonstrated the aptitude of polycations to mediate transfection, those polymers are associated with a considerable degree of cytotoxicity.[15,16] When COS-7 cells (immortalized African green monkey kidney fibroblasts) were incubated with polylysine and PEI, their cell viability was ~50 % at 20 μg/ml and ~2 % at 10 μg/ml after 48 hrs, respectively.[17] In addition, when Vero cells (African green monkey kidney) were exposed to the various concentrations of DOTMA/DOPE (Lipofectin™, a 1:1 (w/w) formulation of the cationic lipid, DOTMA, and at 100 μg/ml there were no viable cells left after 4 days of continuous treatment.[18] Thus, it is needed to develop less toxic and more efficient delivery vehicles for gene or drug based therapeutics. In contrast, LDHs themselves show no discernible cytotoxic effect on HL-60 cells, when administered at levels below 1000 μg/ml for up to 4 days.

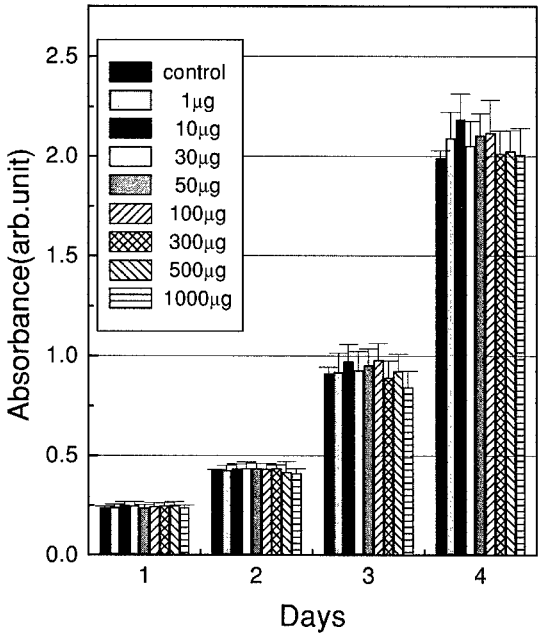


**Figure 2.**Cytotoxicity experiment of LDH in HL-60 cells. Various amounts of LDH were added to cells at final concentrations from 1 μ g/ml to 1000 μg/ml.

## CONCLUSION

This study has shown that inorganic-biomolecular nanohybrids can enter into cell through the cellular uptake experiment using the isotope labeled ATP and the fluorescent FITC. In addition, from the cytotoxicity test, we demonstrate clearly that the inorganic-biomolecular nanohybrids are a safe way of delivering genes or drugs. And we are now developing new inorganic delivery carrier, which can be improvement over conventional delivery carrier in vivo.

## ACKNOWLEDGEMENT

This work was supported by the Korean Ministry of Science and Technology through the National Research Laboratory Program ('99). Seo-Young Kwak express her thanks to the Korea Science and Engineering Foundation for the post-doc. Fellowship (2001).

## REFERENCES


1. J. H. Choy, S. Y. Kwak, J. S. Park, and Y. J. Jeong, *J. Mater. Chem.*, **11(6)**, 1671-1674 (2001)
2. J. H. Choy, S. Y. Kwak, Y. J. Jeong, and J. S. Park, *Angew. Chem. Int. Ed. as a highlight comm.* **39(22)**, 4042-4045 (2000)
3. E. L. Wickstrom, T. A. Bacon, A. Gonzalez, D. L. Freeman, G. H. Lyman, E. Wickstrom, *Proc. Natl. Acad. Sci. USA* **85**, 1028 (1988).
4. R. J. Lee and P. S. Low, *J. Biol. Chem.* **269**, 3198-3204 (1997).
5. Z. W. Lee *et al. Ibid.* **273**, 12710-12715 (1998).
6. K. Vogel, S. Wang, R. J. Lee, J. Chmielewski, P. S. Low, *J. Am. Chem. Soc.* **118**, 1581-1586 (1996).
7. M. B. Hansen, S. E. Nielsen, K. Berg, *J. Immunol. Methods* **119**, 201-203 (1989).
8. J. H. Choy, S. Y. Kwak, J. S. Park, Y. J. Jeong, and J. Portier, *J. Am. Chem. Soc.*, **121**, (1999)1399-1400.
9. S. S. Davis, *Trends Biotechnol.* **15,** 217 (1997).
10. I. M. Verma, N. Somia, *Nature* **389,** 239 (1997).
11. C. F. Bennet, M. Y. Chiang, H. Chan, J. E. E. Shoemaker, C. K. Mirabelli, *Pharmacol.* **41,** 1023 (1992).
12. G. Y. Wu, C. H. Wu, *J. Biol. Chem.* **11**, 1050 (1987).
13. O. Boussif, F. Lesoulac'h, M. A. Zanta, M. D. Mergny, D. Scherman, B. emeneix, J. P. Behr, *Proc. Natl. Acad. Sci. USA* **92,** 7297 (1995).
14. M. A. Zanta, O. Boussif, A. Adib, J. P. Behr, *Bioconjugate Chem.* **8,** 839 (1997).
15. S. Choksakulnimitr, S. Masuda, H. Tokuda, Y. Takakura, M. Hashida, *J. Controlled Release* **34,** 233 (1995).
16. G. A. Brazeau, S. Attia, S. Poxon, J. A. Hughes, *Pharm. Res.* **15,** 680 (1998).
17. D. Putnam, R. Langer, *Macromolecules* **32,** 3658 (1999).
18. K. G. C. Judith, V. Bodepudi, J. S. Bishop, K. Jayaraman, N. Chaudhary, *J. Biol. Chem.* **270,** 31391 (1995).

Mat. Res. Soc. Symp. Proc. Vol. 703 © 2002 Materials Research Society U2.8

# The Coercivity – Remanence Tradeoff in Nanocrystalline Permanent Magnets

Laura H. Lewis and David C. Crew
Materials and Chemical Sciences Division, Energy Sciences and Technology Dept.,
Brookhaven National Laboratory, Upton, New York 11973-5000 USA

## ABSTRACT

The energy product $(BH)_{max}$ is a figure of merit quantifying the maximum amount of useful work that can be performed by the magnet. The energy product is determined by the magnetic remanence and the coercivity which, as extrinsic properties, are determined by the magnets' microstructure. Thus, in principle, magnetic material microstructures may be tailored to obtain defined parameters to produce optimal permanent magnets. However, as asserted by the eponymous Murphy, "Nature favors the hidden flaw". While there is still much undeveloped potential in nanomagnetic materials, with relevant length scales on the order of 100 Å, accumulating evidence strongly suggests that maximum remanence and maximum coercivity are mutually exclusive in nanocrystalline magnetic materials. Diverse experimental and computational results obtained from nanocrystalline $Nd_2Fe_{14}B$-based magnets produced by melt-spinning techniques and subjected to various degrees of thermomechanical deformation confirm this conclusion. Recent results obtained from temperature-dependent magnetic measurement, magnetic force microscopy and simple micromagnetic modeling will be reviewed and summarized. The results, while somewhat discouraging, do hint at possible materials design routes to sidestep the inherent performance limitations of the magnetic nanostructures.

## INTRODUCTION

The permanent magnet material $Nd_2Fe_{14}B$ in its nanocrystalline form exhibits very favorable properties conferred by the rapid solidification process: simplified processing, good corrosion resistance and high magnetic hardness provided by a nanoscale grain size on the order of 200 nm. The metallurgical properties of the $Nd_2Fe_{14}B$ compound allow it to be thermomechanically deformed, or "die-upset", a process that significantly improves the remanence $B_r$ of the magnet [1]. This increase in remanence results stems from two effects: (a) the exchange enhancement of the magnetization in the intergranular regions [2] and (b) an increased degree of crystallographic texture of the magnet. Both effects enhance the energy product $(BH)_{max}$, which is a figure of merit that quantifies the maximum amount of useful work that may be performed by the magnet. The energy product is determined by the magnetic remanence and the coercivity which, as extrinsic properties, are largely determined by the magnets' microstructure. Thus, in principle, it should be possible to tailor magnetic material microstructures to obtain target properties that yield optimal permanent magnets.

Unfortunately, the increase in the remanence upon die-upsetting is always accompanied by a decrease in the coercivity $H_{ci}$ of the magnet. The reasons underlying this phenomenon are unclear. This coercivity decrease dilutes the gains in the energy product produced by the increased remanence and, in some cases, limits the range of applications of the magnet. This decrease in coercivity with increasing level of deformation is in contrast to that expected from an archetypal assemblage of Stoner-Wohlfarth particles that reverse by ideal coherent rotation. The

Stoner-Wohlfarth model, applicable only to homogenous systems of magnetically-isolated uniaxial single-domain particles, yields a coercivity $H_C(\theta)$ as a function of angle $\theta$ between the magnetic easy axis and the applied field that increases with decreasing $\theta$ according to the Eq. [3]

$$H_c(\theta)/H_c(\theta=0) \approx \left(\cos^{2/3}\theta + \sin^{2/3}\theta\right)^{-1/2} \qquad (1)$$

Results of the Stoner-Wohlfarth model imply that nanocrystalline assemblages with $\theta < 45°$ will exhibit increasing coercivity with decreasing angle $\theta$. The model complementary to the Stoner-Wohlfarth model is the Kondorsky pinning model [4] which predicts coercivity to vary with $\theta$ as $1/\cos\theta$, where $\theta$ again is the angle of the easy axis of the grain with respect to the applied field direction. The physical origins of the Kondorsky model lie in the fact that when the coercivity is low relative to the anisotropy field, as in most advanced permanent magnets, field-induced rotation of the moments out of the easy axis may be neglected. In this situation, magnetic reversal is accomplished by the component of applied field acting along the easy axis of a given grain. Crystallographic grain alignment allows the easy axes of an ensemble of magnetic particles to be rotated by a smaller angle $\theta$ with respect to the field. This action results in an increased component of the field acting upon the grain that produces an overall coercivity decrease because the mean coercivity of the grains decreases.

Results computed with the Stoner-Wohlfarth model or the Kondorsky pinning model are in contradiction to behavior observed in die-upset nanocrystalline magnets (Fig. 1), although Givord [5] reports on the existence of similar work by Viadieu that does appear to conform to a $1/\cos\theta$ trend. Fig. 1 shows the correlated, but non-monotonic, relationship between the coercivity and the degree of crystallographic alignment, as quantified by the half-width at half-maximum (HWHM) value of a x-ray diffraction rocking curve for a series of $Nd_2Fe_{14}B$-based die-upset samples with nominal composition $Nd_{13.9}(Fe_{0.92}Co_{0.08})_{80.3}B_{5.3}Ga_{0.5}$ that were deformed to varying degrees [6]. The level of deformation (%) as given in Fig. 1 is the percent change in original height upon deformation.

It is generally accepted that the presence of significant intergranular interactions annul application of the Stoner-Wohlfarth model in nanocrystalline magnets. As summarized by Givord [4], computational models indicate that the field at which magnetic reversal occurs decreases with increasing intergranular exchange. However, the effect of relative crystallographic alignment between constituent nanograins on the magnetic reversal in such materials is less clear. The modeled behavior of two exchange-coupled grains with one grain misaligned by 65° with respect to the applied field [7] indicate that the coercive field of grains coupled by both dipolar and exchange interactions decreases for large granular misalignment, inconsistent with

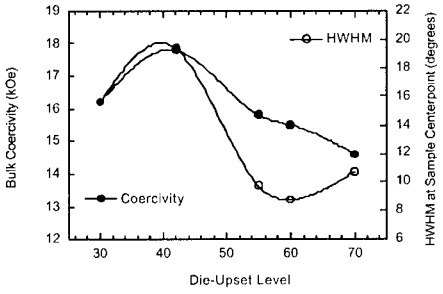


Figure 1. Bulk coercivity and (006) $Nd_2Fe_{14}B$ Bragg reflection rocking curve HWHM data as a function of magnet die-upset level.

experimental observations (Fig. 1). Clarification of the tradeoff in magnetic property optimization with crystallographic alignment of constituent nanograins lies in the relationship between the nanocrystalline grain size and the magnetic exchange, as communicated by the magnetic exchange length $L_{ex}^{0}$:

$$L_{ex}^{0} \approx \sqrt{\frac{A}{K_1}} \tag{2}$$

where A is the exchange stiffness and $K_1$ is the first-order anisotropy constant [8]. The magnetic exchange length describes the thickness of the magnetization transition existing near an interface, where the magnetization direction can deviate from the defined direction existing in the bulk region of a given grain. In the absence of a perpendicular magnetization component across the interface $L_{ex}^{0}$ may be related to the domain wall width $\delta_{DW}$ as [9]:

$$L_{ex}^{0} \approx \frac{\delta_{DW}}{\pi} \tag{3}$$

The room-temperature value of the magnetic exchange length $L_{ex}^{0}$ in $Nd_2Fe_{14}B$ is extremely small, around 21 Å [10]. Further reduction in the magnetic exchange length from its base value is realized from the presence of a perpendicular magnetization component at the interface between nanograins. In this manner a connection between crystallographic alignment and exchange coupling in nanocrystalline magnetic materials is realized.

It is postulated that the magnetic exchange length controls the magnetic behavior in nanocrystalline magnets. When the average grain size of a ferromagnet is much larger than the exchange length, the magnetization deviation at the grain perimeters does not significantly effect the micromagnetics of the system. In such cases the coercivity of the system is largely controlled by lattice imperfections and grain boundary defects, such as a rough grain boundary topography, that furnish regions more susceptible to magnetic reversal relative to the bulk. However, when the grain size descends to the nanoscale the exchange length becomes important; under its influence spins at the peripheries of neighboring nanograins become strongly exchange-coupled. As the relative crystallographic orientation difference between nanograins decreases the intergranular exchange length increases. As the intergranular exchange length increases the local magnetization deviation is likewise reduced, producing a more-uniform micromagnetic state. The exchange-coupling effectively erases the distinction between nanocrystalline grains and decreases the efficacy of the physical grain boundaries to act as barriers to domain wall motion. The peripheral spins on the edges of the nanocrystalline grains constitute a large volume fraction of the total number of spins in the grain; this situation results in magnetic behavior that is very different from that found in the larger-grained counterparts.

Some remarkable phenomena are induced by intergranular exchange coupling in nanocrystalline materials. As the grain size is reduced below the single domain limit intergranular exchange interactions act to bind the magnetic grains into larger units known as "interaction domains", schematically depicted in Fig. 2. These interaction domains, which represent the reversing units of the magnetic structure, can consist of ten to thousands of individual grains. It is important to note that interaction domains may support a domain wall, whereas the individual grains that constitute the interaction domain are typically too small to do so. The scale of the magnetic microstructure, *i.e.*, the size of the interaction domains in nanocrystalline magnets, is

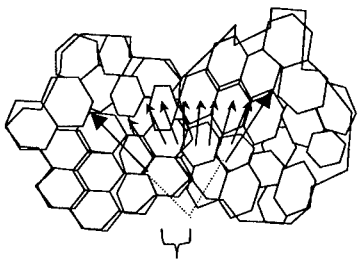

$\Psi < 90°$

Figure 2. Schematic representation of two multi-grain "interaction domains", delineated by the bold outline. The bold arrows indicate the average anisotropy direction of the interaction domains, and the spin rotation angle $\Psi$ is less than 90°.

dependent upon many factors, including the type and magnitude of the magnetocrystalline anisotropy of the compound, the chemical homogeneity and the crystallographic alignment of the constituent grains. Interaction domains are delineated by rotational spin transitions that are distinct from the more-familiar Bloch domain walls found in large-grained materials with magnetization rotations of 180° or 90°. The magnetization transition from one interaction domain to the next subtends an angle $\Psi$ between the collective anisotropy directions of adjacent interaction domains; $\Psi$ is typically less than 90 degrees. It is hypothesized that this divergence in the magnetization is too small to effectively impede domain wall motion.

The above-described factors underlie the structure-sensitive magnetic properties such as coercivity and remanence in nanocrystalline permanent magnet materials and make them unique from their micron-scale counterparts. While there is still much undeveloped potential in nanocrystalline permanent magnet materials, accumulating evidence strongly suggests that the existence of optimal remanence and coercivity are mutually exclusive in nanocrystalline magnetic materials. The microstructural condition found in these materials — that the nanometer grain size is approximately the same size or smaller than the exchange length in $Nd_2Fe_{14}B$ — is hypothesized to underlie this conclusion.

The following sections of this paper present experimental and simple computational results obtained from recent studies of melt-quenched $Nd_2Fe_{14}B$ materials that indicate high remanence and high coercivity seem to be mutually exclusive in nanocrystalline magnets. This conclusion is supported by evidence of increasing magnetic exchange concurrent with increasing grain alignment in nanocrystalline magnets. Investigations of the effect of grain alignment and interaction domain size on coercivity were carried out on a series of $Nd_2Fe_{14}B$-based samples with nominal composition $Nd_{13.9}(Fe_{0.92}Co_{0.08})_{80.3}B_{5.3}Ga_{0.5}$ that were die-upset to varying degrees. The small grain size of these materials guarantees that a significant portion of the constituent atoms reside near grain surfaces and thus these materials represent a good opportunity to examine the effect of intergranular exchange interactions and relative grain alignment upon the magnetic reversal process. A secondary, but still important, microstructural parameter is the change in nanograin shape from quasi-spherical to platelet-type produced by the die-upsetting process. This shape change, while complex and highly nonuniform, nevertheless influences the magnetic coupling and local magnetic reversal mechanism operative in the magnet. In this report the influence of intergrain magnetic exchange coupling on the reversal mechanism and micromagnetic structure in this set of materials is studied with three different techniques: temperature-dependent magnetic measurement [11], magnetic force microscopy [12] and simple micromagnetic modeling [13]. The results, while perhaps discouraging, do hint at possible materials design routes to sidestep the inherent performance limitations of the permanent magnetic nanostructures.

## COERCIVITY AND CRYSTALLOGRAPHIC ALIGNMENT RELATIONS

Information concerning the nature and extent of cooperative magnetic reversal in magnets of differing degrees of intergranular alignment may be obtained from measurements of the coercivity as a function of temperature. A number of approaches have been developed in an attempt to quantify the relationship between microstructure and coercivity. The coercivity is phenomenologically described [14,,15 ,16] as a function of the anisotropy field reduced by dipolar interactions within the material:

$$H_c(T) = \alpha(T) \cdot H_a(T) - 4\pi N_{eff} M_S(T) \qquad (4)$$

with the temperature-dependent parameters $H_c(T)$ (coercivity), $H_a(T)$ (anisotropy field) and $M_s(T)$ (saturation magnetization). The parameter $\alpha(T)$ describes the reduction in coercivity due to the existence of a non-ideal microstructure; in a simplistic sense $\alpha(T)$ characterizes the misalignment of the grains. The parameter $N_{eff}$ is an effective demagnetization factor that encompasses both dipolar interactions and the effects of the demagnetization field at grain corners that tend to assist magnetic reversal and reduce the coercivity. Both $\alpha(T)$ and $N_{eff}$ are expected to decrease as the degree of intergranular alignment increases.

Values of $\alpha(T)$ and $N_{eff}$ were determined by measuring a series of hysteresis loops ($H_{max}$=50 kG) for the die-upset $Nd_2Fe_{14}B$-based samples with increasing temperature from 100 K to room temperature. The samples studied were the previously-mentioned die-upset materials deformed to 0, 30, 42, 55, 60 and 70% reductions in the original sample heights. Using Eq. (4) and plotting $H_c/M_s$ *vs.* $H_a/M_s$ as a function of temperature, the parameters $\alpha$ and $N_{eff}$ were determined by fitting the data to a straight line. The values of $H_a$ used in Eq. (4) were taken from the paper of Grossinger *et al.* [17] and $M_s(T)$ was calculated by extrapolating the high field data. The results for the plots of $H_c/M_s$ *vs.* $H_a/M_s$ for all samples were linear and gave well characterized values of $\alpha$ and $N_{eff}$, as evidenced by the data for the 0, 30 and 70% deformed samples shown in Fig. 3, with resulting values of $\alpha$ and $N_{eff}$ are shown in Fig. 4. The samples are labeled by the degree of die-upset with the corresponding remanence ratio ($M_r/M_s$) given in parentheses. The trend of decreasing coercivity with increased crystallographic alignment is indicated on the figure by the arrow. Also shown in Fig. 3 for comparative purposes is data from the work of Hirosawa and Tsubokawa [16] for sintered $Pr_2Fe_{14}B$-based magnets with varying degrees of particle alignment, labeled by the remanence ratio ($M_r/M_s$).

Fig. 3 shows a distinct linkage between $\alpha$ and $N_{eff}$ as the degree of alignment is varied in both the die-upset samples and the sintered samples. However, the data from the die-upset samples display a trend with coercivity *opposite* to that displayed by the sintered data. The sintered data show the expected Kondorsky-type coercivity behavior, *i.e.* as the degree of alignment is increased the coercivity decreases; additionally $\alpha$ and $N_{eff}$ also decrease in these samples with increasing alignment. While the melt-quenched data also show a decrease in coercivity with increasing alignment, the trend is accompanied by an *increase* in $\alpha$ and $N_{eff}$, contrary to expectation. An explanation of the observed behavior of $\alpha$ and $N_{eff}$ with increased thermomechanical deformation, and hence increased crystallographic alignment, in nano-crystalline materials is provided based on consideration of the active intergrain exchange interaction. Large-grained materials, such as commercial sintered NdFeB magnets, have small

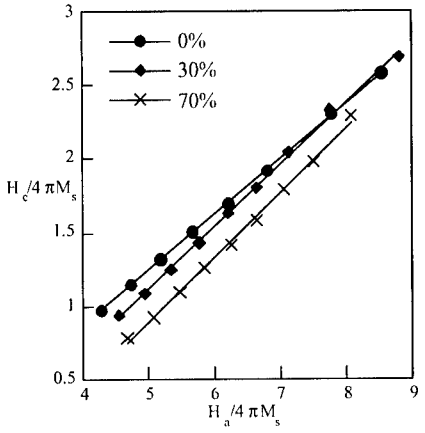


Figure 3. $H_c/4pM_S$ *vs.* $H_a/4pM_S$ for the 0%, 30% and 70% die upset samples. The lines shown are the lines of best fit used to determine $\alpha$ and $N_{eff}$ from Eq. (3).

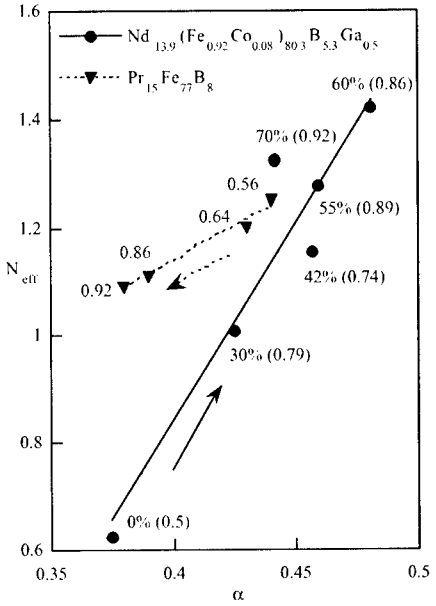


Figure 4. $N_{eff}$ *vs.* $\alpha$ for the melt-quenched NdFeB samples and for a set of sintered PrFeB samples studied by Hirosawa and Tsubokawa [16]. The numerical labels are described in the text. The trend of decreasing coercivity is shown by the arrows

intergrain exchange interactions which favor individual reversal of each grain and provide a coercivity deter mined by the mean coercivity of the individual grains. The coercivity in nanocrystalline materials is determined by a minimum local coercivity which causes reversal of the entire magnet through exchange-coupled avalanche-type magnetization reversal. Thus in these materials the microstructural parameter $\alpha$ is expected to remain relatively unchanged as the degree of crystallographic alignment is increased, because the coercivity is determined by those grains with small orientations to the applied field direction. It is proposed that the coercivity still decreases, despite an approximately constant $\alpha$ in these materials, because nanograin shape changes accompanying the die-upsetting process contribute to increased local stray field configurations that override the expected stray field reduction accompanying grain alignment. The creation of euhedral platelet grains from initially quasi-spherical grains amplifies the stray field gradients at grain corners and triple-point junctions, causing $N_{eff}$ to increase with increasing deformation level. It is hypothesized that only a small population of deformed nanograins is necessary to cause global magnetic reversal because the reversal is rapidly propagated throughout the magnet, underscoring the effect of the intergranular exchange interactions on the coercivity. In summary, remanence increases with deformation, because of greater granular alignment and increased exchange interactions, but these same exchange interactions, combined with other microstructural changes, cause the coercivity to decrease. Thus there is a tradeoff in the two parameters.

## COOPERATIVE MAGNETIC BEHAVIOR OBSERVED WITH MAGNETIC FORCE MICROSCOPY

The character and extent of the intergrain magnetic exchange found in nanocrystalline magnets may be inferred from magnetic domain images. Magnetic force microscopy (MFM) was employed to compare the magnetic domain structure in two well-characterized samples of melt-quenched $Nd_2Fe_{14}B$, one sample hot-pressed (isotropic; 0% die upset) and one sample die-upset to a deformation level of 70%. Images of the domain configurations obtained in different magnetic states from these two microstructurally-distinct samples provide information about the effect of intergranular alignment on the magnetic exchange. MFM samples were prepared from 5 mm cubes cut from the center of the samples; one surface of each cube was polished and examined with the surface normal parallel to the press direction. MFM examination of the domain structures of the samples was performed with a Digital Instruments Nanoscope III using standard low coercivity (commercial MESP-LC) tips. The samples were examined in different remanent magnetic states after magnetization to varying levels in a SQUID magnetometer with a 50 kG superconducting magnet.

The nanoscale grain structure of the samples leads to a complex micromagnetic state that has unique MFM contrast. In this work it is deduced that the use of low-coercivity MESP-LC tips to image nanoscale domain structures produces domain contrast rather than the domain wall contrast. This conclusion is discussed in more detail in recent work [12].

MFM images of the hot-pressed material are shown in Figure 5 for three different magnetic states. In the thermally-demagnetized condition (Fig 5a) the image reveals no large-scale structure. A fine-scale contrast is evident with features approximately 150 - 300 nm, which is 2 ~ 3 times the grain size observed by atomic force microscopy. This sample was then saturated in a 50 kG field and imaged in the remanent state (Fig 5b), with remanent magnetic features that are similar in scale to those seen in the thermally-demagnetized condition. A magnetic field of 19.5 kOe was then applied opposite to the remanent magnetization of the sample and then removed, leaving the sample in a DC-demagnetized state (Fig 5c) as confirmed by the near-zero magnetization of the sample measured by SQUID magnetometry. The features observed in the DC-demagnetized state are similar to those seen in the remanent state. MFM images from the

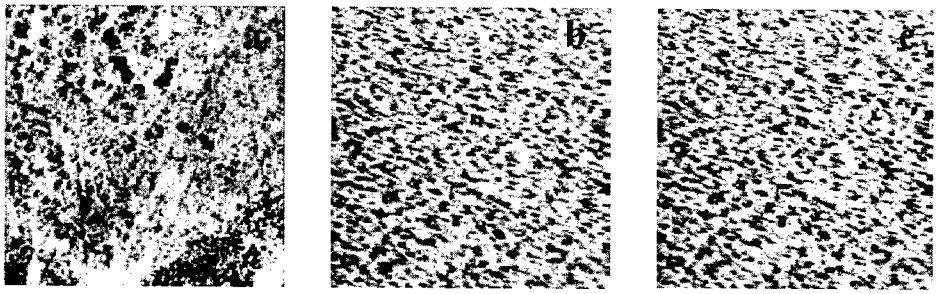


Figure 5: MFM images of hot-pressed $Nd_{13.9}(Fe_{92}Co_8)_{80.3}B_{5.5}Ga_{0.5}$. The image areas are 15 μm by 15 μm. a) Thermally-demagnetized state. b) Remanent state after application of 50 kOe field. c) Coercive state after application and removal of 19.5 kOe reversing field. The press direction is perpendicular to the image plane.

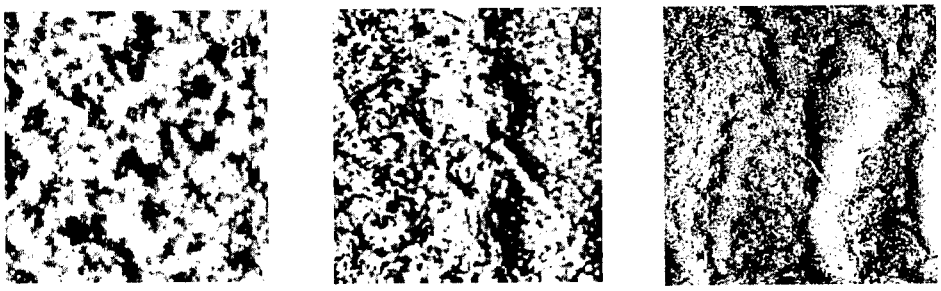


Figure 6: MFM images of thermomechanically-deformed (die-upset) sample $Nd_{13.9}(Fe_{92}Co_8)_{80.3}B_{5.5}Ga_{0.5}$. a) Thermally demagnetized state; image size 15 μm by 15 μm. b) Coercive state after application and removal of a 13.4 kG reversing field; image size 15 μm by 15 μm. c) Same area of the sample as b) except the image size is 50 μm by 50 μm. The press direction is perpendicular to the image plane.

die-upset sample are shown in Fig. 6. The scale of the magnetic structure of the die-upset sample is significantly larger in the thermally-demagnetized condition (Fig 6a)) than in the hot-pressed sample (Fig. 5a)). The magnetic contrast of the die-upset sample is on a scale of 1-2 μm with a finer contrast, on the order of 200 nm, evident within the larger-scale contrast. The fine scale structure is 2-3 times larger than the grain size observed with AFM, but is still 5-10 times smaller than the large scale contrast. It is hypothesized that the observed fine-scale MFM contrast is due to small clusters of exchange-coupled grains within the material, while the larger-scale contrast arises from the coalescence of several magnetic clusters with similar magnetization orientations that create an interaction domain. Application and removal of a reverse field of 13.4 kG to the remanent state drove the sample to a DC-demagnetized state that resulted in a significant change in the domain configuration. The fine-scale magnetic domain structure shown in Fig. 6b) is of a similar scale to the fine-scale structure observed in the thermally-demagnetized condition (*i.e.* approximately 200 nm). However, the image of a larger area, shown in Fig. 6c) and obtained from the same region of the sample as fig. 6b), demonstrates the existence of elongated interaction domains that extend 50 μm or more perpendicular to the magnetization.

In both samples the inherent intergranular exchange interaction is manifest in the finest-scale magnetic contrast, postulated to arise from individual magnetic clusters in the size range 150 - 300 nm that correspond to a volume of approximately 10 exchange-coupled grains. Henceforth the term "cluster" will be used to refer to this fine-scale magnetic contrast, while the term "interaction domain" will be reserved for groups of clusters with similar magnetization orientations existing on length scales of 1 μm to greater than 50 μm. In the hot-pressed material the size of the magnetic cluster domains changes only slightly between thermally-demagnetized, remanent and DC-demagnetized states, indicating that magnetic reversal occurs individually for each cluster. The absence of large multi-cluster interaction domains upon DC-demagnetization in the hot-pressed sample suggest that nucleation of magnetic reversal likely occurs homogeneously throughout the material and the magnetic state of neighboring clusters has only a small effect on cluster reversal. The lack of large interaction domains in the hot-pressed sample is attributed to isotropic crystallographic orientation of the constituent grains. This random crystallographic orientation supplies a perpendicular magnetization component to the cluster interface that reduces the original intergrain magnetic exchange length and ensures small magnetic clusters. In contrast, while the die-upset material exhibits small interaction domains (~ 1-2 μm) in

the thermally-demagnetized condition Figs. 6b) and 6c) indicate the presence of very large interaction domains, extending over 50 μm or more, in the DC-demagnetized condition of this material. It is concluded upon reversal from magnetic saturation the exchange interactions force the reversal of one grain cluster to accelerate the reversal of neighboring clusters. Magnetic reversal in this material thus probably proceeds by a combination of reversal of clusters of grains existing at the peripheries of reversed regions and by an avalanche-type reversal of many clusters simultaneously. Supporting magnetic measurements [18] suggest that magnetic reversal occurs mostly via nucleation of clusters of grains at the peripheries of already-reversed interaction domains, rather than by domain wall unpinning and propagation. The large interaction domains within the die-upset material indicate that the constituent grains with a low coercivity influence the reversal of the entire material to a much greater degree than do similar grains in the hot-pressed material. This effect is, again, attributed to the increased degree and extent of intergranular exchange coupling that accompanies crystallographic alignment in nanocrystalline materials. These measurements show that as alignment proceeds and remanence increases, exchange interactions act to bind grains into larger reversing units. Larger reversing units result in the need for fewer nucleation sites to attain full magnetic reversal and the coercivity decreases as a result.

## COERCIVITY AND CRYSTALLOGRAPHIC ALIGNMENT RELATIONS FROM MICROMAGNETIC MODELLING

While previous micromagnetic studies [19, 20] of nanocrystalline magnetic material have largely concentrated on the influence of grain size and phase composition on the bulk magnetic properties, simple computational models may also provide useful information concerning the effect of crystallographic grain alignment on the coercivity of nanocrystalline magnetic materials. In the present work a micromagnetic model has been used to investigate the influence of grain texture upon the scale of the magnetic structure during reversal.

Micromagnetic calculations were performed using a modified version of the 2-dimensional Object Oriented Micromagnetic Framework (OOMMF) software available from NIST [21]. In this model, 3-dimensional spins arranged on a 2-dimensional mesh are relaxed using a Landau-Lifshitz ordinary differential equation solver. A magnetic field is applied to the system and each spin is allowed to precess, under the action of the total field acting on that spin and a damping term, in accordance with the Landau-Lifshitz equation. The total field acting on a spin is composed of the applied field and effective fields representing magnetocrystalline anisotropy, exchange and self-magnetostatic energies. The system is allowed to evolve until the total torque on all spins is below an arbitrary limit. The presented model was modified from the code available from NIST by allowing the material parameters — saturation magnetization ($M_s$), magnitude and direction of the uniaxial magnetocrystalline anisotropy (K) and exchange parameter (A) — to vary from spin to spin. In this way a granular structure could be simulated and the properties of the system examined as the degree of easy axis alignment was varied.

The material simulated consisted of a two-dimensional slice of $Nd_2Fe_{14}B$, 600 nm long in the x-direction by 300 nm high in the y-direction. Two different schema were used for the simulation, each consisting of 18 grains in total. In the first scheme — the isotropic case — the easy axis of each grain was chosen randomly to lie in the plane of the slice. In the second scheme — the anisotropic case — the easy axis of each grain was chosen to lie in the plane of

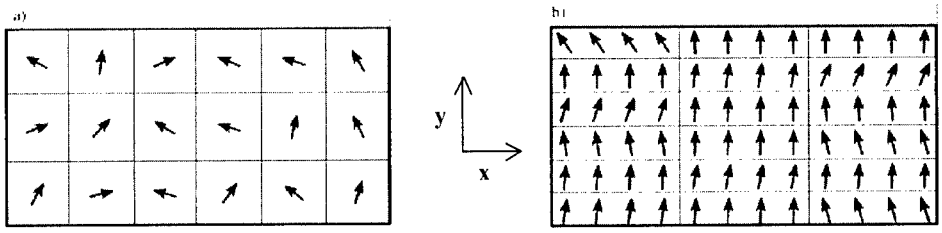


Fig. 7. Figures representing the grain boundaries and easy axis directions for the two schema described in the text. The field was applied such that the x-component was $1/6^{th}$ the y-component in magnitude, which is approximately 9.5° from the y-direction. a) The isotropic scheme. The grains dimensions are 100 nm by 100 nm and the total simulation is 600 nm by 300 nm. b) The anisotropic scheme. The grains dimensions are 200 nm by 50 nm and the total simulation is the same size as a).

the slice from a Gaussian distribution with a standard deviation of 10° about the y-direction. These easy axis distributions simulate, in two dimensions, the experimental easy axis distributions found in hot-pressed and optimally die-upset magnets respectively [6]. In the isotropic scheme each of the 18 grains was 100 nm by 100 nm in size. In the anisotropic scheme each of the 18 grains was 200 nm by 50 nm in size. The change in shape corresponds to that produced by the die-upsetting procedure which is used to develop crystallographic and magnetic texture in melt-quenched $Nd_2Fe_{14}B$. For simplicity the grain size was the same for all grains in each scheme. The directions of the easy axes and the positions of the grain boundaries are shown in Fig. 7 for the two schema considered in this work. The magnetic field was applied in the plane of the slice with a y-component 6 times that of the x-component. A full three-dimensional treatment was used in the self-magnetostatic energy calculation, known as the "3Dslab" calculation in the OOMMF code. The computational cell size chosen for the simulations was 1.5 nm, which is sufficiently small to allow accurate modeling of domain walls in $Nd_2Fe_{14}B$. The physical properties chosen for $Nd_2Fe_{14}B$ were $M_s$ = 1274 kA/m, A = 100 pJ/m, K =5 MJ/m$^3$. The exchange parameter across the grain boundary was assumed to be equal to the bulk value to simulate the upper limit of exchange coupling possible.

Normalized hysteresis loops for the demagnetization section of the curve for the two schema considered are shown in Fig. 8. The isotropic curve has a remanence above the expected value of 0.5 because only 18 grains were considered in the simulation, a number that is too small to allow proper statistical sampling of the isotropic distribution. The remanence of the anisotropic curve is much larger, consistent with the aligned nature of the texture distribution assumed. The coercivity of the anisotropic curve is nearly twice that of the isotropic curve, contrary to experimental findings. However, in micromagnetic simulations the coercivity is expected to increase as the degree of alignment increases because the nucleation field increases as the applied field is aligned more nearly with the easy axis of the grain [22]. The calculated form of the demagnetization curve is more diagnostic of the effect of intergranular alignment. The isotropic curve shows a two-stage magnetic reversal, the first reversal occurring at 1 T with the second reversal occurring at a higher field of 2 T. For the anisotropic curve, apart from a small amount of reversible rotation which occurs in larger negative fields, the entire reversal occurs in a single jump at H = 4 T.

The reasons underlying the two-stage reversal process in the isotropic case were revealed once the magnetization distributions at each field were examined. The magnetization distribu-

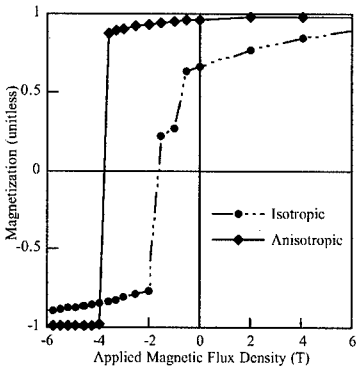


Fig. 8. Second-quadrant normalized hysteresis loops for the isotropic and anisotropic schema. The isotropic case displays a two-stage reversal while the anisotropic case displays only a single-stage reversal.

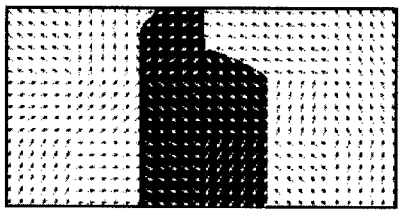

Fig 9. Magnetization distribution in a stable state at 1.5 T for the isotropic scheme. The arrows represent average magnetization of a 12 x 12 element square; black-white shading represents parallel or anti-parallel polarization to the applied field. Domain walls can be seen crossing the two upper grains of the black shaded region.

tion for the isotropic scheme in a field of 1.5 T is shown in Fig. 9. Although the first nucleation event occurred at a field of 1 T, only a portion of the grains in the isotropic material were reversed by this nucleation, in contrast to the reversal of the anisotropic material. It may be concluded that not only does grain misalignment lower the remanence of the ensemble, it also reduces the exchange length that communicates the magnetization information from grain to grain and changes the scale of the interaction domains. This result arises from the isotropic nature of the material with a perpendicular magnetization component at the grain peripheries that convey a reduced exchange length. This reduced exchange length is accompanied by a magnetization misalignment across the grain boundaries that pins domain walls at stray field inhomogeneities, creating smaller interaction domains by virtue of an increased density of domain wall pinning sites. It is thus seen that the grain alignment of a material has consequences not only on the coercivity and remanence, but upon the expected scale of the interaction domains as well.

## SUMMARY AND CONCLUSIONS

The three experimental scenarios previously described all consistently support the hypothesis that granular alignment in nanocrystalline materials is accompanied by an increased degree and extent of magnetic exchange coupling. The increase in the exchange coupling is attributed to an increase in the magnetic exchange length $L_{ex}^{0}$ as the interfacial perpendicular magnetization component is reduced. This increased magnetic exchange coupling increases the interaction domain size and suppresses the coercivity, although at the same time produces an exchange-enhanced remanence. An unavoidable conclusion is that high remanence and high coercivity seem to be mutually exclusive in nanocrystalline magnets.

It may, however, still be possible to engineer aligned nanocrystalline magnetic materials with a high remanence and a robust coercivity. The key to the optimal microstructure lies in the materials design, and associated processing, of the grain boundary the separates the constituent nanograins. It is necessary to keep the magnetic intergrain correlation length smaller than the exchange length $L_{ex}^{0}$ to avoid the formation of extended interaction domains that degrade the co-

ercivity. This may be accomplished with a non-magnetic grain boundary phase of dimensions on the order of the pertinent exchange length. At the same time grain alignment is necessary to provide a large remanence via alignment of moments with a small angular dispersion about a defined axis, but not necessarily from exchange enhancement. In bulk materials these design parameters might be satisfied by the addition of as-yet unidentified elements to the $Nd_2Fe_{14}B$ base composition that would serve to both lower the melting point of the eutectic liquid phase necessary for successful die-upsetting as well as render that phase non-magnetic. In any case the attainment of the truly optimal nanostructure that provides both high remanence and high coercivity in advanced permanent magnets is a challenging task..

## ACKNOWLEDGMENTS

Research performed at Brookhaven National Laboratory under the auspices of the U.S. Dept. of Energy, Division of Materials Sciences, Office of Basic Energy Sciences under contract No. DE-AC02-98CH10886.

## REFERENCES

[1]. C. D. Fuerst and E. G. Brewer, *J. Appl. Phys.* **73** (1993) 5751.
[2]. H. A. Davies, *J. Magn. Magn. Mater.* **157/158** 11 (1996).
[3]. E. C. Stoner and E. P. Wohlfarth, *Philos. Trans. Roy. Soc. London A* 240 (1948) 599.
[4]. E. J. Kondorsky, *J. Exp. Theor. Fiz.* **10** (1940) 420.
[5]. D. Givord and M. F. Rossignol, "Coercivity" Ch. 5 in Rare-earth Iron Permanent Magnets, J. M. D. Coey, Ed., Clarendon Press, Oxford (1996).
[6]. L. H. Lewis, T. R. Thurston, V. Panchanathan, U. Wildgruber and D. O. Welch, *J. Appl. Phys.* **82** (7) (1997) 3430.
[7]. H. Kronmüller and T. Schrefl, *J. Magn. Magn. Mater.*, **129** (1994) 66.
[8]. Gisclher Herzer, *Materials Science and Engineering* **A133** (1991) 1.
[9]. R. C. O'Handley, Modern Magnetic Materials, John Wiley & Sons, New York (2000) 294.
[10]. J. M. D. Coey, "Introduction" Ch. 1 in Rare-earth Iron Permanent Magnets, J. M. D. Coey, Ed., Clarendon Press, Oxford (1996).
[11]. D. C. Crew, L. H. Lewis and V. Panchanathan, *J. Magn. Magn. Mater.* **223** (3) (2001) 261.
[12]. D.C. Crew, L.H. Lewis and V. Panchanathan, *J. Magn. Magn. Mater.* in press.
[13]. D. C. Crew and L. H. Lewis, *IEEE Trans. Magn.* in press.
[14]. W.F. Brown, *Rev. Mod. Phys.* **17** (1945) 15.
[15]. A. Aharoni, *Rev. Mod. Phys.* **34** (1962) 227.
[16]. S. Hirosawa and Y. Tsubokawa, *J. Magn. Magn. Mater.* **84** (1990) 309.
[17]. R. Grossinger, X.K. Sun, R. Eibler, K.H.J. Buschow and H.R. Kirchmayr, *J. Magn. Magn. Mater.* **58** (1986) 55.
[18]. D. C. Crew, L. H. Lewis, D. O. Welch, V. Panchanathan, *J. Appl. Phys.* **87** (2000) 6571.
[19]. T. Schrefl, J. Fidler and H. Kronmüller, *Phys. Rev.* **B 49** (9) (1994) 6100.
[20]. M. K. Griffiths, J. E. L. Bishop, J. W. Tucker and H. A. Davies, *J. Magn. Magn. Mater.* **183** (1998) 49.
[21]. M. J. Donohue and D. G. Porter <URL: http://math.nist.gov/oommf/> version 1.1.
[22]. T. Schrefl, H. F. Schmidts, J. Fidler, H. Kronmüller, *J. Appl. Phys.* **73** (1993) 6510-6512.

Mat. Res. Soc. Symp. Proc. Vol. 703 © 2002 Materials Research Society T3.3

# Growth of Nanosize and Colloid Particles by Controlled Addition of Singlets

Vladimir Privman
Center for Advanced Materials Processing,
Clarkson University, Potsdam, NY 13699-5820, U.S.A.

## ABSTRACT

We outline a theoretical framework for estimating the evolution of the particle size distribution in colloid and nanoparticle synthesis, when the primary growth mode is by externally controlled addition of singlet building blocks. The master equations, analyzed in the leading "non-diffusive" expansion approximation, are reduced to a set of easily numerically programmable relations that yield information on the time evolution of the particle size distribution.

## INTRODUCTION

Recently, we have developed a theoretical model [1,2] that can describe semiquantitatively, without adjustable parameters, growth of monodispersed colloids by precipitation from homogeneous solutions [3-8]. It has been established [1-8] that most monodispersed colloids, i.e., particles of narrow size distribution, with sizes ranging from submicron to few microns, consist of crystalline subunits. The latter are formed as primary particles in a supersaturated solution by the burst-nucleation mechanism [1,9,10]. They then further grow and aggregate, primarily by the mechanism of singlet capture by growing aggregates. At the same time, the resulting aggregates rapidly restructure to form compact, frequently spherical, polycrystalline secondary particles, of density close to that of the bulk material and of narrow size distribution.

This two-stage growth mechanism is illustrated in Figure 1. Many important theoretical issues have remained unsolved or only partially addressed in the literature. These include, in particular, shape selection [11-13] and particle morphology properties. Another important open topic involves extensions to nanosize particles. Such particles of sizes less than colloid, from few tens to single nanometers, involve several new interesting challenges and paradigms related to nanotechnology.

Firstly, what do we mean by "monodispersed" on the nanoscale? It is quite likely that for most truly large-molecule-dimension nanotechnology applications, uniform size (and shape) really means "atomically identical." This is particularly true for future electronic devices that involve quantum effects or quantum control. For many other applications, requirements for uniformity will be also quite strict. Therefore, methods of controlling size and shape distribution, which found numerous applications for colloids, will be even more important for nanotechnology.

In this work, we outline an evaluation method of particle growth controlled by addition of singlet building blocks. We hope that these ideas will initiate the application of some of the techniques developed in colloid science to nanoparticle synthesis. Our results will be also of interest in interpreting growth, specifically after seeding, in colloidal synthesis.

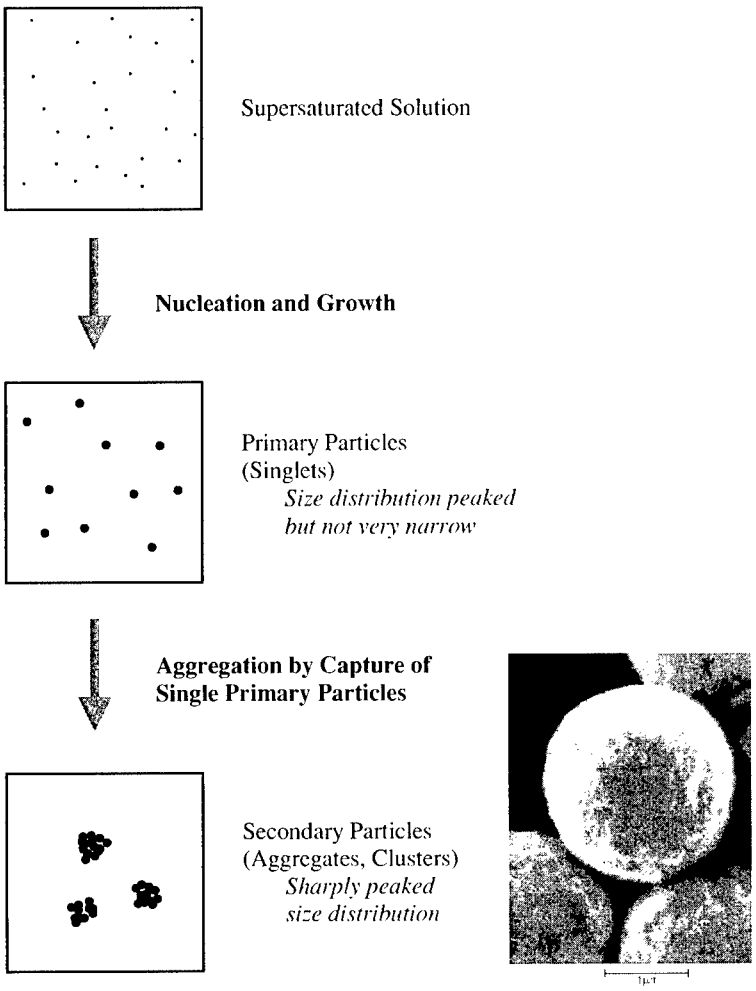


**Figure 1.** In colloid synthesis, initially, solutes are formed to yield a supersaturated solution, leading to nucleation. The formed nuclei may further grow by diffusive mechanism. The resulting primary particles (singlets) aggregate to form secondary particles. This latter process is sometimes facilitated by changes in the chemical conditions in the system: the ionic strength may increase, or the pH may change, causing the surface potential to approach the isoelectric point. Formation of the final (secondary) particles, of narrow size distribution, is a diffusion-controlled aggregation process, proceeding via the addition-polymerization type growth by irreversible capture of primary particles by the aggregates. At the same time, the aggregates also restructure into compact final particles, exemplified here by the SEM image of a gold colloid particle.

## GROWTH BY ADDITION OF SINGLETS

The singlet building blocks in nanoparticle synthesis in solution are atomic-size species (atoms, ions, molecules), whereas for colloid synthesis of the type described in Figure 1, they are the (nanosize) primary particles. Furthermore, in the process of Figure 1, the supply of singlets is "naturally" controlled by the features of their nucleation process. However, in principle the singlets can be added externally. In nearly any such process, the initial components are supplied over some interval of time. Their mixing in, must be fast enough to ensure uniform volume distribution. This represents an important practical chemical engineering problem.

In is therefore quite natural to consider the time dependence of the singlet addition, and its impact on the size distribution of the products. Specifically, for nanosize particle preparation, there has been recent interest in stepwise processes [14,15]: after achieving the initial particle distribution, batches of singlets are added to induce further growth.

Let $N_s(t)$ denote the volume density of particles, consisting of $s$ singlets, at time $t$. We are interested in the situation illustrated in Figure 2, when the particle size distribution evolves in time with a sharp peak eventually present at some rather large $s$ values. For convenience, let us denote the singlet concentration by

$$C(t) = N_1(t) \ . \tag{1}$$

The singlets can be supplied at the rate $\rho(t)$ per unit volume. They are consumed by the processes involving the production of the small clusters, in the "shoulder" in Figure 2. They are also consumed by the growing large clusters in the peak. There are two issues to consider in such growth: how is the peak created in the first place, and how to grow it without much broadening.

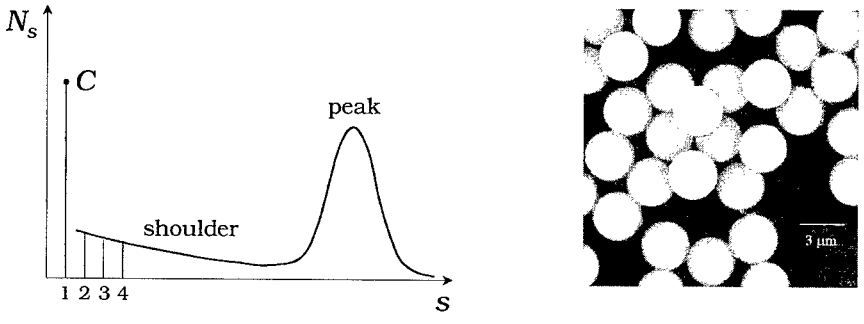


**Figure 2.** The expected form of the particle size distribution in uniform colloid or nanoparticle synthesis in solution. The peak at the large cluster sizes is growing at the expense of the supplied singlets, the concentration of which is controlled externally. The distribution for $s > 1$ can be usually assumed to be a smooth function of $s$, though the vertical bars at $s = 2,3,4$ emphasize that the $s$ values are actually discrete. The SEM image of cadmium sulfide colloid particles illustrates the attainable sharpness of the size distribution.

We will consider growth dominated by the irreversible capture of singlets by the larger growing aggregates. Thus, we use the rate equations, with $\Gamma_s$ denoting the rate constants for singlet capture by the $s \geq 1$ aggregates,

$$\frac{dN_s}{dt} = (\Gamma_{s-1}N_{s-1} - \Gamma_s N_s)C\,, \qquad s > 2\,, \tag{2}$$

$$\frac{dN_2}{dt} = (\frac{1}{2}\Gamma_1 C - \Gamma_2 N_2)C\,, \tag{3}$$

where $C = N_1$, as defined in (1), and

$$\frac{dC}{dt} = \rho - \sum_{s=2}^{\infty} s\frac{dN_s}{dt} = \rho - \Gamma_1 C^2 - C\sum_{s=2}^{\infty}\Gamma_s N_s\,. \tag{4}$$

Let us point out that the assumption that the *only* process involving the $s > 1$ aggregates is that of capturing singlets at the rate proportional to the concentration of the latter, $\Gamma_s C$, is drastic but commonly used in the colloid literature, e.g., [1,2,12,16-18]. In fact, more complex processes, such as cluster-cluster aggregation [19,20], detachment [21] and exchange of singlets (ripening), etc., also contribute to particle growth. However, in uniform colloid synthesis they are typically much slower than the singlet-consumption growth. In addition, they broaden the particle size distribution.

Another important approximation involved in writing the relations (2)-(4) is that of ignoring particle shape distribution and their morphology. We avoid this issue, which is not well understood, by assuming that the growing aggregates rapidly restructure into compact bulk-like particles, of an approximately fixed shape, typically, but not always, spherical. This has been experimentally observed in uniform colloid particle synthesis [1,3-8]. Without such restructuring, the aggregates would be fractal [20-22].

For nanosize particle synthesis, the only assumption in the above summary that can be questioned is that of ignoring singlet detachment for the particles in the shoulder in Figure 2. Indeed, unlike colloid growth, which is fast and irreversible for all $s$ in such synthesis processes, the nanosize particle growth will be typically held back by a nucleation barrier [1,14]. During the late stage growth, that follows the initial nucleation burst [9,10], the barrier can be quite high. The distribution in the shoulder will approach the equilibrium Boltzmann form, governed by the excess free energy of the aggregate formation. It is interesting to note that this fast equilibration means that the singlets "stored" in the small, "shoulder" aggregates will be released and available for consumption by larger aggregates in the peak, provided the latter indeed primarily feed on "free" singlets.

If the singlets are supplied constantly, then the distribution, both for colloids and nanoparticles, will develop a large shoulder at small aggregates, with no pronounced peak at $s >> 1$. If the supply is limited, then only small aggregates will be formed. An interesting recent observation in studies of colloid synthesis [1,2] has been that there exist "protocols" of singlet supply, at the rate $\rho(t)$ which is a slowly decaying, sometimes rather complicated function of

time, that yield peaked size distributions at large times. Furthermore, the primary process summarized in Figure 1, naturally "feeds" the secondary process just at a rate like this.

For nanoparticle synthesis, the main mechanism of the early formation of the peak is by burst nucleation, when nuclei of sizes larger than the critical size form by growing over the nucleation barrier. Of course, *seeding* is another way of initiating the peaked size distribution both for colloid and nanosize growth.

## GROWTH OF THE PEAKED SIZE DISTRIBUTION

Solution of the rate (master) equations (2)-(4) requires numerical approaches and is not particularly illuminating as to the nature of the particle growth. Therefore, we will introduce several additional assumptions which will allow us to go a long way in simplifying the problems in closed analytical form. The main idea is that, once the peak is formed after some transient time or by seeding, the particles in the peak are the main consumers of the available singlets.

This assumes that the singlet concentration is controlled by adding them externally [14,15]. For nanoparticle growth, the addition is at such a rate that the nucleation barrier remains high. The shoulder will then adjust to assume an approximately equilibrium shape, but the production of new larger, supercritical aggregates will be negligible. For colloid growth, the shoulder will also evolve, and new larger particles will be generated. However, if the number of larger aggregates is already significant, they will dominate the consumption of singlets.

Thus, to prevent generation of new small aggregates, we put

$$\Gamma_1 = 0, \tag{5}$$

which is an approximation. Furthermore, we will assume that $s$ is a continuous variable, since we are interested in $s >> 1$, and that $s$ varies in the range

$$0 \le s < \infty. \tag{6}$$

For calculations assuming singlet transport by diffusion, one can take the large $s$ Smoluchowski expression for the rates [21,23],

$$\Gamma_{s>>1} = As^{1/3}, \tag{7}$$

where $A$ is a known constant. Note that $\Gamma_{s>>1}$ is proportional to the aggregate linear dimension (which includes the factor $s^{1/3}$) and singlet diffusion constant. Our results apply for general $\Gamma_s$.

Our last approximation is introduced in writing the continuous $s$ form of the master equations (2). We retain only the leading $s$ derivative, ignoring the "diffusive" second-derivative term (and higher-order terms). The consequences of this approximation, already used in the literature, e.g., [12], will be discussed later. Thus, we replace (2) by

$$\frac{\partial N(s,t)}{\partial t} = -C(t)\frac{\partial}{\partial s}\left[\Gamma(s)N(s,t)\right], \tag{8}$$

with (4) replaced by

$$\frac{dC(t)}{dt} = \rho(t) - C(t)\int_0^\infty ds\left[\Gamma(s)N(s,t)\right]. \tag{9}$$

Let us now define the variable [1,16,18]

$$\tau(t) = \int_0^t dt' C(t') \geq 0, \tag{10}$$

and then introduce the function $u(s,\tau)$ via the relation

$$\tau = \int_u^s \frac{ds'}{\Gamma(s')}. \tag{11}$$

We point out that usually $\Gamma(s) > 0$, and the lower limit of integration can be taken to zero. The asymptotic rate expression (7) does vanish at $s = 0$ because of our cavalier treatment of the small $s$ behavior. However, the integral happens to converge, so no additional care is needed. We can safely define the quantity $s_{\min}(\tau)$ via

$$\tau = \int_0^{s_{\min}} \frac{ds'}{\Gamma(s')}. \tag{12}$$

As $u$ is increased from zero to infinity, the corresponding $s(u,\tau)$, for fixed $\tau$, increases from $s_{\min}(\tau)$ to infinity.

Next, we notice that the relation between the differentials implied by (11), namely,

$$d\tau = \frac{ds}{\Gamma(s)} - \frac{du}{\Gamma(u)}, \tag{13}$$

allows us to calculate various partial derivatives in terms of $\Gamma(s)$ and $\Gamma(u) = \Gamma\left(u\left(s,\tau(t)\right)\right)$. This, in turn, allows one to verify, by a cumbersome calculation not reproduced here, that (8) is solved by

$$N(s,t) = \frac{\Gamma\left(u\left(s,\tau(t)\right)\right)}{\Gamma(s)} N\left(u\left(s,\tau(t)\right),0\right), \qquad s \geq s_{\min}\left(\tau(t)\right), \tag{14}$$

$$N(s,t) = 0, \qquad 0 \leq s \leq s_{\min}\left(\tau(t)\right), \tag{15}$$

where the discontinuity at $s_{\min}(\tau(t))$ is possible if the initial distribution at time zero, $N(s,0)$, is nonzero at $s=0$. Actually, within the present approximation of ignoring the effects of the details of the size distribution for small $s$, we could as well require that $N(0,0)=0$.

Let us summarize the above observations by emphasizing that we consider a particle size distribution which at time $t=0$ already has a well-developed significant peak at large cluster sizes. Relations (14)-(15) will provide an approximate description of the evolution of this peak with time, owing to supply of singlets at the rate $\rho(t)$. The form of the distribution at small particle sizes plays no role in the derivation.

In fact, neglecting the second-derivative in $s$, "diffusive" term in writing (8), leads to certain artificial conclusions. Specifically, sharp features and discontinuities of the initial distribution (as well as its derivatives, etc.) will not be smoothed out. The fact that the initial distribution is only meaningful for $s \geq 0$ translates into the sharp cutoff at $s_{\min}$ for times $t>0$. Had we included the diffusive term, the distribution would extend smoothly to $s=0$ for all times. However, no analytical solution (14)-(15) would be available.

While this lack of smoothness is probably not important for a semiquantitative evaluation of the size distribution, one aspect should be emphasized as critical: if the initial distribution is already very sharp, then the neglect of the diffusive term in our expressions may result in underestimating the *width* of the evolving peak.

To complete the description of the particle size distribution within the non-diffusive approximation, we have to discuss the estimation of the function $\tau(t)$. This is taken up in the next section, where we also further mention the matter of the non-diffusive approximation.

## EVALUATION OF THE PEAKED PARTICLE SIZE DISTRIBUTION

Relations (9)-(10) can be rewritten, using (14), as a system of coupled differential equations for two unknown functions $\tau(t)$ and $C(t)$, with $\tau(0)=0$, and $C(0)$ externally controlled,

$$\frac{d\tau}{dt} = C(t), \tag{16}$$

$$\frac{dC}{dt} = \rho(t) - C(t)F(\tau), \tag{17}$$

where

$$F(\tau) = \int_{s_{\min}(\tau)}^{\infty} ds\left[\Gamma\left(u(s,\tau)\right)N\left(u(s,\tau),0\right)\right]. \tag{18}$$

These equations are easily programmed for numerical evaluation, especially if the function $F(\tau)$ is calculable analytically, so that numerical integration can be avoided. The latter is likely for the power-law rate in (7), provided the initial distribution $N(s,0)$ is not too complicated.

Within the approximation developed here, the number of particles larger than singlet, $M$, obviously remains constant,

$$M = \int_{s_{\min}(t)}^{\infty} dsN(s,t) = \int_{0}^{\infty} dsN(s,0). \tag{19}$$

The change in the average size of the particles larger than singlet,

$$\langle s \rangle_t = \frac{1}{M} \int_{s_{\min}(t)}^{\infty} ds[sN(s,t)], \tag{20}$$

can be evaluated directly from $C(t)$,

$$\langle s \rangle_t = \langle s \rangle_0 + \frac{1}{M}[C(0) - C(t) + \int_0^t dt' \rho(t')]. \tag{21}$$

Furthermore, consideration of the increment relations following from (13), suggests that the width of the peak, $W_t$, grows according to

$$W_t \approx \frac{\Gamma(\langle s \rangle_0)}{\Gamma(u(\langle s \rangle_0, \tau(t)))} W_0 > W_0. \tag{22}$$

The inequality follows from the definition (11), assuming that for large $s$, $\Gamma(s)$ is an increasing (positive) function. This excludes an important case of constant $\Gamma$, appropriate for certain models of polymerization. In this case, however, the discrete equations (2)-(4) can be analyzed directly in great detail [16,18], so that the present formulation is not needed.

In connection with (22), the reader must be cautioned that additional broadening will result from the second-derivative "diffusive" term neglected in our continuous $s$ equations. The model with the diffusive term included, requires serious numerical efforts, as does the original, discrete $s$ model [1,2].

In summary, with the reservations regarding the width estimates, numerical calculation of the functions $\tau(t)$ and $C(t)$, via (16)-(18), goes a long way in estimating various properties of the growing, peaked particle size distribution. Results and applications, specifically for the case of the Smoluchowski rate (7), and comparison with large-scale simulation results of the discrete $s$ equations of the type (2)-(4), will be reported in forthcoming publications.

Even at the level of the approximation (22), it is obvious that the size distribution never actually narrows in absolute terms. All the experimentally realized monodispersed particle synthesis procedures in solution, investigated thus far primarily in the colloid domain, actually yield small *relative* peak width, $W_t/\langle s \rangle_t$, by utilizing fast increase in $\langle s \rangle_t$ via consumption of singlets, on the time scales short for the "diffusive" broadening to set in.

## ACKNOWLEDGEMENTS

The author gratefully acknowledges helpful discussions and collaboration with M. Lawrence Glasser, Dan Goia, Sergiy Libert, Egon Matijevic, Dima Mozyrsky, Jongsoon Park and Yitzhak Shnidman. This research has been supported by the National Science Foundation (grant DMR-0102644) and by the Donors of the Petroleum Research Fund, administered by the American Chemical Society (grant 37013-AC5,9).

## REFERENCES

1. V. Privman, D. V. Goia, J. Park and E. Matijevic, *J. Colloid Interf. Sci.* **213**, 36 (1999).
2. J. Park, V. Privman and E. Matijevic, accepted for publication in *J. Phys. Chem.* **B**, online preprint: http://arxiv.org/ftp/cond-mat/papers/0102/0102079.pdf, online journal draft http://pubs.acs.org/isubscribe/journals/jpcbfk/asap/pdf/jp011306a.pdf (2001).
3. E. Matijevic, *Ann. Rev. Mater. Sci.* **15**, 483 (1985).
4. M. Haruta and B. Delmon, *J. Chim. Phys.* **83**, 859 (1986).
5. T. Sugimoto, *Adv. Colloid Interf. Sci.* **28**, 65 (1987).
6. T. Sugimoto, *J. Colloid Interf. Sci.* **150**, 208 (1992).
7. E. Matijevic, *Langmuir* **10**, 8 (1994).
8. D. V. Goia and E. Matijevic, *Colloids Surf.* **146**, 139 (1999).
9. V. K. LaMer and R. H. Dinegar, *J. Amer. Chem. Soc.* **72**, 4847 (1950).
10. V. K. LaMer, *Ind. Eng. Chem.* **44**, 1270 (1952).
11. J. A. Dirksen and T. A. Ring, *Chem. Eng. Sci.* **46**, 2389 (1991).
12. J. A. Dirksen, S. Benjelloun and T. A. Ring, *Colloid Polym. Sci.* **268**, 864 (1990).
13. T. A. Ring, T. A., *Powder Technol.* **65**, 195 (1991).
14. G. Schmid, *Chem. Rev.* **92**, 1709 (1992).
15. T. Teranishi, M. Hosoe, T. Tanaka and M. Miyake, *J. Phys. Chem.* **103**, 3818 (1999).
16. P. G. J. van Dongen and M. H. Ernst, *J. Statist. Phys.* **37**, 301 (1984).
17. A. D. Randolph and M. A. Larson, *Theory of Particulate Processes* (Academic Press, San Diego, 1988).
18. N. V. Brilliantov and P. L. Krapivsky, *J. Phys.* **A24**, 4787 (1991).
19. J. Krug and H. Spohn, in *Solids Far from Equilibrium*, edited by C. Godreche (Cambridge University Press, 1991).
20. F. Family and T. Vicsek, *Dynamics of Fractal Surfaces* (World Scientific, Singapore, 1991).
21. D. Mozyrsky and V. Privman, *J. Chem. Phys.* **110**, 9254 (1999).
22. D. W. Schaefer, J. E. Martin, P. Wiltzius and D. S. Cannell, *Phys. Rev. Lett.* **52**, 2371 (1984).
23. G. H. Weiss, *J. Statist. Phys.* **42**, 3 (1986).

# AUTHOR INDEX


Akimov, B.A., 349
Allen, C. W., 463
Anderson, W.A., 393
Anikeeva, Olga B., 259
Arantes, Vera L., 159
Arregui, Eduardo Ogando, 271

Bai, G.-R., 179
Baker, C., 193
Barakat, I., 83
Barboux, P., 497
Bauer, Hans-Dietrich, 199
Baughman, R.H., 369, 517
Beaty, K.S., 331, 413
Becker, M.F., 209
Belomoin, G., 475
Beloshapkin, S.A., 529
Bessais, L., 135
Besser, R.S., 297
Bhandarkar, Suhas, 147
Bhattacharya, V., 535
Birtcher, R. C., 463
Black, M.R., 439
Boatner, L.A., 331, 413
Boilot, J.-P., 497
Borca-Tasciuc, Diana-Andra, 65
Borshchevsky, Alexander, 65
Botton, G.A., 407
Boulova, M.N., 349
Bradley, John, 33
Braidy, N., 407
Bright, David S., 249
Broadwater, S. T., 421
Brotzman, R. W., 317
Browning, N.D., 489
Budnick, J.I., 19, 111, 237
Bulusheva, Lyubov G., 381
Burgard, Detlef, 185
Burghard, Marko, 505
Burns, Andrew, 193
Butenko, Yuriy V., 259, 381
Byrne, H.J., 517

Calderon, H. A., 223
Campbell, Sandi, 215
Cappellini, Giancarlo, 93
Caro, Alfredo, 271
Caro, Magdalena, 271
Carrière, D., 497
Casula, Francesco, 93
Cayton, Roger H., 317
Chaieb, S., 475
Chambers, G., 517
Chan, W.-B., 427
Chang, Ko-wei, 129
Chao, Kuei Jung, 541
Chareev, D.A., 349
Chattopadhyay, K., 535
Chen, Chenggang, 3
Chen, Gang, 65
Chen, George Z., 553
Chen, Kang Hung, 547
Chen, Liang-Yih, 129
Choy, Jin-Ho, 453, 559
Chuvilin, Andrew L., 259, 381
Cornett, K., 223
Crew, David C., 565
Cronin, S.B., 439
Cummins, E., 517
Curliss, David, 3

Dahmen, U., 463
Dalton, A.B, 517
Dean, C. J., 421
Derevyankin, A.Ya., 529
Dickey, Elizabeth C., 123
Djega-Mariadassou, C., 135
Dobley, Arthur, 323
Dong, C., 259
Donnelly, S. E., 463
Doorn, Arie van, 185
Doronin, V.P., 529
Douglas, Elliot P., 43
Dresselhaus, Mildred S., 65, 439
Du, Henry, 147
Dunn, Matthew F., 291

Eastman, J.A., 179
Eckert, Jürgen, 199
El Khakani, M.A., 407

Emekalam, A., 399
Esquivel-Sirvent, Raúl, 99

Farrell, G.F., 517
Fattakhova, Dina, 165
Fenelonov, V.B., 529
Feng, Zhechuan, 59
Feresenbet, E., 399
Fink, Y., 439
Fleurial, Jean-Pierre, 65
Franck, J.P., 331
Fray, Derek J., 553
Furuya, K., 463
Furuya, Yasubumi, 265

Gaskov, A.M., 349
Ge, Shihui, 19, 111, 237
Ghan, R.C., 297
Goldberg, Eugene P., 33
Grandfils, C., 83
Granqvist, Claes-Göran, 185
Gromek, J. M., 111
Gupta, Gaurav K., 469
Gupta, S., 481

Hahn, Horst, 173
He, Peng, 277
Heggie, Malcolm I., 381
Heinemann, André, 199
Henderson, Don O., 159
Hepel, M., 427
Hermann, Helmut, 199
Hines, W.A., 19, 111, 237
Hirao, Kazuyuki, 523
Hoel, Anders, 185
Holmes, G., 399
Honda, S., 331
Hong, Franklin Chau-Nan, 129
Huerta, A., 223
Hughes, Mark, 553
Hui, S., 19, 237
Hultåker, Annette, 185
Hwang, Sung-Ho, 559

Inceoglu, A. Baran, 387
in het Panhuis, M., 517

Ito, Y., 489

Janssen, G.C.A.M., 153
Janzen, Christian, 173
Jeong, Yong-Joo, 559
Jérôme, R., 83
Jeung, J-H., 393
Johnson, Jr., David W., 147
Jongerius, Michel J., 185

Kaddouri, H., 445
Kalia, Rajiv K., 117
Kamminga, J.-D., 153
Kanatzidis, Mercouri G., 433
Karakhanyan, R.K., 511
Kaski, Kimmo, 231
Keto, J.W., 209
Kim, Deok-Yang, 147
Kim, Gyu-Tae, 505
Kimura, K., 375
King, Alexander H., 343, 469
Kityk, I.V., 445
Klemmer, Timothy J., 105
Kochubei, D.I., 529
Kolomiichuk, V.N., 529
Konin, G.A., 529
Krtil, Petr, 165
Kubota, Takeshi, 265
Kühn, Uta, 199
Kumar, D., 355
Kuroda, Kazuyuki, 71
Kuronen, Antti, 231
Kuznetsov, Vladimir L., 259, 381
Kuznetsova, T.G., 529
Kvit, A., 355
Kwak, Seo-Young, 559

Lalanne, V., 135
Lam, M., 413
Lamparth, I., 303
Lebon, F., 83
Lee, Hak-Gue, 393
Lee, In-Kyum, 173
Lei, Y., 489
Lewis, Laura H., 565
Li, W., 193

Lian, Guoda, 123
Lian, Jie, 277
Lin, Jianyi, 59
Lin, Y.M., 439
Lin, Yueh, 283
Lin, Yu-Ming, 65
Lindackers, Dirk, 173
Liu, Sai-Chang, 49, 129
Livingston, Thurston, 159
Lopasso, Edmundo M., 271
Lou, Y., 427
Lu, Chung-Hsin, 283
Lu, Gao Q., 9, 25
Luo, J., 427
Lutta, Samuel T., 323
Lvov, Y., 297
Ly, N. K., 427

Malkhasyan, R.T., 511
Malyavanatham, G., 209
Maskaly, K.R., 439
Mattern, Norbert, 199
Matyshak, V.A., 529
Maye, M.M., 427
Mazanec, T.J., 489
McNamara, M., 517
Meldrum, A., 331, 413
Mishra, Sanjay R., 363
Mitas, L., 475
Moreau, M., 497
Morell, G., 481
Moroz, E.M., 529
Mu, Richard R., 159
Muster, Jörg, 505

Nair, Balakrishnan G., 337
Naito, Takashi, 523
Nakano, Aiichiro, 117
Narayan, J., 355
Nayfeh, M.H., 475
Nazaryan, M.N., 511
Ngala, Katana, 323
Ni, Y., 259
Nichols, W.T., 209
Noguez, Cecilia, 99
Novgorodov, B.N., 529

O'Brien, D.T., 209
Ogino, T., 141
Okazaki, Teiko, 265
Okotrub, Alexander V., 259, 381

Padi, M., 439
Park, Jong-Sang, 559
Park, Seung Bin, 255
Paukshtis, E.A., 529
Percheron-Guégan, A., 135
Petrykin, Valery, 165
Phillip, E., 427
Plucinski, K.J., 445
Popovic, Zoran, 59
Prabhakaran, K., 141
Privman, Vladimir, 577

Rabin, Oded, 65, 439
Raghavan, D., 399
Rangan, Krishnaswamy K., 433
Rao, S., 475
Rim, Ji Youn, 255
Romanenko, Anatoliy I., 259
Ross, J.R.H., 529
Roth, Paul, 173
Roth, Siegmar, 505
Rountree, Cindy L., 117
Rumyntseva, M.N., 349
Ryabova, L.I., 349
Ryan, Margaret A., 65

Sadykov, V.A., 529
Saiz, E., 291
Sartore, L., 83
Sato, Mitsutaka, 265
Sato, S., 375
Satta, Guido, 93
Saunders, Vanessa, 159
Scheiman, Daniel, 215
Scott, J. L., 421
Shaffer, Milo S.P., 553
Shafi, K.V.P.M., 141
Shah, S.I., 193
Sharma, Shashank, 123
Shi, Donglu, 277
Shimojima, Atsushi, 71

Slamovich, Elliott B., 343
Sloof, W.G.M., 153
Smith, A., 475
Song, M., 463
Song, Shin Ae, 255
Song, Yanning, 309
Sorge, K., 331
Sorokina, T.P., 529
Southward, Robin E., 421
Sunkara, Mahendra K., 123
Szabó, D.V., 303

Tadd, Erica H., 33
Tannenbaum, Rina, 33
Teng, Lihong, 393
Therrien, J., 475
Thompson, D. W., 421
Thompson, J. R., 331
Thompson, L.J., 179
Tomsia, Antoni P., 291
Trikalitis, Pantelis N., 433
Troiani, H.E., 19, 111, 237
Tsai, A. P., 535
Turner, Shirley, 249
Twesten, R., 475

Ueda, Akira, 159
Ulman, A., 141
Umemoto, M., 223

Vaia, Richard A., 243
Van Brutzel, Laurent, 117
van Ooij, Wim J., 277
Vashishta, Priya, 117
Vasiliu, Elena, 243
Viano, Ann M., 363
Villarreal, Carlos, 99
Vittal, Jagadese J., 59
Vollath, D., 303
von Alfthan, Sebastian, 231

Wagner, L., 475
Wang, Chyi-Shan, 243
Wang, Hsien-Cheng, 283
Wang, L. M., 277
Weiner, B. R., 481
Wen, Ming-Chang, 283
White, C.W., 413, 331
Whittingham, M. Stanley, 309, 323
Wiedenmann, Albrecht, 199
Wiezorek, Jörg M.K., 105
Wiley, J.B., 369
Windle, Alan H., 553
Winterer, Markus, 173
Wise, Adam T., 105
Wu, Jih-Jen, 49, 129
Wu, Marvin H., 159
Wu, Mingzhong, 19, 111, 237
Wuttig, Manfred, 265

Xiao, T.D., 19, 111, 237, 291
Xu, Gu, 59
Xu, Huiping, 105
Xu, L., 369

Yacaman, M.J., 19, 111, 237
Yamamoto, Hiroki, 523
Yamamoto, N., 375
Yang, Chia Min, 541
Yang, Ho-Soon, 179
Yang, Shoufeng, 309, 323
Yang, Sze Ming, 547
Yao, H., 375
Ye, Zhiyuan, 343
Yebassa, D., 399
Yilmazer, Ulku, 387

Zakhidov, A.A., 369
Zavalij, Peter Y., 309, 323
Zhang, J., 135
Zhang, Y.D., 19, 111, 237
Zhang, Zongtao, 111, 291
Zhao, Hanying, 43
Zhong, C.J., 427
Zhou, Honghui, 355
Zhou, W.L., 369
Zhu, Huai Y., 9, 25
Zuhr, R.A., 331, 413
Zyuzin, D.A., 529

# SUBJECT INDEX


alumina, 65
  nanofibers, 25
amorphous, 511
  materials, 231
a-Si, 393

band energy and molecular dynamics
  simulations, 445
bismuth, 65
block co-polymers, 33

carbon, 93
  coating, 309
  nanotube(s), 407
    -polypyrrole composites, 553
Casimir forces, 99
catalysis, 427
CdS nanoparticles, 43
ceramic, 337
clay, 399
coated nanoparticles, 303
coating, 277
cobalt nanoclusters, 33
coercivity, 135, 565
colloid, 577
$Co_3O_4$ thin film, 523
copper aluminium oxide, 255
cyclodextrin, 517

damage effects, 271
DFT-LDA simulations, 93

ECR-CVD deposition, 393
EELS, 489
electrodeposition, 369
energy, 469
epoxy, 547

$Fe_2O_3$ nanoparticles, 141
ferromagnetic shape memory alloy, 265

$Ga_2O_3$ nanowires, 129
gasphase process, 173
$GdCeO_{2-x}$, 489
gene and drug delivery carrier, 559
gold, 159, 375
graphite/diamond nanocomposites, 259

hardness, 153
HFCVD, 481

high
  frequency, 111
  resolution x-ray diffraction, 59
highly oriented, 49
hydrothermal, 165
  processing, 343

inorganic-
  biomolecular nanohybrid, 559
  organic hybrid, 71
ion
  exchange, cross-links, 277
  implantation, 331
iron(-)
  nitride, 363
  palladium, 105
irradiation, 413

large scale, 129
laser ablation, 209
layered silicates, 243
lead titanate, 343
lithium manganese oxide, 283

magnetic
  nanocomposites, 331
  properties, 223
magnetostriction, 265
mesoporous silica, 541
mesostructured, 433
metal, 541
  oxide, 9
microfabrication, 337
molecular dynamics, 117
monodispersed, 577
montmorillonite, 387, 547
morphology, 3

nanocomposite(s), 3, 9, 19, 111, 215, 223,
  237, 309, 349, 363, 387, 399
nanocrystalline, 565
  alumina, 317
nanocrystals, 209, 413
nano-cylinder structure, 59
nanohybrid, 453
nanomaterials, 135
nanoparticle(s), 185, 277, 317, 427, 475, 577
nanoscale structure, 199
nanosize, 511
nanowires, 123, 159, 439

nc-Si, 393
Nd-Fe-B, 565
nickel(-), 355
  iron, 19
  membrane, 369
nonlinear optical property, 523

onion-like carbon, 259, 381
optical absorption, 439
oxides, 303

photocatalysis, 193
plasma, 277
polyacrylamide, 83
polyamidoamine, 83
polyimide, 215, 421
polymer, 277
  nanocomposites, 243
porous silica, 147
proton conductivity, 497
pulsed laser deposition, 355

Raman spectroscopy, 407
reverse-micelle process, 283
rutile, 249

salt-induced micelles, 43
samarium, cobalt, 135
Schottky diode, 505
self-assembly, 297, 375
self-organization, 71
semiconductor(s), 123, 433
SiCON nanocrystallites, 445
silica, 117
silicon, 141, 475
  carbide, nanoparticles, 173
silver, 421
single-walled nanotubes, 517
small-angle neutron scattering, 199
soft magnetic material, 237
solid solutions, 271
spinel, 165
stress, 153
sulfur-incorporated nanocrystalline
  carbon, 481
supercapacitors, 553
superconducting film, 453
surface tension, 463
surfactant directed oriented growth, 25
synthesis, pillaring solutions, 529

tetramethyl ammonium silicate, 147
thermal
  conduction, 231
  stability, 349
  transport, 179
tin
  doped indium oxide, 185
  oxide, 297
titania, 193
transmission electron microscopy, 105, 249
transparent conducting oxide, 255
triple junction, 469

vanadium oxide(s), 99
  nanofiber, 505
  nanotubes, 323

Xe in Al, 463
x-ray emission spectroscopy, 381

yttria-stabilized zirconia, 179

zirconia, 497
  nanopillars, clays, 529
ZnO nanorods, 49